ISSN 2095-8137
CN 53-1229/Q
Volume 45 Issue 4
18 July 2024

# ZR

# Zoological Research



CODEN: DOYADI
www.zoores.ac.cn
Science Press

# ZOOLOGICAL RESEARCH

**Volume 45, Issue 4 18 July 2024**

## CONTENTS

Mitogenomic phylogeny, biogeography, and cryptic divergence of the genus *Silurus* (Siluriformes: Siluridae) ····· *Weitao Chen*, *Nicolas Hubert*, *Yuefei Li*, *Shuli Zhu*, *Jun Wang*, *Denggao Xiang*, *Shang Gao*, *Chunni Kou*, *Jilong Wang*, *Tai Wang*, *Zhiqiang Liang*, *Junjie Wu*, *Xinhui Li*, *Jie Li* ( 711 )

Skeletal phenotypes and molecular mechanisms in aging mice ····· *Qiao Guan*, *Yuan Zhang*, *Zhi-Kun Wang*, *Xiao-Hua Liu*, *Jun Zou*, *Ling-Li Zhang* ( 724 )

Immunobiology of COVID-19: Mechanistic and therapeutic insights from animal models ····· *Hong-Yi Zheng*, *Tian-Zhang Song*, *Yong-Tang Zheng* ( 747 )

A new era of mutation rate analyses: Concepts and methods ····· *Kun Wu*, *Danqi Qin*, *Yang Qian*, *Haoxuan Liu* ( 767 )

Engineered AAV13 variants with enhanced transduction and confined spread ····· *Neng-Song Luo*, *Yu-Xiang Cai*, *Zeng-Peng Han*, *Xiao-Kai Sui*, *Wen-Jia Yuan*, *Zi-Lian Zhang*, *Hao-Dong Guo*, *Jie Wang*, *Kun-Zhang Lin*, *Fu-Qiang Xu* ( 781 )

Metabolomic-based analysis reveals bile acid-mediated ovarian failure induced by low temperature in zebrafish ····· *Wen-Hao Li*, *Zhi-Qiang Li*, *Meng-Di Bu*, *Jia-Zhen Li*, *Liang-Biao Chen* ( 791 )

Microplastic exposure disturbs sleep structure, reduces lifespan, and decreases ovary size in *Drosophila melanogaster* ····· *Wei Yan*, *Zi-Jie Li*, *Zi-Yi Lin*, *Shu-Qin Ji*, *William Ka Fai Tse*, *Zhi-Qiang Meng*, *Chang Liu*, *Lei Li* ( 805 )

On the evolutionary trail of MagRs ····· *Jing Zhang*, *Yafei Chang*, *Peng Zhang*, *Yanqi Zhang*, *Mengke Wei*, *Chenyang Han*, *Shun Wang*, *Hui-Meng Lu*, *Tiantian Cai*, *Can Xie* ( 821 )

Proteins as nanomagnets and magnetoreceptors ····· *P. J. Hore* ( 831 )

Genetically modified pigs with CD163 point mutation are resistant to HP-PRRSV infection ····· *Ying Liu*, *Lin Yang*, *Hong-Yong Xiang*, *Ming Niu*, *Jia-Cheng Deng*, *Xue-Yuan Li*, *Wen-Jie Hao*, *Hong-Sheng Ou-Yang*, *Tong-Yu Liu*, *Xiao-Chun Tang*, *Da-Xin Pang*, *Hong-Ming Yuan* ( 833 )

SIL1 improves cognitive impairment in APP23/PS45 mice by regulating amyloid precursor protein processing and Aβ generation ····· *Qunxian Wang*, *Yanshuang Jiang*, *Zijun Meng*, *Xiangjun Dong*, *Dongjie Hu*, *Liangye Ji*, *Weihui Zhou*, *Weihong Song* ( 845 )

NLRP3-mediated autophagy dysfunction links gut microbiota dysbiosis to tau pathology in chronic sleep deprivation ····· *Na Zhao*, *Xiu Chen*, *Qiu-Gu Chen*, *Xue-Ting Liu*, *Fan Geng*, *Meng-Meng Zhu*, *Fu-Ling Yan*, *Zhi-Jun Zhang*, *Qing-Guo Ren* ( 857 )

Targeting synaptic pathology in Alzheimer's disease ····· *Jing Cao*, *Yun-Wu Zhang* ( 875 )

Study of tree shrew biology and models: A booming and prosperous field for biomedical research ····· *Yong-Gang Yao*, *Li Lu*, *Rong-Jun Ni*, *Rui Bi*, *Ceshi Chen*, *Jia-Qi Chen*, *Eberhard Fuchs*, *Marina Gorbatyuk*, *Hao Lei*, *Hongli Li*, *Chunyu Liu*, *Long-Bao Lv*, *Kyoko Tsukiyama-Kohara*, *Michinori Kohara*, *Claudia Perez-Cruz*, *Gregor Rainer*, *Bao-Ci Shan*, *Fang Shen*, *An-Zhou Tang*, *Jing Wang*, *Wei Xia*, *Xueshan Xia*, *Ling Xu*, *Dandan Yu*, *Feng Zhang*, *Ping Zheng*, *Yong-Tang Zheng*, *Jumin Zhou*, *Jiang-Ning Zhou* ( 877 )

Updated roles of the gut microbiota in exploring shrimp etiology, polymicrobial pathogens, and disease incidence ····· *Jin-Bo Xiong*, *Hao-Nan Sha*, *Jiong Chen* ( 910 )

Rotating magnetic field inhibits Aβ protein aggregation and alleviates cognitive impairment in Alzheimer's disease mice ····· *Ruo-Wen Guo*, *Wen-Jing Xie*, *Biao Yu*, *Chao Song*, *Xin-Miao Ji*, *Xin-Yu Wang*, *Mei Zhang*, *Xin Zhang* ( 924 )

TAX1BP1 and FIP200 orchestrate non-canonical autophagy of p62 aggregates for mouse neural stem cell maintenance ····· *Yi-Fu Zhu*, *Rong-Hua Yu*, *Shuai Zhou*, *Pei-Pei Tang*, *Rui Zhang*, *Yu-Xin Wu*, *Ran Xu*, *Jia-Ming Wei*, *Ying-Ying Wang*, *Jia-Li Zhang*, *Meng-Ke Li*, *Xiao-Jing Shi*, *Yu-Wei Zhang*, *Guang-Zhi Liu*, *Rick F. Thorne*, *Xu Dong Zhang*, *Mian Wu*, *Song Chen* ( 937 )

Tumor necrosis factor α deficiency promotes myogenesis and muscle regeneration ····· *Yu Fu*, *Jing-Ru Nie*, *Peng Shang*, *Bo Zhang*, *Da-Wei Yan*, *Xin Hao*, *Hao Zhang* ( 951 )

**Cover Image:** Illustration of systemic health risks from microplastic pollutant exposure using *Drosophila melanogaster* as a model

**Cover design:** Lei Li, Li-Bin Wu, Chang Liu, BioRender

Chen et al. *Zool. Res.* 2024, 45(4): 711−723
https://doi.org/10.24272/j.issn.2095-8137.2023.311

ZR | Zoological Research

Article Open Access

# Mitogenomic phylogeny, biogeography, and cryptic divergence of the genus *Silurus* (Siluriformes: Siluridae)

Weitao Chen[1,2,3,4], Nicolas Hubert[5,*], Yuefei Li[1,2,3,4], Shuli Zhu[1,2,3,4], Jun Wang[6], Denggao Xiang[1], Shang Gao[1], Chunni Kou[1], Jilong Wang[7], Tai Wang[8], Zhiqiang Liang[9], Junjie Wu[10], Xinhui Li[1], Jie Li[1,2,3,4,*]

[1] *Pearl River Fisheries Research Institute*, *Chinese Academy of Fishery Sciences*, *Guangzhou*, *Guangdong* 510380, *China*
[2] *China Key Laboratory of Aquatic Animal Immune Technology of Guangdong Province*, *Guangzhou*, *Guangdong* 510380, *China*
[3] *Key Laboratory of Prevention and Control for Aquatic Invasive Alien Species*, *Ministry of Agriculture and Rural Affairs*, *Guangzhou*, *Guangdong* 510380, *China*
[4] *Scientific Observing and Experimental Station of National Fisheries Resources and Environment*, *Guangzhou*, *Guangdong* 510380, *China*
[5] *Institut de Recherche pour le Développement*, *Montpellier*, *UMR* 226 *ISEM (UM-CNRS-IRD)*, *France*
[6] *State Key Laboratory of Eco-hydraulic in Northwest Arid Region of China*, *Xi'an University of Technology*, *Xi'an*, *Shaanxi* 710048, *China*
[7] *Heilongjiang River Fisheries Research Institute*, *Chinese Academy of Fishery Sciences*, *Harbin*, *Heilongjiang* 150076, *China*
[8] *Gansu Fisheries Research Institute*, *Lanzhou*, *Gansu* 730030, *China*
[9] *Hunan Fisheries Science Institute*, *Changsha*, *Hunan* 410153, *China*
[10] *Yunnan Institute of Fishery Sciences Research*, *Kunming*, *Yunnan* 650111, *China*

## ABSTRACT

The genus *Silurus*, an important group of catfish, exhibits heterogeneous distribution in Eurasian freshwater systems. This group includes economically important and endangered species, thereby attracting considerable scientific interest. Despite this interest, the lack of a comprehensive phylogenetic framework impedes our understanding of the mechanisms underlying the extensive diversity found within this genus. Herein, we analyzed 89 newly sequenced and 20 previously published mitochondrial genomes (mitogenomes) from 13 morphological species to reconstruct the phylogenetic relationships, biogeographic history, and species diversity of *Silurus*. Our phylogenetic reconstructions identified eight clades, supported by both maximum-likelihood and Bayesian inference. Sequence-based species delimitation analyses yielded multiple molecular operational taxonomic units (MOTUs) in several taxa, including the *Silurus asotus* complex (four MOTUs) and *Silurus microdorsalis* (two MOTUs), suggesting that species diversity is underestimated in the genus. A reconstructed time-calibrated tree of *Silurus* species provided an age estimate of the most recent common ancestor of approximately 37.61 million years ago (Ma), with divergences among clades within the genus occurring between 11.56 Ma and 29.44 Ma, and divergences among MOTUs within species occurring between 3.71 Ma and 11.56 Ma. Biogeographic reconstructions suggested that the ancestral area for the genus likely encompassed China and the Korean Peninsula, with multiple inferred dispersal events to Europe and Central and Western Asia between 21.78 Ma and 26.67 Ma and to Japan between 2.51 Ma and 18.42 Ma. Key factors such as the Eocene-Oligocene extinction event, onset and intensification of the monsoon system, and glacial cycles associated with sea-level fluctuations have likely played significant roles in shaping the evolutionary history of the genus *Silurus*.

**Keywords:** Maximum likelihood; Bayesian inferences; Ancestral area estimation; Cryptic diversity; Dispersal pathways; Mitogenomes; Sea levels

## INTRODUCTION

Understanding phylogenetic relationships, biogeographic history, and species diversity is not only fundamental to evolutionary biology and ecology but also to conservation biology (Alfaro et al., 2009; Donoghue, 2008; Smith et al., 2005; Winter et al., 2013). However, this task is challenging with respect to globally distributed taxa. Notably, widely distributed taxa have generally undergone multiple

This is an open-access article distributed under the terms of the Creative Commons Attribution Non-Commercial License (http://creativecommons.org/licenses/by-nc/4.0/), which permits unrestricted non-commercial use, distribution, and reproduction in any medium, provided the original work is properly cited.
Copyright ©2024 Editorial Office of Zoological Research, Kunming Institute of Zoology, Chinese Academy of Sciences

Received: 27 November 2023; Accepted: 25 December 2023; Online: 26 December 2023
Foundation items: This study was supported by the National Natural Science Foundation of China (32000306), Project of Innovation Team of Survey and Assessment of the Pearl River Fishery Resources (2023TD-10), and Natural Science Foundation of Shaanxi Province (2023-JC-YB-325)
*Corresponding authors, E-mail: nicolas.hubert@ird.fr; lijie1561@163.com

colonization and/or speciation events by virtue of topographic and climatic changes, resulting in complex (and often unresolved) phylogenetic relationships (Crisp et al., 2009; Hotaling et al., 2021; Jetz et al., 2014; Murphy & Austin, 2005; Swenson, 2011). Furthermore, species diversity has often been underestimated due to limited spatial, hence taxonomic, coverage and potential cryptic diversity (Bickford et al., 2007; Cicconardi et al., 2013; Pfenninger & Schwenk, 2007; Sholihah et al., 2021a, 2021b, Siler et al., 2011; Utami et al., 2022). Consequently, to accurately assess the biodiversity of widely distributed taxa and to improve our understanding of their evolutionary history, it is necessary to conduct phylogenetic and biogeographic analyses, as well as large-scale evaluations of species diversity using molecular approaches.

The genus *Silurus*, an important group of catfish species belonging to the family Siluridae, is found throughout the freshwaters of Eurasia. The genus includes notably large species (e.g., *Silurus glanis* Linnaeus 1758), which can exceed 2 m in length and weigh up to 100 kg. To date, researchers have described 16 species worldwide (Britz & Win, 2010; Hibino & Tabata, 2018; Li et al., 2019), including 13 species in East Asia and three species in Europe and Central and Western Asia (https://www.fishbase.org/) (Lu et al., 2023). Both *Silurus asotus* Linnaeus 1758 and *S. glanis* are widely distributed across the Eurasian continent and are considered of economic importance in many countries (https://www.fishbase.org/), whereas the remaining 14 species exhibit more narrow distribution ranges, with over half classified as endangered or threatened (Jiang et al., 2016; EU Habitat Directive IV). For example, *Silurus mento* Regan 1904, once abundant in Dianchi Lake in Yunnan, China, has long been commercially fished, resulting in a dramatic decline in its population since the 1970s, remaining scarce for decades (Chu & Chen, 1989; Yang et al., 2008). As such, various species within the genus have attracted substantial research interest due to their economic value and precarious conservation status (Copp et al., 2009; Gao et al., 2011; Leonardos et al., 2009; Loannis et al., 2007; Luo & Xie, 2008; Yang et al., 2008).

Evaluating phylogenetic relationships and species diversity within a genus are fundamental steps toward the implementation of conservation measures for endangered and threatened species. Previous studies have explored the phylogenetic affiliations of *Silurus* species using complete mitochondrial genome (mitogenome) sequences (Kappas et al., 2016; Kishimoto et al., 2022; Mabuchi et al., 2020; Park et al., 2020; Schedel et al., 2022; Székvári et al., 2021; Vittas et al., 2011; Wang et al., 2015a, 2015b; Wu et al., 2021; Yang et al., 2019; Zeng et al., 2011). Nevertheless, these studies primarily relied on a limited number of species and restricted sampling ranges, leaving many taxa unexamined and the overall phylogeny unresolved. Furthermore, the diversity within the genus remains only partially understood, as evidenced by the identification of three new species (i.e., *Silurus duanensis* Hu, Lan & Zhang 2004, *Silurus longibarbatus* Li, Li, Zhang & He 2019, and *Silurus tomodai* Hibino & Tabata 2018) in the past two decades (Hibino & Tabata, 2018; Hu et al., 2004; Li et al., 2019).

The biogeographic history of a taxon generally results from complex interactions between past ecological processes and geological events, acting together over time (Hoorn et al., 2010; Hubert & Renno, 2006; Olden et al., 2010). Deciphering the biogeographic history of the genus *Silurus* could help elucidate the patterns of diversification within the group and to clarify the various processes that have influenced these patterns across different spatial and temporal scales. A deeper understanding of the biogeographic history of a taxon not only sheds light on the mechanisms underlying uneven distribution patterns but also provides opportunities to test hypotheses regarding the origins of species and their long-distance dispersal. To date, however, a comprehensive biogeographic study of the genus *Silurus* has yet to be conducted, with the origin and spatial expansion of the genus remaining largely unexplored.

As a freshwater fish lineage, the evolutionary history of *Silurus* is likely influenced by major biogeographic barriers in East Asia, such as the Korean Strait, Nanling Mountains, and Baekdudaegan Mountains (Chen et al., 2022; Feng et al., 2023; Kim et al., 2012). In addition, fragmentation and multiple vicariance events are expected, given the high number of endemic species with narrow distribution ranges. This pattern is also expected to favor the emergence of high levels of cryptic diversity within ancient and widely distributed species, challenging traditional taxonomies and calling into question current estimates of species diversity. For example, genetic analyses using the mitochondrial cyt *b* gene have revealed that *S. asotus* populations in several major Chinese watersheds consist of multiple genetic lineages (Xu et al., 2017), suggesting an underestimation of species diversity in the genus. Consequently, it is expected that other species within *Silurus* are still awaiting discovery.

In this context, we sequenced and annotated 89 new mitogenomes from *Silurus* species collected in China (83 specimens involving six species), Uzbekistan (five *S. glanis* specimens), and Germany (one *S. glanis* specimen). Combined with 20 previously published *Silurus* mitogenomes (11 species), we assembled a dataset consisting of 109 mitogenomes representing 13 recognized species to investigate the phylogenetic relationships and divergence history within the *Silurus* lineage. Based on extensive spatial coverage and multiple samples from different biogeographic regions for widely distributed species, we further explored the phylogeographic patterns in the genus. We aimed to: (a) reconstruct a robust mitochondrial phylogeny for the genus *Silurus*; (b) infer the biogeographic history of the genus and identify its origin, timing and pathways of dispersal; and (c) assess species diversity within the genus using standardized DNA sequence-based species delimitation.

## MATERIALS AND METHODS

### Sample collection and DNA extraction

We collected 89 *Silurus* samples belonging to eight morphospecies from 20 localities in Eurasian drainages (Supplementary Table S1; Figure 1). We failed to obtain samples of three species, including *Silurus burmanensis* Thant 1966 (only found in Myanmar), *S. mento* (only found in Dianchi Lake, Yunnan, China), and *Silurus triostegus* Heckel 1843 (only found in Iraq), due to their very restricted distribution ranges and limited information concerning their abundance and ecology (Britz & Win, 2010; Hibino & Tabata, 2018; Yang et al., 2008; www.fishbase.org). The 24 localities covered most of the geographic distribution ranges of the *Silurus* species. For widespread species, multiple samples were collected from different localities. Samples of fin and/or

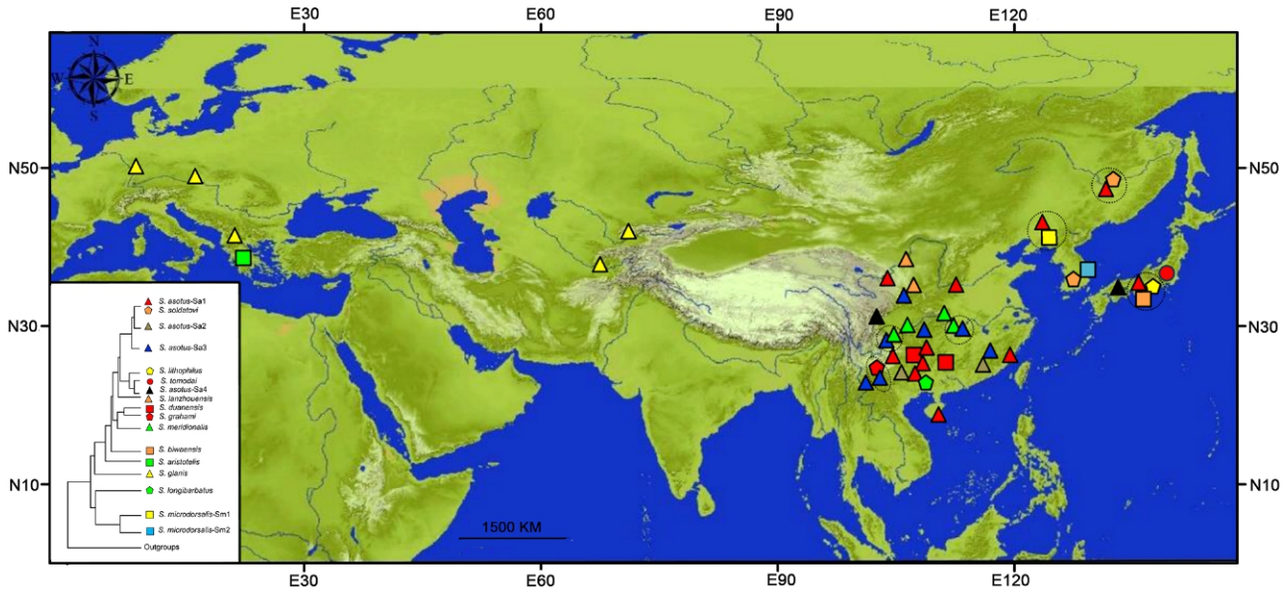



**Figure 1 Geographic distribution of 13 valid *Silurus* species used in the present study**

Phylogenetic tree at left bottom corresponds to topology inferred in the present study and different shapes and colors indicate distinct morphological species. Shapes in dashed ellipses represent identical localities. Detailed sampling information of *Silurus* specimens can be found in Supplementary Table S1.

muscle tissue were obtained and preserved in 95% ethanol. Total genomic DNA was extracted from fin or muscle samples of each specimen using a Qiagen DNeasy Tissue Kit (Hilden, Germany) according to the manufacturer's instructions.

**Mitogenome sequencing, sequence quality control, assembly, and annotation**

To maximize the efficiency of genome assembly, 1 μg of DNA from each sample was used for library construction. The libraries were prepared using an Illumina SeqTM DNA Sample Prep Kit (Illumina, USA) with an insert size of 300–500 bp. Each library was sequenced on the Illumina HiSeq 4000 platform (Illumina, USA), generating 150 bp paired-end reads.

All sequence reads were filtered using the NGS QC Toolkit v.2.3.3 (Patel & Jain, 2012). Cutoff values of 50 for the percentage of read length and 20 for the PHRED quality score were used for editing reads. MITOZ v.2.3 was used to assemble high-quality reads into contigs (Meng et al., 2019). Mitogenome annotations were performed using MitoAnnotator v.3.32 (Iwasaki et al., 2013). Gene boundaries were manually checked by aligning homologous annotated gene sequences of published *Silurus* species using MEGA v.6 (Tamura et al., 2013). To ensure the quality of the assembled mitogenomes, mitochondrial contig mapping was performed using Geneious R11 (Kearse et al., 2012). All novel mitogenomes were deposited in GenBank under accession numbers OQ791283, OQ835313–OQ835316, OQ843503–OQ843543, and OQ851421–OQ851463 (Supplementary Table S1).

**Mitogenome alignment**

We downloaded 19 publicly available *Silurus* mitogenomes from the NCBI database, representing 10 morphological species (Supplementary Table S1), although relevant DNA sequences were not found for *S. burmanensis*, *S. mento*, or *S. triostegus*. A total of 35 localities from Eurasian drainages were included, covering most of the distribution ranges of *Silurus* species. In addition, four Siluridae species belonging to different genera (*Ompok bimaculatus* Bloch 1794, *Pterocryptis cochinchinensis* Valenciennes 1840, and *Kryptopterus vitreolus* Ng & Kottelat 2013), as well as a representative of four Siluriformes families (Ictaluridae, Cranoglanididae, Clariidae, and Saccobranchidae) and two Cypriniformes (*Danio rerio* Hamilton 1822 and *Cyprinus carpio* Linnaeus 1758) were used as outgroups (Supplementary Table S1).

The mitogenomes were aligned using MUSCLE (Edgar, 2004), with 22 transfer RNA (tRNA) genes, 13 protein-coding genes (PCGs), and two ribosomal RNA (rRNA) genes manually extracted using MEGA v.6. The control region from the final matrix were excluded as it presented repetitive patterns that are generally poorly assembled using short reads. For the PCGs, stop codons were removed from each sequence.

**Phylogenetic analyses**

To determine the saturation of each gene sequence, we performed substitution saturation using DAMBE v.6.4.20 (Xia, 2013; Xia & Lemey, 2009). No substitution saturation was found for the 13 PCGs, 12S rRNA, 16S rRNA, or 22 tRNAs, even in the third positions of the 13 PCGs (Table 1). Therefore, 37 mitochondrial genes were concatenated as a "supergene" dataset (15 656 bp) using local Perl scripts. The sequence alignment was partitioned into 42 subsets: a total of 39 sets for three codon positions of each PCG, two for the 12S and 16S rRNA genes, and one for the 22 tRNA genes. The best partitioning schemes and corresponding nucleotide substitution models for the supergene dataset were chosen using PartitionFinder v.2.1 (Lanfear et al., 2012). Scores for different models were calculated based on the Bayesian Information Criterion.

Maximum likelihood (ML) and Bayesian inference (BI) reconstructions of the phylogenetic relationships within *Silurus* were performed using the best partitioning schemes (Table 2). The GTR+I+Γ model was used to perform bootstrapping in RAxML-VI-HPC v.2.0.1 (Stamatakis, 2006), with a random seed and 1 000 replicates. The BI analyses were performed in MrBayes v3.1.2 (Ronquist & Huelsenbeck, 2003) with two independent runs, each with four Markov Chain Monte Carlo

**Table 1 Saturation tests of three codon positions in PCGs, 12S rRNA, 16S rRNA, and combined tRNAs using Xia's method in DAMBE5**

| Gene region | Symmetrical tree | | | Asymmetrical tree | |
|---|---|---|---|---|---|
| | *Iss* | *Iss.c* | *P* | *Iss.c* | *P* |
| All positions of 13 PCGs | 0.120 | 0.818 | <0.0001 | 0.572 | <0.0001 |
| 1st positions of 13 PCGs | 0.063 | 0.809 | <0.0001 | 0.555 | <0.0001 |
| 2nd positions of 13 PCGs | 0.021 | 0.809 | <0.0001 | 0.555 | <0.0001 |
| 3rd positions of 13 PCGs | 0.312 | 0.809 | <0.0001 | 0.555 | <0.0001 |
| 12S rRNA | 0.166 | 0.747 | <0.0001 | 0.440 | <0.0001 |
| 16S rRNA | 0.126 | 0.782 | <0.0001 | 0.506 | <0.0001 |
| 22 tRNAs | 0.084 | 0.777 | <0.0001 | 0.497 | <0.0001 |

**Table 2 Best partitioning schemes and corresponding nucleotide substitution models of all mitogenomes used in phylogenetic inferences within *Silurus***

| Scheme number | Partition scheme | Best model |
|---|---|---|
| 1 | ATP6_1$^{st}$, ND1_1$^{st}$, ND2_1$^{st}$, ND3_1$^{st}$, ND4_1$^{st}$, ND5_1$^{st}$, CYTB _1$^{st}$ | GTR+I+G |
| 2 | ATP6_2$^{ed}$, ATP8_2$^{ed}$, ND1_2$^{ed}$, ND2_2$^{ed}$, ND3_2$^{ed}$, ND4_2$^{ed}$, ND5_2$^{ed}$ | GTR+I+G |
| 3 | ATP6_3$^{rd}$, COIII_3$^{rd}$, ND1_3$^{rd}$, ND2_3$^{rd}$, ND3_3$^{rd}$, ND4_3$^{rd}$, ND4L_3$^{rd}$, ND5_3$^{rd}$, CYTB_3$^{rd}$ | GTR+I+G |
| 4 | ATP8_2$^{ed}$, 22tRNAs | HKY+I+G |
| 5 | ATP8_3$^{rd}$, 12sRNA, 16sRNA | GTR+I+G |
| 6 | COIII_1$^{st}$, COI_1$^{st}$, COII_1$^{st}$, ND4L_1$^{st}$ | TIMEF+I+G |
| 7 | COI_2$^{ed}$, COII_2$^{ed}$, COIII_2$^{ed}$, ND4L_2$^{st}$, CYTB_2$^{ed}$ | HKY+I |
| 8 | COI_3$^{rd}$, COII_3$^{rd}$ | TRN+I+G |
| 9 | ND6_1$^{st}$, ND6_2$^{ed}$ | HKY+I+G |
| 10 | ND6_3$^{rd}$ | TRN+G |

(MCMC) chains. All nucleotide substitution models were unlinked across partitions, and different partitions were allowed to evolve at different rates. An independent run was performed for 20 million generations, sampling every 1 000 generations, with the first 25% discarded as a burn-in, while the remaining samples were used to summarize Bayesian posterior probabilities (BPPs). Convergence of the BI analyses was assessed based on the average standard deviation of split frequencies being less than 0.01, and the potential scale reduction factors (PSRF) being close to 1.0 for all parameters. The convergence of BI analyses was checked using Tracer v.1.5 (Rambaut & Drummond, 2007). Genetic divergence among observed clades and/or subclades was calculated in MEGA using the Kimura two-parameter model (Kimura, 1980).

**Delimitation of molecular operational taxonomic units (MOTUs)**

Three PCGs, i.e., COI, CYTB, and ND2, were selected for delimitation analyses. Distance- and tree-based methods were applied to determine whether multiple MOTUs were present among the most widespread species, *S. asotus* and *Silurus microdorsalis* Mori 1936. *Silurus lithophilus* Tomoda 1961, *S. tomodai*, and *Silurus soldatovi* Nikolskii & Soin 1948 were included in delimitation analyses due to their close phylogenetic relationships with the *S. asotus* clades. First, genetic distances among different clades/subclades determined using the K2P model were input into MEGA. Second, automatic barcode gap discovery (ABGD) was performed using the default value for the relative gap width (X=1.5) and K2P distance (Puillandre et al., 2012). Third, the Poisson tree process (PTP; Kapli et al., 2017) in its multiple rates version was run using the web server (http://mptp.h-its.org). An ML tree was constructed in RAxML-VI-HPC using the GTR + I +Γ model selected by MrModeltest (Nylander, 2004). Fourth, the general mixed Yule-coalescent (GMYC) model (Fujisawa & Barraclough, 2013) based on single- and multiple-thresholds was run using the GMYC web server (http://species.h-its.org/gmyc/). A fully resolved ultrametric gene tree used in the GMYC analysis was built in BEAST v.1.8 (Drummond & Rambaut, 2007) by employing a Yule pure-birth model tree with the GTR + I + Γ substitution model and an uncorrelated relaxed lognormal clock model. Two MCMC chains of 50 million steps, sampled every 1 000 steps, were run and convergence was assessed using Tracer v.1.5.

**Dating analyses**

Divergence dating with an approximate likelihood calculation was performed using MCMCTREE in PAML v.4.9 (Yang, 2007). Due to the low genetic divergence among sequences within MOTUs, one representative sequence for each MOTUs was chosen. Both *S. soldatovi* and *S. lithophilus* were included, although they clustered with different morphospecies with low divergence. To estimate divergence times, a BI phylogenetic tree was reconstructed using selected specimens with MrBayes v.3.1.2 with the same parameters used for BI analyses above and the best partitioning schemes selected by PartitionFinder (Table 3). For this reconstruction, two outgroups outside Siluriformes (*Danio rerio* and *Cyprinus carpio*) were added.

One fossil calibration and three estimated calibrations were employed, including the: (i) most recent common ancestor (MRCA) of the root was the oldest fossil of the crown-group Ostariophysi, the stem gonorynchiform † *Rubiesichthys gregalis* (Benton et al., 2015; Fara et al., 2010) from the Berriasian of Spain (145.5–140.2 million years ago (Ma)). A lower bound of 140.2 Ma and an upper bound of 145.5 Ma were employed as age constraints of the root. (ii) divergence time between Cyprinidae and Danionidae was estimated at 59–122 Ma (www.timetree.org). (iii) divergence time between Siluridae and Cranoglanididae was estimated at 49–66 Ma (www.timetree.org). (iv) first appearance of the African Clariidae was in the Lower Eocene (34–56 Ma), lower age constraint of the clade (*Clarias*, *Heteropneustes*)=34 Ma, and soft upper bound=140.2 Ma. The overall substitution rate was

**Table 3 Best partitioning schemes and corresponding nucleotide substitution models of selected mitogenomes per MOTUs in Bayesian inference used in dating analyses**

| Scheme number | Partition scheme | Best model |
|---|---|---|
| 1 | ATP6_1st, ND1_1st, ND2_1st, ND3_1st, ND4_1st, ND4L_1st, CYTB _1st | GTR+I+G |
| 2 | ATP6_2ed, ND1_2ed, ND2_2ed, ND4L_2st, ND3_2ed, ND4_2ed | GTR+I+G |
| 3 | ATP6_3rd, ND1_3rd, ND2_3rd, ND3_3rd, ND4_3rd, ND4L_3rd, CYTB_3rd | GTR+I+G |
| 4 | ATP8_2ed, 22tRNAs, ATP8_2ed, ND5_1st, | TVM+I+G |
| 5 | ATP8_3rd, ND5_3rd | GTR+I+G |
| 6 | COIII_1st, COI_1st, COII_1st | TIMEF+I+G |
| 7 | COI_2ed, COII_2ed, COIII_2ed, CYTB_2ed | K81UF+I |
| 8 | COI_3rd, COII_3rd, COIII_3rd, ND5_2ed | GTR+I+G |
| 9 | ND6_1st, ND6_2ed | K81UF+I |
| 10 | ND6_3rd | TRN +G |
| 11 | 12sRNA, 16sRNA | GTR+I+G |

estimated using the BASEML program in PAML with a root age of 145.5 Ma. The first 200 000 cycles in MCMCTREE were discarded as burn-in, with sampling every 50 cycles to obtain a total of 20 000 samples. Three independent MCMC runs were conducted with different random seeds to check the convergence of each run. The distributions of the parameter values from the MCMC samples were assessed using Tracer v.1.6, with the values of effective sample size exceeding 200.

**Ancestral area reconstruction**

The dated BI tree described above was used for biogeographical analyses and Reconstruct Ancestral State in Phylogenies (RASP v.4.2 (Yu et al., 2020)) was used for ancestral area reconstructions. The optimal model was selected using the model selection function in the BioGeoBEARS package within RASP v.4.2, which compared AIC values to determine the best fit for the data. Geographic units for biogeographic reconstructions were based on recognized biogeographical regions separated by well-known biogeographic barriers in Eurasia, i.e., Qinghai-Xizang Plateau and Korea Strait. Given that, three regions were defined: China and Korean Peninsula (A), Europe and Central and Western Asia (B), and Japan (C).

## RESULTS

**Taxonomic coverage and mitogenome characteristics**

The 89 newly sequenced mitogenomes of *Silurus* were circular, with lengths ranging from 16 419 to 17 610 bp and average sequencing depths ranging from 556× to 3 254× (Supplementary Table S1). Among these 89 new mitogenomes, a total of 43, seven, six, one, six, seven, 13, and six were generated for *S. asotus*, *S. duanensis*, *S. glanis*, *S. graham* Regan 1907, *Silurus lanzhouensis* Chen 1977, *S. longibarbatus*, *Silurus meridionalis* Chen 1977, and *S. microdorsalis*, respectively. The mitogenomes contained 13 PCGs, 22 tRNA genes, two rRNA genes (12S and 16S RNAs), and a putative control region. The observed variations in length were mostly due to the variable length of the control region. Gene order was identical to that of other Osteichthyes.

**Phylogenetic relationships**

The length of the "supergene" dataset containing the 13 PCGs, 22 tRNAs, and two rRNAs reached 15 656 bp. The best-fit partitioning scheme determined by PartitionFinder for the 116 mitogenomes (including *Clarias fuscus* Lacepède 1803, *Cranoglanis bouderius* Richardson 1846, *Heteropneustes fossilis* Bloch 1794, *Ictalurus punctatus* Rafinesque 1818, *Kryptopterus vitreolus*, *Ompok bimaculatus*, and *Pterocryptis cochinchinensis* as outgroups) included 10 partitions, with corresponding evolutionary models (Table 2). The genus *Silurus* formed a strongly supported monophyletic group in the BI and ML trees, with a posterior probability of 1.0 and bootstrap score of 100 (Figure 2). The ML and BI trees yielded identical topologies and resolved eight well-supported clades: Clade A, most specimens of *S. asotus* and all specimens of *S. soldatovi*; Clade B, two *S. asotus* individuals, *S. lithophilus*, and *S. tomodai*; Clade C, *S. lanzhouensis*; Clade D, *S. meridionalis*, *S. duanensis*, and *S. grahami*; Clade E, *Silurus biwaensis* Tomoda 1961; Clade F, *Silurus aristotelis* Garman 1890; Clade G, *S. glanis*; and Clade H, *S. longibarbatus* and *S. microdorsalis* (Figure 2). Both analyses supported *S. longibarbatus* and *S. microdorsalis* as sister taxa, occupying the basal position of all remaining *Silurus* species, with high bootstrap values. The monophyly of *S. microdorsalis*, *S. longibarbatus*, *S. glanis*, *S. aristotelis*, *S. biwaensis*, *S. grahami*, *S. duanensis*, *S. lanzhouensis*, and *S. meridionalis* was highly supported.

For the *S. asotus* complex, two major clades (A and B) and three subclades (A1, A2, and A3) within Clade A were observed. With respect to *S. microdorsalis*, two sublineages (H1 and H2; Figure 2) with relatively high genetic divergence (K2P distance of 3.75%) were recovered. The phylogenetic trees showed that *S. soldatovi* was clustered with *S. asotus* within subclade A1 (Figure 2). Furthermore, *S. lithophilus* and *S. tomodai* were nested within *S. asotus* in Clade B and displayed shallow genetic divergence, with K2P distances ranging from 0.15% to 1.11% among *S. lithophilus*, *S. tomodai*, and the closest mitogenome of *S. asotus.*

**MOTU delimitation in *S. asotus* complex and *S. microdorsalis***

The K2P, ABGD, and PTP analyses indicated that *S. asotus* and *S. microdorsalis* could be delimited into four and two MOTUs, respectively (Figure 3A). GMYC analyses yielded congruent delimitations (only single threshold model was presented in Figure 3A), except for the identification of a fifth MOTU within *S. asotus* (Figure 3A). Using a majority rule consensus, four MOTUs (Sa1 to Sa4) and two MOTUs (Sm1 and Sm2) were delimited in the *S. asotus* complex and *S. microdorsalis*, respectively. The average K2P genetic distance between the MOTUs ranged from 2.37% to 6.68% in the *S. asotus* complex and reached 4.49% for *S. microdorsalis* (Table 4).

Within the *S. asotus* complex, MOTU Sa1 showed widespread distribution, covering most rivers in East Asia;

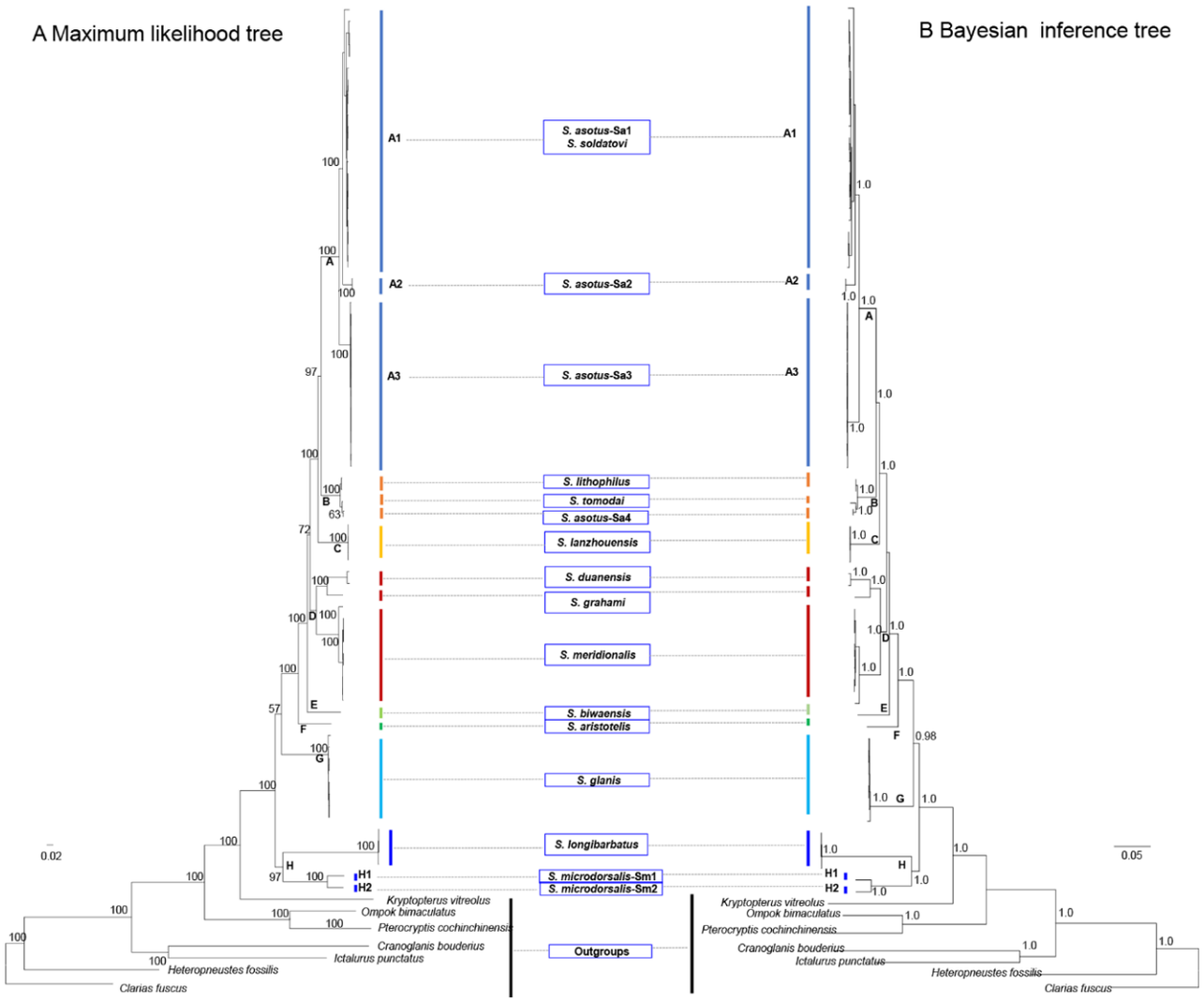



**Figure 2 Phylogenetic trees based on 108 *Silurus* mitogenomes and nine outgroups**

A: Maximum-likelihood (ML) tree. B: Bayesian inference tree. Values on branches indicate bootstrap proportions from ML analysis and Bayesian posterior probabilities. Triangles and rectangles indicate two pairs and one pair of mandibular barbels, respectively.

MOTU Sa2 was observed in the Pearl River only; MOTU Sa3 was found in the Yangtze River and Pearl River; and MOTU Sa4 was observed in the Yangtze River and Japanese rivers (Figure 3B). As the type locality of *S. asotus* was not reported in detail in its original description, it was not possible to identify the MOTU in the type locality of the species. The two *S. microdorsalis* MOTUs were found in Northeast China (Sm1) and South Korea (Sm2) at the species type locality (Figure 3C), showing relatively close spatial distances (Figure 3C).

### Divergence time estimates and biogeography

Divergence age estimates suggested that the split between *Silurus* and closely related genera occurred approximately 37.61 Ma (95% highest posterior density (HPD), 27.93–47.72 Ma; Figure 4). The divergences within the eight clades ranged from 11.56 Ma (95% HPD, 7.23–16.41 Ma) for Clade A to 29.44 Ma for Clade H (95% HPD, 21.64–37.66 Ma). The MOTUs within *S. asotus* diverged between 3.71 Ma (95% HPD, 1.92–5.88 Ma) and 11.56 Ma (95% HPD, 7.23–16.41 Ma), and the two *S. microdorsalis* MOTUs diverged approximately 8.74 Ma (95% HPD, 3.23–15.51 Ma).

The best-fit model in BioGeoBEARS was BAYAREALIKE. The common ancestor of all *Silurus* species was most likely originated from China and the Korean Peninsula (88.2%; Figure 4). The *Silurus* species spread to Europe and Central and Western Asia from China and the Korean Peninsula between 21.78 Ma and 26.67 Ma (Figure 4). Furthermore, *Silurus* species dispersed independently eastward to Japan at least three times. In turn, *S. asotus* recolonized China and the Korean Peninsula approximately 0.45 Ma.

## DISCUSSION

### Phylogenetic reconstructions

Most previous phylogenetic studies of *Silurus* have focused on the mitogenomic structures of individual species or inferred phylogenetic positions using a limited number of taxa (Kappas et al., 2016; Kishimoto et al., 2022; Mabuchi et al., 2020; Park et al., 2020; Székvári et al., 2021; Vittas et al., 2011; Wang et al., 2015a, 2015b; Wu et al., 2021; Yang et al., 2019; Zeng et al., 2011), providing only a partial view of the phylogenetic relationships within the genus. In the present study, we established a comprehensive phylogenetic framework for *Silurus*, utilizing the largest spatial and taxonomic coverage of whole mitogenome sequences to date.

The recovery of *Silurus* as monophyletic is consistent with

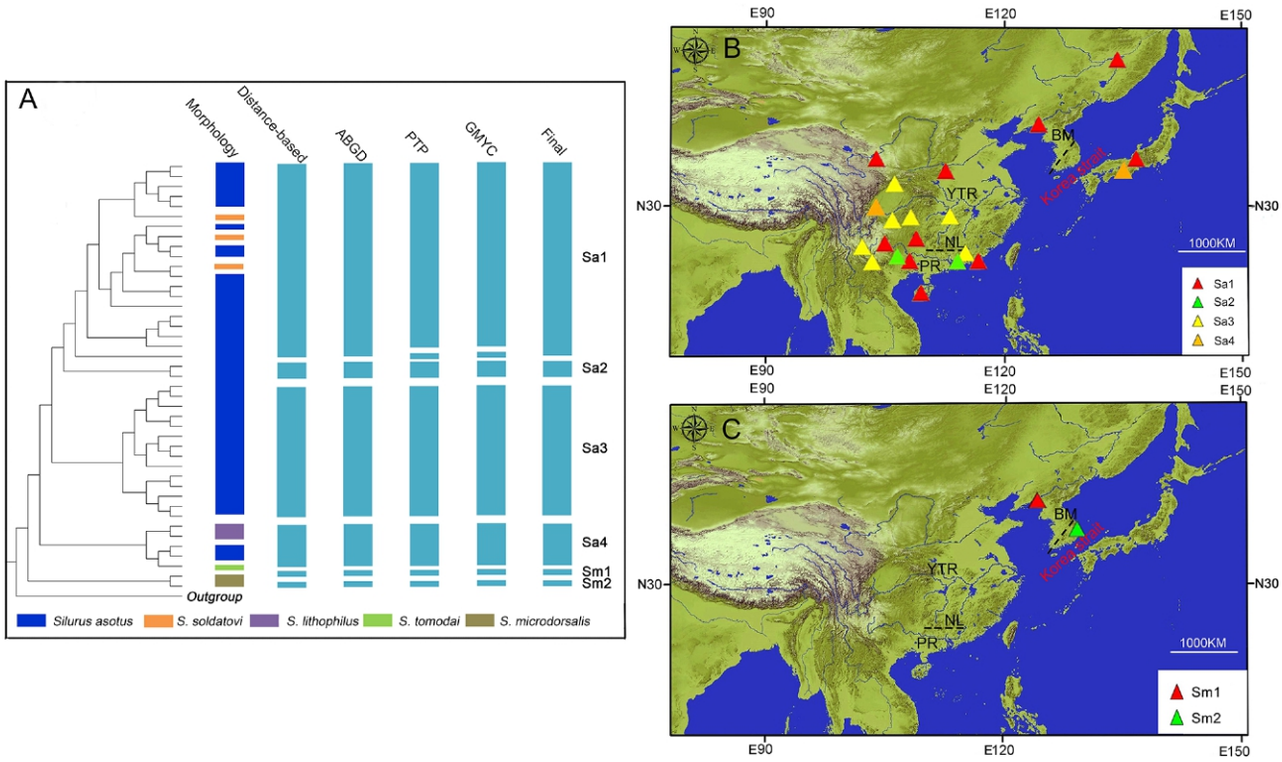



**Figure 3 DNA-based species delimitation and distribution patterns of identified putative species of *Silurus asotus* and *S. microdorsalis***

A: DNA-based species delimitation. B: Distribution patterns of identified putative species of *S. asotus*. C: Distribution patterns of identified putative species of *S. microdorsalis*. Bars with different colors indicate different valid species. MOTU delimitation schemes collected from ABGD, PTP, and GMYC algorithms, including consensus delimitation scheme. BM, Baekdudaegan Mountains; NL, Nanling Mountains; YTR, Yangtze River; PR, Pearl River.

**Table 4 Genetic K2P distances between MOTUs of *Silurus asotus* and *S. microdorsalis***

| Taxon 1 | Taxon 2 | Genetic distance (%) |
|---|---|---|
| Sa1 | Sa2 | 2.38 |
| Sa1 | Sa3 | 3.02 |
| Sa2 | Sa3 | 3.64 |
| Sa1 | Sa4 | 6.22 |
| Sa2 | Sa4 | 6.68 |
| Sa3 | Sa4 | 6.30 |
| Sm1 | Sm2 | 4.49 |

previous phylogenetic analyses (Kappas et al., 2016; Park et al., 2020; Schedel et al., 2022; Székvári et al., 2021; Wang et al., 2015a; Wu et al., 2021; Yang et al., 2019). Our study confirmed strong congruence between molecular delimitations and morphology-based taxonomic hypotheses in nine species, i.e., *S. microdorsalis*, *S. longibarbatus*, *S. glanis*, *S. aristotelis*, *S. biwaensis*, *S. grahami*, *S. duanensis*, *S. lanzhouensis*, and *S. meridionalis*, and robustly supported *S. microdorsalis* and *S. longibarbatus* as sister taxa located in the basal position of the *Silurus* phylogeny (Figure 2). The sister relationship between *S. microdorsalis* and *S. longibarbatus* was unexpected due to their distant distribution ranges, separated by at least 2 000 km, and remarkable morphological differences, including counts of mandibular barbel pairs and anal-fin rays (Chu et al., 1999; Li et al., 2019).

Surprisingly, *S. soldatovi* was clustered within the *S. asotus* subclade A1, exhibiting very shallow genetic distances. This finding contrasts with previous phylogenetic studies (Alam et al., 2019; Mabuchi et al., 2020; Schedel et al., 2022; Yang et al., 2019), which may be attributed to their use of a limited number of taxa and circumscribed sample ranges, thereby overlooking important intraspecific genetic variations in widespread species, thus leading to the classification of *S. soldatovi* as monophyletic. Our results suggest that *S. soldatovi* may have recently diverged from the closely related *S. asotus*, or that *S. asotus* may comprise a complex of cryptic taxa, given the significant morphological differences between the two species despite their intertwined mitochondrial genealogies (Chu et al., 1999). The most salient morphological distinction is that *S. asotus* possesses one pair of mandibular barbels, whereas *S. soldatovi* possesses two (Chu et al., 1999). Furthermore, the phylogenetic trees placed *S. lithophilus*, *S. tomodai*, and *S. asotus* within Clade B, exhibiting shallow divergence. While these species were reciprocally monophyletic, their phylogenetic relationships showed only moderate statistical support. These phylogenetic relationships are consistent with previous findings (Mabuchi et al., 2020; Schedel et al., 2022). Dating analyses indicated that the three species within Clade B diverged approximately 2 Ma, in line with the conclusions reported in Tabata et al. (2016). These results underscore the close relationship among *S. lithophilus*, *S. tomodai*, and the lineage known as *S. asotus*, suggesting that *S. asotus* is clearly polyphyletic. Future research should incorporate larger population-level sample sizes, nuclear gene analysis, and detailed morphological descriptions to clarify the phylogenetic relationships among these closely related species and unravel the complex evolutionary history of the *S. asotus* complex.

### Biogeographic history

The BioGeoBEARS reconstructions supported the origin of *Silurus* in China and the Korean Peninsula. This scenario is

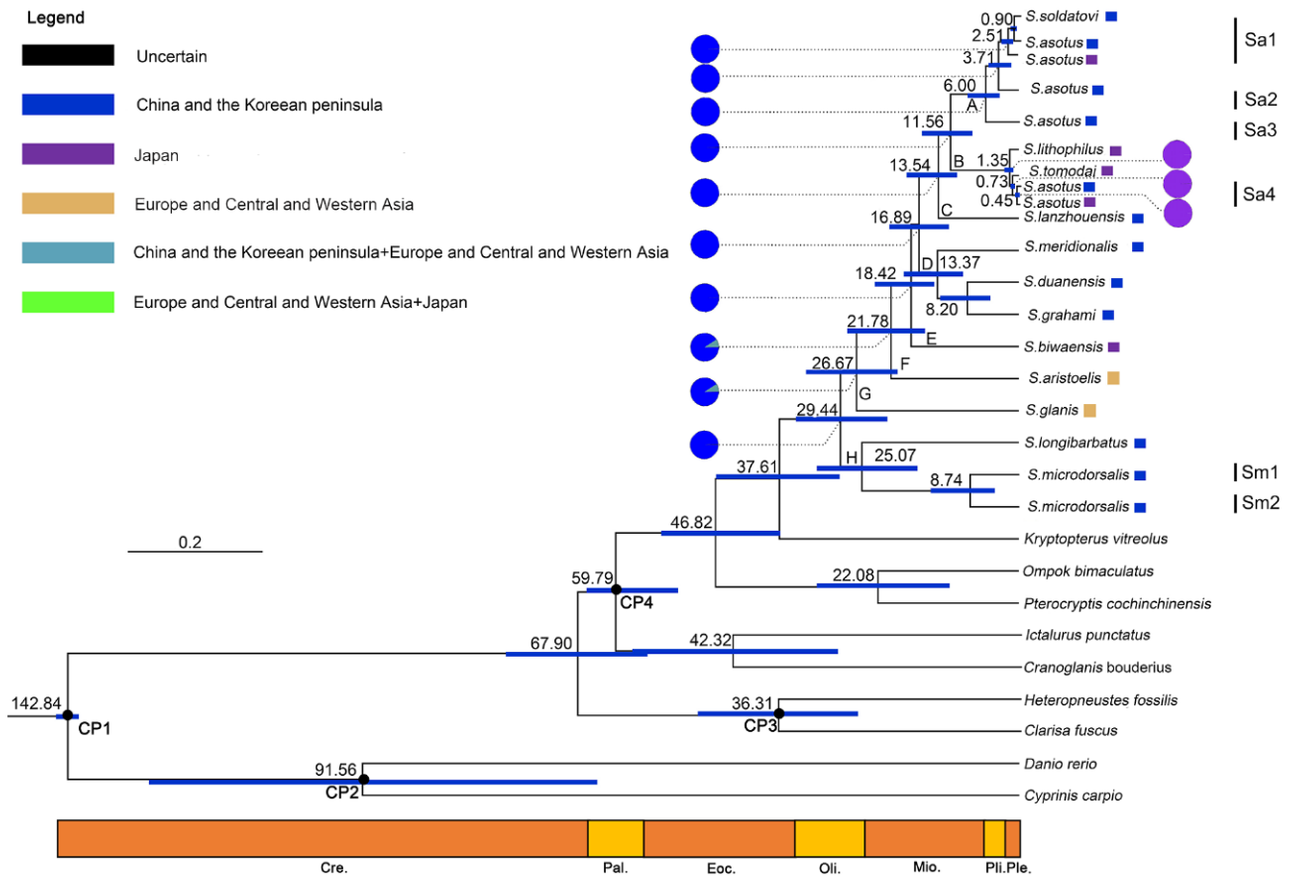



**Figure 4 Chronogram of selected species derived from divergence time estimations in MCMCTREE and ancestral area reconstructions**

Black dots (CP1–4) refer to calibration points. Shaded blue horizontal bars show 95% highest posterior densities (HPD) for divergence times. Pie charts depict ancestral geographic ranges of corresponding nodes inferred with BioGeoBEARS using the BAYAREALIKE model, with different colors representing different biogeographic regions. On the timescale, Cre., Cretaceous; Pal., Paleogene; Eoc., Eocene; Oli., Oligocene; Mio., Miocene; Pli., Pliocene; Ple., Pleistocene.

consistent with the highest species richness observed in these regions, which host 10 of the 16 known species of *Silurus* (www://fishbase.org/; accessed on 1 January 2023). Our results suggested that *Silurus* appeared during the late Eocene, coinciding with the Eocene-Oligocene extinction event (Hren et al., 2013; Ivany et al., 2000), which led to the creation of many empty ecological niches, likely facilitating the emergence of *Silurus* (Hren et al., 2013; Ivany et al., 2000). In addition, the substantial diversification of *Silurus* occurred during the Miocene, coinciding with the Mid-Miocene Climatic Optimum (MMCO) and intensification of the Asian monsoon (Clift et al., 2008; Favre et al., 2015; Guo et al., 2002; Lu & Guo, 2014). Previous studies have also noted that the intensification of the monsoon was accompanied by intense diversification in the East Asian fish fauna (Cheng, 2015; Clift & Plumb, 2008; Feng et al., 2023).

We inferred three major colonization events in the genus *Silurus* from the late Oligocene to the Miocene (Figure 4). Two dispersal events occurred, one from China and the Korean Peninsula to Europe and Central and Western Asia, and another from China and the Korean Peninsula to Japan between the late Oligocene and early Miocene. This period coincides with the onset of the East Asian monsoon climate, when heavy rainfall induced by the summer monsoon led to increased continental erosion rates, potentially accelerating dispersal between China and the Korean Peninsula, and Europe and Central and Western Asia (Colin et al., 2010; Liu et al., 2012). Moreover, the increased rainfall may have enhanced fluvial discharge into the marginal marine environment, creating dispersal pathways between the Eurasian continent and islands such as Japan (Colin et al., 2010; Liu et al., 2012). A subsequent dispersal event from China and the Korean peninsula to Japan occurred approximately 11.19 Ma (Late Miocene) (Figure 4), likely driven by periodic connections of rivers between the Asian mainland and Japan, induced by recurrent marine transgression and regression in East Asia (Kocsis & Scotese, 2021; Scotese & Wright, 2018). Feng et al. (2023) reported similar findings, examining the roles of marine transgression and regression in East Asia on the dispersal of endemic East Asian carp from the Asian mainland to Japan.

Two dispersal events between the Asian mainland and Japan during the Pleistocene were also identified. Initially, *S. asotus* in Japan (Sa4) recolonized the Asian mainland during the Late Pleistocene, although this conclusion is somewhat tentative due to the inclusion of only one mitogenome. Subsequently, a third colonization from the Asian mainland to Japan occurred during the early Pleistocene. Various studies have demonstrated that East Asia underwent multiple large-scale glaciation events during the Pleistocene, leading to periodic fluctuations in sea levels (von Wissmann, 1937; Voris, 2000; Zachos et al., 2001). Similar patterns of dispersion are evident among freshwater fish taxa between the Asian mainland and Japan (Tsao et al., 2016) and/or other islands

such as Taiwan and Hainan (Chen et al., 2020; Gao et al., 2023; Wang et al., 2000; Yang et al., 2012b).

We argue that paleoecological events, including the onset and intensification of the monsoon system, recurrent marine transgression and regression, and glacial cycles have significantly influenced the biogeographic history of the genus *Silurus*. However, given that *S. triostegus* in Europe and Central and Western Asia was not included in the current study, some biogeographic events may have been overlooked.

**Phylogeographic patterns within *S. asotus* and *S. microdorsalis***

Many cryptic species with identical morphological traits have been recognized using molecular tools (Bickford et al., 2007). In our study, species delimitation analyses revealed four (Sa1 to Sa4) and two (Sm1 and Sm2) MOTUs in *S. asotus* and *S. microdorsalis*, respectively, characterized by substantial genetic divergence (K2P distance >2%; Table 1). In this context, *S. asotus* was not monophyletic as Sa4 was closely related to *S. tomodai* and *S. lithophilus* (Figure 2), suggesting that the taxonomic characters used to separate *S. asotus* from other closely related species are varyingly conserved among species and represent a mosaic of converging and/or ancestral character states. These results highlight the need to re-examine the utility of these morphological characters in taxonomy considering our current phylogenetic reconstruction.

The four observed MOTUs in *S. asotus* and their overlapping distributions suggest that the *S. asotus* complex has experienced a complex evolutionary history. Xu et al. (2017) also reported overlapping distributions for members of the four observed MOTUs using mitochondrial cyt *b* fragments. MOTU Sa4 is believed to have initially emerged in the Japanese archipelago during the Late Miocene, isolated by the Korean Strait, and then dispersed to the Asian mainland during the Late Pleistocene due to falling sea levels (von Wissmann, 1937; Voris, 2000; Zachos et al., 2001). MOTU Sa2 and Sa3 are thought to be the byproducts of the rapid uplift of the Qinghai-Xizang Plateau from the Late Miocene (8.0 Ma) to Late Pleistocene (Molnar, 2005). The rapid rise of the plateau significantly influenced the regional climate and reshaped the landscape features of eastern Asia, including the drainage systems (Jia et al., 2003). This geological change is hypothesized to be a crucial driving force in the formation and colonization of many fish taxa in East Asia (Guo et al., 2005; He & Chen, 2006; He et al., 2001; Yang et al., 2012a). Furthermore, MOTU Sa2 underwent local divergence in the Pearl River and was unable to disperse northward due to the Nanling Mountains barrier (Figure 5A). The most recently diverged MOTU, Sa1, has become the most widely distributed species in the East Asian ranges, which may be due to recent population expansion after the Late Pleistocene glacial retreat (Gao et al., 2012) and/or frequent summer flooding (Chen et al., 2017).

Regarding *S. microdorsalis*, the discovery of two MOTUs exhibiting deep divergence was unexpected, given the restricted distribution of the species and the relatively close distributions of the two MOTUs (<800 km). Divergence dating suggested that the two MOTUs split during the late Miocene, implying a period of long-term isolation. The Baekdudaegan Mountain range appears to have acted as a biogeographic barrier, facilitating the separation of the two MOTUs. Previous reports have confirmed that the Baekdudaegan Mountain range has played an important role in the divergence and/or speciation of multiple freshwater fish species in the Korean Peninsula (Jeon et al., 2022; Kim et al., 2012).

Given that the formal taxonomy of DNA-based cryptic lineages often lacks stability (Satler et al., 2013), the MOTUs identified herein merely conform to the primary species

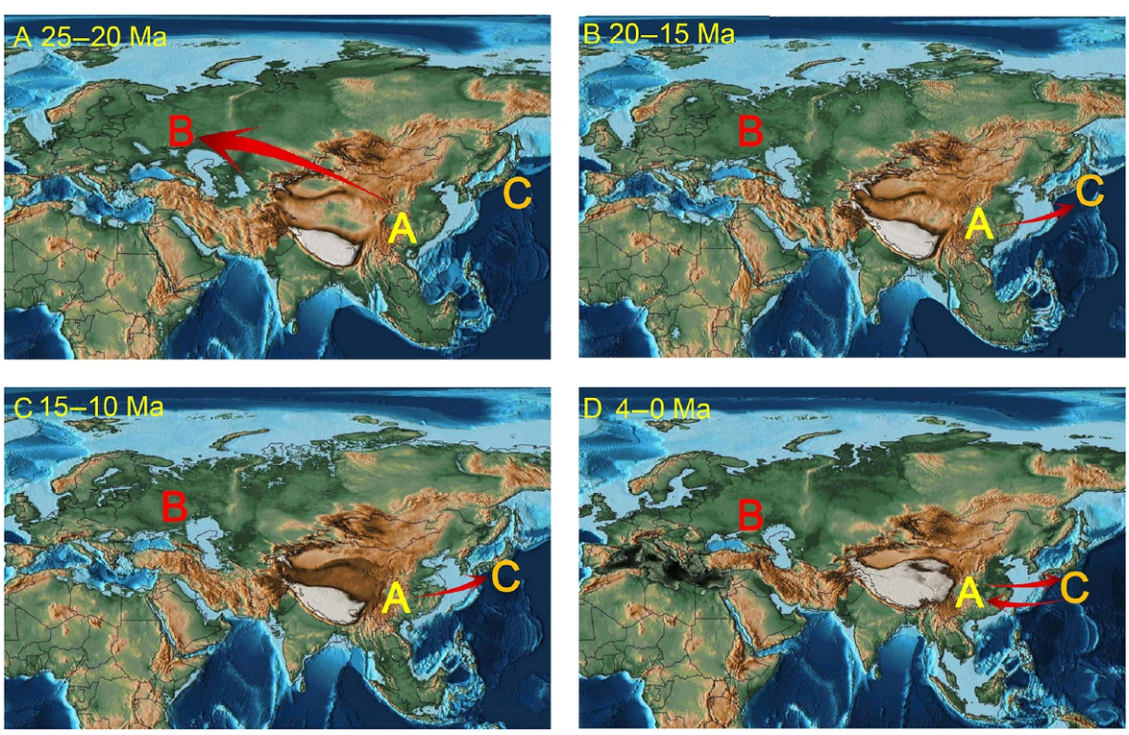



**Figure 5 Dispersal routes of *Silurus* inferred from biogeographic analyses at different time scales**

A: 25–20 Ma. B: 20–15 Ma. C: 15–10 Ma. D: 4–0 Ma. A, B, and C on each map represent three recognized biogeographical regions, i.e., China and Korean Peninsula, Europe and Central and Western Asia, and Japan, respectively.

hypotheses. Additional morphological and phylogenetic evidence is required to clarify the taxonomic status of each MOTU under the criteria of secondary species hypotheses. Furthermore, the species diversity within the genus *Silurus* has likely been seriously underestimated, necessitating further investigation with expanded sample ranges and sizes.

## CONCLUSIONS

Our study employed a comprehensive phylogenetic framework and biogeographic history to examine cryptic diversity within the genus *Silurus*. Phylogenetic trees resolved eight main clades and indicated that *S. soldatovi*, *S. lithophilus*, and *S. tomodai* were not monophyletic, as they clustered with different lineages of *S. asotus*. Biogeographic reconstruction identified China and the Korean Peninsula as the regions of origin, with multiple dispersal events triggered by the Eocene-Oligocene extinction event, onset and intensification of the monsoon system, recurrent marine transgression and regression, and glacial cycles. In addition, DNA-based delimitation identified four and two MOTUs in *S. asotus* and *S. microdorsalis*, respectively, although further research is required to clarify their taxonomic status. These findings not only improve our understanding of the phylogenetic relationships and evolutionary history of *Silurus* species but also pave the way for future ichthyological research on this group.

## SUPPLEMENTARY DATA

Supplementary data to this article can be found online.

## COMPETING INTERESTS

The authors declare that they have no competing interests.

## AUTHORS' CONTRIBUTIONS

W.T.C., N.H., and J.L. conceived and designed the project. W.T.C., Y.F.L., S.L.Z., J.W., D.G.X., S.G., C.N.K., J.LW., T.W., Z.Q.L., J.J.W., and X.H.L. performed sample collection. W.T.C. and N.H. prepared and edited the draft of the manuscript. All authors read and approved the final version of the manuscript.


## ACKNOWLEDGMENTS

We are grateful to Prof. Zuo-Gang Peng in the Southwest University for contributing valuable tissue samples.


## REFERENCES


Alam MJ, Khalil MAS, Kim KS, et al. 2019. Characterization of the complete mitochondrial genome of *Silurus soldatovi* in Korean River. *Mitochondrial DNA Part B*, **4**(2): 3886–3887.

Alfaro ME, Santini F, Brock C, et al. 2009. Nine exceptional radiations plus high turnover explain species diversity in jawed vertebrates. *Proceedings of the National Academy of Sciences of the United States of America*, **106**(32): 13410–13414.

Benton MJ, Donoghue PCJ, Asher RJ, et al. 2015. Constraints on the timescale of animal evolutionary history. *Palaeontologia Electronica*, **18**(1): 1–107.

Bickford D, Lohman DJ, Sodhi NS, et al. 2007. Cryptic species as a window on diversity and conservation. *Trends in Ecology & Evolution*, **22**(3): 148–155.

Bloch ME. 1794. Naturgeschichte der Ausländischen Fische, Vol. 8. i-iv + 1-174. Berlin, 361–396.

Britz R, Win T. 2010. Redescription of *Silurus burmanensis* thant 1967: a *Silurus* not a *Pterocryptis* (Teleostei: Siluriformes: Siluridae). *Zootaxa*, **2647**(1): 61–68.

Chen HL. 1977. A review of the Chinese Siluridae. *Acta Hydrobiologica Sinica*, **6**(2): 197–218. (in Chinese)

Chen WT, Hubert N, Li YF, et al. 2022. Large‐scale DNA barcoding of the subfamily Culterinae (Cypriniformes: Xenocyprididae) in east Asia unveils a geographical scale effect, taxonomic warnings and cryptic diversity. *Molecular Ecology*, **31**(14): 3871–3887.

Chen WT, Li C, Chen FC, et al. 2020. Phylogeographic analyses of a migratory freshwater fish (*Megalobrama terminalis*) reveal a shallow genetic structure and pronounced effects of sea-level changes. *Gene*, **737**: 144478.

Chen WT, Zhong ZX, Dai W, et al. 2017. Phylogeographic structure, cryptic speciation and demographic history of the sharpbelly (*Hemiculter leucisculus*), a freshwater habitat generalist from Southern China. *BMC Evolutionary Biology*, **17**(1): 216.

Cheng PL. 2015. Studies on Phylogenetic Pattern and Macroevolutionary Characteristics of the East Asian Endemic Group of Cyprinids. Ph. D. dissertation, University of Chinese Academy of Sciences, Beijing. (in Chinese)

Chu XL, Chen YR. 1989. The Fishes of Yunnan. Beijing: Science Press. (in Chinese)

Chu XL, Zheng BS, Dai DY. 1999. Fauna Sinica, Class Teleostei, Siluriformes. Beijing: Science Press. (in Chinese)

Cicconardi F, Fanciulli PP, Emerson BC. 2013. Collembola, the biological species concept and the underestimation of global species richness. *Molecular Ecology*, **22**(21): 5382–5396.

Clift PD, Hodges KV, Heslop D, et al. 2008. Correlation of Himalayan exhumation rates and Asian monsoon intensity. *Nature Geoscience*, **1**(12): 875–880.

Clift PD, Plumb RA. 2008. The Asian Monsoon: Causes, History and Effects. Cambridge: Cambridge University Press.

Colin C, Siani G, Sicre MA, et al. 2010. Impact of the east Asian monsoon rainfall changes on the erosion of the Mekong River Basin over the past 25, 000 yr. *Marine Geology*, **271**(1-2): 84–92.

Copp GH, Robert Britton J, Cucherousset J, et al. 2009. Voracious invader or benign feline? A review of the environmental biology of European catfish *Silurus glanis* in its native and introduced ranges. *Fish and Fisheries*, **10**(3): 252–282.

Crisp MD, Arroyo MTK, Cook LG, et al. 2009. Phylogenetic biome conservatism on a global scale. *Nature*, **458**(7239): 754–756.

Donoghue MJ. 2008. A phylogenetic perspective on the distribution of plant diversity. *Proceedings of the National Academy of Sciences of the United States of America*, **105**(S1): 11549–11555.

Drummond AJ, Rambaut A. 2007. BEAST: Bayesian evolutionary analysis by sampling trees. *BMC Evolutionary Biology*, **7**: 214.

Edgar RC. 2004. MUSCLE: multiple sequence alignment with high accuracy and high throughput. *Nucleic Acids Research*, **32**(5): 1792–1797.

Fara E, Gayet M, Taverne L. 2010. The fossil record of Gonorynchiformes. *In*: Grande T. Gonorynchiformes and Ostariophysan Relationships: A Comprehensive Review. Boca Raton: CRC Press, 173–226.

Favre A, Päckert M, Pauls SU, et al. 2015. The role of the uplift of the Qinghai‐Tibetan Plateau for the evolution of Tibetan biotas. *Biological Reviews*, **90**(1): 236–253.

Feng CG, Wang K, Xu WJ, et al. 2023. Monsoon boosted radiation of the endemic east Asian carps. *Science China Life Sciences*, **66**(3): 563–578.

Fujisawa T, Barraclough TG. 2013. Delimiting species using single-locus data and the generalized mixed Yule coalescent approach: a revised method and evaluation on simulated data sets. *Systematic Biology*, **62**(5): 707–724.

Gao S, Li YF, Li J, et al. 2023. Genetic structure and demographic history of *Mastacembelus armatus* in Southern China. *South China Fisheries Science*, **19**(2): 42–49. (in Chinese)

Gao Y, Kim SG, Lee JY. 2011. Effects of pH on fertilization and the

hatching rates of far eastern catfish *Silurus asotus*. *Fisheries and Aquatic Sciences*, **14**(4): 417–420.

Gao Y, Wang SY, Luo J, et al. 2012. Quaternary palaeoenvironmental oscillations drove the evolution of the Eurasian *Carassius auratus* complex (Cypriniformes, Cyprinidae). *Journal of Biogeography*, **39**(12): 2264–2278.

Garman S. 1890. *Silurus* (Parasilurus) *aristotelis*. *Bulletin of the Essex Institute*, **22**: 56–59.

Guo XG, He SP, Zhang YG. 2005. Phylogeny and biogeography of Chinese sisorid catfishes re-examined using mitochondrial cytochrome *b* and 16S rRNA gene sequences. *Molecular Phylogenetics and Evolution*, **35**(2): 344–362.

Guo ZT, Ruddiman WF, Hao QZ, et al. 2002. Onset of Asian desertification by 22 Myr ago inferred from loess deposits in China. *Nature*, **416**(6877): 159–163.

Hamilton F. 1822. An Account of the Fishes Found in the River Ganges and Its Branches. Edinburgh: Constable.

He DK, Chen YF. 2006. Biogeography and molecular phylogeny of the genus *Schizothorax* (Teleostei : Cyprinidae) in China inferred from cytochrome *b* sequences. *Journal of Biogeography*, **33**(8): 1448–1460.

He SP, Cao WX, Chen YY. 2001. The uplift of Qinghai–Xizang (Tibet) Plateau and the vicariance speciation of glyptosternoid fishes (Siluriformes: Sisoridae). *Science in China Series C: Life Sciences*, **44**(6): 644–651.

Heckel JJ. 1843. Ichthyologie in Russeger's Reisen. *Stuttg*, **8**: 234.

Hibino Y, Tabata R. 2018. Description of a new catfish, *Silurus tomodai* (Siluriformes: Siluridae) from central Japan. *Zootaxa*, **4459**(3): 507–524.

Hoorn C, Wesselingh FP, Ter Steege H, et al. 2010. Amazonia through time: Andean uplift, climate change, landscape evolution, and biodiversity. *Science*, **330**(6006): 927–931.

Hotaling S, Borowiec ML, Lins LSF, et al. 2021. The biogeographic history of eelpouts and related fishes: linking phylogeny, environmental change, and patterns of dispersal in a globally distributed fish group. *Molecular Phylogenetics and Evolution*, **162**: 107211.

Hren MT, Sheldon ND, Grimes ST, et al. 2013. Terrestrial cooling in northern Europe during the Eocene-Oligocene transition. *Proceedings of the National Academy of Sciences of the United States of America*, **110**(19): 7562–7567.

Hu XY, Lan JH, Zhang CG. 2004. A new species of the genus *Duanensis* (Siluriformes, Siluridae) from Guangxi China. *Acta Zootaxonomica Sinica*, **29**(3): 586–590. (in Chinese)

Hubert N, Renno JF. 2006. Historical biogeography of south American freshwater fishes. *Journal of Biogeography*, **33**(8): 1414–1436.

Ivany LC, Patterson WP, Lohmann KC. 2000. Cooler winters as a possible cause of mass extinctions at the Eocene/Oligocene boundary. *Nature*, **407**(6806): 887–890.

Iwasaki W, Fukunaga T, Isagozawa R, et al. 2013. MitoFish and MitoAnnotator: a mitochondrial genome database of fish with an accurate and automatic annotation pipeline. *Molecular Biology and Evolution*, **30**(11): 2531–2540.

Jeon HB, Song HY, Suk HY, et al. 2022. Phylogeography of the Korean endemic *Coreoleuciscus* (Cypriniformes: Gobionidae): the genetic evidence of colonization through Eurasian continent to the Korean Peninsula during Late Plio-Pleistocene. *Genes & Genomics*, **44**(6): 709–719.

Jetz W, Thomas GH, Joy JB, et al. 2014. Global distribution and conservation of evolutionary distinctness in birds. *Current Biology*, **24**(9): 919–930.

Jia GD, Peng PA, Zhao QH, et al. 2003. Changes in terrestrial ecosystem since 30 Ma in east Asia: stable isotope evidence from black carbon in the South China Sea. *Geology*, **31**(12): 1093–1096.

Jiang ZG, Jiang JP, Wang YZ, et al. 2016. Red list of China's vertebrates. *Biodiversity Science*, **24**(5): 500–551. (in Chinese)

Kapli P, Lutteropp S, Zhang J, et al. 2017. Multi-rate Poisson tree processes for single-locus species delimitation under maximum likelihood and Markov chain Monte Carlo. *Bioinformatics*, **33**(11): 1630–1638.

Kappas I, Vittas S, Pantzartzi CN, et al. 2016. A time-calibrated mitogenome phylogeny of catfish (Teleostei: Siluriformes). *PLoS One*, **11**(12): e0166988.

Kearse M, Moir R, Wilson A, et al. 2012. Geneious basic: an integrated and extendable desktop software platform for the organization and analysis of sequence data. *Bioinformatics*, **28**(12): 1647–1649.

Kim KY, Nam YK, Bang IC. 2012. Phylogeny and divergence time estimation of *Coreoleuciscus splendidus* populations (Teleostei: Cypriniformes) endemic to Korea based on complete mitogenome sequences. *Genes & Genomics*, **34**(2): 149–156.

Kimura M. 1980. A simple method for estimating evolutionary rates of base substitutions through comparative studies of nucleotide sequences. *Journal of Molecular Evolution*, **16**(2): 111–120.

Kishimoto Y, Okuyama H, Takahashi JI. 2022. Complete mitochondrial DNA sequence of the eastern Asian catfish *Silurus asotus* (Siluriformes: Siluridae) from Lake Biwa in Japan. *Mitochondrial DNA Part B*, **7**(2): 356–357.

Kocsis ÁT, Scotese CR. 2021. Mapping paleocoastlines and continental flooding during the Phanerozoic. *Earth-Science Reviews*, **213**: 103463.

Lacepède BGE. 1803. Histoire Naturelle des Poissons (Tome cinquième). Paris: Chez Plassan.

Lanfear R, Calcott B, Ho SYW, et al. 2012. PartitionFinder: combined selection of partitioning schemes and substitution models for phylogenetic analyses. *Molecular Biology and Evolution*, **29**(6): 1695–1701.

Leonardos ID, Tsikliras AC, Batzakas I, et al. 2009. Life‐history characteristics of the endangered Aristotle's catfish (*Silurus aristotelis* Garman, 1890), Lake Pamvotis, north‐western Greece. *Journal of Applied Ichthyology*, **25**(6): 746–751.

Li J, Li XH, Zhang G, et al. 2019. A diminutive new species of *Silurus* (Teleostei: Siluridae) from Guangxi, Southern China. *Ichthyological Exploration of Freshwaters*, **29**(40): 305–312.

Linnaeus C. 1758. Systema Naturae (Vol. 1). 10th ed. Holmiae: Laurentii Salvii.

Liu ZF, Wang H, Hantoro WS, et al. 2012. Climatic and tectonic controls on chemical weathering in tropical southeast Asia (Malay Peninsula, Borneo, and Sumatra). *Chemical Geology*, **291**: 1–12.

Loannis L, Lfigenia K, Triantafyllidis A. 2007. Threatened fishes of the world: *Silurus aristotelis* (Agassiz 1856) (Siluridae). *Environmental Biology of Fishes*, **78**(3): 285–286.

Lu HY, Guo ZT. 2014. Evolution of the monsoon and dry climate in east Asia during Late Cenozoic: a review. *Science China Earth Sciences*, **57**(1): 70–79.

Lu YR, Fang CC, He SP. 2023. cnfishbase: A cyber Chinese fish database. *Zoological Research*, **44**(5): 950–953.

Luo YP, Xie XJ. 2008. Effects of temperature on the specific dynamic action of the southern catfish, *Silurus meridionalis*. *Comparative Biochemistry and Physiology Part A*: *Molecular & Integrative Physiology*, **149**(2): 150–156.

Mabuchi K, Nishida K, Nakajima N. 2020. The complete mitochondrial genome of *Silurus lithophilus*, a catfish endemic to Lake Biwa, Japan. *Mitochondrial DNA Part B*, **5**(2): 1311–1312.

Meng GL, Li YY, Yang CT, et al. 2019. MitoZ: a toolkit for animal mitochondrial genome assembly, annotation and visualization. *Nucleic Acids Research*, **47**(11): e63.

Molnar P. 2005. Mio-Pliocene growth of the Tibetan Plateau and evolution of east Asian climate. *Palaeontologia Electronica*, **8**(1): 2A.

Mori T. 1936. Studies on the geographical distribution of freshwater fishes in chosen. *Bulletin of the Biogeographical Society of Japan*, **6**: 35–61.

Murphy NP, Austin CM. 2005. Phylogenetic relationships of the globally distributed freshwater prawn genus *Macrobrachium* (Crustacea: Decapoda:

Palaemonidae): biogeography, taxonomy and the convergent evolution of abbreviated larval development. *Zoologica Scripta*, **34**(2): 187–197.
Ng HH, Kottelat M. 2013. After eighty years of misidentification, a name for the glass catfish (Teleostei: Siluridae). *Zootaxa*, **3630**(2): 308–316.
Nikolskii GV, Soin SG. 1948. On catfishes (family Siluridae) in the Amur Basin. *Doklady Akademii Nauk SSSR*, **59**(7): 1357–1360.
Nylander JAA. 2004. MrModeltest Version 2. Program Distributed by the Author. Uppsala: Evolutionary Biology Centre, Uppsala University.
Olden JD, Kennard MJ, Leprieur F, et al. 2010. Conservation biogeography of freshwater fishes: recent progress and future challenges. *Diversity and Distributions*, **16**(3): 496–513.
Park CE, Park YJ, Kim MC, et al. 2020. The first complete mitochondrial genome sequence of the korean endemic catfish *Silurus microdorsalis* (Actinopteri, Siluriformes, Siluridae). *Mitochondrial DNA Part B*, **5**(1): 131–132.
Patel RK, Jain M. 2012. NGS QC Toolkit: a toolkit for quality control of next generation sequencing data. *PLoS One*, **7**(2): e30619.
Pfenninger M, Schwenk K. 2007. Cryptic animal species are homogeneously distributed among taxa and biogeographical regions. *BMC Evolutionary Biology*, **7**: 121.
Puillandre N, Lambert A, Brouillet S, et al. 2012. ABGD, automatic barcode gap discovery for primary species delimitation. *Molecular Ecology*, **21**(8): 1864–1877.
Rafinesque CS. 1818. Description of a new species of north American marten, (*Mustela vulpina*). *American Journal of Science*, **1**: 82.
Rambaut A, Drummond A. 2007[2022-01-21]. Tracer v1.4. http://beast.bio.ed.ac.uk.Tracer.
Regan CT. 1904. XX. —On a collection of fishes made by Mr. John Graham at Yunnan Fu. *Annals and Magazine of Natural History*, **13**(75): 190–194.
Richardson J. 1846. Report on the Ichthyology of the Seas of China and Japan. London: Richard and John E. Taylor.
Ronquist F, Huelsenbeck JP. 2003. MrBayes 3: Bayesian phylogenetic inference under mixed models. *Bioinformatics*, **19**(12): 1572–1574.
Satler JD, Carstens BC, Hedin M. 2013. Multilocus species delimitation in a complex of morphologically conserved trapdoor spiders (Mygalomorphae, Antrodiaetidae, *Aliatypus*). *Systematic Biology*, **62**(6): 805–823.
Schedel FDB, Chakona A, Sidlauskas BL, et al. 2022. New phylogenetic insights into the African catfish families mochokidae and Austroglanididae. *Journal of Fish Biology*, **100**(5): 1171–1186.
Scotese C, Wright N. 2018[2023-01-21]. PALEOMAP paleodigital elevation models (PaleoDEMS) for the Phanerozoic Project. Paleomap Proj.https://www.earthbyte.org/paleodem-resource.
Sholihah A, Delrieu-Trottin E, Condamine FL, et al. 2021a. Impact of Pleistocene eustatic fluctuations on evolutionary dynamics in southeast Asian biodiversity hotspots. *Systematic Biology*, **70**(5): 940–960.
Sholihah A, Delrieu-Trottin E, Sukmono T, et al. 2021b. Limited dispersal and in situ diversification drive the evolutionary history of Rasborinae fishes in Sundaland. *Journal of Biogeography*, **48**(9): 2153–2173.
Siler CD, Diesmos AC, Alcala AC, et al. 2011. Phylogeny of Philippine slender skinks (Scincidae: *Brachymeles*) reveals underestimated species diversity, complex biogeographical relationships, and cryptic patterns of lineage diversification. *Molecular Phylogenetics and Evolution*, **59**(1): 53–65.
Smith SA, Stephens PR, Wiens JJ. 2005. Replicate patterns of species richness, historical biogeography, and phylogeny in Holarctic treefrogs. *Evolution*, **59**(11): 2433–2450.
Stamatakis A. 2006. RAxML-VI-HPC: maximum likelihood-based phylogenetic analyses with thousands of taxa and mixed models. *Bioinformatics*, **22**(21): 2688–2690.
Swenson NG. 2011. The role of evolutionary processes in producing biodiversity patterns, and the interrelationships between taxonomic, functional and phylogenetic biodiversity. *American Journal of Botany*, **98**(3): 472–480.
Székvári K, Szabolcsi Z, Kutasy B, et al. 2021. New complete mitogenome datasets and their characterization of the European catfish (*Silurus glanis*). *Data in Brief*, **38**: 107418.
Tabata R, Kakioka R, Tominaga K, et al. 2016. Phylogeny and historical demography of endemic fishes in Lake Biwa: the ancient lake as a promoter of evolution and diversification of freshwater fishes in western Japan. *Ecology and Evolution*, **6**(8): 2601–2623.
Tamura K, Stecher G, Peterson D, et al. 2013. MEGA6: molecular evolutionary genetics analysis version 6.0. *Molecular Biology and Evolution*, **30**(12): 2725–2729.
Thant MK. 1966. *Silurus burmanensis*, a new species of fish from the Inlé Lake, southern Shan State, Burma. *Journal of the Burma Research Society*, **49**: 219–221.
Tomoda Y. 1961. Two new catfishes of the genus *Parasilurus* found in Lake Biwa-ko. *Memoirs of the College of Science, University of Kyoto. Series B*, **28**(3): 347–354.
Tsao YF, Lin WW, Chang CH, et al. 2016. Phylogeography, historical demography, and genetic structure of the Rose Bitterling, *Rhodeus ocellatus* (Kner, 1866) (Cypriniformes: Acheilognathidae), in east Asia. *Zoological Studies*, **55**: e49.
Utami CY, Sholihah A, Condamine FL, et al. 2022. Cryptic diversity impacts model selection and macroevolutionary inferences in diversification analyses. *Proceedings of the Royal Society B: Biological Sciences*, **289**(1987): 20221335.
Valenciennes A. 1840. Siluroidei. Cuvier G, Valenciennes A. Natural History of the Fishes. Paris and Strasbourg: Chez PITOIS.
Vittas S, Drosopoulou E, Kappas I, et al. 2011. The mitochondrial genome of the European catfish *Silurus glanis* (Siluriformes, Siluridae). *Journal of Biological Research*, **15**: 25–35.
von Wissmann H. 1937. The Pleistocene glaciation in China. *Acta Geologica Sinica: English Edition*, **17**(2): 145–168.
Voris HK. 2000. Maps of Pleistocene sea levels in southeast Asia: shorelines, river systems and time durations. *Journal of Biogeography*, **27**(5): 1153–1167.
Wang JP, Hsu KC, Chiang TY. 2000. Mitochondrial DNA phylogeography of *Acrossocheilus paradoxus* (Cyprinidae) in Taiwan. *Molecular Ecology*, **9**(10): 1483–1494.
Wang K, Xu J, Cui J, et al. 2015a. Complete mitochondrial genome of northern Sheatfish (*Silurus soldatovi*). *Mitochondrial DNA*, **26**(6): 891–892.
Wang QR, Xu C, Xu CR, et al. 2015b. Complete mitochondrial genome of the southern catfish (*Silurus meridionalis* Chen) and Chinese catfish (*S. asotus* Linnaeus): structure, phylogeny, and intraspecific variation. *Genetics and Molecular Research*, **14**(4): 18198–18209.
Winter M, Devictor V, Schweiger O. 2013. Phylogenetic diversity and nature conservation: where are we?. *Trends in Ecology & Evolution*, **28**(4): 199–204.
Wu JJ, Lei CY, Zhao JX, et al. 2021. The complete mitochondrial genome of *Silurus grahami* Regan, 1907 (Siluriformes: Siluridae), a native catfish in Fuxian Lake. *Mitochondrial DNA Part B*, **6**(3): 835–836.
Xia XH. 2013. DAMBE5: a comprehensive software package for data analysis in molecular biology and evolution. *Molecular Biology and Evolution*, **30**(7): 1720–1728.
Xia XH, Lemey P. 2009. Assessing substitution saturation with DAMBE. *In*: Lemey P, Salemi M, Vandamme AM. The Phylogenetic Handbook: A Practical Approach to Phylogenetic Analysis and Hypothesis Testing. 2nd ed. Cambridge: Cambridge University Press, 615–630.
Xu DD, Huang Y, Zeng Q, et al. 2017. Genetic diversity and population history among geographic populations of *Silurus asotus* in different water systems in China based on mtDNA *Cytb* gene sequences. *Journal of*

*Fisheries of China*, **41**(10): 1489–1499. (in Chinese)

Yang B, Chen XY, Yang JX. 2008. Threatened fishes of the world: *Silurus mento* Regon, 1904 (Siluriformes: Siluridae). *Environmental Biology of Fishes*, **83**(3): 307.

Yang J, Yang JX, Chen XY. 2012a. A re-examination of the molecular phylogeny and biogeography of the genus *Schizothorax* (Teleostei: Cyprinidae) through enhanced sampling, with emphasis on the species in the Yunnan-Guizhou Plateau, China. *Journal of Zoological Systematics and Evolutionary Research*, **50**(3): 184–191.

Yang JQ, Tang WQ, Liao TY, et al. 2012b. Phylogeographical analysis on *Squalidus argentatus* recapitulates historical landscapes and drainage evolution on the island of Taiwan and Mainland China. *International Journal of Molecular Sciences*, **13**(2): 1405–1425.

Yang N, Li YW, Liu ZH, et al. 2019. The complete mitochondrial genome of *Silurus asotus* (Siluriformes: Siluridae: *Silurus*) and its phylogenetic analysis. *Mitochondrial DNA Part B*, **4**(2): 2377–2378.

Yang ZH. 2007. PAML 4: phylogenetic analysis by maximum likelihood. *Molecular Biology and Evolution*, **24**(8): 1586–1591.

Yu Y, Blair C, He XJ. 2020. RASP 4: ancestral state reconstruction tool for multiple genes and characters. *Molecular Biology and Evolution*, **37**(2): 604–606.

Zachos J, Pagani M, Sloan L, et al. 2001. Trends, rhythms, and aberrations in global climate 65 Ma to present. *Science*, **292**(5517): 686–693.

Zeng Q, Wang ZJ, Peng ZG. 2011. Mitochondrial genome of *Silurus asotus* (Teleostei: Siluriformes). *Mitochondrial DNA*, **22**(5-6): 162–164.

Guan et al. *Zool. Res.* 2024, 45(4): 724−746
https://doi.org/10.24272/j.issn.2095-8137.2023.397

ZR | Zoological Research

Review Open Access

# Skeletal phenotypes and molecular mechanisms in aging mice

Qiao Guan[1], Yuan Zhang[2], Zhi-Kun Wang[1], Xiao-Hua Liu[1], Jun Zou[1], Ling-Li Zhang[2,*]

[1] *School of Exercise and Health*, *Shanghai University of Sport*, *Shanghai* 200438, *China*
[2] *College of Athletic Performance*, *Shanghai University of Sport*, *Shanghai* 200438, *China*

## ABSTRACT

Aging is an inevitable physiological process, often accompanied by age-related bone loss and subsequent bone-related diseases that pose serious health risks. Research on skeletal diseases caused by aging in humans is challenging due to lengthy study durations, difficulties in sampling, regional variability, and substantial investment. Consequently, mice are preferred for such studies due to their similar motor system structure and function to humans, ease of handling and care, low cost, and short generation time. In this review, we present a comprehensive overview of the characteristics, limitations, applicability, bone phenotypes, and treatment methods in naturally aging mice and prematurely aging mouse models (including *SAMP6*, *POLG* mutant, *LMNA*, *SIRT6*, *ZMPSTE24*, *TFAM*, *ERCC1*, *WERNER*, and *KL/KL*-deficient mice). We also summarize the molecular mechanisms of these aging mouse models, including cellular DNA damage response, senescence-related secretory phenotype, telomere shortening, oxidative stress, bone marrow mesenchymal stem cell (BMSC) abnormalities, and mitochondrial dysfunction. Overall, this review aims to enhance our understanding of the pathogenesis of aging-related bone diseases.

**Keywords:** Aging; Premature aging; Mice; Bone; Gene knockout

## INTRODUCTION

The global population is aging. According to the World Health Organization (WHO), individuals are categorized as young if they are under 44 years old, middle-aged if they are 45–59 years old, young elderly if they are 60–74 years old, elderly if they are 75–89 years old, and longevity elderly if they are over 90 years old. At present, approximately 1 in 11 people worldwide are 65 years of age or older, a number predicted to increase to one in six people by 2050 (United Nations, 2019). Diseases of the skeletal system, such as osteoporosis (OP), are commonly associated with aging. Bone provides leverage and structural support to muscles, promotes movement, stores minerals and growth factors, regulates mineral and acid-base balance, and serves as a site for hematopoiesis. Peak bone mass typically occurs before the age of 40 in both sexes. Women experience significant bone loss around menopause, accounting for approximately one-third of the total calcium mass in bone. This rapid bone loss occurs during the perimenopausal period, which lasts approximately 8 to 10 years. In men, bone mass decreases progressively from age 60, with age-related bone loss occurring at the same rate from age 70 in both men and women (Pignolo, 2023). Therefore, studying the effects of aging on bone is critical.

A suitable animal model of aging is essential for in-depth studies of the etiology, pathology, development, and mechanisms of age-related diseases, as well as for screening and developing antiaging drugs. At present, commonly used models for exploring aging include *Drosophila*, nematodes, mice, rabbits, and nonhuman primates. Mice, in particular, share many aspects of bone biology with humans, including patterns of aging-related bone loss, bone turnover, and bone healing (Foessl et al., 2021). Moreover, the mouse genome is highly similar to the human genome, and advanced gene manipulation technologies allow for detailed studies of disease pathogenesis via gene knockout. As such, mice are considered a more suitable animal model for exploring human-related diseases and the effects of aging on bone compared to other animal models. Herein, we summarize the characteristics, limitations, applicability, bone phenotypes, and treatment approaches for both naturally aging mice and prematurely aging mouse models (including *SAMP6*, POLG mutant, *LMNA*, *SIRT6*, *ZMPSTE24*, *TFAM*, *ERCC1*, *WERNER*, and *KL/KL* -deficient mice).

## ANIMAL MODELS OF AGING

The selection of appropriate animal models is crucial for aging

This is an open-access article distributed under the terms of the Creative Commons Attribution Non-Commercial License (http://creativecommons.org/licenses/by-nc/4.0/), which permits unrestricted non-commercial use, distribution, and reproduction in any medium, provided the original work is properly cited.
Copyright ©2024 Editorial Office of Zoological Research, Kunming Institute of Zoology, Chinese Academy of Sciences

Received: 19 February 2024; Accepted: 28 March 2024; Online: 29 March 2024
Foundation items: The work was supported by the National Natural Science Foundation of China (82272608), 2021 Capacity Building of Shanghai Universities (21010503600), and Shanghai Key Lab of Human Performance (Shanghai University of Sport) (11DZ2261100)
*Corresponding author, E-mail: lingliwdc@163.com

research. While current animal models for exploring aging include *Drosophila*, nematodes, rabbits, and nonhuman primates, mice are more suitable for studying the effects of aging on bone due to their comparable skeletal structure, similar physiological and pathophysiological bone processes, lower time and economic costs, and fewer ethical concerns.

Given its simple body structure, lack of many mammalian anatomical and physiological features, including a skeletal system, and evolutionary distance from humans, *Caenorhabditis elegans* cannot adequately reflect the effects of aging on the skeleton (Tissenbaum, 2015). Although *Drosophila* can be used to investigate the regulatory mechanisms of bone morphogenetic proteins (Matsuda et al., 2016), its significantly different body structure from humans makes it unsuitable for bone aging research. Therefore, mammals are generally preferred for such studies, with rodents considered conducive to aging-related research due to their availability, environmental adaptability, low cost, extensive research background, and genetic manipulability. Their short lifespan compared to humans also facilitates easier study compared to long-lived animals (Mitchell et al., 2015).

In addition to rodents, other animals have been used in studies of bone aging. For example, rhesus monkeys are commonly used in biomedical research due to their genetic, endocrine, physiological, neuroanatomical, and cognitive similarities to humans (Mitchell et al., 2015). Research has shown that forearm bone mineral density (BMD) and whole-body bone mineral content in both male and female rhesus monkeys decrease with age (Black et al., 2001), similar to the changes observed in the human skeleton. However, female rhesus monkeys reach peak bone mass at 11 years of age (Champ et al., 1996), which is later than occurs in humans. Furthermore, in addition to their expense, the strict social hierarchy and potentially aggressive behavior of monkeys necessitate special care and unique environments, with ethical issues further limiting their use in research (Mitchell et al., 2015). Research has shown that *LMNA* knockout (KO) rabbits exhibit reduced cortical bone width, significantly reduced osteoblasts and osteoclasts, irregularly arranged growth plates, and increased porous areas (Sui et al., 2019), consistent with observations in progeria patients and mice harboring *LMNA* gene mutations (Mounkes et al., 2003; Schmidt et al., 2012). However, rabbits have a lifespan of 9–10 years (Lennox, 2010), which makes their use in experiments relatively long and costly compared to rodents. Additionally, there are fewer studies on aging-associated OP using rabbits than mice. Although rats are also used to study aging-related OP, with both sexes showing declines in bone density and bone mass, as well as increased bone marrow fat and decreased bone turnover with age, as observed in humans (Al Saedi et al., 2020; Duque et al., 2009), mice offer significant advantages. Mice are physiologically similar to rats and are suitable for molecular genetic studies on aging and age-related human diseases (Duque et al., 2009). They are also more cost effective to maintain, require less space, and have a much shorter lifecycle of 1–3 years (Dutta & Sengupta, 2016). Furthermore, while genetic manipulation technology for rats has advanced, mouse genome experimental technology remains superior. The first generation of knockout rats were created using zinc finger nuclease technology in 2009 (Geurts et al., 2009), followed shortly thereafter by the first knockout rats generated using modified embryonic stem cells (Tong et al., 2010). With the advent of CRISPR/Cas9, rats are expected to be more widely used for genome engineering research (Homberg et al., 2017). However, targeted gene mutagenesis in mouse embryonic stem cells began as early as 1987 (Thomas & Capecchi, 1987), with knockout techniques in use from 1989 (Capecchi, 1989). Advancements in genome manipulation technologies have enabled researchers to mimic human genetic defects and mutations in mice through knockouts, mutations, and transgenesis. This has established mice as the preferred model for mammalian biology and genetic disease research, particularly for studying genetic deletions and their impact on bone loss. Consequently, mice are superior to other models, including rats, for in-depth studies on bone aging through gene knockout.

## BONE PHENOTYPES IN NATURALLY AGED MICE

### Definition and bone phenotype of naturally aged mice

Natural aging mouse models involve maintaining mice under laboratory conditions until they reach the desired age. The classification of age and aging in such mice can vary. Wang et al. (2020) categorized mice as adults at 6–10 months, late adults at 13–14 months, and old mice at 18–24 months. Supporting this, several studies have shown that C57Bl/6J, DBA/2J, A/J, and 129/SvJ strain mice older than 18 months have markedly lower motor activity compared to mice under six months of age (Bordner et al., 2011; Fahlström et al., 2012; Forster et al., 1996; Goodrick, 1975; Hengemihle et al., 1999; Ingram et al., 1981; Lhotellier & Cohen-Salmon, 1989; Meliska et al., 1997; Sprott & Eleftheriou, 1974). Radulescu et al. (2021) defined age categories for inbred laboratory mice (*Mus musculus*) as juveniles (birth to one month), young adults (1–4 months), adults (4–10 months), late adults (10–14 months), aging adults (14–24 months), and aged adults (>24 months), while other studies have classified mice as young (one month) (Hoerder-Suabedissen & Molnár, 2015), young adults (3–6 months) (Flurkey et al., 2007), middle-aged adults (6–14 months) (Lesné et al., 2006), and old adults (14–24 months) (Flurkey et al., 2007). Naturally aging mice are characterized by decreased immune function (Segre & Segre, 1977), decreased cognitive function, including impaired learning and memory formation (Murphy et al., 2006), and poor performance in hippocampal-dependent memory paradigms such as the Morris water maze, environmental fear conditioning, and object location recognition tasks (Neff et al., 2013). Most notably, naturally aging mice exhibit signs of senile OP (SOP) (Perkins et al., 1994).

In theory, natural aging mouse models closely mirror human aging and avoid the need for drug administration or surgery, reducing the risk of unexpected complications. However, these models have several disadvantages. For example, obtaining old mice is challenging due to inconsistent sources, the lengthy time required for young mice to age, high costs, poor health conditions, high mortality rates, and significant variability in drug absorption, metabolism, and distribution. Therefore, artificial aging mouse models are often used in experimental studies.

C57BL/6 laboratory mice, which typically live for 2–3 years, reach peak bone mass at 4–8 months and experience declines in bone mass and quality with age, leading to SOP (Bikle et al., 2002; Cao et al., 2003; Ferguson et al., 2003; Perkins et al., 1994). Both trabecular (Tb) and cortical bones undergo dynamic changes with age. The trabecular bone

volume fraction (BV/TV) significantly decreases from six weeks to 24 months of age, while cortical thickness increases until peak bone mass, then declines (Bikle et al., 2002). The receptor activator of nuclear factor-kappa B ligand (RANKL), a membrane-associated cytokine expressed by osteoblasts essential for osteoclastogenesis (Yasuda et al., 1998), increases with age and is correlated with cancellous bone volume (Cao et al., 2003). Research has shown that 24–month-old BALB/c mice, a common mouse strain, exhibit reduced osteogenic stem cell proliferative potential, contributing to age-related bone loss (Bergman et al., 1996).

**Mechanisms underlying effects of natural aging on bone**

At present, there are several viewpoints on the mechanisms of bone aging. Firstly, cellular DNA damage responses (DDRs) are considered significant triggers of aging. DNA damage disrupts skeletal homeostasis, and increased DNA damage causes reduced bone formation and bone loss (Hoeijmakers, 2009). Furthermore, the function and efficiency of various DNA repair pathways are thought to decline with age (Stead & Bjedov, 2021). When DNA damage outpaces repair, osteoblasts undergo senescence, resulting in imbalanced bone remodeling. This is evident in models with defective DNA repair, where ataxia-telangiectasia mutated (ATM), a core component of the DNA repair system, is activated upon DNA double-strand breaks to enhance the homologous recombination repair pathway (Jin & Oh, 2019). ATM is a kinase and an important effector of the DDR signaling pathway (Maréchal & Zou, 2013). ATM-deficient mouse models exhibit reduced bone mass, particularly in Tb, accompanied by reduced bone formation, defective osteoblast differentiation, and increased osteoclast formation (Hishiya et al., 2005; Rasheed et al., 2006). Osteoclasts lacking ATM are more resistant to apoptosis and have longer lifespans (Hirozane et al., 2016), leading to dysregulation of bone remodeling. Secondly, the generation of the senescence-associated secretory phenotype (SASP) accelerates cellular senescence in response to DDRs (Rodier et al., 2009). SASP contains several proinflammatory cytokines (e.g., interleukins), proteases (e.g., matrix metalloproteinases), and growth factors that can affect surrounding cells (Coppé et al., 2010). The production of SASP, in turn, triggers DDR and SASP activation in neighboring cells, generating a proinflammatory environment that extends locally and eventually becomes systemic (Olivieri et al., 2015). Increased proinflammatory SASP in the bone microenvironment acts on osteoblasts to impair bone formation, osteoclasts to increase bone resorption, and mesenchymal stem cells to bias differentiation into adipocytes (Khosla et al., 2022). This leads to fat accumulation in the bone marrow cavity, threatening the survival of osteoblasts (Mirsaidi et al., 2014). In addition, age-related telomere shortening contributes to skeletal aging, with telomere dysfunction inducing defects in osteogenic differentiation by increasing P53/P21 expression and down-regulating Runt-related transcription factor (RUNX2) expression (Wang et al., 2012a). Mouse models exhibiting telomere dysfunction show substantial osteoblast dysfunction, with significantly reduced rates of bone mineral deposition and bone formation (Brennan et al., 2014), as well as enhanced osteoclast function due to a proinflammatory microenvironment (Saeed et al., 2011). Furthermore, oxidative stress during aging negatively impacts bone remodeling. This process involves increased levels of reactive oxygen species (ROS), crucial regulators of bone cell function. The effects of ROS on bone metabolism are twofold. Under physiological conditions, ROS produced by osteoclasts contribute to the accelerated destruction of calcified tissues, thus contributing to bone remodeling (Wauquier et al., 2009). Conversely, during aging, ROS production exceeds the average defense capacity due to the accumulation of dysfunctional mitochondria and progressive inefficiency of antioxidant defense mechanisms (Farr et al., 2016). The increase in ROS levels markedly affects the production and survival of osteoclasts, osteoblasts, and osteocytes (Manolagas, 2010). Previous research has shown that aged B6 mice subjected to oxidative stress exhibit peroxisome proliferator-activated receptor γ (PPARγ) signaling in osteoblasts, which reduces Wnt signaling and decreases osteoblast numbers, thereby inhibiting bone formation and increasing bone adipocyte formation (Almeida et al., 2009). Notably, oxidative stress-induced telomere damage may also accelerate telomere shortening, exacerbating its effects on bone remodeling (Muller, 2009) (Figure 1).

## BONE PHENOTYPE OF PREMATURELY AGING MICE

In addition to natural aging, there is an abnormal pattern known as premature aging. Understanding premature aging is crucial for understanding aging. As such, prematurely aging mice should also be considered in studies related to bone aging.

**SAMP6 premature aging mouse model**

Senescence-accelerated mice (SAM) are a series of rapidly aging mouse models developed by Professors Toshio Takeda and Masanori Hosokawa from Kyoto University, Japan. These mice can be divided into the rapid aging P (SAMP) strain and normal aging R (SAMR) strain (Takeda et al., 1997). After a normal growth period, SAMP mice exhibit rapid and irreversible aging from 4 to 6 months of age, with a significantly shortened lifespan (Mori & Higuchi, 2019). In contrast, SAMR mice age similarly to normal aging mice (Aoyama et al., 2013), with SAMR1 mice often used as a control for SAMP strains (Liu et al., 2022). SAMP mice show increased ROS production by mitochondria and other cellular sites, leading to mitochondrial damage, degradation, and senescence (Manczak et al., 2005). Due to their short lifespan, strain-specific pathological features (Chen et al., 2016), and low bone mass in the vertebrae, femur, and tibia (Chen et al., 2009), SAMP mice have been widely used as experimental models for studying age-related diseases.

The *SAMP6* mouse, a spontaneous OP model, is characterized by low BMD, low peak bone mass, and bone microstructure degradation, uniquely demonstrating bone fragility fractures with aging and significantly lower peak bone mass in 4–5-month-old mice compared to SAMR strains (Matsushita et al., 1986). *SAMP6* mice also exhibit thinner cortical bones, larger periosteal and intraosseous diameters (Chen et al., 2009; Jilka et al., 1996; Matsushita et al., 1986; Silva et al., 2005), lower BV/TV and BMD (Chen et al., 2004, 2005, 2009; Jilka et al., 1996; Matsushita et al., 1986), increased bone marrow cavity and trabecular bone separation (Tb.Sp), decreased maximum elastic stress and load, and reduced osteoblasts (Ji et al., 2023). At four months, *SAMP6* mice display comprehensive SOP with low global BMD, diminished bone marrow osteogenesis, defects in cortical mineralized surfaces, and reduced calcium and phosphorus

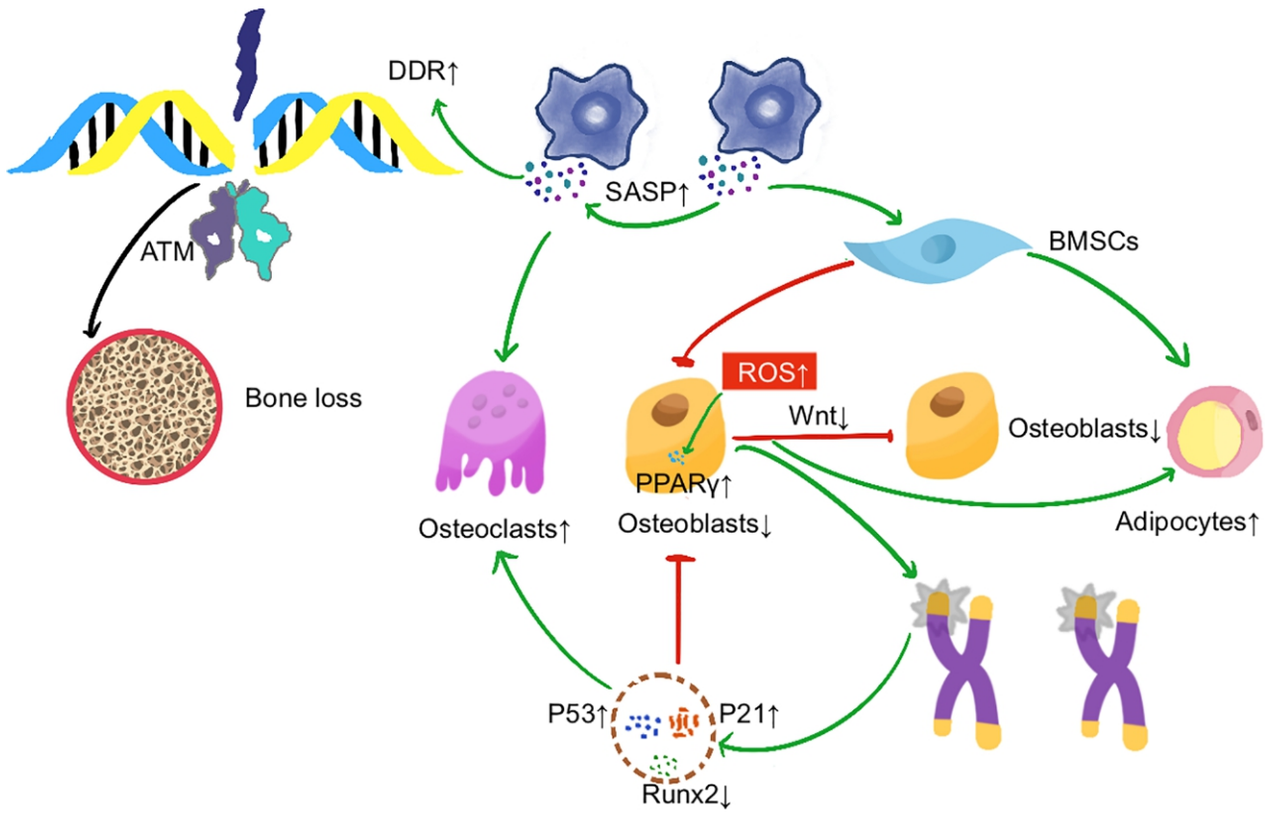



**Figure 1 Naturally aging mouse phenotypes**

The primary viewpoints on the mechanisms of bone aging are as follows. Firstly, increased DNA damage response (DDR) activates ataxia-telangiectasia mutated (ATM), leading to bone loss. Senescence-associated secretory phenotype (SASP) triggers DDR and SASP activation in neighboring cells. Increased proinflammatory SASP in the bone microenvironment promotes mesenchymal stem cell differentiation into adipocytes, inhibits osteoblast formation, and promote osteoclast formation. Telomere dysfunction leads to defective osteogenic differentiation and enhanced osteoclast function by up-regulating P53/P21 levels and down-regulating Runx2 levels. Oxidative stress activates PPARγ signaling in osteoblasts. As a result, Wnt signaling and osteoblast number are reduced, inhibiting bone formation and increasing bone adipocyte formation. In addition, oxidative stress accelerates telomere shortening.

levels. Furthermore, *SAMP6* mice are characterized by age-dependent inhibition of osteoblast and osteoclast formation but enhanced adipogenesis, leading to an early disturbance of bone homeostasis (Chen et al., 2009; Ichioka et al., 2002; Niimi & Takahashi, 2014). Osteoblasts and osteocytes in the Tb of *SAMP6* mice at two and five months of age show degenerative changes, including mitochondrial swelling and fragmentation, and myelin-like structures (Chen et al., 2004). Additionally, these mice contain fewer osteoblasts on the Tb and inner surface of the bone (Chen et al., 2004; Jilka et al., 1996) and increased bone marrow adiposity, with a high frequency of spontaneous leg fractures due to OP (Al-Azab et al., 2020; Matsushita et al., 1986; Stein et al., 1999).

Bone marrow transplantation experiments have indicated that the cause of OP in *SAMP6* mice is abnormal BMSCs (Takada et al., 2006). Senescence of bone marrow progenitors disrupts their differentiation, favoring adipogenesis over osteogenesis. This mechanism is thought to be responsible for the low activity and OP of osteoblasts in *SAMP6* mice and older humans (Matsushita et al., 1986). Notably, compared to healthy BALB/c mice, BMSCs from *SAMP6* mice display lower survival, increased apoptosis, increased mitochondrial membrane depolarization, impaired mitochondrial network dynamics, enhanced adipogenic differentiation, and higher accumulation of lipid droplets (Sikora et al., 2021). Aged *SAMP6* mice also demonstrate decreased osteoblasts and accelerated fat production (Takahashi et al., 1994; Kajkenova et al., 1997), along with high levels of secreted frizzled-related protein (Sfrp4) in the bone, which inhibits the Wnt signaling pathway, leading to diminished Wnt signaling in osteoblasts, inhibition of osteoblast proliferation, and decreased BMD (Haraguchi et al., 2016; Nakanishi et al., 2006). In addition, the expression of miR-494-3p in exosomes derived from aged osteocytes in *SAMP6* mice is decreased, inhibiting osteogenic differentiation and accelerating age-related bone mass loss via the PTEN/PI3K/AKT pathway (Yao et al., 2024). Increased adipogenesis in the bone marrow of *SAMP6* mice is also associated with up-regulated PPARγ, the master regulator of adipogenesis (Cao et al., 2015), leading to a significant increase in PPARγ-positive cells (Azuma et al., 2018) and enhanced lipogenesis in the bone. Overall, the bone phenotype of SAMP6 mice is characterized by decreased osteogenesis and increased adipogenesis.

Unlike *LMNA*-deficient mice (Mounkes et al., 2003), *Zmpste24-deficient* mice (Pendás et al., 2002), $polg^{mut/mut}$ mice (Trifunovic et al., 2004), Klotho-deficient mice (Kuro-O et al., 1997), and *ERCC1*-deficient mice (Niedernhofer et al., 2006), the pathogenesis of aging and aging-related diseases in SAM mice is caused by single gene variants, making them similar to humans in this respect (Mori & Higuchi, 2019). In addition, fractures in aged *SAMP6* mice result from low maximal bone mass, consistent with the cause of SOP in humans (Azuma et al., 2018). Single nucleotide polymorphisms on the SFRP4

gene are known to determine BMD in postmenopausal women (Lee et al., 2010), while *SFRP4* is reported to be overexpressed in the bone tissue of SAMP6 mice, suggesting shared molecular genetic pathways in bone mass regulation between humans and mice (Mori & Higuchi, 2019). Although SAMP6 mice exhibit various properties relevant to human SOP, they also possess certain limitations. Notably, they exhibit lower bone mass in the mid-axis and coccygeal regions compared to age-matched SAMR1 mice, with little further reduction in bone mass from 5 to 12 months of age (Chen et al., 2009). In addition, aging, lifespan, and pathological changes can vary markedly in SAMP mice under different feeding environments and dietary conditions, with proper microbial control and environmental management in laboratories shown to delay aging and prolong lifespan (Mori & Higuchi, 2019). SAMP6 mice have been extensively used to explore the pathogenesis, prevention, and treatment of SOP. Notably, studies have shown that compound 125 can up-regulate BMP2, accelerate bone turnover, and increase osteoblast proportion (Zhou et al., 2023), *Dolichos lablab* Linne can up-regulate BMP-2/Smad and Wnt/β-catenin to promote osteoblast and calcified nodule formation (Kim et al., 2023), and orcinol glucoside can alleviate bone mass loss, inhibit osteoclast formation and bone resorption activity, and reduces oxidative stress in osteoclasts (Gong et al., 2022).

**POLG$^{mut/mut}$ premature aging mouse model**

DNA polymerase gamma (polg) is the only DNA polymerase in mitochondria, thought to be responsible for all DNA synthesis reactions, including mitochondrial DNA (mtDNA) replication and repair (Kaguni, 2004). Its exonuclease activity is crucial for preventing errors in mtDNA synthesis *in vivo* (Vanderstraeten et al., 1998). Polg$^{mut/mut}$ mice, generated from mitochondrial mutations in *POLG* (nucleus-encoded catalytic subunit of mtDNA polymerase) (Kujoth et al., 2005; Trifunovic et al., 2004), were the first model to demonstrate the pathogenic role of mtDNA variants in the premature aging phenotype (Trifunovic et al., 2004). *POLG* mutations significantly reduce the 3'–5' exonuclease activity required for proofreading (Kujoth et al., 2005; Trifunovic et al., 2004), leading to the accumulation of mtDNA mutations, accelerated aging, and premature death. Aging in these mice is characterized by alopecia, gray hair, hunchback, decreased physical activity, decreased body weight and BMD, cardiac enlargement, and hypoglycemia (Trifunovic et al., 2004; Yu et al., 2022). The accumulation of mtDNA mutations and deletions results in highly localized mitochondrial dysfunction and increased oxidative stress, which may contribute to the multitarget aging process (Fayet et al., 2002; Larsson, 2010; Lei et al., 2021; Liang et al., 2020). In addition, markers of mitochondrial oxidative damage, such as protein carbonyls, and markers of lipid oxidation, such as 4-hydroxy-2-nonenal, nitrotyrosine, and 8-OHDG, are significantly increased in polg mutant mice (Kolesar et al., 2014). While the levels of mitochondrial complexes I and IV in osteoblasts decrease with age in wild-type (WT) mice, their levels are even lower in polg mutant mice (Dobson et al., 2016).

Whole-body BMD is significantly reduced in polg$^{mut/mut}$ mice at 40 weeks of age, consistent with the clinical features of OP. These mice also exhibit significant kyphosis and a decreasing trend in whole-body bone mineral content to length ratios (Trifunovic et al., 2004), as well as accelerated bone turnover, leading to the sudden occurrence of OP (Dobson et al., 2020). Several studies have shown that mitochondrial dysfunction contributes to the pathogenesis of OP (Miyazaki, 2013; Trifunovic et al., 2004). The mitochondrial dysfunction caused by the *POLG A* mutation results in decreased osteoblast cell density and increased osteoclast cell density, leading to respiratory chain dysfunction in both cell types. This dysfunction enhances osteoclast activity and reduces the ability of osteoblasts to form new bone, leading to a premature osteoporotic phenotype in mutant mice (Dobson et al., 2020). Polg$^{mut/mut}$ mice display increased respiratory chain defects in osteoblasts, providing insight into the pathology and causes of SOP at the protein and cellular levels (Haas, 2019). Given the higher ROS levels associated with the accumulation of mtDNA mutations, polg$^{mut/mut}$ mice also demonstrate telomere attrition, chromosome fusion and breakage, and elevated 8-oxoguanine (8-oxoGua) levels (Liu et al., 2002). Increased 8-oxoGua leads to telomere shortening and impairs mtDNA integrity and mitochondrial function, which, in turn, leads to increased ROS and 8-oxoGua production, further accelerating aging (Yu et al., 2022).

Polg$^{mut/mut}$ model mice are generated by mtDNA mutations. Unlike other aging mouse models, polg$^{mut/mut}$ mice exhibit premature OP due to impaired cellular respiratory chains (Dobson et al., 2020) and increased ROS production resulting from mitochondrial dysfunction (Liu et al., 2002). While they do not fully replicate the complete pathological process of OP, they are valuable for exploring the role of mitochondria in OP. Additionally, polg$^{mut/mut}$ mice can be used to study age-related kyphosis. Highly kyphotic homozygous polg (D257A) mice show extensive osteopenia, more pronounced in the posterior than anterior thoracolumbar spine (Roessinger et al., 2022).

**LMNA premature aging mouse model**

The *LMNA* gene, consisting of 12 exons on chromosome one, encodes lamin A and C, which are integral components of the nuclear envelope (Sui et al., 2019). Mutations in the *LMNA* gene are associated with various human genetic diseases, including Hutchinson-gilford progeria syndrome (HGPS) and mandibuloacral dysplasia (MAD) (Eriksson et al., 2003). HGPS is a sporadic, rare, fatal, autosomal dominant pediatric segmental disease (Ahmed et al., 2018), most commonly caused by mutations in the *LMNA* gene (Scaffidi & Misteli, 2006). Although patients appear normal at birth, symptoms begin to appear in the first few years of life, including severe growth retardation, loss of subcutaneous adipose tissue, alopecia, skin atrophy and wrinkles, micrognathia, delayed tooth eruption, irregular secondary dentin formation, pulp occlusion, and joint stiffness (Gardner & Majka, 1969; Gordon et al., 2007; Merideth et al., 2008; Ullrich & Gordon, 2015), as well as skeletal abnormalities in bone morphology and structure (Gordon et al., 2011). Mutations in lamin A disrupt the nuclear membrane, leading to impaired cellular functions such as DNA repair, gene transcription, and signal transduction (Villa-Bellosta et al., 2013). Moreover, studies have shown that loss of inner lamin A may lead to defects in nuclear function (Gordon et al., 2012).

Various mouse models of progressive HGPS have been established to study the underlying disease mechanisms (Vidak & Foisner, 2016). One model involves the knockout of the mutant *LMNA* allele *LMNA HG*, which produces only the precursor protein and no WT lamin A or lamin C. This knockout mouse exhibits a phenotype similar to that of HGPS children, including alopecia, partial lipodystrophy, OP, and

premature death, but lacks cardiovascular defects (Yang et al., 2005). Homozygous *LMNA HG/HG* mice, which express only progerin but not lamin A or C, show severe skeletal abnormalities, including spontaneous limb fractures, poor bone mineralization, and premature death (Yang et al., 2006). Progerin is a truncated form of prolamin A produced by a point mutation in the *LMNA* gene that activates a hidden splice donor site (De Sandre-Giovannoli et al., 2003). This mutation leads to permanent farnesylation and the accumulation of progerin around the nucleus, resulting in the loss of progerin in the inner nuclear region (Dechat et al., 2008). Another established model involves human *LMNA* carrying the *G608G* mutation on a 164 kb bacterial artificial chromosome, which shows progressive loss of vascular smooth muscle cells, a feature of HGPS patients, but does not display most other pathological features (Varga et al., 2006). The *LMNAL530P/L530P* model, involving exon 9 skipping and resulting in the in-frame deletion of 40 amino acids in the C-terminal globular domain of lamin A and C proteins, exhibits a phenotype that overlaps with HGPS (Hernandez et al., 2010; Mounkes et al., 2003). Another model involves a mouse knockout strain carrying the HGPS mutant gene in the mouse *LMNA* gene, producing a precursor protein due to the aberrant splicing of endogenous lmna Mrna (Osorio et al., 2011). The genetically engineered LMNA-deficient mouse model also exhibits several defects, including growth retardation, muscular dystrophy, and weakened myocardium (Sullivan et al., 1999).

HGPS patients show irregular cortical bones with poor biomechanical properties, extensive osteocyte and osteoblast loss, bone mineralization defects, decreased red bone marrow cells, and significant reductions in long bone type I collagen and osteoblast markers such as alkaline phosphatase (ALP) and osteocalcin (OCN). Bone mineralization defects occur because HGPS mutant osteoblast-specific expression increases DNA damage and affects Wnt signaling, leading to possible inflammation (Schmidt et al., 2012). Similarly, the cortical bones of five-week-old HGPS mice (long bones, spine, thorax, skull, and mandible) show a marked loss of lamellae, an increase in the embedded non-remodeling and nonmineralized matrix, an increase in the number of osteocytes, a decrease in cells in the bone marrow cavity, and an increase in adipocytes in the bone marrow space. These mutant mice exhibit growth retardation, gait imbalance, and spontaneous fractures (Schmidt et al., 2012). The increase in adipocytes may be associated with PPARγ, a positive regulator of adipocyte differentiation (Moerman et al., 2004). PPARγ ligands are normally restricted to the nuclear periphery via lamin A/C, so the absence of lamin promotes their release, activating PPARγ and inducing MSCs to differentiate into adipocytes (Boguslavsky et al., 2006). At 13 weeks, HGPS mice show increased cortical bone area and thickness. In addition, HGPS mutant osteoblast-specific expression disrupts cell-cell interactions among osteoblasts, osteoclasts, and osteocytes, leading to significant reductions in osteoblast-specific markers (ALP and OCN) and in Wnt-mediated lymphoid enhancer-binding factor one, a regulator of osteoblast maturation. The expression of osteocyte and osteoclast-related genes (Phex, Mepe, and Mmp9) is also inhibited (Schmidt et al., 2012). Consistent with this, osteoblasts, osteocytes, and osteoclasts are significantly reduced in $lmna^{-/-}$ mice compared to WT mice, with abnormal changes in the shape and size of osteoclasts (Li et al., 2011). This reduction in related to the nuclear envelope protein MAN-1. Loss of lamin A/C can disrupts nuclear membrane proteins, such as MAN-1, against osteogenic proteins, thereby affecting the migration and activation of RUNX2. MAN-1, a protein on the nuclear envelope, is closely regulated by lamin A through direct physical interactions (Östlund et al., 2006).

$Lmna^{-/-}$ mice are a widely used and established model for studying premature aging. Their pathological features are similar to those of zmpste24-deficient mice, but distinct from other premature aging mouse models. These mice are established by *LMNA* gene deletion, which disrupts lamin A/C synthesis and triggers nuclear dysfunction, leading to HGPS (Gordon et al., 2012). As a classic HGPS model, $lmna^{-/-}$ mice accumulate presenile proteins, exhibit histological and transcriptomic features of premature aging, and present key clinical manifestations of human HGPS, including shortened lifespan and bone senescence. Thus, $lmna^{-/-}$ mice are instrumental in studying the pathological mechanisms of premature aging syndrome (Cenni et al., 2018). However, the use of gene knockout techniques in $lmna^{-/-}$ mice presents limitations, as different knockout methods can result in varying pathologies, making it challenging to accurately mimic human HGPS. In addition, $lmna^{-/-}$ mice can also serve as a model to investigate the role of lamin A/C in bone metabolism, given their essential functions in osteoblast differentiation and normal bone biogenesis (Li et al., 2011; Vidal et al., 2012).

**Sirtuin 6 (SIRT6) premature senescence mouse model**

Sirt6 is a highly specific histone deacetylase that targets H3K9 and H3K56, playing a vital role in DNA repair, telomerase function, genome stability, and cellular senescence (Michishita et al., 2008). It regulates telomere chromatin stability (Kawahara et al., 2009) and the nuclear factor kappa-B (NF-κB)-mediated inflammatory microenvironment, thereby providing bone protection in OP patients (Wu et al., 2015).

Sirt6-deficient mice exhibit a short lifespan, multiorgan aging, decreased blood glucose and insulin-like growth factor concentrations, increased DNA instability, and early bone loss (Lombard et al., 2008). These mice show approximately 30% bone loss and die at approximately four weeks of age (Mostoslavsky et al., 2006). *SIRT6* knockout mice exhibit reduced cartilage, lower long bone calcification, significantly impaired TB formation, reduced trabecular number (Tb.N) and trabecular volume, significantly reduced serum OCN concentration, and significantly increased TRAP5b concentration, indicating enhanced bone resorption, decreased bone formation, smaller bone size, lower BMD (Zhang et al., 2016), and impaired osteoblast differentiation (Zhang et al., 2017). *SIRT6* knockout directly promotes osteoclast differentiation, leading to excess osteoclasts and hyperactive bone resorption (Zhang et al., 2016), which is related to the up-regulation of NF-κB signaling-related genes, including NEMO, ICAM-1N, C/EBPa, and INOS, caused by *SIRT6* deficiency (Zhang et al., 2018). Additionally, *SIRT6* deficiency inhibits osteogenesis by promoting H3K9 hyperacetylation of the Dickkopf-related protein 1 (Dkk1) promoter, a potent negative regulator of osteoblast formation (Sugatani et al., 2015). Of note, mice with specific knockout of *SIRT6* in osteoblasts/osteocytes exhibit severe bone loss and deformities (Zhang et al., 2021b).

*SIRT6* can interact directly with NF-κB to antagonize NF-κB-induced gene expression, inhibit NF-κB signaling, partially restore lifespan, and improve short-lived sirt6-deficient mice

(Kawahara et al., 2009). Deletion of SIRT6 impairs the proliferation, migration, and oxidative stress tolerance of BMSCs (Zhai et al., 2016). Sirt6-deficient mice also develop rapid bone loss in parallel with accelerated aging, making them a classic model for the study of aging-related OP (Mostoslavsky et al., 2006).

Sirt6 attenuates NF-κB signaling through H3K9 deacetylation, while hyperactive NF-κB signaling may trigger premature aging (Liao & Kennedy, 2014). Excessive ROS generation *in vivo* decreases sirt6 levels (Carreira et al., 2018), which activates the NF-κB signaling pathway, leading to decreased bone quality. However, sirt6 levels in human BMSCs (hBMSCs) increase with age, indicating compensatory overexpression (Zhai et al., 2016). Sirt6 also regulates osteoblast proliferation and differentiation, weakens bone mineralization, and directly regulates osteoclast differentiation (Zhang et al., 2016). Additionally, sirt6 enhances the regulation of OP by BMSCs via the regulation of mitophagy. Inhibition of sirt6 decreases autophagy levels and the osteogenic ability of BMSCs (Shen et al., 2020).

Compared to other premature aging mouse models, sirt6$^{-/-}$ mice have a notably shorter lifespan, with most dying within four weeks and displaying severe bone loss characteristic of human low turnover osteopenia (Xu et al., 2023). Sirt6 plays a complex regulatory role in the human body, with its impact on the same signaling pathway potentially differing across diseases (Liu et al., 2021). Therefore, the therapeutic effects observed in sirt6 knockout mice must be extensively verified for their clinical applicability to humans. Sirt6$^{-/-}$ mice, which exhibit rapid bone loss synchronously with accelerated aging, can serve as a classic model for studying aging-related OP (Mostoslavsky et al., 2006). In addition, their premature aging and early death before four weeks make them valuable for premature aging research (Xu et al., 2023).

**ZMPSTE24 premature senescence mouse model**

Zmpste24, the mouse homolog of human FACE-1, is a multi-transmembrane protein widely distributed in mammalian tissues (Freije et al., 1999; Tam et al., 1998), consisting of 10 exons along a 38 kb genomic segment (Pendás et al., 2002). Structurally, Zmpste24 is related to the yeast metalloprotease Afc1p/ste24p, involved in the maturation of fungal pheromones (Boyartchuk et al., 1997). Functionally, Zmpste24 is an intact membrane metalloproteinase in the endoplasmic reticulum, and mice lacking this gene exhibit abnormal growth, early death, fur loss, kyphosis, abnormal gait, muscle weakness, average or low blood glucose levels, and abnormal anterior layer protein A processing (Bergo et al., 2002; Varela et al., 2005).

*ZMPSTE24* knockout mice are generated by replacing the exon encoding the zinc-binding domain with a neomycin resistance cassette (Leung et al., 2001). These mice show markedly reduced RUNX2 levels, significantly decreased numbers of osteoblasts and osteocytes, and increased expression of adipogenic genes PPARγ and C/EBPα (Rivas et al., 2009).

Both *ZMPSTE24* and *LMNA* are involved in lamin A synthesis, and mutations in *ZMPSTE24* can also induce HGPS. However, the two genes have different roles, with *LMNA* encoding the precursor of lamin A, prelamin A, and *ZMPSTE24* encoding the zinc metalloproteinase Zmpste24, which processes prelamin A (Worman & Michaelis, 2023). When Zmpste24 cleavage is blocked, farnesylated and carboxy-methylated prelamin A accumulates, leading to HGPS (Worman & Michaelis, 2018; Young et al., 2005).

In addition, mutations in the *ZMPSTE24* gene can result in atypical precursor syndrome, which includes restrictive dermatosis and MAD (Navarro et al., 2005). Patients with MAD exhibit aging symptoms similar to those with HGPS, which appear 1–2 years after birth. However, MAD symptoms typically manifest at approximately 4–5 years and include skeletal abnormalities, partial alopecia, insulin resistance, lipodystrophy, and abnormal skin pigmentation. MAD is classified into type A and type B. Type A includes *LMNA* mutations that affect Zmpste24 protease processing, while type B involves mutations that impair the hydrolytic activity of Zmpste24 protease (Cenni et al., 2018). Patients with type B disease show marked skeletal abnormalities, including fractured vertebrae, amorphous subcutaneous calcium deposits, progressive submental changes at the proximal end of long bones, and severe OP with fractures and delayed union (Cunningham et al., 2010).

Zmpste24-deficient mice develop spontaneous fractures. By 24 to 30 weeks of age, rib fractures are visible near the junction of almost every rib, surrounded by dense fibrous tissue. These fracture sites are cell-free, with minimal inflammatory infiltration and little evidence of healing. Multiple fractures also occur in the scapula, clavicle, sternum, zygomatic arch, mandible, and humerus (Bergo et al., 2002).

Homozygous deletion of *LMNA* in mice or haploid *LMNA* in humans results in mature lamin A deficiency, leading to cardiomyopathy and muscular dystrophy. Unlike *LMNA* mutant or null mice, Zmpste24$^{-/-}$ mice do not show a reduction in mature lamin A, but rather exhibit permanent acylation of these proteins, leading to premature germ-like cell defects and disease (Bonne et al., 1999). In addition, Zmpste24$^{-/-}$ mice show overall hypoacetylation of histones H2B and H4, which may contribute to progeroid cell defects and disease (Osorio et al., 2010). Zmpste24$^{-/-}$ mice can serve as research models for HGPS, restrictive dermatosis, MAD, and other diseases. Mating Zmpste24$^{-/-}$ mice with transgenic mice with reduced NF-κB signaling prolongs lifespan and prevents the progression of premature aging traits (Osorio et al., 2012). Furthermore, resveratrol alleviates aging-like characteristics in Zmpste24$^{-/-}$ mice by promoting the interactions between Sirt1 and lamin A, restoring the decline of adult stem cells, improving Tb structure and BMD, and significantly prolonging lifespan (Liu et al., 2012).

**Mitochondrial transcription factor A (TFAM) premature senescence mouse model**

Tfam is a nuclear DNA-encoded protein essential for maintaining and promoting mtDNA transcription and replication (Dairaghi et al., 1995; Ekstrand et al., 2004; Lu et al., 2023; Parisi & Clayton, 1991). Tfam is a 25 kDa protein composed of an amino-terminal high mobility group (HMG) domain, an essential linker region, a secondary HMG structure, and a bare carboxy-terminal tail (Rantanen et al., 2001), which directly regulates mtDNA copy number *in vivo* (Ekstrand et al., 2004). Tfam levels are age-related, showing a reduced binding ability of all protein regions in extremely aged mice compared with aged mice (Lenaers et al., 2020). Tissue-specific knockdown of *TFAM* disrupts mitochondrial genome integrity, inducing the production of inflammatory cytokines and tumor necrosis factor-α (TNF-α), leading to accelerated aging, neuromuscular and vascular dysfunction, and

molecular features of premature aging (Desdín-Micó et al., 2020).

Tfam-deficient mice can be generated using several approaches. Notably, tfam double-floxed mice can be combined with Cre recombinase-containing actin promoter-driven mice to generate tfam-deficient mice, which are then backcrossed 10 times to WTC57BL/6J (B6) mice to remove the Cre transgene and purify the genetic background (Woo et al., 2012). Another approach involves disrupting the *TFAM* gene and generating *TFAM* knockout mice via the introduction of the loxP site by homologous recombination in embryonic stem cells (Gu et al., 1994), followed by excision of *TFAM* exons 6 and 7 by Cre-mediated *in vivo* recombination. The resulting knockout mice are embryonically lethal, surviving only to E8–E10.5, while heterozygous mice are born at standard frequencies but with reduced *TFAM* expression, mtDNA levels, and mitochondria-encoded protein levels (Larsson et al., 1998). Tissue-specific deletion of the tfam protein results in mtDNA defects, mtDNA deletion, and severe respiratory chain defects (Wang et al., 1999).

Limb mesenchyme-specific *TFAM* knockout (Prx1-Cre: TFAM-cKO) mice exhibit significantly shortened limbs after birth, spontaneous fractures, severe limb deformities, bone hypoplasia, and significantly reduced bone matrix mineralization. Tfam plays a crucial role in $Ca^{2+}$ storage and bone matrix mineralization in osteoblasts (Yoshioka et al., 2022). The bone fragility observed in tfam-cKO mice is associated with inhibition of type I collagen deposition, impaired bone matrix mineralization, and poor apatite localization (Yoshioka et al., 2022). Additionally, tfam deficiency leads to adenosine triphosphate (ATP) depletion and increased bone resorption activity, with endogenous ATP release negatively regulating osteoclast function through an autocrine/paracrine feedback loop (Miyazaki, 2013).

$Tfam^{-/-}$ mice, similar to polg $A^{-/-}$ mice (Dobson et al., 2020), show impaired osteoblast differentiation and proliferation due to mitochondrial dysfunction, resulting in reduced expression of Col1a1, which encodes collagen I. However, tfam-cKO mice have a higher incidence of postnatal fractures and severe limb deformities, suggesting that tfam and polg A may have additional functions beyond maintaining mtDNA during bone formation (Yoshioka et al., 2022). $Tfam^{-/-}$ mice also display aging characteristics such as decreased BMD and muscle atrophy, making them an effective model for studying aging. However, the molecular and cellular changes in $tfam^{-/-}$ mice are complex and involve multiple tissues and organs, complicating the interpretation of specific aging mechanisms and bone disease occurrence. In practical applications, $tfam^{-/-}$ mice are primarily used to study diseases caused by tfam-mediated mitochondrial dysfunction, such as mitochondrial myopathy (Chatel et al., 2021) and OP.

**ERCC1 premature senescence mouse model**

The *ERCC1* gene encodes a protein essential for DNA binding (Tsodikov et al., 2005) and repair (Chen et al., 2013). *ERCC1* deficiency leads to persistent DNA damage and cellular senescence in primary osteoblasts and BMSCs (Chen et al., 2013), further leading to premature cellular replicative senescence (Coppé et al., 2010; Rodier et al., 2009) and bone tissue senescence in $ercc1^{-/\Delta}$ mice. The aging process is associated with increased levels of p16INK4A, a cysteinyl kinase inhibitor linked to cellular senescence (Sharpless & Depinho, 2004).

The $ercc1^{-/\Delta}$ mouse model was initially constructed by disrupting exon 5 of *ERCC1*, resulting in the deletion of the last four exons of the transcript, which contain the xeroderma pigmentosum group F (XPF) interaction domain (Enzlin & Schärer, 2002; Sijbers et al., 1996). The second established knockout model was generated by inserting a neomycin resistance cassette into exon 7 of *ERCC1* (Weeda et al., 1997).

ERCC1-XPF is a structurally specific nuclease composed of two subunits, ERCC1 and XPF (Gaillard & Wood, 2001), which are unstable in the absence of each other (Biggerstaff et al., 1993). Human ERCC1-XPF is one of two DNA endonucleases required for the dual incision step of nucleotide excision repair (NER). The ERCC1-XPF enzyme recognizes the junction between single- and double-stranded DNA and cleaves with specific polarity. NER is a DNA repair pathway that removes a wide range of lesions caused by ultraviolet radiation and chemicals from the genome (Lindahl & Wood, 1999). $Ercc1^{-/\Delta}$ mice, which express about 5% of the normal level of ERCC1-XPF, are well-suited models of human diseases such as premature aging (Gurkar & Niedernhofer, 2015; Yousefzadeh et al., 2019). These mice accumulate spontaneously generated endogenous DNA damage at a faster rate than naturally aging mice, resulting in a comparable senescent cell burden (Wong et al., 2020; Yousefzadeh et al., 2019). Thus,$ercc1^{-/\Delta}$ mice can serve as a representative model of early onset of age-related diseases (Harkema et al., 2016), spontaneously developing multiple age-related diseases during their seven-month lifespan, including OP, cardiovascular disease, cataracts, hearing and vision loss, peripheral neuropathy, hepatic fibrosis, brain atrophy with cognitive decline, and intervertebral disc degeneration (Dollé et al., 2011; Gregg et al., 2012; Harkema et al., 2016). In mice deficient in this gene, the skeleton exhibits severe, progressive OP (Chen et al., 2013; Gregg et al., 2011; Vo et al., 2010), including microcephaly, bilateral microphthalmia, micrognathia, brachycephaly, and clubfoot (Chen et al., 2013). Furthermore, ERCC1-deficient mice show substantial reductions in bone volume, trabecular thickness (Tb.Th), and Tb.N, with increased Tb.Sp, accompanied by a significant reduction in osteoblasts, an increase in osteoclast surface area and number, and a reduction in osteogenic progenitor cells in BMSCs, leading to accelerated senescence of BMSCs and osteoblasts. This senescence is characterized by decreased proliferation, accumulation of DNA damage, and a senescence-associated secretory phenotype that promotes the secretion of inflammatory cytokines such as interleukin-6 (IL-6), TNF-α, and RANKL in osteoclasts, creating an inflammatory bone microenvironment that facilitates osteoclast formation (Chen et al., 2013).

$Ercc1^{-/\Delta}$ mice exhibit an aging pattern similar to naturally aging mice across multiple tissues, including the liver, large intestine, kidney, pancreas, and spleen (Yousefzadeh et al., 2020). Due to rapid DNA damage accumulation, ercc1−/Δ mice exhibit accelerated aging and enhanced cellular senescence, showing similarities with WT mouse and human aging. They serve as a precise model of aging, with the process occurring approximately six times faster than normal, and the hierarchical order of aging marker expression closely mirroring that in WT mice (Gurkar & Niedernhofer, 2015; Yousefzadeh et al., 2020). ERCC1 proteins are involved in nucleotide excision repair, interstrand cross-linking repair, and homologous recombination, playing an essential role in

genomic maintenance and body health (Dollé et al., 2011). Thus, ercc1$^{-/\Delta}$ mice exhibit damage to multiple systems, facilitating the study of multiple organs but may present with more severe symptoms when focusing on a single system or organ.

ERCC1-XPF is a nuclease that cleaves the junction between double- and single-stranded DNA (Manandhar et al., 2015). Reduced levels of ERCC1-XPF lead to accelerated aging in humans and mice, manifesting as XPF-ERCC1 (XFE) progeroid syndrome (Niedernhofer et al., 2006). Mice mimicking human XFE age approximately six times faster than WT mice due to the absence of the ERCC1-XPF DNA repair endonuclease complex (Gurkar & Niedernhofer, 2015; Niedernhofer et al., 2006). Ercc1$^{-/\Delta}$ mice also experience increased DNA damage, particularly cyclosporine adducts, in multiple organs with age (Wang et al., 2012b), as well as longer and larger nuclei (Choi et al., 2011). Notably, the symptoms of human progeria syndrome due to ERCC1-XPF deficiency are strikingly similar to those of ercc1-deficient mice, including osteopenia (Niedernhofer et al., 2006).

Ercc1-deficient mice exhibit accelerated epigenetic senescence associated with human-related diseases due to DNA repair defects leading to persistent, irreparable DNA damage (Perez et al., 2024). Ercc1$^{-/\Delta}$ mice have a short and highly uniform lifespan, making them an ideal model for studying the relationship between DNA damage and aging, possessing many features of natural aging across various tissues (Birkisdóttir et al., 2022). Ercc1$^{-/\Delta}$ mice, with lifespans shortened to less than 6 months, exhibit anatomical, physiological, and molecular features of aging in multiple tissues (Weeda et al., 1997; Yousefzadeh et al., 2020). They provide a rapid and cost-effective model for evaluating aging therapeutics (Yousefzadeh et al., 2020) and are an effective tool for accelerating vascular aging to explore the underlying mechanisms (Golshiri et al., 2021).

Cellular senescence in ercc1$^{-/\Delta}$ mice is promoted due to enhanced endogenous DNA damage (Nidadavolu et al., 2013; Niedernhofer et al., 2018; Robinson et al., 2018; Yousefzadeh et al., 2020). The accelerated senescence associated with ERCC1-XPF deficiency is attributed to cellular senescence and death rather than a consequence of telomere-dependent replicative senescence (Gregg et al., 2011). XPF mutations lead to increased cytoplasmic localization of the human XPF-ERCC1 nuclease complex, preventing it from participating in DNA repair (Ahmad et al., 2010).

**WERNER premature aging mouse model**

Werner (Wrn) is a member of the RecQ family of DNA helicases, characterized by an N-terminal 3'-5' exonuclease domain (Huang et al., 1998; Opresko et al., 2004). Wrn is localized to telomeres exclusively during the S phase of the cell cycle (Crabbe et al., 2004; Opresko et al., 2004), where it plays a crucial role in telomere metabolism. It is required for efficient replication of lagging strand telomeric DNA (Crabbe et al., 2004; Griffith et al., 1999; Opresko et al., 2004), and most of the pleiotropic effects observed in Wrn defects are due to critical telomere shortening (Chang, 2005b). Werner syndrome (WS) in humans is also associated with telomere dysfunction (Chang, 2005b).

Human WS is an autosomal recessive genetic disease characterized by clinical symptoms of premature aging and aging-related diseases, such as cardiovascular disease, OP, and cancer (Kipling & Faragher, 1997). The disorder results from mutations in Wrn, Rec-Q helicase, and exonuclease, which hydrolyze ATP to separate double-stranded DNA into single strands for replication, recombination, transcription, and repair (Monnat, 2010). Mutations in the *Wrn* gene lead to early onset aging phenotypes, including skin atrophy, hair graying and loss, OP, malignancy, and shortened lifespan (Vanhooren & Libert, 2013). The incidence of spinal bone deformities is higher in male WS patients than in females, with both sexes exhibiting decreased cortical bone thickness (Shiraki et al., 1998). One of the primary targets of Wrn helicase is telomeric DNA. Given that laboratory mouse telomeres are approximately five times longer than human telomeres, mice must lack telomerase for 3–6 generations before phenotypic defects become evident (Herrera et al., 1999; Rudolph et al., 1999). However, when the telomerase RNA gene (*Terc*), which encodes the RNA component of telomerase, is deleted alongside *Wrn*, Wrn$^{-/-}$-Terc$^{-/-}$ mice rapidly develop a WRN-like phenotype (Chang et al., 2004). These mice show low bone mass and age-related OP due to a shortened lifespan of BMSCs and impaired osteogenic potential and osteoblast differentiation under normal osteoclast differentiation (Pignolo et al., 2008). In juvenile Wrn$^{-/-}$-Terc$^{-/-}$ mice, bone volume, number, and Tb.Th are reduced, while Tb.Sp is increased; in young mice, cortical bone thickness decreases, porosity and bone marrow fat content increase, with these changes accelerating in aged mice (Brennan et al., 2014).

In the absence of telomerase activity in mice, telomeres become shorter after several generations, leading to telomere replicative senescence (Chang, 2005a). When telomere damage surpasses a certain threshold, osteoblast differentiation is impaired, associated with increased expression of p53 and p21 Waf1/Cip1 (p21) and decreased expression of RUNX2 (Wang et al., 2012a). This results in p53-mediated osteoblast injury and mesenchymal progenitor cell (MPC) senescence. The cyclin-dependent kinase inhibitor p21, downstream of p53, is significantly up-regulated, while RUNX2 is inhibited in the MPCs of Wrn$^{-/-}$-Terc$^{-/-}$ mice (Wang et al., 2012a). The fibroblast growth factor p21 inhibits osteoblast differentiation and protects the stem cell pool by regulating cell proliferation and turnover (Bellosta et al., 2003). Additionally, p16 promotes cell senescence by inhibiting cell proliferation, with p16-deficient WS mice showing a reduction in DNA damage response pathways, leading to decreased apoptosis and cell senescence, and an attenuated aging phenotype (Zhang et al., 2021a).

Werner-defective mouse models differ from other aging mouse models due to a lack of *Wrn*, which leads to telomere dysfunction and induces various diseases (Chang, 2005a). The Wrn$^{-/-}$-Terc$^{-/-}$ mouse model redefines the overall mechanism of bone mass loss during human aging (Pignolo et al., 2008). However, the distribution of OP in WS is abnormal, with greater impact on the limbs than on the axial skeleton (Hofer et al., 2005; Mason et al., 2005). *Wrn*$^{-/-}$-*Terc*$^{-/-}$ mutations cause a bone phenotype similar to age-related bone loss in humans, making it a suitable model for studying SOP. Notably, these mutant mouse model may recapitulate the senescence of osteoblasts and their precursors (Pignolo et al., 2008). In addition, WS is a typical premature aging syndrome that mimics natural aging and can also be used in the study of immune inflammation (Goto, 2008).

**KLOTHO premature aging mouse model**

Klotho, a transmembrane protein mainly expressed in the renal distal convoluted tubules and choroid plexus (Kuro-O

et al., 1997), primarily functions as a coreceptor for fibroblast growth factor 23 (FGF23) (Kurosu et al., 2006; Urakawa et al., 2006). Klotho is a potent regulator of bone formation and bone mass in osteocytes (Komaba et al., 2017), with the Klotho gene considered a potential candidate for the genetic regulation of common age-related diseases, such as OP and cervical spondylosis (Ogata et al., 2002). *KLOTHO* locus gene-deficient (Kl/Kl) mice can be generated by crossing heterozygous Klotho mice (Kawaguchi et al., 1999).

Kl/Kl mice generally develop symptoms at 3–4 weeks of age, exhibiting syndromes similar to human premature aging, including arteriosclerosis, emphysema, premature thymus degeneration, skin atrophy, reduced spontaneous activity, ectopic calcification, OP, growth retardation, infertility, and shortened lifespan, with death occurring at approximately two months of age (Kuro-O et al., 1997). Interestingly, the marked decrease in osteoclast activity and population in Kl/Kl-deficient mice coincides with high serum calcium, phosphate (Kuro-O et al., 1997), and osteoprotegerin (OPG) levels (Yamashita et al., 2001). Kl/Kl mice also show a reduction in osteoblast progenitors and lower osteoblast ALP activity and matrix nodule formation (Kawaguchi et al., 1999). Overexpression of *KLOTHO* in cultured osteoblasts inhibits mineralization and osteogenic activity during osteocyte differentiation (Komaba et al., 2017), while *KLOTHO* gene deletion accelerates osteocyte senescence and affects the spatial distribution of osteocytes and synthesis of bone matrix proteins (Suzuki et al., 2005). The bone matrix of *Kl/Kl*-deficient mice contains extensive unmineralized areas, while mineralized osteocytes and their lacunae show a large amount of OCN and dentin matrix protein-1 (DMP-1) staining. This may be due to the excessive production of calcium-binding molecules, such as OCN and DMP-1, by osteocytes, leading to concentrated mineralization around these cells and disruption of mineralization integrity in the bone matrix (Sasaki et al., 2013). BMSCs from Kl/Kl mice exhibit hyperactive proliferation *in vivo* and *in vitro* but decreased function (Feng et al., 2023). However, BMSCs overexpressing *KLOTHO* show enhanced proliferation, secretion, and migration (Ni et al., 2021), with *KLOTHO* overexpression also prolonging the lifespan of Kl/Kl-deficient mice (Kurosu et al., 2005). Kl/Kl mice develop osteopenia and OP, characterized by elongated long bones, thin cortical bone in the diaphysis, and increased epiphyseal trabeculae in the vertebral body (Yamashita et al., 2000). They show increased bone volume of the proximal tibial epiphysis, with an 8AA0% increase in Tb.N, a 300% increase in Tb.Th, a 60% decrease in Tb.Sp, and low bone turnover (Yamashita et al., 2000). The cancellous bone volume in the epiphysis of *Kl/Kl* mice is three times that of WT mice, with osteopenia in vertebrae and long bones. The elongation of trabecular bone is due to relatively low levels of bone resorption (Yamashita et al., 1998). T The number and surface area of osteoclasts and osteoblasts are significantly reduced (Kawaguchi et al., 1999; Kuro-O et al., 1997; Yamashita et al., 1998). Additionally, high OPG expression is observed in the femora of *Kl/Kl* mice, with *Klotho* gene deletion inhibiting bone resorption two weeks after bone marrow ablation (Yamashita et al., 2000).

FGF23 is a bone-derived circulating hormone, crucial for phosphate and vitamin D metabolism (Kurosu et al., 2006; Urakawa et al., 2006). Membrane-anchored Klotho, an important regulator of mineral homeostasis, functions as a coreceptor for FGF23 (Kurosu et al., 2006; Martin et al., 2012; Urakawa et al., 2006). While FGF23 is primarily a growth factor, in the presence of soluble Klotho, it directly affects osteocyte differentiation and mineralization (Baron & Kneissel, 2013). This effect is partially mediated by the induction of Dkk1 and subsequent inhibition of the Wnt/β-catenin pathway (Baron & Kneissel, 2013; Carrillo-López et al., 2016). The Wnt/β-catenin pathway plays a vital role in osteoblast activity, bone development and bone mass maintenance (Baron & Kneissel, 2013). Dkk1 antagonizes Wnt signaling by inhibiting the binding of Wnt ligands to the receptor complex consisting of frizzled protein and lipoprotein receptor-associated protein 5/6. However, loss of Klotho function in osteocytes impairs FGF23-induced Dkk1 effects, resulting in Wnt pathway activation and increased osteoblast activity (Komaba & Lanske, 2018).

Kl/Kl mice are a well-established model that mimics human aging characteristics, including OP (Suzuki et al., 2005). These mice exhibit osteopenia, predominantly cortical osteopenia, similar to human SOP, and die prematurely at around two months of age (Kawaguchi, 2006). This bone loss indicates that decreased bone formation exceeds bone resorption, resulting in net bone loss and mirroring the pathophysiology of SOP in humans (Kawaguchi et al., 2000). *KLOTHO* gene defects lead to independent impairment of osteoblast and osteoclast differentiation, resulting in reduced low-turnover bone mass, also characteristic of human SOP. Therefore, Kl/Kl mice are an important model for studying the molecular mechanisms underlying age-related bone loss (Kawaguchi et al., 1999), and have also been used to study chronic kidney disease (Kuro-O, 2011). However, although disease manifestations in *KLOTHO* knockout mice are similar to those in humans in many respects, species differences still exist. Multiple factors regulate premature aging in humans, which must be comprehensively considered.

We summarized the mechanisms of bone aging in mice (Table 1) and compared the bone phenotypes of aging mice and humans (Table 2). We also described the phenotypic and pathological characteristics of premature aging mice (Figure 2, 3).

However, mice may not always be the most suitable model for studying skeletal phenotypes. Despite apparent similarities in skeletal biology between mice and humans, significant differences also exist between the two species, including variations in organizational structures, remodeling activity, genetic evolution, and mechanical loading patterns (Elefteriou & Yang, 2011). For instance, bone growth in mice is affected by total bone growth plate height, resting zone height, and cell proliferation activity, but is correlated with the width of the bone growth plate rather than its height in humans (Wilson et al., 2021). Therefore, when selecting mice as a model for bone studies, it is essential to carefully consider the similarities and differences between mouse and human bones to choose the most appropriate model.

## TREATMENT

Bone loss naturally occurs with aging in humans, leading to complications such as bone fragility and associated fractures, which can be disabling and fatal. OP is an incurable degenerative disease in both Chinese and Western medicine, directing scientific efforts towards alleviating bone loss and preventing OP. Methods to mitigate bone loss include drug therapy, exercise, and stem cell transplantation. Drug therapy is a primary approach and can help reduce bone loss. For

**Table 1 Summary of bone aging mechanisms in mice**

| Mouse type | Mechanism |
|---|---|
| Naturally aged mice | ① Accumulation of DDR leads to reduced bone formation and bone loss (Hoeijmakers, 2009).<br>② Generation of SASP activates DDR and SASP of neighboring cells (Rodier et al., 2009).<br>③ Telomere dysfunction increases expression of P53/P21 and decreases expression of RUNX2, leading to defects in osteogenic differentiation (Wang et al., 2012a).<br>④ Oxidative stress inhibits bone formation and increases bone adipocyte formation (Almeida et al., 2009), while deepening effects of telomere shortening on bone remodeling (Muller, 2009). |
| *SAMP6* mice | BMSCs are abnormally differentiated and differentiate in favor of adipogenesis rather than osteogenesis (Chen et al., 2009; Ichioka et al., 2002; Niimi & Takahashi, 2014). |
| *POLG*$^{mut/mut}$ mice | ① Polg A mutations cause mitochondrial dysfunction, leading to respiratory chain dysfunction in both osteoblasts and osteoclasts, resulting in reduced osteoblast number and osteogenic ability, increased osteoclast number and activity, and premature OP phenotype (Dobson et al., 2020).<br>② Higher levels of ROS cause telomere attrition and loss, chromosome fusion and fragmentation, and premature senescence (Liu et al., 2002). |
| *LMNA* mice | Mutations and deletions of lmna, which cause lamin A/C synthesis disorders, leading to nuclear membrane structural changes, such as DNA repair-related proteins, gene transcription and signal transduction abnormalities, cellular function destruction, and skeletal abnormalities (Villa-Bellosta et al., 2013). |
| *SIRT6* mice | Loss of *SIRT6* results in uninhibited NF-kB signaling, with hyperactive NF-κB signaling potentially triggering premature aging, leading to skeletal abnormalities (Liao & Kennedy, 2014). |
| *ZMPSTE24* mice | Mutations or deletions in *ZMPSTE24* gene cause loss of Zmpste24 protease function, leading to skeletal abnormalities. |
| *TFAM* mice | Deletion or mutation of *TFAM* gene disrupts mitochondrial genome integrity, leading to impaired mtDNA maintenance, transcription and replication, premature senescence, and skeletal abnormalities (Desdín-Micó et al., 2020). |
| *ERCC1* mice | *ERCC1* deficiency leads to persistent DNA damage and cellular senescence in primary osteoblasts and BMSCs, associated with increased p16INK4A levels (Sharpless & Depinho, 2004). |
| *WERNER* mice | *WERNER* deletion causes telomere dysfunction, up-regulates p21, and inhibits osteoblast differentiation and defective telomere-mediated osteoblast differentiation (Bellosta et al., 2003). |
| *KLOTHO* mice | Functional loss of Klotho in osteocytes impairs biological effects of FGF23-induced Dkk1, resulting in Wnt pathway activation and increased bone formation in osteoblasts (Komaba & Lanske, 2018). |

example, calcium supplementation can prevent bone calcium from entering the bloodstream, reduce bone resorption, and slow bone loss (Zhu & Prince, 2012). Vitamin D can promote calcium absorption, directly acting on osteoblasts and osteoclasts to promote bone mineralization and inhibit bone resorption (Hou et al., 2018). Strontium ranelate (SrR), a clinically used drug containing strontium salt (Pilmane et al., 2017), is more effective than vitamin D3 in treating postmenopausal OP (Kołodziejska et al., 2021). However, SrR can cause a variety of adverse effects, including skin damage, ischemic heart disease, peripheral vascular disease, and cerebrovascular disease (Abrahamsen et al., 2014), limiting its use in OP treatment (Reginster et al., 2015). The most widely used anti-resorptive drugs are bisphosphonates and the RANKL inhibitor denosumab.

Bisphosphonates are the primary treatment for OP (Center et al., 2020) and can be taken with calcium supplements. Bisphosphonates bind to hydroxyapatite on the bone surface, preventing the release of cytokines that activate osteoclasts. This inhibition leads to increased osteoclast apoptosis and decreased bone resorption (Camacho et al., 2020). Denosumab, a fully human RANKL monoclonal antibody, prevents RANKL from activating its receptor on osteoclasts and preosteoclasts, leading to increased bone mass. Compared to bisphosphonates, denosumab more rapidly improves BMD in both cortical and cancellous bone, thereby reducing fracture risk (Camacho et al., 2020). Additionally, teriparatide treatment significantly reduces both vertebral and nonvertebral fractures while improving quality of life. Furthermore, intermittent low-dose parathyroid hormone analogues increase osteoclast activity, promote bone formation, and reduce bone resorption (Augustine & Horwitz, 2013). Estrogen replacement therapy and estrogen plus progesterone therapy are also viable options for treating bone loss in postmenopausal women (Levin et al., 2018). Exercise is another strategy used to mitigate bone loss, with aerobic endurance and resistance exercise shown to exert positive effects on bone metabolism (Stunes et al., 2022). Sustained sprinting and strength training can improve tibial characteristics in middle-aged and elderly male sprinters (Suominen et al., 2021). Additionally, tai chi can benefit patients by increasing BMD and bone Gla protein levels while alleviating OP-induced pain (Zhang et al., 2019). Stem cell therapy can also mitigate bone loss (Sanghani-Kerai et al., 2018), with localized transplantation of BMSCs resulting in an increase in Tb and improvement in bone microarchitecture and stiffness (Hu et al., 2018). Similarly, local injection of human umbilical cord mesenchymal stem cells promotes osteoblast differentiation and Tb formation and reduces bone loss (Hendrijantini et al., 2018).

In addition to the commonly used treatments for alleviating bone loss mentioned above, we also summarize the specific therapeutic approaches targeting skeletal injury in the prematurely aging mouse models discussed in this paper. Orcinol glucoside, a phenolic glycoside isolated from *Curculigo orchioides* Gaertn, has shown promise in SAMP6 mice by preventing SOP through the activation of the Nrf2/Keap1 and mTOR signaling pathways, thereby attenuating oxidative stress and osteoclast autophagy (Gong et al., 2022). *Dolichos lablab* Linné treatment in SAMP6 mice promotes osteoblast and calcified nodule formation by up-regulating BMP-2/Smad and Wnt/β-linker protein pathways, enhancing BMD and fracture healing (Kim et al., 2023). Acupuncture on the Shenshu point in SAMP6 mice has been shown to enhance testosterone secretion, decreases bone renewal, and partially alleviate OP by promoting bone formation, restoring bone mass, and improving bone structure (Zhang et al., 2009). Additionally, allogeneic bone marrow cell transplantation directly into the bone marrow cavity of irradiated SAMP6 mice promotes the normalization of cancellous bone and BMD (Takada et al., 2006). Lactoferrin, an iron-binding glycoprotein, promotes the normalization of bone formation and structure in SAMP6 mice by promoting osteogenesis (Chen et al., 2019). Additionally, glucagon-like

**Table 2 Summary of bone phenotypes in mice and humans**

| Type | Bone phenotypes in mice | Bone phenotypes in humans |
|---|---|---|
| Naturally aged | Bone mass, cancellous bone volume fraction, and cortical bone thickness, after reaching peak values, decrease with age and exhibit SOP (Bikle et al., 2002). | Bone remodeling homeostasis is disrupted, and bone resorption exceeds bone formation in SOP, leading to thinning of cortical bone, reduction in Tb.Th and Tb.N, increase in Tb.Sp in patients, bone mass and strength reduction, bone fragility and increased risk of fracture (Khandelwal & Lane, 2023). |
| SAMP6 | Compared with aging R-strain mice, SAMP6 mice exhibit thinner cortex, larger periosteal and intraosseous diameters (Chen et al., 2009; Jilka et al., 1996; Matsushita et al., 1986; Silva et al., 2005), and lower BV/TV and BMD (Chen et al., 2004, 2005, 2009; Jilka et al., 1996; Matsushita et al., 1986). | Skeletal phenotype of SAMP6 mice corresponds to SOP. |
| *POLG* $^{mut/mut}$ | OP appears prematurely. Polg$^{mut/mut}$ mice at 40 weeks show significantly reduced whole-body BMD, significant kyphosis, and decreasing tendency in whole-body bone mineral content to length ratio (Trifunovic et al., 2004). | No relevant skeletal studies have been conducted on patients with POLG deletion. However, the discovery of mitochondrial complex defects in osteoblasts from older adults compared to younger adults is consistent with this mouse model (Hipps et al., 2022), suggesting that respiratory chain defects, resulting from accumulation of age-related pathogenic mtDNA mutations, are associated with an increased risk of death. These findings may be significant in the pathogenesis of age-related OP in humans. |
| *LMNA* | Irregular cortical bone with poor biomechanical properties, extensive loss of osteocytes and osteoblasts, defects in bone mineralization, decreased red marrow cells, and significant reductions in type I collagen, ALP, and OCN in long bones (Schmidt et al., 2012). | Patients with HGPS exhibit slender, long bones, thin but abnormally dense cortical bone, sparse and narrow Haversia canals, unclear bone trabeculae, and insufficient mineralization (Lee et al., 2012). Ossific defects show an extensive patent anterior fontanelle, which may remain open during childhood and adolescence (Debusk, 1972). In HGPS patients, osteolysis commonly occurs in distal phalanges, clavicle, mandible, neurocranial and visceral skull (Lamis et al., 2022), and first rib (Sivaraman et al., 1999). |
| *SIRT6* | Bone resorption is enhanced, bone formation is decreased, bones show smaller body size and lower BMD, long bones show lower calcification, trabecular bone formation is significantly impaired, and number and volume are reduced (Zhang et al., 2016). | There are no relevant skeletal studies with *sirt6*-deficient patients, but sirt6-KO mice exhibit similar SOP symptoms to humans. Sirt6 plays an essential role in DNA repair, telomerase function, genome stability and cellular senescence, especially in preventing premature senescence of human cells (Michishita et al., 2008). |
| *ZMPSTE24* | Spontaneous fractures and severe OP. RUNX2 expression is markedly reduced, osteoblasts and osteocytes are significantly reduced, and expression of adipogenic genes PPARγ and C/EBPα is increased (Rivas et al., 2009). | Patients harbor two heterozygous compound mutations in *ZMPSTE24* gene and present with different skeletal features, including coracoid process of vertebrae, development of amorphous subcutaneous calcified deposits, progressive epiphyseal changes in proximal long bones, and severe OP with fractures and delayed healing. Skull exhibits typical features of MAD-A, including mandibular hypoplasia, premature teething and crowding of dentition (Cunningham et al., 2010). Patients may present with skeletal disorders, including decreased bone density in spine and limbs, multiple spontaneous fractures, osteolysis of femoral head, and cranial sutures that remain unhealed. These symptoms typically appear at around 15 years old (Ben Yaou et al., 2011). Patients with MAD-B caused by *ZMPSTE24* mutation exhibit growth retardation, partial lipodystrophy, skin pigmentation, and prominent bone defects, including mandibular hypoplasia and progressive bone resorption in distal phalanges and clavicles (Worman & Michaelis, 2023). |
| *TFAM* | Significant shortening of limbs with spontaneous fractures, severe limb deformities, bone hypoplasia, and significantly reduced mineralization of bone matrix, impaired osteoblast proliferation, differentiation, and function (Yoshioka et al., 2022). | There are no relevant skeletal studies on patients with *TFAM* deficiency. However, tfam is a core component of the human mitochondrial transcription machinery and is vital in maintaining mitochondrial function (Shi et al., 2012). |
| *ERCC1* | Skeletal manifestations are severe, with progressive OP (Chen et al., 2013; Gregg et al., 2011; Vo et al., 2010), microcephaly, bilateral microphthalmia, micrognathia, brachycephaly, and clubfoot. Bone tissue volume, Tb.Th, and Tb.N are significantly decreased, and Tb.Sp is increased (Chen et al., 2013). | Patients with Ercc1 show microcephaly, premature closure of fontanelles, bilateral microphthalmia (Jaspers et al., 2007), and osteopenia (Niedernhofer et al., 2006). Due to severe symptoms in Ercc1 patients and few related cases, few studies have been conducted on Ercc1 patient bone, and in-depth research is lacking. |
| *WERNER* | ① Lifespan of BMSCs is shortened, and osteogenic potential and osteoblast differentiation are impaired (Pignolo et al., 2008).<br>② Juvenile Wrn$^{-/-}$-Terc$^{-/-}$ mice show reduced trabecular volume, Tb.Th, and Tb.N, and increased trabecular spacing (Brennan et al., 2014).<br>③ Young Wrn$^{-/-}$-Terc$^{-/-}$ mice show thinner cortical bone, increased porosity, and increased bone marrow fat content (Brennan et al., 2014).<br>④ In aged Wrn$^{-/-}$-Terc$^{-/-}$ mice, changes in trabecular bone, cortical bone and bone marrow fat content are accelerated (Brennan et al., 2014). | Patients lacking werner exhibit OP (Neveling et al., 2007), low serum levels of insulin-like growth factor 1, which can promote bone formation, and reduced osteoblast activity (Rubin et al., 1994). |

Continued

| Type | Bone phenotypes in mice | Bone phenotypes in humans |
|---|---|---|
| *KLOTHO* | Kl/Kl-deficient mice develop osteopenia and OP, including thinning of epiphyseal trabeculae of vertebral body and cortical bone of diaphysis, but lengthening of bone, increased bone volume (Yamashita et al., 2000), and extensive unmineralized areas in bone matrix (Sasaki et al., 2013). At the cellular level, the number and surface area of osteoclasts (Kuro-O et al., 1997) and osteoblasts (Kawaguchi et al., 1999) are significantly reduced in Kl/Kl-deficient mice, and BMSCs show excess proliferation and functional impairment (Sasaki et al., 2013). | Klotho gene deficiency in humans increases bone resorption and causes chronic renal failure (Koh et al., 2001). In addition, bone loss in SOP in humans is characterized by a decrease in bone formation over bone resorption, similar to the mechanism in Kl/Kl-deficient mice (Kawaguchi et al., 2000). |

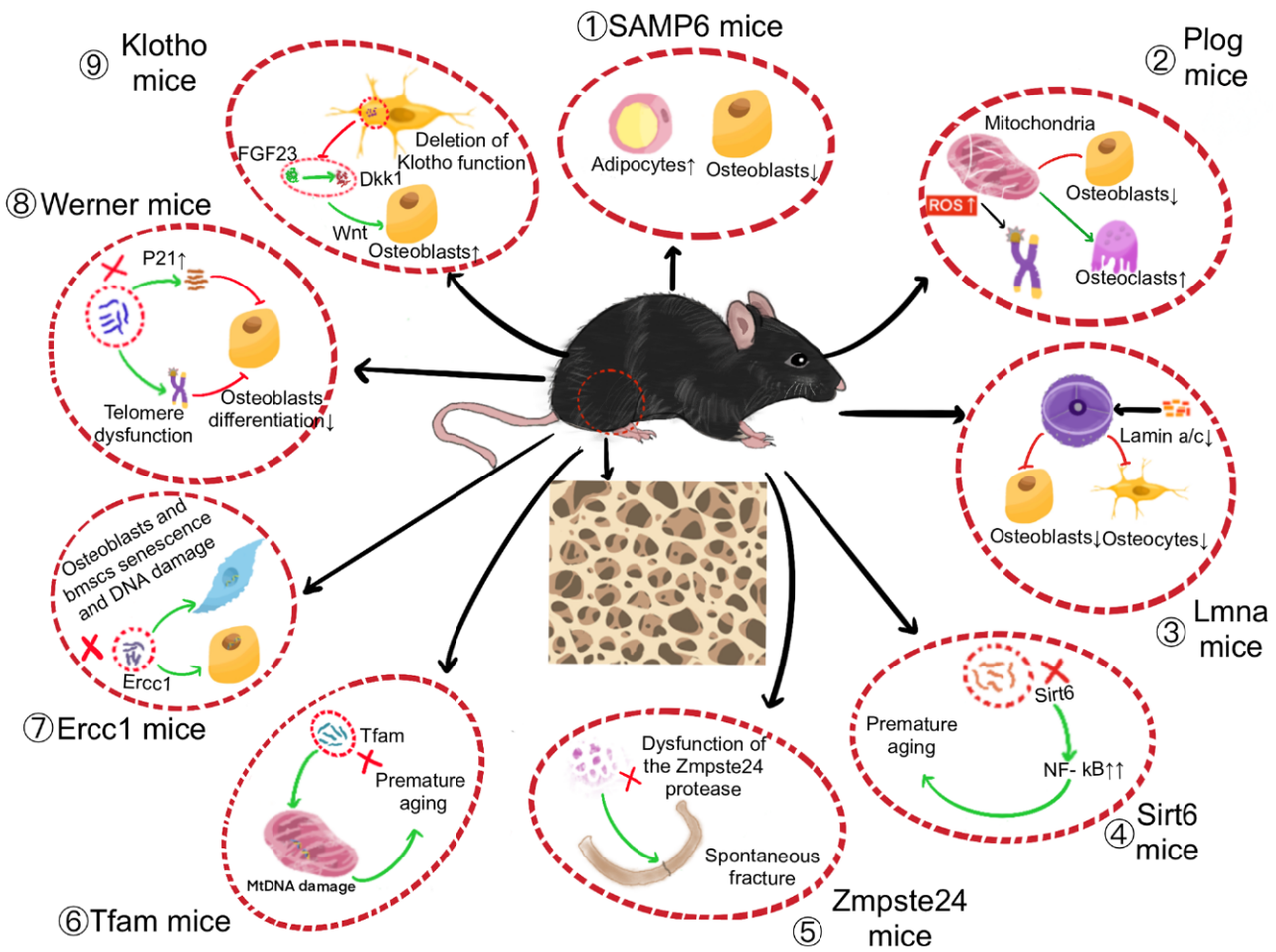



**Figure 2 Phenotypes of prematurely aging mice**

SAMP6 mutant prematurely aging mice: Abnormal differentiation of bone marrow stem cells, increased adipogenesis, and decreased osteoblasts. Polg$^{mut/mut}$ premature aging mice: Mitochondrial dysfunction reduces number and osteogenic ability of osteoblasts, increases number and activity of osteoclasts, and increases ROS, leading to telomere dysfunction, chromosome fusion, and breakage. Lmna premature aging mice: *LMNA* mutation and deletion cause lamin A/C synthesis disorder, resulting in nuclear membrane structural changes, destruction of cellular functions, and extensive loss of osteocytes and osteoblasts. Sirt6 premature aging mice: Loss of sirt6 leads to uninhibited NF-κB signaling, with hyperactive NF-κB signaling potentially triggering premature aging. Zmpste24 premature senescence mice: Loss of Zmpste24 protease function, resulting in spontaneous fracture. Tfam premature senescence mice: Deletion or mutation of *TFAM* gene results in impaired mtDNA maintenance, transcription, and replication, inducing premature senescence in mice. Ercc1 premature senescence mice: *ERCC1* deficiency leads to persistent DNA damage and cellular senescence in primary osteoblasts and BMSCs. Werner premature aging mice: *WERNER* deletion causes telomere dysfunction, significantly up-regulated p21, and inhibited osteoblast differentiation. Klotho premature aging mice: Functional loss of Klotho in osteocytes impairs the biological effects of FGF23–induced Dkk1, resulting in Wnt pathway activation and increased osteoblast activity.

peptide-2 treatment attenuates bone loss in SAMP6 mice, as evidenced by increased BMD, improved femoral microarchitecture, and enhanced osteogenic activity (Huang et al., 2023). Human parathyroid hormone 1–34 (PTH 1–34), administered subcutaneously at 20 μg/kg three times per week for 12 weeks in SAMP6 mice, significantly reduces BMD loss and improves trabeculae microstructure and femoral epiphysis bone strength (Washimi et al., 2010). Similarly, low-dose PTH (10 μg/kg per day) administration in SAMP6 mice effectively promotes senescent bone loss, increases bone mass, and enhances bone formation by increasing osteoblast activity and modulating specific Wnt effectors, suggesting the therapeutic potential of intermittent low doses of PTH to increase bone formation activity in skeletal senescence

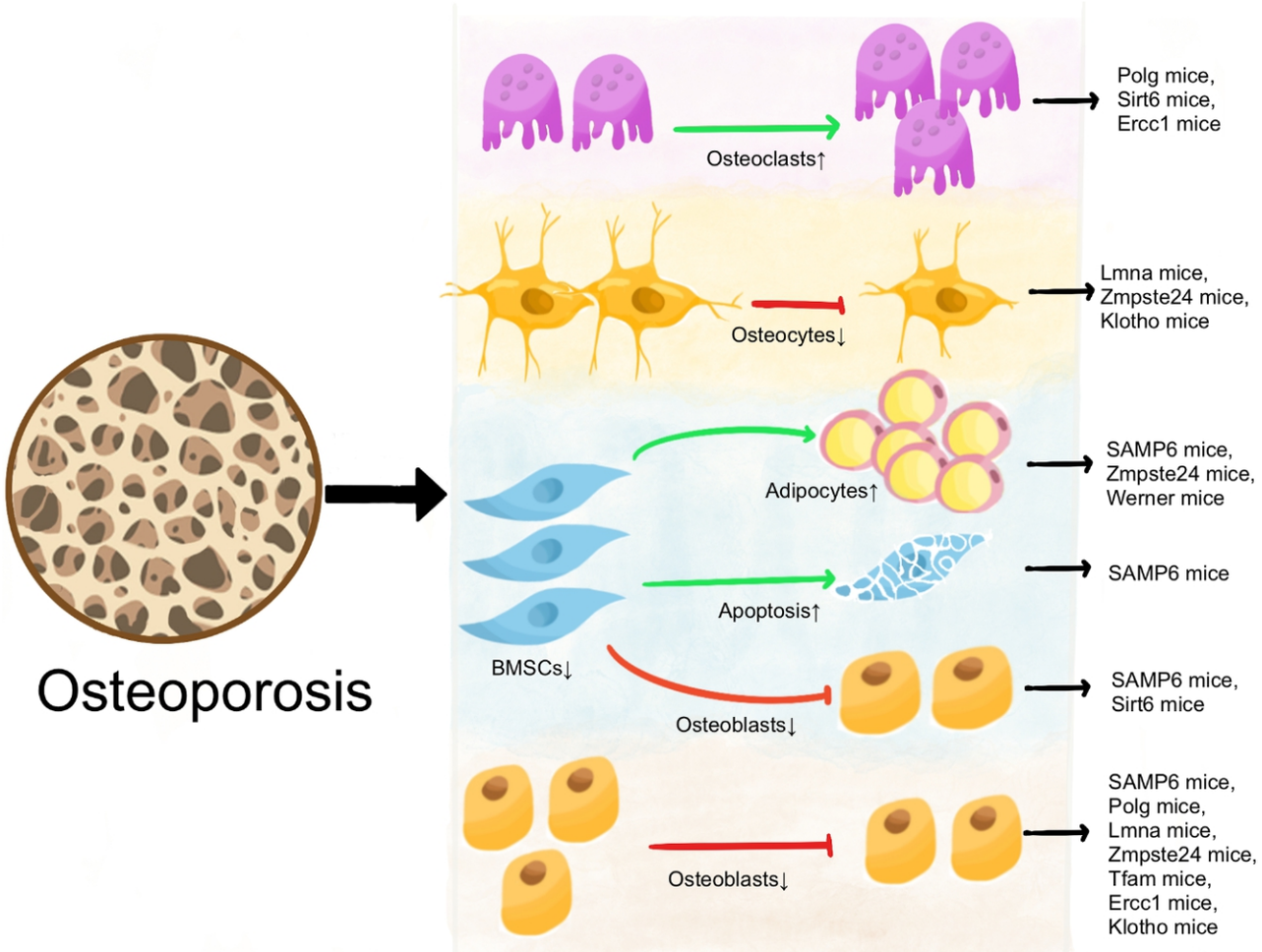



**Figure 3 Pathological features of each premature aging mouse models**

Polg, Sirt6, and Ercc1 mice show increased number of osteoclasts. Lmna, Zmpste24, and Klotho mice show reduced number of osteocytes. BMSCs in mice are also affected, with increased apoptosis, as in SAMP6 mice, increased adipogenic differentiation, as in SAMP6, Zmpste24, and Werner mice, and decreased osteogenic differentiation, as in SAMP6 and Sirt6 mice. Osteoblasts are also reduced in SAMP6, Polg, Lmna, Zmpste24, Tfam, Ercc1, and Klotho mice.

(Saidak et al., 2014).

In 100-day-old polg$^{mut/mut}$ mice, treatment with the mitochondrially targeted antioxidant 10-(6'-plastoquinonyl) decyltriphenylphosphonium cation (SkQ1) ameliorates most syndromes associated with polg dysfunction and significantly delays aging characteristics, resulting in increased bone mineral content from the scapula to lumbar spinal cord, reduced spinal kyphosis, and increased lifespan (Shabalina et al., 2017).

In the lmna mouse model, three main treatments are used. The first involves inhibiting IL-6 activity using tocilizumab, a neutralizing antibody against the IL-6 receptor, which counteracts the premature aging features in *LMNA G609G/G609G* mice. Notably, *in vivo* administration of tocilizumab improves osteoblast differentiation, Tb organization, and femoral biomechanical length in *LMNA G609G/G609G* mutant mice, while also preventing locomotor deficits and maintaining a good quality of life (Squarzoni et al., 2021). Additionally, bone defects associated with HGPS can be reversed by silencing the *LMNA* mutant gene at postnatal week 3, resulting in restored bone marrow and osteoclast activity and improved bone mineralization at 12 and 48 weeks. HGPS mice silenced at postnatal week 3 show faster improvement than those silenced at postnatal week 5, indicating that earlier suppression induces a greater chance of recovery (Strandgren et al., 2015). *In vivo* treatment of *LMNA* mutant mice with morpholino antisense-based oligonucleotides blocks pathogenic *LMNA* splicing and significantly reduces progerin accumulation and its associated nuclear defects (Osorio et al., 2011). Morpholinos are small modifying oligonucleotides that can block splicing events by preventing the splicing machinery from accessing the splice site (Parra et al., 2011).

Among the main treatments targeting sirt6 premature aging mice, metformin significantly promotes *SIRT6* expression and inhibits NF-kB phosphorylation during the proliferation and differentiation of mouse preosteoblasts (Mu et al., 2018). Additionally, pyrrolo[1,2-a]quinoxaline derivatives, synthesized as sirt6 activators, bind directly to the sirt6 catalytic core and activate sirt6-dependent deacetylation of peptide substrates and intact nucleosomes (You et al., 2017). Long-chain fatty acids have also been shown to effectively enhance SIRT6 enzyme activity (Feldman et al., 2013). Similarly, quercetin binds to SIRT6-selective acyl-binding channels at high concentrations, increasing SIRT6 activity (Rahnasto-Rilla et al., 2017; You et al., 2019).

Targeted treatments have been shown to improve skeletal symptoms in zmpste24-deficient mice. Notably, combining

pravastatin and zoledronate significantly improves HGPS phenotypes in Zmpste24–deficient mice, including growth retardation, weight loss, lipodystrophy, alopecia, bone defects, bone mineralization, and cortical thickness (Varela et al., 2008). Senolytic drugs, such as dasatinib, quercetin, and fisetin, effectively target and eliminate senescent cells, improving skeletal age-related degeneration in HGPS in Zmpste24 prematurely aging mice. Although dasatinib plus quercetin do not significantly attenuate Tb loss, fisetin reduces BMD loss in Zmpste24-deficient mice (Hambright et al., 2023). Inhibition of isoprenylcysteine carboxyl methyltransferase (ICMT) expression in Zmpste24$^{-/-}$ mice improves the disease phenotype, resulting in higher Tb.N, Tb.Th, BMD, bone volume, and bone content at 13–15 weeks of age (Ibrahim et al., 2013). Furthermore, Zmpste24-deficient mice treated with farnesyltransferase inhibitors (FTIs) (ABT-100) exhibit enhanced body weight, grip strength, bone integrity, and survival at 20 weeks of age (Fong et al., 2006).

Various methods can enhance the bone phenotype of ercc1$^{-/\Delta}$ mice. Notably, ercc1$^{-/\Delta}$ mice heterozygous for Atm exhibit significantly reduced NF-κB activity, decreased cellular senescence, improved myogenic stem/progenitor cell function, and attenuated age-related skeletal and intervertebral disc pathology, resulting in an extension of a healthy lifespan and improved bone quality, including reduced vertebral OP and Tb.Sp and increased TH.N (Zhao et al., 2020). Transplantation of BMSCs derived from young mice prolongs lifespan and health in ercc1$^{-/-}$ mice, as extracellular vesicles released by young BMSCs rescue cellular senescence and stem cell dysfunction in culture and reduce the senescent cell burden in vivo, effects not observed with BMSCs derived from old mice (Dorronsoro et al., 2021). Additionally, treatment with the HSP90 inhibitor 17-DMAG prolongs healthy lifespan, delays the onset of several age-associated symptoms, and reduces p16INK4a expression in ercc1$^{-/\Delta}$ mice (Fuhrmann-Stroissnigg et al., 2017).

Therapeutic approaches targeting werner premature aging mice primarily involve inhibiting the expression of specific genes. For instance, the absence of p16 significantly rescues the senescent phenotype of WS mice, as evidenced by reduced cellular senescence and apoptosis, along with increased telomere length and cell proliferation (Zhang et al., 2021a).

Regarding treatment of the Kl/Kl mouse bone phenotype, two approaches are used. Rapamycin, a general inhibitor of mTORC1 signaling, coordinates mTORC1 activity and autophagy in Kl/Kl mice, promoting BMSC rejuvenation, restoring the bone phenotype, and prolonging lifespan (Feng et al., 2023). Additionally, treatment with growth hormone increases trabecular volume and BMD in the tibial epiphyseal region of Klotho mice, although it does not improve osteoporotic alterations of cortical bone present in the mutant mice (Kashimada et al., 2002).

## DISCUSSION

Skeletal system diseases are prevalent in aging populations. Many genes and signaling pathways are conserved between mice and humans, making mice excellent research models that can overcome many complex ethical issues involved in human aging research. As such, various prematurely aging mouse models have been established. Bone mass in naturally aging mice peaks between 4 and 8 months of age, then declines with age. However, SAMP6 mice develop spontaneous OP markedly earlier than naturally aging mice. Furthermore, polg$^{mut/mut}$ knockout mice exhibit a significant decrease in BMD at 40 weeks of age. Lmna knockout mice exhibit damaged cortical bone structure, defective bone mineralization, and disordered production of osteoblasts, osteoclasts, and osteocytes. Sirt6 knockout mice are characterized by substantial bone loss and impaired bone trabeculation. Zmpste24 knockout mice display frequent spontaneous fractures at 24–39 weeks. Tfam knockout mice are noted for short bones in the extremities, often accompanied by spontaneous fractures, bone hypoplasia, and significantly reduced bone matrix mineralization. *ERCC1* knockout mice exhibit severe and progressive OP, with significantly reduced bone volume, Tb.Th, and Tb.N and increased Tb.Sp. Aged werner knockout mice display a bone phenotype very similar to that of human age-related bone loss. Kl/Kl mice demonstrate osteopenia, OP, and disturbed production of bone-related cells, including osteocytes, osteoclasts, and osteoblasts.

While SAMP6 and Klotho mice both regulate osteogenesis via the Wnt signaling pathway, they also exhibit some differences. Notably, SAMP6 mice inhibit the Wnt signaling pathway by increasing the level of Sfrp4 to suppress the formation of osteoblasts (Haraguchi et al., 2016; Nakanishi et al., 2006). In contrast, defective *Klotho* in osteocytes impairs the biological effects of FGF23-induced Dkk1, resulting in Wnt pathway activation and increased bone formation in osteoblasts (Komaba & Lanske, 2018).

The bone phenotypes of naturally and prematurely aging mice show a declining trend in bone mass and quality from birth to a particular stage after reaching peak bone mass. In naturally aging mice, the decrease in bone mass post-peak is mainly due to aging-related factors, such as reduced bone turnover and bone mass loss due to defective osteoblast progenitor cells and impaired osteoblast differentiation or function. Prematurely aging mice have shorter lifespans than naturally aging mice, with bone aging caused by the loss of specific gene functions, leading to disrupted bone balance, bone formation disorder, and reduced bone mass. Although prematurely aging mouse models exhibit bone phenotypes similar to naturally aging mice, such accelerated aging models cannot fully recapitulate the pathogenesis of bone aging-related diseases. Therefore, appropriate mice must be selected for bone aging studies. For example, the *SAMP6* knockout mouse model is suitable for studying the mechanisms of OP, while *LMNA* knockout mice are ideal for researching the disease mechanisms of OP in patients with premature aging syndrome.

## COMPETING INTERESTS

The authors declare that they have no competing interests.

## AUTHORS' CONTRIBUTIONS

L.L.Z. provided a brief introduction to this article. Q.G., Y.Z., Z.K.W., and X.H.L. were responsible for manuscript writing. Q.G. drew the figures. L.L.Z. and J.Z. revised the manuscript. All authors read and approved the final version of the manuscript.

## REFERENCES

Abrahamsen B, Grove EL, Vestergaard P. 2014. Nationwide registry-based analysis of cardiovascular risk factors and adverse outcomes in patients treated with strontium ranelate. *Osteoporosis International*, **25**(2): 757–762.

Ahmad A, Enzlin JH, Bhagwat NR, et al. 2010. Mislocalization of XPF-

ERCC1 nuclease contributes to reduced DNA repair in XP-F patients. *PLoS Genetics*, **6**(3): e1000871.

Ahmed MS, Ikram S, Bibi N, et al. 2018. Hutchinson-gilford progeria syndrome: a premature aging disease. *Molecular Neurobiology*, **55**(5): 4417–4427.

Al Saedi A, Chen LL, Phu S, et al. 2020. Age-related increases in marrow fat volumes have regional impacts on bone cell numbers and structure. *Calcified Tissue International*, **107**(2): 126–134.

Al-Azab M, Wang B, Elkhider A, et al. 2020. Indian hedgehog regulates senescence in bone marrow-derived mesenchymal stem cell through modulation of ROS/mTOR/4EBP1, p70S6K1/2 pathway. *Aging*, **12**(7): 5693–5715.

Almeida M, Ambrogini E, Han L, et al. 2009. Increased lipid oxidation causes oxidative stress, increased peroxisome proliferator-activated receptor-γ expression, and diminished pro-osteogenic wnt signaling in the skeleton. *Journal of Biological Chemistry*, **284**(40): 27438–27448.

Aoyama Y, Kim TY, Yoshimoto T, et al. 2013. Impaired motor function in senescence-accelerated mouse prone 1 (SAMP1). *Brain Research*, **1515**: 48–54.

Augustine M, Horwitz MJ. 2013. Parathyroid hormone and parathyroid hormone-related protein analogs as therapies for osteoporosis. *Current Osteoporosis Reports*, **11**(4): 400–406.

Azuma K, Zhou Q, Kubo KY. 2018. Morphological and molecular characterization of the senile osteoporosis in senescence-accelerated mouse prone 6 (SAMP6). *Medical Molecular Morphology*, **51**(3): 139–146.

Baron R, Kneissel M. 2013. WNT signaling in bone homeostasis and disease: From human mutations to treatments. *Nature Medicine*, **19**(2): 179–192.

Bellosta P, Masramon L, Mansukhani A, et al. 2003. $P21^{WAF1/CIP1}$ acts as a brake in osteoblast differentiation. *Journal of Bone and Mineral Research*, **18**(5): 818–826.

Ben Yaou R, Navarro C, Quijano-Roy S, et al. 2011. Type B mandibuloacral dysplasia with congenital myopathy due to homozygous *ZMPSTE24* missense mutation. *European Journal of Human Genetics*, **19**(6): 647–654.

Bergman RJ, Gazit D, Kahn AJ, et al. 1996. Age-related changes in osteogenic stem cells in mice. *Journal of Bone and Mineral Research*, **11**(5): 568–577.

Bergo MO, Gavino B, Ross J, et al. 2002. *Zmpste24* deficiency in mice causes spontaneous bone fractures, muscle weakness, and a prelamin A processing defect. *Proceedings of the National Academy of Sciences of the United States of America*, **99**(20): 13049–13054.

Biggerstaff M, Szymkowski DE, Wood RD. 1993. Co-correction of the ERCC1, ERCC4 and xeroderma pigmentosum group F DNA repair defects in vitro. *The EMBO Journal*, **12**(9): 3685–3692.

Bikle DD, Sakata T, Leary C, et al. 2002. Insulin-like growth factor I is required for the anabolic actions of parathyroid hormone on mouse bone. *Journal of Bone and Mineral Research*, **17**(9): 1570–1578.

Birkisdóttir MB, van Galen I, Brandt RMC, et al. 2022. The use of progeroid DNA repair-deficient mice for assessing anti-aging compounds, illustrating the benefits of nicotinamide riboside. *Frontiers in Aging*, **3**: 1005322.

Black A, Tilmont EM, Handy AM, et al. 2001. A nonhuman primate model of age-related bone loss: a longitudinal study in male and premenopausal female rhesus monkeys. *Bone*, **28**(3): 295–302.

Boguslavsky RL, Stewart CL, Worman HJ. 2006. Nuclear lamin a inhibits adipocyte differentiation: implications for dunnigan-type familial partial lipodystrophy. *Human Molecular Genetics*, **15**(4): 653–663.

Bonne G, Di Barletta MR, Varnous S, et al. 1999. Mutations in the gene encoding lamin A/C cause autosomal dominant emery-dreifuss muscular dystrophy. *Nature Genetics*, **21**(3): 285–288.

Bordner KA, Kitchen RR, Carlyle B, et al. 2011. Parallel declines in cognition, motivation, and locomotion in aging mice: association with immune gene upregulation in the medial prefrontal cortex. *Experimental Gerontology*, **46**(8): 643–659.

Boyartchuk VL, Ashby MN, Rine J. 1997. Modulation of ras and a-factor function by carboxyl-terminal proteolysis. *Science*, **275**(5307): 1796–1800.

Brennan TA, Egan KP, Lindborg CM, et al. 2014. Mouse models of telomere dysfunction phenocopy skeletal changes found in human age-related osteoporosis. *Disease Models & Mechanisms*, **7**(5): 583–592.

Camacho PM, Petak SM, Binkley N, et al. 2020. American association of clinical endocrinologists/american college of endocrinology clinical practice guidelines for the diagnosis and treatment of postmenopausal osteoporosis-2020 update. *Endocrine Practice*, **26** Suppl 1: 1–46.

Cao J, Ou GM, Yang NL, et al. 2015. Impact of targeted PPARγ disruption on bone remodeling. *Molecular and Cellular Endocrinology*, **410**: 27–34.

Cao J, Venton L, Sakata T, et al. 2003. Expression of RANKL and OPG correlates with age-related bone loss in male C57BL/6 mice. *Journal of Bone and Mineral Research*, **18**(2): 270–277.

Capecchi MR. 1989. Altering the genome by homologous recombination. *Science*, **244**(4910): 1288–1292.

Carreira MC, Izquierdo AG, Amil M, et al. 2018. Oxidative stress induced by excess of adiposity is related to a downregulation of hepatic sirt6 expression in obese individuals. *Oxidative Medicine and Cellular Longevity*, **2018**: 6256052.

Carrillo-López N, Panizo S, Alonso-Montes C, et al. 2016. Direct inhibition of osteoblastic Wnt pathway by fibroblast growth factor 23 contributes to bone loss in chronic kidney disease. *Kidney International*, **90**(1): 77–89.

Cenni V, D'Apice MR, Garagnani P, et al. 2018. Mandibuloacral dysplasia: a premature ageing disease with aspects of physiological ageing. *Ageing Research Reviews*, **42**: 1–13.

Center JR, Lyles KW, Bliuc D. 2020. Bisphosphonates and lifespan. *Bone*, **141**: 115566.

Champ JE, Binkley N, Havighurst T, et al. 1996. The effect of advancing age on bone mineral content of female rhesus monkeys. *Bone*, **19**(5): 485–492.

Chang S, Multani AS, Cabrera NG, et al. 2004. Essential role of limiting telomeres in the pathogenesis of werner syndrome. *Nature Genetics*, **36**(8): 877–882.

Chang S. 2005a. Modeling aging and cancer in the telomerase knockout mouse. *Mutation Research/Fundamental and Molecular Mechanisms of Mutagenesis*, **576**(1-2): 39–53.

Chang S. 2005b. Modeling premature aging syndromes with the telomerase knockout mouse. *Current Molecular Medicine*, **5**(2): 153–158.

Chatel B, Ducreux S, Harhous Z, et al. 2021. Impaired aerobic capacity and premature fatigue preceding muscle weakness in the skeletal muscle *Tfam*-knockout mouse model. *Disease Models & Mechanisms*, **14**(9): dmm048981.

Chen H, Shoumura S, Emura S. 2004. Ultrastructural changes in bones of the senescence-accelerated mouse (SAMP6): a murine model for senile osteoporosis. *Histology and Histopathology*, **19**(3): 677–685.

Chen HY, Emura S, Isono H, et al. 2005. Effects of traditional Chinese medicine on bone loss in SAMP6: a murine model for senile osteoporosis. *Biological and Pharmaceutical Bulletin*, **28**(5): 865–869.

Chen HY, Zhou XR, Emura S, et al. 2009. Site-specific bone loss in senescence-accelerated mouse (SAMP6): a murine model for senile osteoporosis. *Experimental Gerontology*, **44**(12): 792–798.

Chen Q, Liu K, Robinson AR, et al. 2013. DNA damage drives accelerated bone aging via an NF-κB-dependent mechanism. *Journal of Bone and Mineral Research*, **28**(5): 1214–1228.

Chen X, Li LH, Guo JM, et al. 2016. Treadmill running exercise prevents senile osteoporosis and upregulates the wnt signaling pathway in SAMP6 mice. *Oncotarget*, **7**(44): 71072–71086.

Chen XW, Li YH, Zhang MJ, et al. 2019. Lactoferrin ameliorates aging-

suppressed osteogenesis via IGF1 signaling. *Journal of Molecular Endocrinology*, **63**(1): 63–75.

Choi S, Wang W, Ribeiro AJS, et al. 2011. Computational image analysis of nuclear morphology associated with various nuclear-specific aging disorders. *Nucleus*, **2**(6): 570–579.

Coppé JP, Desprez PY, Krtolica A, et al. 2010. The senescence-associated secretory phenotype: the dark side of tumor suppression. *Annual Review of Pathology: Mechanisms of Disease*, **5**: 99–118.

Crabbe L, Verdun RE, Haggblom CI, et al. 2004. Defective telomere lagging strand synthesis in cells lacking WRN helicase activity. *Science*, **306**(5703): 1951–1953.

Cunningham VJ, D'Apice MR, Licata N, et al. 2010. Skeletal phenotype of mandibuloacral dysplasia associated with mutations in *ZMPSTE24. Bone*, **47**(3): 591–597.

Dairaghi DJ, Shadel GS, Clayton DA. 1995. Addition of a 29 residue carboxyl-terminal tail converts a simple HMG box-containing protein into a transcriptional activator. *Journal of Molecular Biology*, **249**(1): 11–28.

De Sandre-Giovannoli A, Bernard R, Cau P, et al. 2003. Lamin a truncation in hutchinson-gilford progeria. *Science*, **300**(5628): 2055.

DeBusk FL. 1972. The Hutchinson-Gilford progeria syndrome: report of 4 cases and review of the literature. *The Journal of Pediatrics*, **80**(4): 697–724.

Dechat T, Pfleghaar K, Sengupta K, et al. 2008. Nuclear lamins: major factors in the structural organization and function of the nucleus and chromatin. *Genes & Development*, **22**(7): 832–853.

Desdín-Micó G, Soto-Heredero G, Aranda JF, et al. 2020. T cells with dysfunctional mitochondria induce multimorbidity and premature senescence. *Science*, **368**(6497): 1371–1376.

Dobson PF, Dennis EP, Hipps D, et al. 2020. Mitochondrial dysfunction impairs osteogenesis, increases osteoclast activity, and accelerates age related bone loss. *Scientific Reports*, **10**(1): 11643.

Dobson PF, Rocha MC, Grady JP, et al. 2016. Unique quadruple immunofluorescence assay demonstrates mitochondrial respiratory chain dysfunction in osteoblasts of aged and PolgA$^{-/-}$ mice. *Scientific Reports*, **6**: 31907.

Dollé MET, Kuiper RV, Roodbergen M, et al. 2011. Broad segmental progeroid changes in short-lived *Ercc1*$^{-/\Delta 7}$ mice. *Pathobiology of Aging & Age-related Diseases*, **1**(1): 7219.

Dorronsoro A, Santiago FE, Grassi D, et al. 2021. Mesenchymal stem cell-derived extracellular vesicles reduce senescence and extend health span in mouse models of aging. *Aging Cell*, **20**(4): e13337.

Duque G, Rivas D, Li W, et al. 2009. Age-related bone loss in the LOU/c rat model of healthy ageing. *Experimental Gerontology*, **44**(3): 183–189.

Dutta S, Sengupta P. 2016. Men and mice: relating their ages. *Life Sciences*, **152**: 244–248.

Ekstrand MI, Falkenberg M, Rantanen A, et al. 2004. Mitochondrial transcription factor A regulates mtDNA copy number in mammals. *Human Molecular Genetics*, **13**(9): 935–944.

Elefteriou F, Yang XL. 2011. Genetic mouse models for bone studies-Strengths and limitations. *Bone*, **49**(6): 1242–1254.

Enzlin JH, Schärer OD. 2002. The active site of the DNA repair endonuclease XPF-ERCC1 forms a highly conserved nuclease motif. *The EMBO Journal*, **21**(8): 2045–2053.

Eriksson M, Brown WT, Gordon LB, et al. 2003. Recurrent *de novo* point mutations in lamin A cause Hutchinson-Gilford progeria syndrome. *Nature*, **423**(6937): 293–298.

Fahlström A, Zeberg H, Ulfhake B. 2012. Changes in behaviors of male C57BL/6J mice across adult life span and effects of dietary restriction. *Age*, **34**(6): 1435–1452.

Farr JN, Fraser DG, Wang HT, et al. 2016. Identification of senescent cells in the bone microenvironment. *Journal of Bone and Mineral Research*, **31**(11): 1920–1929.

Fayet G, Jansson M, Sternberg D, et al. 2002. Ageing muscle: Clonal expansions of mitochondrial DNA point mutations and deletions cause focal impairment of mitochondrial function. *Neuromuscular Disorders*, **12**(5): 484–493.

Feldman JL, Baeza J, Denu JM. 2013. Activation of the protein deacetylase SIRT6 by long-chain fatty acids and widespread deacylation by mammalian sirtuins. *Journal of Biological Chemistry*, **288**(43): 31350–31356.

Feng R, Wu S, Li RF, et al. 2023. mTORC1-induced bone marrow-derived mesenchymal stem cell exhaustion contributes to the bone abnormalities in *Klotho*-deficient mice of premature aging. *Stem Cells and Development*, **32**(11-12): 331–345.

Ferguson VL, Ayers RA, Bateman TA, et al. 2003. Bone development and age-related bone loss in male C57BL/6J mice. *Bone*, **33**(3): 387–398.

Flurkey K, Currer JM, Harrison DE. 2007. Mouse models in aging research. *In*: Fox JG, Davisson MT, Quimby FW, et al. The Mouse in Biomedical Research. 2nd ed. Amsterdam: Elsevier, 637–672.

Foessl I, Bassett JHD, Bjørnerem Å, et al. 2021. Bone phenotyping approaches in human, mice and zebrafish - expert overview of the EU cost action GEMSTONE ("genomics of musculoskeletal traits translational network"). *Frontiers in Endocrinology*, **12**: 720728.

Fong LG, Frost D, Meta M, et al. 2006. A protein farnesyltransferase inhibitor ameliorates disease in a mouse model of progeria. *Science*, **311**(5767): 1621–1623.

Forster MJ, Dubey A, Dawson KM, et al. 1996. Age-related losses of cognitive function and motor skills in mice are associated with oxidative protein damage in the brain. *Proceedings of the National Academy of Sciences of the United States of America*, **93**(10): 4765–4769.

Freije JMP, Blay P, Pendás AM, et al. 1999. Identification and chromosomal location of two human genes encoding enzymes potentially involved in proteolytic maturation of farnesylated proteins. *Genomics*, **58**(3): 270–280.

Fuhrmann-Stroissnigg H, Ling YY, Zhao J, et al. 2017. Identification of HSP90 inhibitors as a novel class of senolytics. *Nature Communications*, **8**(1): 422.

Gaillard PHL, Wood RD. 2001. Activity of individual ERCC1 and XPF subunits in DNA nucleotide excision repair. *Nucleic Acids Research*, **29**(4): 872–879.

Gardner DG, Majka M. 1969. The early formation of irregular secondary dentine in progeria. *Oral Surgery, Oral Medicine, Oral Pathology*, **28**(6): 877–884.

Geurts AM, Cost GJ, Freyvert Y, et al. 2009. Knockout rats via embryo microinjection of zinc-finger nucleases. *Science*, **325**(5939): 433.

Golshiri K, Ataei Ataabadi E, Rubio-Beltran E, et al. 2021. Selective phosphodiesterase 1 inhibition ameliorates vascular function, reduces inflammatory response, and lowers blood pressure in aging animals. *Journal of Pharmacology and Experimental Therapeutics*, **378**(2): 173–183.

Gong W, Liu MQ, Zhang Q, et al. 2022. Orcinol glucoside improves senile osteoporosis through attenuating oxidative stress and autophagy of osteoclast via activating Nrf2/Keap1 and mTOR signaling pathway. *Oxidative Medicine and Cellular Longevity*, **2022**: 5410377.

Goodrick CL. 1975. Behavioral differences in young and aged mice: strain differences for activity measures, operant learning, sensory discrimination, and alcohol preference. *Experimental Aging Research*, **1**(2): 191–207.

Gordon CM, Gordon LB, Snyder BD, et al. 2011. Hutchinson-gilford progeria is a skeletal dysplasia. *Journal of Bone and Mineral Research*, **26**(7): 1670–1679.

Gordon LB, Kleinman ME, Miller DT, et al. 2012. Clinical trial of a farnesyltransferase inhibitor in children with Hutchinson-Gilford progeria syndrome. *Proceedings of the National Academy of Sciences of the United States of America*, **109**(41): 16666–16671.

Gordon LB, McCarten KM, Giobbie-Hurder A, et al. 2007. Disease

progression in hutchinson-gilford progeria syndrome: impact on growth and development. *Pediatrics*, **120**(4): 824–833.

Goto M. 2008. Elevation of soluble fas (APO-1, CD95) ligand in natural aging and werner syndrome. *Bioscience Trends*, **2**(3): 124–127.

Gregg SQ, Gutiérrez V, Robinson AR, et al. 2012. A mouse model of accelerated liver aging caused by a defect in DNA repair. *Hepatology*, **55**(2): 609–621.

Gregg SQ, Robinson AR, Niedernhofer LJ. 2011. Physiological consequences of defects in ERCC1-XPF DNA repair endonuclease. *DNA Repair*, **10**(7): 781–791.

Griffith JD, Comeau L, Rosenfield S, et al. 1999. Mammalian telomeres end in a large duplex loop. *Cell*, **97**(4): 503–514.

Gu H, Marth JD, Orban PC, et al. 1994. Deletion of a DNA polymerase β gene segment in T cells using cell type-specific gene targeting. *Science*, **265**(5168): 103–106.

Gurkar AU, Niedernhofer LJ. 2015. Comparison of mice with accelerated aging caused by distinct mechanisms. *Experimental Gerontology*, **68**: 43–50.

Haas RH. 2019. Mitochondrial dysfunction in aging and diseases of aging. *Biology*, **8**(2): 48.

Hambright WS, Mu XD, Gao XQ, et al. 2023. The senolytic drug fisetin attenuates bone degeneration in the *Zmpste24*$^{-/-}$ progeria mouse model. *Journal of Osteoporosis*, **2023**: 5572754.

Haraguchi R, Kitazawa R, Mori K, et al. 2016. sFRP4-dependent Wnt signal modulation is critical for bone remodeling during postnatal development and age-related bone loss. *Scientific Reports*, **6**: 25198.

Harkema L, Youssef SA, de Bruin A. 2016. Pathology of mouse models of accelerated aging. *Veterinary Pathology*, **53**(2): 366–389.

Hendrijantini N, Kusumaningsih T, Rostiny R, et al. 2018. A potential therapy of human umbilical cord mesenchymal stem cells for bone regeneration on osteoporotic mandibular bone. *European Journal of Dentistry*, **12**(3): 358–362.

Hengemihle JM, Long JM, Betkey J, et al. 1999. Age-related psychomotor and spatial learning deficits in 129/SvJ mice. *Neurobiology of Aging*, **20**(1): 9–18.

Hernandez L, Roux KJ, Wong ESM, et al. 2010. Functional coupling between the extracellular matrix and nuclear lamina by wnt signaling in progeria. *Developmental Cell*, **19**(3): 413–425.

Herrera E, Samper E, Martín-Caballero J, et al. 1999. Disease states associated with telomerase deficiency appear earlier in mice with short telomeres. *The EMBO Journal*, **18**(11): 2950–2960.

Hipps D, Dobson PF, Warren C, et al. 2022. Detecting respiratory chain defects in osteoblasts from osteoarthritic patients using imaging mass cytometry. *Bone*, **158**: 116371.

Hirozane T, Tohmonda T, Yoda M, et al. 2016. Conditional abrogation of *Atm* in osteoclasts extends osteoclast lifespan and results in reduced bone mass. *Scientific Reports*, **6**: 34426.

Hishiya A, Ito M, Aburatani H, et al. 2005. Ataxia telangiectasia mutated (*Atm*) knockout mice as a model of osteopenia due to impaired bone formation. *Bone*, **37**(4): 497–503.

Hoeijmakers JHJ. 2009. DNA damage, aging, and cancer. *New England Journal of Medicine*, **361**(15): 1475–1485.

Hoerder-Suabedissen A, Molnár Z. 2015. Development, evolution and pathology of neocortical subplate neurons. *Nature Reviews Neuroscience*, **16**(3): 133–146.

Hofer AC, Tran RT, Aziz OZ, et al. 2005. Shared phenotypes among segmental progeroid syndromes suggest underlying pathways of aging. *The Journals of Gerontology: Series A*, **60**(1): 10–20.

Homberg JR, Wöhr M, Alenina N. 2017. Comeback of the rat in biomedical research. *ACS Chemical Neuroscience*, **8**(5): 900–903.

Hou YC, Wu CC, Liao MT, et al. 2018. Role of nutritional vitamin D in osteoporosis treatment. *Clinica Chimica Acta*, **484**: 179–191.

Hu LF, Yin C, Zhao F, et al. 2018. Mesenchymal stem cells: CEll fate decision to osteoblast or adipocyte and application in osteoporosis treatment. *International Journal of Molecular Sciences*, **19**(2): 360.

Huang SR, Li BM, Gray MD, et al. 1998. The premature ageing syndrome protein, WRN, is a 3'->5' exonuclease. *Nature Genetics*, **20**(2): 114–116.

Huang YM, Xu B, Kuai Z, et al. 2023. Glucagon-like peptide-2 ameliorates age-associated bone loss and gut barrier dysfunction in senescence-accelerated mouse prone 6 mice. *Gerontology*, **69**(4): 428–449.

Ibrahim MX, Sayin VI, Akula MK, et al. 2013. Targeting isoprenylcysteine methylation ameliorates disease in a mouse model of progeria. *Science*, **340**(6138): 1330–1333.

Ichioka N, Inaba M, Kushida T, et al. 2002. Prevention of senile osteoporosis in SAMP6 mice by intrabone marrow injection of allogeneic bone marrow cells. *Stem Cells*, **20**(6): 542–551.

Ingram DK, London ED, Reynolds MA, et al. 1981. Differential effects of age on motor performance in two mouse strains. *Neurobiology of Aging*, **2**(3): 221–227.

Jaspers NGJ, Raams A, Silengo MC, et al. 2007. First reported patient with human ERCC1 deficiency has cerebro-oculo-facio-skeletal syndrome with a mild defect in nucleotide excision repair and severe developmental failure. *The American Journal of Human Genetics*, **80**(3): 457–466.

Ji CJ, Dong QY, Liu HH, et al. 2023. Acyl-protein thioesterase1 alleviates senile osteoporosis by promoting osteoblast differentiation via depalmitoylation of BMPR1a. *Regenerative Therapy*, **24**: 351–360.

Jilka RL, Weinstein RS, Takahashi K, et al. 1996. Linkage of decreased bone mass with impaired osteoblastogenesis in a murine model of accelerated senescence. *The Journal of Clinical Investigation*, **97**(7): 1732–1740.

Jin MH, Oh DY. 2019. ATM in DNA repair in cancer. *Pharmacology & Therapeutics*, **203**: 107391.

Kaguni LS. 2004. DNA polymerase γ, the mitochondrial replicase. *Annual Review of Biochemistry*, **73**: 293–320.

Kajkenova O, Lecka-Czernik B, Gubrij I, et al. 1997. Increased adipogenesis and myelopoiesis in the bone marrow of SAMP6, a murine model of defective osteoblastogenesis and low turnover osteopenia. *Journal of Bone and Mineral Research*, **12**(11): 1772–1779.

Kashimada K, Yamashita T, Tsuji K, et al. 2002. Defects in growth and bone metabolism in *klotho* mutant mice are resistant to GH treatment. *Journal of Endocrinology*, **174**(3): 403–410.

Kawaguchi H. 2006. Molecular backgrounds of age-related osteoporosis from mouse genetics approaches. *Reviews in Endocrine and Metabolic Disorders*, **7**(1-2): 17–22.

Kawaguchi H, Manabe N, Chikuda H, et al. 2000. Cellular and molecular mechanism of low-turnover osteopenia in the klotho-deficient mouse. *Cellular and Molecular Life Sciences CMLS*, **57**(5): 731–737.

Kawaguchi H, Manabe N, Miyaura C, et al. 1999. Independent impairment of osteoblast and osteoclast differentiation in *klotho* mouse exhibiting low-turnover osteopenia. *The Journal of Clinical Investigation*, **104**(3): 229–237.

Kawahara TLA, Michishita E, Adler AS, et al. 2009. SIRT6 links histone H3 lysine 9 deacetylation to NF-κB-dependent gene expression and organismal life span. *Cell*, **136**(1): 62–74.

Khandelwal S, Lane NE. 2023. Osteoporosis: review of etiology, mechanisms, and approach to management in the aging population. *Endocrinology and Metabolism Clinics of North America*, **52**(2): 259–275.

Khosla S, Farr JN, Monroe DG. 2022. Cellular senescence and the skeleton: pathophysiology and therapeutic implications. *The Journal of Clinical Investigation*, **132**(3): e154888.

Kim M, Kim JH, Hong S, et al. 2023. Dolichos lablab linné inhibits bone density loss and promotes bone union in senile osteoporosis through osteogenesis. *Pharmaceuticals*, **16**(10): 1350.

Kipling D, Faragher RG. 1997. Progeroid syndromes: probing the molecular basis of aging?. *Molecular Pathology*, **50**(5): 234–241.

Koh N, Fujimori T, Nishiguchi S, et al. 2001. Severely reduced production of klotho in human chronic renal failure kidney. *Biochemical and Biophysical Research Communications*, **280**(4): 1015–1020.

Kolesar JE, Safdar A, Abadi A, et al. 2014. Defects in mitochondrial DNA replication and oxidative damage in muscle of mtDNA mutator mice. *Free Radical Biology and Medicine*, **75**: 241–251.

Kołodziejska B, Stępień N, Kolmas J. 2021. The influence of strontium on bone tissue metabolism and its application in osteoporosis treatment. *International Journal of Molecular Sciences*, **22**(12): 6564.

Komaba H, Kaludjerovic J, Hu DZ, et al. 2017. Klotho expression in osteocytes regulates bone metabolism and controls bone formation. *Kidney International*, **92**(3): 599–611.

Komaba H, Lanske B. 2018. Role of Klotho in bone and implication for CKD. *Current Opinion in Nephrology and Hypertension*, **27**(4): 298–304.

Kujoth GC, Hiona A, Pugh TD, et al. 2005. Mitochondrial DNA mutations, oxidative stress, and apoptosis in mammalian aging. *Science*, **309**(5733): 481–484.

Kuro-O M, Matsumura Y, Aizawa H, et al. 1997. Mutation of the mouse *klotho* gene leads to a syndrome resembling ageing. *Nature*, **390**(6655): 45–51.

Kuro-O M. 2011. Phosphate and Klotho. *Kidney International*, **79** Suppl 121: S20–S23.

Kurosu H, Ogawa Y, Miyoshi M, et al. 2006. Regulation of fibroblast growth factor-23 signaling by klotho. *Journal of Biological Chemistry*, **281**(10): 6120–6123.

Kurosu H, Yamamoto M, Clark JD, et al. 2005. Suppression of aging in mice by the hormone klotho. *Science*, **309**(5742): 1829–1833.

Lamis A, Siddiqui SW, Ashok T, et al. 2022. Hutchinson-gilford progeria syndrome: a literature review. *Cureus*, **14**(8): e28629.

Larsson NG, Wang JM, Wilhelmsson H, et al. 1998. Mitochondrial transcription factor A is necessary for mtDNA maintance and embryogenesis in mice. *Nature Genetics*, **18**(3): 231–236.

Larsson NG. 2010. Somatic mitochondrial DNA mutations in mammalian aging. *Annual Review of Biochemistry*, **79**: 683–706.

Lee DY, Kim H, Ku SY, et al. 2010. Association between polymorphisms in Wnt signaling pathway genes and bone mineral density in postmenopausal Korean women. *Menopause*, **17**(5): 1064–1070.

Lee JS, Ward WO, Ren HZ, et al. 2012. Meta-analysis of gene expression in the mouse liver reveals biomarkers associated with inflammation increased early during aging. *Mechanisms of Ageing and Development*, **133**(7): 467–478.

Lei YJ, Guerra Martinez C, Torres-Odio S, et al. 2021. Elevated type i interferon responses potentiate metabolic dysfunction, inflammation, and accelerated aging in mtDNA mutator mice. *Science Advances*, **7**(22): eabe7548.

Lenaers G, Bonneau D, Delneste Y, et al. 2020. Dysfunctional t cell mitochondria lead to premature aging. *Trends in Molecular Medicine*, **26**(9): 799–800.

Lennox AM. 2010. Care of the geriatric rabbit. *Veterinary Clinics of North America: Exotic Animal Practice*, **13**(1): 123–133.

Lesné S, Koh MT, Kotilinek L, et al. 2006. A specific amyloid-β protein assembly in the brain impairs memory. *Nature*, **440**(7082): 352–357.

Leung GK, Schmidt WK, Bergo MO, et al. 2001. Biochemical studies of *Zmpste24*–deficient mice. *Journal of Biological Chemistry*, **276**(31): 29051–29058.

Levin VA, Jiang X, Kagan R. 2018. Estrogen therapy for osteoporosis in the modern era. *Osteoporosis International*, **29**(5): 1049–1055.

Lhotellier L, Cohen-Salmon C. 1989. Genetics and senescence. I. Age-related changes in activity and exploration in three inbred strains of mice. *Physiology & Behavior*, **45**(3): 491–493.

Li W, Yeo LS, Vidal C, et al. 2011. Decreased bone formation and osteopenia in lamin A/C-deficient mice. *PLoS One*, **6**(4): e19313.

Liang KX, Kristiansen CK, Mostafavi S, et al. 2020. Disease-specific phenotypes in iPSC-derived neural stem cells with *POLG* mutations. *EMBO Molecular Medicine*, **12**(10): e12146.

Liao CY, Kennedy BK. 2014. Mouse models and aging: longevity and progeria. *Current Topics in Developmental Biology*, **109**: 249–285.

Lindahl T, Wood RD. 1999. Quality control by DNA repair. *Science*, **286**(5446): 1897–1905.

Liu BH, Ghosh S, Yang X, et al. 2012. Resveratrol rescues SIRT1-dependent adult stem cell decline and alleviates progeroid features in laminopathy-based progeria. *Cell Metabolism*, **16**(6): 738–750.

Liu G, Chen HY, Liu H, et al. 2021. Emerging roles of SIRT6 in human diseases and its modulators. *Medicinal Research Reviews*, **41**(2): 1089–1137.

Liu L, Trimarchi JR, Smith PJS, et al. 2002. Mitochondrial dysfunction leads to telomere attrition and genomic instability. *Aging Cell*, **1**(1): 40–46.

Liu N, Qi BY, Zhang YL, et al. 2022. Bu-gu-sheng-sui decoction promotes osteogenesis via activating the ERK/smad signaling pathways. *Frontiers in Pharmacology*, **13**: 976121.

Lombard DB, Schwer B, Alt FW, et al. 2008. SIRT6 in DNA repair, metabolism and ageing. *Journal of Internal Medicine*, **263**(2): 128–141.

Lu TQ, Zhang ZQ, Bi ZF, et al. 2023. TFAM deficiency in dendritic cells leads to mitochondrial dysfunction and enhanced antitumor immunity through cGAS-STING pathway. *Journal for ImmunoTherapy of Cancer*, **11**(3): e005430.

Manandhar M, Boulware KS, Wood RD. 2015. The *ERCC1* and *ERCC4* (*XPF*) genes and gene products. *Gene*, **569**(2): 153–161.

Manczak M, Jung Y, Park BS, et al. 2005. Time-course of mitochondrial gene expressions in mice brains: implications for mitochondrial dysfunction, oxidative damage, and cytochrome *c* in aging. *Journal of Neurochemistry*, **92**(3): 494–504.

Manolagas SC. 2010. From estrogen-centric to aging and oxidative stress: a revised perspective of the pathogenesis of osteoporosis. *Endocrine Reviews*, **31**(3): 266–300.

Maréchal A, Zou L. 2013. DNA damage sensing by the ATM and ATR kinases. *Cold Spring Harbor Perspectives in Biology*, **5**(9): a012716.

Martin A, David V, Quarles LD. 2012. Regulation and function of the FGF23/Klotho endocrine pathways. *Physiological Reviews*, **92**(1): 131–155.

Mason PJ, Wilson DB, Bessler M. 2005. Dyskeratosis congenita - a disease of dysfunctional telomere maintenance. *Current Molecular Medicine*, **5**(2): 159–170.

Matsuda S, Harmansa S, Affolter M. 2016. BMP morphogen gradients in flies. *Cytokine & Growth Factor Reviews*, **27**: 119–127.

Matsushita M, Tsuboyama T, Kasai R, et al. 1986. Age-related changes in bone mass in the senescence-accelerated mouse (SAM). SAM-R/3 and SAM-P/6 as new murine models for senile osteoporosis. *The Americal Journal of Pathology*, **125**(2): 276–283.

Meliska CJ, Burke PA, Bartke A, et al. 1997. Inhibitory avoidance and appetitive learning in aged normal mice: comparison with transgenic mice having elevated plasma growth hormone levels. *Neurobiology of Learning and Memory*, **68**(1): 1–12.

Merideth MA, Gordon LB, Clauss S, et al. 2008. Phenotype and course of hutchinson-gilford progeria syndrome. *New England Journal of Medicine*, **358**(6): 592–604.

Michishita E, McCord RA, Berber E, et al. 2008. SIRT6 is a histone H3 lysine 9 deacetylase that modulates telomeric chromatin. *Nature*, **452**(7186): 492–496.

Mirsaidi A, Genelin K, Vetsch JR, et al. 2014. Therapeutic potential of adipose-derived stromal cells in age-related osteoporosis. *Biomaterials*,

**35**(26): 7326–7335.

Mitchell SJ, Scheibye-Knudsen M, Longo DL, et al. 2015. Animal models of aging research: implications for human aging and age-related diseases. *Annual Review of Animal Biosciences*, **3**: 283–303.

Miyazaki T. 2013. Role of mitochondria in osteoclast function. *Clinical Calcium*, **23**(11): 1577–1583.

Moerman EJ, Teng K, Lipschitz DA, et al. 2004. Aging activates adipogenic and suppresses osteogenic programs in mesenchymal marrow stroma/stem cells: the role of PPAR-γ2 transcription factor and TGF-β/BMP signaling pathways. *Aging Cell*, **3**(6): 379–389.

Monnat RJ Jr. 2010. Human RECQ helicases: roles in DNA metabolism, mutagenesis and cancer biology. *Seminars in Cancer Biology*, **20**(5): 329–339.

Mori M, Higuchi K. 2019. The senescence-accelerated mouse as a model for geriatrics and aging biology. *Folia Pharmacologica Japonica*, **153**(4): 179–185.

Mostoslavsky R, Chua KF, Lombard DB, et al. 2006. Genomic instability and aging-like phenotype in the absence of mammalian SIRT6. *Cell*, **124**(2): 315–329.

Mounkes LC, Kozlov S, Hernandez L, et al. 2003. A progeroid syndrome in mice is caused by defects in A-type lamins. *Nature*, **423**(6937): 298–301.

Mu W, Wang ZR, Ma CY, et al. 2018. Metformin promotes the proliferation and differentiation of murine preosteoblast by regulating the expression of *sirt6* and *oct4. Pharmacological Research*, **129**: 462–474.

Muller M. 2009. Cellular senescence: molecular mechanisms, *in vivo* significance, and redox considerations. *Antioxidants & Redox Signaling*, **11**(1): 59–98.

Murphy GG, Rahnama NP, Silva AJ. 2006. Investigation of age-related cognitive decline using mice as a model system: behavioral correlates. *The American Journal of Geriatric Psychiatry*, **14**(12): 1004–1011.

Nakanishi R, Shimizu M, Mori M, et al. 2006. Secreted frizzled-related protein 4 is a negative regulator of peak BMD in SAMP6 mice. *Journal of Bone and Mineral Research*, **21**(11): 1713–1721.

Navarro CL, Cadiñanos J, De Sandre-Giovannoli A, et al. 2005. Loss of ZMPSTE24 (FACE-1) causes autosomal recessive restrictive dermopathy and accumulation of lamin a precursors. *Human Molecular Genetics*, **14**(11): 1503–1513.

Neff F, Flores-Dominguez D, Ryan DP, et al. 2013. Rapamycin extends murine lifespan but has limited effects on aging. *Journal of Clinical Investigation*, **123**(8): 3272–3291.

Neveling K, Bechtold A, Hoehn H. 2007. Genetic instability syndromes with progeroid features. *Zeitschrift für Gerontologie und Geriatrie*, **40**(5): 339–348.

Ni WH, Zhang Y, Yin ZC. 2021. The protective mechanism of Klotho gene-modified bone marrow mesenchymal stem cells on acute kidney injury induced by rhabdomyolysis. *Regenerative Therapy*, **18**: 255–267.

Nidadavolu LS, Niedernhofer LJ, Khan SA. 2013. Identification of microRNAs dysregulated in cellular senescence driven by endogenous genotoxic stress. *Aging*, **5**(6): 460–473.

Niedernhofer LJ, Garinis GA, Raams A, et al. 2006. A new progeroid syndrome reveals that genotoxic stress suppresses the somatotroph axis. *Nature*, **444**(7122): 1038–1043.

Niedernhofer LJ, Gurkar AU, Wang YS, et al. 2018. Nuclear genomic instability and aging. *Annual Review of Biochemistry*, **87**: 295–322.

Niimi K, Takahashi E. 2014. Characterization of senescence-accelerated mouse prone 6 (SAMP6) as an animal model for brain research. *Experimental Animals*, **63**(1): 1–9.

Ogata N, Matsumura Y, Shiraki M, et al. 2002. Association of *klotho* gene polymorphism with bone density and spondylosis of the lumbar spine in postmenopausal women. *Bone*, **31**(1): 37–42.

Olivieri F, Albertini MC, Orciani M, et al. 2015. DNA damage response (DDR) and senescence: shuttled inflamma-mirnas on the stage of inflamm-aging. *Oncotarget*, **6**(34): 35509–35521.

Opresko PL, Otterlei M, Graakjær J, et al. 2004. The werner syndrome helicase and exonuclease cooperate to resolve telomeric D loops in a manner regulated by TRF1 and TRF2. *Molecular Cell*, **14**(6): 763–774.

Osorio FG, Bárcena C, Soria-Valles C, et al. 2012. Nuclear lamina defects cause ATM-dependent NF-κB activation and link accelerated aging to a systemic inflammatory response. *Genes & Development*, **26**(20): 2311–2324.

Osorio FG, Navarro CL, Cadiñanos J, et al. 2011. Splicing-directed therapy in a new mouse model of human accelerated aging. *Science Translational Medicine*, **3**(106): 106ra107.

Osorio FG, Varela I, Lara E, et al. 2010. Nuclear envelope alterations generate an aging-like epigenetic pattern in mice deficient in Zmpste24 metalloprotease. *Aging Cell*, **9**(6): 947–957.

Östlund C, Sullivan T, Stewart CL, et al. 2006. Dependence of diffusional mobility of integral inner nuclear membrane proteins on a-type lamins. *Biochemistry*, **45**(5): 1374–1382.

Parisi MA, Clayton DA. 1991. Similarity of human mitochondrial transcription factor 1 to high mobility group proteins. *Science*, **252**(5008): 965–969.

Parra MK, Gee S, Mohandas N, et al. 2011. Efficient *in vivo* manipulation of alternative Pre-mRNA splicing events using antisense morpholinos in mice. *Journal of Biological Chemistry*, **286**(8): 6033–6039.

Pendás AM, Zhou ZJ, Cadiñanos J, et al. 2002. Defective prelamin A processing and muscular and adipocyte alterations in Zmpste24 metalloproteinase-deficient mice. *Nature Genetics*, **31**(1): 94–99.

Perez K, Parras A, Picó S, et al. 2024. DNA repair-deficient premature aging models display accelerated epigenetic age. *Aging Cell*, **23**(2): e14058.

Perkins SL, Gibbons R, Kling S, et al. 1994. Age-related bone loss in mice is associated with an increased osteoclast progenitor pool. *Bone*, **15**(1): 65–72.

Pignolo RJ. 2023. Aging and bone metabolism. *Comprehensive Physiology*, **13**(1): 4355–4386.

Pignolo RJ, Suda RK, McMillan EA, et al. 2008. Defects in telomere maintenance molecules impair osteoblast differentiation and promote osteoporosis. *Aging Cell*, **7**(1): 23–31.

Pilmane M, Salma-Ancane K, Loca D, et al. 2017. Strontium and strontium ranelate: historical review of some of their functions. *Materials Science and Engineering: C*, **78**: 1222–1230.

Radulescu CI, Cerar V, Haslehurst P, et al. 2021. The aging mouse brain: cognition, connectivity and calcium. *Cell Calcium*, **94**: 102358.

Rahnasto-Rilla MK, McLoughlin P, Kulikowicz T, et al. 2017. The identification of a SIRT6 activator from brown algae *Fucus distichus. Marine Drugs*, **15**(6): 190.

Rantanen A, Jansson M, Oldfors A, et al. 2001. Downregulation of Tfam and mtDNA copy number during mammalian spermatogenesis. *Mammalian Genome*, **12**(10): 787–792.

Rasheed N, Wang XY, Niu QT, et al. 2006. Atm-deficient mice: an osteoporosis model with defective osteoblast differentiation and increased osteoclastogenesis. *Human Molecular Genetics*, **15**(12): 1938–1948.

Reginster JY, Brandi ML, Cannata-Andía J, et al. 2015. The position of strontium ranelate in today's management of osteoporosis. *Osteoporosis International*, **26**(6): 1667–1671.

Rivas D, Li W, Akter R, et al. 2009. Accelerated features of age-related bone loss in Zmpste24 metalloproteinase-deficient mice. *The Journals of Gerontology: Series A*, **64**(10): 1015–1024.

Robinson AR, Yousefzadeh MJ, Rozgaja TA, et al. 2018. Spontaneous DNA damage to the nuclear genome promotes senescence, redox imbalance and aging. *Redox Biology*, **17**: 259–273.

Rodier F, Coppé JP, Patil CK, et al. 2009. Persistent DNA damage signalling triggers senescence-associated inflammatory cytokine secretion. *Nature Cell Biology*, **11**(8): 973–979.

Roessinger O, Hügle T, Walker UA, et al. 2022. *Polg* mtDNA mutator mice reveal limited involvement of vertebral bone loss in premature aging-related thoracolumbar hyperkyphosis. *Bone Reports*, **17**: 101618.

Rubin CD, Reed B, Sakhaee K, et al. 1994. Treating a patient with the werner syndrome and osteoporosis using recombinant human insulin-like growth factor. *Annals of Internal Medicine*, **121**(9): 665–668.

Rudolph KL, Chang S, Lee HW, et al. 1999. Longevity, stress response, and cancer in aging telomerase-deficient mice. *Cell*, **96**(5): 701–712.

Saeed H, Abdallah BM, Ditzel N, et al. 2011. Telomerase-deficient mice exhibit bone loss owing to defects in osteoblasts and increased osteoclastogenesis by inflammatory microenvironment. *Journal of Bone and Mineral Research*, **26**(7): 1494–1505.

Saidak Z, Le Henaff C, Azzi S, et al. 2014. Low-dose PTH increases osteoblast activity via decreased *Mef2c/Sost* in senescent osteopenic mice. *Journal of Endocrinology*, **223**(1): 25–33.

Sanghani-Kerai A, McCreary D, Lancashire H, et al. 2018. Stem cell interventions for bone healing: fractures and osteoporosis. *Current Stem Cell Research & Therapy*, **13**(5): 369–377.

Sasaki M, Hasegawa T, Yamada T, et al. 2013. Altered distribution of bone matrix proteins and defective bone mineralization in *klotho*-deficient mice. *Bone*, **57**(1): 206–219.

Scaffidi P, Misteli T. 2006. Lamin a-dependent nuclear defects in human aging. *Science*, **312**(5776): 1059–1063.

Schmidt E, Nilsson O, Koskela A, et al. 2012. Expression of the hutchinson-gilford progeria mutation during osteoblast development results in loss of osteocytes, irregular mineralization, and poor biomechanical properties. *Journal of Biological Chemistry*, **287**(40): 33512–33522.

Segre D, Segre M. 1977. Age-related changes in B and T lymphocytes and decline of humoral immune responsiveness in aged mice. *Mechanisms of Ageing and Development*, **6**(2): 115–129.

Shabalina IG, Vyssokikh MY, Gibanova N, et al. 2017. Improved health-span and lifespan in mtDNA mutator mice treated with the mitochondrially targeted antioxidant SkQ1. *Aging*, **9**(2): 315–339.

Sharpless NE, Depinho RA. 2004. Telomeres, stem cells, senescence, and cancer. *Journal of Clinical Investigation*, **113**(2): 160–168.

Shen X, Chen X, Huang JD, et al. 2020. Age-dependent role of SIRT6 in jawbone via regulating senescence and autophagy of bone marrow stromal cells. *Journal of Molecular Histology*, **51**(1): 67–76.

Shi YH, Dierckx A, Wanrooij PH, et al. 2012. Mammalian transcription factor A is a core component of the mitochondrial transcription machinery. *Proceedings of the National Academy of Sciences of the United States of America*, **109**(41): 16510–16515.

Shiraki M, Aoki C, Goto M. 1998. Bone and calcium metabolism in werner's syndrome. *Endocrine Journal*, **45**(4): 505–512.

Sijbers AM, van der Spek PJ, Odijk H, et al. 1996. Mutational analysis of the human nucleotide excision repair gene *ERCC1*. *Nucleic Acids Research*, **24**(17): 3370–3380.

Sikora M, Śmieszek A, Marycz K. 2021. Bone marrow stromal cells (BMSCs $CD45^-/CD44^+/CD73^+/CD90^+$) isolated from osteoporotic mice SAM/P6 as a novel model for osteoporosis investigation. *Journal of Cellular and Molecular Medicine*, **25**(14): 6634–6651.

Silva MJ, Brodt MD, Ko M, et al. 2005. Impaired marrow osteogenesis is associated with reduced endocortical bone formation but does not impair periosteal bone formation in long bones of SAMP6 mice. *Journal of Bone and Mineral Research*, **20**(3): 419–427.

Sivaraman DMT, D'Souza M, Ratnakar C. 1999. Progeria (hutchinson-gilford): a case report. *The Journal of Dermatology*, **26**(5): 324–328.

Sprott RL, Eleftheriou BE. 1974. Open-field behavior in aging inbred mice. *Gerontologia*, **20**(3): 155–162.

Squarzoni S, Schena E, Sabatelli P, et al. 2021. Interleukin-6 neutralization ameliorates symptoms in prematurely aged mice. *Aging Cell*, **20**(1): e13285.

Stead ER, Bjedov I. 2021. Balancing DNA repair to prevent ageing and cancer. *Experimental Cell Research*, **405**(2): 112679.

Stein GH, Drullinger LF, Soulard A, et al. 1999. Differential roles for cyclin-dependent kinase inhibitors p21 and p16 in the mechanisms of senescence and differentiation in human fibroblasts. *Molecular and Cellular Biology*, **19**(3): 2109–2117.

Strandgren C, Nasser HA, Mckenna T, et al. 2015. Transgene silencing of the Hutchinson-Gilford progeria syndrome mutation results in a reversible bone phenotype, whereas resveratrol treatment does not show overall beneficial effects. *The FASEB Journal*, **29**(8): 3193–3205.

Stunes AK, Brobakken CL, Sujan MaJ, et al. 2022. Acute effects of strength and endurance training on bone turnover markers in young adults and elderly men. *Frontiers in Endocrinology*, **13**: 915241.

Sugatani T, Agapova O, Malluche HH, et al. 2015. SIRT6 deficiency culminates in low-turnover osteopenia. *Bone*, **81**: 168–177.

Sui TT, Liu D, Liu TJ, et al. 2019. *LMNA*-mutated rabbits: a model of premature aging syndrome with muscular dystrophy and dilated cardiomyopathy. *Aging and Disease*, **10**(1): 102–115.

Sullivan T, Escalante-Alcalde D, Bhatt H, et al. 1999. Loss of a-type lamin expression compromises nuclear envelope integrity leading to muscular dystrophy. *Journal of Cell Biology*, **147**(5): 913–920.

Suominen TH, Alén M, Törmäkangas T, et al. 2021. Regular strength and sprint training counteracts bone aging: a 10 year follow up in male masters athletes. *JBMR Plus*, **5**(7): e10513.

Suzuki H, Amizuka N, Oda K, et al. 2005. Histological evidence of the altered distribution of osteocytes and bone matrix synthesis in klotho-deficient mice. *Archives of Histology and Cytology*, **68**(5): 371–381.

Takada K, Inaba M, Ichioka N, et al. 2006. Treatment of senile osteoporosis in SAMP6 mice by intra-bone marrow injection of allogeneic bone marrow cells. *Stem Cells*, **24**(2): 399–405.

Takahashi K, Tsuboyama T, Matsushita M, et al. 1994. Modification of strain-specific femoral bone density by bone marrow-derived factors administered neonatally: a study on the spontaneously osteoporotic mouse, SAMP6. *Bone and Mineral*, **24**(3): 245–255.

Takeda T, Hosokawa M, Higuchi K. 1997. Senescence-accelerated mouse (SAM): a novel murine model of senescence. *Experimental Gerontology*, **32**(1-2): 105–109.

Tam A, Nouvet FJ, Fujimura-Kamada K, et al. 1998. Dual roles for ste24p in yeast a-factor maturation: $NH_2$-terminal proteolysis and COOH-terminal CAAX processing. *The Journal of Cell Biology*, **142**(3): 635–649.

Thomas KR, Capecchi MR. 1987. Site-directed mutagenesis by gene targeting in mouse embryo-derived stem cells. *Cell*, **51**(3): 503–512.

Tissenbaum HA. 2015. Using *C. elegans* for aging research. *Invertebrate Reproduction & Development*, **59**(S1): 59–63.

Tong C, Li P, Wu NL, et al. 2010. Production of *p53* gene knockout rats by homologous recombination in embryonic stem cells. *Nature*, **467**(7312): 211–213.

Trifunovic A, Wredenberg A, Falkenberg M, et al. 2004. Premature ageing in mice expressing defective mitochondrial DNA polymerase. *Nature*, **429**(6990): 417–423.

Tsodikov OV, Enzlin JH, Schärer OD, et al. 2005. Crystal structure and DNA binding functions of ERCC1, a subunit of the DNA structure-specific endonuclease XPF-ERCC1. *Proceedings of the National Academy of Sciences of the United States of America*, **102**(32): 11236–11241.

Ullrich NJ, Gordon LB. 2015. Hutchinson-Gilford progeria syndrome. *Handbook of Clinical Neurology*, **132**: 249–264.

United Nations. 2019. World population prospects 2019.

https://www.un.org/development/desa/pd/news/world-population-prospects-2019-0.

Urakawa I, Yamazaki Y, Shimada T, et al. 2006. Klotho converts canonical FGF receptor into a specific receptor for FGF23. *Nature*, **444**(7120): 770–774.

Vanderstraeten S, Van den Brûle S, Hu JP, et al. 1998. The role of 3'-5' exonucleolytic proofreading and mismatch repair in yeast mitochondrial DNA error avoidance. *Journal of Biological Chemistry*, **273**(37): 23690–23697.

Vanhooren V, Libert C. 2013. The mouse as a model organism in aging research: usefulness, pitfalls and possibilities. *Ageing Research Reviews*, **12**(1): 8–21.

Varela I, Cadiñanos J, Pendás AM, et al. 2005. Accelerated ageing in mice deficient in Zmpste24 protease is linked to p53 signalling activation. *Nature*, **437**(7058): 564–568.

Varela I, Pereira S, Ugalde AP, et al. 2008. Combined treatment with statins and aminobisphosphonates extends longevity in a mouse model of human premature aging. *Nature Medicine*, **14**(7): 767–772.

Varga R, Eriksson M, Erdos MR, et al. 2006. Progressive vascular smooth muscle cell defects in a mouse model of Hutchinson-Gilford progeria syndrome. *Proceedings of the National Academy of Sciences of the United States of America*, **103**(9): 3250–3255.

Vidak S, Foisner R. 2016. Molecular insights into the premature aging disease progeria. *Histochemistry and Cell Biology*, **145**(4): 401–417.

Vidal C, Bermeo S, Fatkin D, et al. 2012. Role of the nuclear envelope in the pathogenesis of age-related bone loss and osteoporosis. *BoneKEy Reports*, **1**(5): 62.

Villa-Bellosta R, Rivera-Torres J, Osorio FG, et al. 2013. Defective extracellular pyrophosphate metabolism promotes vascular calcification in a mouse model of hutchinson-gilford progeria syndrome that is ameliorated on pyrophosphate treatment. *Circulation*, **127**(24): 2442–2451.

Vo N, Seo HY, Robinson A, et al. 2010. Accelerated aging of intervertebral discs in a mouse model of progeria. *Journal of Orthopaedic Research*, **28**(12): 1600–1607.

Wang F, Ren SY, Chen JF, et al. 2020. Myelin degeneration and diminished myelin renewal contribute to age-related deficits in memory. *Nature Neuroscience*, **23**(4): 481–486.

Wang HT, Chen QJ, Lee SH, et al. 2012a. Impairment of osteoblast differentiation due to proliferation-independent telomere dysfunction in mouse models of accelerated aging. *Aging Cell*, **11**(4): 704–713.

Wang J, Clauson CL, Robbins PD, et al. 2012b. The oxidative DNA lesions 8, 5'-cyclopurines accumulate with aging in a tissue-specific manner. *Aging Cell*, **11**(4): 714–716.

Wang JM, Wilhelmsson H, Graff C, et al. 1999. Dilated cardiomyopathy and atrioventricular conduction blocks induced by heart-specific inactivation of mitochondrial DNA gene expression. *Nature Genetics*, **21**(1): 133–137.

Washimi Y, Chen H, Ito A, et al. 2010. Effect of intermittent treatment with human parathyroid hormone 1–34 in SAMP6 senescence-accelerated mice. *Journal of Endocrinological Investigation*, **33**(6): 395–400.

Wauquier F, Leotoing L, Coxam V, et al. 2009. Oxidative stress in bone remodelling and disease. *Trends in Molecular Medicine*, **15**(10): 468–477.

Weeda G, Donker I, de Wit J, et al. 1997. Disruption of mouse *ERCC1* results in a novel repair syndrome with growth failure, nuclear abnormalities and senescence. *Current Biology*, **7**(6): 427–439.

Wilson K, Usami Y, Hogarth D, et al. 2021. Analysis of association between morphometric parameters of growth plate and bone growth of tibia in mice and humans. *Cartilage*, **13**(S2): 315S–325S.

Wong A, Kieu T, Robbins PD. 2020. The Ercc1$^{-/\Delta}$ mouse model of accelerated senescence and aging for identification and testing of novel senotherapeutic interventions. *Aging*, **12**(24): 24481–24483.

Woo DK, Green PD, Santos JH, et al. 2012. Mitochondrial genome instability and ROS enhance intestinal tumorigenesis in *APC*$^{Min/+}$ mice. *The American Journal of Pathology*, **180**(1): 24–31.

Worman HJ, Michaelis S. 2018. Permanently farnesylated prelamin a, progeria, and atherosclerosis. *Circulation*, **138**(3): 283–286.

Worman HJ, Michaelis S. 2023. Prelamin A and ZMPSTE24 in premature and physiological aging. *Nucleus*, **14**(1): 2270345.

Wu YS, Chen LW, Wang Y, et al. 2015. Overexpression of Sirtuin 6 suppresses cellular senescence and NF-κB mediated inflammatory responses in osteoarthritis development. *Scientific Reports*, **5**: 17602.

Xu K, Guo YN, Wang YD, et al. 2023. Decreased Enterobacteriaceae translocation due to gut microbiota remodeling mediates the alleviation of premature aging by a high-fat diet. *Aging Cell*, **22**(2): e13760.

Yamashita T, Nifuji A, Furuya K, et al. 1998. Elongation of the epiphyseal trabecular bone in transgenic mice carrying a *klotho* gene locus mutation that leads to a syndrome resembling aging. *Journal of Endocrinology*, **159**(1): 1–8.

Yamashita T, Sekiya I, Kawaguchi N, et al. 2001. *Klotho*-deficient mice are resistant to bone loss induced by unloading due to sciatic neurectomy. *Journal of Endocrinology*, **168**(2): 347–351.

Yamashita T, Yoshitake H, Tsuji K, et al. 2000. Retardation in bone resorption after bone marrow ablation in *Klotho* mutant mice. *Endocrinology*, **141**(1): 438–445.

Yang SH, Bergo MO, Toth JI, et al. 2005. Blocking protein farnesyltransferase improves nuclear blebbing in mouse fibroblasts with a targeted Hutchinson-Gilford progeria syndrome mutation. *Proceedings of the National Academy of Sciences of the United States of America*, **102**(29): 10291–10296.

Yang SH, Meta M, Qiao X, et al. 2006. A farnesyltransferase inhibitor improves disease phenotypes in mice with a Hutchinson-Gilford progeria syndrome mutation. *Journal of Clinical Investigation*, **116**(8): 2115–2121.

Yao C, Sun J, Luo WX, et al. 2024. Down-expression of miR-494–3p in senescent osteocyte-derived exosomes inhibits osteogenesis and accelerates age-related bone loss via PTEN/PI3K/AKT pathway. *Bone & Joint Research*, **13**(2): 52–65.

Yasuda H, Shima N, Nakagawa N, et al. 1998. Osteoclast differentiation factor is a ligand for osteoprotegerin/osteoclastogenesis-inhibitory factor and is identical to TRANCE/RANKL. *Proceedings of the National Academy of Sciences of the United States of America*, **95**(7): 3597–3602.

Yoshioka H, Komura S, Kuramitsu N, et al. 2022. Deletion of *Tfam* in *Prx1-Cre* expressing limb mesenchyme results in spontaneous bone fractures. *Journal of Bone and Mineral Metabolism*, **40**(5): 839–852.

You WJ, Rotili D, Li TM, et al. 2017. Structural basis of sirtuin 6 activation by synthetic small molecules. *Angewandte Chemie International Edition*, **56**(4): 1007–1011.

You WJ, Zheng W, Weiss S, et al. 2019. Structural basis for the activation and inhibition of Sirtuin 6 by quercetin and its derivatives. *Scientific Reports*, **9**(1): 19176.

Young SG, Fong LG, Michaelis S. 2005. *Thematic Review Series: Lipid Posttranslational Modifications*. Prelamin A, Zmpste24, misshapen cell nuclei, and progeria-new evidence suggesting that protein farnesylation could be important for disease pathogenesis. *Journal of Lipid Research*, **46**(12): 2531–2558.

Yousefzadeh MJ, Melos KI, Angelini L, et al. 2019. Mouse models of accelerated cellular senescence. *In*: Demaria M. Cellular Senescence. New York: Humana Press, 203–230.

Yousefzadeh MJ, Zhao J, Bukata C, et al. 2020. Tissue specificity of senescent cell accumulation during physiologic and accelerated aging of mice. *Aging Cell*, **19**(3): e13094.

Yu TH, Slone J, Liu WS, et al. 2022. Premature aging is associated with higher levels of 8-oxoguanine and increased DNA damage in the polg mutator mouse. *Aging Cell*, **21**(9): e13669.

Zhai XY, Yan P, Zhang J, et al. 2016. Knockdown of SIRT6 enables human bone marrow mesenchymal stem cell senescence. *Rejuvenation Research*, **19**(5): 373–384.

Zhang DM, Cui DX, Xu RS, et al. 2016. Phenotypic research on senile osteoporosis caused by SIRT6 deficiency. *International Journal of Oral Science*, **8**(2): 84–92.

Zhang DM, Jing JJ, Lou F, et al. 2018. Evidence for excessive osteoclast activation in SIRT6 null mice. *Scientific Reports*, **8**(1): 10992.

Zhang P, Liu YS, Wang YJ, et al. 2017. SIRT6 promotes osteogenic differentiation of mesenchymal stem cells through BMP signaling. *Scientific Reports*, **7**(1): 10229.

Zhang XZ, Peng YM, Yu JC, et al. 2009. Changes in histomorphometric and mechanical properties of femurs induced by acupuncture at the shenshu point in the SAMP6 mouse model of senile osteoporosis. *Gerontology*, **55**(3): 322–332.

Zhang YJ, Shao CH, Li HL, et al. 2021a. The distinct function of $p21^{Waf1/Cip1}$ with $p16^{Ink4a}$ in modulating aging phenotypes of werner syndrome by affecting tissue homeostasis. *Frontiers in Genetics*, **12**: 597566.

Zhang YL, Chai Y, Pan XJ, et al. 2019. Tai chi for treating osteopenia and primary osteoporosis: a meta-analysis and trial sequential analysis. *Clinical Interventions in Aging*, **14**: 91–104.

Zhang ZK, Song YP, Wang SI, et al. 2021b. Osteoblasts/osteocytes sirtuin6 is vital to preventing ischemic osteonecrosis through targeting VDR-RANKL signaling. *Journal of Bone and Mineral Research*, **36**(3): 579–590.

Zhao J, Zhang L, Lu AP, et al. 2020. ATM is a key driver of NF-κB-dependent DNA-damage-induced senescence, stem cell dysfunction and aging. *Aging*, **12**(6): 4688–4710.

Zhou ZY, Sun LQ, Han XY, et al. 2023. Efficacy, mechanism, and structure-activity relationship of 6-methoxy benzofuran derivatives as a useful tool for senile osteoporosis. *Journal of Medicinal Chemistry*, **66**(3): 1742–1760.

Zhu K, Prince RL. 2012. Calcium and bone. *Clinical Biochemistry*, **45**(12): 936–942.

Zheng et al. *Zool. Res.* 2024, 45(4): 747−766
https://doi.org/10.24272/j.issn.2095-8137.2024.062

ZR | Zoological Research

Review Open Access

# Immunobiology of COVID-19: Mechanistic and therapeutic insights from animal models

Hong-Yi Zheng[1], Tian-Zhang Song[1], Yong-Tang Zheng[1,2,*]

[1] *State Key Laboratory of Genetic Evolution & Animal Models*, *KIZ-CUHK Joint Laboratory of Bioresources and Molecular Research in Common Diseases*, *Center for Biosafety Mega-Science*, *Kunming Institute of Zoology*, *Chinese Academy of Sciences*, *Kunming*, *Yunnan* 650223, *China*

[2] *National Resource Center for Non-Human Primates*, *National Research Facility for Phenotypic & Genetic Analysis of Model Animals (Primate Facility)*, *Kunming Institute of Zoology*, *Chinese Academy of Sciences*, *Kunming*, *Yunnan* 650107, *China*

## ABSTRACT

The distribution of the immune system throughout the body complicates *in vitro* assessments of coronavirus disease 2019 (COVID-19) immunobiology, often resulting in a lack of reproducibility when extrapolated to the whole organism. Consequently, developing animal models is imperative for a comprehensive understanding of the pathology and immunology of severe acute respiratory syndrome coronavirus 2 (SARS-CoV-2) infection. This review summarizes current progress related to COVID-19 animal models, including non-human primates (NHPs), mice, and hamsters, with a focus on their roles in exploring the mechanisms of immunopathology, immune protection, and long-term effects of SARS-CoV-2 infection, as well as their application in immunoprevention and immunotherapy of SARS-CoV-2 infection. Differences among these animal models and their specific applications are also highlighted, as no single model can fully encapsulate all aspects of COVID-19. To effectively address the challenges posed by COVID-19, it is essential to select appropriate animal models that can accurately replicate both fatal and non-fatal infections with varying courses and severities. Optimizing animal model libraries and associated research tools is key to resolving the global COVID-19 pandemic, serving as a robust resource for future emerging infectious diseases.

**Keywords:** SARS-CoV-2; COVID-19; Animal models; Infection immunology; Immunotherapy

## INTRODUCTION

Severe acute respiratory syndrome coronavirus 2 (SARS-CoV-2) is the pathogen responsible for coronavirus disease 2019 (COVID-19), which can manifest as mild to severe respiratory illness and can cause death in humans (Riggioni et al., 2020). Since its emergence in late 2019, the highly transmissible and variable nature of this virus has posed a significant challenge to the global medical community. As of February 2024, the pandemic has led to over 774 million confirmed cases and more than 7 million deaths worldwide (https://covid19.who.int/). Despite the continuous evolution of the virus, the current prevalent variants are not associated with increased disease severity (Statement from the Fifteenth Meeting of the International Health Regulations (IHR) (2005) Emergency Committee on the COVID-19 Pandemic). Consequently, on 4 May 2023, the World Health Organization (WHO) declared that COVID-19 no longer constituted a “public health emergency of international concern” (PHEIC). Nonetheless, considerable research challenges remain, particularly in our understanding of the role of the host immune system in disease progression, as well as the development of broad-spectrum vaccines capable of targeting rapidly mutating SARS-CoV-2 strains and the implementation of different immunotherapies. Therefore, animal model research remains a priority for advancing our knowledge of COVID-19.

Studying the immunobiology of COVID-19 using only *in vitro* tools is difficult due to the complexity of the human immune system. Animal models offer significant advantages as they enable the simulation and control of various factors, such as host characteristics, viral dosage, and antiviral interventions. These models facilitate procedures such as transgene expression, cell selection, and tissue sampling, which are challenging in humans, thereby providing valuable experimental data. Hence, animal models are essential for the

This is an open-access article distributed under the terms of the Creative Commons Attribution Non-Commercial License (http://creativecommons.org/licenses/by-nc/4.0/), which permits unrestricted non-commercial use, distribution, and reproduction in any medium, provided the original work is properly cited.

Copyright ©2024 Editorial Office of Zoological Research, Kunming Institute of Zoology, Chinese Academy of Sciences

Received: 23 February 2024; Accepted: 22 April 2024; Online: 23 April 2024

Foundation items: The work was supported by the National Key Research and Development Program of China (2022YFC2303700, 2021YFC2301300), Yunnan Key Research and Development Program (202303AC100026), National Natural Science Foundation of China (82302002, 82341069), Yunnan Fundamental Research Project (202201AS070047), and Strategic Priority Research Program of the Chinese Academy of Sciences (XDB0490000)

*Corresponding author, E-mail: zhengyt@mail.kiz.ac.cn

advancement of immunological research and immunotherapy for COVID-19, particularly those involving higher mammals. During the early stages of the pandemic, various animal models were established to support vaccine and drug development, and to investigate SARS-CoV-2 pathogenesis (Muñoz-Fontela et al., 2020). To date, naturally susceptible animals such as non-human primates (NHPs), Syrian hamsters (*Mesocricetus auratus*), ferrets (*Mustela furo*), and mice (*Mus musculus*) — either sensitized through transgenic techniques or infected with SARS-CoV-2-adapted strains — have been widely utilized. Various studies have documented the creation, pathology, and application of animal models for COVID-19 (Bi et al., 2021; Chu et al., 2022; Kane et al., 2023; Muñoz-Fontela et al., 2020; Shou et al., 2021; Zhang et al., 2023; Zhao et al., 2023), which will not be repeated here. Other reviews have also summarized the immune responses to SARS-CoV-2 infection in both patients and animals, highlighting the unique immune characteristics of diverse animal models (Chen et al., 2024; Saravanan et al., 2022). This review focuses on current advancements in our understanding of the immunological characteristics and mechanisms of animal models for COVID-19, as well as their applications in studying immune prevention and treatment strategies, emphasizing the effective use of each model to address specific problems (Figure 1).

## ANIMAL MODELS OF COVID-19

In response to the rapid global spread of SARS-CoV-2, various animal species, including NHPs, mice, ferrets, tree shrews, and Syrian hamsters, have been established as models to facilitate COVID-19 research. The suitability of these animals as models predominantly depends on the molecular structure of the primary binding receptor (ACE2) for the virus. Catarrhine primates, including apes and African/Asian monkeys, have ACE2 amino acid residues identical to those in human ACE2 (hACE2), while New World monkeys exhibit over 90% similarity, making both groups highly susceptible to SARS-CoV-2 (Gao & Zhang, 2020; Karki et al., 2021; Melin et al., 2020). However, the high costs associated with using large animal models often limit their utility in research, prompting a shift towards smaller animals. Tree shrews, which possess certain primate-like characteristics, show a divergence of 10 amino acids in their ACE2 key domain compared to hACE2, resulting in lower susceptibility to SARS-CoV-2 infection, characterized by mild viral shedding and lung lesions (Xu et al., 2020a; Zhao et al., 2020). Furthermore, mice and ferrets have ACE2 sequences that differ from hACE2 by eight and seven amino acids, respectively. Although mice are naturally resistant to SARS-CoV-2, humanized mouse models are widely utilized in COVID-19 research due to advancements in gene-editing techniques, including transgenic expression, clustered

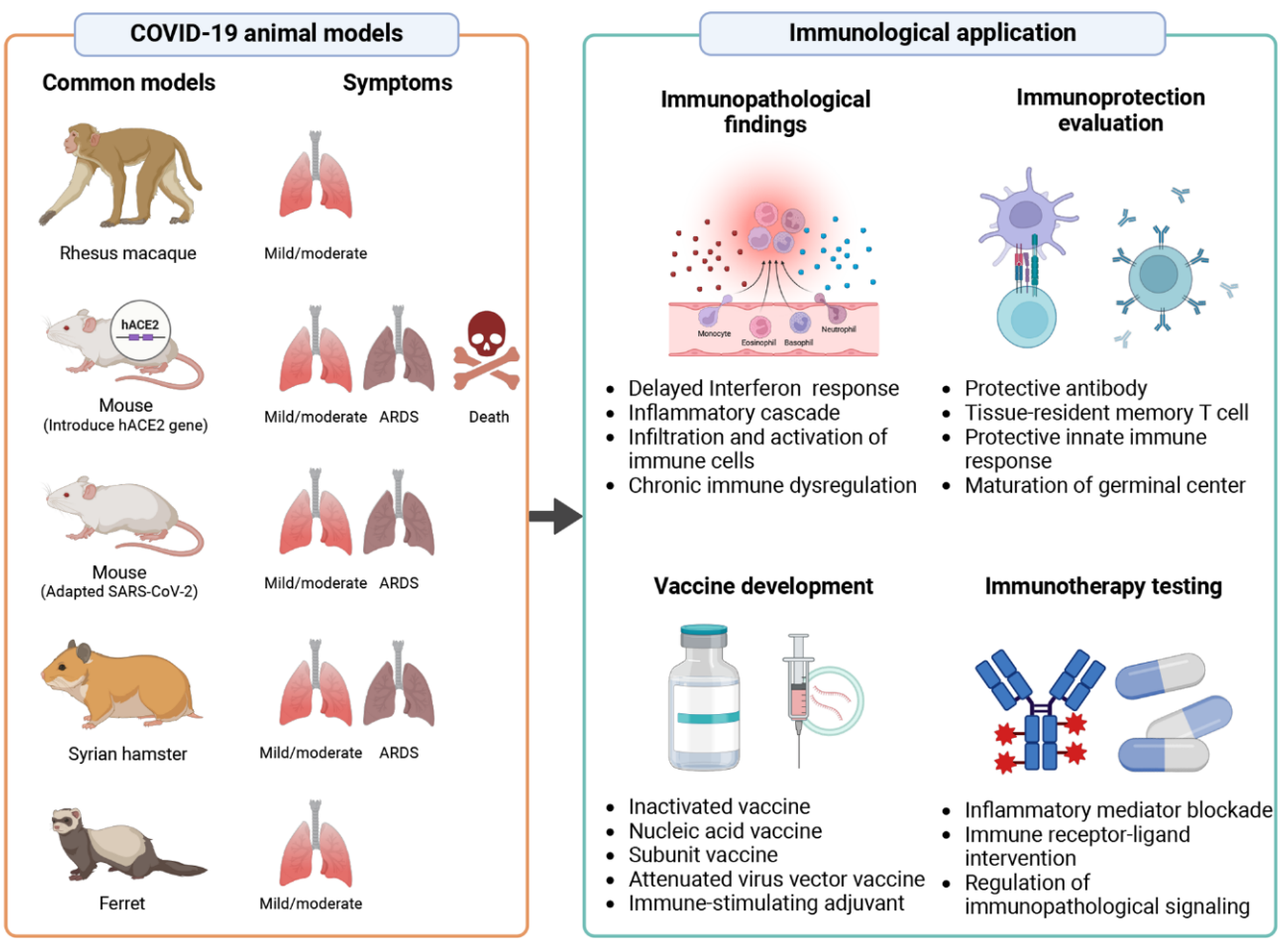



**Figure 1 Immunological applications of common COVID-19 animal models**

Rhesus macaques, mice transduced with human ACE2 gene, mice infected with adaptive SARS-CoV-2, Syrian hamsters, and ferrets are widely used to study immune pathogenesis and immune protection mechanisms of COVID-19, and also play important roles in COVID-19 vaccine and immunotherapeutic drug development. Figure created using BioRender (https://biorender.com/).

regularly interspaced short palindromic repeats (CRISPR)/CRISPR-associated protein 9 (Cas9) editing, and transient overexpression of hACE2 (Sefik et al., 2022; Zhang et al., 2023; Zhou et al., 2023). Conversely, ferrets exhibit a natural susceptibility to SARS-CoV-2, manifesting with mild clinical symptoms and relatively low lung viral titers (Zhao et al., 2023). Syrian hamsters, with only two amino acid differences in ACE2 compared to hACE2, are a preferred model for *in vivo* preclinical assessment of SARS-CoV-2 virulence and for testing vaccines, antivirals, and therapeutics (Handley et al., 2023). Despite these advancements, however, no single animal model can fully replicate all aspects of COVID-19, highlighting the need for tailored research approaches that utilize the unique features of each animal model (Table 1).

**NHPs**

Compared to other laboratory animals, NHPs possess immune and respiratory systems, as well as tissue structures, that closely resemble those of humans (Estes et al., 2018). Old World monkeys, such as rhesus macaques (*Macaca mulatta*), cynomolgus macaques (*Macaca fascicularis*), African green monkeys (*Chlorocebus aethiops*), and baboons (*Papio hamadryas*), and New World monkeys, such as common marmosets (*Callithrix jacchus*), are frequently employed as models for SARS-CoV-2 infection, displaying mild to moderate respiratory symptoms. In rhesus macaques, SARS-CoV-2 infection causes acute localized to widespread pneumonia, but typically without pronounced clinical respiratory symptoms (Shan et al., 2020). Notably, age significantly impacts the severity of SARS-CoV-2 in rhesus macaques, with older animals demonstrating more severe interstitial pneumonia and cytokine storm, despite a delayed immune response, compared to their younger counterparts (Song et al., 2020; Yu et al., 2020b). Cynomolgus macaques, which are smaller and less expensive to maintain, are predominant in China's experimental primate population, with crab-eating monkeys (211 171) far outnumbering rhesus macaques (28 806). Post-infection, cynomolgus macaques show symptoms such as abnormal chest radiographs, elevated body temperature, and weight loss, although their cytokine response and lung disease are less severe than in rhesus macaques (Lu et al., 2020). Despite the abundance of cynomolgus macaques, rhesus macaques are preferred in COVID-19 research due to their higher suitability. Northern pig-tailed macaques (*Macaca leonina*), lacking the retroviral restriction factor tripartite motif-containing protein 5α (TRIM5α), exhibit more severe inflammation and physical impairment from SARS-CoV-2 than rhesus macaques (Kuang et al., 2009; Song et al., 2021). However, limited research on these macaques due to their small number hinders a full understanding of their potential in studies. Common marmosets exhibit lower susceptibility to SARS-CoV-2, with less pronounced and replicable manifestations of COVID-19 (Ireland et al., 2022; Lu et al., 2020). African green monkeys and baboons, though utilized less frequently, can also serve as SARS-CoV-2 models. Compared to macaques, baboons experience prolonged viral RNA shedding and more severe lung inflammation (Singh et al., 2020), while African green monkeys display higher SARS-CoV-2 replication and marked

**Table 1 Common animal models for COVID-19 immunobiology research**

| Animal | Immunopathology | Immune response | Advantage | Disadvantages |
|---|---|---|---|---|
| NHPs | Diffuse alveolar damage<br>Lung consolidation<br>Infiltration of inflammatory cells<br>Thoracic adhesion<br>Glassy opacity<br>Hepatosplenopathy<br>Age-related pathological changes | Neutralizing antibody response<br>Virus-specific T cell response<br>Up-regulation of IL-1, IL-6, IL-10, and other inflammatory factors<br>Transient neutropenia and lymphocytopenia | Closer to human immune response<br>Essential models for preclinical trials | Lack of severe clinical symptoms<br>High technical requirements for biosecurity<br>High experimental costs |
| hACE2 transgenic mice | Severe interstitial pneumonia<br>Infiltration of inflammatory cells<br>Thickening of alveolar septum<br>Unique vascular system damage | Lymphopenia<br>Pulmonary immune cell recruitment<br>Up-regulation of IFN-γ, IL-6, MCP-1 and other inflammatory factors<br>Diffuse microglia activation | Excellent simulation of severe COVID-19<br>Dose-dependent respiratory symptoms and mortality<br>Central nervous system infection | Vastly different ACE2 expression pattern from humans<br>Complex and expensive transgenic operations<br>Lack of genetic diversity and disease models |
| AdV/AAV-hACE2 mice | Infiltration of inflammatory cells from perivascular to mesenchymal<br>Diffuse alveolar intraepithelial infection<br>Alveolar edema<br>Increased vascular congestion and bleeding | Virus-specific T cell response<br>Up-regulation of TNF-α, IFN-γ, IL-10 and other inflammatory factors<br>Reduced activation of $CD4^+$, $CD8^+$, or NK cells | Fast and simple model construction<br>Diverse genetic backgrounds or disease models<br>Suitable for large-scale drug and vaccine research | Interference from anti-Adv/AAV immune response<br>Time and tissue limitations of viral infection |
| Mouse adapted SARS-COV-2 | Interstitial pneumonia<br>Edema<br>Diffuse alveolar damage<br>Mild to moderate lung inflammation | Proinflammatory and monocyte chemokine responses<br>Up-regulation of IL-6, IL-1α, IL-1β and other inflammatory factors | Easy to simulate multiple COVID-19 symptoms<br>Diverse genetic backgrounds or disease models | Clinical SARS-CoV-2 strains cannot be used |
| Syrian hamsters | Alveolar destruction<br>Monocyte infiltration<br>Alveolar collapse<br>Lung consolidation<br>Pulmonary hemorrhage | Neutralizing antibody response<br>Infiltration of macrophages and T lymphocytes<br>Up-regulation of IFN-γ, IL-4, IL-6 and other inflammatory factors | Naturally susceptible to SARS-CoV-2<br>Similar to human COVID-19 symptoms<br>Suitable for large-scale drug and vaccine research | Lack of reagents and tools for immunology research<br>Lack of genetic diversity and disease models |

respiratory issues, including pronounced inflammation and clotting disorders (Woolsey et al., 2021). The correlation between age and COVID-19 severity is consistent across these NHP species, highlighting their utility in exploring the effects of aging and metabolic diseases on SARS-CoV-2 infection (Singh et al., 2020; Song et al., 2020; Yu et al., 2020b). Despite requiring biosafety level 3 (BSL-3) facilities and specialized personnel to handle SARS-CoV-2-infected NHPs, these models are essential for evaluating COVID-19 treatments and vaccines (Guebre-Xabier et al., 2020; Rabdano et al., 2023; Sui et al., 2021b; Vogel et al., 2021).

**Mice**

Due to their small size, large populations, and low feeding costs, mice are extensively used as model organisms for a variety of human diseases. However, significant structural differences between hACE2 and mouse ACE2 (mACE2) inhibit the natural replication of SARS-CoV-2 in wild-type mice (Mahdy et al., 2020). Consequently, current strategies for developing COVID-19-susceptible mouse models involve either introducing the hACE2 gene or adapting mACE2 through viral passage (Knight et al., 2021). The diverse array of genetic and immunological tools available for mice allows for a more effective exploration of COVID-19 pathogenesis, offering advantages not achievable with other animal models and contributing to a more profound understanding of this complex disease.

**hACE2 transgenic mice:** Animal susceptibility to SARS-CoV-2 is influenced by the structural characteristics of ACE2, while COVID-19 severity is closely associated with its expression (Ni et al., 2020). As a result, the transgenic introduction of hACE2 into mice under the control of efficient promoters has become a highly effective strategy for constructing COVID-19 models. In 2007, hACE2 transgenic mice were generated to evaluate SARS-CoV *in vivo* using cytomegalovirus (CMV) immediate enhancer/β-actin (CAG) and keratin-18 (K18) promoters, with the former enabling robust hACE2 expression across various mouse cell types and the latter restricting high hACE2 expression to epithelial cells (McCray et al., 2007; Tseng et al., 2007). The K18-hACE2 mouse model has also been extensively used in COVID-19 research, replicating dose-dependent characteristics of SARS-CoV-2 infection, including loss of olfaction, severe lung pathology, thrombosis, vasculitis, nerve damage, and mortality, similar to those observed in human COVID-19 patients (Zheng et al., 2021b). However, K18-initiated hACE2 is overexpressed in the brain, exceeding ACE2 expression levels in humans (Chen et al., 2021b). Consequently, K18-hACE2 transgenic mice exhibit a disparity in brain infection levels compared to COVID-19 patients (Winkler et al., 2020). To address this issue, hACE2 transgenic mice were developed using the mACE2 promoter to ensure equivalent hACE2 expression in $mACE2^+$ cells (Yang et al., 2007), resulting in a self-limiting and non-lethal course of infection, which is invaluable for assessing the efficacy of antiviral therapeutics and vaccines (Bao et al., 2020). Additionally, CRISPR/Cas9 knock-in technology has been employed to generate transgenic mouse models expressing hACE2, which display detectable SARS-CoV-2 in the lung, trachea, and brain, accompanied by interstitial pneumonia and elevated cytokine levels (Sun et al., 2020b).

**Viral vectors for hACE2 transduction in mice:** Employing adenoviral vectors (AdV) or adeno-associated virus vectors (AAV) to transiently express hACE2 in mouse lungs is considered highly effective for modeling SARS-CoV-2 infection in strains with distinct genetic characteristics or diseases. Notably, intranasal administration of AdV-encoded hACE2 in wild-type BALB/c or C57BL/6 mice, with subsequent SARS-CoV-2 infection at the peak of hACE2 expression at 5 days post-transduction, leads to weight loss, severe lung lesions, and high viral replication in the lungs (Sun et al., 2020a). In general, AAVs are preferred over AdVs due to their lower immunogenicity, prolonged expression of target genes, and enhanced suitability for *in vivo* gene delivery. Intranasal administration of hACE2 encoded by AAV9 and AAV-DJ results in robust hACE2 gene expression in the lungs of mice, while AAV6 yields relatively low expression (Gary et al., 2021; Glazkova et al., 2022; Israelow et al., 2020). Mice humanized with AAV-hACE2, specifically the MSTRG6 strain, exhibit chronic COVID-19 features, including weight loss, persistent viral RNA presence, fibrotic lung pathology, human-like macrophage responses, sustained interferon (IFN)-stimulated gene (ISG) expression, and T cell lymphopenia (Glazkova et al., 2022; Sefik et al., 2022). These AdV/AAV-hACE2 mouse models provide a readily available and genetically varied framework for studying SARS-CoV-2 infection, crucial for rapid preclinical assessments.

**Mouse-adapted viruses:** For research involving COVID-19 animal models where SARS-CoV-2 mutation is not a factor, using a mouse-adapted strain of SARS-CoV-2 may be a preferable option. Dinnon et al. (2020) engineered a mouse-adapted recombinant SARS-CoV-2 variant by modifying the Q498Y/P499T amino acid residue in the receptor-binding domain (RBD) of the spike (S) protein, enabling viral replication in both the upper and lower respiratory tracts of wild-type BALB/c mice, although young mice rapidly cleared the infection within 4 days. Leist et al. (2020) generated the MA10 variant by passaging mouse-adapted SARS-CoV-2 through mice 10 times, inducing pulmonary disease and potential acute respiratory distress syndrome (ARDS) in BALB/c mice, but only mild lung inflammation and weight loss in C57BL/6 mice. Another variant carrying the N501Y substitution, generated by serial passage of SARS-CoV-2 through the respiratory tract of elderly BALB/c mice, induces interstitial pneumonia without visible clinical symptoms or weight loss (Gu et al., 2020). The SARS2-N501Y MA30 strain, produced through successive passages of SARS2-N501Y in mouse lungs, shares spike protein mutations with the Omicron variant and can cause fatal disease in young BALB/c mice (Kibler et al., 2022; Wong et al., 2022). The generation of highly virulent mouse-adapted SARS-CoV-2 through *in vivo* passage alone mirrors unrestricted SARS-CoV-2 transmission in the population without preventative measures, providing a vital model for studying viral transmission dynamics.

**Hamsters**

Hamsters, particularly Syrian hamsters (*Mesocricetus auratus*), are highly susceptible to SARS-CoV-2 infection, making them a preferred model for viral study. SARS-CoV-2 effectively replicates in the pulmonary system of Syrian hamsters, targeting the lower respiratory tract within 12 hours post-inoculation and causing severe pathological alterations and olfactory dysfunction similar to symptoms observed in COVID-19 patients (Clancy et al., 2023; Imai et al., 2020; Merle-Nguyen et al., 2024). SARS-CoV-2 infection in Syrian hamsters is characterized by rapid viral clearance by day 7, resembling infection dynamics in mildly infected humans,

possibly attributed to varying viral infection titers (Sia et al., 2020). Few animal models of COVID-19 exhibit clinical features of ARDS, limiting our understanding of the molecular mechanisms underlying the host immune response to SARS-CoV-2 infection. However, SARS-CoV-2-infected Syrian hamsters display key ARDS characteristics, such as lung injury, increased permeability, acute inflammation, and hypoxemia, particularly when inflammatory mediators are up-regulated and persist after viral clearance (Bednash et al., 2022). Thus, Syrian hamster models of SARS-CoV-2 infection reflect several aspects observed in moderate, self-limiting cases of COVID-19, including respiratory and vascular inflammation and age-related patterns (Bednash et al., 2022; Gruber et al., 2022; Imai et al., 2020). In addition, Roborovski pygmy hamsters (*Phodopus roborovskii*) are highly susceptible to SARS-CoV-2, developing severe acute diffuse alveolar injury and pulmonary hyaline microthrombi similar to severe COVID-19 patients (Trimpert et al., 2020). Chinese hamsters (*Cricetulus griseus*) can also be infected with SARS-CoV-2, presenting with clinical symptoms akin to the Syrian hamster models but with prolonged symptom duration (Bertzbach et al., 2021). As valuable models for SARS-CoV-2 infection, hamsters, mice, and NHPs have been used in combination for the development of viral vaccines and drugs (Baum et al., 2020; Lu et al., 2023; Yu et al., 2023).

**Other animal models**

Various other rodents have been used in studies of SARS-CoV-2 infection. Guinea pigs (*Cavia porcellus*) do not appear to be susceptible to SARS-CoV-2 infection, as the virus cannot be detected despite early histological changes in the lungs by day 3 (Hewitt et al., 2020). In contrast, New Zealand white rabbits (*Oryctolagus cuniculus*) are sensitive to SARS-CoV-2 but remain asymptomatic (Mykytyn et al., 2021), making them unsuitable as a disease model. Interestingly, Yu et al. (2022a) established a SARS-CoV-2-susceptible hACE2-transgenic rat (*Rattus norvegicus*) model but found that wild-type Sprague-Dawley (SD) rats infected with the prototype strain of SARS-CoV-2 showed detectable viral loads in the upper respiratory tract and lung lesions. The increase in demand for COVID-19 research has expanded the range of animals used for testing and model development, beyond conventional primate and rodent models. Studies have indicated that SARS-CoV-2 exhibits limited replication in dogs, pigs, chickens, and ducks, but shows efficient replication in the upper respiratory tract of ferrets and in the respiratory and digestive systems of cats (Shi et al., 2020). The respiratory tract of ferrets, which is physiologically and anatomically similar to that of humans, is naturally sensitive to a variety of human respiratory viruses, including influenza virus, SARS-CoV, and SARS-CoV-2 (Belser et al., 2011; Kim et al., 2020; Shi & Hu, 2008). SARS-CoV-2 infection in ferrets results in fever, mild respiratory symptoms, acute bronchiolitis, and diffuse interstitial histiocytic pneumonia, but not death (Kim et al., 2020; Kreft et al., 2022). Minks (*Neovison vison*), also belonging to the weasel family, experience severe respiratory disease and death following SARS-CoV-2 infection, presenting with pulmonary edema, moderate vasculitis, and fibrinous interstitial pneumonia (Eckstrand et al., 2021). Domestic cats (*Felis catus*) also exhibit high susceptibility to SARS-CoV-2 infection, although their widespread use is impeded by the challenges of non-standard animal models (Shi et al., 2020). Additionally, in-depth study of infection immunology in these models is hindered by the scarcity of specialized immunological research tools.

## INFECTION IMMUNOLOGY IN ANIMAL MODELS OF COVID-19

**Immune pathogenesis of SARS-CoV-2 infection**

The pathophysiology of COVID-19 primarily arises from host dysregulation in controlling SARS-CoV-2 replication and modulating the immune response, resulting in delayed viral clearance, inflammation, and tissue damage that extends beyond pulmonary involvement to systemic manifestations (Arish et al., 2023). The host innate immune system detects RNA viruses, like coronaviruses, through various pattern recognition receptors (PRRs). Toll-like receptor 3 (TLR3), TLR7, and TLR8 recognize viral genomic RNA, double-stranded RNA (dsRNA), and single-stranded RNA (ssRNA). Cytoplasmic RNA sensors, such as retinoic acid-inducible gene I (RIG-I) and melanoma differentiation-associated protein 5 (MDA5), detect dsRNA intermediates formed during viral replication. This detection triggers the activation of IFN regulatory factor 3 (IRF3)/IRF7-dependent type I and III IFN transcription, as well as nuclear factor kappa B (NF-κB)-dependent proinflammatory cytokines and chemokines, initiating the antiviral process (Merad et al., 2022).

SARS-CoV-2 disrupts the innate immune system by targeting viral sensors and blocking downstream antiviral signaling molecules, facilitating successful transmission and adaptation to human hosts (Kasuga et al., 2021). Patients with moderate to severe COVID-19 exhibit impaired responses to both IFN-I and IFN-III, associated with persistent viral load in the bloodstream, while patients with mild disease show early induction and higher levels of IFN (Galani et al., 2021; Hadjadj et al., 2020). As the virus evades immune surveillance and efficiently infects neighboring target cells, leading to acute lung injury, it continues to activate the innate immune response via PRRs and damage-associated molecular patterns (Chu et al., 2020). Uncontrolled immune responses trigger secondary systemic inflammation and a cytokine storm, marked by immune cell overactivation, abnormal blood counts, and elevated levels of circulating cytokines, such as tumor necrosis factor (TNF)-α, IFN-I and IFN-II, interleukin (IL)-1, IL-6, IL-12, IFN-γ-inducible protein 10 (IP-10), and monocyte chemoattractant protein 1 (MCP-1), culminating in septic shock, ARDS, and multiple organ failure (Fajgenbaum & June, 2020; Kasuga et al., 2021).

Initial insights into the pathological mechanisms of COVID-19 were derived from patient blood samples, biopsies, and autopsy specimens. With the advancement of animal models replicating SARS-CoV-2 infection, a more comprehensive understanding of COVID-19 pathogenesis has been achieved (Figure 2). An ideal animal model should capture the key aspects of SARS-CoV-2 pathogenesis and associated immune responses, allow detailed study of multiple anatomical sites of viral infection through invasive sampling, and support experimental approaches to manipulate the immune system. Currently, NHPs, mice, and golden hamsters are commonly used as models of SARS-CoV-2 infection due to their similarity to human patients regarding virus sensitivity, anatomical sites of viral infection, immune system components, and clinical symptoms. However, no single animal model can perfectly replicate all characteristics of COVID-19. By effectively and thoughtfully utilizing each animal

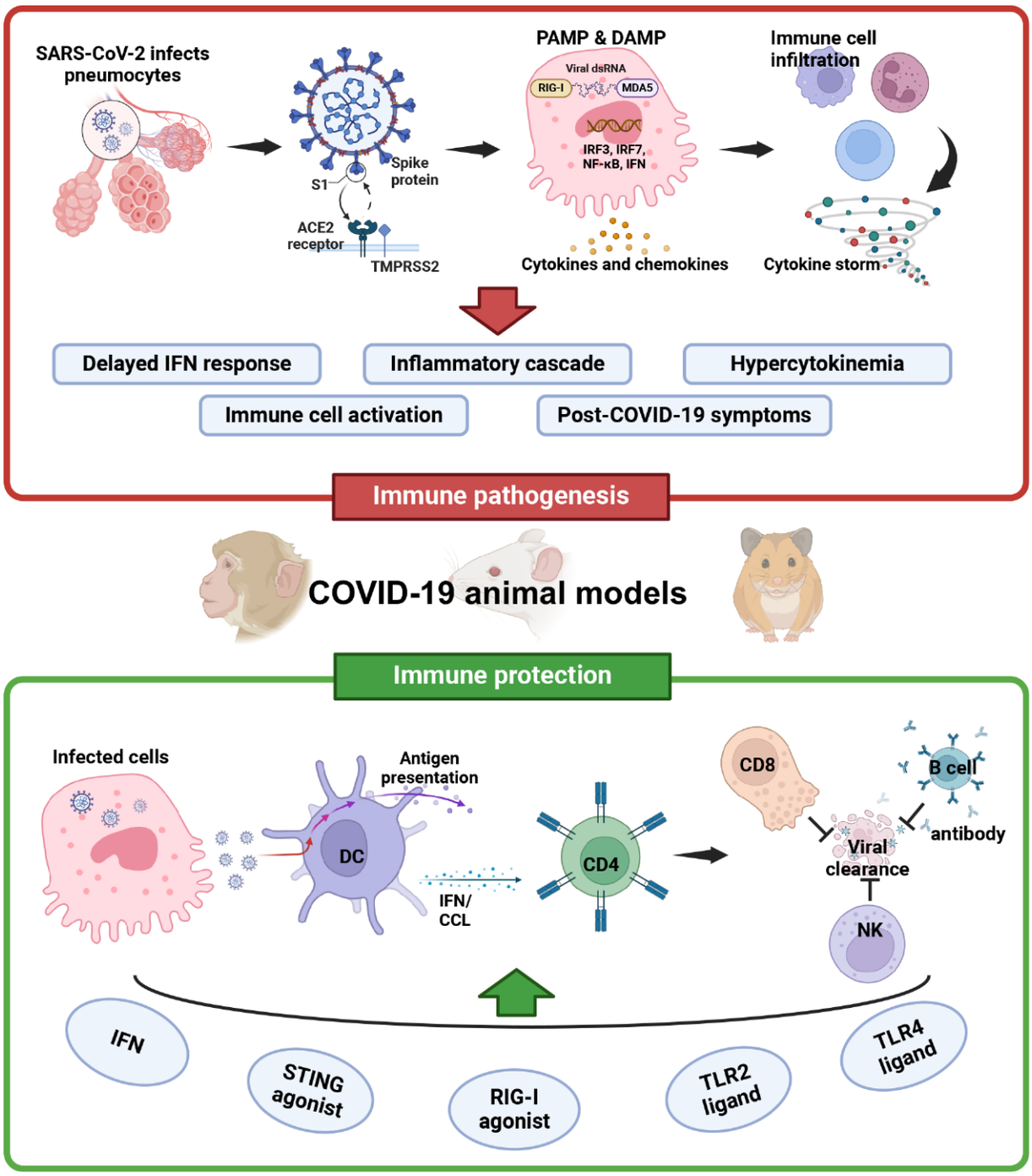



**Figure 2 Infection immunology based on COVID-19 animal models**

Application of animal models of SARS-CoV-2 infection has promoted systematic research on COVID-19 immunopathology. Animal experiments on vaccines and adjuvants have advanced our understanding of the immunoprotective mechanisms against SARS-CoV-2 infection. Figure created using BioRender (https://biorender.com/).

model, we can gain a deeper understanding of the immunopathological mechanism underpinning SARS-CoV-2 infection.

**IFN-I response:** The role of IFN-I in SARS-CoV-2 infection is complex and extensively studied. IFN-I is crucial for antiviral immunity, exerting various antiviral effects and promoting immune cell recruitment, thereby playing a protective role against SARS-CoV-2 infection (Zhang et al., 2020a). However, evidence also links a strong IFN-I response and increased ISG expression with the development of severe COVID-19 (Lee & Shin, 2020; Zhu et al., 2020). This abnormal IFN-I response in COVID-19 is further supported by animal models. Notably, C57BL/6J mice infected with the SARS-CoV-2 MA10 strain do not develop severe disease, while those lacking IFN-I and IFN-II receptors develop more pronounced and longer-lasting pulmonary dysfunction after infection, confirming the protective role of IFN-I signaling (Leist et al., 2020). Studies have shown that SARS-CoV-2 suppresses IFN-I expression, promoting infection in models involving rhesus macaques and Syrian hamsters (Francis et al., 2021; Sui et al., 2021a). However, most animal models have reported an association between IFN-I signal intensity and

disease severity. For instance, AAV-hACE2-transfected IFN-α/β receptor (IFNAR)$^{-/-}$ and IRF3/7$^{-/-}$ mice have revealed that the IFN-I response post-SARS-CoV-2 infection is essential for the recruitment of proinflammatory monocytes and macrophages to lung lesions, which induces inflammation (Israelow et al., 2020). Prolonged IFN signaling in mice with respiratory tract infection disrupts lung epithelial cell repair, thereby increasing disease severity and susceptibility to bacterial infection (Broggi et al., 2020; Major et al., 2020). In baboons, SARS-CoV-2 infection leads to a higher production of inflammatory factors, including IFN-α, compared to rhesus macaques, resulting in more severe lung pathology (Singh et al., 2020). K18-hACE2 transgenic mice infected with SARS-CoV-2 exhibit high and persistent IFN-I, IFN-II, and IFN-III expression, highlighting the correlation between IFN expression and COVID-19 severity (Oladunni et al., 2020; Zheng et al., 2021b).

**Inflammatory response:** Activation of inflammasomes by SARS-CoV-2 infection initiates an inflammatory cascade, which can, in severe cases, lead to a lethal cytokine storm and systemic organ failure (Mehta et al., 2020). Animal models have been instrumental in elucidating the inflammation caused by SARS-CoV-2 infection and its role in disease pathogenesis. NHPs infected with SARS-CoV-2 exhibit typical clinical symptoms, such as fever, cough, dyspnea, and interstitial pneumonia. However, severe lung injury and diffuse alveolitis are primarily observed in rhesus macaques and African green monkeys (Azkur et al., 2020; Yuan et al., 2021). This severe condition is marked by thickening of the alveolar wall and infiltration of numerous monocytes and lymphocytes, as well as a small number of eosinophils (Shan et al., 2020). Beyond the respiratory tract, NHP models also show pathological changes in the heart, liver, kidneys, spleen, lymph nodes, and brain, although direct evidence of SARS-CoV-2 infection in these tissues is still lacking (Lu et al., 2020; Philippens et al., 2022). Research involving K18-hACE2 transgenic mice has shown that lung function impairment is associated with the infiltration of monocytes, neutrophils, and activated T cells, leading to a heightened innate immune response (Winkler et al., 2020). Similarly, Syrian hamsters infected with SARS-CoV-2 exhibit symptoms such as interstitial pneumonia, inflammatory cell infiltration, alveolar septum thickening, and vascular system injury, as well as a pulmonary immune response driven by macrophages (Bednash et al., 2022; Mulka et al., 2022). These findings suggest that inflammatory injury induced by SARS-CoV-2 is more critical than the multiorgan damage resulting from direct viral infection.

The cytokine storm associated with COVID-19 is a key pathogenic factor and potential therapeutic target in COVID-19 patients (Zanza et al., 2022). Clinical studies have highlighted the significant role of cytokines such as IL-6, IL-1, IL-17, and TNF-α in lung injury (Montazersaheb et al., 2022). In cases of severe COVID-19, SARS-CoV-2 induces a chronic immune response mediated by transforming growth factor-β (TGF-β), which promotes fibrosis (Ferreira-Gomes et al., 2021). SARS-CoV-2-infected NHPs also show elevated expression of inflammatory cytokines, including IL-10, IL-1A, IL-8, IL-15, MCP-1, IFN-β, and IP-10, but unlike in severe COVID-19 patients, IL-6 is not highly expressed (Lu et al., 2020; Song et al., 2020), underscoring its critical role in cytokine storms. Transcriptomic analysis of lung tissue from SARS-CoV-2-infected mice with severe disease has shown that antiviral responses in younger mice are dominated by IFN and IL-6 pathway activation, while fatal outcomes in older animals are associated with TNF and TGF-β signaling, highlighting the significant impact of age on cytokine response in COVID-19 (Bader et al., 2023). In the Syrian hamster model of SARS-CoV-2 infection, various cytokines, such as IFN-α, IL-6, IL-1β, and TNF, are associated with severe lung disease, consistent with clinical observations (Fomin et al., 2023; Francis et al., 2021).

**Immune cell activation:** Clinical studies have demonstrated that cytokine storms in COVID-19 are driven by the robust activation of monocytes and macrophages, leading to the development of SARS-CoV-2-related complications, including ARDS, disseminated intravascular coagulation syndrome (DICS), edema, and pneumonia (Kosyreva et al., 2021; Liao et al., 2020). Similarly, SARS-CoV-2-infected K18-hACE2 transgenic mice exhibit pronounced recruitment of pulmonary immune cells, including dendritic cells (DCs), innate myeloid cells (IMMs), and CD4$^+$ and CD8$^+$ T lymphocytes (Zheng et al., 2021b). In rhesus macaques, SARS-CoV-2 infection induces rapid recruitment of macrophage subsets, particularly CD163$^+$ mannose receptor C-type 1 (MRC1)- and triggering receptor expressed on myeloid cells 2 (TREM2)$^+$, which are primary sources of inflammatory cytokines (Upadhyay et al., 2023). In ferrets, SARS-CoV-2 infection also results in notable alterations in the composition of macrophage subsets in bronchoalveolar lavage fluid (BALF), with monocyte-derived M1 and M2 macrophages playing pivotal roles in both early viral clearance and late-phase excessive inflammation (Lee et al., 2021). Furthermore, in Syrian hamsters, SARS-CoV-2 infection induces rapid and extensive infiltration of monocyte-derived macrophages (MDM) in the lungs, contributing to tissue remodeling and fibrosis via the up-regulation of prothrombotic factors, tissue repair, and alveolar cell proliferation (Bagato et al., 2024). Neutrophils, the most abundant white blood cells, are the first to infiltrate infected lungs following viral infection. Chemokine (C-X-C motif) ligand 5 (CXCL5) plays an important role in the process of neutrophil recruitment, with its knockout in SARS-CoV-2-infected mice found to significantly reduce pulmonary inflammation (Liang et al., 2020).

Hospitalized COVID-19 patients, especially those with severe disease, frequently exhibit a notable decrease in blood lymphocyte counts (Liu et al., 2020a; Sekine et al., 2020). Autopsies have revealed T cell infiltration and migration in inflamed tissues, suggesting that the decrease in blood lymphocytes may be due to their relocation to infection sites (Adamo et al., 2021; Jafarzadeh et al., 2020). However, the percentage of CD8 T cells in the BALF is lower in severe patients compared to those with moderate disease, possibly due to apoptotic signals (André et al., 2022; Liao et al., 2020). Despite variations in T cell numbers, their activation in SARS-CoV-2 infection-induced pulmonary inflammation is significantly increased. This heightened activation, characterized by overactivation, depletion, or apoptosis sensitivity, is identified through various cell surface markers, including CD38, human leukocyte antigen-DR isotype (HLA-DR), programmed cell death 1 (PD-1), T cell immunoreceptor with Ig and ITIM domains (TIGIT), T cell immunoglobulin and mucin domain-containing protein 3 (Tim-3), and natural killer (NK) cell receptor A (NKG2A). These activated T cells are closely linked to the development of severe COVID-19 (Du et al., 2021; Georg et al., 2022; Zheng et al., 2020), as supported by various animal models. For example, Zheng

et al. (2021a) observed a significant increase in T cell CXCR3 and CD38 expression in the lung tissues of elderly macaques infected with SARS-CoV-2, indicative of both activation and inflammation and potentially valuable for predicting severe COVID-19. Similarly, SARS-CoV-2-infected rhesus macaques exhibit a marked increase in T cell activation markers in their lung tissues and cerebrospinal fluid (Verma et al., 2021), while SARS-CoV-2-infected mice show a significant up-regulation in $CD44^+CD3^+CD8^+$T cell activation in their lungs, accompanied by alveolar macrophage loss (Winkler et al., 2020). In K18-hACE2 mice, T cell activation is correlated with diffuse microglial activation and plays a critical role in SARS-CoV-2 brain infection (Seehusen et al., 2022). Wu et al. (2021) found that the SARS-CoV-2 membrane (M) protein activates STAT1 phosphorylation and T-bet transcription via TREM-2, contributing to T cell activation. Experiments using CD4-specific conditional TREM-2 knockout mice have demonstrated that TREM-2 enhances the TH1 response and aggravates lung injury.

**Immune protection against SARS-CoV-2**

Following the SARS-CoV-2 outbreak, the development of vaccines and drugs necessitated relevant animal studies to evaluate their safety and efficacy *in vivo*. Various NHP models, particularly rhesus macaques, have been employed to test the efficiency of different SARS-CoV-2 vaccines developed using different technologies, including inactivation (A'La et al., 2023; Chen et al., 2021a), spike protein or RBD subunit expression (Guebre-Xabier et al., 2020; Prenafeta et al., 2023), DNA (Yu et al., 2020a), mRNA (Oh et al., 2023; Vogel et al., 2021), and attenuated viral vectors (Feng et al., 2020; Jacob-Dolan et al., 2021). Mouse and hamster models have primarily been applied for testing new vaccines and adjuvants and studying immunoprotective mechanisms, such as immune-stimulating adjuvant chimeric vaccines (Ashhurst et al., 2022), multivalent vaccines (Afkhami et al., 2022), lipid nanoparticle vaccines (Elia et al., 2021), adenovirus vaccines (Port et al., 2023), DC vaccines (Tada et al., 2023), novel adjuvants (Machado et al., 2023; Vijayanand et al., 2023), and cross-protection mechanisms (Liu et al., 2023a). The effects of different vaccine delivery modes on immune efficacy have also been verified using animal models. In addition to traditional intramuscular injection, oral (Beddingfield et al., 2021; Langel et al., 2022; Yu et al., 2022b) and intranasal vaccines (Langel et al., 2022; Sui et al., 2021b; Tokunoh et al., 2023) have also been shown to provide protection. These animal models have significantly enhanced our understanding of the immunoprotective mechanisms against SARS-CoV-2 (Figure 2).

**Protective adaptive immune response:** Animal models have been instrumental in elucidating the importance of adaptive immune protection in SARS-CoV-2 infection. Speranza et al. (2022) discovered that older rhesus macaques exhibit a sustained inflammatory innate response to SARS-CoV-2 infection, while younger animals initiate an earlier local effector T-cell response, leading to more rapid recovery of immune homeostasis. A key immunological feature of SARS-CoV-2-infected NHPs and hamsters is their ability to develop protective immunity, which not only protects against secondary infection but may also cross-react with other coronaviruses (Chandrashekar et al., 2020; Horiuchi et al., 2021; Jacob-Dolan et al., 2021). McMahan et al. (2021) demonstrated that the transfer of purified IgG from convalescent rhesus macaques protects recipient macaques from SARS-CoV-2, highlighting that $CD8^+$ T cell responses can confer protection even with low or weak antibody levels. The $CD4^+$ T cell response in rhesus macaques is strongly correlated with the efficacy of SARS-CoV-2 spike protein mRNA vaccines and neutralizing antibody levels (Corbett et al., 2021). In mice, the IFN-I pathway-mediated virus-specific T cell immune response is critical for protecting against severe SARS-CoV-2 infection (Zhuang et al., 2021). $CD8^+$ T cells are essential for early control and elimination of SARS-CoV-2, while $CD4^+$ T cells play a crucial role in eliciting antibody responses (Israelow et al., 2021), underscoring the importance of adaptive immunity in mitigating disease progression and preventing secondary infections. Despite the significant role of T cells in recovery from acute SARS-CoV-2 infection in rhesus macaques, their depletion does not result in severe disease, suggesting that T cells alone do not fully account for the innate resistance of rhesus macaques to severe COVID-19 (Hasenkrug et al., 2021).

The respiratory mucosal surface is a crucial site for interactions between SARS-CoV-2 and the immune system, where mucosal antibodies and tissue-resident memory T (TRM) and B cells provide early antiviral immune responses (Lee & Oh, 2022; Zheng & Wakim, 2022). However, challenges in sampling from human mucosal sites, especially the lower respiratory tract, have hindered studies on local immunity to SARS-CoV-2. Animal model vaccination experiments have offered vital insights into mucosal immune memory following SARS-CoV-2 infection. Tang et al. (2022) demonstrated that mice immunized with a combination of systemic mRNA vaccine and mucosal AdV-S protein vaccine exhibit a strong neutralizing antibody response, providing better respiratory mucosal protection than the systemic mRNA vaccine alone. Intratracheal inoculation of rhesus macaques with a bivalent SARS-CoV-2 vaccine based on Ad26 significantly induces humoral and cellular immunity in mucosa, with almost complete protection against SARS-CoV-2 BQ.1.1 challenge (McMahan et al., 2024). Furthermore, intranasal delivery of the ChAdOx1 vaccine induces potent respiratory RBD-specific IgA antibody titers, antibody-dependent neutrophil and monocyte phagocytosis, complement activation, NK cell activation, and reduced viral shedding following SARS-CoV-2 infection (Oh et al., 2021). Intranasal immunization with trivalent COVID-19 AdV vaccine elicits a robust multifunctional respiratory tract mucosal TRM response in K18-hACE2 mice, enhancing mucosal protection and conferring complete protection against SARS-CoV-2 infection-induced disease or mortality (Afkhami et al., 2022). Research on SARS-CoV-2-infected K18-hACE2 mice has also shown that respiratory memory T cells, both $CD4^+$ and $CD8^+$, induced by a subunit-based adjuvant system, can protect against SARS-CoV-2 infection, even in the absence of virus-neutralizing antibodies (Van Doremalen et al., 2021).

**Protective innate immune response:** The efficacy of COVID-19 vaccines may be reduced in certain populations, such as the elderly, highlighting the need for more personalized vaccination regimens. Targeted activation of innate immune signals has gained attention as a strategy to elicit strong immune responses in vaccine development. Studies have shown that mRNA vaccines can enhance the innate immune response in obese mice with impaired adaptive immunity by enhancing IFN-I signaling and providing protection against SARS-CoV-2 infection (Chen et al., 2023).

In rhesus macaques, mRNA-based vaccines can effectively stimulate all immune system components and improve the connection between innate and adaptive immunity after a second dose via key mediators, such as TNFα, IFNγ, IL-21, and chemokine (C-C motif) ligand 3 (CCL3) (Schramm et al., 2023). Marx et al. (2022) found that therapeutic RNA oligonucleotides, acting as RIG-I agonists, can trigger a robust NK cell response in K18-hACE2 mice, providing transient yet potent antiviral protection against SARS-CoV-2 infection. TLR2, an important innate immune receptor on respiratory epithelial and lung immune cells, is crucial for effective defense against infection (Beckett et al., 2012). The TLR2 ligand Pam 2 Cys, when used as a mucosal adjuvant in COVID-19 vaccines, enhances the recruitment of antigen-presenting cells (APCs), including DCs, alveolar macrophages, and monocytes, to the respiratory mucosa, leading to robust activation of the IL-17$^{+}$CD4$^{+}$ T cell response and significantly boosting the protective efficacy of COVID-19 vaccines in murine models (Ashhurst et al., 2022). Lymphoblastoid cells play a crucial role in shaping the microenvironment of lymph nodes and the structure and function of the germinal center (GC). Age-related decline in GC response impedes the establishment of durable humoral immunity post-vaccination (Masters et al., 2018). Denton et al. (2022) discovered that TLR4 agonists can promote the maturation and expansion of follicular DCs (FDCs) and the activation and proliferation of stromal cells, thus enhancing GC immune response initiation and COVID-19 vaccine efficacy in aged mice. Additionally, the RBD dimer fusion protein carrying IFN exhibits potential as a candidate for COVID-19 vaccination by targeting DCs in lymph nodes and stimulating T follicular helper (Tfh) cell differentiation and GC formation, providing complete protection against high-dose SARS-CoV-2 challenge in rhesus macaques (Sun et al., 2021).

**Protective immune response against novel SARS-CoV-2 variants:** In late 2020, after nearly a year of transmission in humans, SARS-CoV-2 underwent significant adaptive changes. These highly mutated variants, referred to as “variants of concern” (VOC), exhibit higher transmission rates than earlier strains. To date, the WHO has identified five SARS-CoV-2 variants as VOCs, including Alpha, Beta, Gamma, Delta, and Omicron, all of which exhibit significant changes in transmissibility or immune escape, warranting close surveillance (Carabelli et al., 2023). As of 9 February 2024, the primary circulating variants of interest include XBB.1.5, XBB.1.16, EG.5, BA.2.86, and JN.1 (https://www.who.int/activities/tracking-SARS-CoV-2-variants). These variants have numerous nonsynonymous mutations in the spike protein and unique phenotypic characteristics, leading to changes in transmissibility and antigenicity, which facilitate evasion of host immune responses. This evolution may reduce the effectiveness of current SARS-CoV-2 vaccines (Kim et al., 2022). Therefore, it is crucial to use appropriate animal models to further study the etiology, transmission, and pathogenesis of the virus and to evaluate the efficacy of vaccines against the latest SARS-CoV-2 variants.

Compared to the Delta variant, the Omicron BA.1 and BA.2 variants have been shown to exhibit weakened lower respiratory tract replication and lower pathogenicity in a variety of animal models, including rodents and NHPs (Boon et al., 2022; Halfmann et al., 2022; Van Doremalen et al., 2022). Halfmann et al. (2023) reported that the Omicron subvariant XBB.1.5 exhibited greater airborne transmissibility than its predecessor BA.2 and partial immune escape from previous infection with BA.1 in Syrian hamsters. Tamura et al. (2024) found that nonsense mutations in ORF8 of XBB.1.5 impaired MHC suppression and were associated with reduced virulence in Syrian hamsters infected with this subvariant. XBB.1.16, an independent variant from XBB.1.5, has two amino acid substitutions in its spike protein compared to XBB.1.5: E180V in the N-terminal domain and T478R in the receptor-binding domain (Yamasoba et al., 2023). Pseudovirus experiments have shown that XBB.1.16 has similar infectivity to XBB.1.5 and similar sensitivity to XBB.1 in convalescent serum as XBB.1 and XBB.1.5 (Tamura et al., 2023). Meehan et al. (2023) developed a digital pathology algorithm to quantitatively assess respiratory lesions caused by SARS-CoV-2, confirming that Omicron subvariants BA.2.75 and EG.5.1 have regained some virulence, although not to the levels previously observed in Omicron. Similar to XBB.1.5, EG.5.1 is more transmissible among hamsters, but exhibits significantly enhanced immune evasion characteristics, and shows no significant differences in replication ability or pathogenicity compared to BA.2 (Uraki et al., 2023). Herder et al. (2023) evaluated the virulence of BA.2.86 and BA.2.75, among the most virulent Omicron subvariants, and found that BA.2.86 exhibited an attenuated phenotype in hamsters, suggesting no greater risk to public health than its parental Omicron subvariants. JN.1, derived from BA.2.86, harbors a key mutation (S:L455S) in the spike protein, which enhances its immune evasion ability and resistance to monovalent XBB.1.5 vaccine serum (Altamimi et al., 2024). However, the lack of animal models associated with JN.1 has hindered pathology and vaccine development.

Several animal-based vaccine studies have been conducted against novel SARS-CoV-2 variants. An Omicron (BA.1)-specific mRNA vaccine has shown effective protection in hamsters against BA.1 at 253 days after immunization, and moderate neutralizing activity against Omicron subvariants in rhesus macaques at 9 months after immunization (Wu et al., 2023b). Immunization of mice and rhesus macaques with the XBB.1.5-based monovalent recombinant spike protein COVID-19 vaccine induces neutralizing antibodies against the XBB.1.5, XBB.1.16, XBB.2.3, EG.5.1, and XBB.1.16.6 subvariants and elicits a CD4$^{+}$ Th1 cell response specific to the XBB subvariant (Patel et al., 2023). The Omicron XBB.1.5 RBD dimer-based vaccine completely protects mice from Omicron XBB.1.16 and significantly reduces respiratory viral infection in Syrian hamsters, demonstrating excellent protective efficacy against SARS-CoV-2 and its variants (Wu et al., 2023a). Wang et al. (2024) identified a highly conserved neutralizing epitope targeted by the broad-spectrum neutralizing antibody BA7535, which was highly neutralizing not only to previous variants (e.g. Alpha, Beta, Gamma, Delta and Omicron BA.1-BA.5) but also to recently emerging Omicron subvariants BF.7, CH.1.1, XBB.1, XBB.1.5, XBB.1.9.1, and EG.5. BA7535 effectively protects female mice from Omicron BA.5 and XBB.1 variants. The novel ChAd-SARS-CoV-2 vaccine, consisting of a bivalent Ad36 vector vaccine encoding SARS-CoV-2 WA1 and BA.5 spike proteins, induces persistent antibody and T cell responses against XBB.1.16 infection in rhesus macaques immunized by intranasal spray or inhalation aerosol (Gagne et al., 2023). The new generation of RBD nano-antibodies neutralizes

Alpha, Delta and Omicron BA.2.75, BA.1, BA.2, BA.4/5 and XBB.1 variants, significantly reducing viral load, weight loss, and pathogenicity in infected hamsters (Aksu et al., 2024).

## IMMUNOLOGICAL INSIGHTS OF POST-COVID-9 SYMPTOMS (LONG COVID-19) FROM ANIMAL MODELS

### Development of long COVID-19

Although most individuals fully recover from SARS-CoV-2 infection within days or weeks, some experience persistent or new symptoms months or even years later, a condition known as long COVID-19 (Schmidt, 2021). This complex multisystem disorder is characterized by over 200 identified symptoms, including fatigue, dyspnea, arthralgia, myalgia, cardiac arrhythmias, and cognitive impairments, affecting up to 75% of those who have recovered from COVID-19 (Jansen et al., 2022). Huang et al. (2022) found that patients infected with the original strain of SARS-CoV-2 continued to experience long-term symptoms more than 2 years after hospital discharge, although most symptoms had improved. Significant risk factors for long COVID-19 include female sex, obesity, and severe COVID-19 disease; however, even outpatients with mild symptoms may experience prolonged COVID-19 manifestations (Frontera et al., 2022; Subramanian et al., 2022). The original SARS-CoV-2 strain is associated with a higher incidence of long COVID-19 compared to the Alpha or Delta variants (Fernández-de-las-Peñas et al., 2022). In contrast, the Omicron variant is associated with a lower risk of long-term pneumonia compared to the Delta variant (Antonelli et al., 2022; Wise, 2022). Older adults infected with SARS-CoV-2 are more likely to suffer from long COVID-19, presenting with fatigue, difficulty breathing, coughing, and joint pain, as well as abnormalities in chest imaging and lung function tests. The situation is more complex for children and adolescents (Daitch et al., 2022), with immunocompromised children showing a higher prevalence of gastrointestinal symptoms associated with long COVID-19, while immunocompetent children report increased levels of fatigue (Roessler et al., 2022).

The mechanisms behind long COVID-19 and reasons for differences in symptoms across viruses and populations are unclear. Key hypotheses include changes in the immune system, persistence of residual viral components driving chronic inflammation, endothelial dysfunction or activation, changes in the microbiome, mitochondrial dysfunction, abnormal metabolites, reactivation of pre-existing chronic viral infections, microbiota dysbiosis, and unrepaired tissue damage (Davis et al., 2023; Liu et al., 2023b; Santopaolo et al., 2023). From an immunological perspective, uncontrolled immune dysregulation following SARS-CoV-2 clearance is an important contributor to the development of long COVID-19. In-depth immunophenotyping analysis has revealed significant gene expression interference in innate immune cells (such as NK cells, low-density neutrophils, and $CXCR3^+$ monocytes) and adaptive immune cells (such as T helper (Th) cells, Tfh cells, and regulatory T cells) in long-term COVID-19 patients (Ryan et al., 2022). Klein et al. (2023) demonstrated that long COVID-19 patients exhibit an excessive humoral response to SARS-CoV-2 and higher levels of antibody response to non-SARS-CoV-2 viral pathogens, especially Epstein-Barr virus. Single-cell omics and serologic studies have also revealed systemic inflammation and immune dysregulation in patients with long COVID-19, characterized by an increased frequency of inflammatory $CD4^+$ T cells and an exhausted phenotype of virus-specific $CD8^+$ T cells, indicating disharmony between humoral and cell-mediated responses (Yin et al., 2024). Despite these findings, clinical challenges remain in identifying potential therapeutic targets for COVID-19, necessitating urgent *in vivo* intervention studies using animal models.

### Animal models of long COVID-19

Animal models for long COVID-19 are still in the early stages. Paidas et al. (2022) inoculated mice with mouse hepatitis virus 1 (MHV-1), a member of the same β-coronavirus family as SARS-CoV-2, for 12 months to simulate long COVID-19, finding severe pathological changes and inflammation in their brain, lungs, and heart. Although not a direct SARS-CoV-2 infection model, these results imply that coronaviruses can have long-term effects, even after viral clearance. Sefik et al. (2022) examined innate and adaptive immune responses to SARS-CoV-2 infection in an AAV-hACE2 mouse model over 28 days, revealing characteristics of chronic COVID-19, such as progressive weight loss, persistent viral RNA presence, lung pathology accompanied by fibrosis, inflammatory macrophage response, sustained expression of ISGs, and depletion of T lymphocytes. Mice infected with SARS-CoV-2 for up to 120 days exhibit persistent inflammation and fibrosis, important features of chronic COVID-19 lung injury, as well as an increase in interstitial macrophages (Dinnon et al., 2022). The neurological symptoms associated with SARS-CoV-2 infection may potentially arise from cytokine storm, neuroimmune stimulation, and systemic infection, rather than direct viral mechanisms of injury (Efstathiou et al., 2022). Evidence suggests that SARS-CoV-2 infection-induced CCL11 evokes a selective microglial response in white matter, leading to dysfunction and structural dysregulation of multiple neuronal lineages in the central nervous system, contributing to cognitive impairment during the acute phase following COVID-19 (Li et al., 2022). In Syrian hamsters, 31 days of SARS-CoV-2 infection results in permanent lung and kidney damage, along with unique effects on the olfactory bulb and olfactory epithelium, including myeloid and T cell activation, proinflammatory cytokine production, and IFN responses, leading to neurobehavioral disorders such as anosmia and depression (Frere et al., 2022). Due to the lack of animal models of long COVID-19 and the high cost of BSL-3 laboratories, it is difficult to summarize the immunological mechanisms underlying COVID-19 development in a small number of cases, hindering the advancement of appropriate treatments. Solving this issue requires the development of pseudovirus and transgenic mouse models suitable for establishing animal models for long COVID-19.

## APPLICATION OF ANIMAL MODELS IN COVID-19 IMMUNOTHERAPY

Following the COVID-19 outbreak, various new and repurposed compounds exhibiting *in vitro* anti-coronavirus activity have rapidly advanced towards clinical application. Prior to the development of an effective SARS-CoV-2 vaccine, the US Food and Drug Administration (FDA) granted emergency use authorization (EUA) for a nucleoside analog and three monoclonal antibodies (MAbs) (Tao et al., 2021). Despite widespread vaccination, developing drug therapy for SARS-CoV-2 remains crucial, particularly for immunocompromised individuals and those who may not respond to the rapidly mutating virus (Boby et al., 2023).

Current COVID-19 antiviral drugs are primarily divided into the following categories: ① Polymerase inhibitors, which act on RNA-dependent RNA polymerase (RdRps), mainly nucleoside analogs, including remdesivir, molnupiravir, and nelfinavir, and have been validated in rhesus monkeys (Johnson et al., 2023; Tao et al., 2021; Williamson et al., 2020) and Syrian hamsters (Abdelnabi et al., 2021); ② Protease inhibitors, which act on 3C-like proteinase protein (3CLpro), mainly nirmatrelvir, PF-07321332, S-217622, ensitrelvir, and have been validated in rhesus monkeys (Rosenke et al., 2023), Syrian hamsters (Sasaki et al., 2023; Tao et al., 2021), and mice (Jeong et al., 2022; Tao et al., 2021); ③ Entry inhibitors, including antibodies, fusion inhibitors, soluble recombinant hACE2, which have achieved good results in SARS-CoV-2 infected rhesus monkeys (Streblow et al., 2023), mice (Morgan et al., 2022; Tao et al., 2021), Syrian hamsters (Linsky et al., 2020; Uraki et al., 2022), and ferrets (De Vries et al., 2021). The rapid development of COVID-19 immunotherapy research, relying on *in vivo* testing, can be attributed to the establishment of diverse animal models for SARS-CoV-2 infection, leading to numerous potential therapeutic drugs and protocols. These findings will serve as a valuable resource for addressing future infections, even if COVID-19 ceases to be a major public health threat. This discussion will not delve into the efficacy and mechanisms of these antivirals but will instead focus on trial outcomes of immunomodulatory drugs in COVID-19 animal models (Figure 3).

**Targeting immune receptors**

Since the early stages of the global pandemic, research has focused on targeting immune receptors for COVID-19. Early studies revealed that severe COVID-19 patients often show reduced T-cell counts, linked to poor clinical outcomes and indicating potential T-cell exhaustion (Liu et al., 2020b; Zheng et al., 2020). Lymphopenia in severe COVID-19 is linked to the overexpression of immune checkpoint receptors PD-1, cytotoxic T-lymphocyte-associated protein 4 (CTLA-4), TIGIT, and Tim-3 (Jin et al., 2023; Yin et al., 2024). With numerous inhibitory receptor antagonists already in clinical trials and available for use, their rapid implementation in COVID-19 trials is likely, minimizing the necessity for preclinical animal testing (Loretelli et al., 2021; Tan & Li, 2022). Given our advancing comprehension of the interactions between SARS-CoV-2 and immune receptors, the validation of novel immune receptor-targeted drugs will largely depend on animal models to confirm their efficacy.

SARS-CoV-2 enters host cells and is recognized by TLRs, NOD-like receptors (NLRs), and NLR protein 3 (NLRP3), initiating IFN-I production and innate immune reactions. Targeting these immune receptors therapeutically may help ameliorate infection-induced inflammation. TLRs, crucial for recognizing SARS-CoV-2 and initiating innate immunity, are expressed in various cell types, including immune cells, fibroblasts, epithelial cells, and ACE2-expressing type II lung cells (Jiang et al., 2022; Qi et al., 2020). TLRs, including those in human (TLR1–TLR10) and mouse cells (TLR1–TLR9 and TLR11–TLR13), are broadly categorized into cell surface TLRs, including TLR1, TLR2, TLR4–6, and TLR10, and intracellular somatic membrane TLRs, including TLR3 and TLR7–9 (O'Neill et al., 2013). Upon activation, TLRs recruit specific bridging molecules like myeloid differentiation primary response protein 88 (MyD88) and Toll/IL-1 receptor (TIR) domain-containing linker-induced interferon β (TRIF), which trigger the IRF and NF-κB signaling pathways to initiate IFN-I and inflammatory cytokine production (Jiang et al., 2022). TLR-mediated immune dysregulation plays a critical role in hyperinflammation and cytokine storm observed in COVID-19, making it a potential target for intervention (Liu et al., 2022). Zheng et al. (2021c) demonstrated that the SARS-CoV-2 E protein induces TLR2-related inflammatory responses in mice,

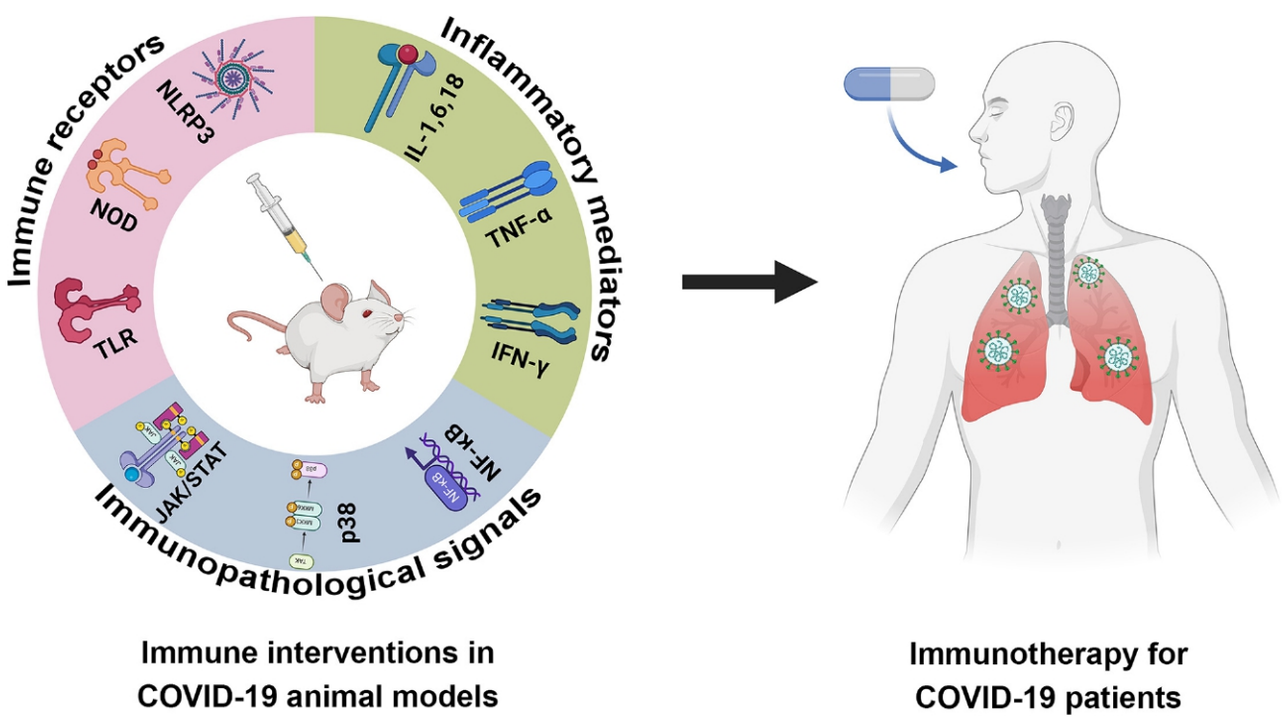



**Figure 3 COVID-19 immunotherapy based on animal models**

Validation of immune interventions targeting immune receptors, inflammatory mediators, and immunopathological signals in SARS-CoV-2-infected animal models is crucial for the development of COVID-19 immunotherapy. Figure created using BioRender (https://biorender.com/).

while inhibition of TLR2 with oxPAPC significantly attenuates the release of proinflammatory cytokines and chemokines. Fontes-Dantas et al. (2023) reported that intracerebral administration of the spike protein in mice induces neuroinflammation and synaptic loss through TLR4-mediated microglial activation, with early intervention with TLR4 inhibitors shown to prevent late neuronal damage in mice, identifying TLR4 as a potential target for long-term cognitive dysfunction induced by COVID-19. The role of TLRs in COVID-19 is complex, extending beyond immunopathology. Pre-COVID-19 studies indicated that MyD88- and TRIF-deficient mice infected with SARS-CoV experience higher mortality rates, weight loss, and viral loads, suggesting that MyD88 and TRIF are essential for preventing fatal SARS-CoV infection (Sheahan et al., 2008; Totura et al., 2015). Furthermore, combining a TLR9 agonist with mRNA enhances both T cell and neutralizing antibody responses against RBD in mice, compared to mRNA alone (Haabeth et al., 2021). Treating K18-hACE2 transgenic mice with a lethal SARS-CoV-2 dose and the synthetic agonist Poly(I:C) for TLR3/MDA5 temporarily boosts the innate immune response in the lungs, subsequently reducing viral load and cytokine storm levels, and significantly improving survival (Tamir et al., 2022).

Inflammatory processes at the cellular level are typically mediated by inflammasomes, particularly NLRP3 inflammasomes, which are highly responsive to RNA viruses. NLRP3 inflammasomes are composed of the NLRP3 receptor, apoptosis-associated speck-like protein containing a C-terminal caspase recruitment domain (ASC), and caspase-1. Upon assembly, caspase-1 is activated by autoproteolytic cleavage, facilitating the maturation of proinflammatory cytokines such as IL-1β, IL-18, IL-6, TNF-α, and gasdermin-D (GSDMD), which all contribute to the development of COVID-19-induced cytokine storm (Broz & Dixit, 2016; Dutta et al., 2022). Increasing evidence suggests that hyperactivation of NLRP3 inflammasomes plays a role in the pathogenesis of SARS-CoV-2-induced multiorgan failure (Ratajczak & Kucia, 2020). Studies have indicated that $Nlrp3^{-/-}$ mice, which lack NLRP3 inflammasomes, exhibit reduced severity of SARS-CoV-2-induced lung pathology compared to wild-type C57BL/6 mice, while specific inhibition of MCC950 reduces excessive lung inflammation in SARS-CoV-2-infected hACE2 transgenic mice, confirming NLRP3 as a potential immunotherapeutic target for COVID-19 (Zeng et al., 2022). Albornoz et al. (2023) discovered that SARS-CoV-2 infection activates NLRP3 inflammasomes in microglia through the NF-κB and ACE2 signaling pathways, leading to neurodegeneration in hACE2 transgenic mice, with these effects significantly mitigated and survival rates improved with oral administration of an NLRP3 inhibitor. These findings suggest that targeting NLRP3 may be beneficial in alleviating neurocognitive disorders associated with long-term SARS-CoV-2 infection.

**Targeting inflammatory mediators**

In the context of acute lung injury in COVID-19, macrophage activation syndrome and ARDS arise from the release of proinflammatory cytokines, such as IL-1, IL-6, IL-18, and TNF-α. Consequently, targeting these cytokines presents significant therapeutic potential for reducing cytokine storm in COVID-19 patients (McGonagle et al., 2020). Rubsamen et al. (2020) noted that early administration of α-IL-6 mAbs in mice infected with Ebola more effectively combated cytokine release syndrome (CRS) than IL-6 receptor blockade alone, offering insights for potential SARS-CoV-2 treatments. Subsequently, Xu et al. (2020b) found that the recombinant human IL-6 mAb tocilizumab binds specifically to soluble and membrane-bound IL-6 receptors (sIL-6R and mIL-6R), inhibiting IL-6-mediated signal transduction and improving clinical outcomes in severe and critically ill COVID-19 patients. IL-18 is also implicated in SARS-CoV-2-induced inflammatory lung injury. Notably, IL-18 is associated with the excessive recruitment, infiltration, and activation of neutrophils observed in the lung tissue of COVID-19 patients, as well as progression of cardiovascular dysfunction (Liang et al., 2023). In hACE2 transgenic mice, exposure to the spike protein increases NF-κB activity and NLRP3-inflammasome-dependent IL-18 levels in heart and lung tissues, with subsequent improvement in cardiac function and reduced NF-κB activity following inhibition of IL-18 (Liang et al., 2023). In K18-hACE2 mice, SARS-CoV-2 infection activates the NLRP3 pyroptosis signaling pathway in the lungs, resulting in IL-1β release, pulmonary vascular injury, and associated protein-rich pulmonary edema, while the selective IL-1 receptor antagonist anastrozole blocks IL-1 receptor signaling and prevents VE-cadherin down-regulation and excessive pulmonary vascular permeability, significantly improving survival (Xiong et al., 2021). Clinical findings indicate that the bispecific IL-1β/IL-18 MAb MAS825 effectively inhibits biomarkers of clinical and inflammatory pathways associated with COVID-19 and promotes the rapid clearance of SARS-CoV-2 (Hakim et al., 2023). Dysregulation of TNF-α, an important proinflammatory cytokine in the innate immune response, can induce CRS (Ragab et al., 2020). Karki et al. (2021) demonstrated that inhibition of TNF-α and IFN-γ can effectively mitigate sepsis, hemophagocytic lymphohistiocytosis (HLH), and cytokine shock in K18-ACE-2 transgenic mice following SARS-CoV-2 infection. Several anti-TNF therapeutics, including Humira (adalimumab), Remicade (infliximab), Simponi (golimumab), Cimzia (certolizumab pegol), and Entyvio (vedolizumab), are currently undergoing clinical trials for COVID-19, with most studies confirming favorable impact on reducing or ameliorating disease progression (Hakim et al., 2023).

**Targeting immunopathological signaling pathways**

The Janus kinase (JAK)-signal transducer and activator of transcription (STAT) pathway is pivotal in the regulation of inflammatory factors and formation of cytokine storms in COVID-19. Consequently, several JAK/STAT signaling inhibitors, including baricitinib, ruxolitinib, and tofacitinib, have been investigated as potential treatments for COVID-19 (Hall et al., 2023; Rein et al., 2022). Despite this, clinical trials have indicated that JAK/STAT signaling inhibitors are less effective than expected in alleviating disease severity in severe COVID-19 cases. Baricitinib effectively inhibits JAK1/2 kinase by competitively blocking adenosine triphosphate (ATP), essential for JAK1/2 activation by inflammatory cytokines such as IL-6, and disrupts various proinflammatory signaling pathways, including IL-6, IL-1β, IL-12, granulocyte-macrophage colony-stimulating factor (GM-CSF), and IL-2 (Ravid et al., 2022; Zhang et al., 2020b). Additionally, baricitinib effectively attenuates pulmonary inflammation in SARS-CoV-2-infected rhesus macaques by suppressing cytokines and chemokines, which, in turn, reduce neutrophil recruitment and pulmonary macrophage inflammation. However, its effect on viral replication and the IFN-I response

is minimal, resulting in incomplete resolution of immunopathology (Hoang et al., 2021).

Bruton's tyrosine kinase (BTK) is essential for B cell development in the bone marrow and plays a key role in the proliferation and survival of leukemia B cells (Hendriks et al., 2014). Elevated BTK activation levels in blood monocytes from severe COVID-19 patients are associated with systemic inflammation (Roschewski et al., 2020). Ibrutinib, a BTK inhibitor, is widely used in the treatment of indolent B cell malignancies and chronic graft-versus-host disease (cGVHD) and shows potential in eliminating inflammatory cytokines in the lungs, minimizing lung injury, and lowering mortality risk in a lethal influenza mouse model (Florence et al., 2018). Ibrutinib effectively inhibits poly I:C and lipopolysaccharide (LPS)-induced activation of BTK, fms-like tyrosine kinase 3 (FLT3), and epidermal growth factor receptor (EGFR)-related pathways, significantly reducing acute lung injury in mice (Rao et al., 2022). These findings suggest that BTK inhibitors may serve as potential therapeutic agents for regulating SARS-CoV-2-induced acute lung injury. BTK inhibitors, including acalabrutinib, ibrutinib, and zanubrutinib, have been utilized in COVID-19 clinical trials, showing protection against lung injury and reduced inflammatory activity (Kifle, 2021; Treon et al., 2020).

Excessive up-regulation of p38 activity may drive the intense inflammatory response observed in COVID-19 infection through two potential mechanisms: first, the loss of ACE2 after viral entry may hinder the conversion of angiotensin II to angiotensin 1–7, thereby releasing the inhibition of p38 activity; second, SARS-CoV-2 may exploit p38 activity to facilitate its replication (Grimes & Grimes, 2020; Higgins et al., 2023). Therefore, p38 inhibition may be a promising therapeutic strategy for alleviating COVID-19. Jimenez-Guardeño et al. (2014) found that during SARS-CoV infection, syntenin binds to the E protein, leading to syntenin redistribution from the nucleus to the cytoplasm, activating the p38 mitogen-activated protein kinase (MAPK) pathway and promoting excessive inflammatory cytokine expression. Furthermore, the application of p38 MAPK inhibitors significantly improves survival in SARS-CoV-2-infected mice by reducing IL-1α and IL-6 levels in the BALF, decreasing neutrophil infiltration, and alleviating interstitial edema (Gu et al., 2021). Selective p38 signaling inhibitors, such as PH-797804 and VX-702, markedly reduce the expression of proinflammatory cytokines IL6, CXCL8, CXCL10, and TNF-α during SARS-CoV-2 infection, while concurrently reducing viral replication and modulating the IFN-mediated antiviral response (Faist et al., 2023).

The NF-κB pathway plays a central role as an immune regulator in COVID-19, contributing to excessive inflammation and cytokine storms. Inhibiting the NF-κB pathway can suppress the release of various proinflammatory cytokines, chemokines, and adhesion molecules, making it an important potential therapeutic target for COVID-19 (Jiang et al., 2022). During the early phase of infection, the SARS-CoV-2 nucleocapsid protein, present in body fluids, activates NF-κB p65 phosphorylation, promotes M1 macrophage polarization and proinflammatory cytokine expression, and induces acute lung injury. The NF-κB inhibitor pyrrolidine dithiocarbamate alleviates the effects of the N protein on acute lung injury in mouse models (Xia et al., 2021). Auranofin, another NF-κB inhibitor, also exerts inhibitory effects on SARS-CoV-2 replication and inflammatory cytokine expression, including IL-6, TNF-α, and IL-1β, *in vitro* (Cirri et al., 2021; Rothan et al., 2020). Oral administration of auranofin significantly attenuates lung tissue damage, cell infiltration, inflammatory response, and IL-6 production in Syrian hamsters infected with SARS-CoV-2 (Biji et al., 2021). Neufeldt et al. (2022) reported that in human epithelial cells, SARS-CoV-2 triggers an inflammatory immune response via cyclic GMP-AMP synthase (cGAS)-stimulator of IFN genes (STING)-mediated NF-κB activation, which can be attenuated by various STING-targeting drugs, suggesting that cGAS-STING may be a potential target for COVID-19 therapy. However, STING-deficient K18-hACE2 mice do not exhibit altered disease progression after SARS-CoV-2 infection, suggesting that STING deficiency does not impact viral replication or IFN and inflammatory cytokine production (Marino et al., 2023). In contrast, the small-molecule STING agonist diABZI limits SARS-CoV-2 replication in mice and effectively inhibits SARS-CoV-2 infection in multiple viral strains (Li et al., 2021). These findings emphasize the need to verify the effects of immunomodulatory drugs via *in vitro* and *in vivo* experiments and conduct comprehensive validations in animal models before advancing with COVID-19 treatment strategies.

## CONCLUSIONS

The COVID-19 pandemic continues to pose unprecedented challenges to global health, particularly in terms of prevention and treatment efforts. While activation of the immune system is critical for defending against invading pathogens, it also plays a key role in COVID-19 pathogenesis. Understanding the interactions between SARS-CoV-2 infection and the host immune system is essential for developing effective prevention and treatment strategies. Animal models have been instrumental in studying COVID-19, uncovering the pathological and immunological mechanisms of SARS-CoV-2 infection and accelerating vaccine and drug development. Future research in COVID-19 immunobiology should focus on optimizing the existing animal model library, incorporating specialized animal strains to better represent diverse human populations, and developing relevant tools and methods to address the challenges posed by the high variability and continuous evolution of novel SARS-CoV-2 variants.

## COMPETING INTERESTS

The authors declare that they have no competing interests.

## AUTHORS' CONTRIBUTIONS

Y.T.Z. conceived the project; H.Y.Z., T.Z.S., and Y.T.Z. wrote the manuscript; Y.T.Z. edited the manuscript. All authors read and approved the final version of the manuscript.

## REFERENCES


Abdelnabi R, Foo CS, De Jonghe S, et al. 2021. Molnupiravir inhibits replication of the emerging SARS-CoV-2 variants of concern in a hamster infection model. *The Journal of Infectious Diseases*, **224**(5): 749–753.

Adamo S, Chevrier S, Cervia C, et al. 2021. Profound dysregulation of T cell homeostasis and function in patients with severe COVID‐19. *Allergy*, **76**(9): 2866–2881.

Afkhami S, D'Agostino MR, Zhang AL, et al. 2022. Respiratory mucosal delivery of next-generation COVID-19 vaccine provides robust protection against both ancestral and variant strains of SARS-CoV-2. *Cell*, **185**(5): 896–915. e19.

Aksu M, Kumar P, Güttler T, et al. 2024. Nanobodies to multiple spike variants and inhalation of nanobody-containing aerosols neutralize SARS-

CoV-2 in cell culture and hamsters. *Antiviral Research*, **221**: 105778.
A'La R, Wijaya AY, Susilowati H, et al. 2023. Inactivated SARS-CoV-2 vaccine candidate immunization on non-human primate animal model: B-cell and T-cell responses immune evaluation. *Heliyon*, **9**(7): e18039.
Albornoz EA, Amarilla AA, Modhiran N, et al. 2023. SARS-CoV-2 drives NLRP3 inflammasome activation in human microglia through spike protein. *Molecular Psychiatry*, **28**(7): 2878–2893.
Altamimi I, Alabdulkarim IM, Alhumimidi AS, et al. 2024. Navigating novel uncertainties of COVID-19: the rise of the JN. 1 variant. *Cureus*, **16**(1): e51497.
André S, Picard M, Cezar R, et al. 2022. T cell apoptosis characterizes severe Covid-19 disease. *Cell Death & Differentiation*, **29**(8): 1486–1499.
Antonelli M, Pujol JC, Spector TD, et al. 2022. Risk of long COVID associated with delta versus omicron variants of SARS-CoV-2. *The Lancet*, **399**(10343): 2263–2264.
Arish M, Qian W, Narasimhan H, et al. 2023. COVID‐19 immunopathology: from acute diseases to chronic sequelae. *Journal of Medical Virology*, **95**(1): e28122.
Ashhurst AS, Johansen MD, Maxwell JWC, et al. 2022. Mucosal TLR2-activating protein-based vaccination induces potent pulmonary immunity and protection against SARS-CoV-2 in mice. *Nature Communications*, **13**(1): 6972.
Azkur AK, Akdis M, Azkur D, et al. 2020. Immune response to SARS‐CoV‐2 and mechanisms of immunopathological changes in COVID‐19. *Allergy*, **75**(7): 1564–1581.
Bader SM, Cooney JP, Sheerin D, et al. 2023. SARS-CoV-2 mouse adaptation selects virulence mutations that cause TNF-driven age-dependent severe disease with human correlates. *Proceedings of the National Academy of Sciences of the United States of America*, **120**(32): e2301689120.
Bagato O, Balkema-Buschmann A, Todt D, et al. 2024. Spatiotemporal analysis of SARS-CoV-2 infection reveals an expansive wave of monocyte-derived macrophages associated with vascular damage and virus clearance in hamster lungs. *Microbiology Spectrum*, **12**(1): e0246923.
Bao LL, Deng W, Huang BY, et al. 2020. The pathogenicity of SARS-CoV-2 in hACE2 transgenic mice. *Nature*, **583**(7818): 830–833.
Baum A, Ajithdoss D, Copin R, et al. 2020. REGN-COV2 antibodies prevent and treat SARS-CoV-2 infection in rhesus macaques and hamsters. *Science*, **370**(6520): 1110–1115.
Beckett EL, Phipps S, Starkey MR, et al. 2012. TLR2, but Not TLR4, is required for effective host defence against *Chlamydia* respiratory tract infection in early life. *PLoS One*, **7**(6): e39460.
Beddingfield BJ, Maness NJ, Fears AC, et al. 2021. Effective prophylaxis of COVID-19 in rhesus macaques using a combination of two parenterally-administered SARS-CoV-2 neutralizing antibodies. *Frontiers in Cellular and Infection Microbiology*, **11**: 753444.
Bednash JS, Kagan VE, Englert JA, et al. 2022. Syrian hamsters as a model of lung injury with SARS-CoV-2 infection: pathologic, physiologic, and detailed molecular profiling. *Translational Research*, **240**: 1–16.
Belser JA, Katz JM, Tumpey TM. 2011. The ferret as a model organism to study influenza A virus infection. *Disease Models & Mechanisms*, **4**(5): 575–579.
Bertzbach LD, Vladimirova D, Dietert K, et al. 2021. SARS‐CoV‐2 infection of Chinese hamsters (*Cricetulus griseus*) reproduces COVID‐19 pneumonia in a well‐established small animal model. *Transboundary and Emerging Diseases*, **68**(3): 1075–1079.
Bi ZF, Hong WQ, Yang JY, et al. 2021. Animal models for SARS‐CoV‐2 infection and pathology. *MedComm*, **2**(4): 548–568.
Biji A, Khatun O, Swaraj S, et al. 2021. Identification of COVID-19 prognostic markers and therapeutic targets through meta-analysis and validation of Omics data from nasopharyngeal samples. *EBioMedicine*, **70**: 103525.
Boby ML, Fearon D, Ferla M, et al. 2023. Open science discovery of potent noncovalent SARS-CoV-2 main protease inhibitors. *Science*, **382**(6671): eabo7201.
Boon ACM, Darling TL, Halfmann PJ, et al. 2022. Reduced airborne transmission of SARS-CoV-2 BA. 1 omicron virus in Syrian hamsters. *PLoS Pathogens*, **18**(12): e1010970.
Broggi A, Ghosh S, Sposito B, et al. 2020. Type III interferons disrupt the lung epithelial barrier upon viral recognition. *Science*, **369**(6504): 706–712.
Broz P, Dixit VM. 2016. Inflammasomes: mechanism of assembly, regulation and signalling. *Nature Reviews Immunology*, **16**(7): 407–420.
Carabelli AM, Peacock TP, Thorne LG, et al. 2023. SARS-CoV-2 variant biology: immune escape, transmission and fitness. *Nature Reviews Microbiology*, **21**(3): 162–177.
Chandrashekar A, Liu JY, Martinot AJ, et al. 2020. SARS-CoV-2 infection protects against rechallenge in rhesus macaques. *Science*, **369**(6505): 812–817.
Chen HB, Xie ZP, Long RX, et al. 2021a. Immunological evaluation of an inactivated SARS-CoV-2 vaccine in rhesus macaques. *Molecular Therapy - Methods & Clinical Development*, **23**: 108–118.
Chen RR, Wang KE, Yu J, et al. 2021b. The spatial and cell-type distribution of SARS-CoV-2 receptor ACE2 in the human and mouse brains. *Frontiers in Neurology*, **11**: 573095.
Chen YX, Song WC, Li C, et al. 2023. COVID-19 mRNA vaccine protects against SARS-CoV-2 Omicron BA. 1 infection in diet-induced obese mice through boosting host innate antiviral responses. *EBioMedicine*, **89**: 104485.
Chen Z, Yuan YC, Hu QT, et al. 2024. SARS-CoV-2 immunity in animal models. *Cellular & Molecular Immunology*, **21**(2): 119–133.
Chu H, Chan JFW, Wang YX, et al. 2020. Comparative replication and immune activation profiles of SARS-CoV-2 and SARS-CoV in human lungs: an ex vivo study with implications for the pathogenesis of COVID-19. *Clinical Infectious Diseases*, **71**(6): 1400–1409.
Chu H, Chan JFW, Yuen KY. 2022. Animal models in SARS-CoV-2 research. *Nature Methods*, **19**(4): 392–394.
Cirri D, Marzo T, Tolbatov I, et al. 2021. In vitro anti-SARS-CoV-2 activity of selected metal compounds and potential molecular basis for their actions based on computational study. *Biomolecules*, **11**(12): 1858.
Clancy CS, Meade-White K, Shaia C, et al. 2023. Histopathologic characterization of experimental peracute SARS-CoV-2 infection in the Syrian hamster. *Veterinary Sciences*, **10**(9): 536.
Corbett KS, Nason MC, Flach B, et al. 2021. Immune correlates of protection by mRNA-1273 vaccine against SARS-CoV-2 in nonhuman primates. *Science*, **373**(6561): eabj0299.
Daitch V, Yelin D, Awwad M, et al. 2022. Characteristics of long-COVID among older adults: a cross-sectional study. *International Journal of Infectious Diseases*, **125**: 287–293.
Davis HE, Mccorkell L, Vogel JM, et al. 2023. Long COVID: major findings, mechanisms and recommendations. *Nature Reviews Microbiology*, **21**(3): 133–146.
De Vries RD, Schmitz KS, Bovier FT, et al. 2021. Intranasal fusion inhibitory lipopeptide prevents direct-contact SARS-CoV-2 transmission in ferrets. *Science*, **371**(6536): 1379–1382.
Denton AE, Dooley J, Cinti I, et al. 2022. Targeting TLR4 during vaccination boosts MAdCAM-1$^{+}$ lymphoid stromal cell activation and promotes the aged germinal center response. *Science Immunology*, **7**(71): eabk0018.
Dinnon KH, Leist SR, Okuda K, et al. 2022. SARS-CoV-2 infection produces chronic pulmonary epithelial and immune cell dysfunction with fibrosis in mice. *Science Translational Medicine*, **14**(664): eabo5070.
Dinnon KH, Leist SR, Schäfer A, et al. 2020. A mouse-adapted model of SARS-CoV-2 to test COVID-19 countermeasures. *Nature*, **586**(7830):

560–566.

Du J, Wei LR, Li GL, et al. 2021. Persistent high percentage of HLA-DR$^{+}$CD38$^{high}$ CD8$^{+}$ T cells associated with immune disorder and disease severity of COVID-19. *Frontiers in Immunology*, **12**: 735125.

Dutta D, Liu JN, Xiong HG. 2022. NLRP3 inflammasome activation and SARS-CoV-2-mediated hyperinflammation, cytokine storm and neurological syndromes. *International Journal of Physiology, Pathophysiology and Pharmacology*, **14**(3): 138–160.

Eckstrand CD, Baldwin TJ, Rood KA, et al. 2021. An outbreak of SARS-CoV-2 with high mortality in mink (*Neovison vison*) on multiple Utah farms. *PLoS Pathogens*, **17**(11): e1009952.

Efstathiou V, Stefanou MI, Demetriou M, et al. 2022. Long COVID and neuropsychiatric manifestations (Review). *Experimental and Therapeutic Medicine*, **23**(5): 363.

Elia U, Rotem S, Bar Haim E, et al. 2021. Lipid nanoparticle RBD-hFc mRNA vaccine protects hACE2 transgenic mice against a lethal SARS-CoV-2 infection. *Nano Letters*, **21**(11): 4774–4779.

Estes JD, Wong SW, Brenchley JM. 2018. Nonhuman primate models of human viral infections. *Nature Reviews Immunology*, **18**(6): 390–404.

Faist A, Schloer S, Mecate-Zambrano A, et al. 2023. Inhibition of p38 signaling curtails the SARS-CoV-2 induced inflammatory response but retains the IFN-dependent antiviral defense of the lung epithelial barrier. *Antiviral Research*, **209**: 105475.

Fajgenbaum DC, June CH. 2020. Cytokine storm. *New England Journal of Medicine*, **383**(23): 2255–2273.

Feng LQ, Wang Q, Shan C, et al. 2020. An adenovirus-vectored COVID-19 vaccine confers protection from SARS-COV-2 challenge in rhesus macaques. *Nature Communications*, **11**(1): 4207.

Fernández-de-las-Peñas C, Cancela-Cilleruelo I, Rodríguez-Jiménez J, et al. 2022. Associated-onset symptoms and Post-COVID-19 symptoms in hospitalized COVID-19 survivors infected with wuhan, alpha or delta SARS-CoV-2 variant. *Pathogens*, **11**(7): 725.

Ferreira-Gomes M, Kruglov A, Durek P, et al. 2021. SARS-CoV-2 in severe COVID-19 induces a TGF-β-dominated chronic immune response that does not target itself. *Nature Communications*, **12**(1): 1961.

Florence JM, Krupa A, Booshehri LM, et al. 2018. Inhibiting Bruton's tyrosine kinase rescues mice from lethal influenza-induced acute lung injury. *American Journal of Physiology-Lung Cellular and Molecular Physiology*, **315**(1): L52–L58.

Fomin G, Tabynov K, Islamov R, et al. 2023. Cytokine response and damages in the lungs of aging Syrian hamsters on a high-fat diet infected with the SARS-CoV-2 virus. *Frontiers in Immunology*, **14**: 1223086.

Fontes-Dantas FL, Fernandes GG, Gutman EG, et al. 2023. SARS-CoV-2 Spike protein induces TLR4-mediated long-term cognitive dysfunction recapitulating post-COVID-19 syndrome in mice. *Cell Reports*, **42**(3): 112189.

Francis ME, Goncin U, Kroeker A, et al. 2021. SARS-CoV-2 infection in the Syrian hamster model causes inflammation as well as type I interferon dysregulation in both respiratory and non-respiratory tissues including the heart and kidney. *PLoS Pathogens*, **17**(7): e1009705.

Frere JJ, Serafini RA, Pryce KD, et al. 2022. SARS-CoV-2 infection in hamsters and humans results in lasting and unique systemic perturbations after recovery. *Science Translational Medicine*, **14**(664): eabq3059.

Frontera JA, Sabadia S, Yang D, et al. 2022. Life stressors significantly impact long-term outcomes and post-acute symptoms 12-months after COVID-19 hospitalization. *Journal of the Neurological Sciences*, **443**: 120487.

Gagne M, Flynn BJ, Andrew SF, et al. 2023. Mucosal adenoviral-vectored vaccine boosting durably prevents XBB. 1.16 infection in nonhuman primates. *BioRxiv*, doi: https://doi.org/10.1101/2023.11.06.565765.

Galani IE, Rovina N, Lampropoulou V, et al. 2021. Untuned antiviral immunity in COVID-19 revealed by temporal type I/III interferon patterns and flu comparison. *Nature Immunology*, **22**(1): 32–40.

Gao S, Zhang LL. 2020. ACE2 partially dictates the host range and tropism of SARS-CoV-2. *Computational and Structural Biotechnology Journal*, **18**: 4040–4047.

Gary EN, Warner BM, Parzych EM, et al. 2021. A novel mouse AAV6 hACE2 transduction model of wild-type SARS-CoV-2 infection studied using synDNA immunogens. *iScience*, **24**(7): 102699.

Georg P, Astaburuaga-García R, Bonaguro L, et al. 2022. Complement activation induces excessive T cell cytotoxicity in severe COVID-19. *Cell*, **185**(3): 493–512. e25.

Glazkova DV, Bogoslovskaya EV, Urusov FA, et al. 2022. Generation of SARS-CoV-2 mouse model by transient expression of the human ACE2 gene mediated by intranasal administration of AAV-hACE2. *Molecular Biology*, **56**(5): 705–712.

Grimes JM, Grimes KV. 2020. p38 MAPK inhibition: a promising therapeutic approach for COVID-19. *Journal of Molecular and Cellular Cardiology*, **144**: 63–65.

Gruber AD, Firsching TC, Trimpert J, et al. 2022. Hamster models of COVID-19 pneumonia reviewed: how human can they be?. *Veterinary Pathology*, **59**(4): 528–545.

Gu HJ, Chen Q, Yang G, et al. 2020. Adaptation of SARS-CoV-2 in BALB/c mice for testing vaccine efficacy. *Science*, **369**(6511): 1603–1607.

Gu TX, Zhao SM, Jin GG, et al. 2021. Cytokine signature induced by SARS-CoV-2 spike protein in a mouse model. *Frontiers in Immunology*, **11**: 621441.

Guebre-Xabier M, Patel N, Tian JH, et al. 2020. NVX-CoV2373 vaccine protects cynomolgus macaque upper and lower airways against SARS-CoV-2 challenge. *Vaccine*, **38**(50): 7892–7896.

Haabeth OaW, Lohmeyer JJK, Sallets A, et al. 2021. An mRNA SARS-CoV-2 vaccine employing charge-altering releasable transporters with a TLR-9 agonist induces neutralizing antibodies and T cell memory. *ACS Central Science*, **7**(7): 1191–1204.

Hadjadj J, Yatim N, Barnabei L, et al. 2020. Impaired type I interferon activity and inflammatory responses in severe COVID-19 patients. *Science*, **369**(6504): 718–724.

Hakim AD, Awili M, O'Neal HR, et al. 2023. Efficacy and safety of MAS825 (anti-IL-1β/IL-18) in COVID-19 patients with pneumonia and impaired respiratory function. *Clinical and Experimental Immunology*, **213**(3): 265–275.

Halfmann PJ, Iida S, Iwatsuki-Horimoto K, et al. 2022. SARS-CoV-2 Omicron virus causes attenuated disease in mice and hamsters. *Nature*, **603**(7902): 687–692.

Halfmann PJ, Uraki R, Kuroda M, et al. 2023. Transmission and re-infection of Omicron variant XBB. 1.5 in hamsters. *eBioMedicine*, **93**: 104677.

Hall FC, Cheriyan J, Cope AP, et al. 2023. Efficacy and safety of baricitinib or ravulizumab in adult patients with severe COVID-19 (TACTIC-R): a randomised, parallel-arm, open-label, phase 4 trial. *The Lancet Respiratory Medicine*, **11**(12): 1064–1074.

Handley A, Ryan KA, Davies ER, et al. 2023. SARS-CoV-2 disease severity in the golden Syrian hamster model of infection is related to the volume of intranasal inoculum. *Viruses*, **15**(3): 748.

Hasenkrug KJ, Feldmann F, Myers L, et al. 2021. Recovery from acute SARS-CoV-2 infection and development of anamnestic immune responses in T cell-depleted rhesus macaques. *mBio*, **12**(4): e0150321.

Hendriks RW, Yuvaraj S, Kil LP. 2014. Targeting Bruton's tyrosine kinase in B cell malignancies. *Nature Reviews Cancer*, **14**(4): 219–232.

Herder V, Mendonca DC, Upfold N, et al. 2023. The SARS-CoV-2 Omicron sub-variant BA. 2.86 is attenuated in hamsters. *BioRxiv*, doi: https://doi.org/10.1101/2023.11.10.566576.

Hewitt JA, Lutz C, Florence WC, et al. 2020. ACTIVating resources for the

COVID-19 pandemic: *in vivo* models for vaccines and therapeutics. *Cell Host & Microbe*, **28**(5): 646–659.
Higgins CA, Nilsson-Payant BE, Bonaventure B, et al. 2023. SARS-CoV-2 hijacks p38β/MAPK11 to promote virus replication. *mBio*, **14**(4): e0100723.
Hoang TN, Pino M, Boddapati AK, et al. 2021. Baricitinib treatment resolves lower-airway macrophage inflammation and neutrophil recruitment in SARS-CoV-2-infected rhesus macaques. *Cell*, **184**(2): 460–475. e21.
Horiuchi S, Oishi K, Carrau L, et al. 2021. Immune memory from SARS-CoV-2 infection in hamsters provides variant-independent protection but still allows virus transmission. *Science Immunology*, **6**(66): eabm3131.
Huang LX, Li X, Gu XY, et al. 2022. Health outcomes in people 2 years after surviving hospitalisation with COVID-19: a longitudinal cohort study. *The Lancet Respiratory Medicine*, **10**(9): 863–876.
Imai M, Iwatsuki-Horimoto K, Hatta M, et al. 2020. Syrian hamsters as a small animal model for SARS-CoV-2 infection and countermeasure development. *Proceedings of the National Academy of Sciences of the United States of America*, **117**(28): 16587–16595.
Ireland RE, Davies CD, Keyser E, et al. 2022. Histopathological and immunological findings in the common marmoset following exposure to aerosolized SARS-CoV-2. *Viruses*, **14**(7): 1580.
Israelow B, Mao TY, Klein J, et al. 2021. Adaptive immune determinants of viral clearance and protection in mouse models of SARS-CoV-2. *Science Immunology*, **6**(64): eabl4509.
Israelow B, Song E, Mao TY, et al. 2020. Mouse model of SARS-CoV-2 reveals inflammatory role of type I interferon signaling. *Journal of Experimental Medicine*, **217**(12): e20201241.
Jacob-Dolan C, Feldman J, McMahan K, et al. 2021. Coronavirus-specific antibody cross reactivity in Rhesus Macaques following SARS-CoV-2 vaccination and infection. *Journal of Virology*, **95**(11): e00117–21.
Jafarzadeh A, Jafarzadeh S, Nozari P, et al. 2020. Lymphopenia an important immunological abnormality in patients with COVID‐19: possible mechanisms. *Scandinavian Journal of Immunology*, **93**(2): e12967.
Jansen EB, Orvold SN, Swan CL, et al. 2022. After the virus has cleared—Can preclinical models be employed for Long COVID research?. *PLoS Pathogens*, **18**(9): e1010741.
Jeong JH, Chokkakula S, Min SC, et al. 2022. Combination therapy with nirmatrelvir and molnupiravir improves the survival of SARS-CoV-2 infected mice. *Antiviral Research*, **208**: 105430.
Jiang YJ, Zhao TM, Zhou XY, et al. 2022. Inflammatory pathways in COVID‐19: mechanism and therapeutic interventions. *MedComm*, **3**(3): e154.
Jimenez-Guardeño JM, Nieto-Torres JL, Dediego ML, et al. 2014. The PDZ-binding motif of severe acute respiratory syndrome coronavirus envelope protein is a determinant of viral pathogenesis. *PLoS Pathogens*, **10**(8): e1004320.
Jin JY, Wang XW, Li YZ, et al. 2023. Weak SARS-CoV-2-specific responses of TIGIT-expressing $CD8^+$ T cells in people living with HIV after a third dose of a SARS-CoV-2 inactivated vaccine. *Chinese Medical Journal*, **136**(24): 2938–2947.
Johnson DM, Brasel T, Massey S, et al. 2023. Evaluation of molnupiravir (EIDD-2801) efficacy against SARS-CoV-2 in the rhesus macaque model. *Antiviral Research*, **209**: 105492.
Kane Y, Wong G, Gao GF. 2023. Animal models, zoonotic reservoirs, and cross-species transmission of emerging human-infecting coronaviruses. *Annual Review of Animal Biosciences*, **11**: 1–31.
Karki R, Sharma BR, Tuladhar S, et al. 2021. Synergism of TNF-α and IFN-γ triggers inflammatory cell death, tissue damage, and mortality in SARS-CoV-2 infection and cytokine shock syndromes. *Cell*, **184**(1): 149–168. e17.
Kasuga Y, Zhu BH, Jang KJ, et al. 2021. Innate immune sensing of coronavirus and viral evasion strategies. *Experimental & Molecular Medicine*, **53**(5): 723–736.
Kibler KV, Szczerba M, Lake D, et al. 2022. Intranasal immunization with a vaccinia virus vaccine vector expressing pre-fusion stabilized SARS-CoV-2 spike fully protected mice against lethal challenge with the heavily mutated mouse-adapted SARS2-$N501Y_{MA30}$ strain of SARS-CoV-2. *Vaccines*, **10**(8): 1172.
Kifle ZD. 2021. Bruton tyrosine kinase inhibitors as potential therapeutic agents for COVID-19: a review. *Metabolism Open*, **11**: 100116.
Kim YI, Casel MaB, Choi YK. 2022. Transmissibility and pathogenicity of SARS-CoV-2 variants in animal models. *Journal of Microbiology*, **60**(3): 255–267.
Kim YI, Kim SG, Kim SM, et al. 2020. Infection and rapid transmission of SARS-CoV-2 in ferrets. *Cell Host & Microbe*, **27**(5): 704–709. e2.
Klein J, Wood J, Jaycox JR, et al. 2023. Distinguishing features of long COVID identified through immune profiling. *Nature*, **623**(7985): 139–148.
Knight AC, Montgomery SA, Fletcher CA, et al. 2021. Mouse models for the study of SARS-CoV-2 infection. *Comparative Medicine*, **71**(5): 383–397.
Kosyreva A, Dzhalilova D, Lokhonina A, et al. 2021. The role of macrophages in the pathogenesis of SARS-CoV-2-associated acute respiratory distress syndrome. *Frontiers in Immunology*, **12**: 682871.
Kreft IC, Winiarczyk RRA, Tanis FJ, et al. 2022. Absence of COVID-19-associated changes in plasma coagulation proteins and pulmonary thrombosis in the ferret model. *Thrombosis Research*, **210**: 6–11.
Kuang YQ, Tang X, Liu FL, et al. 2009. Genotyping of *TRIM5* locus in northern pig-tailed macaques (*Macaca leonina*), a primate species susceptible to Human Immunodeficiency Virus type 1 infection. *Retrovirology*, **6**(1): 58.
Langel SN, Johnson S, Martinez CI, et al. 2022. Adenovirus type 5 SARS-CoV-2 vaccines delivered orally or intranasally reduced disease severity and transmission in a hamster model. *Science Translational Medicine*, **14**(658): eabn6868.
Lee CM, Oh JE. 2022. Resident memory B cells in barrier tissues. *Frontiers in Immunology*, **13**: 953088.
Lee JS, Koh JY, Yi K, et al. 2021. Single-cell transcriptome of bronchoalveolar lavage fluid reveals sequential change of macrophages during SARS-CoV-2 infection in ferrets. *Nature Communications*, **12**(1): 4567.
Lee JS, Shin EC. 2020. The type I interferon response in COVID-19: implications for treatment. *Nature Reviews Immunology*, **20**(10): 585–586.
Leist SR, Dinnon KH, Schäfer A, et al. 2020. A mouse-adapted SARS-CoV-2 induces acute lung injury and mortality in standard laboratory mice. *Cell*, **183**(4): 1070–1085. e12.
Li MH, Ferretti M, Ying BL, et al. 2021. Pharmacological activation of STING blocks SARS-CoV-2 infection. *Science Immunology*, **6**(59): eabi9007.
Li Q, Dang C, Wang LH. 2022. Neuroinflammation in mild respiratory COVID-19: insights into cognitive impairment in milder cases. *Military Medical Research*, **9**(1): 72.
Liang SX, Bao CL, Yang Z, et al. 2023. SARS-CoV-2 spike protein induces IL-18-mediated cardiopulmonary inflammation via reduced mitophagy. *Signal Transduction and Targeted Therapy*, **8**(1): 108.
Liang Y, Li H, Li J, et al. 2020. Role of neutrophil chemoattractant CXCL5 in SARS-CoV-2 infection-induced lung inflammatory innate immune response in an *in vivo* hACE2 transfection mouse model. *Zoological Research*, **41**(6): 621–631.
Liao MF, Liu Y, Yuan J, et al. 2020. Single-cell landscape of bronchoalveolar immune cells in patients with COVID-19. *Nature Medicine*, **26**(6): 842–844.
Linsky TW, Vergara R, Codina N, et al. 2020. De novo design of potent and resilient hACE2 decoys to neutralize SARS-CoV-2. *Science*, **370**(6521): 1208–1214.
Liu DL, Chen CK, Chen DB, et al. 2023a. Mouse models susceptible to HCoV-229E and HCoV-NL63 and cross protection from challenge with

SARS-CoV-2. *Proceedings of the National Academy of Sciences of the United States of America*, **120**(4): e2202820120.

Liu R, Wang Y, Li J, et al. 2020a. Decreased T cell populations contribute to the increased severity of COVID-19. *Clinica Chimica Acta*, **508**: 110–114.

Liu Y, Gu XY, Li HB, et al. 2023b. Mechanisms of long COVID: an updated review. *Chinese Medical Journal Pulmonary and Critical Care Medicine*, **1**(4): 231–240.

Liu ZM, Long W, Tu MQ, et al. 2020b. Lymphocyte subset (CD4+, CD8+) counts reflect the severity of infection and predict the clinical outcomes in patients with COVID-19. *Journal of Infection*, **81**(2): 318–356.

Liu ZM, Yang MH, Yu K, et al. 2022. Toll-like receptor (TLRs) agonists and antagonists for COVID-19 treatments. *Frontiers in Pharmacology*, **13**: 989664.

Loretelli C, Abdelsalam A, D'addio F, et al. 2021. PD-1 blockade counteracts post–COVID-19 immune abnormalities and stimulates the anti–SARS-CoV-2 immune response. *JCI Insight*, **6**(24): e146701.

Lu SY, Zhao Y, Yu WH, et al. 2020. Comparison of nonhuman primates identified the suitable model for COVID-19. *Signal Transduction and Targeted Therapy*, **5**(1): 157.

Lu Y, Shen F, He WQ, et al. 2023. HR121 targeting HR2 domain in S2 subunit of spike protein can serve as a broad-spectrum SARS-CoV-2 inhibitor *via* intranasal administration. *Acta Pharmaceutica Sinica B*, **13**(8): 3339–3351.

Machado RRG, Walker JL, Scharton D, et al. 2023. Immunogenicity and efficacy of vaccine boosters against SARS-CoV-2 Omicron subvariant BA. 5 in male Syrian hamsters. *Nature Communications*, **14**(1): 4260.

Mahdy MaA, Younis W, Ewaida Z. 2020. An overview of SARS-CoV-2 and animal infection. *Frontiers in Veterinary Science*, **7**: 596391.

Major J, Crotta S, Llorian M, et al. 2020. Type I and III interferons disrupt lung epithelial repair during recovery from viral infection. *Science*, **369**(6504): 712–717.

Marino G, Zhang BC, Schmitz A, et al. 2023. STING is redundant for host defense and pathology of COVID-19-like disease in mice. *Life Science Alliance*, **6**(8): e202301997.

Marx S, Kümmerer BM, Grützner C, et al. 2022. RIG-I-induced innate antiviral immunity protects mice from lethal SARS-CoV-2 infection. *Molecular Therapy - Nucleic Acids*, **27**: 1225–1234.

Masters AR, Jellison ER, Puddington L, et al. 2018. Attrition of T cell zone fibroblastic reticular cell number and function in aged spleens. *Immunohorizons*, **2**(5): 155–163.

McCray Jr PB, Pewe L, Wohlford-Lenane C, et al. 2007. Lethal infection of K18-*hACE2* mice infected with severe acute respiratory syndrome coronavirus. *Journal of Virology*, **81**(2): 813–821.

McGonagle D, Sharif K, O'regan A, et al. 2020. The role of cytokines including interleukin-6 in COVID-19 induced pneumonia and macrophage activation syndrome-like disease. *Autoimmunity Reviews*, **19**(6): 102537.

McMahan K, Wegmann F, Aid M, et al. 2024. Mucosal boosting enhances vaccine protection against SARS-CoV-2 in macaques. *Nature*, **626**(7998): 385–391.

McMahan K, Yu JY, Mercado NB, et al. 2021. Correlates of protection against SARS-CoV-2 in rhesus macaques. *Nature*, **590**(7847): 630–634.

Meehan GR, Herder V, Allan J, et al. 2023. Phenotyping the virulence of SARS-CoV-2 variants in hamsters by digital pathology and machine learning. *PLoS Pathogens*, **19**(11): e1011589.

Mehta P, Mcauley DF, Brown M, et al. 2020. COVID-19: consider cytokine storm syndromes and immunosuppression. *The Lancet*, **395**(10229): 1033–1034.

Melin AD, Janiak MC, Marrone F, et al. 2020. Comparative ACE2 variation and primate COVID-19 risk. *Communications Biology*, **3**(1): 641.

Merad M, Blish CA, Sallusto F, et al. 2022. The immunology and immunopathology of COVID-19. *Science*, **375**(6585): 1122–1127.

Merle-Nguyen L, Ando-Grard O, Bourgon C, et al. 2024. Early corticosteroid treatment enhances recovery from SARS-CoV-2 induced loss of smell in hamster. *Brain, Behavior, and Immunity*, **118**: 78–89.

Montazersaheb S, Hosseiniyan Khatibi SM, Hejazi MS, et al. 2022. COVID-19 infection: an overview on cytokine storm and related interventions. *Virology Journal*, **19**(1): 92.

Morgan MS, Yan KX, Le TT, et al. 2022. Monoclonal antibodies specific for SARS-CoV-2 spike protein suitable for multiple applications for current variants of concern. *Viruses*, **15**(1): 139.

Mulka KR, Beck SE, Solis CV, et al. 2022. Progression and resolution of severe acute respiratory syndrome coronavirus 2 (SARS-CoV-2) infection in golden syrian hamsters. *The American Journal of Pathology*, **192**(2): 195–207.

Muñoz-Fontela C, Dowling WE, Funnell SGP, et al. 2020. Animal models for COVID-19. *Nature*, **586**(7830): 509–515.

Mykytyn AZ, Lamers MM, Okba NMA, et al. 2021. Susceptibility of rabbits to SARS-CoV-2. *Emerging Microbes & Infections*, **10**(1): 1–7.

Neufeldt CJ, Cerikan B, Cortese M, et al. 2022. SARS-CoV-2 infection induces a pro-inflammatory cytokine response through cGAS-STING and NF-κB. *Communications Biology*, **5**(1): 45.

Ni WT, Yang XW, Yang DQ, et al. 2020. Role of angiotensin-converting enzyme 2 (ACE2) in COVID-19. *Critical Care*, **24**(1): 422.

Oh DQP, Grothe I, Lukaß H, et al. 2023. Monitoring and immunogenicity of SARS-CoV-2 vaccination of laboratory rhesus monkeys (*Macaca mulatta*). *Scientific Reports*, **13**(1): 3274.

Oh JE, Song E, Moriyama M, et al. 2021. Intranasal priming induces local lung-resident B cell populations that secrete protective mucosal antiviral IgA. *Science Immunology*, **6**(66): eabj5129.

Oladunni FS, Park JG, Pino PA, et al. 2020. Lethality of SARS-CoV-2 infection in K18 human angiotensin-converting enzyme 2 transgenic mice. *Nature Communications*, **11**(1): 6122.

O'Neill LAJ, Golenbock D, Bowie AG. 2013. The history of Toll-like receptors — redefining innate immunity. *Nature Reviews Immunology*, **13**(6): 453–460.

Paidas MJ, Cosio DS, Ali S, et al. 2022. Long-term sequelae of COVID-19 in experimental mice. *Molecular Neurobiology*, **59**(10): 5970–5986.

Patel N, Trost JF, Guebre-Xabier M, et al. 2023. XBB. 1.5 spike protein COVID-19 vaccine induces broadly neutralizing and cellular immune responses against EG. 5.1 and emerging XBB variants. *Scientific Reports*, **13**(1): 19176.

Philippens IHCHM, Böszörményi KP, Wubben JAM, et al. 2022. Brain inflammation and intracellular α-Synuclein aggregates in macaques after SARS-CoV-2 infection. *Viruses*, **14**(4): 776.

Port JR, Yinda CK, Riopelle JC, et al. 2023. Infection- or AZD1222 vaccine-mediated immunity reduces SARS-CoV-2 transmission but increases Omicron competitiveness in hamsters. *Nature Communications*, **14**(1): 6592.

Prenafeta A, Bech-Sàbat G, Moros A, et al. 2023. Preclinical evaluation of PHH-1V vaccine candidate against SARS-CoV-2 in non-human primates. *iScience*, **26**(7): 107224.

Qi FR, Qian S, Zhang SY, et al. 2020. Single cell RNA sequencing of 13 human tissues identify cell types and receptors of human coronaviruses. *Biochemical and Biophysical Research Communications*, **526**(1): 135–140.

Rabdano SO, Ruzanova EA, Pletyukhina IV, et al. 2023. Immunogenicity and in vivo protective effects of recombinant nucleocapsid-based SARS-CoV-2 vaccine convacell®. *Vaccines*, **11**(4): 874.

Ragab D, Salah Eldin H, Taeimah M, et al. 2020. The COVID-19 cytokine storm; What we know so far. *Frontiers in Immunology*, **11**: 1446.

Rao HN, Song XMT, Lei JT, et al. 2022. Ibrutinib prevents acute lung injury via multi-targeting BTK, FLT3 and EGFR in mice. *International Journal of Molecular Sciences*, **23**(21): 13478.

Ratajczak MZ, Kucia M. 2020. SARS-CoV-2 infection and overactivation of Nlrp3 inflammasome as a trigger of cytokine “storm” and risk factor for damage of hematopoietic stem cells. *Leukemia*, **34**(7): 1726–1729.

Ravid JD, Leiva O, Chitalia VC. 2022. Janus kinase signaling pathway and its role in COVID-19 inflammatory, vascular, and thrombotic manifestations. *Cells*, **11**(2): 306.

Rein L, Calero K, Shah R, et al. 2022. Randomized phase 3 trial of ruxolitinib for COVID-19-associated acute respiratory distress syndrome. *Critical Care Medicine*, **50**(12): 1701–1713.

Riggioni C, Comberiati P, Giovannini M, et al. 2020. A compendium answering 150 questions on COVID‐19 and SARS‐CoV‐2. *Allergy*, **75**(10): 2503–2541.

Roessler M, Tesch F, Batram M, et al. 2022. Post-COVID-19-associated morbidity in children, adolescents, and adults: a matched cohort study including more than 157, 000 individuals with COVID-19 in Germany. *PLoS Medicine*, **19**(11): e1004122.

Roschewski M, Lionakis MS, Sharman JP, et al. 2020. Inhibition of Bruton tyrosine kinase in patients with severe COVID-19. *Science Immunology*, **5**(48): eabd0110.

Rosenke K, Lewis MC, Feldmann F, et al. 2023. Combined molnupiravir-nirmatrelvir treatment improves the inhibitory effect on SARS-CoV-2 in macaques. *JCI Insight*, **8**(4): e166485.

Rothan HA, Stone S, Natekar J, et al. 2020. The FDA-approved gold drug auranofin inhibits novel coronavirus (SARS-COV-2) replication and attenuates inflammation in human cells. *Virology*, **547**: 7–11.

Rubsamen R, Burkholz S, Massey C, et al. 2020. Anti-IL-6 Versus Anti-IL-6R blocking antibodies to treat acute ebola infection in BALB/c mice: potential implications for treating cytokine release syndrome. *Frontiers in Pharmacology*, **11**: 574703.

Ryan FJ, Hope CM, Masavuli MG, et al. 2022. Long-term perturbation of the peripheral immune system months after SARS-CoV-2 infection. *BMC Medicine*, **20**(1): 26.

Santopaolo M, Gregorova M, Hamilton F, et al. 2023. Prolonged T-cell activation and long COVID symptoms independently associate with severe COVID-19 at 3 months. *eLife*, **12**: e85009.

Saravanan UB, Namachivayam M, Jeewon R, et al. 2022. Animal models for SARS-CoV-2 and SARS-CoV-1 pathogenesis, transmission and therapeutic evaluation. *World Journal of Virology*, **11**(1): 40–56.

Sasaki M, Tabata K, Kishimoto M, et al. 2023. S-217622, a SARS-CoV-2 main protease inhibitor, decreases viral load and ameliorates COVID-19 severity in hamsters. *Science Translational Medicine*, **15**(679): eabq4064.

Schmidt C. 2021. COVID-19 long haulers. *Nature Biotechnology*, **39**(8): 908–913.

Schramm CA, Moon D, Peyton L, et al. 2023. Interaction dynamics between innate and adaptive immune cells responding to SARS-CoV-2 vaccination in non-human primates. *Nature Communications*, **14**(1): 7961.

Seehusen F, Clark JJ, Sharma P, et al. 2022. Neuroinvasion and neurotropism by SARS-CoV-2 variants in the K18-hACE2 mouse. *Viruses*, **14**(5): 1020.

Sefik E, Israelow B, Mirza H, et al. 2022. A humanized mouse model of chronic COVID-19. *Nature Biotechnology*, **40**(6): 906–920.

Sekine T, Perez-Potti A, Rivera-Ballesteros O, et al. 2020. Robust T cell immunity in convalescent individuals with asymptomatic or mild COVID-19. *Cell*, **183**(1): 158–168. e14.

Shan C, Yao YF, Yang XL, et al. 2020. Infection with novel coronavirus (SARS-CoV-2) causes pneumonia in *Rhesus macaques. Cell Research*, **30**(8): 670–677.

Sheahan T, Morrison TE, Funkhouser W, et al. 2008. MyD88 is required for protection from lethal infection with a mouse-adapted SARS-CoV. *PLoS Pathogens*, **4**(12): e1000240.

Shi JZ, Wen ZY, Zhong GX, et al. 2020. Susceptibility of ferrets, cats, dogs, and other domesticated animals to SARS–coronavirus 2. *Science*, **368**(6494): 1016–1020.

Shi ZL, Hu ZH. 2008. A review of studies on animal reservoirs of the SARS coronavirus. *Virus Research*, **133**(1): 74–87.

Shou SY, Liu MH, Yang Y, et al. 2021. Animal models for COVID-19: hamsters, mouse, ferret, mink, tree shrew, and non-human primates. *Frontiers in Microbiology*, **12**: 626553.

Sia SF, Yan LM, Chin AWH, et al. 2020. Pathogenesis and transmission of SARS-CoV-2 in golden hamsters. *Nature*, **583**(7818): 834–838.

Singh DK, Singh B, Ganatra SR, et al. 2020. Responses to acute infection with SARS-CoV-2 in the lungs of rhesus macaques, baboons and marmosets. *Nature Microbiology*, **6**(1): 73–86.

Song TZ, Zheng HY, Han JB, et al. 2020. Delayed severe cytokine storm and immune cell infiltration in SARS-CoV-2-infected aged Chinese rhesus macaques. *Zoological Research*, **41**(5): 503–516.

Song TZ, Zheng HY, Han JB, et al. 2021. Northern pig-tailed macaques (*Macaca leonina*) infected with SARS-CoV-2 show rapid viral clearance and persistent immune response. *Zoological Research*, **42**(3): 350–353.

Speranza E, Purushotham JN, Port JR, et al. 2022. Age-related differences in immune dynamics during SARS-CoV-2 infection in rhesus macaques. *Life Science Alliance*, **5**(4): e202101314.

Streblow DN, Hirsch AJ, Stanton JJ, et al. 2023. Aerosol delivery of SARS-CoV-2 human monoclonal antibodies in macaques limits viral replication and lung pathology. *Nature Communications*, **14**(1): 7062.

Subramanian A, Nirantharakumar K, Hughes S, et al. 2022. Symptoms and risk factors for long COVID in non-hospitalized adults. *Nature Medicine*, **28**(8): 1706–1714.

Sui YJ, Li JP, Venzon DJ, et al. 2021a. SARS-CoV-2 spike protein suppresses ACE2 and type I interferon expression in primary cells from macaque lung bronchoalveolar lavage. *Frontiers in Immunology*, **12**: 658428.

Sui YJ, Li JP, Zhang RS, et al. 2021b. Protection against SARS-CoV-2 infection by a mucosal vaccine in rhesus macaques. *JCI Insight*, **6**(10): e148494.

Sun J, Zhuang Z, Zheng J, et al. 2020a. Generation of a broadly useful model for COVID-19 pathogenesis, vaccination, and treatment. *Cell*, **182**(3): 734–743. e5.

Sun SY, Cai YQ, Song TZ, et al. 2021. Interferon-armed RBD dimer enhances the immunogenicity of RBD for sterilizing immunity against SARS-CoV-2. *Cell Research*, **31**(9): 1011–1023.

Sun SH, Chen Q, Gu HJ, et al. 2020b. A mouse model of SARS-CoV-2 infection and pathogenesis. *Cell Host & Microbe*, **28**(1): 124–133. e4.

Tada T, Peng JY, Dcosta BM, et al. 2023. Single-epitope T cell–based vaccine protects against SARS-CoV-2 infection in a preclinical animal model. *JCI Insight*, **8**(7): e167306.

Tamir H, Melamed S, Erez N, et al. 2022. Induction of innate immune response by TLR3 agonist protects mice against SARS-CoV-2 infection. *Viruses*, **14**(2): 189.

Tamura T, Irie T, Deguchi S, et al. 2024. Virological characteristics of the SARS-CoV-2 Omicron XBB. 1.5 variant. *Nature Communications*, **15**(1): 1176.

Tamura T, Ito J, Uriu K, et al. 2023. Virological characteristics of the SARS-CoV-2 XBB variant derived from recombination of two Omicron subvariants. *Nature Communications*, **14**(1): 2800.

Tan JX, Li YQ. 2022. Immune checkpoint alterations and their blockade in COVID-19 patients. *Blood Science*, **4**(4): 192–198.

Tang JY, Zeng C, Cox TM, et al. 2022. Respiratory mucosal immunity against SARS-CoV-2 after mRNA vaccination. *Science Immunology*, **7**(76): eadd4853.

Tao KM, Tzou PL, Nouhin J, et al. 2021. SARS-CoV-2 antiviral therapy. *Clinical Microbiology Reviews*, **34**(4): e0010921.

Tokunoh N, Tamiya S, Watanabe M, et al. 2023. A nasal vaccine with inactivated whole-virion elicits protective mucosal immunity against SARS-CoV-2 in mice. *Frontiers in Immunology*, **14**: 1224634.

Totura AL, Whitmore A, Agnihothram S, et al. 2015. Toll-like receptor 3 signaling via TRIF contributes to a protective innate immune response to severe acute respiratory syndrome coronavirus infection. *mBio*, **6**(3): e00638–15.

Treon SP, Castillo JJ, Skarbnik AP, et al. 2020. The BTK inhibitor ibrutinib may protect against pulmonary injury in COVID-19–infected patients. *Blood*, **135**(21): 1912–1915.

Trimpert J, Vladimirova D, Dietert K, et al. 2020. The roborovski dwarf hamster is a highly susceptible model for a rapid and fatal course of SARS-CoV-2 infection. *Cell Reports*, **33**(10): 108488.

Tseng CTK, Huang C, Newman P, et al. 2007. Severe acute respiratory syndrome coronavirus infection of mice transgenic for the human angiotensin-converting enzyme 2 virus receptor. *Journal of Virology*, **81**(3): 1162–1173.

Upadhyay AA, Viox EG, Hoang TN, et al. 2023. TREM2$^{+}$ and interstitial-like macrophages orchestrate airway inflammation in SARS-CoV-2 infection in rhesus macaques. *Nature Communications*, **14**(1): 1914.

Uraki R, Kiso M, Imai M, et al. 2022. Therapeutic efficacy of monoclonal antibodies and antivirals against SARS-CoV-2 Omicron BA. 1 in Syrian hamsters. *Nature Microbiology*, **7**(8): 1252–1258.

Uraki R, Kiso M, Iwatsuki Horimoto K, et al. 2023. Characterization of a SARS-CoV-2 EG. 5.1 clinical isolate *in vitro* and *in vivo. Cell Reports*, **42**(12): 113580.

Van Doremalen N, Purushotham JN, Schulz JE, et al. 2021. Intranasal ChAdOx1 nCoV-19/AZD1222 vaccination reduces viral shedding after SARS-CoV-2 D614G challenge in preclinical models. *Science Translational Medicine*, **13**(607): eabh0755.

Van Doremalen N, Singh M, Saturday TA, et al. 2022. SARS-CoV-2 Omicron BA. 1 and BA. 2 are attenuated in rhesus macaques as compared to Delta. *Science Advances*, **8**(46): eade1860.

Verma A, Hawes CE, Lakshmanappa YS, et al. 2021. Monoclonal antibodies protect aged rhesus macaques from SARS-CoV-2-induced immune activation and neuroinflammation. *Cell Reports*, **37**(5): 109942.

Vijayanand S, Patil S, Menon I, et al. 2023. An adjuvanted inactivated SARS-CoV-2 microparticulate vaccine delivered using microneedles induces a robust immune response in vaccinated mice. *Pharmaceutics*, **15**(3): 895.

Vogel AB, Kanevsky I, Che Y, et al. 2021. BNT162b vaccines protect rhesus macaques from SARS-CoV-2. *Nature*, **592**(7853): 283–289.

Wang YQ, Yan A, Song DY, et al. 2024. Identification of a highly conserved neutralizing epitope within the RBD region of diverse SARS-CoV-2 variants. *Nature Communications*, **15**(1): 842.

Williamson BN, Feldmann F, Schwarz B, et al. 2020. Clinical benefit of remdesivir in rhesus macaques infected with SARS-CoV-2. *Nature*, **585**(7824): 273–276.

Winkler ES, Bailey AL, Kafai NM, et al. 2020. SARS-CoV-2 infection of human ACE2-transgenic mice causes severe lung inflammation and impaired function. *Nature Immunology*, **21**(11): 1327–1335.

Wise J. 2022. Covid-19: long covid risk is lower with omicron than delta, researchers find. *BMJ*, **377**: o1500.

Wong LYR, Zheng J, Wilhelmsen K, et al. 2022. Eicosanoid signalling blockade protects middle-aged mice from severe COVID-19. *Nature*, **605**(7908): 146–151.

Woolsey C, Borisevich V, Prasad AN, et al. 2021. Establishment of an African green monkey model for COVID-19 and protection against re-infection. *Nature Immunology*, **22**(1): 86–98.

Wu Y, Shi J, He XX, et al. 2023a. Protection of the receptor binding domain (RBD) dimer against SARS-CoV-2 and its variants. *Journal of Virology*, **97**(11): e0127923.

Wu Y, Wu NM, Jia XY, et al. 2023b. Long‐term immune response to Omicron‐specific mRNA vaccination in mice, hamsters, and nonhuman primates. *MedComm*, **4**(6): e460.

Wu YJ, Wang MN, Yin H, et al. 2021. TREM-2 is a sensor and activator of T cell response in SARS-CoV-2 infection. *Science Advances*, **7**(50): eabi6802.

Xia J, Tang WQ, Wang JM, et al. 2021. SARS-CoV-2 N protein induces acute lung injury in mice via NF-κB activation. *Frontiers in Immunology*, **12**: 791753.

Xiong SQ, Zhang LH, Qadir AS, et al. 2021. Interleukin-1RA mitigates SARS-CoV-2–induced inflammatory lung vascular leakage and mortality in humanized K18-hACE-2 mice. *Arteriosclerosis, Thrombosis, and Vascular Biology*, **41**(11): 2773–2785.

Xu L, Yu DD, Ma YH, et al. 2020a. COVID-19-like symptoms observed in Chinese tree shrews infected with SARS-CoV-2. *Zoological Research*, **41**(5): 517–526.

Xu XL, Han MF, Li TT, et al. 2020b. Effective treatment of severe COVID-19 patients with tocilizumab. *Proceedings of the National Academy of Sciences of the United States of America*, **117**(20): 10970–10975.

Yamasoba D, Uriu K, Plianchaisuk A, et al. 2023. Virological characteristics of the SARS-CoV-2 omicron XBB. 1.16 variant. *The Lancet Infectious Diseases*, **23**(6): 655–656.

Yang XH, Deng W, Tong Z, et al. 2007. Mice transgenic for human angiotensin-converting enzyme 2 provide a model for SARS coronavirus infection. *Comparative Medicine*, **57**(5): 450–459.

Yin KL, Peluso MJ, Luo XY, et al. 2024. Long COVID manifests with T cell dysregulation, inflammation and an uncoordinated adaptive immune response to SARS-CoV-2. *Nature Immunology*, **25**(2): 218–225.

Yu DD, Long YHP, Xu L, et al. 2022a. Infectivity of SARS-CoV-2 and protection against reinfection in rats. *Zoological Research*, **43**(6): 945–948.

Yu JY, Collins ND, Mercado NB, et al. 2022b. Protective efficacy of gastrointestinal SARS-CoV-2 delivery against intranasal and intratracheal SARS-CoV-2 challenge in rhesus macaques. *Journal of Virology*, **96**(2): e0159921.

Yu JY, Tostanoski LH, Peter L, et al. 2020a. DNA vaccine protection against SARS-CoV-2 in rhesus macaques. *Science*, **369**(6505): 806–811.

Yu P, Qi FF, Xu YF, et al. 2020b. Age‐related rhesus macaque models of COVID‐19. *Animal Models and Experimental Medicine*, **3**(1): 93–97.

Yu WH, Wang JB, Yang Y, et al. 2023. SARS‐CoV‐2 Omicron (B. 1.1. 529) infection in rhesus macaques, hamsters, and BALB/c mice with severe lung histopathological damage. *Journal of Medical Virology*, **95**(6): e28846.

Yuan LZ, Tang QY, Zhu HC, et al. 2021. SARS-CoV-2 infection and disease outcomes in non-human primate models: advances and implications. *Emerging Microbes & Infections*, **10**(1): 1881–1889.

Zanza C, Romenskaya T, Manetti AC, et al. 2022. Cytokine storm in COVID-19: immunopathogenesis and therapy. *Medicina*, **58**(2): 144.

Zeng JX, Xie XC, Feng XL, et al. 2022. Specific inhibition of the NLRP3 inflammasome suppresses immune overactivation and alleviates COVID-19 like pathology in mice. *eBioMedicine*, **75**: 103803.

Zhang Q, Bastard P, Liu ZY, et al. 2020a. Inborn errors of type I IFN immunity in patients with life-threatening COVID-19. *Science*, **370**(6515): eabd4570.

Zhang XH, Zhang Y, Qiao WZ, et al. 2020b. Baricitinib, a drug with potential effect to prevent SARS-COV-2 from entering target cells and control cytokine storm induced by COVID-19. *International Immunopharmacology*, **86**: 106749.

Zhang ZY, Zhang N, Lu XC, et al. 2023. Anti-infection effects of heparin on SARS-CoV-2 in a diabetic mouse model. *Zoological Research*, **44**(6): 1003–1014.

Zhao Y, Wang CL, Gao ZY, et al. 2023. Ferrets: a powerful model of SARS-

CoV-2. *Zoological Research*, **44**(2): 323–330.
Zhao Y, Wang JB, Kuang DX, et al. 2020. Susceptibility of tree shrew to SARS-CoV-2 infection. *Scientific Reports*, **10**(1): 16007.
Zheng HY, He XY, Li W, et al. 2021a. Pro-inflammatory microenvironment and systemic accumulation of CXCR3+ cell exacerbate lung pathology of old rhesus macaques infected with SARS-CoV-2. *Signal Transduction and Targeted Therapy*, **6**(1): 328.
Zheng HY, Zhang M, Yang CX, et al. 2020. Elevated exhaustion levels and reduced functional diversity of T cells in peripheral blood may predict severe progression in COVID-19 patients. *Cellular & Molecular Immunology*, **17**(5): 541–543.
Zheng J, Wong LYR, Li K, et al. 2021b. COVID-19 treatments and pathogenesis including anosmia in K18-hACE2 mice. *Nature*, **589**(7843): 603–607.
Zheng M, Karki R, Williams EP, et al. 2021c. TLR2 senses the SARS-CoV-2 envelope protein to produce inflammatory cytokines. *Nature Immunology*, **22**(7): 829–838.
Zheng MZM, Wakim LM. 2022. Tissue resident memory T cells in the respiratory tract. *Mucosal Immunology*, **15**(3): 379–388.
Zhou XY, Sun WY, Zhang Y, et al. 2023. A novel hACE2 knock-in mouse model recapitulates pulmonary and intestinal SARS-CoV-2 infection. *Frontiers in Microbiology*, **14**: 1175188.
Zhu LN, Yang PH, Zhao YZ, et al. 2020. Single-cell sequencing of peripheral mononuclear cells reveals distinct immune response landscapes of COVID-19 and influenza patients. *Immunity*, **53**(3): 685–696. e3.
Zhuang Z, Lai XM, Sun J, et al. 2021. Mapping and role of T cell response in SARS-CoV-2–infected mice. *Journal of Experimental Medicine*, **218**(4): e20202187.

Wu et al. *Zool. Res.* 2024, 45(4): 767−780
https://doi.org/10.24272/j.issn.2095-8137.2024.058

ZR | Zoological Research

Review Open Access

# A new era of mutation rate analyses: Concepts and methods

Kun Wu[1], Danqi Qin[1], Yang Qian[1], Haoxuan Liu[1,*]

[1] *Center for Evolutionary & Organismal Biology and the Fourth Affiliated Hospital of Zhejiang University*, *Zhejiang University School of Medicine*, *Hangzhou*, *Zhejiang* 310058, *China*

**ABSTRACT**

The mutation rate is a pivotal biological characteristic, intricately governed by natural selection and historically garnering considerable attention. Recent advances in high-throughput sequencing and analytical methodologies have profoundly transformed our understanding in this domain, ushering in an unprecedented era of mutation rate research. This paper aims to provide a comprehensive overview of the key concepts and methodologies frequently employed in the study of mutation rates. It examines various types of mutations, explores the evolutionary dynamics and associated theories, and synthesizes both classical and contemporary hypotheses. Furthermore, this review comprehensively explores recent advances in understanding germline and somatic mutations in animals and offers an overview of experimental methodologies, mutational patterns, molecular mechanisms, and driving forces influencing variations in mutation rates across species and tissues. Finally, it proposes several potential research directions and pressing questions for future investigations.

**Keywords:** Mutation rate; Somatic mutations; Germline mutations; Animal

## INTRODUCTION

In his seminal first chapter of “On the Origin of Species”, Darwin recognized the integral role of natural selection in evolution, deeply intertwined with trait variations among individuals within a population, although he was uncertain about the origins of these variations at the time (Darwin, 1859). Subsequent discoveries revealed that these trait variations predominantly arise from alterations in DNA sequences (Watson & Crick, 1953). Ronald Aylmer Fisher, a pivotal figure in population genetics, mathematically described evolution as shifts in allele frequencies within populations (Fisher, 1930) and identified five key mechanisms influencing these frequencies: mutation, recombination, natural selection, genetic drift, and gene flow.

This is an open-access article distributed under the terms of the Creative Commons Attribution Non-Commercial License (http://creativecommons.org/licenses/by-nc/4.0/), which permits unrestricted non-commercial use, distribution, and reproduction in any medium, provided the original work is properly cited.

Copyright ©2024 Editorial Office of Zoological Research, Kunming Institute of Zoology, Chinese Academy of Sciences

Among these mechanisms, mutation is recognized as the primary and most fundamental source of genetic variation, providing new genetic material upon which other evolutionary forces can act. Consequently, the mutation rate and the fitness effects of emerging mutations are crucial in understanding genetic variation and evolution. These elements are central to theoretical frameworks in evolutionary biology and quantitative genetics (Barton & Keightley, 2002).

In recent decades, various scholars have provided insightful summaries and comprehensive overviews on mutation and mutation rates (Baer et al., 2007; Halligan & Keightley, 2009; Katju & Bergthorsson, 2019; Lynch, 2010; Lynch et al., 2016; Wang & Obbard, 2023). This review diverges from these previous works by adopting a more accessible, popular science approach, avoiding complex theoretical derivations. Our objective is to bridge the disciplines of biomedical science, structural biology, cell biology, and evolutionary biology and to present fundamental concepts of mutations, classic and modern methods for calculating mutation rates, and emerging methodologies based on whole-genome sequencing (WGS, also known as next-generation sequencing) and long-read third-generation sequencing. We also clarify definitions and types of mutations, theoretical underpinnings, methods, workflows, and considerations in mutation analysis. Finally, we explore the evolutionary patterns of mutation rates in animals and consider future directions in mutation research.

### Definitions of genetic mutation, somatic mutation, and germline mutation

In evolutionary biology, a genetic mutation is defined as any change in the genetic material of an organism. For most cellular life and DNA viruses, this involves alterations in DNA sequences. While DNA typically replicates with high fidelity, occasional errors may arise. If these errors are not corrected by cellular repair mechanisms, they result in mutations. In RNA viruses and other organisms that use RNA as their genetic material, mutations constitute changes in the RNA sequence.

In multicellular organisms, the distinction between somatic and germline cells adds complexity to the concept of mutations. Germline mutations, which can be transmitted to subsequent generations, play a pivotal role in evolution (Figure 1A), underpinning various theories and models in evolutionary biology, including those related to inbreeding

Received: 06 April 2024; Accepted: 04 June 2024; Online: 11 June 2024
Foundation items: This work was supported by Zhejiang University
*Corresponding author, E-mail: haoxuan@zju.edu.cn

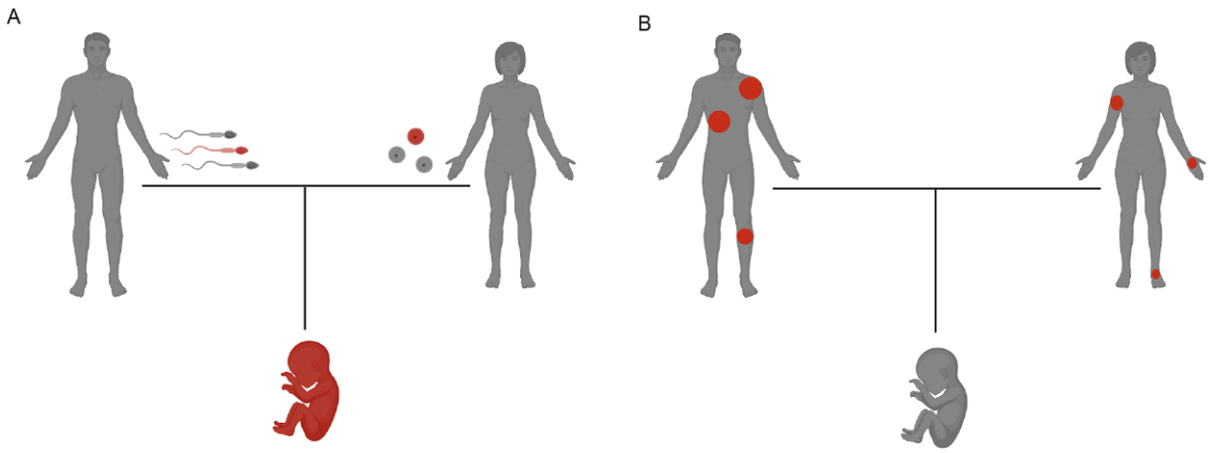



**Figure 1 Schematic of germline mutations (A) and somatic mutations (B)**

A: Germline mutations. Red sperm and egg cell represent germ cells carrying *de novo* mutations. Through a serendipitous encounter, these cells undergo fertilization and develop into an individual, transmitting newly acquired mutations to the offspring. B: Somatic mutations. Red circles represent somatic mutations occurring in different tissues of the body. Unlike germline mutations, somatic mutations do not get passed on to offspring, but they may contribute to the development of genetic diseases.

depression (Charlesworth et al., 1990), the maintenance of genetic variation (Caballero & Keightley, 1994), and the evolutionary fate of duplicate genes (Lynch, 2002; Lynch & Conery, 2000).

Conversely, somatic mutations, which do not transfer to offspring, can significantly impact the individual (Figure 1B). These mutations are of particular interest in the medical field as they are frequently associated with genetic disorders. Notably, the accumulation of somatic mutations over an individual's lifespan can contribute to cancer and aging (Stratton et al., 2009; Vijg & Dong, 2020). Traditionally, mutations implicated in the onset of cancer were thought to primarily originate from intrinsic processes and environmental factors. However, recent research has suggested that approximately two-thirds of cancer-causing mutations emerge from random errors during DNA replication (Tomasetti et al., 2017). These mutations, which occur independently of environmental influences, are considered unavoidable. As such, understanding these mutations is essential for advancing diagnosis, prediction, and treatment of various mutation-related conditions (Li et al., 2020).

## CLASSIFICATIONS OF MUTATIONS

Mutations are diverse and can be classified in several ways. Using the framework established by Hermann Muller, one approach categorizes mutations according to their functional outcomes, known as "Muller's morphs". These include amorphs (loss-of-function mutations leading to product inactivation), hypomorphs (mutations causing partial functional defects), hypermorphs (mutations resulting in more active products), and neomorphs (mutations leading to novel functions). Alternatively, mutations can be categorized based on changes in nucleotides and number of nucleotides involved. Another classification differentiates between spontaneous mutations, arising during a cell's regular life cycle, and induced mutations, induced by external mutagens. This paper will focus on the latter two categorizations, which are more commonly used in contemporary scientific discourse.

### Point mutations, indels, and inversions

Point mutations, indels, and inversions constitute the basis of mutation classification (Figure 2). Point mutations involve the replacement of a matching pair of nucleotides in the DNA double helix by another pair, also referred to as single nucleotide substitutions/variations (Figure 2A, B). These mutations can be further categorized as transitions, substitutions between adenine (A) and guanine (G) or cytosine (C) and thymine (T), and transversions, substitutions between pyrimidines and purines (Figure 2A).

### Synonymous and nonsynonymous mutations

The distinction between synonymous and nonsynonymous mutations is crucial in evolutionary research. Synonymous mutations, which do not alter the amino acid sequence of a protein, have traditionally been viewed as neutral (Figure 2B). As such, the ratio of nonsynonymous/synonymous mutation rate has served as a key parameter for inferring selection, with ratios >1 indicating positive selection and those <1 indicating negative selection (Goldman & Yang, 1994; Kimura, 1980). However, recent studies have reported that synonymous mutations, while not altering the amino acid sequence encoded by a codon, may still influence protein function by creating new splicing sites, disrupting exonic splicing enhancers (Cartegni et al., 2002), affecting pre-mRNA splicing, mRNA folding, and mRNA degradation, altering transfer RNA (tRNA) translation efficiency (Grantham et al., 1980; Sharp et al., 1988), disrupting binding sites for transcription factor, and altering translational initiation, efficiency, accuracy, and co-translational protein folding, thereby potentially altering protein sequence or abundance (Buschauer et al., 2020; Deng et al., 2022; Kristofich et al., 2018; Shen et al., 2022). For example, while synonymous mutations have traditionally been viewed as nonfunctional in the context of cancer, Supek et al. proposed that these seemingly silent mutations may possess oncogenic potential by influencing transcript splicing and consequently impacting protein function (Supek et al., 2014; Zheng et al., 2014). Notably, recent advancements have revealed that synonymous mutations can markedly impact various biological processes, challenging earlier assumptions of their neutrality (Shen et al., 2022).

Unlike synonymous mutations, nonsynonymous mutations typically exert more profound effects on individuals. Although many nonsynonymous mutations do not significantly alter

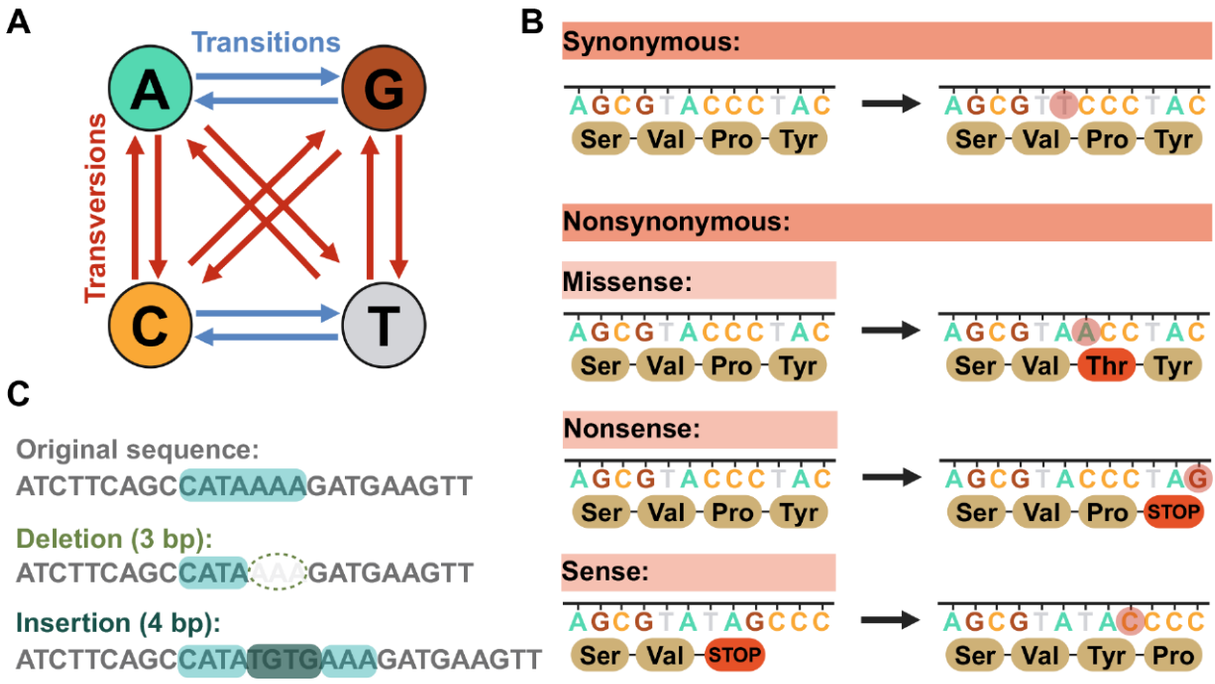



**Figure 2 Classification of mutations**

A: Transitions and transversions. Due to the complexity of distinguishing specific origins in many analysis scenarios, mutations are typically grouped into six categories for analytical simplicity: A:T→G:C, G:C→A:T, A:T→T:A, A:T→C:G, G:C→C:G, and G:C→T:A. B: Synonymous and nonsynonymous mutations. According to the impact of mutations, nonsynonymous mutations can be further categorized into missense, nonsense, and sense mutations. C: Deletions and insertions.

protein function or cause immediate lethality, they can lead to changes in the amino acid sequence of proteins. Such mutations can be subdivided into missense, nonsense, and sense mutations (Figure 2B) based on their specific impacts at the amino acid level.

Missense mutations alter encoded amino acids (Figure 2B), as exemplified in sickle cell anemia (Hoban et al., 2016; Rees et al., 2010) and amyotrophic lateral sclerosis (ALS), where altered superoxide dismutase (SOD) activity from mutations in the *SOD1* gene leads to misfolded proteins (Urushitani et al., 2006). A missense mutation at the start codon can be particularly damaging, potentially halting protein translation entirely. For instance, a nonsynonymous mutation at the initiation codon of the *HBB* gene can abolish the beta-globin chain, causing severe beta$^0$-thalassemia, characterized by growth delays, bone deformities, and organ enlargement (Cao & Galanello, 2010; Musallam et al., 2021).

Nonsense mutations convert a regular codon into a stop codon (Figure 2B), truncating the protein and often leading to dysfunctional products. These mutations account for about 20% of genetic diseases caused by mutations in coding regions (Mort et al., 2008), and are implicated in conditions like Hurler syndrome, neurofibromatosis type 1, and Duchenne muscular dystrophy (Li et al., 2019; Osum et al., 2023; Pichavant et al., 2011). While typically detrimental, nonsense mutations can occasionally become fixed in a population (Hahn & Lee, 2006); however, whether these mutations confer new beneficial traits or contribute to adaptive evolution and species-specific features remains a subject of controversy.

Sense mutations convert a stop codon into a regular codon, extending the protein by incorporating the 3' untranslated region (UTR) into the coding sequence (Graur & Li, 2000), resulting in longer proteins due to a shifted termination site, thus classified as elongating mutations (Figure 2B). For instance, an exon in the Metnase gene may potentially originate from the exonization of noncoding sequences induced by a sense mutation (Cordaux et al., 2006).

**Indels**

Insertions and deletions, collectively referred to as indels due to their shared underlying mechanisms (Figure 2C), arise from various processes, including asymmetric crossover, intra-strand exchange, slippage in repetitive regions, and DNA transposition (Figure 3). Asymmetric crossover may lead to DNA sequence loss on one chromosome and simultaneous insertion on another (Figure 3A). Tandem repeat regions with homologous sequences are particularly susceptible to asymmetric crossovers due to mismatches. Intra-strand exchange, a form of site-specific recombination, frequently leads to DNA deletions when similar segments on a chromosome align and exchange, especially in regions of simple or microsatellite repeats (Figure 3B) (Li et al., 2002).

Indels can vary greatly in size, from massive alterations involving millions of nucleotides to minor changes involving just one nucleotide. During DNA replication, slippage in repetitive sequences can lead to small indels (Figure 3C). In the human genome, areas with simple repeats (such as (CAG/CTG)n) are particularly prone to expansion or contraction (Polleys et al., 2023). Similarly, in single-cell organisms like bacteria or fungi, over 60% of short indel sequences occur in repetitive regions (Katju & Bergthorsson, 2019). Though rarer than single nucleotide mutations, these small indels can profoundly affect biological functions (Audano et al., 2019).

Previous studies have primarily focused on short indels (fragment lengths <50 bp), largely due to the low sensitivity and high false positive rates of short-read sequencing technologies in identifying structural variations (SVs), including

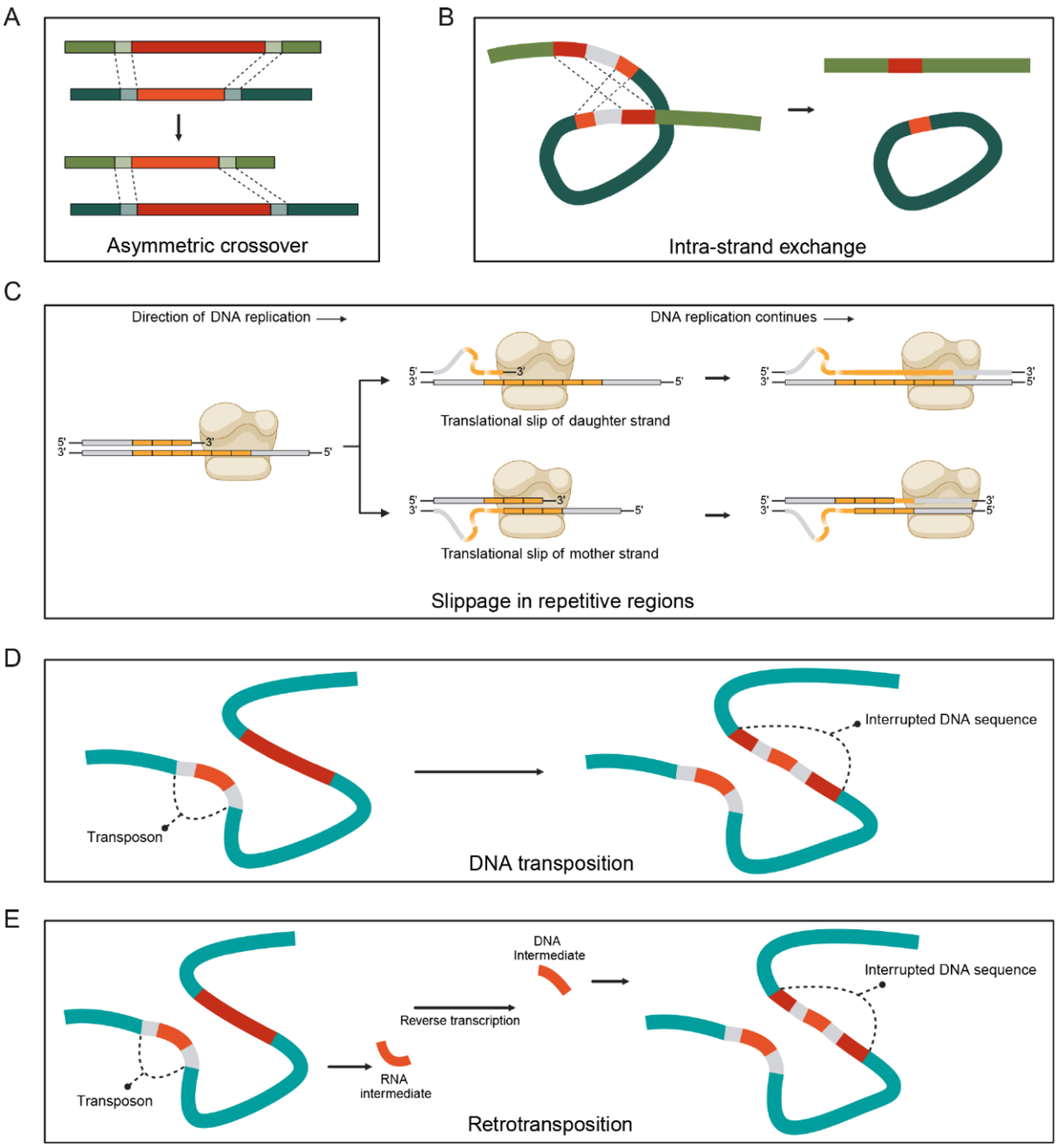



**Figure 3 Mechanisms for insertions and deletions**

A: Asymmetric crossover. Regions connected by dashed lines represent homologous sequences. Asymmetric crossover events can result in the insertion of a sequence in one strand and deletion in the other strand. B: Intra-strand exchange. Intra-strand crossover events lead to deletion of a sequence fragment. C: Indels caused by slippage in repetitive sequences. During DNA replication, slippage at the 3' end of the DNA strand may occur, and if not repaired, it can lead to the occurrence of insertions or deletions. D: DNA transposition. Transposons utilize transposase to randomly introduce insertions or deletions in the genome. E: RNA-mediated transposition. Transposon undergoes an initial transcription process, with conversion into RNA, followed by reverse transcription where it is transformed back into DNA. Subsequently, this DNA is inserted into a new genomic locus.

large indels, translocations, and DNA- and RNA-mediated transpositions (Figure 3D, E) (Huddleston et al., 2017; Jeffares et al., 2017). Large-scale SVs (>50 bp) and genome rearrangements, such as chromosomal fusion, fission, and polyploidy changes, play critical roles in species diversification or genetic polymorphism and are often associated with phenotypic alterations, including the development of cancer and other genetic disorders (Audano et al., 2019). The development and enhancement of long-read sequencing technologies, such as Pacific Biosciences (PacBio) and Oxford Nanopore Technologies (ONT), have opened new avenues for studying SVs. With the ability to sequence millions of base pairs, long-read sequencing enables comprehensive coverage of SVs across the entire genome, thus enhancing the ability to detect large-scale segment alterations, including duplications, deletions, insertions, and translocations.

**Inversions**

Inversions, a type of DNA rearrangement, occur through

mechanisms such as ectopic recombination, chromosomal breakage, and repair (Feschotte & Pritham, 2007; Gray, 2000). These often involve reciprocal exchange of homologous sequences in opposite directions on a chromosome. Especially prevalent in bacterial and archaeal genomes (Eisen et al., 2000; Suyama & Bork, 2001), inversions can span long DNA segments. Although balanced inversions without genetic information loss do not typically cause phenotypic abnormalities, they can suppress recombination, leading to issues like infertility, cancer, and genetic disorders (Antonacci et al., 2009; Feuk, 2010; Guttenbach et al., 1997). Inversions play a crucial role in both evolution and disease. However, identifying their breakpoints is challenging as they are often embedded within similar segmental duplications (Chaisson et al., 2015). Advanced sequencing technologies, including single-cell DNA template strand sequencing and Hi-C, are improving our ability to understand inversions across pedigrees and lineages (Himmelbach et al., 2018; Porubsky et al., 2020).

**Spontaneous and induced mutations**

Spontaneous mutations arise from the cumulative errors that occur in DNA during an organism's normal lifecycle (Glickman et al., 1986). Most spontaneous mutations are single base substitutions, frequently resulting from mismatches during the DNA replication process. Typically, adenine (A) pairs with thymine (T) and guanine (G) with cytosine (C), but errors can lead to abnormal pairings like A:C and A:A (Harris et al., 2003; Topal & Fresco, 1976). The primary cause of these mismatches is the isomerization of bases, where DNA bases switch between keto and enol forms (for G and T) and amino and imino forms (for A and C). For example, G may pair with T when in the enol form, or A with C when in the imino form (Topal & Fresco, 1976), leading to spontaneous mutations if these isomerizations occur during replication. Furthermore, adenine can undergo deamination to form hypoxanthine, which pairs with cytosine, leading to an A to G transition (Figure 4A) (Jung et al., 2020).

Spontaneous mutations are crucial in studies related to spontaneous carcinogenesis, aging, and evolution (Kirkwood, 1989; Long et al., 2016; Totter, 1980). Initial research on spontaneous mutations was limited, with most insights derived from control groups in experiments focusing on induced mutations (Sargentini & Smith, 1985). In 1971, Hartman explored and classified spontaneous mutations, identifying single base substitutions, small-scale indels, and large-scale SVs (Hartman et al., 1971). However, the techniques available at the time, which primarily involved marker gene construction and phenotype assays, significantly underestimated the diversity and frequency of mutations. With the development of DNA sequencing technologies such as Sanger sequencing, more comprehensive mutation frequency data have been documented across various species, including yeast, *Escherichia coli*, and *Salmonella* (Albertini et al., 1982; Giroux et al., 1988; O'Hara & Marnett, 1991). However, earlier studies were limited by their focus on marker genes and the typically deleterious nature of spontaneous mutations, which often disappeared during culture passages, resulting in less accurate mutation data. In the 21st century, significant advancements and cost reductions in WGS have revolutionized the field, enabling researchers to merge mutation accumulation experiments with high-throughput sequencing to explore spontaneous mutations across a wide range of organisms, from viruses and single-cell microorganisms like bacteria, fungi, and protists, to more complex multicellular entities. This comprehensive and integrated approach has greatly enhanced the precision and reliability of spontaneous mutation evaluations, facilitating a thorough understanding of mutation rates and patterns across diverse life forms.

In addition to spontaneous mutations that occur as part of their natural life cycle, organisms are subjected to induced mutations from environmental and artificial factors, such as temperature, ultraviolet (UV) radiation, pH (Brash & Haseltine, 1982; Strauss et al., 2017; Witkin, 1953), mutagens, antibiotics, oxidizing agents, and other toxic substances (Bjelland, 2003; Long et al., 2016; Wu et al., 2023). These factors can directly or indirectly alter DNA due to their persistent effects, with the oxidation of guanine to form 8-oxoG, leading to a G to T mutation, noted as a common type of mutation (Figure 4B) (Tchou et al., 1991). Among physical factors, the deamination of nucleotides due to increased temperature is also considered common. For example, heating can cause cytosine to deaminate, transforming into uracil, a base typically found in RNA. If this uracil pairs with adenine and is not repaired before DNA replication, it can result in a C:G to U:A mutation (Graur & Li, 2000). Similarly, the deamination of methylated cytosine can directly produce thymine (Figure 4C). While cytosine to uracil changes are often recognized and corrected by DNA repair mechanisms, the conversion of methylated cytosine to thymine is more challenging to detect, making it a prevalent source of mutations in CG-rich regions of the genome (Graur & Li, 2000). Additionally, mutagenic UV radiation can induce covalent bonds between neighboring pyrimidines in DNA, leading to structural distortions and potential breakage, further contributing to the mutational burden (Brash & Haseltine, 1982).

## METHODS FOR EVALUATING MUTATION RATES

Mutations are the fundamental source of genetic variations and are therefore critical for the study of genetics and evolutionary biology. However, quantifying mutation rates is a formidable task. In living organisms, mutation rates are exceedingly low —for example, the single-nucleotide substitution rate in *Escherichia coli* is approximately $2\times10^{-10}$ per site per cell division. Moreover, most mutations are deleterious and tend to be eliminated by natural selection, rendering their observation at the population level particularly challenging. Historically, four principal approaches have been employed to assess mutation rates: theoretical estimation (neutral theory), reporter-based (Luria-Delbrück experiment), and sequencing-based methods (parent-progeny sequencing and mutation accumulation).

**Estimation based on substitution rate in selectively neutral regions**

Originating from Kimura's neutral theory (Kimura, 1968), this approach posits that the mutation rate at neutral sites is equivalent to the substitution rate of neutral alleles (Figure 5A). Substitution involves one allele replacing another within a population. Kimura's diffusion approximations elucidate the fixation probability of an allele ($P$) as:

$$P = \frac{1 - e^{-4N_e sq}}{1 - e^{-4N_e s}} \quad (1)$$

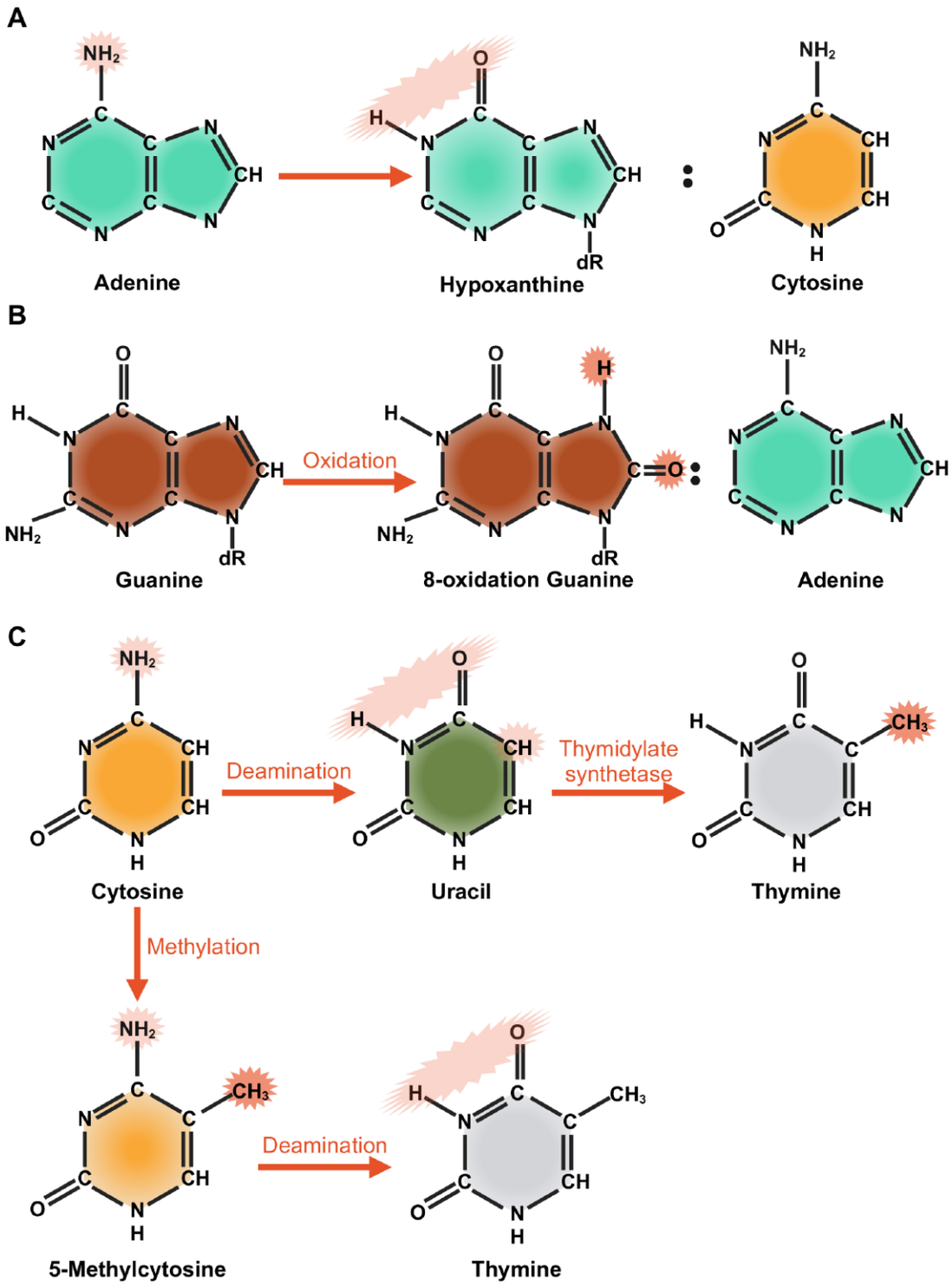



**Figure 4 Molecular mechanisms of single base substitutions**

A: Deamination of A leads to formation of hypoxanthine, which then pairs with C, causing an A to G mutation. B: Guanine oxidation leads to formation of 8-oxoG (8-oxo-7,8-dihydroguanine), which pairs with A, followed by replication, resulting in the replacement of G by T. C: Cytosine undergoes deamination to form uracil, while methylated cytosine directly undergoes deamination to form thymine.

where $q$ is the initial frequency of an allele, $N_e$ is the effective population size, and $s$ is the selective advantage. In a diploid population of $N$ individuals, the allele frequency of a newly arisen mutation is. If $x$ is very small, $e^{-x} \approx 1-x$. Under neutral conditions ($s$=0) and replacing $q$ with $\frac{1}{2N}$, the former equation can be simplified as:

$$P = \frac{1}{2N} \quad (2)$$

For neutral alleles, in a diploid population of $N$ individuals, the number of mutations generated at a locus is $2N\mu$, where $\mu$ is the mutation rate per gene per generation. If the probability of neutral mutations fixed in a population equals $\frac{1}{2N}$, the rate of substitution of neutral alleles ($K$) equals the total mutation number multiplied by the fixation probability:

$$K = 2N\mu \times \frac{1}{2N} = \mu \quad (3)$$

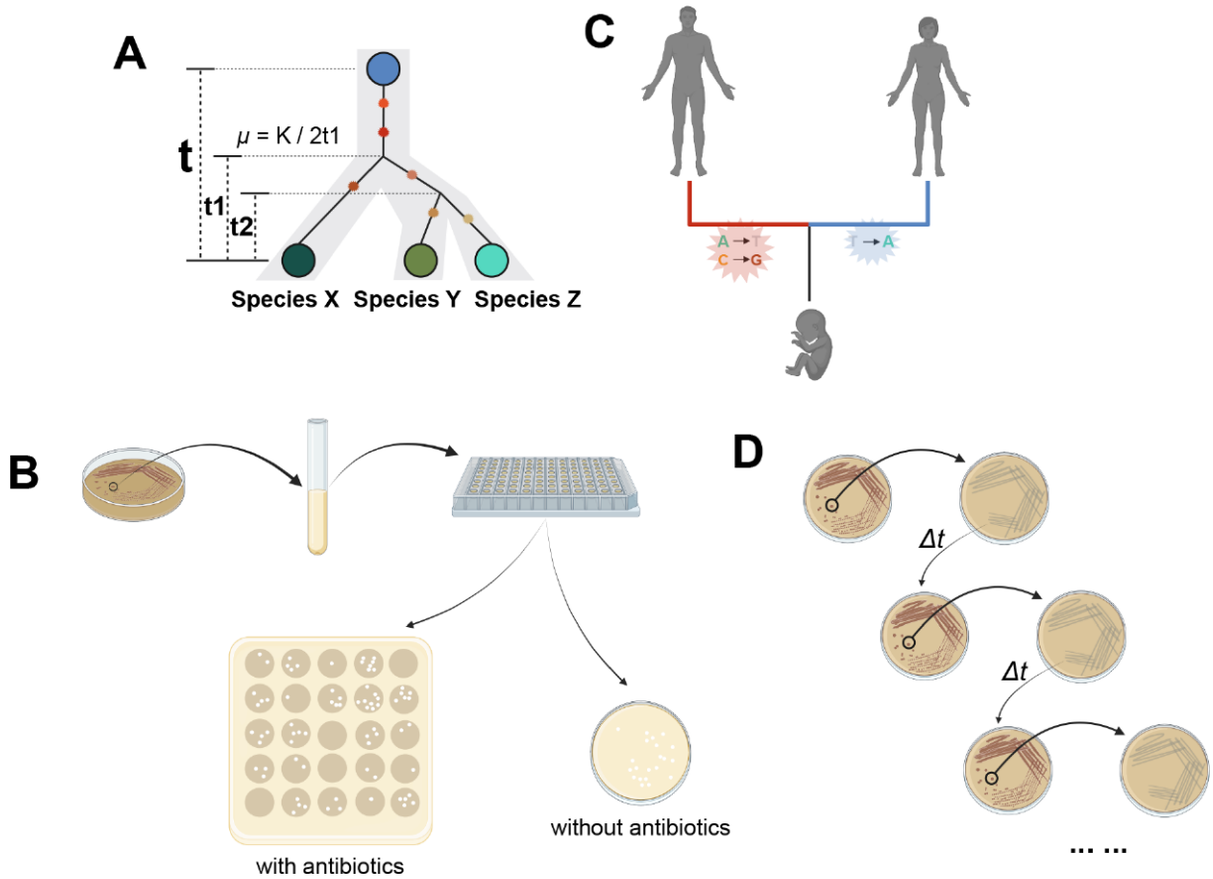



**Figure 5 Methods for evaluating mutation rates**

A: Estimation based on substitution rate in selectively neutral regions. Over time t, three species, X, Y, and Z, evolved. Colored dots along branches represent mutations that occurred during this process. Neutral theory suggests that polymorphisms within a population and substitutions between species are largely neutral, thus, their rate and divergent time can be used to infer the raw mutation rate. In $\mu$=K/2t1, $\mu$ represents the mutation rate, K is the number of neutral substitutions between species X and Z, and t1 is the divergence time between two species. B: Luria-Delbrück experiment. C: Parent-offspring sequencing. Base substitutions in the shaded regions represent mutations. D: Mutation accumulation experiment.

This method has been used to estimate mutation rates in humans. Notably, comparing the sequences of pseudogenes between humans and closely related species revealed a mutation rate of $2.5\times10^{-8}$ mutations per nucleotide site or 175 mutations per diploid genome per generation (Nachman & Crowell, 2000), within the same order as the estimation from direct parent-offspring sequencing ($1.2\times10^{-8}$) (Milholland et al., 2017).

**Luria-Delbrück experiment**

In the 1940s, before the identification of DNA as the source of genetic material, the nature of mutations was a burning question: Did they pre-exist before selection, or were they adaptively induced during or after selection? Through pioneering experiments, Luria and Delbrück formulated a canonical experiment and a mathematical model that demonstrated genetic variations arise spontaneously rather than adaptively (Luria & Delbrück, 1943), a concept that earned them the 1969 Nobel Prize in Physiology or Medicine. The Luria-Delbrück model has since become a pivotal tool for estimating mutation rates in single-celled organisms and viruses.

In the typical fluctuation test, a small batch of cells from the same ancestor is cultured in parallel until reaching a specified density, during which mutations may occur. These cells are then plated on selective media to allow mutants with resistance mutations to form colonies (Figure 5B). By counting these colonies and evaluating the initial and total cell numbers, researchers can derive an accurate mutation rate estimate. Several methods exist for this, including the $p_0$ method, Luria-Delbrück's method of the mean, and Lea-Coulson method of the median, each based on specific assumptions (Drake, 1991; Lea & Coulson, 1949; Luria & Delbrück, 1943). To maximize experimental accuracy, certain conditions must be met, including consistent growth rates for mutants and non-mutants and negligible reverse mutations. With advancements in sequencing technologies, the fluctuation test remains a foundational method for investigating spontaneous mutations, offering precise mutation rates and spectra (Jiang et al., 2021).

**Parent-offspring sequencing**

Parent-offspring or trio sequencing offers the most direct approach to infer mutation rates by analyzing genetic differences between parents and offspring (Figure 5C). This approach calculates mutation rates by tallying the number of mutations over a specific time scale, from years to generations. With the advancement of WGS, this method has been applied to many species, especially those with large genome sizes, such as humans, mice (Milholland et al., 2017), and *Arabidopsis* (Xue et al., 2009; Yang et al., 2015). Parent-offspring sequencing involves sequencing both parents and the affected individual to study genetic disorders, complex diseases, and other conditions related to gene mutations. By

comparing the genome sequences of parents and progeny, scientists can identify genetic mutations that cause specific diseases and traits in offspring (Lelieveld et al., 2016).

**Mutation accumulation experiments**

The fate of mutations in a population is influenced by the mutation rate as well as evolutionary forces such as natural selection and genetic drift (Halligan & Keightley, 2009; Kimura, 1968; Long et al., 2016; Otto & Michalakis, 1998). The deleterious nature of most non-neutral mutations presents a challenge as they are quickly eliminated from natural populations, making it difficult to glean useful information (Drake, 2006; Keightley & Eyre-Walker, 1999). To overcome this, Muller conceptualized various mutation accumulation experiments in 1928, which were later refined by Mukai and Ohnishi (Mukai, 1964; Mukai et al., 1972; Ohnishi, 1977a, 1977b, 1977c). While these experiments are conceptually straightforward, the practical workload is substantial, requiring independent culturing of numerous sublines, all originating from identical inbred ancestors, with each subline undergoing periodic bottlenecks, which reduce selection effectiveness, thereby inducing genetic drift and the accumulation of non-lethal mutations. For example, in microbial systems, this bottleneck can be achieved by streaking individual colonies onto agar plates, with each colony beginning from a single cell (Figure 5D). By employing WGS and mutation calling, researchers can pinpoint specific mutation sites and facilitate analysis of mutation rates and spectra. Given their comprehensive and accurate approach, mutation accumulation experiments in conjunction with WGS are widely acknowledged as one of the most precise methodologies for determining mutation rates.

The four approaches mentioned above each possess unique specializations and data requirements. One of the most concise and elegant conclusions of Kimura's neutral theory is that "the rate of substitution of neutral alleles (*K*) equals the neutral mutation rate", establishing a crucial link between molecular evolution and mutation rates. This concept has been widely applied in various evolutionary fields, including population genomics and molecular evolutionary theory. Mutation rates derived through Kimura's neutral theory align closely with those obtained from modern methods, underscoring its remarkable efficacy. However, as it does not account for certain variables, such as environmental variations, it may not meet the precision requirements for tasks demanding high accuracy. While the fluctuation test is convenient, precise, and efficient at estimating mutation rates, its applicability is restricted to bacteria, single-celled fungi, and viruses, and confined to estimating mutation rates for single loci within the genome. Trio sequencing is among the most direct, efficient, and accurate methods for estimating mutation rates in multicellular organisms, although it is limited to species with large genome sizes, such as vertebrates. For organisms with smaller genomes and shorter generation times, such as bacteria, fungi, fruit flies, and nematodes, mutation accumulation experiments are invaluable. These experiments facilitate the accumulation of a relatively high number of mutations, making mutation rate estimation more cost-effective.

## VARIATIONS IN GERMLINE AND SOMATIC MUTATION RATES ACROSS THE ANIMAL KINGDOM

In the animal kingdom, both germ and somatic cells are susceptible to mutations. Yet, due to their potential for inheritance, germ cell mutations have garnered more attention. Estimating mutation rates is crucial in evolutionary studies, and recent years have seen an increased focus on understanding germline mutation rates and their evolution through analyses within and across species (Bergeron et al., 2022, 2023). To date, WGS has directly measured the germline mutation rate in at least 10 invertebrates and 80 vertebrates (Liu et al., 2023). These rates are typically expressed as number of mutations per site per generation and number of mutations per site per year, with generation time, body mass, and genome size being the strongest predictors of these rates (Figure 6A–F; Supplementary Table S1).

Conversely, somatic mutations in animals have been less studied due to technical challenges. Somatic mutations accumulate as cells divide and the organism develops, resulting in a unique mutational landscape across different tissues and cells (Dou et al., 2018). The identification of these mutations often necessitates single-cell sequencing, which currently lacks the accuracy required for such precise tasks. Consequently, most research in this area has been limited to specific organs, such as intestinal crypts, which originate from a single cell. Recent research sequenced hundreds of intestinal crypts from 16 species, revealing significant differences in mutation numbers between germline and somatic mutations (Cagan et al., 2022). For example, a 40-year-old human may accumulate about 1 500 somatic mutations in one intestinal crypt, compared to only around 40 in a germ cell. There is a near-perfect linear correlation between the accumulation of somatic mutations and age, suggesting a time-dependent mechanism for mutagenic effects. Furthermore, across species, the rate of somatic mutations (per sample per year) shows a correlation with generation time, body mass, and genome size (Figure 6G–L; Supplementary Table S2).

**Variations in somatic mutation rates across different tissues in humans**

Somatic mutations, which accumulate within normal tissues, play pivotal roles in aging, cancer, and various diseases (Stratton et al., 2009; Vijg & Dong, 2020). Both aging and cancer are associated with mutation accumulation over time, precipitating a marked decline in cellular function. However, detecting somatic mutations poses considerable challenges, primarily due to genetic heterogeneity and low allele frequencies in affected cells (Huddleston et al., 2017; Vijg & Dong, 2020). Genetic heterogeneity, or somatic mosaicism, arises from variations in postzygotic mutations across different cells and tissues. These mutations, unique to each cell in every individual, are typically present at low allele frequency in bulk sequencing, necessitating sequencing with sufficient depth and accuracy for detection. Various methods have been developed in recent years to address these challenges, including single-cell *ex vivo* expansion followed by sequencing (Bae et al., 2018), high-depth sequencing of microdissected tissues or single-cell-derived cell clusters (Li et al., 2021), single-cell sequencing (Huang et al., 2022), and duplex sequencing (Abascal et al., 2021). Although differences in sample collection and sequencing methodologies may hinder direct comparison, several discernible trends have emerged with sufficient data collection (Figure 7).

The somatic mutation rates across different tissues in humans, collated from three studies sampling multiple somatic

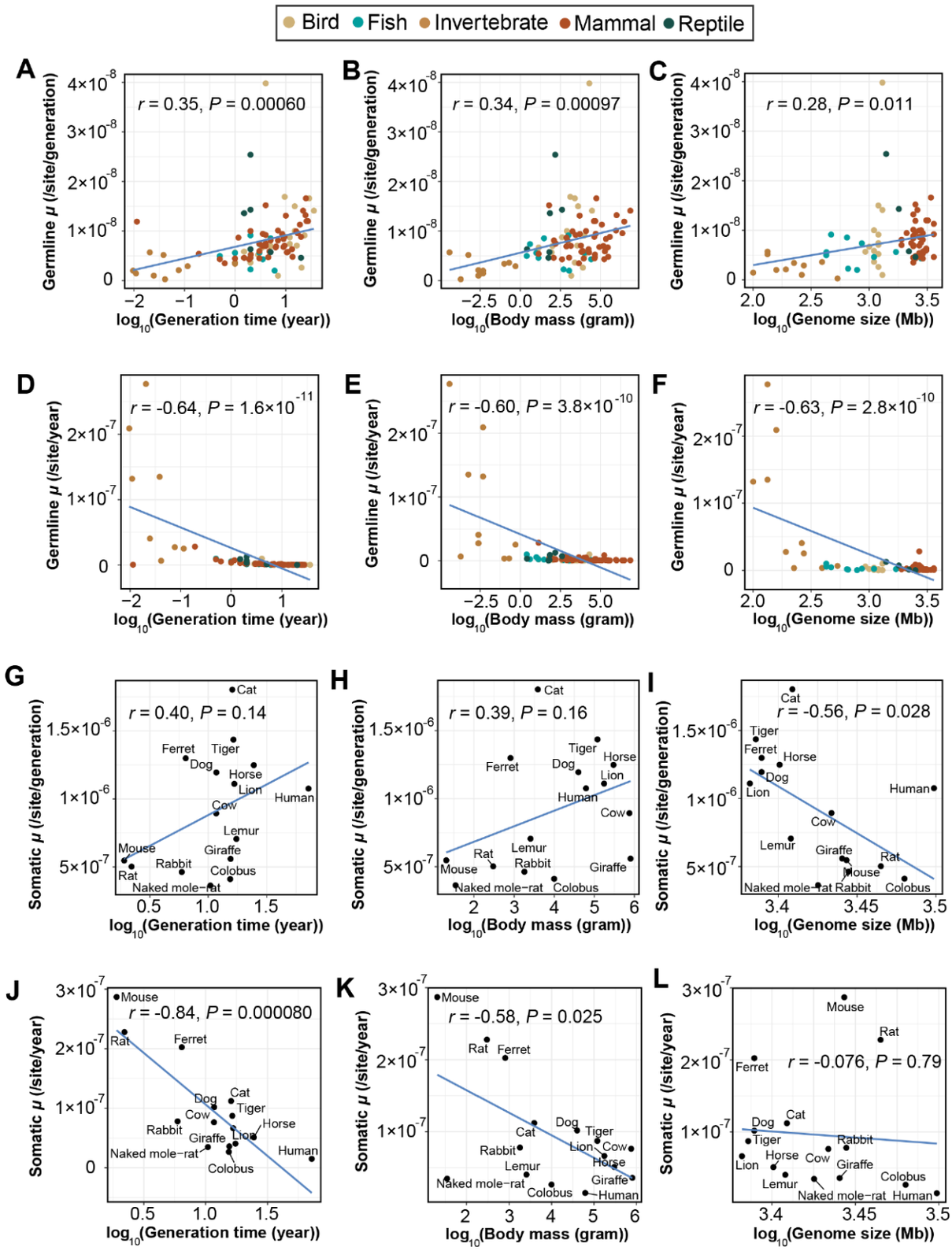



**Figure 6 Correlations between germline and somatic mutation rates ($\mu$) with generation time, body mass, and genome size**

Each dot represents a specific species, and blue lines represent linear regression. Pearson's *r* and *P* values between X-axis and Y-axis are annotated in each panel. Data sources are referenced in Supplementary Tables S1 and S2.

tissues, are summarized in Figure 7. Moore et al. (2021) conducted WGS on hundreds of microdissected samples from dozens of donors, revealing significant within-organ heterogeneity in mutational load. Notably, in a 47-year-old donor, the mutation rates in skin tissues ranged from $7.6\times10^{-11}$ to $1.9\times10^{-8}$ per site per year, whereas rates in stomach tissues varied by less than 3%. Furthermore, mutation rates varied substantially between tissues, with the lowest rate observed in heart tissue (averaging $8.0\times10^{-12}$ per site per year) and the highest in appendix tissue (averaging $1.0\times10^{-8}$ per site per year) (Figure 7). Abascal et al. (2021) applied a low-error-rate duplex sequencing protocol to analyze different cell types and

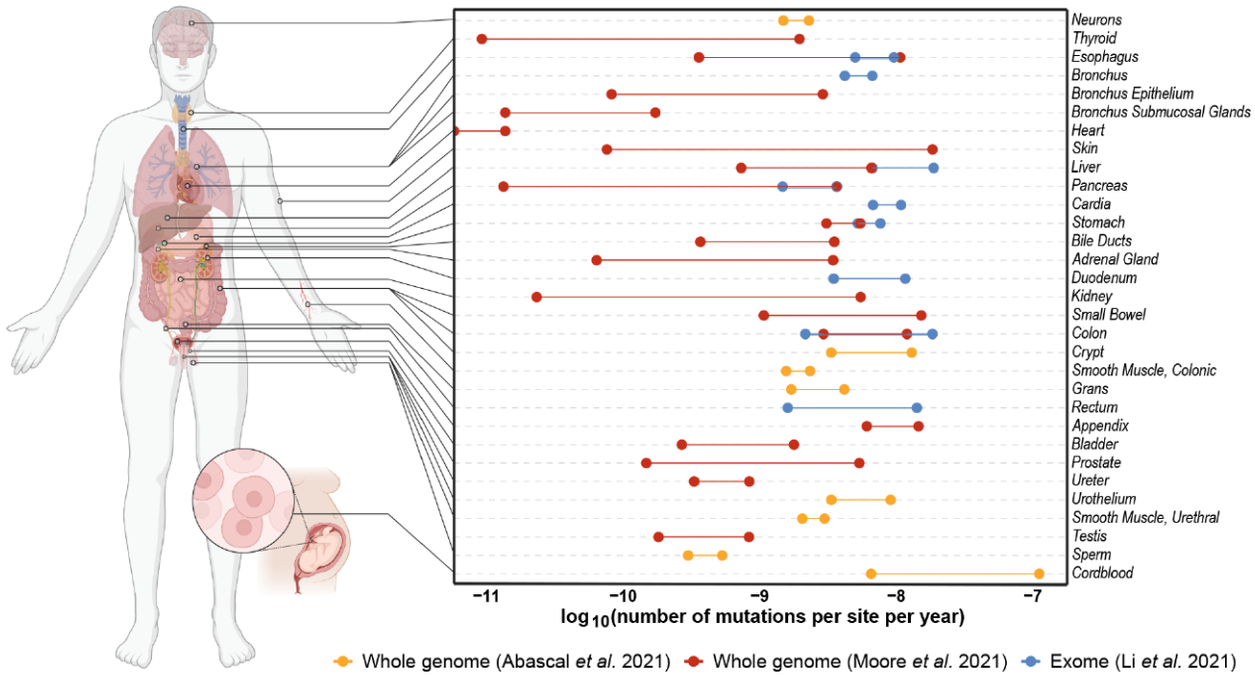



**Figure 7 Somatic mutation rates across different tissues in humans**

Estimated minimal and maximal mutation rates of 31 tissues are shown in the plot panel. Different colors represent different data sources. Age of cord blood was set to 1. For detailed data and references, see Supplementary Table S3.

identified the lowest mutation rate in sperm (Figure 7), consistent with low germline mutation rates identified in parent-offspring studies (Bergeron et al., 2023). Li et al. (2021) performed exome sequencing of 1 737 microdissected tissues from nine organs across five donors, with their findings largely aligning with the aforementioned WGS studies (Figure 7).

**Underlying causes of differences in somatic mutation rates across tissues**

Variations in mutational burden across tissues may stem from multiple intrinsic and environmental factors. Mutation directly impacts the genomes of somatic cells, involving factors such as DNA replication timing, chromatin structure, and gene expression levels (Haradhvala et al., 2016; Polak et al., 2015). Polak et al. (2015) observed asymmetrical distribution of cancer mutations between the two DNA strands, possibly linked to mutations associated with DNA replication and transcription. Moreover, different tissues possess distinct developmental, environmental, and functional characteristics, which can contribute to variation in mutation rates. Early research, mainly on blood cells, indicated that the mutational burden in these cells is primarily influenced by immune-driven somatic mutations, ultimately driving enhanced cell renewal and clonal expansion (Xie et al., 2014).

An alternative hypothesis suggests that the number of somatic cell divisions is correlated with mutation accumulation, as more cell divisions may lead to greater cell-division-dependent mutations. However, accurately estimating the number of cell divisions for each tissue is technologically challenging, and direct evidence is lacking. Contrary to expectations, Abascal et al. (2021) observed that the number of cell divisions may not be the sole determining factor affecting mutation accumulation in some tissues. Notably, despite mature blood cells undergoing significantly more divisions, granulocytes and colonic epithelial cells exhibited comparable mutational burdens and signatures. Additionally, post-mitotic neurons and polyclonal smooth muscle cells accumulated mutations throughout their lifespan, even in the absence of cell division, at rates comparable to actively dividing cells.

Lastly, exposure to environmental mutagens is a major determinant of somatic mutational load. For example, smoking tobacco is a well-recognized preventable risk factor for cancer. Alexandrov et al. (2016) evaluated differences in somatic mutational load between smokers and non-smokers using a dataset of 5 243 cancer samples covering 13 tissues and found significantly increased mutational load in smokers in four tissues—lung, larynx, liver, and kidney—characterized by a C>A mutation signature. Sunlight exposure is another significant mutagenic factor. Notably, Martincorena et al. (2015) observed increased mutational burdens and CC>TT dinucleotide substitutions, some leading to clonal expansion, in normal skin tissues upon sequencing. Moreover, UV radiation exposure is also associated with increases in mutations during aging (García-Nieto et al., 2019). *Aristolochia* and related plants, integral to traditional Chinese pharmacopeias, are known to contain aristolochic acids and similar compounds, which significantly increase A:T>T:A mutations in trinucleotide contexts and contribute to the development of multiple cancers, including bladder, upper tract urothelial (Debelle et al., 2008), kidney (Jelaković et al., 2015), intrahepatic cholangiocarcinoma (Zou et al., 2014), and liver cancers (Ng et al., 2017). Notably, previous research has estimated that 47% of liver cancers in mainland China and 78% in Taiwan are associated with aristolochic acid exposure (Ng et al., 2017).

In conclusion, the variability in mutation numbers among tissues can be attributed to multiple interacting factors, including the molecular mechanisms of mutations, cellular development, tissue-specific regulation, and environmental exposure. Importantly, mutations arising from different mechanisms exhibit distinct mutation spectra, which can be used to infer the mutational environment of a cell. For

instance, the mutation spectrum of a virus often closely mirrors that of its host; for example, the highly similar mutation spectra between bats and SARS-CoV-2 suggest bats as the host (Deng et al., 2022), while the SARS-CoV-2 Omicron variant is believed to have originated from mice, as evidenced by their similar mutation spectra (Wei et al., 2021).

## FUTURE OUTLOOK

As genetic research continues to lead scientific exploration, the trajectory of mutation studies appears expansive and full of potential. Key areas are emerging that promise to shape and amplify the impact of this field significantly.

Technological advancements, particularly in sequencing technologies such as long-read sequencing and single-cell genomics, are set to revolutionize the accurate detection and characterization of mutations. This evolution is expected to deepen our comprehension of complex mutation patterns and their significance across various biological contexts. For instance, while SVs are prevalent in cancer, their detection using short-read sequencing has posed challenges. In a groundbreaking study, Xu et al. (2023) utilized Nanopore sequencing of colorectal cancer samples, achieving unprecedented accuracy and efficiency in detecting SVs. Such advancements indicate a burgeoning future for similar studies research endeavors.

Expanding somatic mutation studies to encompass diverse tissues and species holds the potential to enrich our understanding of genetic variation, natural selection, and evolutionary dynamics. While germline mutation rates across numerous animal species have been measured directly through WGS, data on somatic mutation rates remains relatively scarce, with only a few cross-species estimates available. This scarcity is particularly evident in studies of between-tissue variations, where currently, comprehensive cross-tissue data exist solely for humans, underscoring the urgent need to expand research on somatic mutations to encompass more species and tissues. With the accumulation of data, opportunities arise to probe the underlying mechanisms driving between-tissue variation in mutation rates. Pertinent questions emerge, such as why the heart has the lowest mutational load among organs, potentially explaining its rarity in cancer occurrences, and what molecular mechanisms underlie the disparities in mutation rates between germline and somatic cells. Such investigations harbor immense biomedical potential, as exemplified by the naked mole rat, which exhibits an exceptionally low somatic mutation rate (Cagan et al., 2022), associated with its reduced cancer incidence and extended lifespan (Oka et al., 2023). Investigating the factors that govern the naked mole rat's unique mutation profile promises novel insights for biomedical research.

Ultimately, the mutation rate is shaped by evolutionary forces, including deleterious mutations, beneficial mutations, and the cost of fidelity (Sniegowski et al., 2000). While theoretical studies abound regarding the evolution of germline mutation rates, discussions on somatic mutation rates are notably lacking. Given that somatic mutations seldom confer benefits, their evolution likely hinges on deleterious mutations and the cost of fidelity. In addition to the rate at which mutations occur, the debate on whether the distribution of mutations is selected remains unresolved, with conflicting perspectives regarding the distribution of mutations between genic and intergenic regions (Liu & Zhang, 2020; Xia et al., 2020) and among genes of varying functional importance (Liu & Zhang, 2022; Monroe et al., 2022). As such, a definitive conclusion on these matters remains elusive, underscoring the enduring complexities inherent in mutation research.

## SUPPLEMENTARY DATA

Supplementary data to this article can be found online.

## COMPETING INTERESTS

The authors declare that they have no competing interests.

## AUTHORS' CONTRIBUTIONS

K.W., D.Q., Y.Q., and H.L. conceived the review, prepared the draft and designed the figures. All authors read and approved the final version of the manuscript.


## ACKNOWLEDGMENTS

We thank members of the Liu laboratory for valuable comments.


## REFERENCES


Abascal F, Harvey LMR, Mitchell E, et al. 2021. Somatic mutation landscapes at single-molecule resolution. *Nature*, **593**(7859): 405–410.

Albertini AM, Hofer M, Calos MP, et al. 1982. On the formation of spontaneous deletions: the importance of short sequence homologies in the generation of large deletions. *Cell*, **29**(2): 319–328.

Alexandrov LB, Ju YS, Haase K, et al. 2016. Mutational signatures associated with tobacco smoking in human cancer. *Science*, **354**(6312): 618–622.

Antonacci F, Kidd JM, Marques-Bonet T, et al. 2009. Characterization of six human disease-associated inversion polymorphisms. *Human Molecular Genetics*, **18**(14): 2555–2566.

Audano PA, Sulovari A, Graves-Lindsay TA, et al. 2019. Characterizing the major structural variant alleles of the human genome. *Cell*, **176**(3): 663–675. e19.

Bae T, Tomasini L, Mariani J, et al. 2018. Different mutational rates and mechanisms in human cells at pregastrulation and neurogenesis. *Science*, **359**(6375): 550–555.

Baer CF, Miyamoto MM, Denver DR. 2007. Mutation rate variation in multicellular eukaryotes: causes and consequences. *Nature Reviews Genetics*, **8**(8): 619–631.

Barton NH, Keightley PD. 2002. Understanding quantitative genetic variation. *Nature Reviews Genetics*, **3**(1): 11–21.

Bergeron LA, Besenbacher S, Turner T, et al. 2022. The Mutationathon highlights the importance of reaching standardization in estimates of pedigree-based germline mutation rates. *eLife*, **11**: e73577.

Bergeron LA, Besenbacher S, Zheng J, et al. 2023. Evolution of the germline mutation rate across vertebrates. *Nature*, **615**(7951): 285–291.

Bjelland S. 2003. Mutagenicity, toxicity and repair of DNA base damage induced by oxidation. *Mutation Research/Fundamental and Molecular Mechanisms of Mutagenesis*, **531**(1-2): 37–80.

Brash DE, Haseltine WA. 1982. UV-induced mutation hotspots occur at DNA damage hotspots. *Nature*, **298**(5870): 189–192.

Buschauer R, Matsuo Y, Sugiyama T, et al. 2020. The Ccr4-Not complex monitors the translating ribosome for codon optimality. *Science*, **368**(6488): eaay6912.

Caballero A, Keightley PD. 1994. A pleiotropic nonadditive model of variation in quantitative traits. *Genetics*, **138**(3): 883–900.

Cagan A, Baez-Ortega A, Brzozowska N, et al. 2022. Somatic mutation rates scale with lifespan across mammals. *Nature*, **604**(7906): 517–524.

Cao A, Galanello R. 2010. Beta-thalassemia. *Genetics in Medicine*, **12**(2): 61–76.

Cartegni L, Chew SL, Krainer AR. 2002. Listening to silence and

understanding nonsense: exonic mutations that affect splicing. *Nature Reviews Genetics*, **3**(4): 285–298.

Chaisson MJP, Wilson RK, Eichler EE. 2015. Genetic variation and the *de novo* assembly of human genomes. *Nature Reviews Genetics*, **16**(11): 627–640.

Charlesworth B, Charlesworth D, Morgan MT. 1990. Genetic loads and estimates of mutation rates in highly inbred plant populations. *Nature*, **347**(6291): 380–382.

Cordaux R, Udit S, Batzer MA, et al. 2006. Birth of a chimeric primate gene by capture of the transposase gene from a mobile element. *Proceedings of the National Academy of Sciences of the United States of America*, **103**(21): 8101–8106.

Darwin C. 1859. On the Origin of Species by Means of Natural Selection, or, the Preservation of Favoured Races in the Struggle for Life. London: John Murray.

Debelle FD, Vanherweghem JL, Nortier JL. 2008. Aristolochic acid nephropathy: a worldwide problem. *Kidney International*, **74**(2): 158–169.

Deng SJ, Xing K, He XL. 2022. Mutation signatures inform the natural host of SARS-CoV-2. *National Science Review*, **9**(2): nwab220.

Dou YM, Gold HD, Luquette LJ, et al. 2018. Detecting somatic mutations in normal cells. *Trends in Genetics*, **34**(7): 545–557.

Drake JW. 1991. A constant rate of spontaneous mutation in DNA-based microbes. *Proceedings of the National Academy of Sciences of the United States of America*, **88**(16): 7160–7164.

Drake JW. 2006. Chaos and order in spontaneous mutation. *Genetics*, **173**(1): 1–8.

Eisen JA, Heidelberg JF, White O, et al. 2000. Evidence for symmetric chromosomal inversions around the replication origin in bacteria. *Genome Biology*, **1**(6): research0011.

Feschotte C, Pritham EJ. 2007. DNA transposons and the evolution of eukaryotic genomes. *Annual Review of Genetics*, **41**: 331–368.

Feuk L. 2010. Inversion variants in the human genome: role in disease and genome architecture. *Genome Medicine*, **2**(2): 11.

Fisher R. 1930. The Genetical Theory of Natural Selection. Oxford: Clarendon.

García-Nieto PE, Morrison AJ, Fraser HB. 2019. The somatic mutation landscape of the human body. *Genome Biology*, **20**(1): 298.

Giroux CN, Mis JRA, Pierce MK, et al. 1988. DNA sequence analysis of spontaneous mutations in the *SUP4*-o gene of *Saccharomyces cerevisiae. Molecular and Cellular Biology*, **8**(2): 978–981.

Glickman BW, Burns PA, Fix DF. 1986. Mechanisms of spontaneous mutagenesis: clues from altered mutational specificity in DNA repair-defective strains. *In*: Shankel DM, Hartman PE, Kada T, et al. Antimutagenesis and Anticarcinogenesis Mechanisms. New York: Springer, 259–281.

Goldman N, Yang Z. 1994. A codon-based model of nucleotide substitution for protein-coding DNA sequences. *Molecular Biology and Evolution*, **11**(5): 725–736.

Grantham R, Gautier C, Gouy M, et al. 1980. Codon catalog usage and the genome hypothesis. *Nucleic Acids Research*, **8**(1): r49–r62.

Graur D, Li WH. 2000. Fundamentals of Molecular Evolution. 2nd ed. Sunderland: Sinauer Associates.

Gray YHM. 2000. It takes two transposons to tango: transposable-element-mediated chromosomal rearrangements. *Trends in Genetics*, **16**(10): 461–468.

Guttenbach M, Engel W, Schmid M. 1997. Analysis of structural and numerical chromosome abnormalities in sperm of normal men and carriers of constitutional chromosome aberrations. A review. *Human Genetics*, **100**(1): 1–21.

Hahn Y, Lee B. 2006. Human-specific nonsense mutations identified by genome sequence comparisons. *Human Genetics*, **119**(1-2): 169–178.

Halligan DL, Keightley PD. 2009. Spontaneous mutation accumulation studies in evolutionary genetics. *Annual Review of Ecology, Evolution, and Systematics*, **40**: 151–172.

Haradhvala NJ, Polak P, Stojanov P, et al. 2016. Mutational strand asymmetries in cancer genomes reveal mechanisms of DNA damage and repair. *Cell*, **164**(3): 538–549.

Harris VH, Smith CL, Jonathan Cummins W, et al. 2003. The effect of tautomeric constant on the specificity of nucleotide incorporation during DNA replication: support for the rare tautomer hypothesis of substitution mutagenesis. *Journal of Molecular Biology*, **326**(5): 1389–1401.

Hartman PE, Hartman Z, Stahl RC, et al. 1971. Classification and mapping of spontaneous and induced mutations in the histidine operon of *Salmonella. Advances in Genetics*, **16**: 1–34.

Himmelbach A, Ruban A, Walde I, et al. 2018. Discovery of multi-megabase polymorphic inversions by chromosome conformation capture sequencing in large-genome plant species. *The Plant Journal*, **96**(6): 1309–1316.

Hoban MD, Orkin SH, Bauer DE. 2016. Genetic treatment of a molecular disorder: gene therapy approaches to sickle cell disease. *Blood*, **127**(7): 839–848.

Huang ZQ, Sun SX, Lee M, et al. 2022. Single-cell analysis of somatic mutations in human bronchial epithelial cells in relation to aging and smoking. *Nature Genetics*, **54**(4): 492–498.

Huddleston J, Chaisson MJP, Steinberg KM, et al. 2017. Discovery and genotyping of structural variation from long-read haploid genome sequence data. *Genome Research*, **27**(5): 677–685.

Jeffares DC, Jolly C, Hoti M, et al. 2017. Transient structural variations have strong effects on quantitative traits and reproductive isolation in fission yeast. *Nature Communications*, **8**: 14061.

Jelaković B, Castells X, Tomić K, et al. 2015. Renal cell carcinomas of chronic kidney disease patients harbor the mutational signature of carcinogenic aristolochic acid. *International Journal of Cancer*, **136**(12): 2967–2972.

Jiang PY, Ollodart AR, Sudhesh V, et al. 2021. A modified fluctuation assay reveals a natural mutator phenotype that drives mutation spectrum variation within *Saccharomyces cerevisiae. eLife*, **10**: e68285.

Jung H, Hawkins MA, Lee S. 2020. Structural insights into the bypass of the major deaminated purines by translesion synthesis DNA polymerase. *Biochemical Journal*, **477**(24): 4797–4810.

Katju V, Bergthorsson U. 2019. Old trade, new tricks: insights into the spontaneous mutation process from the partnering of classical mutation accumulation experiments with high-throughput genomic approaches. *Genome Biology and Evolution*, **11**(1): 136–165.

Keightley PD, Eyre-Walker A. 1999. Terumi mukai and the riddle of deleterious mutation rates. *Genetics*, **153**(2): 515–523.

Kimura M. 1968. Evolutionary rate at the molecular level. *Nature*, **217**(5129): 624–626.

Kimura M. 1980. A simple method for estimating evolutionary rates of base substitutions through comparative studies of nucleotide sequences. *Journal of Molecular Evolution*, **16**(2): 111–120.

Kirkwood TBL. 1989. DNA, mutations and aging. *Mutation Research/DNAging*, **219**(1): 1–7.

Kristofich J, Morgenthaler AB, Kinney WR, et al. 2018. Synonymous mutations make dramatic contributions to fitness when growth is limited by a weak-link enzyme. *PLoS Genetics*, **14**(8): e1007615.

Lea DE, Coulson CA. 1949. The distribution of the numbers of mutants in bacterial populations. *Journal of Genetics*, **49**(3): 264–285.

Lelieveld SH, Reijnders MRF, Pfundt R, et al. 2016. Meta-analysis of 2, 104 trios provides support for 10 new genes for intellectual disability. *Nature Neuroscience*, **19**(9): 1194–1196.

Li HY, Yang Y, Hong WQ, et al. 2020. Applications of genome editing technology in the targeted therapy of human diseases: mechanisms,

advances and prospects. *Signal Transduction and Targeted Therapy*, **5**(1): 1.

Li RY, Di L, Li J, et al. 2021. A body map of somatic mutagenesis in morphologically normal human tissues. *Nature*, **597**(7876): 398–403.

Li YC, Korol AB, Fahima T, et al. 2002. Microsatellites: genomic distribution, putative functions and mutational mechanisms: a review. *Molecular Ecology*, **11**(12): 2453–2465.

Li YJ, Tang XY, Meng Y, et al. 2019. A novel compound mutation in alpha-L-iduronidase gene causes mucopolysaccharidosis type I. *Journal of Genetics*, **98**(3): 65.

Liu HX, Sun MY, Zhang JZ. 2023. Genomic estimates of mutation and substitution rates contradict the evolutionary speed hypothesis of the latitudinal diversity gradient. *Proceedings of the Royal Society B: Biological Sciences*, **290**(2009): 20231787.

Liu HX, Zhang JZ. 2020. Higher germline mutagenesis of genes with stronger testis expressions refutes the transcriptional scanning hypothesis. *Molecular Biology and Evolution*, **37**(11): 3225–3231.

Liu HX, Zhang JZ. 2022. Is the mutation rate lower in genomic regions of stronger selective constraints?. *Molecular Biology and Evolution*, **39**(8): msac169.

Long H, Miller SF, Strauss C, et al. 2016. Antibiotic treatment enhances the genome-wide mutation rate of target cells. *Proceedings of the National Academy of Sciences of the United States of America*, **113**(18): E2498–E2505.

Luria SE, Delbrück M. 1943. Mutations of bacteria from virus sensitivity to virus resistance. *Genetics*, **28**(6): 491–511.

Lynch M. 2002. Gene duplication and evolution. *Science*, **297**(5583): 945–947.

Lynch M. 2010. Evolution of the mutation rate. *Trends in Genetics*, **26**(8): 345–352.

Lynch M, Ackerman MS, Gout JF, et al. 2016. Genetic drift, selection and the evolution of the mutation rate. *Nature Reviews Genetics*, **17**(11): 704–714.

Lynch M, Conery JS. 2000. The evolutionary fate and consequences of duplicate genes. *Science*, **290**(5494): 1151–1155.

Martincorena I, Roshan A, Gerstung M, et al. 2015. High burden and pervasive positive selection of somatic mutations in normal human skin. *Science*, **348**(6237): 880–886.

Milholland B, Dong X, Zhang L, et al. 2017. Differences between germline and somatic mutation rates in humans and mice. *Nature Communications*, **8**: 15183.

Monroe JG, Srikant T, Carbonell-Bejerano P, et al. 2022. Mutation bias reflects natural selection in *Arabidopsis thaliana*. *Nature*, **602**(7895): 101–105.

Moore L, Cagan A, Coorens THH, et al. 2021. The mutational landscape of human somatic and germline cells. *Nature*, **597**(7876): 381–386.

Mort M, Ivanov D, Cooper DN, et al. 2008. A meta-analysis of nonsense mutations causing human genetic disease. *Human Mutation*, **29**(8): 1037–1047.

Mukai T. 1964. The genetic structure of natural populations of *Drosophila melanogaster*. I. Spontaneous mutation rate of polygenes controlling viability. *Genetics*, **50**(1): 1–19.

Mukai T, Chigusa SI, Mettler LE, et al. 1972. Mutation rate and dominance of genes affecting viability in *Drosophila melanogaster. Genetics*, **72**(2): 335–355.

Musallam KM, Bou-Fakhredin R, Cappellini MD, et al. 2021. 2021 update on clinical trials in β-thalassemia. *American Journal of Hematology*, **96**(11): 1518–1531.

Nachman MW, Crowell SL. 2000. Estimate of the mutation rate per nucleotide in humans. *Genetics*, **156**(1): 297–304.

Ng AWT, Poon SL, Huang MN, et al. 2017. Aristolochic acids and their derivatives are widely implicated in liver cancers in Taiwan and throughout Asia. *Science Translational Medicine*, **9**(412): eaan6446.

O'Hara SM, Marnett LJ. 1991. DNA sequence analysis of spontaneous and β-methoxy-acrolein-induced mutations in *Salmonella typhimurium hisD 3052. Mutation Research/Fundamental and Molecular Mechanisms of Mutagenesis*, **247**(1): 45–56.

Ohnishi O. 1977a. Spontaneous and ethyl methanesulfonate-induced mutations controlling viability in *Drosophila melanogaster*. I. Recessive lethal mutations. *Genetics*, **87**(3): 519–527.

Ohnishi O. 1977b. Spontaneous and ethyl methanesulfonate-induced mutations controlling viability in *Drosophila melanogaster*. II. Homozygous effect of polygenic mutations. *Genetics*, **87**(3): 529–545.

Ohnishi O. 1977c. Spontaneous and ethyl methanesulfonate-induced mutations controlling viability in *Drosophila melanogaster*. III. Heterozygous effect of polygenic mutations. *Genetics*, **87**(3): 547–556.

Oka K, Yamakawa M, Kawamura Y, et al. 2023. The naked mole-rat as a model for healthy aging. *Annual Review of Animal Biosciences*, **11**: 207–226.

Osum SH, Oribamise EI, Corbière SMAS, et al. 2023. Combining nonsense mutation suppression therapy with nonsense-mediated decay inhibition in neurofibromatosis type 1. *Molecular Therapy-Nucleic Acids*, **33**: 227–239.

Otto SP, Michalakis Y. 1998. The evolution of recombination in changing environments. *Trends in Ecology & Evolution*, **13**(4): 145–151.

Pichavant C, Aartsma-Rus A, Clemens PR, et al. 2011. Current status of pharmaceutical and genetic therapeutic approaches to treat DMD. *Molecular Therapy*, **19**(5): 830–840.

Polak P, Karlić R, Koren A, et al. 2015. Cell-of-origin chromatin organization shapes the mutational landscape of cancer. *Nature*, **518**(7539): 360–364.

Polleys EJ, Del Priore I, Haber JE, et al. 2023. Structure-forming CAG/CTG repeats interfere with gap repair to cause repeat expansions and chromosome breaks. *Nature Communications*, **14**(1): 2469.

Porubsky D, Sanders AD, Höps W, et al. 2020. Recurrent inversion toggling and great ape genome evolution. *Nature Genetics*, **52**(8): 849–858.

Rees DC, Williams TN, Gladwin MT. 2010. Sickle-cell disease. *The Lancet*, **376**(9757): 2018–2031.

Sargentini NJ, Smith KC. 1985. Spontaneous mutagenesis: the roles of DNA repair, replication, and recombination. *Mutation Research/Reviews in Genetic Toxicology*, **154**(1): 1–27.

Sharp PM, Cowe E, Higgins DG, et al. 1988. Codon usage patterns in *Escherichia coli, Bacillus subtilis, Saccharomyces cerevisiae, Schizosaccharomyces pombe, Drosophila melanogaster* and *Homo sapiens*; A review of the considerable within-species diversity. *Nucleic Acids Research*, **16**(17): 8207–8211.

Shen XK, Song SL, Li C, et al. 2022. Synonymous mutations in representative yeast genes are mostly strongly non-neutral. *Nature*, **606**(7915): 725–731.

Sniegowski PD, Gerrish PJ, Johnson T, et al. 2000. The evolution of mutation rates: separating causes from consequences. *Bioessays*, **22**(12): 1057–1066.

Stratton MR, Campbell PJ, Futreal PA. 2009. The cancer genome. *Nature*, **458**(7239): 719–724.

Strauss C, Long H, Patterson CE, et al. 2017. Genome-wide mutation rate response to pH change in the coral reef pathogen *Vibrio shilonii* AK1. *mBio*, **8**(4): e01021–17.

Supek F, Miñana B, Valcárcel J, et al. 2014. Synonymous mutations frequently act as driver mutations in human cancers. *Cell*, **156**(6): 1324–1335.

Suyama M, Bork P. 2001. Evolution of prokaryotic gene order: genome rearrangements in closely related species. *Trends in Genetics*, **17**(1): 10–13.

Tchou J, Kasai H, Shibutani S, et al. 1991. 8-oxoguanine (8-

hydroxyguanine) DNA glycosylase and its substrate specificity. *Proceedings of the National Academy of Sciences of the United States of America*, **88**(11): 4690–4694.

Tomasetti C, Li L, Vogelstein B. 2017. Stem cell divisions, somatic mutations, cancer etiology, and cancer prevention. *Science*, **355**(6331): 1330–1334.

Topal MD, Fresco JR. 1976. Complementary base pairing and the origin of substitution mutations. *Nature*, **263**(5575): 285–289.

Totter JR. 1980. Spontaneous cancer and its possible relationship to oxygen metabolism. *Proceedings of the National Academy of Sciences of the United States of America*, **77**(4): 1763–1767.

Urushitani M, Sik A, Sakurai T, et al. 2006. Chromogranin-mediated secretion of mutant superoxide dismutase proteins linked to amyotrophic lateral sclerosis. *Nature Neuroscience*, **9**(1): 108–118.

Vijg J, Dong X. 2020. Pathogenic mechanisms of somatic mutation and genome mosaicism in aging. *Cell*, **182**(1): 12–23.

Wang YG, Obbard DJ. 2023. Experimental estimates of germline mutation rate in eukaryotes: a phylogenetic meta-analysis. *Evolution Letters*, **7**(4): 216–226.

Watson JD, Crick FHC. 1953. The structure of DNA. *Cold Spring Harbor Symposia on Quantitative Biology*, **18**: 123–131.

Wei CS, Shan KJ, Wang WG, et al. 2021. Evidence for a mouse origin of the SARS-CoV-2 Omicron variant. *Journal of Genetics and Genomics*, **48**(12): 1111–1121.

Witkin EM. 1953. Effects of temperature on spontaneous and induced mutations in *Escherichia coli*. *Proceedings of the National Academy of Sciences of the United States of America*, **39**(5): 427–433.

Wu K, Li HC, Wang YH, et al. 2023. Silver nanoparticles elevate mutagenesis of eukaryotic genomes. *G3 Genes*| *Genomes*| *Genetics*, **13**(3): jkad008.

Xia B, Yan Y, Baron M, et al. 2020. Widespread transcriptional scanning in the testis modulates gene evolution rates. *Cell*, **180**(2): 248–262. e21.

Xie MC, Lu C, Wang JY, et al. 2014. Age-related mutations associated with clonal hematopoietic expansion and malignancies. *Nature Medicine*, **20**(12): 1472–1478.

Xu LM, Wang XY, Lu XH, et al. 2023. Long-read sequencing identifies novel structural variations in colorectal cancer. *PLoS Genetics*, **19**(2): e1010514.

Xue YL, Wang QJ, Long Q, et al. 2009. Human Y chromosome base-substitution mutation rate measured by direct sequencing in a deep-rooting pedigree. *Current Biology*, **19**(17): 1453–1457.

Yang SH, Wang L, Huang J, et al. 2015. Parent–progeny sequencing indicates higher mutation rates in heterozygotes. *Nature*, **523**(7561): 463–467.

Zheng SY, Kim H, Verhaak RGW. 2014. Silent mutations make some noise. *Cell*, **156**(6): 1129–1131.

Zou SS, Li JR, Zhou HB, et al. 2014. Mutational landscape of intrahepatic cholangiocarcinoma. *Nature Communications*, **5**: 5696.

Luo et al. *Zool. Res.* 2024, 45(4): 781−790
https://doi.org/10.24272/j.issn.2095-8137.2023.355

ZR | Zoological Research

Article Open Access

# Engineered AAV13 variants with enhanced transduction and confined spread

Neng-Song Luo[1,#], Yu-Xiang Cai[1,#], Zeng-Peng Han[2,3,4,5,#], Xiao-Kai Sui[6], Wen-Jia Yuan[7], Zi-Lian Zhang[2,4], Hao-Dong Guo[8], Jie Wang[3,5], Kun-Zhang Lin[2,4,*], Fu-Qiang Xu[1,2,3,4,5,9,*]

[1] *Wuhan National Laboratory for Optoelectronics*, *Huazhong University of Science and Technology*, *Wuhan*, *Hubei* 430074, *China*
[2] *Shenzhen Key Laboratory of Viral Vectors for Biomedicine*, *Shenzhen-Hong Kong Institute of Brain Science*, *Shenzhen Institute of Advanced Technology*, *Chinese Academy of Sciences*, *Shenzhen*, *Guangdong* 518055, *China*
[3] *Key Laboratory of Magnetic Resonance in Biological Systems*, *State Key Laboratory of Magnetic Resonance and Atomic and Molecular Physics*, *National Center for Magnetic Resonance in Wuhan*, *Innovation Academy for Precision Measurement Science and Technology*, *Chinese Academy of Sciences*, *Wuhan*, *Hubei* 430071, *China*
[4] *Key Laboratory of Quality Control Technology for Virus-Based Therapeutics*, *Guangdong Provincial Medical Products Administration*, *NMPA Key Laboratory for Research and Evaluation of Viral Vector Technology in Cell and Gene Therapy Medicinal Products*, *Brain Cognition and Brain Disease Institute*, *Shenzhen Institute of Advanced Technology*, *Chinese Academy of Sciences*, *Shenzhen*, *Guangdong* 518055, *China*
[5] *University of Chinese Academy of Sciences*, *Beijing* 100049, *China*
[6] *Zhongnan Hospital*, *Wuhan University*, *Wuhan*, *Hubei* 430072, *China*
[7] *Brain Case Biotechnology Co.*, *Ltd.*, *Shenzhen*, *Guangdong* 518107, *China*
[8] *College of Life Sciences*, *Wuhan University*, *Wuhan*, *Hubei* 430072, *China*
[9] *Center for Excellence in Brain Science and Intelligence Technology*, *Chinese Academy of Sciences*, *Shanghai* 200031, *China*

## ABSTRACT

Precise targeting of specific regions within the central nervous system (CNS) is crucial for both scientific research and gene therapy in the context of brain diseases. Adeno-associated virus 13 (AAV13) is known for its restricted diffusion range within the CNS, making it an ideal choice for precise labeling and administration within small brain regions. However, AAV13 mediates relatively low expression of target genes. Here, we introduced specifically engineered modifications to the AAV13 capsid protein to enhance its transduction efficiency. We first constructed AAV13-YF by mutating tyrosine to phenylalanine on the surface of the AAV13 capsid. We then inserted the 7m8 peptide, known to enhance cell transduction, into positions 587/588 and 585/586 of the AAV13 capsid, resulting in two distinct variants named AAV13-587-7m8 and AAV13-585-7m8, respectively. We found that AAV13-YF exhibited superior *in vitro* infectivity in HEK293T cells compared to AAV13, while AAV13-587-7m8 and AAV13-585-7m8 showed enhanced CNS infection capabilities in C57BL/6 mice, with AAV13-587-7m8 infection retaining a limited spread range. These modified AAV13 variants hold promising potential for applications in gene therapy and neuroscience research.

**Keywords:** Adeno-associated virus 13; AAV13-YF; AAV13-587-7m8; AAV13-585-7m8; transduction efficiency

## INTRODUCTION

Viral vectors, especially adeno-associated viruses (AAV), have attracted considerable attention due to their low immunogenicity, broad host range, and long-term high-level transgene expression (Wang et al., 2019). They serve as valuable tools for delivering target genes to specific tissues, and have been widely applied in studies of neural circuits and gene therapy (Challis et al., 2022; Lykken et al., 2018; Mendell et al., 2021; Ojala et al., 2015; Zheng et al., 2023). Many AAV serotypes exist, including natural serotypes and engineered capsid variants, which exhibit different tissue tropism and

This is an open-access article distributed under the terms of the Creative Commons Attribution Non-Commercial License (http://creativecommons.org/licenses/by-nc/4.0/), which permits unrestricted non-commercial use, distribution, and reproduction in any medium, provided the original work is properly cited.
Copyright ©2024 Editorial Office of Zoological Research, Kunming Institute of Zoology, Chinese Academy of Sciences

Received: 28 February 2024; Accepted: 19 March 2024; Online: 20 March 2024
Foundation items: This study was supported by the National Science and Technology Innovation 2030 Grant (2021ZD0201003), National Natural Science Foundation of China (31830035, 31771156, 21921004), Strategic Priority Research Program of the Chinese Academy of Sciences (XDB32030200), Shenzhen Key Laboratory of Viral Vectors for Biomedicine (ZDSYS20200811142401005), and Key Laboratory of Quality Control Technology for Virus-Based Therapeutics, Guangdong Provincial Medical Products Administration (2022ZDZ13)
[#]Authors contributed equally to this work
*Corresponding authors, E-mail: kz.lin@siat.ac.cn; fq.xu@siat.ac.cn

provide diverse choices for scientific research and clinical practice (Srivastava, 2016; Watakabe et al., 2015).

In neuroscience research, AAV application scenarios can be broadly classified into two types. Firstly, several AAVs enable long-distance transportation through axon terminal absorption, anterograde trans-synaptic spread, or blood-brain barrier transportation. For example, AAV11 (Han et al., 2023), AAV2-Retro (Tervo et al., 2016), and AAV9-Retro (Lin et al., 2020) can mediate the retrograde transportation of target genes to the soma along the axon, high-titer AAV1 and AAV9 (Zingg et al., 2017) can infect downstream neural networks by anterograde trans-synaptic spread, and AAV.CPP.16 (Yao et al., 2022), AAV.CAP-B10 (Goertsen et al., 2022), and AAV-PHP.eB (Chan et al., 2017) facilitate efficient non-invasive gene delivery across the blood-brain barrier to the CNS through intravenous administration. Conversely, there are scenarios where precise *in situ* transduction by AAVs is required, ensuring that neurons are targeted strictly at the injection site with minimal spread. This localized, small-scale spread minimizes off-target delivery to unintended brain regions, which is essential for gene manipulation or disease treatment in specific nuclei. Several AAV serotypes are preferred for transducing localized neuronal populations, with AAV1 and AAV2 often chosen for applications requiring precise targeting due to their more confined diffusion (Duarte Azevedo et al., 2021; Haery et al., 2019). Nonetheless, they can still transduce non-target brain regions through axon terminal uptake or anterograde trans-synaptic transmission (Aschauer et al., 2013; Duarte Azevedo et al., 2021; Tervo et al., 2016; Zingg et al., 2017). AAV13, in contrast, exhibits confined diffusion without retrograde transduction and trans-synaptic transmission in the brain. Its local spread range is smaller than that of AAV2 (Han et al., 2022), making it ideal for precise gene delivery in smaller volume nuclei. However, AAV13-mediated gene expression is relatively weak and does not sufficiently meet the needs for robust gene expression in specific brain areas.

Enhancing the transduction efficiency or expression intensity of target genes driven by AAV13, while preserving its confined diffusion range, presents a crucial challenge. Previous studies have shown that replacing tyrosine (Y) residues exposed on the capsid proteins of AAV2/AAV2-retro with phenylalanine (F) (called “YF mutation”) can reduce viral particle degradation, thereby improving transgene expression efficiency (Nakahama et al., 2022; Zhong et al., 2008). AAV2-7m8, developed by incorporating a 10-amino acid peptide “LALGETTRPA” (known as the 7m8 peptide) at position 588 of the AAV2 capsid protein, exhibits stronger retinal targeting than its parental AAV2 serotype (Dalkara et al., 2013), as well as higher gene transduction strength than AAV2, while retaining the original diffusion range (Khabou et al., 2016). Given the structural similarities between AAV13 and AAV2 capsid proteins (Han et al., 2022; Mietzsch et al., 2021), we tentatively explored the incorporation of YF mutations and 7m8 modifications into AAV13 to enhance its transduction efficiency. In AAV2/AAV2-retro, tyrosine residues at positions Y444, Y500, and Y730 are mutated to phenylalanine (Nakahama et al., 2022). Correspondingly, in AAV13, these residues are located at Y443 and Y728, with F498 naturally occurring in place of Y500. We constructed AAV13-YF and found it to be more efficient at infecting HEK293T cells *in vitro* compared to unmodified AAV13. Additionally, we inserted the 7m8 peptide at positions 587 and 585 of the AAV13 capsid to construct AAV13-587-7m8 and AAV13-585-7m8, respectively, which demonstrated higher transduction efficiency in the mouse brain compared to AAV13.

## MATERIALS AND METHODS

### Plasmid construction

The Fast Mutagenesis System kit, polymerase chain reaction (PCR) was applied to construct and amplify the plasmids pAAV2/13-585-7m8, pAAV2/13-587-7m8, and pAAV13-YF, with pAAV2/13 as the starting template. All primer sequences are provided in Supplementary Table S1. The PCR systems were set to 50 μL and 36 cycles, with 1 μL of the template digestive enzyme DMT (TransGen Biotech, FM111, China) added to the PCR product, followed by digestion at 37°C for 1 h. After digestion, 5 μL of the digested product was used to transform competent Stbl3 cells. Single colonies identified as positive by colony PCR were activated and inoculated in 15 mL of Luria-Bertani (LB) liquid medium. The plasmids were then extracted for sequencing, with the correctly sequenced clones named pAAV2/13-585-7m8, pAAV2/13-587-7m8, and pAAV2/13-YF.

### Cell culture and AAV vector manufacture

HEK293T cells were obtained from the American Type Culture Collection (USA) and maintained in suspension culture in Balance CD (Cell-wise, CW01001, China) medium supplemented with 1% penicillin/streptomycin (BasalMedia, S110JV, China) at 37°C and 5% $CO_2$. At 16 h before transfection, the cells were transferred to adherent culture in Dulbecco’s Modified Eagle Medium (DMEM, BasalMedia, L110KJ, China) with 2% fetal bovine serum (GIBCO, 10099141C, USA) and 1% penicillin/streptomycin (BasalMedia, S110JV, China). AAV vectors were produced by triple plasmid transient transfection with linear polyethylenimine (Polysciences, 24765-1, USA). Viral particles were harvested at 72 h post-transfection, purified by iodixanol gradient ultracentrifugation (Fripont et al., 2019), and subjected to buffer exchange in Amicon® Ultra centrifugal filters (Millipore, UFC910024, USA) using phosphate-buffered saline (PBS) with 0.001% Pluronic F68 (Thermo Fisher Scientific, 24040032, USA). The purified AAVs were titered by quantitative real-time PCR (qPCR) using an iQ SYBR Green Supermix kit (Bio-Rad, 1708884, USA). The obtained virus titers are shown in Supplementary Table S2. All viral vectors were aliquoted and stored at −80°C until use.

### Research animals

All procedures were approved by the Animal Care and Use Committee of the Innovation Academy for Precision Measurement Science and Technology, Chinese Academy of Sciences (approval No. APM20026A) on 12 December 2020. Adult male C57BL/6 mice (8–10 weeks old, *n*=48, Hunan SJA Laboratory Animal Company) were used for the experiments.

### Stereotaxic AAV injection

Mice were deeply anaesthetized using 1% pentobarbital intraperitoneally (i.p., 50 mg/kg body weight) and placed in a stereotaxic apparatus (68025-stereotaxic apparatus and 68030-mice adaptor, RWD, China). The injection coordinates were selected according to *The Mouse Brain in Stereotaxic Coordinates*, 4th edition (Paxinos & Franklin, 2013). Three brain regions were used: primary somatosensory area (SSp) (relative to bregma: anterior-posterior-axis (AP) +0.50 mm,

medial-lateral-axis (ML) ±3.00 mm, and dorsal-ventral-axis (DV) –2.00 mm), primary motor cortex (MOp) (relative to bregma: AP +1.54 mm, ML ±1.60 mm, and DV –1.60 mm), and ventral tegmental area (VTA) (relative to bregma: AP –3.20 mm, ML ±0.45 mm, and DV –4.30 mm). The virus was administered at a rate of 0.03 μL/min using a stereotaxic injector equipped with a pulled glass capillary (Stoelting, 53311). Following the injection, the micropipette was held for an additional 10 min before being withdrawn. The mice were then allowed to recover from anesthesia on a heating pad. Three weeks post-injection, the mice were sacrificed and their brain tissues were collected via transcardial perfusion with PBS and 4% paraformaldehyde.

**Slice preparation and imaging**

Brain slice preparation and imaging were performed according to previously reported methods (Lin et al., 2020). The brains were soaked overnight in 4% paraformaldehyde solution. After dehydration with 30% sucrose solution, the brains were sectioned (thickness of 40 μm) using a microtome (Thermo Fisher Scientific, USA), collected in anti-freeze fluid, and stored at −20°C for further use. After washing with PBS, the brain slices attached to microscope slides were counterstained with 4',6-diamidino-2-phenylindole (DAPI, 1:4 000, Beyotime, C1002, China) and sealed with 70% glycerol. Imaging was completed using an Olympus VS120 Slide Scanner microscope (Olympus, Japan).

**Data analysis**

Data analysis (student's *t*-test) was performed using GraphPad Prism v.9.0 (GraphPad Software, USA). Average fluorescence intensity was quantified using ImageJ v.1.8.0 (National Institutes of Health, USA). All statistical data were presented as means±standard error of the mean (SEM). Statistical significance was set to $^{*}$: $P$<0.05; $^{**}$: $P$<0.01; $^{***}$: $P$<0.001, and $^{****}$: $P$<0.0001. The AAV13, AAV13-YF, AAV13-585-7m8, and AAV13-587-7m8 capsid protein structures were predicted using the ColabFold algorithm on the Beikunyun supercomputing platform. The three-dimensional structural alignment of the VP1 proteins of AAV13, AAV2, AAV13-585-7m8, and AAV13-587-7m8 was determined using UCSF ChimeraX software (Goddard et al., 2018; Pettersen et al., 2021).

## RESULTS

**Engineered AAVs possess higher production efficiency**

The capsid protein sequences and structures between AAV13 and AAV2 are highly similar (Han et al., 2022). To identify a suitable site for engineering modifications in AAV13, we compared the VP1 protein structure of AAV13 with that of AAV2 (Figure 1A). Previous studies have suggested that replacing surface-exposed tyrosine with phenylalanine in the capsid of AAV2-retro enhances the intracellular transduction efficiency of virions (Nakahama et al., 2022). Therefore, we employed this strategy to modify the AAV13 capsid (Figure 1B). Additionally, structural prediction results revealed that the 585th amino acid site of the AAV13 capsid aligns with the 587th amino acid site of the AAV2 capsid, a commonly targeted engineering modification site located within the triple-axis protrusion. Therefore, we selected the 585th amino acid site of the AAV13 capsid for engineering modifications. Furthermore, to investigate the impact of similar sites on engineering modifications, we also designated the 587th amino acid of the AAV13 capsid as the site for engineering modifications. Subsequently, the 7m8 peptide (LALGETTRPA) was inserted after positions 587 and 585 of the AAV13 capsid, resulting in the construction of the AAV13-587-7m8 and AAV13-585-7m8 variants, respectively (Figure 1B). For practical production of these vectors based on the triple transfection method, the packaging plasmids pAAV2/13-YF, pAAV2/13-585-7m8, and pAAV2/13-587-7m8 were constructed. The same packaging plasmid pAAV-CMV-EGFP-WPRE was used for viral packaging to identify the packaging efficiency variation of the engineered AAVs. Subsequently, qPCR assays were used to detect viral titers in the supernatants and cellular lysates of transfected HEK293T cells. We found that AAV13-YF contained the maximum number of viral particles in the cell lysates, while AAV13-585-7m8 contained the maximum number of viral particles in the supernatants (Figure 1C, D). Silver staining showed that the constructed AAVs were of high purity (Figure 1E). These results indicate that the engineered AAVs had higher packaging efficiency than the parental AAV13.

**Significant variation in cell tropism of engineered vectors *in vitro***

To assess their infectivity, the prepared AAV13 mutants, including AAV2/13-CMV-EGFP, AAV2/13-YF-CMV-EGFP, AAV2/13-587-7m8-CMV-EGFP, and AAV2/13-585-7m8-CMV-EGFP, were individually added to adherent HEK293T cells at a multiplicity of infection (MOI) of $2\times10^5$. Fluorescence signals were prominently observed in the AAV13- and AAV13-YF-infected cells at 24 and 48 h post-infection, whereas signals were weaker in the AAV13-587-7m8- and AAV13-585-7m8-infected cells (Figure 2A). Based on mean fluorescence intensity of green fluorescent protein, both AAV13 and AAV13-YF exhibited the highest levels of fluorescence expression at 24 h post-infection, with no significant difference between them (Figure 2B, $P$=0.1761). Furthermore, the fluorescence intensity mediated by AAV13 surpassed that of AAV13-585-7m8 (Figure 2B, $P$=0.0034) and AAV13-587-7m8 (Figure 2B, $P$=0.0029). At 48 h post-infection, AAV13-YF mediated the strongest fluorescence expression, exceeding that of AAV13 (Figure 2B, $P$<0.0001), while the fluorescence intensity mediated by AAV13 remained higher than that of AAV13-585-7m8 (Figure 2B, $P$<0.0001) and AAV13-587-7m8 (Figure 2B, $P$<0.0001). These results suggest that AAV13-587-7m8 and AAV13-585-7m8 exhibit lower transduction efficiency than AAV13 *in vitro* on HEK293T cells.

**Enhanced *in-situ* transduction efficiency of engineered variants**

To assess the performance of the variants *in situ* tagging, AAV13-CMV-EGFP, AAV13-YF-CMV-EGFP, AAV13-587-7m8-CMV-EGFP, and AAV13-585-7m8-CMV-EGFP were injected into layer 4 of the SSp (Figure 3A). Three weeks post-injection, the mice were perfused and their brains were sampled, sectioned, and imaged. Only a small cluster of green fluorescent-positive neurons were observed in the SSp of mice injected with AAV13 and AAV13-YF, while a cluster of positive neurons with strong fluorescence signals was detected in the SSp of mice injected with AAV13-587-7m8. In addition, positive neurons with a large *in situ* diffusion range and strong fluorescence signals were observed in the SSp of mice injected with AAV13-585-7m8 (Figure 3B). When these viral vectors were separately injected into the SSp, distinct labeling patterns were observed in other brain regions.

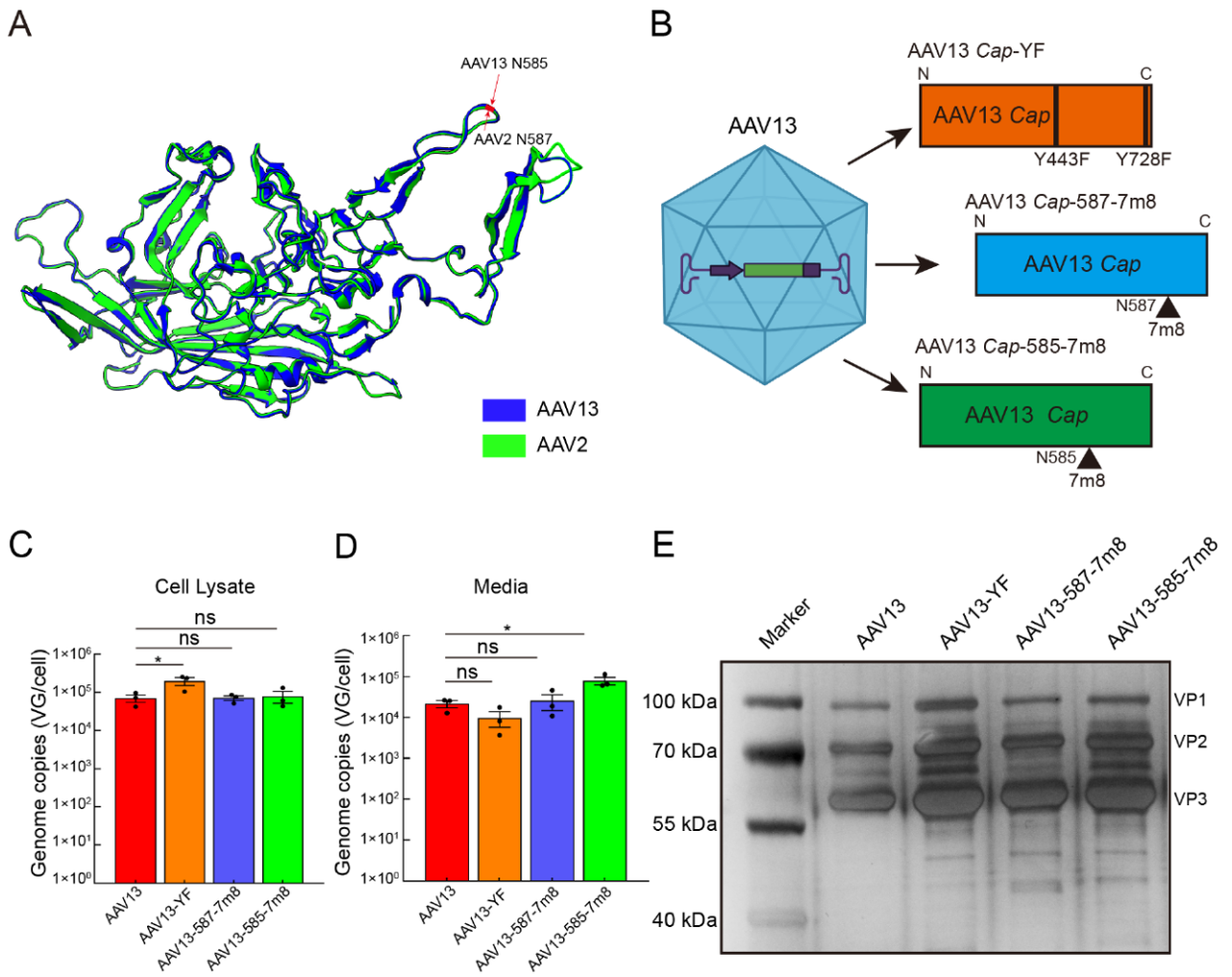



**Figure 1 Construction strategies for engineered AAVs and evaluation of packaging characteristics**

A: Structure comparison between AAV13 and AAV2. Structural information was obtained from the Protein Database (PDB) (AAV13, 7L6H; AAV2, 6IH9), and graph was generated using UCSF ChimeraX. Red segment indicates that the 585 amino acid site of AAV13 coincides with the 587 amino acid site of AAV2. B: Strategies for engineering AAV13, including YF mutations (Y443F, Y728F) and insertion of 7m8 peptides after 585 and 587 positions of AAV13 VP1. C, D: Crude lysate PCR assays were performed on cellular lysates (C) and media (D) of HEK239T cells subjected to triple transfection to produce AAV13, AAV13-YF, AAV13-587-7m8, and AAV13-585-7m8. Values represent mean±SEM, *n*=3/group. Statistical analysis was completed using one-way analysis of variance (ANOVA) followed by Tukey's multiple comparisons test with an alpha value of 0.05. ns: Not significant; *: *P*<0.05. E: Detection of virus purity. AAV13 mutant purity was detected by silver staining, with AAV13 as the control. Results showed that AAV13 mutants had high purity.

Initially, following injection of AAV13 and AAV13-YF into the SSp, no fluorescence-labeled cell signals were detected in the ventral posteromedial nucleus of the thalamus (VPM) region. Subsequently, upon injection of AAV13-587-7m8 and AAV13-585-7m8 into the SSp, a limited number of cells were fluorescently labeled in the VPM (Supplementary Figure S1). This phenomenon may be attributed to the ability of these two engineered vectors to undergo retrograde labeling through minimal uptake by axon terminals. Based on average fluorescence intensity of the same area, no differences in average fluorescence intensity were detected between AAV13 and AAV13-YF in the SSp (Figure 3C, *P*=0.9987), while average fluorescence intensity of AAV13 was significantly lower than that of AAV13-587-7m8 (Figure 3C, *P*=0.0024) and AAV13-585-7m8 (Figure 3C, *P*<0.0001). When injected into the VTA, fluorescent expression mediated by AAVs exhibited the same characteristics (Figure 4A, B). Based on average fluorescence intensity of the same area, no differences in average fluorescence intensity were detected between AAV13 and AAV13-YF in the VTA (Figure 4C, *P*=0.8005), while average fluorescence intensity of AAV13 was significantly lower than that of AAV13-587-7m8 (Figure 4C, *P*=0.0138) and AAV13-585-7m8 (Figure 4C, *P*=0.0001). These results indicate that AAV13-587-7m8 and AAV13-585-7m8 exhibit higher transduction efficiency than AAV13 in the CNS of mice.

**AAV13-587-7m8 permits highly efficient transduction at low doses**

Based on the aforementioned findings, AAV13-587-7m8 emerged as one of the three engineered vectors characterized by a comparatively restricted diffusion range and enhanced transduction efficiency. Consequently, it holds greater promise as a gene delivery vector for small nuclei. To determine whether AAV13-587-7m8 retains its restricted diffusion range and efficient neuron infection with reduced injection volume, we decreased the injection volume of AAV13-587-7m8 and AAV13 to 50 nL in layer 5 of the MOp brain region (Figure 5A). Three weeks post-injection, the mice were perfused and their

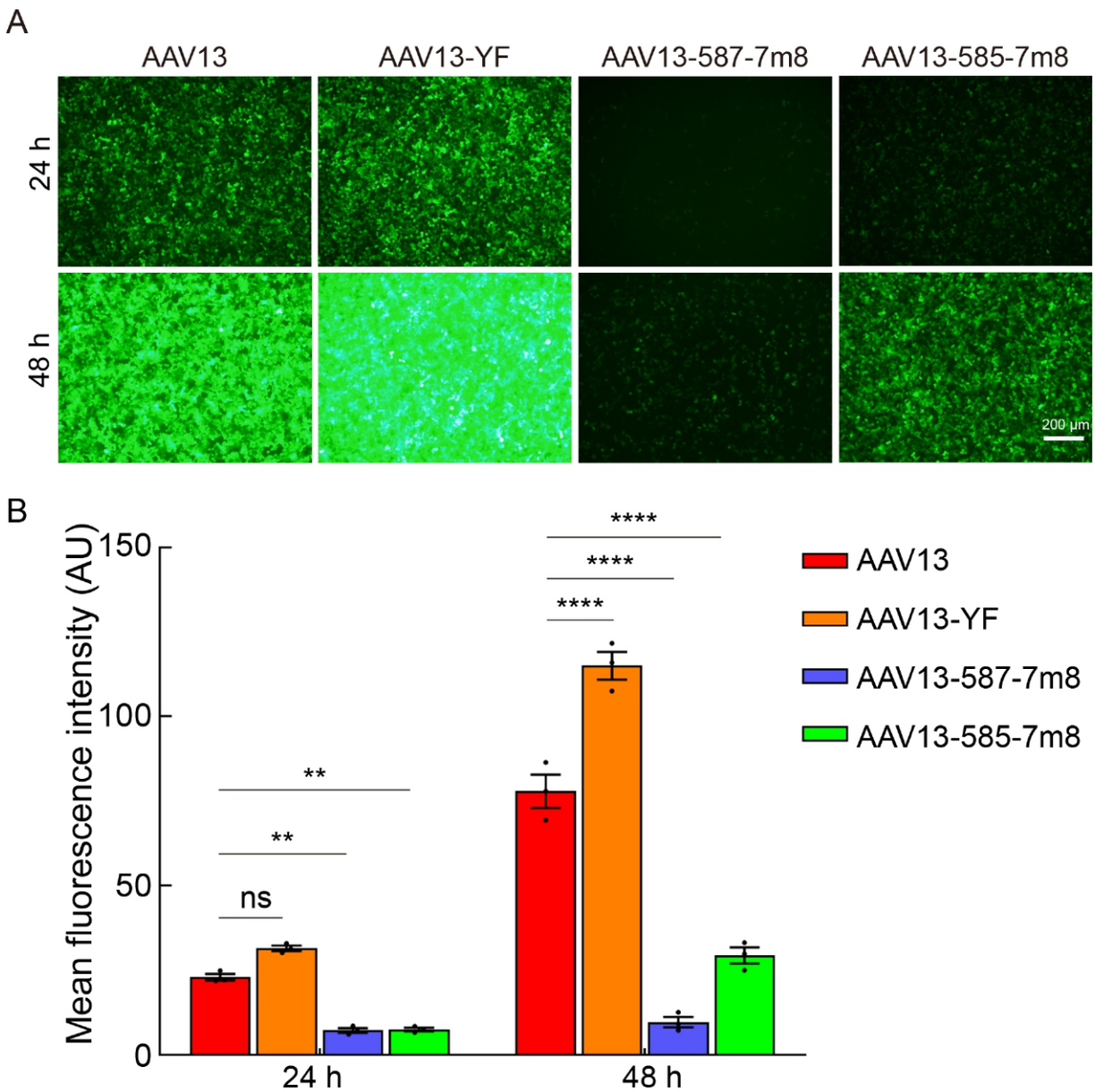



**Figure 2 Characterization of transduction properties of novel AAV variants *in vitro***

A: Fluorescence expression of AAV13, AAV13-YF, AAV13-587-7m8, and AAV13-585-7m8 in HEK293T cells at 24 h and 48 h post-infection, respectively. B: Quantification of mean fluorescence intensities for different AAV transductions *in vitro*. Values represent mean±SEM, *n*=3/group. Statistical analysis was completed using two-way ANOVA followed by Tukey's multiple comparisons test with an alpha value of 0.05. AU, arbitrary units; ns: Not significant; **: $P<0.01$; ****: $P<0.0001$.

brain tissues were sampled, sectioned, and imaged. Results showed that reducing the injection volume resulted in weaker expression of AAV13, whereas AAV13-587-7m8 maintained strong transduction ability (Figure 5B). Quantifying average fluorescence density indicated that AAV13-587-7m8 mediated significantly brighter fluorescence expression compared to AAV13 (Figure 5C, $P=0.0031$). Given that AAV13-585-7m8 exhibited the strongest average fluorescence intensity but largest diffusion range, we aimed to investigate whether reducing the viral particle quantity of AAV13-585-7m8 by half could balance the transduction efficiency of diluted AAV13-585-7m8 with that of undiluted AAV13-587-7m8. AAV13-585-7m8-CMV-EGFP and AAV13-587-7m8-CMV-EGFP were respectively injected into layer 4 of the SSp (Figure 5D). Three weeks post-injection, the mice were perfused and their brain tissues were sampled, sectioned, and imaged (Figure 5E). Calculating the effective area with fluorescence expression in the injection region, we found that even after two-fold dilution, the diffusion range of AAV13-585-7m8 remained larger than that of AAV13-587-7m8 (Figure 5F, $P=0.0030$). Additionally, assessing average fluorescence intensity within the effective range showed that the average fluorescence intensity of AAV13-585-7m8 was weaker than that of AAV13-587-7m8 (Figure 5G, $P=0.0005$). These results indicate that AAV13-587-7m8 is more suitable for gene delivery in small-volume brain regions.

**AAV13-587-7m8 is suitable for sparsely labeling neurons**

To verify whether AAV can be used for sparse labeling of neurons, we employed a dual viral vector strategy utilizing the Cre-*lox* recombinant enzyme system to control the expression of fluorescent genes driven by a strong promoter (Nagy,

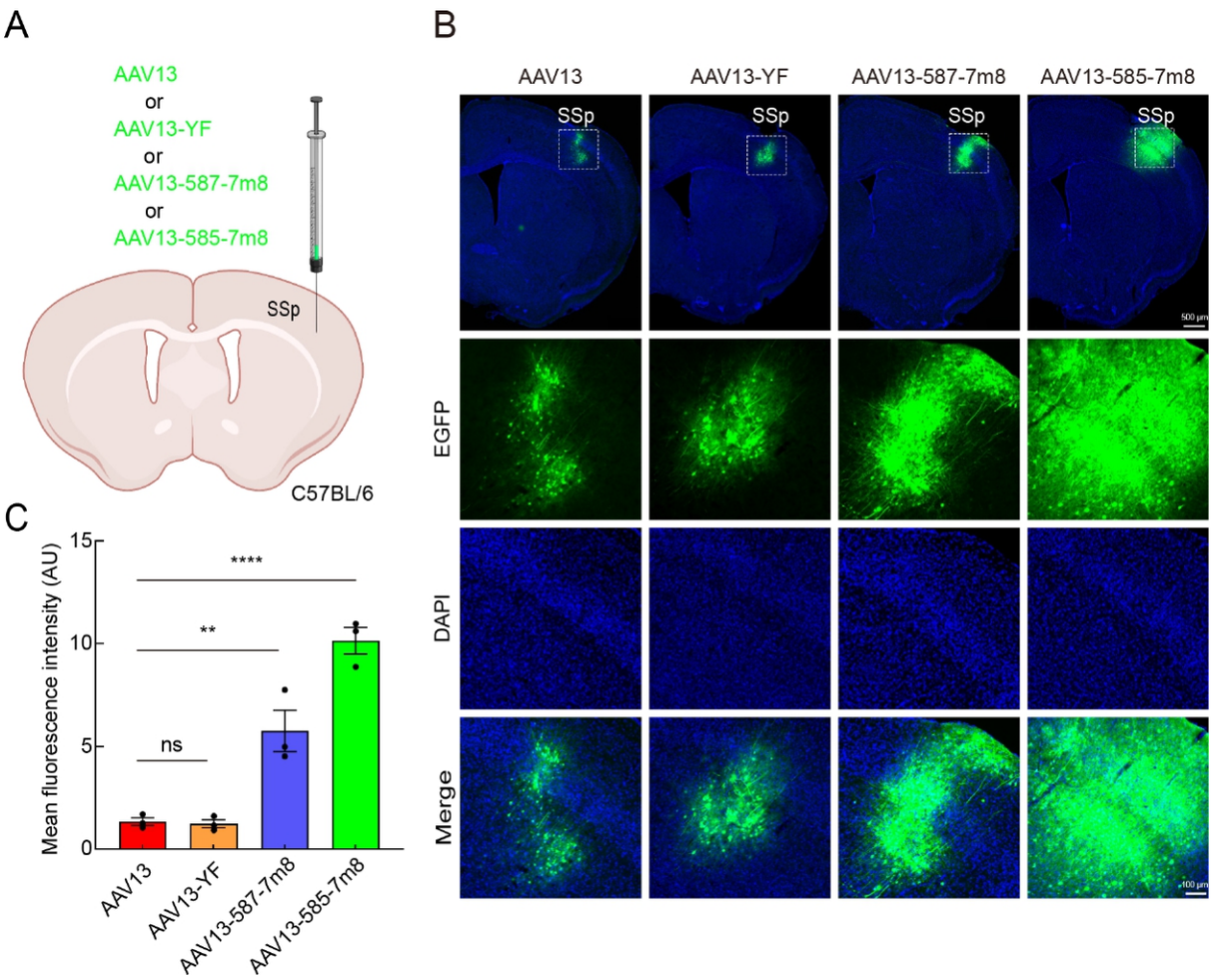



**Figure 3 Characterization of transduction properties of engineered variants in the cortex**

A: Schematic of virus injection. AAV13-CMV-EGFP, AAV13-YF-CMV-EGFP, AAV13-587-7m8-CMV-EGFP, and AAV13-585-7m8-CMV-EGFP viruses ($2\times10^9$ VG) were individually injected into the SSp of C57BL/6 mice. B: Fluorescence distribution of EGFP in the SSp. AAV13-CMV-EGFP, AAV13-YF-CMV-EGFP, AAV13-587-7m8-CMV-EGFP, and AAV13-585-7m8-CMV-EGFP viruses (200 nL, $2\times10^9$ VG in total) were separately injected into the SSp of C57BL/6 mice ($n$=3 in each group, $n$=12 in total). C: Quantification of mean fluorescence intensities of EGFP in the SSp after transduction with different AAVs. Values represent mean±SEM, $n$=3/group. Statistical analyses were completed using one-way ANOVA followed by Tukey's multiple comparisons test with an alpha value of 0.05. ns: Not significant; **: $P$<0.01; ****: $P$<0.0001. Schematics in Figure 3A were created with BioRender.com.

2000). The working principle of the dual virus labeling strategy is illustrated in Figure 6A. AAV9, known for its efficient neuron infection and high gene expression levels, was used in conjunction with AAV13-hSyn-Cre and AAV13-587-7m8-hSyn-Cre as "controllers". These were separately mixed with AAV9-CAG-DIO-EGFP and injected into the MOp of C57BL/6 mice (Figure 6B). When AAV13-hSyn-Cre and AAV13-587-7m8-hSyn-Cre were diluted 1 000-fold, only a few sparse neurons were labeled (Figure 6C). However, the experimental group injected with AAV13-587-7m8-hSyn-Cre was still able to efficiently label more cells in the MOp of C57BL/6 mice (Figure 6D, $P$=0.0183). These results indicate that AAV13-587-7m8 is effective for the sparse labeling of neurons, achieving a higher number of labeled neurons compared to AAV13 and suggesting it can achieve the desired sparse labeling effect even at lower doses.

## DISCUSSION

This study focused on the rational design-based modification of AAV13. Initially, tyrosine residues at positions 443 and 728 on the AAV13 capsid were mutated to phenylalanine (Y-F). The rationale behind this approach was based on the fact that proteasome inhibitors can enhance AAV transduction both *in vitro* and *in vivo* (Nakahama et al., 2022; Zhong et al., 2008), suggesting that modification of the AAV capsid to reduce ubiquitination may help AAV viral particles avoid proteasome-mediated cytoplasmic degradation. Specifically, mutating surface-exposed tyrosine residues on the AAV2 capsid prevents phosphorylation, subsequent ubiquitination, and proteasome-mediated degradation, thereby improving transgene expression efficiency (Nakahama et al., 2022; Zhong et al., 2008). Our constructed AAV13-YF variant exhibited higher transduction efficiency in HEK293T cells *in vitro* compared to AAV13. However, there was no marked improvement in the infection efficiency of AAV13-YF in neurons within the mouse CNS, possibly because there was no significant enhancement in its ability to enter neurons or in its ability to inhibit intracellular proteasome degradation.

Secondly, we inserted the 7m8 peptide (LALGETTRPA), which enhances cell transduction, between amino acids 585/586 and 587/588 of AAV13. This peptide was derived from previous research, in which an engineered AAV variant,

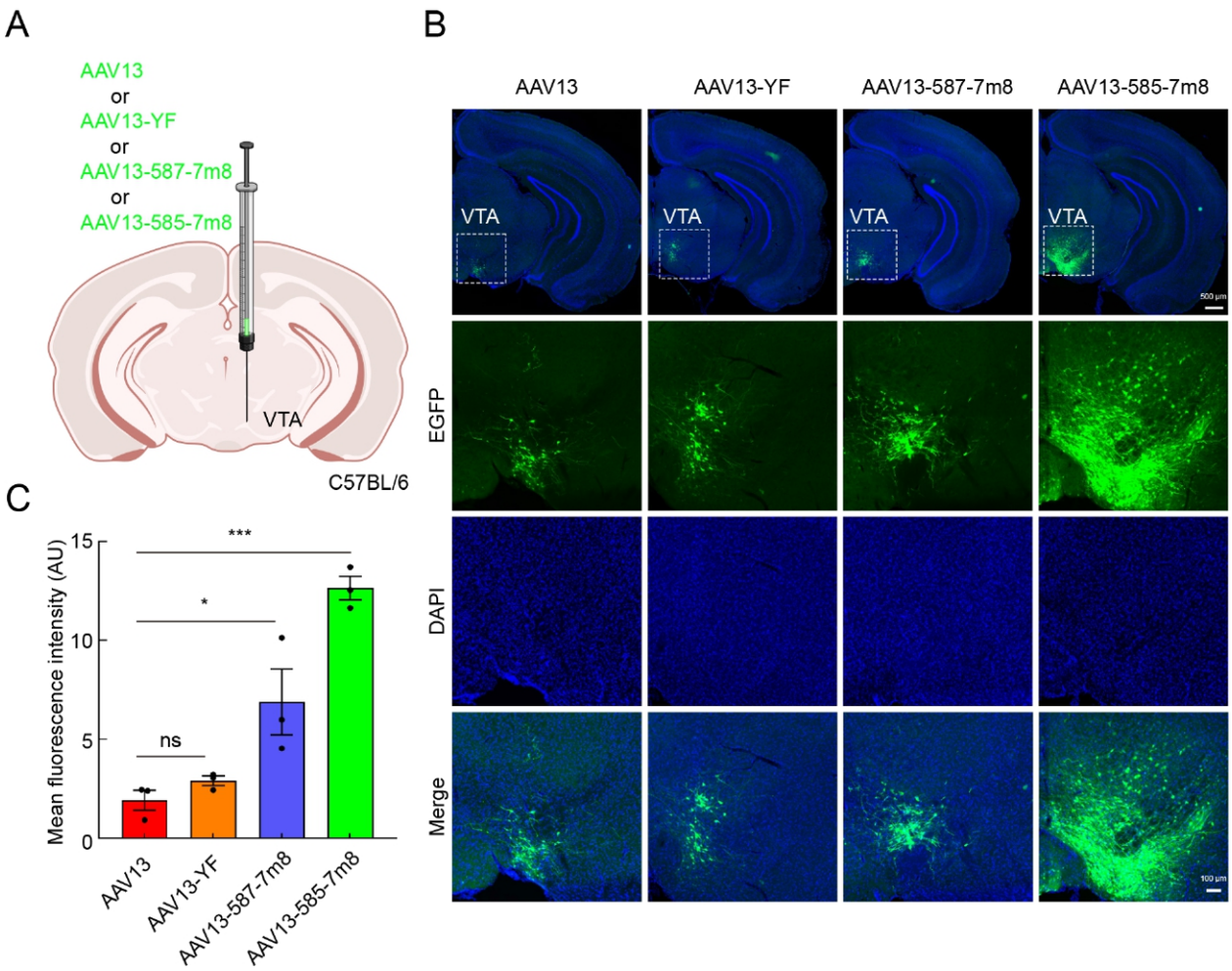



**Figure 4 Characterization of transduction properties of engineered variants in the subcortical brain area**

A: Schematic of virus injection. AAV13-CMV-EGFP, AAV13-YF-CMV-EGFP, AAV13-587-7m8-CMV-EGFP, and AAV13-585-7m8-CMV-EGFP viruses ($2\times10^9$ VG) were individually injected into the VTA of C57BL/6 mice. B: Fluorescence distribution of EGFP in the VTA. AAV13-CMV-EGFP, AAV13-YF-CMV-EGFP, AAV13-587-7m8-CMV-EGFP, and AAV13-587-7m8-CMV-EGFP viruses (200 nL, $2\times10^9$ VG in total) were respectively injected into the VTA of C57BL/6 mice ($n$=3 in each group, $n$=12 in total). C: Quantification of mean fluorescence intensities of EGFP in the VTA after transduction with different AAVs *in vivo*. Values represent mean±SEM, $n$=3/group. Statistical analyses were completed using one-way ANOVA followed by Tukey's multiple comparisons test with an alpha value of 0.05. ns: Not significant; $^*$: $P$<0.05; $^{***}$: $P$<0.001. Schematics in Figure 4A were created with BioRender.com.

AAV2-7m8, was developed with stronger retinal targeting abilities than its parental AAV2 serotype via modification at the trimerization site of the AAV2 capsid protein (Dalkara et al., 2013). Subsequent research showed that although the insertion of the 7m8 peptide increased the gene expression abundance in AAV2-7m8, it did not change its diffusion range compared to the parental AAV2 serotype (Khabou et al., 2016). Here, the AAV13-585-7m8 and AAV13-587-7m8 constructs exhibited lower transduction efficiency in HEK293T cells *in vitro* compared to AAV13. This may be due to the insertion site of the peptide disrupting the critical binding structure of AAV13 with HEK293T cells. However, in the CNS, AAV13-585-7m8 and AAV13-587-7m8 demonstrated an enhanced ability to infect neurons compared to AAV13, with AAV13-587-7m8 maintaining a relatively limited diffusion range. This could be because the two serotypes recognize different receptors for viral entry, and receptor expression varies across brain regions, or because they have different binding abilities with the same receptor. This finding is significant, indicating that these two positions in AAV13 offer different potentials and capabilities for engineering modifications.

We integrated a point mutation strategy with a peptide insertion strategy to investigate changes in transduction efficiency, leading to the construction of AAV13-587-7m8-YF. When injected into the SSP, AAV13-587-7m8-YF showed significantly weaker neuronal transduction ability compared to AAV13-587-7m8 (Supplementary Figure S2), indicating the need for further study of the mechanisms underlying this phenomenon.

Although AAV13-585-7m8 exhibited a much larger diffusion range in the CNS than AAV13, its transduction ability was significantly improved, making it suitable for gene delivery in large brain nuclei, such as the VTA. Conversely, AAV13-587-7m8 achieved the same labeling effects and gene delivery efficiency in small brain nuclei as AAV13 but at a lower dose or smaller volume. This reduction in viral dose decreases potential neuronal toxicity and minimizes the immune response. Even at high dilution ratios and using a dual virus labeling strategy, AAV13-587-7m8 maintained stronger *in vivo* transduction capabilities than AAV13, making it effective for sparse neuronal labeling. Using the protein structure

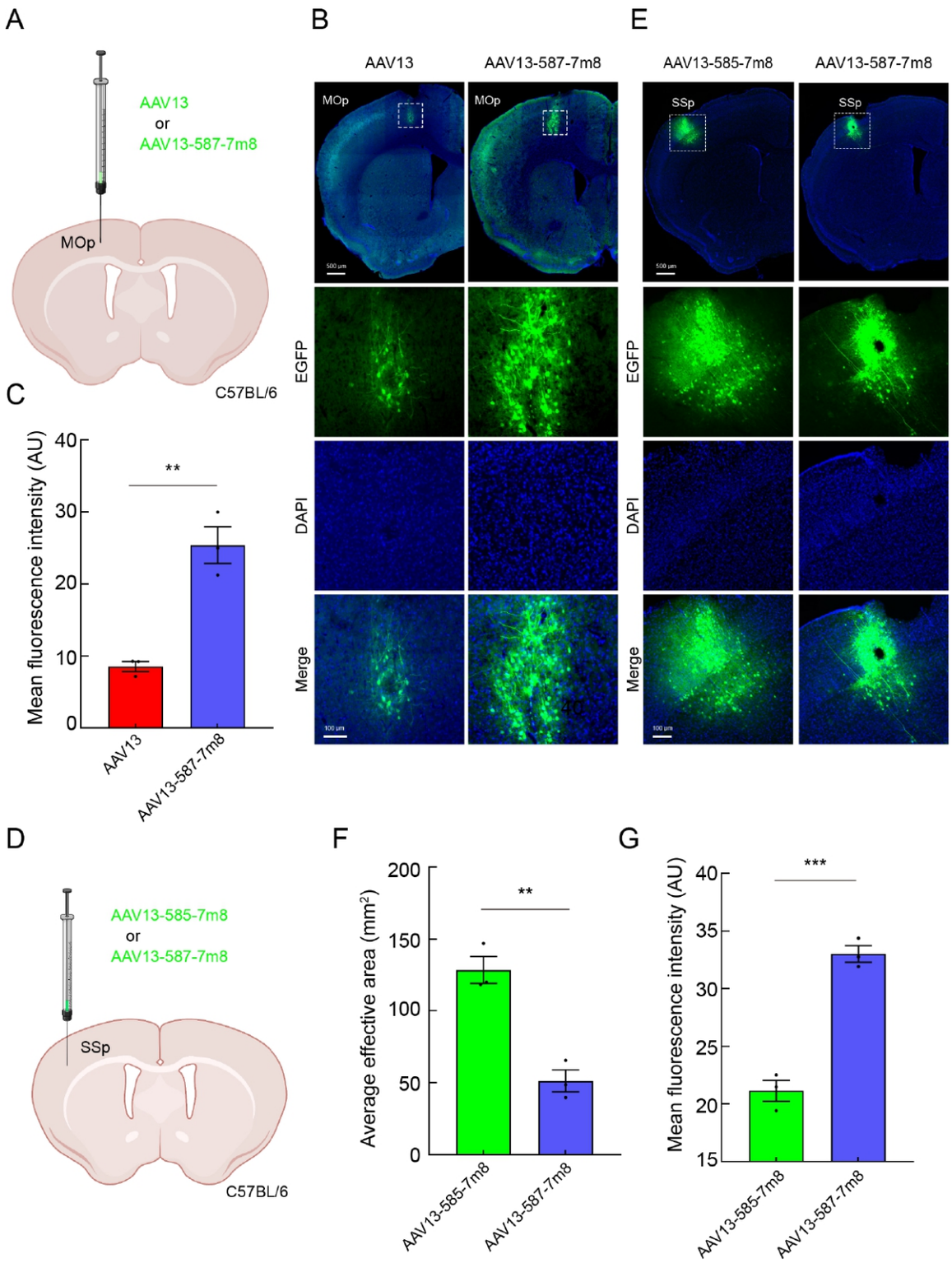



**Figure 5 AAV13-587-7m8 permits efficient *in situ* transduction at low doses**

A: Schematic of single-viral vector injection in the MOp. AAV13-CMV-EGFP and AAV13-587-7m8-CMV-EGFP ($2.5\times10^8$ VG) were individually injected into the MOp region of C57BL/6 mice. B: Fluorescence distribution of EGFP in the MOp by single-viral labeling at low doses. Compared with AAV13, AAV13-587-7m8 achieved stronger fluorescence expression at a reduced injection dose. C: Quantification of mean fluorescence intensities of EGFP in the MOp after transduction with different AAVs at lower injection doses. D: Schematic comparing transduction efficiency between reduced quantities of AAV13-585-7m8 and AAV13-587-7m8. AAV13-585-7m8-CMV-EGFP (200 nL, $1\times10^9$ VG in total) and AAV13-587-7m8-CMV-EGFP viruses (200 nL, $2\times10^9$ VG in total) were separately injected into the SSp of C57BL/6 mice ($n$=3 in each group, $n$=6 in total). E: Fluorescence distribution of EGFP in the SSp. AAV13-585-7m8 was diluted two-fold. F: Quantitative statistics of average effective range of fluorescence expression after *in situ* injection of two viruses. G: Quantitative statistics of average fluorescence intensity within the effective range after *in situ* injection of two viruses. Values represent mean±SEM, $n$=3/group. Statistical analyses were completed using unpaired two-tailed Student's $t$-test with an alpha value of 0.05. $^{**}$: $P$<0.01; $^{***}$: $P$<0.001. Schematics in Figure 5A and 5D were created with BioRender.com.

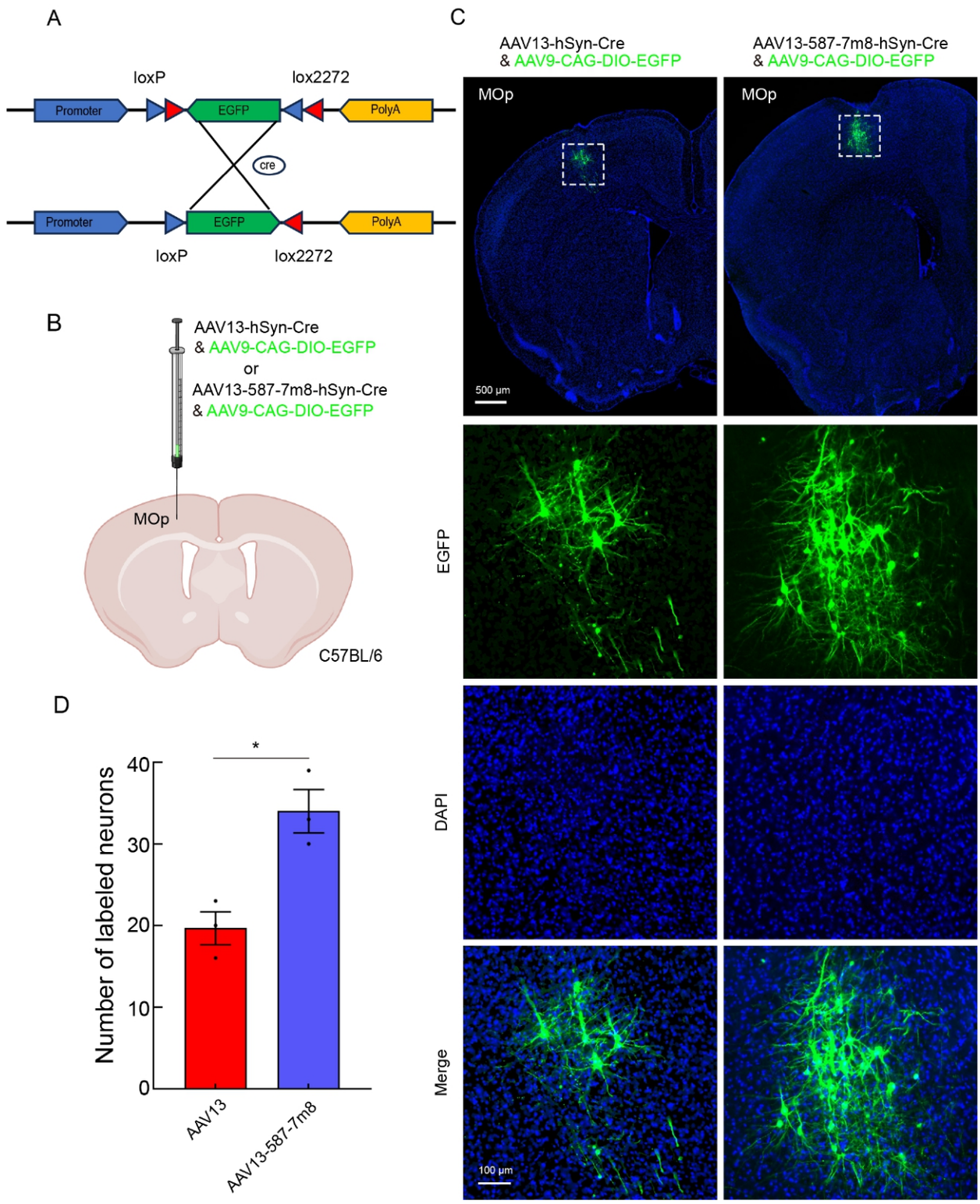



**Figure 6 AAV13-587-7m8 permits efficient sparse labeling of neurons**

A: Schematic of working principle of the Cre-*lox* system. B: Schematic of dual-viral vector injection in the MOp. AAV13-hSyn-Cre ($1\times10^6$ VG) mixed with AAV9-CAG-DIO-EGFP ($5\times10^8$ VG) or AAV13-587-7m8-hSyn-Cre ($1\times10^6$ VG) mixed with AAV9-CAG-DIO-EGFP ($5\times10^8$ VG) was injected into the MOp region of C57BL/6 mice. C: Fluorescence distribution of EGFP in the MOp by dual-viral labeling strategy. Compared with AAV13, AAV13-587-7m8 more efficiently transduced neurons to deliver target genes under high dilution conditions. D: Quantitative analysis of sparse labeling of neurons. Values represent mean±SEM, *n*=3/group. Statistical analyses were completed using unpaired two-tailed Student's *t*-test with an alpha value of 0.05. *: $P<0.05$. Schematics in Figure 6B were created with BioRender.com.

prediction tool ColabFold, we predicted the monomer structures of AAV13, AAV13-YF, AAV13-587-7m8, and AAV13-585-7m8, and compared these structures using UCSF ChimeraX. Results showed that the structure of AAV13 completely overlapped with AAV13-YF, whereas AAV13-587-7m8 and AAV13-585-7m8 showed structural differences at the

trimerization site, explaining the differences in their properties (Supplementary Figure S3).

In conclusion, our preliminary exploration of AAV13 capsid protein modification indicates that AAV13-585-7m8 and AAV13-587-7m8 are effective for *in situ* gene delivery in the CNS. Further experiments are needed to explore other characteristics of these two viral vectors, such as their transduction efficiency in the retina and other brain regions. This rational design strategy, involving peptide insertions, can be applied to modify other natural AAV serotypes to meet the demands of advancing neuroscience and gene therapy.

## SUPPLEMENTARY DATA

Supplementary data to this article can be found online.

## COMPETING INTERESTS

The authors declare that they have no competing interests.

## AUTHORS' CONTRIBUTIONS

K.L. and F.X. contributed to the study idea and design; F.X. and J.W. contributed to funding acquisition and resources; N.L., Y.C., Z.H., X.S., W.Y., Z.Z., and H.G. performed the experiments and data acquisition; N.L., Z.H., and K.L. conducted data analyses; N.L., Z.H., K.L., and F.X. drafted the manuscript, and contributed to review and editing. All authors read and approved the final version of the manuscript.

## REFERENCES


Aschauer DF, Kreuz S, Rumpel S. 2013. Analysis of transduction efficiency, tropism and axonal transport of AAV serotypes 1, 2, 5, 6, 8 and 9 in the mouse brain. *PLoS One*, **8**(9): e76310.

Challis RC, Ravindra Kumar S, Chen XH, et al. 2022. Adeno-associated virus toolkit to target diverse brain cells. *Annual Review of Neuroscience*, **45**: 447–469.

Chan KY, Jang MJ, Yoo BB, et al. 2017. Engineered AAVs for efficient noninvasive gene delivery to the central and peripheral nervous systems. *Nature Neuroscience*, **20**(8): 1172–1179.

Dalkara D, Byrne LC, Klimczak RR, et al. 2013. In vivo-directed evolution of a new adeno-associated virus for therapeutic outer retinal gene delivery from the vitreous. *Science Translational Medicine*, **5**(189): 189ra76.

Duarte Azevedo M, Sander S, Jeanneret C, et al. 2021. Selective targeting of striatal parvalbumin-expressing interneurons for transgene delivery. *Journal of Neuroscience Methods*, **354**: 109105.

Fripont S, Marneffe C, Marino M, et al. 2019. Production, purification, and quality control for adeno-associated virus-based vectors. *Journal of Visualized Experiments*, (143), doi: 10.3791/58960.

Goddard TD, Huang CC, Meng EC, et al. 2018. UCSF ChimeraX: meeting modern challenges in visualization and analysis. *Protein Science*, **27**(1): 14–25.

Goertsen D, Flytzanis NC, Goeden N, et al. 2022. AAV capsid variants with brain-wide transgene expression and decreased liver targeting after intravenous delivery in mouse and marmoset. *Nature Neuroscience*, **25**(1): 106–115.

Haery L, Deverman BE, Matho KS, et al. 2019. Adeno-associated virus technologies and methods for targeted neuronal manipulation. *Frontiers in Neuroanatomy*, **13**: 93.

Han ZP, Luo NS, Ma WY, et al. 2023. AAV11 enables efficient retrograde targeting of projection neurons and enhances astrocyte-directed transduction. *Nature Communications*, **14**(1): 3792.

Han ZP, Luo NS, Wu Y, et al. 2022. AAV13 enables precise targeting of local neural populations. *International Journal of Molecular Sciences*, **23**(21): 12806.

Khabou H, Desrosiers M, Winckler C, et al. 2016. Insight into the mechanisms of enhanced retinal transduction by the engineered AAV2 capsid variant -7m8. *Biotechnology and Bioengineering*, **113**(12): 2712–2724.

Lin KZ, Zhong X, Li L, et al. 2020. AAV9-Retro mediates efficient transduction with axon terminal absorption and blood-brain barrier transportation. *Molecular Brain*, **13**(1): 138.

Lykken EA, Shyng C, Edwards RJ, et al. 2018. Recent progress and considerations for AAV gene therapies targeting the central nervous system. *Journal of Neurodevelopmental Disorders*, **10**(1): 16.

Mendell JR, Al-Zaidy SA, Rodino-Klapac LR, et al. 2021. Current clinical applications of *in vivo* gene therapy with AAVs. *Molecular Therapy*, **29**(2): 464–488.

Mietzsch M, Jose A, Chipman P, et al. 2021. Completion of the AAV structural atlas: serotype capsid structures reveals clade-specific features. *Viruses*, **13**(1): 101.

Nagy A. 2000. Cre recombinase: the universal reagent for genome tailoring. *Genesis*, **26**(2): 99–109.

Nakahama R, Saito A, Nobe S, et al. 2022. The tyrosine capsid mutations on retrograde adeno-associated virus accelerates gene transduction efficiency. *Molecular Brain*, **15**(1): 70.

Ojala DS, Amara DP, Schaffer DV. 2015. Adeno-associated virus vectors and neurological gene therapy. *The Neuroscientist*, **21**(1): 84–98.

Paxinos G, Franklin KBJ. 2013. The Mouse Brain in Stereotaxic Coordinates. Amsterdam: Elsevier.

Pettersen EF, Goddard TD, Huang CC, et al. 2021. UCSF ChimeraX: structure visualization for researchers, educators, and developers. *Protein Science*, **30**(1): 70–82.

Srivastava A. 2016. *In vivo* tissue-tropism of adeno-associated viral vectors. *Current Opinion in Virology*, **21**: 75–80.

Tervo DGR, Hwang BY, Viswanathan S, et al. 2016. A designer AAV variant permits efficient retrograde access to projection neurons. *Neuron*, **92**(2): 372–382.

Wang D, Tai PWL, Gao GP. 2019. Adeno-associated virus vector as a platform for gene therapy delivery. *Nature Reviews Drug Discovery*, **18**(5): 358–378.

Watakabe A, Ohtsuka M, Kinoshita M, et al. 2015. Comparative analyses of adeno-associated viral vector serotypes 1, 2, 5, 8 and 9 in marmoset, mouse and macaque cerebral cortex. *Neuroscience Research*, **93**: 144–157.

Yao YZ, Wang J, Liu Y, et al. 2022. Variants of the adeno-associated virus serotype 9 with enhanced penetration of the blood-brain barrier in rodents and primates. *Nature Biomedical Engineering*, **6**(11): 1257–1271.

Zheng R, Zhang DX, Shao YJ, et al. 2023. Multiplex gene editing reduces oxalate production in primary hyperoxaluria type 1. *Zoological Research*, **44**(6): 993–1002.

Zhong L, Li BZ, Jayandharan G, et al. 2008. Tyrosine-phosphorylation of AAV2 vectors and its consequences on viral intracellular trafficking and transgene expression. *Virology*, **381**(2): 194–202.

Zingg B, Chou XL, Zhang ZG, et al. 2017. AAV-mediated anterograde transsynaptic tagging: mapping corticocollicular input-defined neural pathways for defense behaviors. *Neuron*, **93**(1): 33–47.

Li et al. *Zool. Res.* 2024, 45(4): 791−804
https://doi.org/10.24272/j.issn.2095-8137.2023.369

ZR | Zoological Research

Article Open Access

# Metabolomic-based analysis reveals bile acid-mediated ovarian failure induced by low temperature in zebrafish

Wen-Hao Li[1,2,3,#], Zhi-Qiang Li[1,3,#], Meng-Di Bu[1,3,#], Jia-Zhen Li[1,3], Liang-Biao Chen[1,3,*]

[1] *Key Laboratory of Exploration and Utilization of Aquatic Genetic Resources*, *Ministry of Education*, *College of Fisheries and Life Sciences*, *Shanghai Ocean University*, *Shanghai* 201306, *China*

[2] *Laboratory for Marine Biology and Biotechnology*, *Qingdao National Laboratory for Marine Science and Technology*, *Qingdao*, *Shandong* 266237, *China*

[3] *International Research Center for Marine Biosciences*, *Ministry of Science and Technology*, *College of Fisheries and Life Sciences*, *Shanghai Ocean University*, *Shanghai* 201306, *China*

## ABSTRACT

As ectotherms, fish are highly sensitive to temperature fluctuations, which can profoundly impact their reproductive cycles. In this study, we investigated the fertility and histological characteristics of zebrafish (*Danio rerio*) ovaries exposed to a temperature gradient ranging from the thermopreferendum temperature of the species, 27°C, to lower temperatures of 22°C, 20°C, and 13°C over a period of two weeks. Comparative metabolomic (six biological replicates for each temperature) and transcriptomic (four biological replicates for each temperature) analyses were conducted under the four temperature conditions. Results indicated that lower temperatures inhibited oocyte development and differential metabolites were involved in steroid hormone production, antioxidant function, and lipid and protein catabolism. Disrupted reproductive hormones, increased proteolysis, and lipid degradation significantly impeded oocyte development and egg maturation. Notably, a significant increase in bile acid content was noted in the ovaries of the cold-treated fish, indicating that bile acids play a critical role in ovarian failure. Overall, these findings provide valuable insights into the mechanisms governing the reproductive response of fish to cold stress.

**Keywords:** Cold stress; Ovarian failure; Metabolome; Zebrafish

## INTRODUCTION

Reproductive performance in fish is closely associated with the economic outcomes of aquaculture (Gjerde, 1986). Cold temperatures present a major challenge in completing the reproductive cycles for many farmed species, such as tilapia (*Oreochromis niloticus*) and largemouth bass (*Micropterus salmoides*). The inhibition of reproduction due to cold temperatures not only prolongs the farming period but also negatively impacts the quality and quantity of spawned eggs, leading to higher larval mortality and lower productivity (El-Naggar et al., 2000; Islam et al., 2022). Studying how the reproductive system responds to cold temperatures provides crucial biological insights for enhancing reproductive performance in fish aquaculture. Temperature strongly influences animal survival and reproduction (Alix et al., 2020; Ou et al., 2018), particularly in poikilothermic animals such as fish (Dahlke et al., 2020; Hu et al., 2015). As fish cannot regulate their body temperature internally, they are heavily reliant on their surrounding environment for thermoregulation (Lushchak, 2011). Genomic (Chen et al., 2008, 2019), transcriptomic (Chen et al., 2008; Hu et al., 2015, 2016; Long et al., 2013; Windisch et al., 2011), and epigenomic (Campos et al., 2013; Han et al., 2016) analyses have been instrumental in unraveling the genetic networks associated with the response of fish to cold stress. Prior studies on cold-induced apoptosis in fish have shown that different tissues respond variably to cold stress, with gill and kidney tissues exhibiting higher sensitivity to critical thermal limits (Hu et al., 2016; Wang et al., 2023). When ambient temperatures drop below the preferred thermal range for fish, female gamete production may be inhibited. Spawning adults, like developing embryos, represent the most temperature-sensitive life stage (Dahlke et al., 2020), with thermal fertility limits (TFLs) typically preceding critical thermal limits (CTLs) (Parratt et al., 2021). This can result in significant damage to the ovaries, leading to infertility in many species, even if other tissues are not notably affected (Servili et al., 2020). Even mild non-life-

This is an open-access article distributed under the terms of the Creative Commons Attribution Non-Commercial License (http://creativecommons.org/licenses/by-nc/4.0/), which permits unrestricted non-commercial use, distribution, and reproduction in any medium, provided the original work is properly cited.

Copyright ©2024 Editorial Office of Zoological Research, Kunming Institute of Zoology, Chinese Academy of Sciences

Received: 18 February 2024; Accepted: 11 March 2024; Online: 12 March 2024

Foundation items: This work was supported by the National Natural Science Foundation of China (32130109) and Open Project Fund from Laboratory for Marine Biology and Biotechnology, Qingdao National Laboratory for Marine Science (OF2019NO01)

[#]Authors contributed equally to this work

*Corresponding author, E-mail: lbchen@shou.edu.cn

threatening temperature changes can disturb fish reproduction (Dahlke et al., 2020).

As fish evolved and underwent adaptive radiation, they expanded from equatorial to polar regions, with each species developing optimal reproductive temperatures (Donelson et al., 2010; Kock, 1992; Lopes et al., 2020). The thermal sensitivity of fish ovaries varies markedly among tropical, temperate, and polar species (Van Der Kraak & Pankhurst, 1997). At their optimal temperatures, vertebrates maintain body temperatures that closely align with their metabolic and reproductive optima (Kennedy & Mihursky, 1967). In adverse conditions, organisms can adapt through their stress response system, which comprises a set of physiological responses enabling survival while sacrificing energy-intensive functions such as reproduction (Barton, 2002). Cold stress (18°C or 10°C for 48h) results in the dysregulation of multiple genes associated with reproduction in female zebrafish, leading to ovarian damage (Zhao et al., 2023). However, the physiological mechanisms underlying the effects of "cold noxious" temperatures on fish ovaries, especially in gradient cold temperatures, remains largely unknown.

Metabolomic adjustments are fundamental for fish adaptation to environmental stress, primarily attributable to stress-induced coordinated genetic and epigenetic reprograming (Liu et al., 2022b). Previous gas chromatography-time-of-flight mass spectrometry (GC-TOF-MS)-based metabolomic analyses found that metabolites involved in energy metabolism and basic amino acids increased significantly in black rockfish (*Sebastes schlegelii*) exposed to acute high thermal stress (27°C for 12 h), while certain fatty acids increased after acute cold stress (5°C for 12 h) (Song et al., 2019). Another study using GC-MS analyzed the serum metabolic responses of Nile tilapia (*Oreochromis niloticus*) subjected to *Streptococcus agalactiae* infection at normal (25°C) and high (35°C) temperatures and found that glycolysis was inhibited and arachidonic acid consumption may be associated with mortality following high-temperature infection (Hu et al., 2020). To date, however, research on the impact of cold temperatures on metabolomic changes in the reproductive organs of fish remains limited.

The aim of this study was to identify metabolite biomarkers that respond to cold stress and assess the impact of cold stress on fish reproduction. The female reproductive system was selected to investigate ovarian impairment following 2 weeks of exposure to a cold-stress gradient, measuring fertility and histological changes. Reproductive metabolic changes and adaptations to cold were assessed in the ovaries of cold-exposed fish using a global metabolomics approach based on liquid chromatography-tandem mass spectrometry (LC-MS/MS). We identified several cold-responsive biomolecules and biomarkers in the ovary and revealed bile acid-mediated ovarian failure in cold stress.

## MATERIALS AND METHODS

### Low temperature treatment and sample preparation

The optimal temperature range for zebrafish is 26°C to 28°C (López-Olmeda & Sánchez-Vázquez, 2011), so we selected 27°C as the control group. The temperature range for zebrafish embryo development is 22°C to 34°C (Urushibata et al., 2021), so we chose 22°C as the first treatment temperature. The critical temperature determining the survival of embryonic development is 20°C (Schnurr et al., 2014), which we selected as the second treatment temperature. The critical temperature resulting in the death of most zebrafish within 24 h is 12°C (Wu et al., 2015), thus we adopted a sublethal temperature (13°C) as the third treatment temperature. After treating the zebrafish at the four different temperatures for 7 days, the histological changes were not pronounced. However, distinct phenotypic changes were observed after 14 days and a significantly reduced number of mature follicles were noted by day 30 (Supplementary Figure S1). As our objective was to observe the process of ovarian failure, we opted for a treatment duration of 14 days.

Wild-type (WT) AB strain zebrafish breeding was conducted in the laboratory of Shanghai Ocean University. Sexually mature female zebrafish (7–8 months old), cultured under normal temperatures (27°C), were transferred to tanks with four separate flow circulation systems, where water temperature could be adjusted. The selected zebrafish were uniform in weight and size. Starting at 27°C, the water temperature in three tanks was gradually cooled to 22°C, 20°C, and 13°C respectively, at a rate of 0.5°C/h, while one tank remained at 27°C. The flow circulation systems were then activated at the set temperatures, and the fish were exposed to these temperatures for 14 days under a light/dark cycle of 14 h/10 h. The four sets of fish were fed with freshly hatched *Artemia* twice daily (0900h and 1800h). Six biological replicates were established for each temperature, with each replicate containing five fish. Fish from each temperature treatment were sampled for ovarian imaging, histological analysis, and LC-MS/MS measurement. All animal experiments adhered to the guidelines of, and were approved by, the Animal Research and Ethics Committees of Shanghai Ocean University (SHOU-DW-2021-061).

### Histological analysis

The ovaries were collected and immersed in 4% paraformaldehyde (Sangon Biotech, China) overnight, with subsequent dehydration through a serial gradient of alcohol (Sangon Biotech, China) at 50%, 70%, 80%, 90%, and 100% (1 h each). The dehydrated ovaries were transferred to lemosol (Wako, Japan) to increase transparency, then immersed in paraffin for 2 h and embedded in wax blocks. The samples were sliced into 5 μm sections using a Leica microtome (Leica biosystems, Germany), dried overnight at 37°C, dewaxed in xylene, rehydrated in decreasing concentrations of ethanol (Sangon Biotech, China), washed in distilled water, and stained with hematoxylin-eosin (H&E, Beyotime, China). The sections were then dehydrated under increasing concentrations of ethanol and xylene (Sangon Biotech, China), dried in a fume hood, and mounted on glass slides with a neutral balsam (Sangon Biotech, China) mounting medium for photography using a microscope (Nikon, Japan).

### Ultra-high performance (UHP) LC-MS/MS metabolomic analysis

Fresh ovarian tissues were rapidly frozen in liquid nitrogen and stored at –80°C. Subsequently, 100 mg of each tissue sample was homogenized in liquid nitrogen, with the resulting homogenate resuspended with pre-chilled 80% methanol (ThermoFisher, USA) containing 0.1% formic acid (ThermoFisher, USA) through vigorous vortexing. The samples were then incubated on ice for 5 min and centrifuged at 15 000 ×*g* and 4°C for 20 min. The supernatant (400 μL) was further diluted to a final concentration of 53% methanol using LC-MS grade water (Merck, Germany). The resulting

samples were transferred to fresh Eppendorf tubes and subjected to centrifugation step at 15 000 ×*g* and 4°C for 20 min. Finally, the supernatant was injected into the LC-MS/MS system for analysis. Quality control (QC) samples were established by taking 10 μL of each experimental sample and mixing it evenly.

The raw data files produced by UHPLC-MS/MS were processed using Compound Discoverer v.3.1 (CD3.1, ThermoFisher, USA) to execute peak alignment, peak picking, and quantitation for each metabolite. Key parameters were configured as follows: retention time tolerance of 0.2 min; actual mass tolerance of 5 ppm; signal intensity tolerance of 30%; signal/noise ratio of 3; and minimum intensity. Following this, peak intensities were normalized to total spectral intensity. The normalized data were utilized to predict the molecular formula based on additive ions, molecular ion peaks, and fragment ions. Subsequently, peaks were matched with the mzCloud (https://www.mzcloud.org/), mzVault, and MassList databases to acquire accurate qualitative and relative quantitative results. Statistical analyses were conducted using R statistical software (v.3.4.3) and Python (v.3.5.0). In cases where data deviated from normal distribution, attempts at normalization were made using the area normalization method: metabolite original quantitative value/(sum of metabolite quantitative values in sample/sum of metabolite quantitative values in QC1).

After metabolomic data transformation using metaX package in R, principal component analysis (PCA) and partial least squares discriminant analysis (PLS-DA) were performed. Metabolites with coefficients of variance (CV) less than 0.3 were retained through filtering. Three sets of differential metabolite data, namely 27°C vs. 22°C, 27°C vs. 20°C, and 27°C vs. 13°C, were screened using the NovoMagic platform (https://magic.novogene.com/). Differential metabolites (DMs) were screened based on a variable importance for projection (VIP) score>1, $P$<0.05, and fold-change>1.5 or <0.67. Metabolites were annotated using the Kyoto Encyclopedia of Genes and Genomes database (KEGG; https://www.genome.jp/kegg/pathway.html), Human Metabolome Database (HMDB; https://hmdb.ca/metabolites), and LIPID MAPS database (https://lipidmaps.org).

**Metabolite enrichment**

The KEGG database in MetaboAnalyst (https://www.metaboanalyst.ca/MetaboAnalyst/upload/EnrichUploadView.xhtml) was used to perform enrichment analyses of all differential metabolites obtained from LC-MS/MS. Subsequently, the ggplot2 package in R was used to generate a bubble plot for metabolic pathways with $P$<0.05.

**Soft clustering analysis**

Clustering analysis was conducted to investigate differentially expressed metabolites using the Mfuzz package. The Fuzzy C-Means (FCM) clustering algorithm, a component of the package, employs soft partition clustering, which requires two primary parameters (c=number of clusters, m=fuzzification parameter). The iterative refinement procedure was used to determine the optimal values of c and m, calculated to be 16 and Mestimate (data), respectively.

**Transcriptome analysis**

Total RNA was extracted using TRIzol reagent (Sigma-Aldrich, USA). Strand-specific RNA-seq libraries were prepared using the VAHTS Stranded mRNA-seq Library Prep Kit for Illumina v.2 (Vazyme Biotech, China) and subjected to 150 bp paired-end sequencing on the Illumina NovaSeq 6000 platform (USA). Trimmomatic (v.0.36) was employed to remove low-quality reads and sequencing adapters, followed by clean read alignment to the zebrafish reference genome GRCz11 (v.106) using STAR (v.2.7.10a). Read counts for each gene were calculated using featureCounts (v.2.0.1). Finally, fragments per kilobase million (FPKM) values for each gene were obtained using DESeq2.

**Correlation analysis of transcriptomic and metabolomic data**

To assess the concordance of changes between the transcriptome and metabolome, Pearson correlation analysis was performed between differentially expressed genes in the transcriptome and metabolites in the metabolome. First, genes with significant changes from the transcriptome data were identified. Subsequently, Pearson correlation coefficients and $P$-values between the selected genes and target metabolites were calculated. The Benjamini-Hochberg method was applied for multiple testing correction using the $P$-adjust function in R to control the false discovery rate (FDR). Genes with adjusted $P$-values less than 0.05 and functionally relevant to the target metabolites were selected, and Pearson correlation coefficients were used for visualization. The corrplot package in R was used to present the correlation plots.

**Glycodeoxycholic acid (GDCA) treatment**

Adult female zebrafish (7–8 months old), without any abnormal temperature treatment, were maintained at 27°C in tanks with 10 L of filtered water. Subsequently, 40 mg of GDCA hydrate (Xianding Biotechnology, China, B-HI304) dissolved in 400 μL of dimethyl sulfoxide (DMSO, Sangon Biotech, China) was added to 1 L of water (40 mg/L), while 400 μL of DMSO without GDCA was added to 1 L of water for the control group. The selection of 40 mg/L GDCA for zebrafish treatment was based on assays showing that total bile acids can reach 20–25 mg/L in human plasma under bile metabolic disorders (Roy-Chowdhury et al., 2020) and serum bile acid content can exceed 100 mg/L in cases of obstructive jaundice (Song & Kew, 1983). In addition, previous experiments have demonstrated no negative impact on zebrafish survival at a concentration of 40 mg/L GDCA (Liu et al., 2022a). During GDCA treatment, half of the water was replaced with fresh, filtered water daily. The diel rhythm, temperature, and GDCA concentration were maintained for 14 days. Three replicates, each containing 10 fish, were conducted.

## RESULTS

**Low temperature disrupted oocyte development**

Adult female zebrafish were exposed to four different temperatures for two weeks, representing normal (27°C), mild (22°C and 20°C), and severe (13°C) cold stress conditions. Cold stress altered ovarian histology, as revealed by H&E staining of ovarian sections (Figure 1). At 27°C, the ovaries were well-developed, with a high proportion of mature oocytes and yolk-filled eggs. A similar histological appearance was found in the ovaries of fish acclimated to 22°C, with a slightly reduced percentage of maturing eggs and overall ovary size compared to the normal group. However, when the treatment temperature decreased to 20°C, the percentage of immature

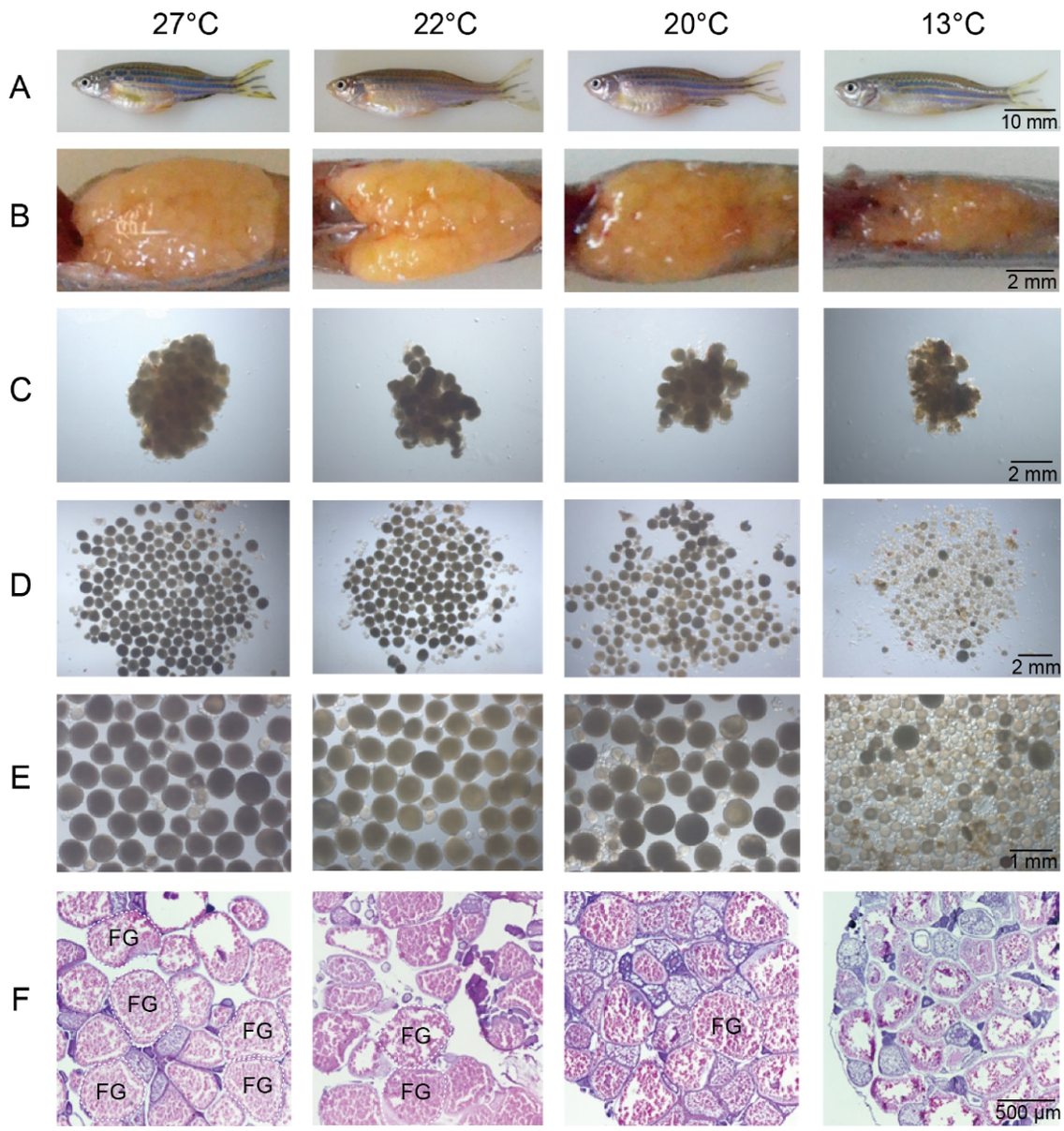



**Figure 1 Morphology of ovaries and eggs in zebrafish acclimated to different cold temperatures**

Zebrafish and their ovaries were examined after 14 days of exposure to four different temperature treatments. A: Appearance of zebrafish exposed to four different temperatures. B: Morphological appearance of ovaries from fish exposed to different temperatures. C: Central region of ovary was extracted using forceps and photographed under a ZEISS microscope (ZEISS, Germany) (12.5×). D, E: Retrieved ovaries were dispersed using a pipette and imaged under the same ZEISS microscope (10× and 25×). F: H&E-stained ovarian sections, photographed under a Nikon microscope (Nikon, Japan) (40×). FG: Fully-grown stage.

oocytes increased significantly, worsening under 13°C treatment. These results indicated that consistent cold stress compromised oocyte maturation by disrupting oocyte development. More pronounced phenotypes were achieved under 30 days of 13°C treatment, with oocyte development primarily halting at the early vitellogenic stage, and mid-vitellogenic oocytes shrinking (Supplementary Figure S1). Severe cold exposure resulted in defects in oocyte development and oogenesis in zebrafish.

**Metabolite profiling in ovaries exposed at different temperatures**

UHPLC-MS/MS was conducted to elucidate the metabolomic signature of ovaries exposed to cold stress. A total of 1 605 metabolites were identified in the ovaries of zebrafish from the four different temperature groups (Supplementary Tables S1, S2). Correlation analyses of the six QC samples based on total ion chromatograms (TIC) demonstrated high retention time and response intensity of the mass spectral peaks, indicating high stability and repeatability (Supplementary Figure S2). The PLS-DA results showed a clear separation of the 27°C group from the 13°C, 20°C, and 22°C groups, respectively. The 20°C group profile was more similar to that of the 22°C group than to the other groups (Figure 2A). These results suggested that cold temperatures exerted a significant impact on the metabolic profiles of the zebrafish ovary.

In total, 451, 449, and 515 differential metabolites were identified in the 22°C vs. 27°C, 20°C vs. 27°C, and 13°C vs. 27°C comparisons, respectively (Supplementary Table S3). Venn plot analysis revealed 101 up-regulated and 49 down-regulated metabolites common to all three comparisons (Figure 2B). The up-regulated differential metabolites were

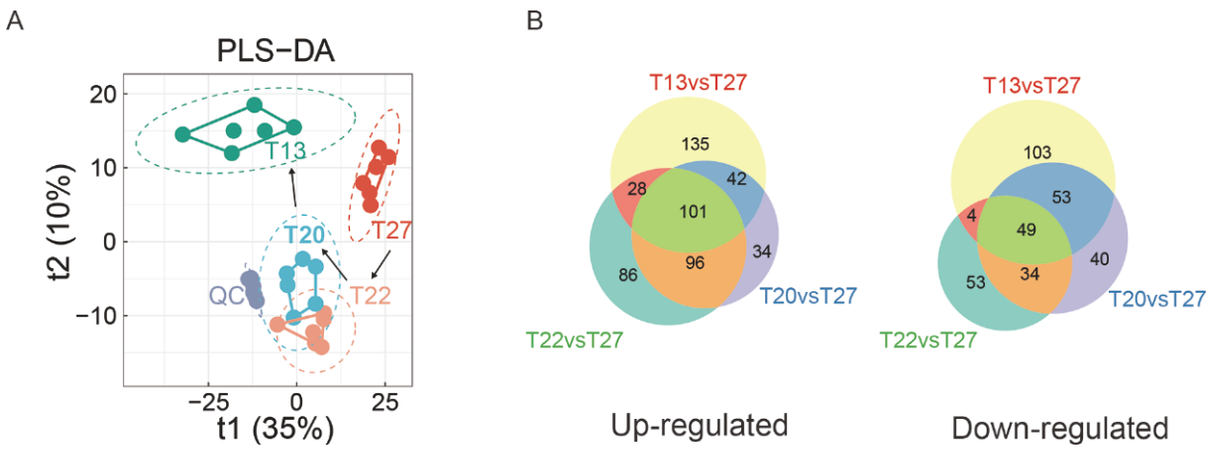



**Figure 2 Metabolite screening**

A: PLS-DA was performed on ovarian metabolome of zebrafish treated for 14 days at 27°C, 22°C, 20°C, and 13°C. B: Venn diagram of up-regulated or down-regulated metabolites in 13°C vs. 27°C, 20°C vs. 27°C, and 22°C vs. 27°C comparisons and their overlap. In total, 101 up-regulated and 49 down-regulated metabolites were identified.

enriched in androgens, bile acids, and protein derived metabolites (i.e., amino acids and dipeptides), while the down-regulated differential metabolites were enriched in molecular functions such as antioxidants and the neuroendocrine factor epinephrine (Supplementary Table S4). Furthermore, specifically increased metabolites in the 13°C group revealed that several amino acids were significantly up-regulated at this temperature (Supplementary Figure S3).

KEGG enrichment analysis identified 15 differential metabolic pathways (Supplementary Figure S4), including pathways related to antioxidant metabolism (e.g., glutathione metabolism), steroid metabolism (e.g., steroid hormone biosynthesis), and amino acid metabolism pathways (e.g., arginine biosynthesis and glycine, serine, and threonine metabolism).

Utilizing the Mfuzz R package, metabolites were clustered to reflect change trends with decreasing temperatures, yielding 16 clusters (Figure 3). Clusters 2, 4, 10, and 14 exhibited the opposite trend of change with decreasing treatment temperature (Figure 3A), while clusters 1, 5, 9, and 16 showed a gradual decreasing trend (Figure 3B), and the remaining clusters displayed irregular patterns of change (Figure 3C).

**Effects of cold stress on steroid hormones and prostaglandins (PGs)**

Tracing the biochemical pathways for synthesizing the reproductive steroid hormones, we found significant alteration of several metabolites after cold treatment (Figure 4A). Among these metabolites, pregnenolone, 5β-androstane-3,17-dione, and testosterone were generally increased with the decreasing of the exposure temperatures. However, no significant changes were found in the amount of estrone and estradiol (E2) albeit the upregulation of its precursor 5β-androstane-3,17-dione, suggesting a biased increase of male hormone testosterone in the cold stressed ovaries. Besides the upregulation of the male hormones, four types of PGs were steadily increased in the cold exposed ovaries (Figure 4B).

**Reduced anti-oxidants and increased protein and triglyceride degradation products**

A marked decrease was found in several compounds involved in oxidative stress, including S-(methyl)glutathione, L-ascorbate, reduced L-glutathione (GSH), and oxidized L-glutathione (GSSG) (Figure 5A), suggesting a reduction in anti-oxidative capacity in cold exposed ovaries. Proteolysis also increased, as evidenced from the accumulation of various dipeptides and free amino acids, such as N-glycyl-L-proline, Gly-Val, H-Gly-Pro-OH, L-alanyl-L-proline, Val-Ser, glycyl-proline, leucyl-proline, prolyl-leucine, L-threonine, L-lysine, threonine, DL-arginine, and L-cystine (Figure 5A). Similarly, a steady increase in various long-chain polyunsaturated fatty acids (LPUFAs) was detected, including docosahexaenoic acid (DHA), eicosapentaenoic acid (EPA), docosapentaenoic acid (DPA), and arachidonic acid (ARA) (Figure 5A). Various fatty acyl esters of hydroxy fatty acids (FAHFAs) were also identified, which can enhance insulin-stimulated glucose transport and help meet energy demands (Tan et al., 2019; Yore et al., 2014) (Supplementary Figure S5). Through combined transcriptomic and metabolomic analysis, we identified genes associated with protein metabolism (Figure 5B). As anticipated, genes involved in protein degradation showed a positive correlation with up-regulated amino acids, and their expression levels significantly increased, including proteasome (*psm*) and *cacul1* (Supplementary Figure S6). Conversely, genes involved in protein synthesis exhibited a negative correlation with up-regulated amino acids, and their expression levels were significantly decreased, including *kri1*, *mrps34*, and *mtg2* (Supplementary Figure S6). These findings indicate a shift from protein synthesis to protein catabolism in zebrafish ovaries exposed to low temperatures.

**Accumulation of bile acids in the ovary**

With the decrease in treatment temperature, there was a general increasing trend in several bile acids and their derivatives, including GDCA (hydrate), taurolithocholic acid 3-sulfate, lithocholic acid, tauroursodeoxycholic acid dihydrate, and taurolithocholic acid sodium salt (Figure 6). All five bile acids, derived from cholesterol, facilitate fat and vitamin absorption (Smith et al., 2009).

**Bile acid treatment caused ovarian degradation in zebrafish**

To test whether an increase in bile acids plays a role in ovarian failure, we treated adult female zebrafish with GDCA, which showed a steady and largest increase in the low

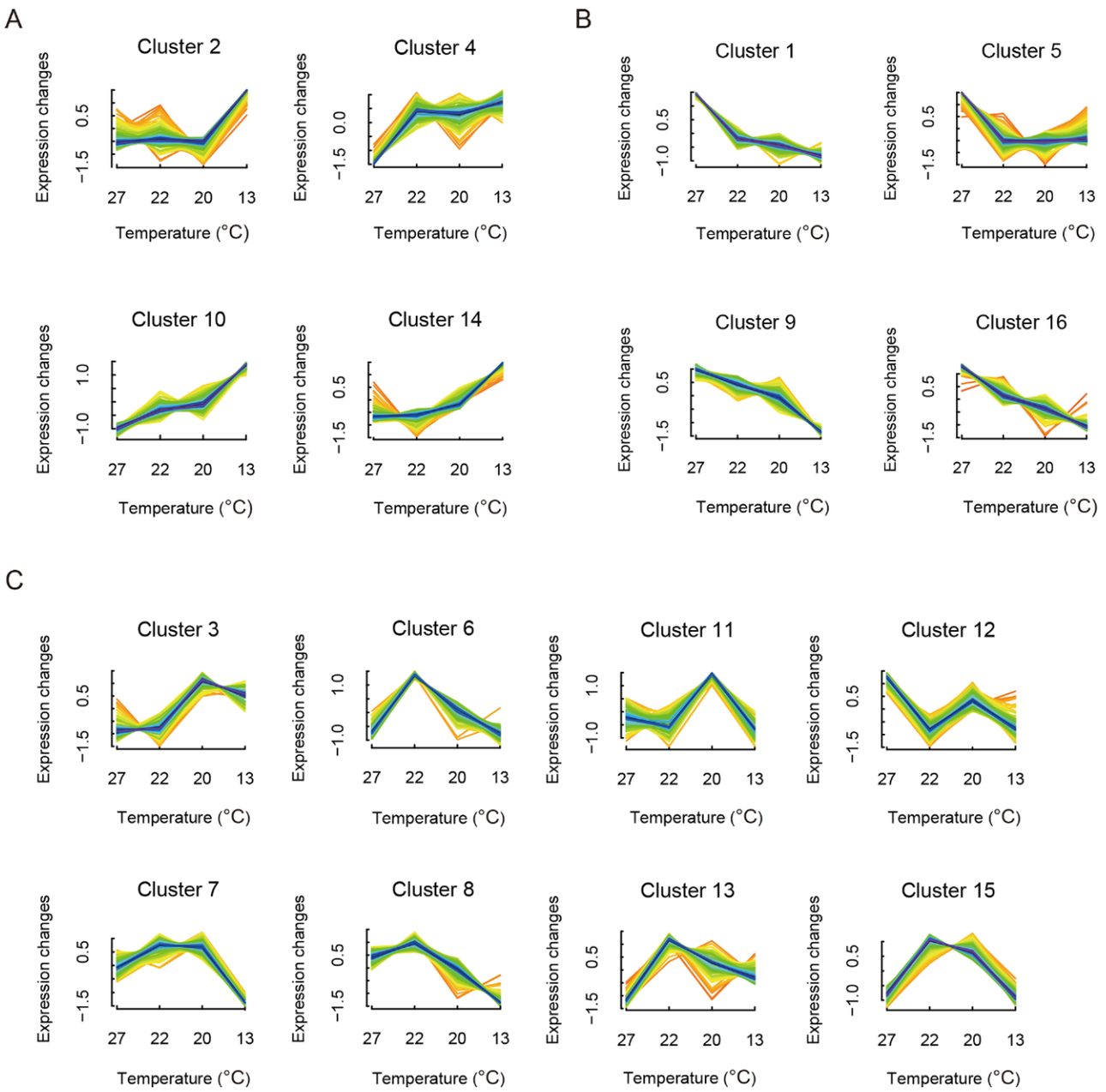



**Figure 3 Cluster analysis of metabolites**

A: Metabolites were clustered using Mfuzz based on changes with decreasing temperature, resulting in 16 clusters. Clusters 2, 4, 10, and 14 exhibited a gradual increase in metabolites with decreasing temperature. B: Clusters 1, 5, 9, and 16 exhibited a gradual decrease in metabolites with decreasing temperature. C: Remaining clusters exhibited irregular variations with temperatures.

temperature-exposed ovaries. At a final concentration of 40 mg/L, GDCA was used to treat aged-matched adult female zebrafish derived from the same parent with temperatures maintained at 27°C for both the GDCA-treated and untreated groups (Figure 7A).

After 14 days of treatment, ovarian weight, body weight, and the gonadosomatic index (GSI) were calculated (Supplementary Table S5). Results indicated that GSI was significantly lower in the GDCA-treated group than in the control group, suggesting a significant adverse effect of GDCA on ovarian development (Figure 7B). Histological analysis of the GDCA-treated zebrafish ovaries revealed no significant changes in the proportions of oocytes at the primary growth (PG) and mid-vitellogenic (MV) stages. However, there was a significant increase in oocytes at the previtellogenic (PV) and early vitellogenic (EV) stages, while the proportion of fully grown (FG) stage (mature) oocytes decreased by 11% compared to the control group (Figure 7C). The GDCA-treated ovaries showed atrophy (Figure 7D; Supplementary Figures S7, S8). These results suggest that a bile acid increase inhibits oocyte development at the PV and EV stages, while simultaneously inhibiting yolk accumulation (Figure 7).

## DISCUSSION

### Reproductive capacity of female fish is limited by cold stress

At present, there is a limited understanding of the molecular mechanisms underlying the impact of reduced temperatures on ovarian development in fish. Exploring this phenomenon could provide novel insights into fish reproduction under low-

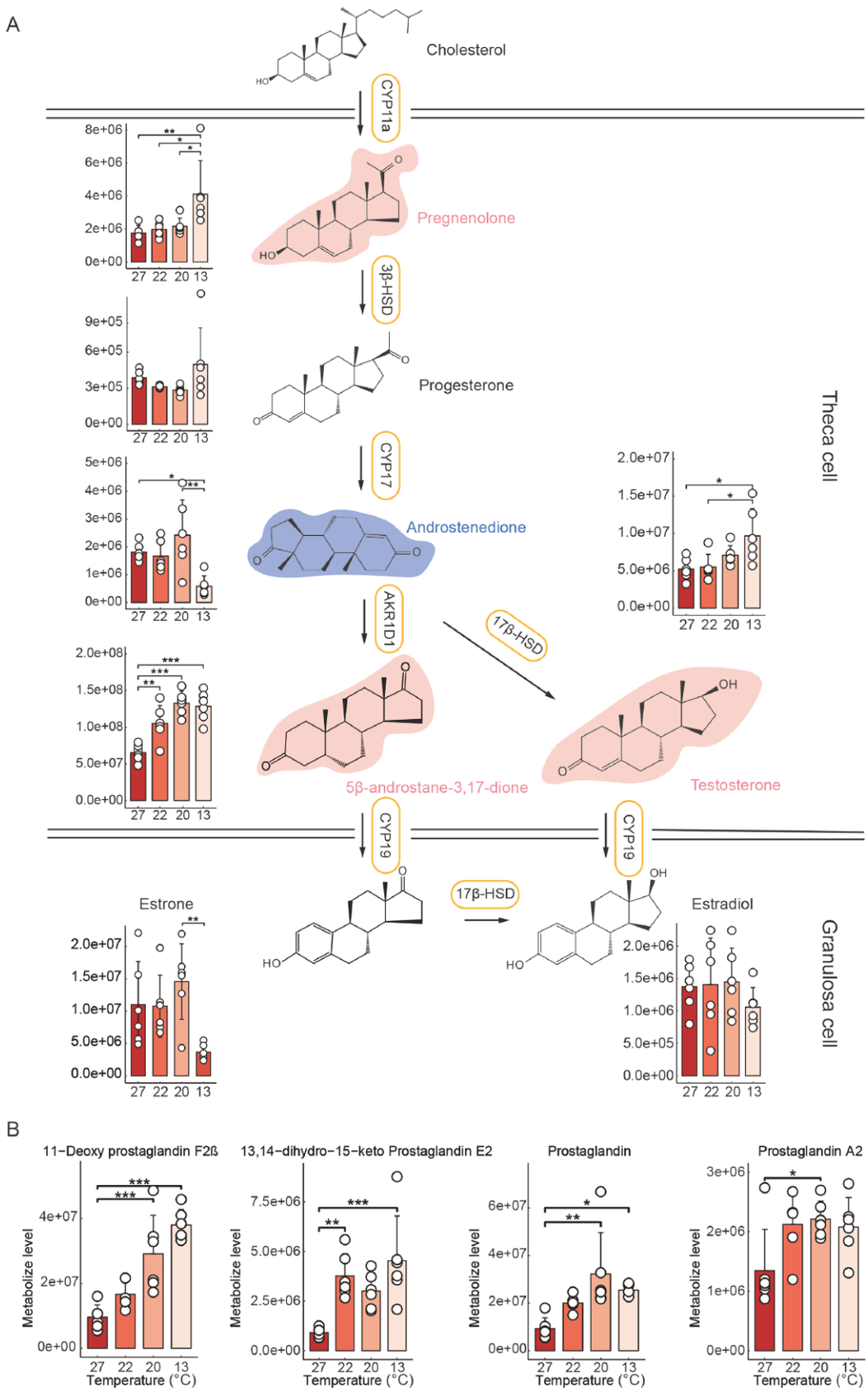



**Figure 4 Intermediate product of estradiol synthesis and up-regulated PGs**

A: Flowchart shows estradiol synthesis from cholesterol, with enzymes in yellow rectangles (Javitt et al., 2001; Nerusu et al., 2017; Stocco, 2000; Swart et al., 2003). Bar charts next to metabolites show changes in zebrafish ovaries post low-temperature treatment. X-axis is temperature (°C), y-axis is metabolite levels. Red-shaded areas indicate hormone up-regulation, blue-shaded areas indicate down-regulation under low temperatures. Asterisks denote significance ($^{*}$: $P$<0.05; $^{**}$: $P$<0.01; $^{***}$: $P$<0.001). Hormone molecular formulas were from http://www.chemspider.com. B: Levels of four prostaglandins (PGF2β, PGE2, PG, and PGA2) in cold-acclimated ovaries.

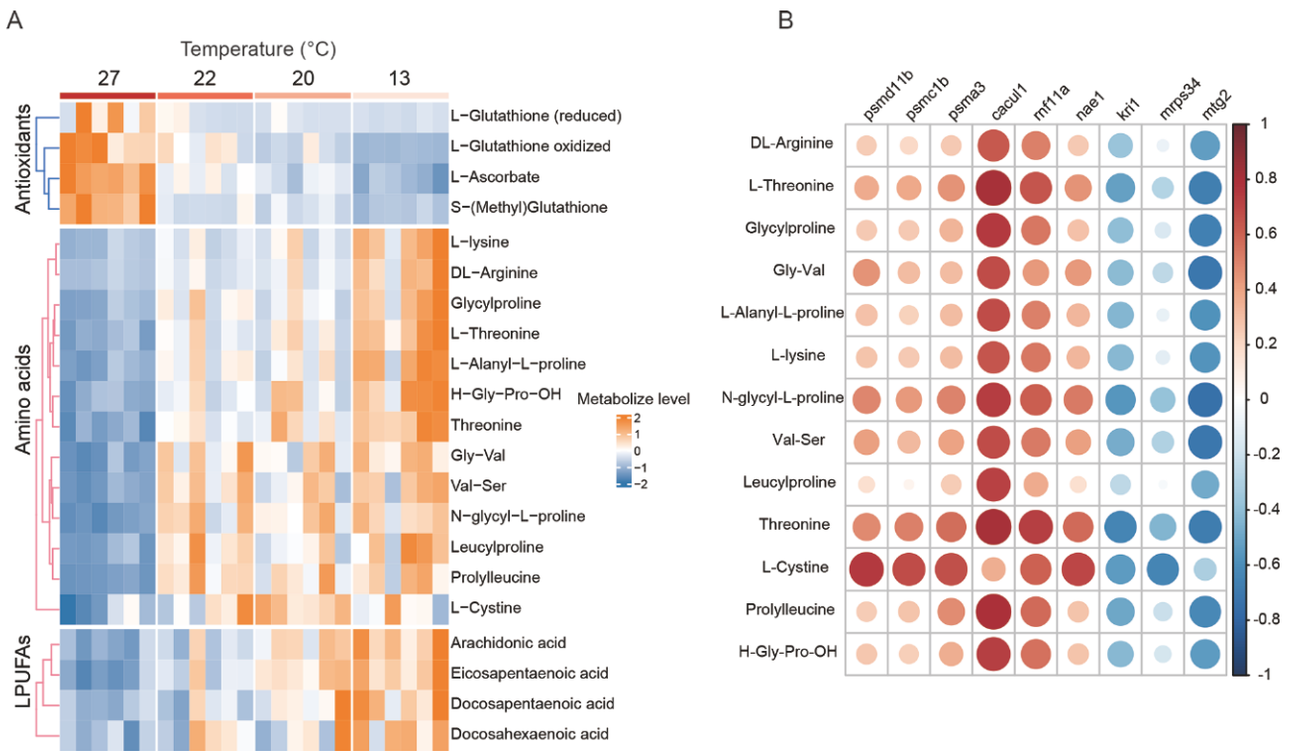



**Figure 5 Down-regulated antioxidants, up-regulated amino acids, LPUFAs, and Pearson correlation analysis**

A: As temperature decreased from 27°C to 13°C, levels of four antioxidants declined in zebrafish ovaries, while multiple amino acids and various LPUFAs showed an up-regulation. Numerical values of metabolite levels were standardized. B: Pearson correlation between up-regulated amino acids and genes associated with protein metabolism.

temperature challenges. In our investigation, we initially employed H&E staining to illustrate that exposure to low temperatures resulted in a reduction in zebrafish ovary size, suppression of oocyte development, and a decline in the mature oocyte population (Figure 8A). We also explored the mechanisms underlying the inhibition of zebrafish oocyte development at low temperatures using untargeted metabolomic analyses. Our findings revealed that cold stress perturbed sex hormones, altered both protein and fatty acid metabolism, reduced antioxidant levels, and increased bile acid content. These metabolic changes synergistically contributed to ovarian failure in zebrafish under cold stress (Figure 8B).

**Cold treatment up-regulates amino acids, LPUFAs, and FAHFAs**

The *psm* family ring finger protein 11a (*rnf11a*) (Chen et al., 2011; Joazeiro & Weissman, 2000), CDK2-associated cullin domain 1 (*cacul1*), and NEDD8 activating enzyme E1 (*nae1*) (Chiba & Tanaka, 2004) regulate protein degradation as components of ubiquitin ligases. Conversely, the loss of *kri1l* (Jia et al., 2015), mitochondrial ribosomal proteins (MRPS), and mitochondrial ribosome-associated GTPase 2 (*mtg2*) (Miller et al., 2004) impairs protein synthesis. In our study, low temperatures led to the up-regulation of genes involved in protein degradation (*psm* family and *cacul1*) and the down-regulation of genes involved in protein synthesis (*kri1l*, *mrps34* and *mtg2*), ultimately leading to an increase in free amino acid levels in the ovaries under cold treatment.

Our data indicated that cold treatment significantly increased the accumulation of LPUFAs and FAHFAs in the ovary. Recent research has shown that endogenously synthesized DHA promotes pregnenolone production by regulating the transcription of cyp11a1, thereby enhancing oocyte maturation and quality (Li et al., 2024). As an LPUFA, EPA plays an important role in various organisms, from microorganisms to mammals, by maintaining plasma membrane fluidity and facilitating cell division (Andersson et al., 2007; Kawamoto et al., 2009; Sato et al., 2008). *Bangia fuscopurpurea* cultured at 4°C shows a 29.8% increase in EPA content, along with an up-regulation in desaturase and elongase genes associated with EPA biosynthesis, which contributes to improved membrane fluidity and cold tolerance (Cao et al., 2017). ARA has been shown to induce oocyte maturation (Jiang et al., 2019), respond to cold stress (Song et al., 2019), and inhibit activation of channel transient receptor potential (melastatin)-8 (TRPM8) (Andersson et al., 2007). Additionally, ARA increases in the ovary, which may serve to maintain stability of the immune system to cope with prolonged cold stress (Qi et al., 2022). It is hypothesized that low temperatures lead to the conversion of lipids into LPUFAs and FAHFAs, providing energy for zebrafish to withstand the cold (Tan et al., 2011; Wood, 2020), consistent with the increase in LPUFA content in Nile tilapia exposed to suboptimal cold conditions (Corrêa et al., 2023).

We speculate that the degradation of proteins and fatty acids may contribute to ovarian decline. Previous research has shown that disruption of lipid homeostasis in zebrafish is detrimental to reproductive development (Xu et al., 2023). Temperature stress induces the redistribution of protein and lipid metabolism from anabolism toward catabolism, strongly impeding growth and reproduction (Iwama et al., 1997; Schreck & Tort, 2016). Under long-term cold treatment, metabolic energy is likely redirected towards cold resistance at the expense of reproduction, resulting in ovarian shrinkage.

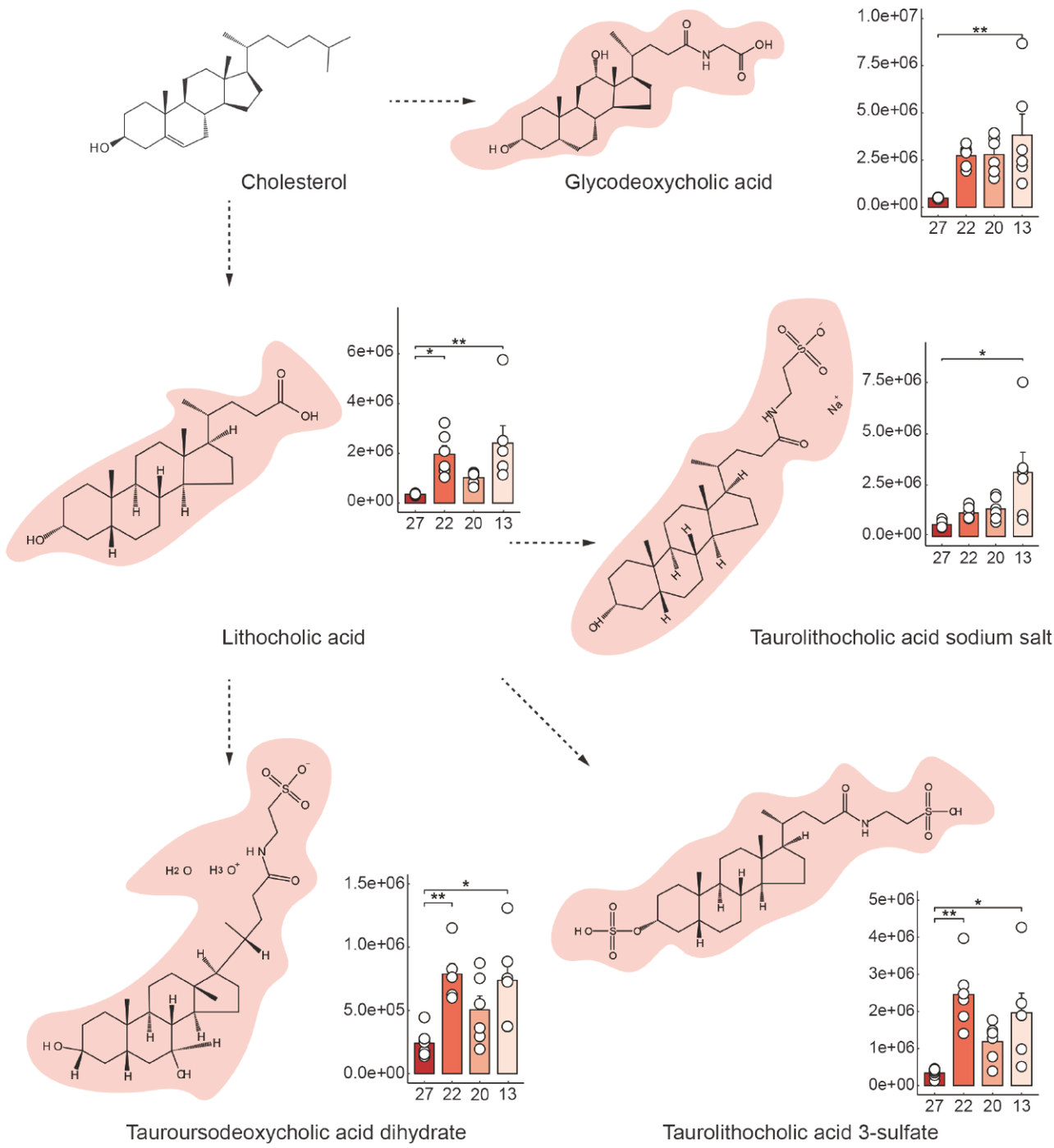



**Figure 6 Substances involved in bile acid formation at low temperature**

Levels of five bile acids formed indirectly through cholesterol metabolism were significantly elevated under low temperatures. X-axis represents temperature (°C), y-axis represents metabolite levels. Asterisks indicate significant differences ($^{*}$: $P$<0.05; $^{**}$: $P$<0.01; $^{***}$: $P$<0.001). Normalization process: metabolite original quantitative value/(sum of metabolite quantitative values in sample/sum of metabolite quantitative values in QC1).

**Cold treatment reduces antioxidant levels**

Previous studies have shown that marked reductions in temperature can elevate antioxidative compound levels in various plants and animals (Lubkowska et al., 2019; Proietti et al., 2009; Wang et al., 2022b). However, changes in antioxidant levels depend on the duration of cold treatment. For example, Wang et al. (2022a) observed a sharp increase in antioxidant enzymes, including GSH, in zebrafish embryonic fibroblast (ZF4) cells after 2 days of cold stress, but a significant decrease in antioxidant enzymes compared to the control group after three months of cold acclimation. And, we observed a decrease in both GSH and GSSG levels during cold treatment (Figure 5A), similar to findings in the liver of the high-altitude frog *Nanorana pleskei* (Zhang et al., 2021). Cold exposure in juvenile Chinese soft-shelled turtles (*Pelodiscus sinensis*) leads to a decrease in brain ascorbate concentration (Chen et al., 2015), while the brain levels of ascorbic acid and GSH are lower in winter than in summer in *Trachemys scripta elegans* turtles (Pérez-Pinzón & Rice, 1995). Our study revealed a decline in GSH and ascorbic acid levels in the zebrafish ovary. We postulate two potential causes for the decline: First, low temperatures may hinder ovarian

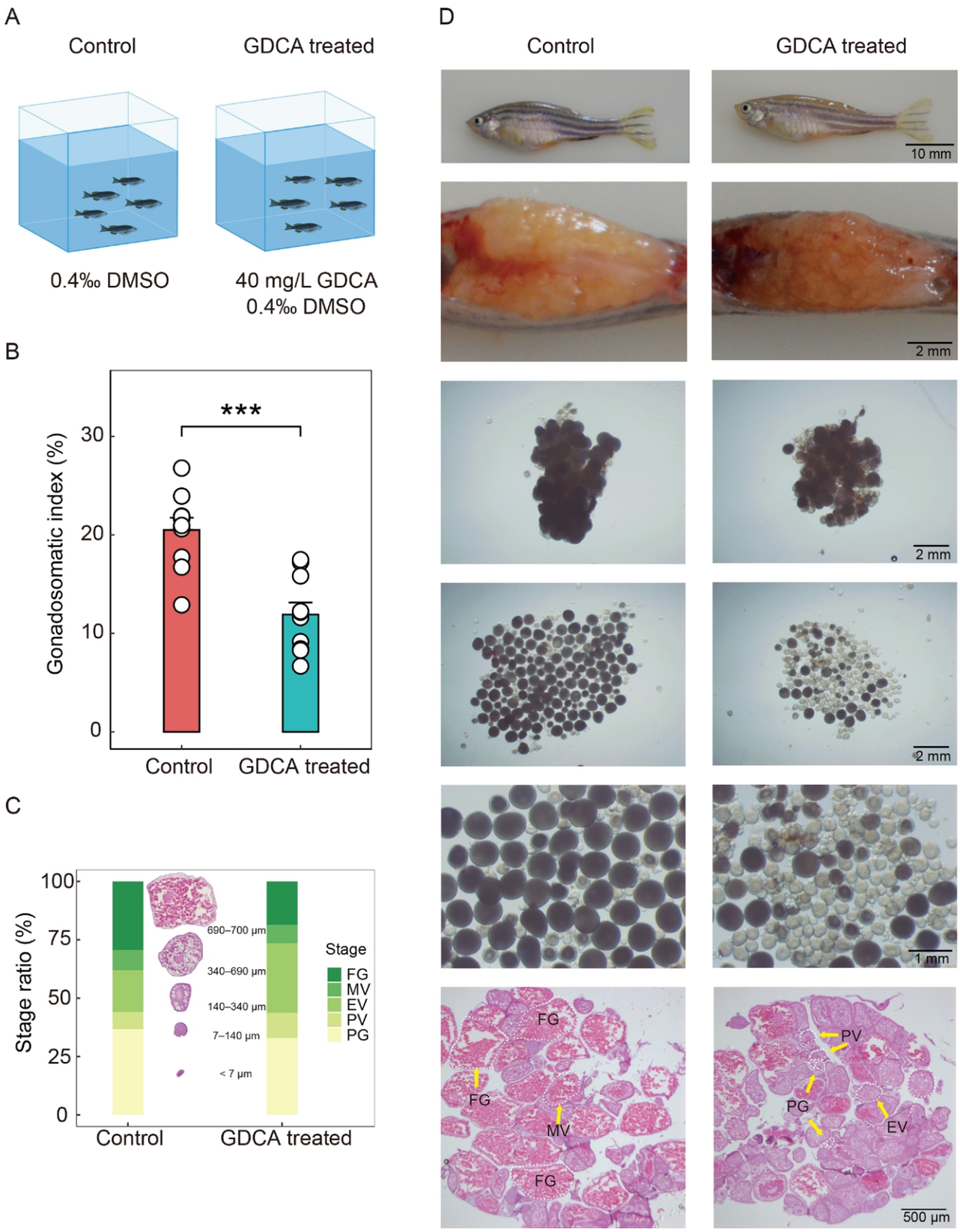



**Figure 7 Comparation between control and GDCA-treated groups**

A: Experimental set up. B: Bar graph shows GSI. C: Proportions of oocytes in five developmental stages. D: From top to bottom: external appearance of zebrafish, appearance of ovary after abdominal dissection, partial ovary, dispersed ovary, enlarged dispersed imaged under ZEISS microscope (25×), H&E-stained ovary paraffin section, imaged using a Nikon microscope (40×). FG: Fully-grown stage; MV: Mid-vitellogenic stage; EV: Early vitellogenic stage; PV: Previtellogenic stage; PG: Primary growth stage.

development, increasing the proportion of immature oocytes, which generally exhibit lower concentrations of GSH and ascorbic acid compared to mature oocytes (Funahashi et al., 1994). Second, the ovary may require greater consumption of

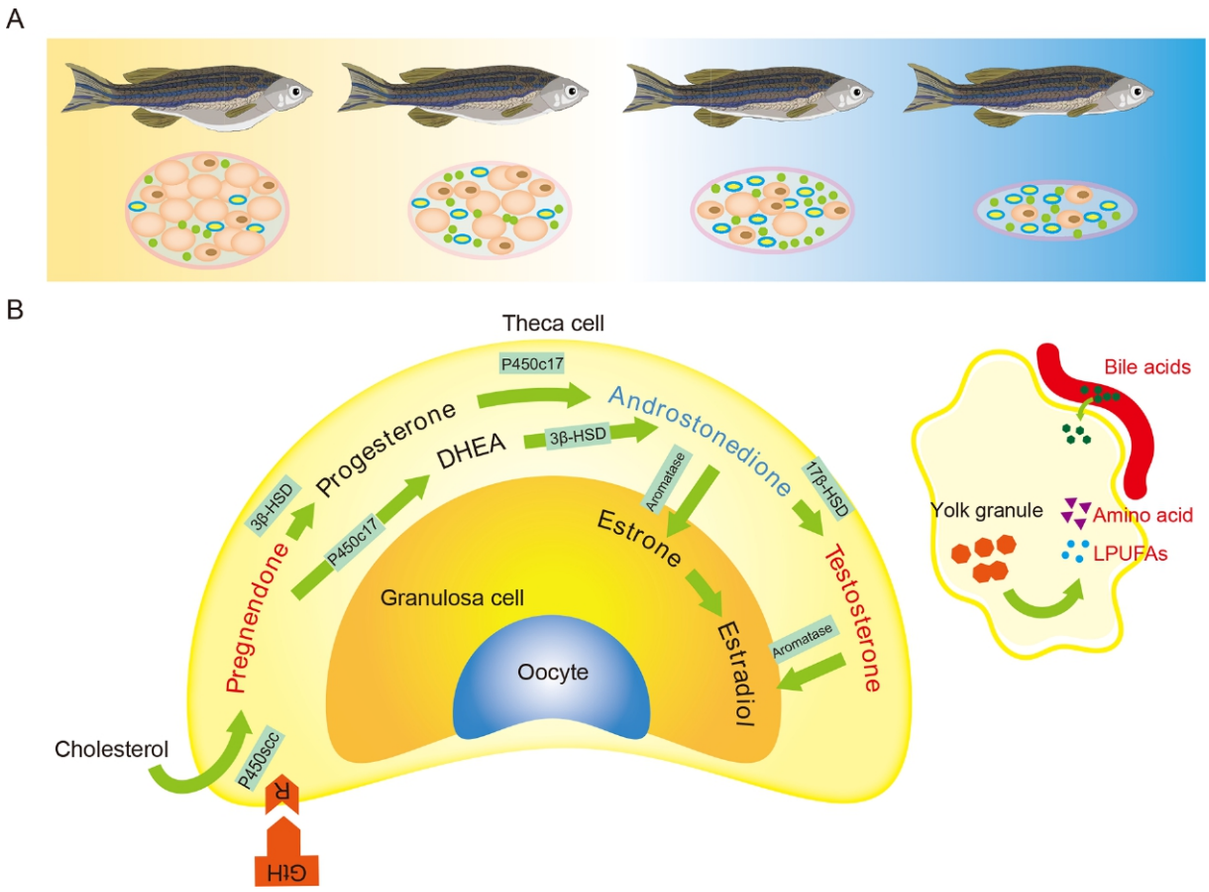



**Figure 8 Model diagram of ovarian abortion in zebrafish induced by low temperature**

A: Conditions of subnormal rearing temperature inhibited the growth and development of zebrafish oocytes. Decrease in temperature led to a gradual reduction in number of mature oocytes. B: Left side shows steps involved in synthesis of estradiol from cholesterol. Right side shows bile acids entering oocyte, leading to the breakdown of yolk granules into amino acids and long-chain polyunsaturated fatty acids (LPUFAs), ultimately inhibiting further oocyte maturation.

antioxidant molecules to neutralize reactive oxygen species (ROS) and maintain oocyte redox status under cold exposure. Consequently, GSH and ascorbic acid levels decrease in response to the increased demand for antioxidant defense. These factors may act synergistically to reduce GSH and ascorbic acid levels in the zebrafish ovary under cold treatment.

The down-regulation of antioxidants can lead to an overproduction of ROS. Oxidative stress negatively impacts the reproductive system and can even lead to pathological conditions (Agarwal et al., 2006). The pathological consequences of a decreased antioxidant defense system include reproductive disorders such as polycystic ovary syndrome (PCOS) and infertility (Ruder et al., 2008; Sabuncu et al., 2001). Similar to our findings, a significant increase in atretic antral follicles in rat ovaries occurs after blocking GSH synthesis with the inhibitor buthionine sulfoximine (Lopez & Luderer, 2004). Therefore, the down-regulation of antioxidants under low temperatures may be a significant contributor to ovarian failure in zebrafish.

**Cold stress up-regulates cholesterol metabolism, altering profile of steroid hormone and accumulation of bile acids**

Testosterone is synthesized from cholesterol through a process catalyzed by cholesterol side-chain cleavage enzymes (CYP11a), producing pregnenolone. Pregnenolone is then converted into testosterone through a series of enzymatic reactions involving 3β-hydroxysteroid dehydrogenase (3β-HSD), cytochrome P450 17α-hydroxylase/17,20-lyase (CYP17), and 17β-hydroxysteroid dehydrogenase (17β-HSD) (Figure 4A). High concentrations of testosterone can impede follicular development, resulting in reduced reproductive capacity (Beloosesky et al., 2004; Liu et al., 2015, 2021; Yu et al., 2020). Additionally, the accumulation of PGs may correspond to an increase in undeveloped eggs under cold stress, as oocytes failing to mature to stage III can lead to the accumulation of PGs and their metabolites in the ovary (Clelland & Peng, 2009; Wu et al., 2000). In our study, we observed that cold temperature stimulation led to elevated levels of prostaglandins and androgens, including androstenedione and testosterone. Based on these observations, we hypothesize that the increased androgen levels may constitute a primary inhibitory factor affecting oocyte production and maturation.

Bile acids are synthesized from cholesterol in the liver and subsequently secreted into the intestinal tract to facilitate lipid absorption (Norlin & Wikvall, 2007). Despite their primary synthesis in the liver, bile acids are also linked to ovarian processes. Liu et al. (2003) demonstrated substantial expression of liver receptor homologue 1 (LRH-1), a key participant in cholesterol metabolism and bile acid synthesis, within rat ovaries. Cheng et al. (2021) discovered that late atretic follicles in the Chinese buffalo accumulate substantial amounts of bile acid-related substances in their follicular fluid. Smith et al. (2009) confirmed the existence of bile acid

synthesis pathways within human ovaries. Our study revealed that low-temperature exposure significantly increased bile acid content in zebrafish ovaries. Similarly, Worthmann et al. (2017) found that cold exposure in mice accelerates the conversion of cholesterol to bile acids, accompanied by increased heat production.

**Bile acids promote ovarian failure**

It is important to recognize that bile acids possess systemic endocrine functions that modulate triglycerides, cholesterol, energy, and glucose homeostasis (Houten et al., 2006). In this study, administering GDCA to zebrafish resulted in ovarian failure, characterized by slower oocyte development and a reduced number of mature oocytes. This phenotype mirrors the effects observed in zebrafish ovaries under cold stress, suggesting that elevated bile acid levels may constitute a notable determinant in ovarian failure during cold stress. A similar association is found in human reproductive disorders, such as PCOS, characterized by chronic anovulation, hyperandrogenism, and polycystic ovarian morphology, where elevated bile acid levels within the follicular fluid are accompanied by increased serum concentrations of total testosterone and androstenedione (Yang et al., 2021; Zhang et al., 2019). This similarity to the metabolic perturbations observed in zebrafish ovaries exposed to low temperatures highlights the potential role of bile acids and unbalanced steroid hormones in ovarian failure.

In summary, we identified significant metabolite alterations in zebrafish ovaries under cold stress. Notably, changes in protein and lipid metabolism, reduced antioxidant levels, disrupted steroid hormones, and elevated bile acids collectively contributed to ovarian failure. Our findings provide new perspectives into the mechanisms of metabolic rebalance between survival and reproduction in ectothermic fish facing cold stress.

## DATA AVAILABILITY

All Illumina RNA sequencing data from this project were deposited in the Genome Sequence Archive (GSA) database under accession number CRA015402, Science Data Bank (DOI: 10.57760/sciencedb.16619), and NCBI under BioProjectID PRJNA1020641. The metabolome data that support the findings of this study were deposited in the CNGB Sequence Archive (CNSA) of the China National GeneBank Database (CNGBdb) under accession number CNP0004915.

## SUPPLEMENTARY DATA

Supplementary data to this article can be found online.

## COMPETING INTERESTS

The authors declare that they have no competing interests.

## AUTHORS' CONTRIBUTIONS

W.H.L. and L.B.C. conceived and designed the research; Z.Q.L., M.D.B., and J.Z.L. performed the experiments; W.H.L., Z.Q.L., and M.D.B. analyzed the data; Z.Q.L., M.D.B., and L.B.C. wrote the manuscript. All authors read and approved the final version of the manuscript.


## ACKNOWLEDGEMENTS

We thank Qiang-Hua Xu from Shanghai Ocean University for technical assistance during the study.


## REFERENCES


Agarwal A, Gupta S, Sikka S. 2006. The role of free radicals and antioxidants in reproduction. *Current Opinion in Obstetrics & Gynecology*, **18**(3): 325–332.

Alix M, Kjesbu OS, Anderson KC. 2020. From gametogenesis to spawning: how climate‐driven warming affects teleost reproductive biology. *Journal of Fish Biology*, **97**(3): 607–632.

Andersson DA, Nash M, Bevan S. 2007. Modulation of the cold-activated channel TRPM8 by lysophospholipids and polyunsaturated fatty acids. *The Journal of Neuroscience*, **27**(12): 3347–3355.

Barton BA. 2002. Stress in fishes: a diversity of responses with particular reference to changes in circulating corticosteroids. *Integrative and Comparative Biology*, **42**(3): 517–525.

Beloosesky R, Gold R, Almog B, et al. 2004. Induction of polycystic ovary by testosterone in immature female rats: modulation of apoptosis and attenuation of glucose/insulin ratio. *International Journal of Molecular Medicine*, **14**(2): 207–215.

Campos C, Valente L, Conceição L, et al. 2013. Temperature affects methylation of the *myogenin* putative promoter, its expression and muscle cellularity in Senegalese sole larvae. *Epigenetics*, **8**(4): 389–397.

Cao M, Wang DM, Mao YX, et al. 2017. Integrating transcriptomics and metabolomics to characterize the regulation of EPA biosynthesis in response to cold stress in seaweed *Bangia fuscopurpurea. PLoS One*, **12**(12): e0186986.

Chen BJ, Niu CJ, Yuan L. 2015. Ascorbic acid regulation in stress responses during acute cold exposure and following recovery in juvenile Chinese soft-shelled turtle (*Pelodiscus sinensis*). *Comparative Biochemistry and Physiology Part A: Molecular & Integrative Physiology*, **184**: 20–26.

Chen LB, Lu Y, Li WH, et al. 2019. The genomic basis for colonizing the freezing Southern Ocean revealed by Antarctic toothfish and Patagonian robalo genomes. *Gigascience*, **8**(4): giz016.

Chen MF, Gutierrez GJ, Ronai ZA. 2011. Ubiquitin-recognition protein Ufd1 couples the endoplasmic reticulum (ER) stress response to cell cycle control. *Proceedings of the National Academy of Sciences of the United States of America*, **108**(22): 9119–9124.

Chen ZZ, Cheng CHC, Zhang JF, et al. 2008. Transcriptomic and genomic evolution under constant cold in Antarctic notothenioid fish. *Proceedings of the National Academy of Sciences of the United States of America*, **105**(35): 12944–12949.

Cheng JR, Pan Y, Yang SF, et al. 2021. Integration of transcriptomics and non-targeted metabolomics reveals the underlying mechanism of follicular atresia in Chinese buffalo. *The Journal of Steroid Biochemistry and Molecular Biology*, **212**: 105944.

Chiba T, Tanaka K. 2004. Cullin-based ubiquitin ligase and its control by NEDD8-conjugating system. *Current Protein and Peptide Science*, **5**(3): 177–184.

Clelland E, Peng C. 2009. Endocrine/paracrine control of zebrafish ovarian development. *Molecular and Cellular Endocrinology*, **312**(1-2): 42–52.

Corrêa CF, Nobrega RO, Mattioni B, et al. 2023. LC-PUFA endogenous biosynthesis is improved in Nile tilapia fed plant-oil sources at cold suboptimal temperature. *Aquaculture*, **562**: 738832.

Dahlke FT, Wohlrab S, Butzin M, et al. 2020. Thermal bottlenecks in the life cycle define climate vulnerability of fish. *Science*, **369**(6499): 65–70.

Donelson JM, Munday PL, Mccormick MI, et al. 2010. Effects of elevated water temperature and food availability on the reproductive performance of a coral reef fish. *Marine Ecology Progress Series*, **401**: 233–243.

El-Naggar GO, El Nady MA, Kamar MG, et al. 2000. Effect of photoperiod, dietary protein and temperature on reproduction in Nile tilapia (*Oreochromis niloticus*). *In*: The 21st Century Proceedings from the Fifth International Symposium on Tilapia Aquaculture. Rio die Janeiro, Brazil: American Tilapia, 352–358.

Funahashi H, Cantley TC, Stumpf TT, et al. 1994. Use of low-salt culture medium for in vitro maturation of porcine oocytes is associated with elevated oocyte glutathione levels and enhanced male pronuclear formation

after in vitro fertilization. *Biology of Reproduction*, **51**(4): 633–639.

Gjerde B. 1986. Growth and reproduction in fish and shellfish. *Aquaculture*, **57**(1-4): 37–55.

Han BS, Li WH, Chen ZZ, et al. 2016. Variation of DNA methylome of zebrafish cells under cold pressure. *PLoS One*, **11**(8): e0160358.

Houten SM, Watanabe M, Auwerx J. 2006. Endocrine functions of bile acids. *The EMBO Journal*, **25**(7): 1419–1425.

Hu P, Liu ML, Liu YM, et al. 2016. Transcriptome comparison reveals a genetic network regulating the lower temperature limit in fish. *Scientific Reports*, **6**: 28952.

Hu P, Liu ML, Zhang D, et al. 2015. Global identification of the genetic networks and *cis*-regulatory elements of the cold response in zebrafish. *Nucleic Acids Research*, **43**(19): 9198–9213.

Hu WT, Bai JY, Fei X, et al. 2020. Metabolomic responses of Nile tilapia (*Oreochromis niloticus*) maintained under different temperatures and challenged with *Streptococcus agalactiae. Aquaculture*, **524**: 735209.

Islam MJ, Kunzmann A, Slater MJ. 2022. Responses of aquaculture fish to climate change‐induced extreme temperatures: a review. *Journal of the World Aquaculture Society*, **53**(2): 314–366.

Iwama GK, Pickering A, Sumpter J, et al. 1997. Fish stress and health in aquaculture. *In*: Proc. Society for Experimental Biology Seminar Series.

Javitt NB, Lee YC, Shimizu C, et al. 2001. Cholesterol and hydroxycholesterol sulfotransferases: identification, distinction from dehydroepiandrosterone sulfotransferase, and differential tissue expression. *Endocrinology*, **142**(7): 2978–2984.

Jia XE, Ma K, Xu T, et al. 2015. Mutation of *kri1l* causes definitive hematopoiesis failure via PERK-dependent excessive autophagy induction. *Cell Research*, **25**(8): 946–962.

Jiang YX, Shi WJ, Ma DD, et al. 2019. Dydrogesterone exposure induces zebrafish ovulation but leads to oocytes over-ripening: an integrated histological and metabolomics study. *Environment International*, **128**: 390–398.

Joazeiro CAP, Weissman AM. 2000. RING finger proteins: mediators of ubiquitin ligase activity. *Cell*, **102**(5): 549–552.

Kawamoto J, Kurihara T, Yamamoto K, et al. 2009. Eicosapentaenoic acid plays a beneficial role in membrane organization and cell division of a cold-adapted bacterium, *Shewanella livingstonensis* Ac10. *Journal of Bacteriology*, **191**(2): 632–640.

Kennedy VS, Mihursky J. 1967. Bibliography on the effects of temperature in the aquatic environment and addendum. Contribution no. 326. Solomons: Maryland University.

Kock KH. 1992. Antarctic Fish and Fisheries. Cambridge: Cambridge University Press.

Li Y, Li XH, Ye D, et al. 2024. Endogenous biosynthesis of docosahexaenoic acid (DHA) regulates fish oocyte maturation by promoting pregnenolone production. *Zoological Research*, **45**(1): 176–188.

Liu CC, Yue S, Solarz J, et al. 2021. Improving the sexual activity and reproduction of female zebrafish with high testosterone levels. *Scientific Reports*, **11**(1): 3822.

Liu CP, Chao B, Feng YZ, et al. 2022a. Establishment of transgenic zebrafish model regulated by *nr1h4* and related studies. *Chinese Journal of Pharmacovigilance*, **19**(8): 873–880.

Liu DL, Liu WZ, Li QL, et al. 2003. Expression and functional analysis of liver receptor homologue 1 as a potential steroidogenic factor in rat ovary. *Biology of Reproduction*, **69**(2): 508–517.

Liu T, Cui YQ, Zhao H, et al. 2015. High levels of testosterone inhibit ovarian follicle development by repressing the FSH signaling pathway. *Journal of Huazhong University of Science and Technology [Medical Sciences]*, **35**(5): 723–729.

Liu ZJ, Zhou T, Gao DY. 2022b. Genetic and epigenetic regulation of growth, reproduction, disease resistance and stress responses in aquaculture. *Frontiers in Genetics*, **13**: 994471.

Long Y, Song GL, Yan JJ, et al. 2013. Transcriptomic characterization of cold acclimation in larval zebrafish. *BMC Genomics*, **14**: 612.

Lopes AF, Faria AM, Dupont S. 2020. Elevated temperature, but not decreased pH, impairs reproduction in a temperate fish. *Scientific Reports*, **10**(1): 20805.

Lopez SG, Luderer U. 2004. Effects of cyclophosphamide and buthionine sulfoximine on ovarian glutathione and apoptosis. *Free Radical Biology and Medicine*, **36**(11): 1366–1377.

López-Olmeda JF, Sánchez-Vázquez FJ. 2011. Thermal biology of zebrafish (*Danio rerio*). *Journal of Thermal Biology*, **36**(2): 91–104.

Lubkowska A, Bryczkowska I, Gutowska I, et al. 2019. The effects of swimming training in cold water on antioxidant enzyme activity and lipid peroxidation in erythrocytes of male and female aged rats. *International Journal of Environmental Research and Public Health*, **16**(4): 647.

Lushchak VI. 2011. Environmentally induced oxidative stress in aquatic animals. *Aquatic Toxicology*, **101**(1): 13–30.

Miller C, Saada A, Shaul N, et al. 2004. Defective mitochondrial translation caused by a ribosomal protein (MRPS16) mutation. *Annals of Neurology*, **56**(5): 734–738.

Nerusu A, Reddy PS, Ramachary DB, et al. 2017. Unraveling the stability of plasma proteins upon interaction of synthesized androstenedione and its derivatives-a biophysical and computational approach. *ACS Omega*, **2**(10): 6514–6524.

Norlin M, Wikvall K. 2007. Enzymes in the conversion of cholesterol into bile acids. *Current Molecular Medicine*, **7**(2): 199–218.

Ou JX, Ball JM, Luan YZ, et al. 2018. iPSCs from a hibernator provide a platform for studying cold adaptation and its potential medical applications. *Cell*, **173**(4): 851–863. e16.

Parratt SR, Walsh BS, Metelmann S, et al. 2021. Temperatures that sterilize males better match global species distributions than lethal temperatures. *Nature Climate Change*, **11**(6): 481–484.

Pérez-Pinzón MA, Rice ME. 1995. Seasonal- and temperature-dependent variation in CNS ascorbate and glutathione levels in anoxia-tolerant turtles. *Brain Research*, **705**(1-2): 45–52.

Proietti S, Moscatello S, Famiani F, et al. 2009. Increase of ascorbic acid content and nutritional quality in spinach leaves during physiological acclimation to low temperature. *Plant Physiology and Biochemistry*, **47**(8): 717–723.

Qi HQ, Liu Y, Jian FJ, et al. 2022. Effects of dietary arachidonic acid (ARA) on immunity, growth and fatty acids of *Apostichopus japonicus. Fish & Shellfish Immunology*, **127**: 901–909.

Roy-Chowdhury N, Wang X, Roy-Chowdhury J. 2020. Bile pigment metabolism and its disorders. *In*: Pyeritz RE, Korf BR, Grody WaW. Emery and Rimoin's Principles and Practice of Medical Genetics and Genomics. 7th ed. Amsterdam: Elsevier, 507–553.

Ruder EH, Hartman TJ, Blumberg J, et al. 2008. Oxidative stress and antioxidants: exposure and impact on female fertility. *Human Reproduction Update*, **14**(4): 345–357.

Sabuncu T, Vural H, Harma M, et al. 2001. Oxidative stress in polycystic ovary syndrome and its contribution to the risk of cardiovascular disease. *Clinical Biochemistry*, **34**(5): 407–413.

Sato S, Kurihara T, Kawamoto J, et al. 2008. Cold adaptation of eicosapentaenoic acid-less mutant of *Shewanella livingstonensis* Ac10 involving uptake and remodeling of synthetic phospholipids containing various polyunsaturated fatty acids. *Extremophiles*, **12**(6): 753–761.

Schnurr ME, Yin Y, Scott GR. 2014. Temperature during embryonic development has persistent effects on metabolic enzymes in the muscle of zebrafish. *Journal of Experimental Biology*, **217**(8): 1370–1380.

Schreck CB, Tort L. 2016. The concept of stress in fish. *Fish Physiology*, **35**: 1–34.

Servili A, Canario AVM, Mouchel O, et al. 2020. Climate change impacts on fish reproduction are mediated at multiple levels of the brain-pituitary-gonad axis. *General and Comparative Endocrinology*, **291**: 113439.

Smith LP, Nierstenhoefer M, Yoo SW, et al. 2009. The bile acid synthesis pathway is present and functional in the human ovary. *PLoS One*, **4**(10): e7333.

Song E, Segal I, Hodkinson J, et al. 1983. Sinus bradycardia in obstructive jaundice-correlation with total serum bile acid concentrations. *South African Medical Journal*, **64**(14): 548–551.

Song M, Zhao J, Wen HS, et al. 2019. The impact of acute thermal stress on the metabolome of the black rockfish (*Sebastes schlegelii*). *PLoS One*, **14**(5): e0217133.

Stocco DM. 2000. The role of the StAR protein in steroidogenesis: challenges for the future. *Journal of Endocrinology*, **164**(3): 247–253.

Swart P, Lombard N, Swart AC, et al. 2003. Ovine steroid 17α-hydroxylase cytochrome P450: characteristics of the hydroxylase and lyase activities of the adrenal cortex enzyme. *Archives of Biochemistry and Biophysics*, **409**(1): 145–152.

Tan D, Ertunc ME, Konduri S, et al. 2019. Discovery of FAHFA-containing triacylglycerols and their metabolic regulation. *Journal of the American Chemical Society*, **141**(22): 8798–8806.

Tan SY, Batterham M, Tapsell L. 2011. Increased intake of dietary polyunsaturated fat does not promote whole body or preferential abdominal fat mass loss in overweight adults. *Obesity Facts*, **4**(5): 352–357.

Urushibata H, Sasaki K, Takahashi E, et al. 2021. Control of developmental speed in zebrafish embryos using different incubation temperatures. *Zebrafish*, **18**(5): 316–325.

Van Der Kraak G, Pankhurst N. 1997. Temperature effects on the reproductive performance of fish. *In*: Wood CM, McDonald DG. Global Warming: Implications for Freshwater and Marine Fish. Cambridge: Cambridge University Press, 159–176.

Wang HM, Wang Y, Niu MH, et al. 2022a. Cold acclimation for enhancing the cold tolerance of zebrafish cells. *Frontiers in Physiology*, **12**: 813451.

Wang HY, Guo L, Zha RF, et al. 2022b. Histological, metabolomic and transcriptomic analyses reveal mechanisms of cold acclimation of the Moso bamboo (*Phyllostachys edulis*) leaf. *Tree Physiology*, **42**(11): 2336–2352.

Wang Y, Wang HM, Zhou Y, et al. 2023. Dusp1 regulates thermal tolerance limits in zebrafish by maintaining mitochondrial integrity. *Zoological Research*, **44**(1): 126–141.

Windisch HS, Kathöver R, Pörtner HO, et al. 2011. Thermal acclimation in Antarctic fish: transcriptomic profiling of metabolic pathways. *American Journal of Physiology-Regulatory, Integrative and Comparative Physiology*, **301**(5): R1453–R1466.

Wood PL. 2020. Fatty acyl esters of hydroxy fatty acid (FAHFA) lipid families. *Metabolites*, **10**(12): 512.

Worthmann A, John C, Rühlemann MC, et al. 2017. Cold-induced conversion of cholesterol to bile acids in mice shapes the gut microbiome and promotes adaptive thermogenesis. *Nature Medicine*, **23**(7): 839–849.

Wu SM, Liu JH, Shu LH, et al. 2015. Anti-oxidative responses of zebrafish (*Danio rerio*) gill, liver and brain tissues upon acute cold shock. *Comparative Biochemistry and Physiology Part A: Molecular & Integrative Physiology*, **187**: 202–213.

Wu TT, Patel H, Mukai S, et al. 2000. Activin, inhibin, and follistatin in zebrafish ovary: expression and role in oocyte maturation. *Biology of Reproduction*, **62**(6): 1585–1592.

Xu SS, Li Y, Wang HP, et al. 2023. Depletion of *stearoyl-CoA desaturase* (*scd*) leads to fatty liver disease and defective mating behavior in zebrafish. *Zoological Research*, **44**(1): 63–77.

Yang X, Wu RC, Qi D, et al. 2021. Profile of bile acid metabolomics in the follicular fluid of PCOS patients. *Metabolites*, **11**(12): 845.

Yore MM, Syed I, Moraes-Vieira PM, et al. 2014. Discovery of a class of endogenous mammalian lipids with anti-diabetic and anti-inflammatory effects. *Cell*, **159**(2): 318–332.

Yu GQ, Liu X, Zhang DW, et al. 2020. Zebrafish Nedd8 facilitates ovarian development and the maintenance of female secondary sexual characteristics via suppression of androgen receptor activity. *Development*, **147**(18): dev194886.

Zhang BJ, Shen SM, Gu TW, et al. 2019. Increased circulating conjugated primary bile acids are associated with hyperandrogenism in women with polycystic ovary syndrome. *The Journal of Steroid Biochemistry and Molecular Biology*, **189**: 171–175.

Zhang XJ, Niu YG, Zhang HY, et al. 2021. The effect of long-term cold acclimation on redox state and antioxidant defense in the high-altitude frog. *Nanorana pleskei*. *Journal of Thermal Biology*, **99**: 103008.

Zhao C, Wang SJ, Liu YX, et al. 2023. Acute cold stress leads to zebrafish ovarian dysfunction by regulating miRNA and mRNA. *Comparative Biochemistry and Physiology Part D: Genomics and Proteomics*, **48**: 101139.

Yan et al. *Zool. Res.* 2024, 45(4): 805−820
https://doi.org/10.24272/j.issn.2095-8137.2024.038

ZR | Zoological Research

Article Open Access

# Microplastic exposure disturbs sleep structure, reduces lifespan, and decreases ovary size in *Drosophila melanogaster*

Wei Yan[1,2,#], Zi-Jie Li[1,#], Zi-Yi Lin[1,2], Shu-Qin Ji[1], William Ka Fai Tse[3], Zhi-Qiang Meng[1,2,4], Chang Liu[1,2,*], Lei Li[1,2,5,*]

[1] *Shenzhen-Hong Kong Institute of Brain Science*, *Shenzhen Institute of Advanced Technology*, *Chinese Academy of Sciences*, *Shenzhen*, *Guangdong* 518000, *China*

[2] *CAS Key Laboratory of Brain Connectome and Manipulation*, *the Brain Cognition and Brain Disease Institute*, *Shenzhen Institute of Advanced Technology*, *Chinese Academy of Sciences*, *Shenzhen*, *Guangdong* 518000, *China*

[3] *Laboratory of Developmental Disorders and Toxicology*, *Center for Promotion of International Education and Research*, *Faculty of Agriculture*, *Kyushu University*, *Fukuoka*, *Fukuoka* 819-0395, *Japan*

[4] *Shenzhen Key Laboratory of Drug Addiction*, *the Brain Cognition and Brain Disease Institute*, *Shenzhen Institute of Advanced Technology*, *Chinese Academy of Sciences*, *Shenzhen*, *Guangdong* 518000, *China*

[5] *Guangdong Provincial Key Laboratory of Brain Connectome and Behavior*, *Brain Cognition and Brain Disease Institute*, *Shenzhen Institute of Advanced Technology*, *Chinese Academy of Sciences*, *Shenzhen*, *Guangdong* 518000, *China*

## ABSTRACT

The organ-specific toxicity resulting from microplastic (MP) exposure has been extensively explored, particularly concerning the gut, liver, testis, and lung. However, under natural conditions, these effects are not restricted to specific organs or tissues. Investigating whether MP exposure presents a systemic threat to an entire organism, impacting factors such as lifespan, sleep, and fecundity, is essential. In this study, we investigated the effects of dietary exposure to two different doses of MPs (1–5 μm) using the terrestrial model organism *Drosophila melanogaster*. Results indicated that the particles caused gut damage and remained within the digestive system. Continuous MP exposure significantly shortened the lifespan of adult flies. Even short-term exposure disrupted sleep patterns, increasing the length of daytime sleep episodes. Additionally, one week of MP exposure reduced ovary size, with a trend towards decreased egg-laying in mated females. Although MPs did not penetrate the brain or ovaries, transcriptome analysis revealed altered gene expression in these tissues. In the ovary, Gene Ontology (GO) analysis indicated genotoxic effects impacting inflammation, circadian regulation, and metabolic processes, with significant impacts on extracellular structure-related pathways. In the brain, GO analysis identified changes in pathways associated with proteolysis and carbohydrate metabolism. Overall, this study provides compelling evidence of the systemic negative effects of MP exposure, highlighting the urgent need to address and mitigate environmental MP pollution.

**Keywords:** Microplastics; Sleep; Lifespan; Reproduction; Risk assessment; *Drosophila melanogaster*

## INTRODUCTION

An estimated 5 billion tons of plastics exist on Earth, with an additional 400 million tons produced annually (Lim, 2021). Recently, intensive attention has been directed towards microplastic (MP) pollutants, which result from the degradation of disposed plastics into particle fragments smaller than 5 mm in diameter (Hartmann et al., 2019). These MPs are ubiquitously distributed in the environment (Lim, 2021), with more than 5 trillion plastic pieces, containing at least 14.9 trillion MP particles and weighing more than $25\times10^4$ tons (Eriksen et al., 2014), floating in the ocean (Van Sebille et al., 2015). MP deposition occurs both indoors and outdoors, with central London samples showing deposition rates between

This is an open-access article distributed under the terms of the Creative Commons Attribution Non-Commercial License (http://creativecommons.org/licenses/by-nc/4.0/), which permits unrestricted non-commercial use, distribution, and reproduction in any medium, provided the original work is properly cited.

Copyright ©2024 Editorial Office of Zoological Research, Kunming Institute of Zoology, Chinese Academy of Sciences

Received: 04 February 2024; Accepted: 22 March 2024; Online: 23 March 2024

Foundation items: This work was supported by the Key Collaborative Research Program of the Alliance of International Science Organizations (ANSO-CR-KP-2021-12 to L.L.), National Natural Science Foundation of China (32071009, 32371063, 82341248 to C.L., 31971072 and 32171154 to L.L.), Guangdong Basic and Applied Basic Research Foundation (2024A1515011500 to C.L.), and Shenzhen Science Technology and Innovative Commission (SZSTI JCYJ20180508152336419 to L.L. and GJHZ20200731095406021 to S.J.)

[#]Authors contributed equally to this work

*Corresponding authors, E-mail: chang.liu3@siat.ac.cn; saralilei@siat.ac.cn

575 and 1 008 microplastics/$m^2$/day (Wright et al., 2020). In eastern China, indoor air MP concentrations (1 583±1 180 n/$m^3$) exceed outdoor air concentrations (189±85 n/$m^3$), and urban air concentrations (224±70 n/$m^3$) are higher than those in rural areas (101±47 n/$m^3$) (Liao et al., 2021).

Humans are not exempt from MP exposure. Studies have demonstrated the transfer of MPs from the environment to organisms (Mallik et al., 2021; Van Raamsdonk et al., 2020). Previous research has suggested that children and adults may ingest more than $10^5$ MPs daily (Nor et al., 2021), and MPs have been detected in human fecal samples (Schwabl et al., 2019; Zhang et al., 2021; Ho et al., 2022). Although concerns about the potential public health risks of MPs are increasing, direct evidence from the general population remains scarce. Animal studies have shown that MP exposure can pose health risks to organisms, including the gut (Jin et al., 2019; Lu et al., 2018; Zhang et al., 2020b), liver (Lu et al., 2016, 2018), testes (Deng et al., 2021; Hou et al., 2021; Jin et al., 2021; Wang et al., 2019a; Lin et al., 2024a, 2024b), developing embryos (Park et al., 2020; Zhang et al., 2020a), respiratory system (Lu et al., 2021), and locomotion function (Zhang et al., 2020b). RNA sequencing (RNA-seq) has also provided a better understanding of the detrimental effects of MP on organisms, revealing that MP exposure can induce an inflammatory response in the lungs of mice and alter gene expression related to the immune system and programmed cell death (Lu et al., 2021). Exposure to di-(2-ethylhexyl) phthalate (DEHP)-contaminated MPs affects the oxidative response, lipid metabolism, and immune response in mice (Deng et al., 2020). Recent studies have also highlighted genotoxic effects of MP, associated with oxidative stress, inflammation, and DNA repair disruption (Jin et al., 2018; Lei et al., 2018; Tagorti & Kaya, 2022).

The detrimental effects of MP exposure appear to extend beyond specific organs or tissues, posing a systemic threat to the entire organism (Deng et al., 2017). Various studies have explored the relationship among environmental pollutants, sleep, and longevity (Bushey et al., 2010; Chuang et al., 2018; Yu et al., 2019). A recent cohort analysis of the UK Biobank linked sleep quality to accelerated biological aging resulting from air pollution (i.e., $PM_{2.5}$ and $NO_2$) (Gao et al., 2022). However, direct evidence regarding the impact of MP exposure as inert pollutants on broader health aspects, such as sleep and lifespan, remains limited. Due to ethical and technical constraints, animal studies are indispensable for such research. *Drosophila melanogaster*, commonly known as the fruit fly, inhabits diverse environments, ranging from tropical to temperate climates (Skevington & Dang, 2002). This species shares many conserved functions with mammals, including gastrointestinal and reproductive functions. Fruit flies are attracted to rotting fruits and vegetables, which may be contaminated with MPs via plant uptake or airborne deposition (Azeem et al., 2021; Conti et al., 2020). Additionally, fruit fly larvae develop in the soil until the pupal stage, likely encountering MPs from contaminated soil (Ashburner et al., 1986; Wang et al., 2019b). Thus, *D. melanogaster* is an ideal organism for assessing MP toxicity due to its short life cycle, high reproductive rate, ease of handling, and extensive genetic tools, making it a highly tractable and powerful model for investigating molecular and cellular mechanisms (Aime & Adamantidis, 2022; Jiang & Pan, 2022; Ma et al., 2022; Wan et al., 2023; Wei et al., 2023).

In the present study, we evaluated the systemic toxicity of MPs in *D. melanogaster*, focusing on general health concepts, such as sleep, lifespan, and fecundity. The flies were exposed to food mixed with two concentrations of MPs: 1×MPs (0.02 mg/mL) and 10×MPs (0.2 mg/mL) (EFSA Panel on Contaminants in the Food Chain, 2016; Matthews et al., 2021; Zhong et al., 2022). Exposure periods covered different developmental stages, ranging from 2 days to 10 weeks. Results indicated that MP exposure led to intestinal damage, disrupted sleep patterns, reduced ovary size, shortened lifespan, and genotoxic effects, as revealed by RNA-seq analysis.

## MATERIALS AND METHODS

### *Drosophila melanogaster* stock and maintenance

Wild-type Canton-S flies were maintained in an environment with a temperature of 25°C and relative humidity of 60% under a 12 h light/dark cycle. All experiments were performed under these conditions. The flies were divided into three groups, with the control group raised on standard cornmeal-dextrose-yeast-agar food (per batch: 4.4 L of $H_2O$, 24 g of agar, 80 g of yeast, 280 g of cornmeal, 200 g of sucrose, 40 g of soymeal, and 12 g of methylparaben). Female flies were used for most experiments unless otherwise specified.

### Microplastics (MPs)

Spherical MPs were purchased from Cospheric (Cat# FMG-Green Fluorescent Polymer Microspheres 1.3 g/cc 1–5 μm–500 mg, USA) (Barboza et al., 2018; Bringer et al., 2020; Lu et al., 2021). The MP size ranged from 1 to 5 μm, with excitation and emission wavelengths of 450 nm and 520 nm, respectively. MPs were added to the standard food at 60°C before solidification and stored in the dark (wrapped in foil paper). Flies were raised on standard food or standard food containing 0.02 mg/mL MP (1×MP group, particle concentration: $3.68\times10^6$/mL) or 0.2 mg/mL MP (10×MP group, particle number concentration: $3.68\times10^7$/mL), respectively (EFSA Panel on Contaminants in the Food Chain, 2016; Marsden et al., 2019; Matthews et al., 2021; Panacek et al., 2011; Posgai et al., 2011; World Health Organization, 2022; Zhang et al., 2020b; Zhong et al., 2022).

### Histological analysis of guts and ovaries

Whole adult flies were anesthetized with $CO_2$ and visualized under bright-field or fluorescent light using a fluorescence microscope (MF43-N, Mshot, China). Brains, guts, and ovaries were dissected at room temperature (24°C) in 1×phosphate-buffered saline (PBS). Fresh samples for immediate quantification of gut leakage and ovary size were imaged without fixation. Samples for qualitative analysis were fixed in 4% paraformaldehyde (Cat# 1.17701.018, GHTECH, China) for 30 min at 4°C, followed by 3×5 min washing in 1×PBS with 0.5% Triton (0.5% PBST). The fixed samples were then stained with 4',6-diamidino-2-phenylindole (DAPI, 1 μg/mL, Cat# C1005, Beyotime, China) for 5 min at room temperature. After rinsing with 0.5% PBST for 3×5 min, samples were mounted in VECTASHIELD antifade mounting medium (Cat# H-1000, Vector Laboratories, USA) and imaged using a 5×objective lens and an Apotome fluorescence microscope (Image 2Z, Zeiss, Germany). Images were analyzed using ZEN imaging (black edition) (https://www.zeiss.com/microscopy/en/products/software/zeiss-zen.html, Zeiss, Germany).

**Dye exclusion method using trypan blue**

Virgin flies aged 0–2 days were raised on standard food with 1×MPs, 10×MPs, or no MPs (control) for 6 days. On day 7, all groups were starved for 16 h prior to trypan blue treatment, then fed 2 mol/L sucrose solution with 10% trypan blue stain (Cat# 15-250-061, Gibco, USA) using 0.3 mm capillary tubes (Shanghai Changcheng, China) for 2 h. Subsequently, crops and guts were dissected in 1×PBS and imaged at 3×objective under a stereomicroscope (MZ101, Mshot, China) and digital camera (YH-1600, Yuehe, China). ImageJ (v.1.52P, https://imagej.nih.gov/ij/download.html) was used for image quantification. The width of the trypan blue-positive area and the cross-section diameter of each gut sample were measured, with the ratio used to evaluate the level of gut leakage.

**Sleep assays and sleep changes**

Flies were raised on standard cornmeal food at 25°C. Virgin flies (0–1 day old) were collected and individually placed in 65 mm×5 mm glass tubes containing 5% sucrose and 2% agar food at one end. These tubes, each holding a single fly, were loaded into the DAM2 system (TriKinetics, USA) at 25°C under a 12 h light/dark (LD) cycle. After 2 days of entrainment, baseline sleep was recorded for 2 days. On day 3, immediately after lights-on, flies were transferred to new tubes containing fresh food with 1×MPs, 10×MPs, or no MPs (control), and sleep was recorded for another 6 days. Sleep profiles were plotted in 30 min bins over the entire recording period. Sleep parameters, including total sleep, maximum episode length, mean episode length, number of episodes, and activity while awake, were analyzed for both the light and dark periods (LP and DP, respectively). Each parameter after 5 days of MP exposure was quantified as the change on day 8, normalized to the average of the baseline days (Δ=day 8−(day 1+day 2)/2). Analysis was performed using DAMFileScan113 and SCAMP 2019v2 (TriKinetics; https://www.trikinetics.com/) in MATLAB (RRID: SCR_001622).

**Lifespan assay**

Thirty virgin flies aged 0–1 day were placed into a vial containing standard cornmeal food with 1×MPs, 10×MPs, or no MPs (control). Virgin flies were used to exclude the possible influence of mating experience and oviposition on lifespan, thus ensuring baseline consistency. Flies were transferred to fresh food tubes every 2–3 days. Eight vial replicates were established for each treatment group. The number of living flies in each vial was recorded when the transfer occurred until all flies in each vial died.

**Ovary size evaluation**

Virgin flies aged 0–3 days were raised on three kinds of food containing 1×MPs, 10×MPs, or no MPs (control). Ovaries were collected and dissected in 1×PBS every 7 days from days 0 to 28, then imaged using a stereomicroscope and digital camera under the same settings as described above. Each ovary from a single fly was outlined as the region of interest (ROI) and measured using ImageJ (v.1.52P) (https://imagej.nih.gov/ij/download.html). The average ROI area from a pair of ovaries from a single fly was quantified for analysis.

**Female fecundity assay**

Forty virgin female flies (F0) and 40 male flies were allowed to mate overnight, with 10 females and 10 males per group selected and transferred to a Petri dish the following morning for egg collection for 2 h. Each dish contained 5% sucrose and 2% agar medium with yeast paste on top. To determine the effects of MPs on female fecundity during development, approximately 2 000 eggs were collected and distributed evenly into 48 vials with either standard food or 1×MP food until adulthood (F1). After eclosion, 15 F1 virgin females were collected and allowed to mate with 12 males without MP exposure, then transferred to a Petri dish for female fecundity tests for 6 consecutive days. Egg number was counted every 24 h using a microscope (MZ101, Mshot, China). Six control F1 and 1×MP-treated F1 group replicates were established for analysis.

To assess the effects of MPs on fertilization ability, 2–3-day-old virgins were raised on standard cornmeal food containing 1×MPs, 10×MPs, or no MPs (control) for 5 days. On day 6, male flies were introduced to mate with the virgin females for 2 days. On day 8, the females were transferred to a Petri dish for egg collection over a 24 h period.

To evaluate the effects of MPs on reproductive capacity, 2–3-day-old mated females were raised on standard cornmeal food containing 1×MPs, 10×MPs, or no MPs (control) for 7 days. On day 8, the females were transferred to a Petri dish for egg collection over a 24 h period.

Each Petri dish contained 2% yeast solution on top of an apple juice-agar medium to provide better contrast for the eggs, which were imaged using a digital camera (VARIO-SUMMILUX-H 1:1.9-2.4/17-80 ASPH, Leica, Germany). Egg number was counted using the Cell Counter plugin in ImageJ (v.1.52P) (https://imagej.nih.gov/ij/download.html). Sixteen replicates were established for each group for analysis.

**RNA-seq analysis**

Virgin female flies aged 0–5 days were divided into 1×MP and control groups. Each group initially consisted of four vials containing 40 flies each. Flies were raised for 48 days, with transfer to new vials containing fresh food with/without 1×MPs every 2–3 days. Brain and ovary samples were first dissected in ice-cold adult hemolymph-like saline solution (AHL; 3.156 g of NaCl (Cat# 7647-14-5, Macklin, China), 1.712 g of sucrose (Cat# 57-50-1, Sigma-Aldrich, USA), 0.946 g of trehalose (Cat# 6138-23-4, Sigma-Aldrich, USA), 0.834 g of $MgCl_2$-$6H_2O$ (Cat# 7791-18-6, Sigma-Aldrich, USA), 0.596 g of HEPES (Cat# 7365-45-9, Sigma-Aldrich, USA), 0.186 g of KCl (Cat# 7447-40-7, Sigma-Aldrich, USA), 0.168 g of $NaHCO_3$ (Cat# 144-55-8,Sigma-Aldrich, USA), 0.147 g of $CaCl_2$ (Cat# 10035-04-8, Macklin, China), and 0.069 g of $NaH_2PO_4$-$H_2O$ (Cat# 10049-21-5, Macklin, China) in 500 mL; pH 7.5), then transferred to a centrifuge tube in liquid nitrogen. The brains of 40 flies from either the control or 1×MP group were pooled together as one sample for RNA extraction. Three samples from the control group and two samples from the 1×MP group with high-quality RNA (RNA integrity number, RIN>7.0) were included for further RNA-seq analysis. Similarly, the ovaries of 40 flies from either the control group or 1×MP group were pooled together as one sample. Four samples from the control group and three samples from the 1×MP group were included for further RNA-seq analysis.

RNA extraction, library construction, and sequencing of samples were completed by Hangzhou Lianchuan Biotechnology (China). Total RNA was extracted using Trizol reagent (Cat# 15596018, Thermo Fisher, USA) following the manufacturer's procedures. Total RNA quantity and purity were analyzed using a Bioanalyzer 2100 and RNA 6000 Nano

LabChip Kit (Cat# 5067-1511, Agilent, USA), with high-quality RNA samples (RIN>7.0) used to construct the sequencing library. After extraction, mRNA was purified from the total RNA (5 μg) using Dynabeads Oligo (dT) (Cat# 61002, Thermo Fisher, USA), with two rounds of purification. The mRNA was then fragmented into short fragments using a Magnesium RNA Fragmentation Module (Cat# 6150S NEB, USA). The cleaved RNA fragments were reverse-transcribed to create cDNA using SuperScript™ II Reverse Transcriptase (Cat# 18064014, Invitrogen, USA), which was then used to synthesize U-labeled second-stranded DNA with *Escherichia coli* DNA polymerase I (Cat# M0209S, NEB, USA), RNase H (Cat# 0297S, NEB, USA), and dUTP Solution (Cat# R0133, Thermo Fisher, USA). An A-base was then added to the blunt ends of each strand for ligation to the indexed adapters. Each adapter contained a T-base overhang for ligation of the adapter to the A-tailed fragmented DNA. Dual-index adapters were ligated to the fragments, and size selection was performed with AMPureXP beads (Cat# A63882, Beckman Coulter, USA). After heat-labile UDG enzyme (Cat# 0280S, NEB, USA) treatment of the U-labeled second-stranded DNA, the ligated products were amplified by polymerase chain reaction (PCR) under the following conditions: initial denaturation at 95°C for 3 min; eight cycles of denaturation at 98°C for 15 s, annealing at 60°C for 15 s, extension at 72°C for 30 s; and final extension at 72°C for 5 min. The average insert size for the final cDNA libraries was 300±50 bp. Finally, 2×150 bp paired-end sequencing (PE150) was performed using the Illumina NovaSeq™ 6000 platform (LC-Bio Technologies, China) following the vendor's recommended protocols. To obtain high-quality clean reads, reads were filtered using Cutadapt (v.1.9, https://cutadapt.readthedocs.io/en/stable/) and sequence quality was verified using FastQC (v.0.11.9, http://www.bioinformatics.babraham.ac.uk/projects/fastqc/). Differentially expressed gene (DEG) analysis between two different groups was performed using DESeq2 (https://bioconductor.org/packages/release/bioc/html/DESeq2.html) (Love et al., 2014; Sahraeian et al., 2017) based on $|\log_2$ fold-change$|\geq 1$ and *Q*-value<0.05. The DEGs were then subjected to Gene Ontology (GO) enrichment analysis (Ashburner et al., 2000; Gene Ontology Consortium, 2021). Data analysis and visualization were performed using R (https://www.r-project.org/) and the OmicStudio platform of LC-Bio Technologies (China; https://www.omicstudio.cn/tool).

### Statistical analysis

All statistical analyses were performed using GraphPad Prism v.8 (RRID:SCR_002798) (GraphPad Software, USA). Data are presented as mean±standard error of the mean (SEM) with individual values. For normally distributed data, one-way analysis of variance (ANOVA) followed by Bonferroni's multiple comparison test or student *t*-test was applied, while for non-normally distributed data, the Kruskal-Wallis test followed by Dunn's multiple comparison test was used. Significance was set to $P<0.05$. All statistical analyses are summarized in Supplementary Tables S1, S2.

## RESULTS

### MPs were detected in the digestive system

The MP particles used to treat flies were first verified using bright-field and fluorescence microscopy (Figure 1A). The green fluorescent microspheres ranged in size from 1 to 5 μm, with a density of 1.3 g/cc, zeta potential of 23.14 mV, and softening point and decomposition temperature of 290°C, as described in our previous study (Lu et al., 2021). To confirm whether the MPs mixed in food were ingested and retained in the digestive system, flies were exposed to standard cornmeal food with 1×MPs, 10×MPs, or standard food alone (control) for 2 days (Figure 1B). Fluorescence signals were examined in the whole body, followed by collection and further examination of the digestive organs. After 2 days of exposure, MPs were observed in the thorax and abdomen, with strong signals detected in the crops and guts (Figure 1C).

### MP exposure caused gut damage in adult flies

Previous research has shown that MP exposure leads to gut damage in fly larvae (Zhang et al., 2020b). To examine whether MP exposure also causes gut damage in adult flies, adult flies were exposed to standard food or MP-mixed food at two doses (1×MPs and 10×MPs) from days 1–7. The trypan blue dye exclusion method, which selectively stains dead tissues or cells (Strober, 2001) (Figure 2A), revealed visible trypan blue in the abdomens of intact flies exposed to 1×MPs and 10×MPs but not in control flies (Figure 2B). The ratio of trypan blue-positive areas in gut sections exhibited a significant increase in the 1×MP and 10×MP groups compared

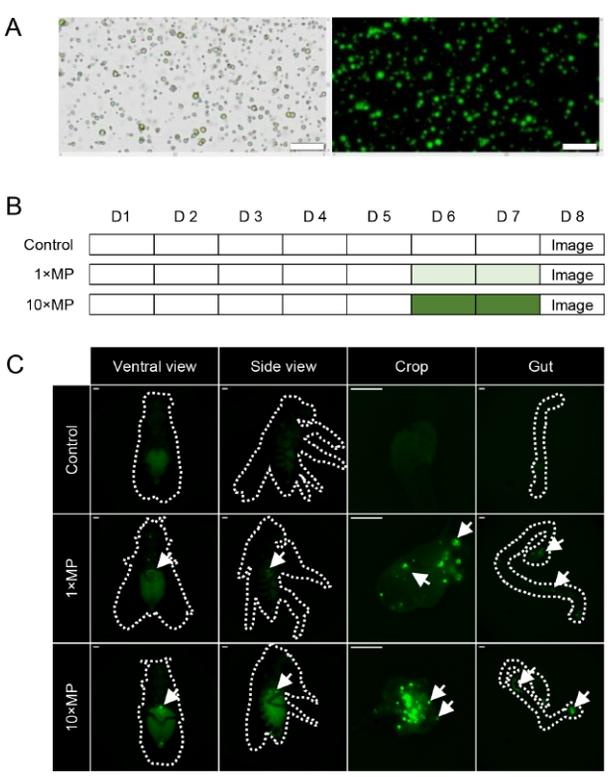



**Figure 1 Microplastics (MP) were ingested and retained in the digestive system**

A: MPs used for exposure were characterized under light and fluorescent microscopy. Scale bars: 20 μm. B: Flies of the treatment groups were raised on standard food for 5 days and exposed to MPs at two doses: 1×MPs (0.02 mg/mL MP mixed in food) and 10×MPs (0.2 mg/mL mixed in food) from days 6 to 7. Control and MP-treated groups were sampled on day 8 and subjected to imaging analysis (D represents day). C: Fluorescence-labeled MPs were detected in crops and guts after 2 days of MP treatment (dashed lines indicate outlines of flies, arrows indicate MP with fluorescence; *n*=5–7 per group. Scale bars: 200 μm).

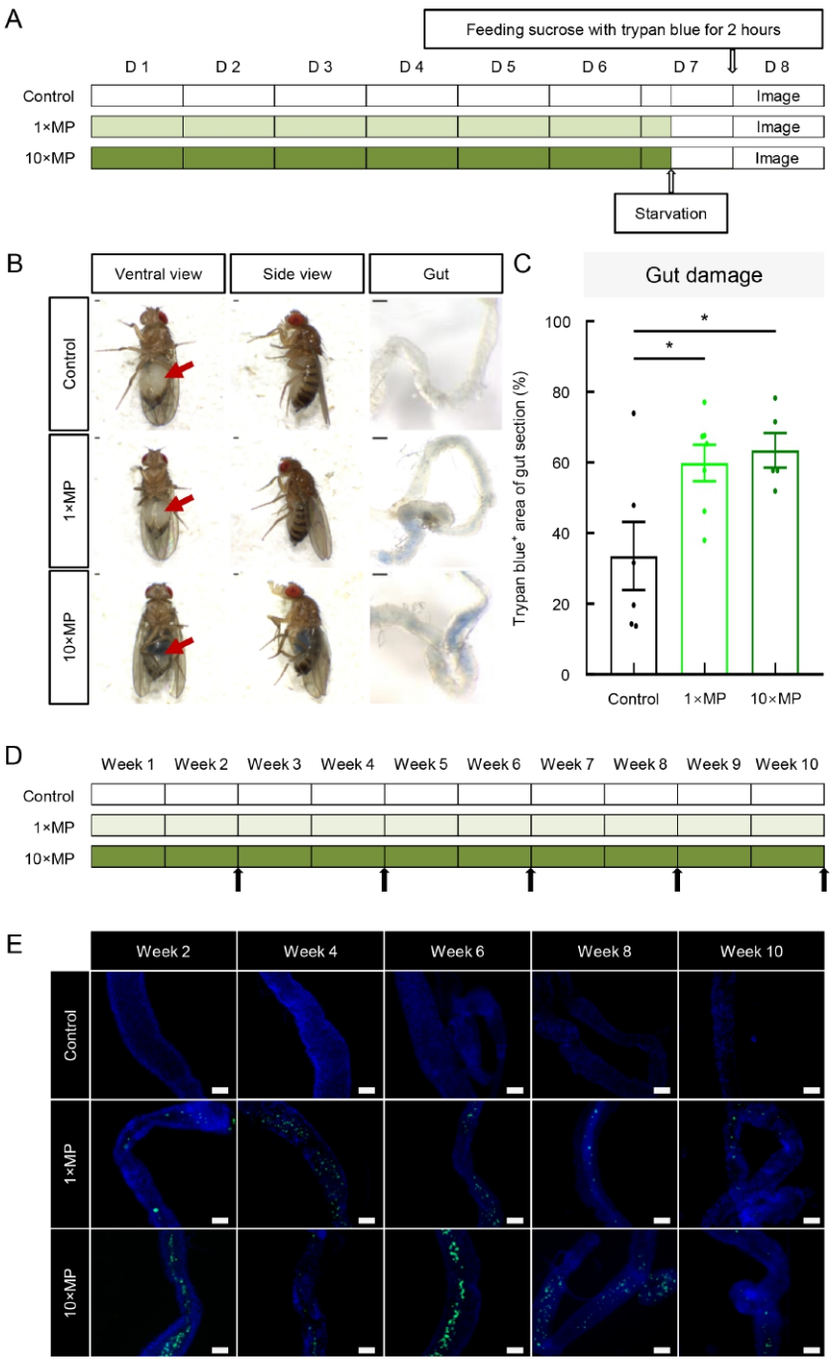



**Figure 2 Intestinal cell damage was detected in MP-treated groups using trypan blue dye exclusion method**

A: Adult flies were exposed to standard food or MP mixed in food at two doses: 1×MPs and 10×MPs from days 1 to 7. On day 7, flies were starved for 16 h, then fed sucrose with trypan blue on day 8 for 2 h, with images taken 2 h later (D represents day). B: Gut leakage was revealed by trypan blue staining of gut walls of 1×MP and 10×MP treatment groups compared to controls (arrows indicate trypan blue in abdomen) . Scale bars: 200 μm. C: Quantitative analysis of trypan blue-colored proportion of gut section showed a significant increase of gut-damaged area in 1×MP and 10×MP groups compared to controls ($n$=5–7 per group, one-way ANOVA followed by Bonferroni's *post-hoc* analysis, *: $P$<0.05). D: Following chronic MP exposure for 10 weeks, sub-groups of flies were dissected, and guts were imaged at the end of weeks 2, 4, 6, 8, and 10 (arrows indicate sampling and imaging time points). E: MPs were observed in the guts at all examined time points ($n$=3 per group). Scale bars: 100 μm.

to the controls (Figure 2B, C), suggesting that MP-induced gut damage occurred as early as 7 days of treatment in adult flies. To determine how long MP remain in the digestive system, flies were chronically exposed to MP for up to 10 weeks (Figure 2D). Results showed that MPs were robustly detected in gut samples collected every 2 weeks over the 10 week period (Figure 2E). These findings demonstrate that MPs mixed in food are ingested, cause significant gut damage, and remain in the digestive system.

### MP exposure reduced *D. melanogaster* lifespan

Previous studies have demonstrated an association between gut homeostasis and lifespan (Fan et al., 2018; Galenza & Foley, 2021). Given the observed gut damage following MP exposure, we hypothesized that continuous MP exposure would reduce lifespan. As expected, flies in the MP-treated groups exhibited a reduction in lifespan compared to flies in

the control group (Figure 3A). We further quantified survival rates on days 7, 14, and 21 (Figure 3B). Although the 1×MP group exhibited a declining survival trend, the difference was not significant at any time point. In contrast, the 10×MP group showed significantly lower survival rates on days 14 and 21 compared to the control group. These findings indicate that MP exposure reduces lifespan, with the onset of death occurring as early as day 9 of treatment (Figure 3A).

**MP exposure disturbed sleep structure and altered brain gene expression**

Gut function has been linked to sleep regulation (Tang et al., 2022; Vaccaro et al., 2020). To investigate whether MP-induced gut damage leads to abnormal sleep, flies were placed in a *D. melanogaster* activity monitor system (DAM2) for continuous observation under standard, 1×MP, or 10×MP food conditions (Figure 4A). Results indicated that the sleep profiles showed no significant differences among the groups before or after MP exposure (Figure 4B). On day 8, after 5 days of exposure, the daytime maximum sleep episode length was significantly increased in the 1×MP group compared to the control, while no significant change was observed in the 10×MP group (Figure 4C, middle panel). Furthermore, no significant changes in total sleep, mean episode duration, number of episodes, or locomotion were detected (Figure 4C). These findings suggest that MP exposure can disturb sleep structure by increasing daytime maximum sleep episode length, supporting the link between gut function and daytime sleepiness.

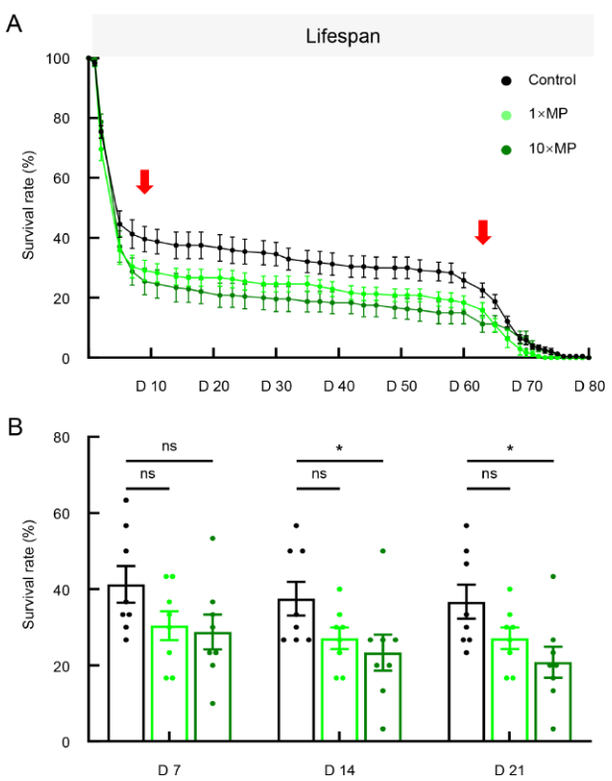



**Figure 3 MP exposure reduced lifespan in flies**

A: Both 1×MP and 10×MP treatments reduced lifespan. B: Quantitative analysis of the survival rate at different time points: days 7, 14, and 21 showed that 10×MP treatment resulted in a significant decrease in fly survival rate ($n$=8 tubes per group, 30 flies per tube initially; one-way ANOVA followed by Bonferroni's *post-hoc* analysis, *: $P$<0.05; ns: Not significant). D represents day. Solid red arrows indicate range of significant differences between control and 10×MP groups.

Although no accumulation of MP signals was detected in fly brains over the 10 week period (Figure 5A), 48 days of MP exposure led to changes in gene expression in the brain. Notably, transcriptomic analysis identified 98 DEGs, including nine up-regulated and 89 down-regulated genes, which were subjected to GO enrichment analysis (Figure 5B, C; Table 1). Results showed that MP exposure significantly altered the expression of genes related to hydrolase activity, peptidase activity, serine-type peptidase activity, proteolysis, and carbohydrate metabolism. Despite the absence of MP signals in the brain, our findings suggest potential involvement in regulating the brain-gut axis through pathways that modulate neuropeptide and metabolite levels and stability, influence the balance of energy supply and consumption, and participate in cell signaling and the release of inflammatory mediators during inflammatory responses.

**MP exposure impacted ovarian size and response**

Previous studies have reported MP penetration in rodent ovaries (An et al., 2021). To examine the potential presence and impact of MPs in fruit fly ovaries, flies were exposed to varying durations and concentrations of MPs, with the ovaries then dissected and measured at weeks 0, 1, 2, 3, and 4 (Figure 6A). At baseline (week 0), ovary sizes were similar across all groups. In the control group, ovary size increased during the first week and remained at a comparable level until the end of week 4 (Figure 6C, D). In contrast, MP-treated flies had significantly smaller ovaries compared to the control group, with notable size reductions observed at weeks 1, 3, and 4 for the 1×MP group and weeks 1 and 2 for the 10×MP group (Figure 6C, D), suggesting that MP exposure inhibits ovarian development.

Mendes & Mirth (2016) showed that different nutrient conditions significantly influence ovary size plasticity and ovariole number. An egg-laying assay was conducted to assess the impacts of MP exposure on female fecundity. Regardless of whether MP exposure occurred in larvae during development (Figure 7A, B), adult virgin females (Figure 7C), or adult mated females (Figure 7D), no significant difference in the number of eggs laid was observed between the MP-treated and control groups (Figure 7B–D).

To determine why ovary size decreased despite normal egg-laying ability, we first tested for MP penetration over a 10 week period. Results showed that, unlike in rodents, no MP signals were detected in the ovaries of fruit flies (Figure 8A).

For further insight into the impact of MP exposure, ovarian samples from flies exposed to 1×MPs for 48 days were subjected to transcriptomic analysis. Notably, 732 DEGs were identified, including 688 up-regulated and 44 down-regulated genes, which were subjected to GO enrichment analysis (Figure 8B, C). Results showed that MP exposure altered the expression of genes involved in extracellular region/space, hydrolase activity, lipid metabolism, fatty acid elongation and biosynthesis, and regulation of egg-laying behavior (Figure 8C; Table 2). Despite the absence of MPs in the ovary, the proximity of the gut to the ovary suggests that MPs leaking from the gut may affect ovarian development. These findings indicate that MP exposure can affect the extracellular matrix (ECM) surrounding the ovary and disrupt ovarian development.

## DISCUSSION

The distribution and concentration of MPs in the environment

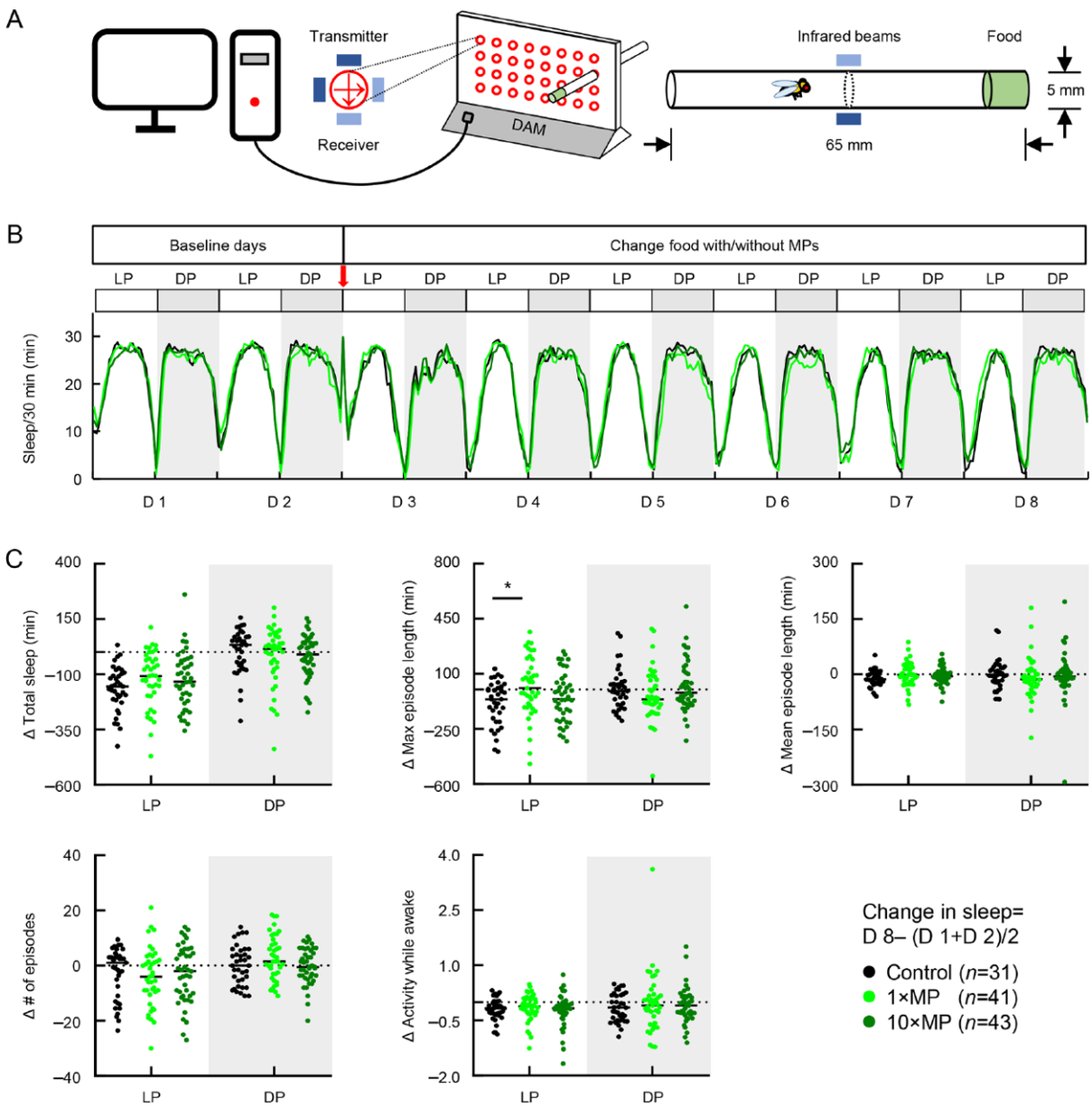



**Figure 4 MP exposure disturbed sleep structure in flies**

A: Schematic of *D. melanogaster* activity monitoring system. Sleep activity was detected by recording crossing changes in infrared beams at the tube center. B: Adult flies were raised on standard food from days 1–2, then transferred to standard food or MP mixed in food at two doses: 1×MPs and 10×MPs from days 3–8. Sleep profile of total sleep with/without MP food across 8 days (D represents day). C: Quantitative analysis of changes in sleep amount, maximum episode length, mean episode length, number of episodes, and activity while awake during daytime (LP, light period) and nighttime (DP, dark period) showed that 1×MP treatment resulted in a significant increase in maximum episode length during daytime ($n$=31–43 per group; one-way ANOVA followed by Bonferroni's *post-hoc* analysis, *: $P$<0.05).

have been extensively documented (Fu et al., 2020; Yu et al., 2016), and their potential adverse effects have been studied in various organs and tissues using animal models, including both invertebrates and vertebrates (Prokić et al., 2021). In the present study, we used *D. melanogaster* as a terrestrial animal model to study the impacts of chronic MP exposure on sleep, lifespan, and reproduction. We used two doses of MPs (0.02 mg/mL and 0.2 mg/mL mixed in food) previously reported to adversely affect normal fly development and mating behavior (Panacek et al., 2011; Posgai et al., 2011; Zhang et al., 2020b).

Following dietary exposure to MPs, fluorescence-labeled MP particles were detected in the digestive system of the flies, with retention in the crops and guts. Gut leakage and cell damage were revealed by trypan blue staining. The detrimental impact of MPs on gut physiology is consistent with findings in adult zebrafish (Jin et al., 2018, 2019; Qiao et al., 2019), marine medaka (Kang et al., 2021), mice (Lu et al., 2018), larval flies (Demir et al., 2022), and adult flies (Zhang et al., 2020b), albeit with MP concentrations approximately 100 times higher than those used in the current study. Ingested MPs have also been detected in other organs, including the liver (Collard et al., 2017) and placenta (Ragusa et al., 2021), suggesting that ingested MPs may potentially affect other organs beyond the digestive system.

The gut serves as a crucial interface between the body and environment, initiating the pathophysiological processes of various multisystem diseases. In addition to gut damage, MP

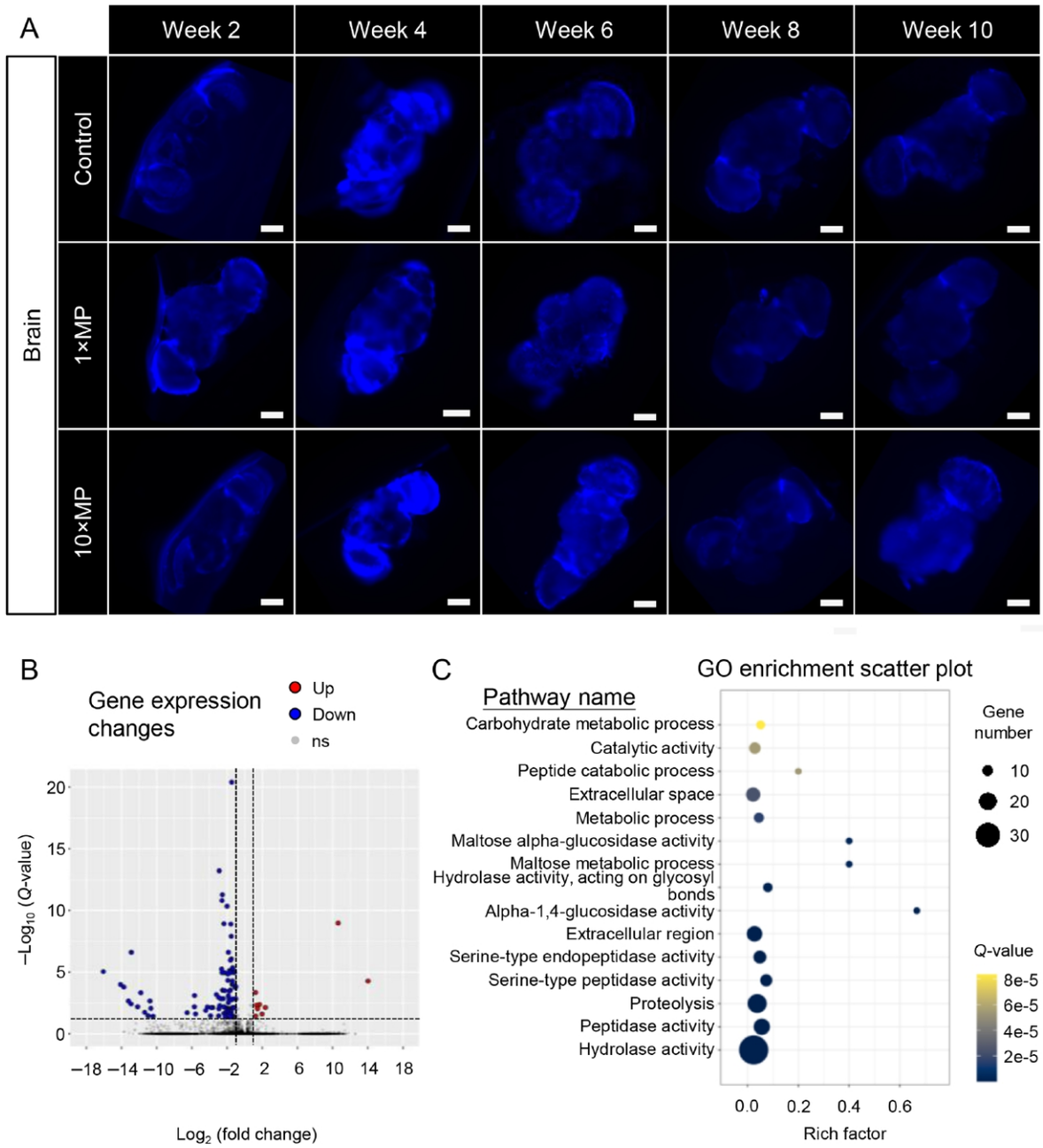



**Figure 5 No MPs were detected in brains after 10 weeks of MP treatment, but altered brain gene expression was observed**

A: Adult flies were exposed to standard food or MP mixed in food at two doses. Treatment continued for 10 weeks, and sub-groups of flies were dissected and imaged at the end of weeks 2, 4, 6, 8, and 10. No MPs were observed in fly brains at any time point (scale bars=100 μm). B: MP exposure led to differential gene expression in fly brains. C: Gene Ontology (GO) enrichment analysis showed brain pathways altered by MP exposure (rich factor indicates degree of pathway enrichment score. *Q*-value represents significance of enriched pathway).

exposure significantly increased the length of daytime sleep episodes without affecting locomotion ability. This subtle yet significant impact on daytime sleep episode length should not be neglected, as both sleep quantity and quality are vital for overall physiological health (Pilcher et al., 1997; Wesselius et al., 2018). For instance, patients with obstructive sleep apnea exhibit markedly higher levels of intestinal barrier markers (Li et al., 2021), suggesting a link between gut impairment and sleep abnormalities. The “gut-brain axis” is associated with sleep via the immune response, endocrine regulation, and neural modulation (Sgro et al., 2022; Tang et al., 2022). Here, transcriptome GO analysis revealed that MP exposure altered molecular pathways related to hydrolase, peptidase, and serine-type peptidase activity, as well as proteolysis and carbohydrate metabolism, in the brain. These observations suggest that MP exposure may affect the regulation of the brain-gut axis, altering the levels and stability of neuropeptides and metabolites, as well as the balance of energy supply and consumption. Previous studies have shown that changes in sleep duration and quality can affect protein hydrolysis (Piovezan et al., 2015), while protein hydrolysates can alleviate stress and enhance sleep (Qian et al., 2021). GO enrichment analysis indicated that the hydrolase and proteolysis pathways may play a role in sleep structure modulation. GO analysis also indicated that MP exposure down-regulated carbohydrate metabolism, consistent with

**Table 1 Pathway-related genes shown in GO scatter plot of the brain**

| Terms | *Q*-value | Genes |
|---|---|---|
| Hydrolase activity | 3.88E-15 | *Mal-A1, CG12374, CG31198, LysD, Jon25Biii, Bace, Alp10, βTry, Cht9, Jon99Ci, Jon25Bi, LManVI, LManV, Jon99Cii, primo-2, CG6295, mus312, CG15255, CG31343, εTry, Alp9, CG10472, CG18180, Jon99Ciii, CG3841, CG8773, CG15534, Alp2, CG31233, CG6048, LysP, Jon74E, Jon99Fi, Mal-A2, Phae1, CG6696, CG6283* |
| Peptidase activity | 2.12E-12 | *CG31198, Bace, βTry, Jon99Ci, Jon25Bi, Jon99Cii, CG15255, CG31343, εTry, CG10472, CG18180, Jon99Ciii, CG8773, CG31233, CG6048, Jon74E, Jon99Fi, CG6696* |
| Proteolysis | 3.65E-12 | *CG12374, CG31198, Jon25Biii, Bace, βTry, Jon99Ci, Jon25Bi, Jon99Cii, CG15255, CG31343, εTry, CG10472, CG18493, CG18180, Jon99Ciii, CG8773, CG31233, CG6048, Jon74E, Jon99Fi, Phae1, CG6696* |
| Serine-type peptidase activity | 1.60E-09 | *βTry, Jon99Ci, Jon25Bi, Jon99Cii, εTry, CG10472, CG18493, CG18180, Jon99Ciii, CG6048, Jon74E, Jon99Fi* |
| Serine-type endopeptidase activity | 3.26E-08 | *Jon25Biii, βTry, Jon99Ci, Jon25Bi, Jon99Cii, εTry, CG10472, CG18180, Jon99Ciii, CG6048, Jon74E, Jon99Fi, Phae1* |
| Extracellular region | 3.08E-07 | *Obp56e, yellow-d, βTry, Cht9, CG6295, Obp99a, CG10725, Diedel, εTry, CG34426, Ag5r, Cp36, lectin-37Da, Mur18B, Lsp1α, js, CG6283* |
| Alpha-1,4-glucosidase activity | 3.27E-07 | *Mal-A1, Mal-A7, Mal-A4, Mal-A2* |
| Hydrolase activity, acting on glycosyl bonds | 1.09E-06 | *Mal-A1, LysD, Cht9, LManVI, LManV, CG15534, LysP, Mal-A2* |
| Maltose metabolic process | 3.15E-06 | *Mal-A1, Mal-A7, Mal-A4, Mal-A2* |
| Maltose alpha-glucosidase activity | 3.15E-06 | *Mal-A1, Mal-A7, Mal-A4, Mal-A2* |
| Metabolic process | 1.56E-05 | *Mal-A1, LysD, Cht9, LManVI, LManV, CG15534, Ugt35E2, LysP, Mal-A2* |
| Extracellular space | 2.37E-05 | *Obp56e, CG12374, LysD, βTry, Cht9, Listericin, Jhbp12, Obp99a, Diedel, εTry, Ag5r, CG15534, CG14913, LysP, Lsp1α* |
| Peptide catabolic process | 5.39E-05 | *CG31198, CG31343, CG8773, CG31233* |
| Catalytic activity | 5.50E-05 | *Mal-A1, LysD, Mal-A7, Alp10, LManVI, LManV, Alp9, Alp2, Mal-A4, LysP, Mal-A2* |
| Carbohydrate metabolic process | 8.35E-05 | *Mal-A1, Mal-A7, Cht9, LManVI, LManV, Mal-A4, Mal-A2* |
| Metalloaminopeptidase activity | 1.12E-04 | *CG31198, CG31343, CG8773, CG31233* |
| Peptide binding | 1.24E-04 | *CG31198, CG31343, CG8773, CG31233* |
| Metallopeptidase activity | 1.43E-04 | *CG31198, CG15255, CG31343, CG8773, CG31233, CG6696* |
| Aminopeptidase activity | 4.72E-04 | *CG31198, CG31343, CG8773, CG31233* |
| Alpha-glucosidase activity | 1.02E-03 | *Mal-A1, Mal-A2* |
| Carbohydrate binding | 1.08E-03 | *LManVI, LManV, CG15818, lectin-37Da, CG14500* |
| Alkaline phosphatase activity | 1.14E-03 | *Alp10, Alp9, Alp2* |
| Phosphatidylserine 1-acylhydrolase activity | 2.81E-03 | *CG6295, CG6283* |
| 1-acyl-2-lysophosphatidylserine acylhydrolase activity | 2.81E-03 | *CG6295, CG6283* |
| Chitin binding | 3.94E-03 | *Cht9, CG10725, CG34426, Mur18B, js* |
| Phospholipase A1 activity | 5.41E-03 | *CG6295, CG6283* |
| Cytolysis | 8.56E-03 | *LysD, LysP* |
| Alpha-mannosidase activity | 8.56E-03 | *LManVI, LManV* |
| Rhythmic behavior | 9.95E-03 | *tim, vri* |
| Mannose metabolic process | 9.95E-03 | *LManVI, LManV* |
| Cell wall macromolecule catabolic process | 1.40E-02 | *LysD, LysP* |
| Chitin metabolic process | 1.63E-02 | *CG10725, CG34426, Mur18B, js* |
| Protein deglycosylation | 2.31E-02 | *LManVI, LManV* |
| Endopeptidase activity | 2.31E-02 | *Jon25Biii, Jon99Ci, Jon25Bi* |
| Lysozyme activity | 2.52E-02 | *LysD, LysP* |
| Defense response to Gram-positive bacterium | 2.99E-02 | *LysD, Listericin, LysP* |
| Obsolete nuclear telomeric heterochromatin | 2.99E-02 | *SuUR* |
| Protein localization to chromosome | 2.99E-02 | *SuUR* |
| Photoperiodism | 2.99E-02 | *tim* |
| Negative regulation of transcription regulatory region DNA binding | 2.99E-02 | *tim* |
| Aspartic-type endopeptidase activity involved in amyloid precursor protein catabolic process | 2.99E-02 | *Bace* |
| Neuromuscular junction development, skeletal muscle fiber | 2.99E-02 | *Act57B* |
| Neutral L-amino acid transmembrane transporter activity | 2.99E-02 | *NAAT1* |
| Neutral amino acid transport | 2.99E-02 | *NAAT1* |
| L-amino acid transport | 2.99E-02 | *NAAT1* |

Continued

| Terms | Q-value | Genes |
|---|---|---|
| D-amino acid transport | 2.99E-02 | *NAAT1* |
| D-amino acid transmembrane transporter activity | 2.99E-02 | *NAAT1* |
| Imaginal disc-derived wing hair organization | 3.07E-02 | *vri, qua* |
| Cell surface | 3.11E-02 | *Alp10, Alp9, Alp2* |
| Chitinase activity | 3.80E-02 | *LysD, Cht9* |
| Phosphatase activity | 3.86E-02 | *Alp10, Alp9, Alp2* |
| Actin filament | 4.84E-02 | *Act57B, qua* |
| Negative regulation of DNA-templated DNA replication | 4.84E-02 | *SuUR* |
| Amyloid precursor protein catabolic process | 4.84E-02 | *Bace* |
| Non-membrane spanning protein tyrosine phosphatase activity | 4.84E-02 | *primo-2* |
| Slx1-Slx4 complex | 4.84E-02 | *mus312* |
| Homologous recombination | 4.84E-02 | *mus312* |
| 3'-flap endonuclease activity | 4.84E-02 | *mus312* |

previous research showing that mice on a carbohydrate-restricted diet exhibit decreased survival and accelerated aging, along with alterations in gut microbiota that promote inflammation (He et al., 2020). MP exposure may trigger an inflammatory response, increasing the duration of sleep episodes (Besedovsky et al., 2019). Our transcriptomic analysis demonstrated that MP exposure altered the expression of *achl*, a gene involved in signal transduction from neurons to immune tissues. The up-regulation of *achl*, which inhibits the expression of immune response genes (Li et al., 2017), may decrease the resistance of flies, negatively impacting immune function and overall physiological state, including lifespan. However, several recent studies have indicated that exposure to higher MP concentrations can significantly shorten the total amount of sleep in *D. melanogaster* (Jin et al., 2024; Tang et al., 2023). These differing results may be due to the dose effect, but further research is needed to clarify the underlying mechanisms.

All living organisms are continuously exposed to MPs, which are widely distributed in the environment and negatively impact organisms across their entire lives. Our assays on flies revealed that both MP doses caused a significant decrease in lifespan. Although no significant dose-dependent effect of MP treatment was detected, there was a trend towards further reduction in lifespan under the 10×MP dose compared to the 1×MP dose, in alignment with recent findings at even higher doses (1 000× and 2 000×) (Kauts et al., 2023). Previous studies have shown that exposure to polystyrene microbeads reduces growth rates and lifespan in monogonont rotifers (Jeong et al., 2016), while ingestion of high concentrations of polyethylene MPs increases mortality rates in sea bass larvae (Mazurais et al., 2015). Comparable adverse effects on lifespan have also been observed in *Caenorhabditis elegans* larvae after 3 days of MP exposure (Shang et al., 2020), as well as in flies exposed to MPs for 28 days (El Kholy & Al Naggar, 2023; Urbisz et al., 2024). However, to the best of our knowledge, the present study is the first to demonstrate the detrimental effects of MP exposure on *D. melanogaster* lifespan (up to 80 days), highlighting potentially sensitive and resistant windows. Although direct evidence linking MP exposure to human lifespan is lacking, the urgency to address environmental MP pollutants remains critical. Further studies are needed to elucidate the cellular and molecular mechanisms underlying MP-induced shortened lifespan. Our findings of gut damage from MP exposure, as revealed by trypan blue staining, suggest a possible link between gut homeostasis and lifespan (Fan et al., 2018; Galenza & Foley, 2021). Several animal models have reported disturbed gut microbiota linked to the adverse effects of MP exposure (Fackelmann & Sommer, 2019; Jin et al., 2018; Lu et al., 2018, 2019). For instance, Newell & Douglas (2014) demonstrated that axenic flies show longer developmental stages and elevated glucose and triglyceride levels. Gould et al. (2018) reported that fly lifespan and fecundity are impacted by gut microbiome diversity. The intestine, a plastic organ influenced by both external and internal factors (Colombani & Andersen, 2020), coordinates physiological activities. Altered gut microbiota from intermittent fasting is associated with lifespan extension in flies via target of rapamycin (TOR)-independent pathways (Catterson et al., 2018). Reactive oxygen species (ROS) may be another candidate pathway by which MP exposure reduces lifespan, as ROS accumulation in the gut contributes to sleep dysfunction and death (Vaccaro et al., 2020). Proteolysis, a hallmark of aging, is disrupted by MP exposure, leading to increased oxidative stress, cellular damage, DNA damage, and aging processes, ultimately impacting lifespan (Korovila et al., 2017). Our GO enrichment analyses identified proteolysis as one of the top significant pathways, providing molecular insight into the MP-induced reduction in survival rates.

Beyond individual lifespan, fecundity is essential for species reproduction and population survival. The effects of MP exposure on animal reproductive systems have been extensively studied, including zebrafish (Qiang & Cheng, 2021), male mice (Deng et al., 2021; Hou et al., 2021; Jin et al., 2021), and female rats (An et al., 2021). In our study, we observed a decrease in ovary size in flies after just one week of MP exposure, which persisted during the chronic 4 week MP exposure period. Consistent with previous studies (Goodman et al., 2021), cell morphology was altered in cells exposed to MPs. Transcriptomic analysis also suggested that MP exposure altered ECM gene expression. Fly ovaries can regenerate three types of cells, namely, germline (GSC), somatic (SSC) and escort stem cells (ESC) (Kirilly & Xie, 2007). The ECM plays a pivotal role in maintaining and shaping the ovary and organizing ovarian stem cell niches (Díaz-Torres et al., 2021; Pearson et al., 2016). GO analysis also revealed that MP exposure altered fatty acid biosynthesis and elongation, consistent with findings of increased

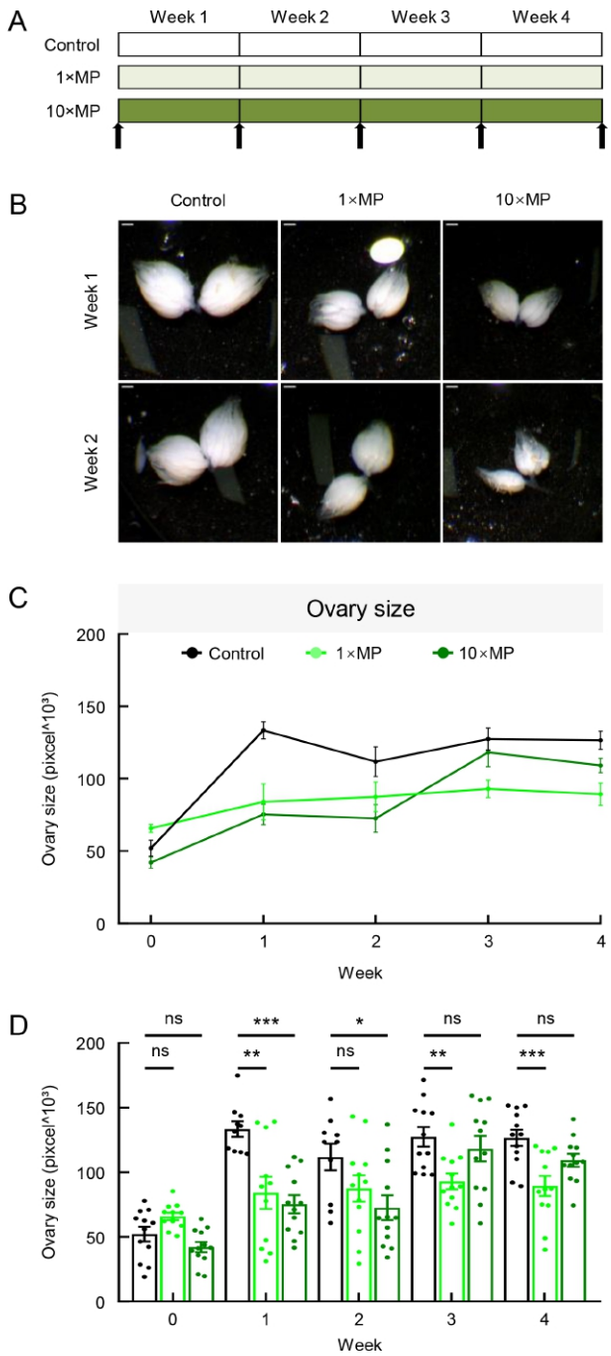



**Figure 6 MP exposure resulted in a reduction in ovary size**

A: Adult flies were exposed to standard food or MP mixed in food at two doses: 1×MPs and 10×MPs. Treatment continued for 4 weeks, and sub-groups of flies were dissected and imaged at weeks 0, 1, 2, 3, and 4 (arrows indicate dissection and imaging time points). B, C: 1×MP and 10×MP treatments both led to a reduction in ovary size. Scale bars: 200 μm. D: Quantitative analysis showed significant differences in 1×MP group at weeks 1, 3, and 4 and in 10×MP group at week 1 compared to controls ($n$=10–12 per group; one-way ANOVA followed by Bonferroni's *post-hoc* analysis, *: $P$<0.05; **: $P$<0.01; ***: $P$<0.001; ns: Not significant).

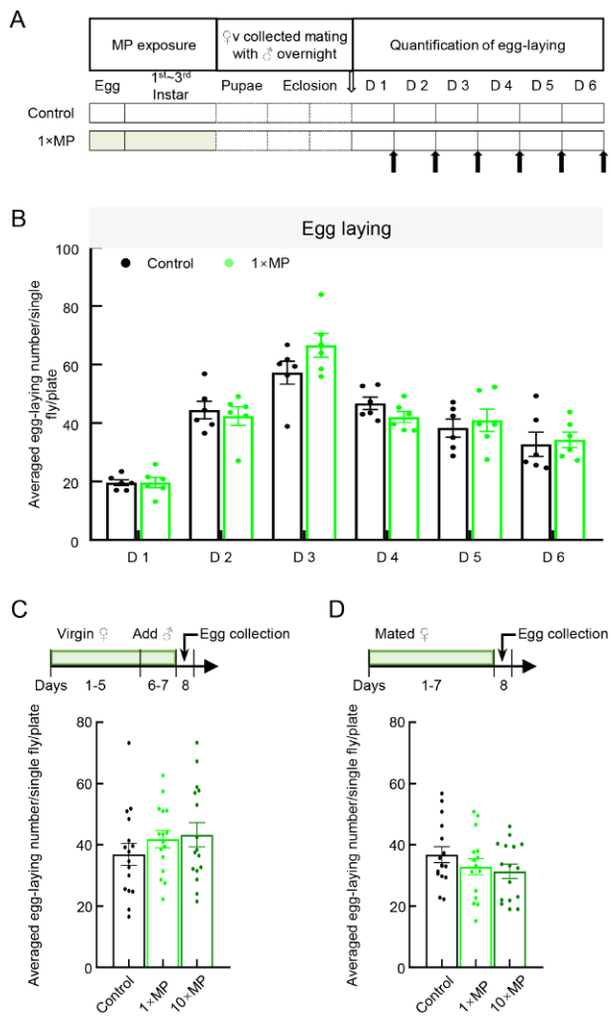



**Figure 7 Female fecundity showed resistance to exposure to 0.02 mg/mL and 0.2 mg/mL MP mixed in food**

A: To test the effect of MP exposure during development on female fecundity, embryos were exposed to 1×MPs until eclosion, with virgin flies mated with untreated males used for fertility tests. B: A 6-day egg-laying assay showed that MP treatment had no effect on egg-laying number ($n$=6 plates per group, 15 females per plate; Student $t$-test). C: To test the effect of MP exposure during adulthood on female fecundity of virgin flies, virgin flies were exposed to standard food or MP mixed in food at two doses: 1×MPs and 10×MPs from days 1–7. On day 6, untreated male flies were introduced and allowed to mate with females for 2 days. On day 8, females were transferred to a Petri dish for egg collection and images were taken and counted 24 h later. D: To test the effect of MP exposure during adulthood on female fecundity of mated flies, mated untreated female flies were exposed to standard food or MP mixed in food at two doses: 1×MPs and 10×MPs from days 1–7. On day 8, flies were transferred to a Petri dish for egg collection and images were taken and counted 24 h later. C, D: Quantitative analysis of number of eggs laid after MP exposure during adulthood in virgin and mated flies showed no significant difference between the control and MP-treated groups ($n$=16 per group, one-way ANOVA followed by Bonferroni's *post-hoc* analysis). D represent day.

unsaturated lipid concentrations in the ovaries of aged female flies (Li et al., 2022). Our results suggest MP exposure can alter ovarian structure by shifting unsaturated lipid biosynthesis and modifying the surrounding ECM. Ovarian development is influenced by nutritional conditions. For example, third instar larvae fed with 20% sucrose food exhibit decreased ovariole number compared to those fed with standard food (Mendes & Mirth, 2016). The smaller ovary size observed in our study upon MP exposure may be due to limited nutrient absorption resulting from MP-induced gut

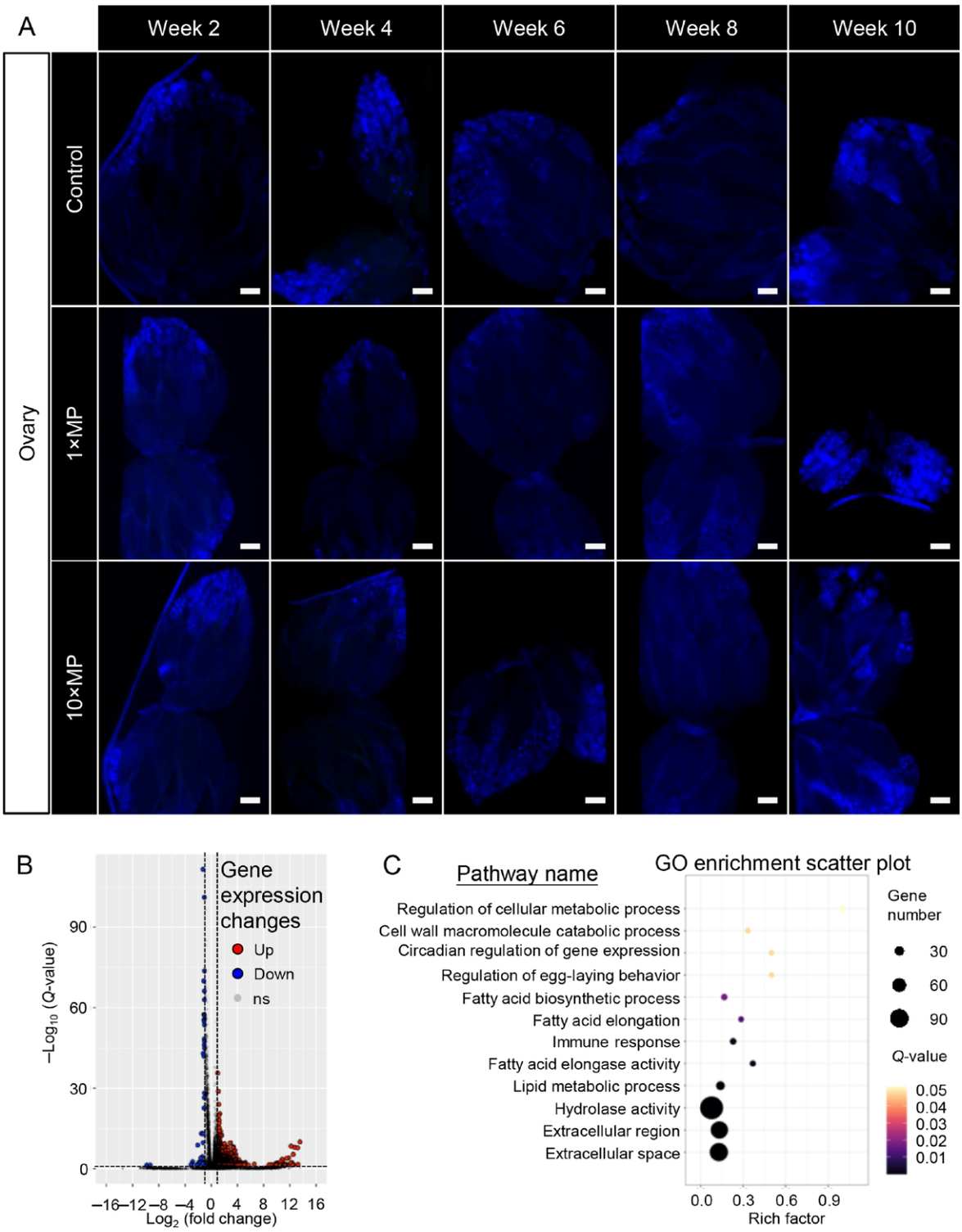



**Figure 8 No MPs were observed in the ovaries after 10 weeks of treatment, but ovarian gene expression was altered**

A: Adult flies were exposed to standard food or MP mixed in food at two doses: 1×MPs and 10×MPs. Treatment continued for 10 weeks, and sub-groups of flies were dissected and imaged at the end of weeks 2, 4, 6, 8, and 10. No MPs were observed in the ovaries at any time point (scale bars=100 μm; *n*=3–4 per group). B: MP exposure led to differential gene expression in the fly ovaries. C: GO enrichment analysis showed pathways altered in the ovaries following MP exposure (rich factor indicates degree of pathway enrichment score. *Q*-value represents significance of enriched pathway).

damage. Moreover, structural interaction between the ovary and parts of the midgut and hindgut housed in the abdomen may contribute to this effect. Gut leakage can initiate local immune responses, indirectly affecting the ovaries, as supported by GO enrichment in the immune response pathway. Although GO analysis showed MP exposure altered genes related to circadian regulation and egg-laying behavior, no significant changes in egg-laying were detected, even at distinct developmental stages. This finding aligns with previous studies using MP concentrations 1 000 times higher

**Table 2 Pathway-related genes shown in GO scatter plot of the ovaries**

| Terms | Q-value | Genes |
|---|---|---|
| Extracellular space | 5.97E-15 | *ImpL2, mfas, CG10433, Swim, CG17633, Ance, Timp, gbb, retinin, CG8562, PGRP-LB, Ag5r2, Obp99c, Mmp1, CG6959, SPARC, CG5162, CG3868, CG42342, CG5867, PGRP-LC, NLaz, nec, CG5945, Adgf-D, CG18585, LysP, CG8093, PGRP-SC1a, CG5397, Est-6, Ag5r, CG7142, PGRP-LA, Ance-4, Spn43Ab, CG14820, Spn42Dd, CG33127, CG8560, LysX, CG16799, Spn77Ba, Npc2e, Spn47C, CG17919, etaTry, CCHa2, CG15534, CG9400, Apoltp, Ilp7, CG18628, CG4546, CG31997, Fst, PGRP-SC2, CG44008, CG16820, Peritrophin-15a, upd3, LysS, iotaTry, CG3604, Tep3, CG9673, PGRP-SC1b, CG42780, CG9672, CG14661, Vm32E, Npc2h, BG642312, daw, upd1, Spn28Dc, CG15533, CG18067, Gasp, CG32984, ssp7, Phk-3, CG31207, serp, Spn42Dc, tsl, CG8539, Pde1c* |
| Extracellular region | 9.18E-15 | *ImpL2, Fs, CG18749, CG17633, Ance, Timp, gbb, retinin, Nplp3, PGRP-LB, CG6283, Ag5r2, Obp99c, Vm26Aa, CG4666, Vm26Ab, Yp2, CG5162, Yp1, Vm34Ca, CG42397, CG42486, Muc26B, bou, lectin-37Da, PGRP-SC1a, CG5177, Gbp2, Idgf1, Est-6, EbpIII, Yp3, Ag5r, Npc2g, CG6277, Spn42Dd, Muc68E, yellow-k, Glt, l (2)34Fc, CG14526, Spn77Ba, CG18258, fon, shf, CG32284, etaTry, CCHa2, CG15293, CG9400, Ilp7, NimB3, spheroide, ckd, PGRP-SC2, yellow-d, CG3505, upd3, dec-1, iotaTry, Tep3, CG13075, Lectin-galC1, PGRP-SC1b, Vm32E, Npc2h, CG6933, daw, NimB2, upd1, Spn28Dc, fat-spondin, Gasp, yellow-c, grass, Phk-3, yellow-d2, CG10116, Nplp4, serp, tsl, CG7298* |
| Hydrolase activity | 9.15E-06 | *alpha-Man-IIb, Swim, Jon25Biii, CG17633, laza, Ance, Jon99Fii, CG10477, CG8562, PGRP-LB, LManVI, CG4822, Mipp1, CG10472, Jon99Fi, CG6283, nrv2, lambdaTry, Mmp1, CG30100, alpha-Est7, CG11911, Yp2, FASN2, CG16749, CG5162, LManV, CG17571, eya, PGRP-LC, Yp1, CG15255, CG14120, CG7378, CG31343, CG33346, CG43110, Adgf-D, CG18585, LysP, CG33082, Mal-A2, CG9449, CG8093, PGRP-SC1a, CG10827, Jon65Aii, CG5397, CG5177, hiro, Est-6, mag, Yp3, CG11842, Jon65Ai, CG5171, CG7142, CG9701, PGRP-LA, Ance-4, CG18180, CG14820, alpha-Est8, CG6277, Amy-p, LManI, Jon44E, Decay, CG33127, CG8560, Glt, LysX, CG16799, CG30002, CG3819, CG10970, CG9676, CG14526, Mal-A3, CG4653, CG18258, etaTry, CG15534, kappaTry, spheroide, CG31198, PGRP-SC2, CG3505, CG11841, CG30371, CG11912, LysS, iotaTry, CG11147, CG9673, CG9649, CG9780, PGRP-SC1b, CG4301, CG9672, CG6067, Phae2, CG31326, CG1809, DNaseII, Nlg1, alpha-Est2, CG15533, grass, CG31200, CG31265, Jon66Ci, CG42335, Btnd, CG10116, Vha100-5, serp, CG8539, Pde1c* |
| Lipid metabolic process | 2.24E-04 | *CG8303, CG30008, CG5326, CG9743, melt, CG16904, CG6283, CG5162, CG18609, NLaz, Fad2, CG8093, mag, GstE14, CG9458, CG6277, CG18258, CG10097, CG6660, Npc1b, eloF, CG17562, FarO, CG15531, Cyt-b5-r* |
| Immune response | 1.16E-03 | *Swim, PGRP-LB, Thor, PGRP-LC, nec, PGRP-SC1a, PGRP-LA, PGRP-SC2, upd3, PGRP-SC1b, CG15529* |
| Fatty acid elongase activity | 1.16E-03 | *CG30008, CG5326, CG16904, CG18609, CG9458, CG6660, eloF* |
| Fatty acid elongation | 1.16E-02 | *CG30008, CG5326, CG16904, CG18609, CG9458, eloF* |
| Fatty acid biosynthetic process | 1.58E-02 | *CG30008, CG5326, CG9743, CG16904, CG18609, Fad2, CG9458, CG6660, eloF, CG15531* |
| Cell wall macromolecule catabolic process | 4.39E-02 | *LysP, LysX, CG16799, LysS* |
| Circadian regulation of gene expression | 4.39E-02 | *nej, cry, Clk* |
| Regulation of egg-laying behavior | 4.39E-02 | *Gadd45, Drip, Est-6* |
| Regulation of cellular metabolic process | 4.76E-02 | *hry, melt* |

than ours (Jin et al., 2024). However, several earlier studies have reported impaired female reproductive function, possibly due to a dose effect (Shen et al., 2021; Tang et al., 2023). As such, further investigation is needed to clarify how different MP concentrations impact reproductive functions and to explore potential generational/cross-generational impacts. Another study in flies reported a reduction in egg-laying after 28 days of MP exposure (Urbisz et al., 2024). We speculate that these differences in results may be attributable to an interactive effect of age and accumulated MP impact, as egg-laying typically peaks around 8–10 days after eclosion (Aigaki & Ohba, 1984), and no detectable MP entry into the ovary was observed in our study, even after 10 weeks of exposure.

Our study has several limitations. Although we observed a decrease in ovary size after 4 weeks of MP exposure, the underlying mechanisms and subtle effects on reproduction, including potential impacts on future generations, require further investigation. Additionally, efforts should be made to explore the link between reduced lifespan and diminished ovaries. Furthermore, the combined effects of MPs with potentially accumulated organic pollutants or heavy metals could exacerbate the adverse impacts on lifespan and reproduction, given the release of phthalate esters (Deng et al., 2020), polychlorinated biphenyls (Nor & Koelmans, 2019), and Cd, Pb, and Zn heavy metals (Yan et al., 2020) from MPs and other small particles (Alaraby et al., 2020; Anand et al., 2019). Reported MP concentrations in the natural environment also vary widely, ranging from $2.5\times10^{-5}$ to 121 mg/mL (EFSA Panel on Contaminants in the Food Chain, 2016), with fresh/drinking water concentrations ranging from $3.75\times10^{-5}$ to 0.162 mg/mL (Marsden et al., 2019) and indoor and outdoor air concentrations ranging from $16.7\times10^{-3}$ to $1\times10^{3}$ f/mL (Li et al., 2020; Wright & Kelly, 2017). Further studies are needed to investigate the impacts of different MP exposure concentrations and provide a more realistic understanding of animal responses.

## DATA AVAILABILITY

The raw metagenomics sequencing reads can be downloaded from the NCBI (PRJNA1101743), China National Center for Bioinformation (PRJCA025077), and Science Data Bank databases (DOI:10.57760/sciencedb.j00139.00127).

## COMPETING INTERESTS

The authors declare that they have no competing interests.

## AUTHORS' CONTRIBUTIONS

W.Y. and Z.J.L.: Conceptualization, Investigation, Methodology, Formal analysis, Visualization, Writing-original draft. Z.Y.L.: Investigation, Resources. S.Q.J.: Investigation, Funding acquisition. W.K.F.T.: Investigation and editing. Z.Q.M.: Formal analysis, Writing-review & editing. L.L. and C.L.: Conceptualization, Writing-original draft, review & editing, Supervision, Project administration, Funding acquisition. All authors read and approved the final version of the manuscript.

## REFERENCES


Aigaki T, Ohba S. 1984. Individual analysis of age-associated changes in reproductive activity and lifespan of *Drosophila virilis*. *Experimental Gerontology*, **19**(1): 13–23.

Aime M, Adamantidis AR. 2022. Sleep to survive predators. *Neuroscience Bulletin*, **38**(9): 1114–1116.

Alaraby M, Demir E, Domenech J, et al. 2020. *In vivo* evaluation of the toxic and genotoxic effects of exposure to cobalt nanoparticles using *Drosophila melanogaster*. *Environmental Science: Nano*, **7**(2): 610–622.

An R, Wang XF, Yang L, et al. 2021. Polystyrene microplastics cause granulosa cells apoptosis and fibrosis in ovary through oxidative stress in rats. *Toxicology*, **449**: 152665.

Anand AS, Gahlot U, Prasad DN, et al. 2019. Aluminum oxide nanoparticles mediated toxicity, loss of appendages in progeny of *Drosophila melanogaster* on chronic exposure. *Nanotoxicology*, **13**(7): 977–989.

Ashburner M, Ball CA, Blake JA, et al. 2000. Gene ontology: tool for the unification of biology. *Nature Genetics*, **25**(1): 25–29.

Ashburner M, Carson HL, Thompson Jr JN. 1986. The Genetics and Biology of Drosophila. vol. 3e. London: Academic Press.

Azeem I, Adeel M, Ahmad MA, et al. 2021. Uptake and accumulation of nano/microplastics in plants: a critical review. *Nanomaterials* (*Basel*), **11**(11): 2935.

Barboza LGA, Vieira LR, Branco V, et al. 2018. Microplastics increase mercury bioconcentration in gills and bioaccumulation in the liver, and cause oxidative stress and damage in *Dicentrarchus labrax* juveniles. *Scientific Reports*, **8**(1): 15655.

Besedovsky L, Lange T, Haack M. 2019. The sleep-immune crosstalk in health and disease. *Physiological Reviews*, **99**(3): 1325–1380.

Bringer A, Cachot J, Prunier G, et al. 2020. Experimental ingestion of fluorescent microplastics by pacific oysters, *Crassostrea gigas*, and their effects on the behaviour and development at early stages. *Chemosphere*, **254**: 126793.

Bushey D, Hughes KA, Tononi G, et al. 2010. Sleep, aging, and lifespan in *Drosophila*. *BMC Neuroscience*, **11**: 56.

Catterson JH, Khericha M, Dyson MC, et al. 2018. Short-term, intermittent fasting induces long-lasting gut health and TOR-independent lifespan extension. *Current Biology*, **28**(11): 1714–1724. e4.

Chuang HC, Su TY, Chuang KJ, et al. 2018. Pulmonary exposure to metal fume particulate matter cause sleep disturbances in shipyard welders. *Environmental Pollution*, **232**: 523–532.

Collard F, Gilbert B, Compère P, et al. 2017. Microplastics in livers of European anchovies (*Engraulis encrasicolus*, L. ). *Environmental Pollution*, **229**: 1000–1005.

Colombani J, Andersen DS. 2020. The *Drosophila* gut: A gatekeeper and coordinator of organism fitness and physiology. *WIREs Developmental Biology*, **9**(6): e378.

Conti GO, Ferrante M, Banni M, et al. 2020. Micro- and nano-plastics in edible fruit and vegetables. The first diet risks assessment for the general population. *Environmental Research*, **187**: 109677.

Demir FT, Akkoyunlu G, Demir E. 2022. Interactions of ingested polystyrene microplastics with heavy metals (Cadmium or Silver) as environmental pollutants: a comprehensive in vivo study using *Drosophila melanogaster*. *Biology* (*Basel*), **11**(10): 1470.

Deng YF, Yan ZH, Shen RQ, et al. 2020. Microplastics release phthalate esters and cause aggravated adverse effects in the mouse gut. *Environment International*, **143**: 105916.

Deng YF, Yan ZH, Shen RQ, et al. 2021. Enhanced reproductive toxicities induced by phthalates contaminated microplastics in male mice (*Mus musculus*). *Journal of Hazardous Materials*, **406**: 124644.

Deng YF, Zhang Y, Lemos B, et al. 2017. Tissue accumulation of microplastics in mice and biomarker responses suggest widespread health risks of exposure. *Scientific Reports*, **7**: 46687.

Díaz-Torres A, Rosales-Nieves AE, Pearson JR, et al. 2021. Stem cell niche organization in the *Drosophila* ovary requires the ECM component Perlecan. *Current Biology*, **31**(8): 1744–1753. e5.

EFSA Panel on Contaminants in the Food Chain. 2016. Presence of microplastics and nanoplastics in food, with particular focus on seafood. *EFSA Journal*, **14**(6): e04501.

El Kholy S, Al Naggar Y. 2023. Exposure to polystyrene microplastic beads causes sex-specific toxic effects in the model insect *Drosophila melanogaster*. *Scientific Reports*, **13**(1): 204.

Eriksen M, Lebreton LCM, Carson HS, et al. 2014. Plastic pollution in the world's oceans: more than 5 trillion plastic pieces weighing over 250, 000 tons afloat at sea. *PLoS One*, **9**(12): e111913.

Fackelmann G, Sommer S. 2019. Microplastics and the gut microbiome: How chronically exposed species may suffer from gut dysbiosis. *Marine Pollution Bulletin*, **143**: 193–203.

Fan XL, Gaur U, Yang MY. 2018. Intestinal homeostasis and longevity: drosophila gut feeling. *Advances in Experimental Medicine and Biology*, **1086**: 157–168.

Fu DD, Chen CM, Qi HY, et al. 2020. Occurrences and distribution of microplastic pollution and the control measures in China. *Marine Pollution Bulletin*, **153**: 110963.

Galenza A, Foley E. 2021. A glucose-supplemented diet enhances gut barrier integrity in *Drosophila*. *Biology Open*, **10**(3): bio056515.

Gao X, Huang NH, Guo XB, et al. 2022. Role of sleep quality in the acceleration of biological aging and its potential for preventive interaction on air pollution insults: Findings from the UK Biobank cohort. *Aging Cell*, **21**(5): e13610.

Goodman KE, Hare JT, Khamis ZI, et al. 2021. Exposure of human lung cells to polystyrene microplastics significantly retards cell proliferation and triggers morphological changes. *Chemical Research in Toxicology*, **34**(4): 1069–1081.

Gould AL, Zhang V, Lamberti L, et al. 2018. Microbiome interactions shape host fitness. *Proceedings of the National Academy of Sciences of the United States of America*, **115**(51): E11951–E11960.

Hartmann NB, Huffer T, Thompson RC, et al. 2019. Are we speaking the same language? Recommendations for a definition and categorization framework for plastic debris. *Environmental Science & Technology*, **53**(3): 1039–1047.

He CQ, Wu QM, Hayashi N, et al. 2020. Carbohydrate-restricted diet alters the gut microbiota, promotes senescence and shortens the life span in senescence-accelerated prone mice. *The Journal of Nutritional Biochemistry*, **78**: 108326.

Ho YW, Lim JY, Yeoh YK, et al. 2022. Preliminary Findings of the High Quantity of Microplastics in Faeces of Hong Kong Residents. *Toxics*, **10**(8).

Hou BL, Wang FY, Liu T, et al. 2021. Reproductive toxicity of polystyrene microplastics: In vivo experimental study on testicular toxicity in mice. *Journal of Hazardous Materials*, **405**: 124028.

Jeong CB, Won EJ, Kang HM, et al. 2016. Microplastic size-dependent

toxicity, oxidative stress induction, and p-JNK and p-p38 activation in the monogonont rotifer (*Brachionus koreanus*). *Environmental Science & Technology*, **50**(16): 8849–8857.

Jiang XY, Pan YF. 2022. Neural control of action selection among innate behaviors. *Neuroscience Bulletin*, **38**(12): 1541–1558.

Jin H, Xu YF, Kong FH, et al. 2024. Chronic exposure to polytetrafluoroethylene microplastics caused sex-specific effects in the model insect, *Drosophila melanogaster* (Diptera: Drosophilidae). *Journal of Economic Entomology*, doi: 10.1093/jee/toae015.

Jin HB, Ma T, Sha XX, et al. 2021. Polystyrene microplastics induced male reproductive toxicity in mice. *Journal of Hazardous Materials*, **401**: 123430.

Jin YX, Lu L, Tu WQ, et al. 2019. Impacts of polystyrene microplastic on the gut barrier, microbiota and metabolism of mice. *Science of the Total Environment*, **649**: 308–317.

Jin YX, Xia JZ, Pan ZH, et al. 2018. Polystyrene microplastics induce microbiota dysbiosis and inflammation in the gut of adult zebrafish. *Environmental Pollution*, **235**: 322–329.

Kang HM, Byeon E, Jeong H, et al. 2021. Different effects of nano- and microplastics on oxidative status and gut microbiota in the marine medaka *Oryzias melastigma. Journal of Hazardous Materials*, **405**: 124207.

Kauts S, Mishra Y, Yousuf S, et al. 2023. Toxicological profile of polyethylene terephthalate (PET) microplastic in ingested *Drosophila melanogaster* (Oregon $R^+$) and its adverse effect on behavior and development. *Toxics*, **11**(9): 782.

Kirilly D, Xie T. 2007. The *Drosophila* ovary: an active stem cell community. *Cell Research*, **17**(1): 15–25.

Korovila I, Hugo M, Castro JP, et al. 2017. Proteostasis, oxidative stress and aging. *Redox Biology*, **13**: 550–567.

Lei LL, Wu SY, Lu SB, et al. 2018. Microplastic particles cause intestinal damage and other adverse effects in zebrafish *Danio rerio* and nematode *Caenorhabditis elegans. Science of the Total Environment*, **619–620**: 1–8.

Li JJ, Terry EE, Fejer E, et al. 2017. *Achilles* is a circadian clock-controlled gene that regulates immune function in *Drosophila. Brain, Behavior, and Immunity*, **61**: 127–136.

Li QJ, Xu T, Zhong H, et al. 2021. Impaired intestinal barrier in patients with obstructive sleep apnea. *Sleep and Breathing*, **25**(2): 749–756.

Li YJ, Bagheri P, Chang P, et al. 2022. Direct imaging of lipid metabolic changes in *Drosophila* ovary during aging using DO-SRS microscopy. *Frontiers in Aging*, **2**: 819903.

Li YW, Shao LY, Wang WH, et al. 2020. Airborne fiber particles: Types, size and concentration observed in Beijing. *Science of the Total Environment*, **705**: 135967.

Liao ZL, Ji XL, Ma Y, et al. 2021. Airborne microplastics in indoor and outdoor environments of a coastal city in Eastern China. *Journal of Hazardous Materials*, **417**: 126007.

Lim XZ. 2021. Microplastics are everywhere - but are they harmful?. *Nature*, **593**(7857): 22–25.

Lin Z, Li Z, Ji S, et al. 2024a. Size-dependent deleterious effects of nano- and microplastics on sperm motility. *Toxicology*, **506**: 153834.

Lin Z, Li Z, Ji S, et al. 2024b. Microplastics from face mask impairs sperm motility. *Mar Pollut Bull*, **203**: 116422.

Love MI, Huber W, Anders S. 2014. Moderated estimation of fold change and dispersion for RNA-seq data with DESeq2. *Genome Biology*, **15**(12): 550.

Lu K, Lai KP, Stoeger T, et al. 2021. Detrimental effects of microplastic exposure on normal and asthmatic pulmonary physiology. *Journal of Hazardous Materials*, **416**: 126069.

Lu L, Luo T, Zhao Y, et al. 2019. Interaction between microplastics and microorganism as well as gut microbiota: A consideration on environmental animal and human health. *Science of the Total Environment*, **667**: 94–100.

Lu L, Wan ZQ, Luo T, et al. 2018. Polystyrene microplastics induce gut microbiota dysbiosis and hepatic lipid metabolism disorder in mice. *Science of the Total Environment*, **631–632**: 449–458.

Lu YF, Zhang Y, Deng YF, et al. 2016. Uptake and accumulation of polystyrene microplastics in zebrafish (*Danio rerio*) and toxic effects in liver. *Environmental Science & Technology*, **50**(7): 4054–4060.

Ma BX, Wang RC, Liu YH, et al. 2022. Serotonin signaling modulates sexual receptivity of virgin female *Drosophila. Neuroscience Bulletin*, **38**(11): 1277–1291.

Mallik A, Xavier KAM, Naidu BC, et al. 2021. Ecotoxicological and physiological risks of microplastics on fish and their possible mitigation measures. *Science of the Total Environment*, **779**: 146433.

Marsden P, Koelmans AA, Bourdon-Lacombe J, et al. 2019. Microplastics in drinking water. Geneva: World Health Organization.

Matthews S, Xu EG, Dumont ER, et al. 2021. Polystyrene micro- and nanoplastics affect locomotion and daily activity of *Drosophila melanogaster. Environmental Science: Nano*, **8**(1): 110–121.

Mazurais D, Ernande B, Quazuguel P, et al. 2015. Evaluation of the impact of polyethylene microbeads ingestion in European sea bass (*Dicentrarchus labrax*) larvae. *Marine Environmental Research*, **112**: 78–85.

Mendes CC, Mirth CK. 2016. Stage-specific plasticity in ovary size is regulated by insulin/insulin-like growth factor and ecdysone signaling in *Drosophila. Genetics*, **202**(2): 703–719.

Newell PD, Douglas AE. 2014. Interspecies interactions determine the impact of the gut microbiota on nutrient allocation in *Drosophila melanogaster. Applied and Environmental Microbiology*, **80**(2): 788–796.

Nor NHM, Koelmans AA. 2019. Transfer of PCBs from microplastics under simulated gut fluid conditions is biphasic and reversible. *Environmental Science & Technology*, **53**(4): 1874–1883.

Nor NHM, Kooi M, Diepens NJ, et al. 2021. Lifetime accumulation of microplastic in children and adults. *Environmental Science & Technology*, **55**(8): 5084–5096.

Panacek A, Prucek R, Safarova D, et al. 2011. Acute and chronic toxicity effects of silver nanoparticles (NPs) on *Drosophila melanogaster. Environmental Science & Technology*, **45**(11): 4974–4979.

Park EJ, Han JS, Park EJ, et al. 2020. Repeated-oral dose toxicity of polyethylene microplastics and the possible implications on reproduction and development of the next generation. *Toxicology Letters*, **324**: 75–85.

Pearson JR, Zurita F, Tomás-Gallardo L, et al. 2016. ECM-regulator *timp* is required for stem cell niche organization and cyst production in the *Drosophila* ovary. *PLoS Genetics*, **12**(1): e1005763.

Pilcher JJ, Ginter DR, Sadowsky B. 1997. Sleep quality versus sleep quantity: relationships between sleep and measures of health, well-being and sleepiness in college students. *Journal of Psychosomatic Research*, **42**(6): 583–596.

Piovezan RD, Abucham J, Dos Santos RVT, et al. 2015. The impact of sleep on age-related sarcopenia: Possible connections and clinical implications. *Ageing Research Reviews*, **23**: 210–220.

Posgai R, Cipolla-Mcculloch CB, Murphy KR, et al. 2011. Differential toxicity of silver and titanium dioxide nanoparticles on *Drosophila melanogaster* development, reproductive effort, and viability: size, coatings and antioxidants matter. *Chemosphere*, **85**(1): 34–42.

Prokić MD, Gavrilović BR, Radovanović TB, et al. 2021. Studying microplastics: Lessons from evaluated literature on animal model organisms and experimental approaches. *Journal of Hazardous Materials*, **414**: 125476.

Qian JJ, Zheng L, Su GW, et al. 2021. Identification and screening of potential bioactive peptides with sleep-enhancing effects in bovine milk casein hydrolysate. *Journal of Agricultural and Food Chemistry*, **69**(38): 11246–11258.

Qiang LY, Cheng JP. 2021. Exposure to polystyrene microplastics impairs gonads of zebrafish (*Danio rerio*). *Chemosphere*, **263**: 128161.

Qiao RX, Sheng C, Lu YF, et al. 2019. Microplastics induce intestinal inflammation, oxidative stress, and disorders of metabolome and microbiome in zebrafish. *Science of the Total Environment*, **662**: 246–253.

Ragusa A, Svelato A, Santacroce C, et al. 2021. Plasticenta: First evidence of microplastics in human placenta. *Environment International*, **146**: 106274.

Sahraeian SME, Mohiyuddin M, Sebra R, et al. 2017. Gaining comprehensive biological insight into the transcriptome by performing a broad-spectrum RNA-seq analysis. *Nature Communications*, **8**(1): 59.

Schwabl P, Koppel S, Konigshofer P, et al. 2019. Detection of various microplastics in human stool: a prospective case series. *Annals of Internal Medicine*, **171**(7): 453–457.

Sgro M, Kodila ZN, Brady RD, et al. 2022. Synchronizing our clocks as we age: the influence of the brain-gut-immune axis on the sleep-wake cycle across the lifespan. *Sleep*, **45**(3): zsab268.

Shang X, Lu JW, Feng C, et al. 2020. Microplastic (1 and 5 μm) exposure disturbs lifespan and intestine function in the nematode *Caenorhabditis elegans*. *Science of the Total Environment*, **705**: 135837.

Shen J, Liang BY, Zhang DK, et al. 2021. Effects of PET microplastics on the physiology of *Drosophila*. *Chemosphere*, **283**: 131289.

Skevington JH, Dang PT. 2002. Exploring the diversity of flies (Diptera). *Biodiversity*, **3**(4): 3–27.

Strober W. 2001. Trypan blue exclusion test of cell viability. *Current Protocols in Immunology*, **Appendix 3**: Appendix 3B.

Tagorti G, Kaya B. 2022. Genotoxic effect of microplastics and COVID-19: The hidden threat. *Chemosphere*, **286**(Pt 3): 131898.

Tang H, Zhong LC, Xu YF, et al. 2023. Polypropylene microplastics affect the physiology in Drosophila model. *Bulletin of Entomological Research*, **113**(3): 355–360.

Tang MS, Song XR, Zhong WW, et al. 2022. Dietary fiber ameliorates sleep disturbance connected to the gut-brain axis. *Food & Function*, **13**(23): 12011–12020.

The Gene Ontology Consortium. 2021. The Gene Ontology resource: enriching a GOld mine. *Nucleic Acids Research*, **49**(D1): D325–D334.

Urbisz AZ, Malota K, Chajec Ł, et al. 2024. Size-dependent and sex-specific negative effects of micro- and nano-sized polystyrene particles in the terrestrial invertebrate model *Drosophila melanogaster*. *Micron*, **176**: 103560.

Vaccaro A, Dor YK, Nambara K, et al. 2020. Sleep loss can cause death through accumulation of reactive oxygen species in the gut. *Cell*, **181**(6): 1307–1328. e15.

Van Raamsdonk LWD, Van Der Zande M, Koelmans AA, et al. 2020. Current insights into monitoring, bioaccumulation, and potential health effects of microplastics present in the food Chain. *Foods*, **9**(1): 72.

Van Sebille E, Wilcox C, Lebreton L, et al. 2015. A global inventory of small floating plastic debris. *Environmental Research Letters*, **10**(12): 124006.

Wan XL, Shen P, Shi K, et al. 2023. A neural circuit controlling virgin female aggression induced by mating-related cues in *Drosophila*. *Neuroscience Bulletin*, **39**(9): 1396–1410.

Wang J, Li YJ, Lu L, et al. 2019a. Polystyrene microplastics cause tissue damages, sex-specific reproductive disruption and transgenerational effects in marine medaka (*Oryzias melastigma*). *Environmental Pollution*, **254**: 113024.

Wang J, Liu XH, Li Y, et al. 2019b. Microplastics as contaminants in the soil environment: A mini-review. *Science of the Total Environment*, **691**: 848–857.

Wei YB, Zhang H, Liu Y. 2023. Charting normative brain variability across the human lifespan. *Neuroscience Bulletin*, **39**(2): 362–364.

Wesselius HM, Van Den Ende ES, Alsma J, et al. 2018. Quality and quantity of sleep and factors associated with sleep disturbance in hospitalized patients. *JAMA Internal Medicine*, **178**(9): 1201–1208.

World Health Organization. 2022. Dietary and inhalation exposure to nano- and microplastic particles and potential implications for human health. Geneva: WHO.

Wright SL, Kelly FJ. 2017. Plastic and human health: a micro issue?. *Environmental Science & Technology*, **51**(12): 6634–6647.

Wright SL, Ulke J, Font A, et al. 2020. Atmospheric microplastic deposition in an urban environment and an evaluation of transport. *Environment International*, **136**: 105411.

Yan W, Hamid N, Deng S, et al. 2020. Individual and combined toxicogenetic effects of microplastics and heavy metals (Cd, Pb, and Zn) perturb gut microbiota homeostasis and gonadal development in marine medaka (*Oryzias melastigma*). *Journal of Hazardous Materials*, **397**: 122795.

Yu HJ, Chen PP, Gordon SP, et al. 2019. The association between air pollution and sleep duration: a cohort study of freshmen at a university in Beijing, China. *International Journal of Environmental Research and Public Health*, **16**(18): 3362.

Yu XB, Peng JP, Wang JD, et al. 2016. Occurrence of microplastics in the beach sand of the Chinese inner sea: the Bohai Sea. *Environmental Pollution*, **214**: 722–730.

Zhang N, Li YB, He HR, et al. 2021. You are what you eat: Microplastics in the feces of young men living in Beijing. *Science of the Total Environment*, **767**: 144345.

Zhang R, Wang M, Chen XP, et al. 2020a. Combined toxicity of microplastics and cadmium on the zebrafish embryos (*Danio rerio*). *Science of the Total Environment*, **743**: 140638.

Zhang Y, Wolosker MB, Zhao YP, et al. 2020b. Exposure to microplastics cause gut damage, locomotor dysfunction, epigenetic silencing, and aggravate cadmium (Cd) toxicity in *Drosophila*. *Science of the Total Environment*, **744**: 140979.

Zhong LC, Jin H, Tang H, et al. 2022. Intake of polyamide microplastics affects the behavior and metabolism of Drosophila. *Chemosphere*, **308**: 136485.

Zhang et al. *Zool. Res.* 2024, 45(4): 821−830
https://doi.org/10.24272/j.issn.2095-8137.2024.074

ZR | Zoological Research

Article Open Access

# On the evolutionary trail of MagRs

Jing Zhang[1,2], Yafei Chang[1,2], Peng Zhang[1,2], Yanqi Zhang[1,2], Mengke Wei[3], Chenyang Han[3], Shun Wang[3], Hui-Meng Lu[4], Tiantian Cai[1,2,5,*], Can Xie[1,2,5,*]

[1] *High Magnetic Field Laboratory*, *Hefei Institutes of Physical Science*, *Chinese Academy of Sciences*, *Science Island*, *Hefei*, *Anhui* 230031, *China*

[2] *Science Island Branch of Graduate School*, *University of Science and Technology of China*, *Hefei*, *Anhui* 230036, *China*

[3] *Institutes of Physical Science and Information Technology*, *Anhui University*, *Hefei*, *Anhui* 230039, *China*

[4] *School of Life Sciences*, *Key Laboratory for Space Bioscience and Biotechnology*, *Northwestern Polytechnical University*, *Xi'an*, *Shaanxi* 710072, *China*

[5] *Institute of Quantum Sensing*, *Zhejiang University*, *Hangzhou*, *Zhejiang* 310027, *China*

**ABSTRACT**

Magnetic sense, or termed magnetoreception, has evolved in a broad range of taxa within the animal kingdom to facilitate orientation and navigation. MagRs, highly conserved A-type iron-sulfur proteins, are widely distributed across all phyla and play essential roles in both magnetoreception and iron-sulfur cluster biogenesis. However, the evolutionary origins and functional diversification of MagRs from their prokaryotic ancestor remain unclear. In this study, MagR sequences from 131 species, ranging from bacteria to humans, were selected for analysis, with 23 representative sequences covering species from prokaryotes to Mollusca, Arthropoda, Osteichthyes, Reptilia, Aves, and mammals chosen for protein expression and purification. Biochemical studies revealed a gradual increase in total iron content in MagRs during evolution. Three types of MagRs were identified, each with distinct iron and/or iron-sulfur cluster binding capacity and protein stability, indicating continuous expansion of the functional roles of MagRs during speciation and evolution. This evolutionary biochemical study provides valuable insights into how evolution shapes the physical and chemical properties of biological molecules such as MagRs and how these properties influence the evolutionary trajectories of MagRs.

**Keywords:** Magnetoreception; Magnetoreceptor (MagR); Iron-sulfur cluster; Stability; Evolutionary biochemistry

## INTRODUCTION

The Earth's geomagnetic field is a natural environmental component influencing all living organisms during evolution. Magnetic sense, or magnetoreception, has evolved across a broad range of animal taxa to facilitate orientation and navigation (Begall et al., 2013; Johnsen & Lohmann, 2008; Mouritsen, 2018; Qin et al., 2016; Wang et al., 2023; Wiltschko & Wiltschko, 1995, 2006, 2005). This sensory ability enables the extraction of two types of information: (1) directional or "compass" information, and (2) positional or "map" information. These are derived from three geomagnetic field parameters, including polarity (direction of the horizontal component), inclination (angle between the Earth's magnetic field lines and its surface), and intensity (Naisbett-Jones & Lohmann, 2022).

Several models have been proposed to explain the mechanism underlying animal magnetoreception, including the magnetite-based model for polarity detection (Cadiou & Mcnaughton, 2010; Kirschvink & Gould, 1981; Kirschvink et al., 2001; Walcott et al., 1979), the cryptochrome (Cry)-based radical-pair model or quantum compass for inclination detection (Hore & Mouritsen, 2016; Maeda et al., 2008; Ritz et al., 2000; Rodgers & Hore, 2009; Schulten & Weller, 1978), and the MagR/Cry-based biocompass model for both polarity and inclination detection (Lohmann, 2016; Qin et al., 2016; Xie, 2022).

Remarkably diverse animals, from invertebrates such as mollusks and insects to vertebrates such as sea turtles and birds, perceive guidance cues from the geomagnetic field. Different organisms inhabit various environments, ranging from oceans to land and air, and may have undergone distinct evolutionary paths to sense and utilize geomagnetic field cues for various purposes including long-distance migration, short-distance movement, homing, nesting, body alignment, and food searching. In the ocean, the marine mollusk *Tritonia*

This is an open-access article distributed under the terms of the Creative Commons Attribution Non-Commercial License (http://creativecommons.org/licenses/by-nc/4.0/), which permits unrestricted non-commercial use, distribution, and reproduction in any medium, provided the original work is properly cited.

Copyright ©2024 Editorial Office of Zoological Research, Kunming Institute of Zoology, Chinese Academy of Sciences

Received: 05 March 2024; Accepted: 22 April 2024; Online: 23 April 2024

Foundation items: This study was supported by the National Natural Science Foundation of China (31640001 and T2350005 to C.X.), Ministry of Science and Technology of China (2021ZD0140300 to C.X.), and Presidential Foundation of Hefei Institutes of Physical Science, Chinese Academy of Sciences (Y96XC11131, E26CCG27, and E26CCD15 to C.X., E36CWGBR24B and E36CZG14132 to T.C.)

*Corresponding authors, E-mail: tiantiancai@zju.edu.cn; canxie@zju.edu.cn

*diomedea* can orient to the Earth's magnetic field to navigate between shallow and deeper areas (Lohmann & Willows, 1987). Salmon, coral reef fish, lobsters, and sea turtles also exhibit magnetic sense for navigation (Naisbett-Jones & Lohmann, 2022). On land, termites (*Amitermes meridionalis*) use geomagnetic cues for mound construction (Jacklyn & Munro, 2002), while mole-rats display a strong innate preference for building nests in the southeastern sector of circular arenas (Burda et al., 2020, 1990) and can navigate over both short and long distances (Kimchi et al., 2004). In the air, monarch butterflies (*Danaus plexippus*) take four generations to complete a migration of approximately 8 000 km from Mexico, across the USA to Canada, and back annually (Brower, 1996). Birds, the most mobile creatures in the animal kingdom, often undertake long-distance annual journeys guided by their innate magnetic sense (Wiltschko & Wiltschko, 2019). The Arctic tern (*Sterna paradisaea*) completes the longest roundtrip migration annually, traveling from pole to pole (Alerstam et al., 2019; Egevang et al., 2010). Both the migratory European robin (*Erithacus rubecula*) and homing pigeon (*Columba livia*) have been extensively studied in the field and laboratory for their ability to sense the geomagnetic field during navigation (Biro, 2010; Mouritsen & Ritz, 2005; Qin et al., 2016; Wang et al., 2024; Wiltschko & Wiltschko, 2006; Xie, 2022; Xu et al., 2021; Zhou et al., 2023). Of note, the existence of a human magnetic sense remains the subject of ongoing study, debate, and controversy (Baker, 1980, 1988; Chae et al., 2022; Foley et al., 2011; Wang et al., 2019; Westby & Partridge, 1986).

The broad distribution and phylogenetic diversity of animals with a magnetic sense suggest that this sensory modality evolved before the major evolutionary radiations, motivating the exploration of the evolutionary history of the putative magnetoreceptor. In the biocompass model, the magnetoreceptor MagR forms a rod-like complex with Cry, indicating a possible mechanism of biomagnetism and implying a connection between the biocompass and quantum compass (Xie, 2022).

MagRs, or the homologous bacterial iron-sulfur cluster assembly (IscA) protein, are dual-functional proteins involved in both magnetoreception and iron-sulfur cluster (Fe–S) biogenesis and are highly evolutionarily conserved from bacteria to humans (Lu et al., 2020). MagRs exhibit various unique and sophisticated features. First, the binding of iron and/or iron-sulfur clusters in MagRs is highly complex and likely species-specific. In *Escherichia coli*, IscA (ecIscA), the homologous protein of eukaryotic MagRs, binds to iron (Ding & Clark, 2004; Ding et al., 2007; Landry et al., 2013), while in pigeons and humans, MagRs bind to both iron and iron-sulfur clusters (Guo et al., 2021; Song et al., 2009; Weiler et al., 2020; Zhou et al., 2023). Additionally, two forms of iron-sulfur clusters [2Fe-2S] and [3Fe-4S] have been identified in pigeon MagR, which show different magnetic properties (Guo et al., 2021), potentially serving as a magnetic switch to modulate magnetoreceptor sensitivity. Second, the functional roles of the N-terminal sequences in MagRs remain incompletely understood. The highly variable N-terminal region of MagRs, present only in eukaryotic MagR/IscA1 and not in prokaryotic IscA, is proposed to play essential roles in the formation of MagR tetramers and the MagR/Cry biocompass complex, as evidenced by sequence analysis and molecular dynamics (Friis et al., 2017; Lu et al., 2020) and recently validated by biochemical analysis in pigeon MagR (Zhang et al., 2024). The same region also contributes to the high affinity binding of iron and iron-sulfur clusters (Zhang et al., 2024). Furthermore, the MagR proteins from European robin and pigeon differ markedly in their iron and iron-sulfur binding capacity and conformation, despite only three residues varying between them (Wang et al., 2024). Therefore, elucidating the conservation and variation of this dual-functional protein from both sequence and biochemical perspectives will extend our understanding of MagRs as iron-sulfur cluster proteins and magnetoreceptors.

In this study, MagR sequences from 131 species across a wide range of taxa, from bacteria to humans, were analyzed, with 23 representative sequences selected for protein expression and purification. The biochemical properties of the 23 MagR proteins from different species were compared, leading to the identification of three distinct types based on their iron and iron-sulfur cluster binding capacities. Interestingly, the binding capacity for iron and iron-sulfur clusters in MagR proteins increased progressively from prokaryotes to mammals, correlating with the increasing body complexity. Furthermore, iron-sulfur cluster binding appears to be a requisite feature of eukaryotic MagRs, in addition to the mononuclear iron binding observed in bacterial IscA. Four MagRs from bacteria, worms, and pigeons and humans, representing the three different types, were selected for further systematic analysis and comparison. The stability of MagRs was also found to increase gradually during evolution and speciation. Overall, this study provides a comprehensive overview of the evolutionary trajectory of MagRs, both as iron-sulfur proteins and magnetoreceptors, shedding light on how animal magnetoreception evolved from an ancient prokaryotic iron-sulfur protein.

## MATERIALS AND METHODS

### Multiple sequence alignment and phylogenetic analysis

The MagR and IscA protein sequences from 131 species were downloaded from the NCBI database. The common English name of the species and accession numbers of the protein sequences are provided in Supplementary Figure S1 alongside each sequence. The MagR sequences from the monarch butterfly and pigeon were obtained from a previous study (Qin et al., 2016), while the MagR sequence from the sea slug (*Elysia leucolegnote*) was shared by Dr. Yinglang Wan from Hainan University. All sequences were aligned using ClustalW (https://www.megasoftware.net/citations) and colored according to identity percentage with ESPript v.3.0 (https://espript.ibcp.fr/ESPript/ESPript/index.php) (Figure 1A; Supplementary Figure S1). Among these sequences, 23 representatives were chosen for further phylogenetic analysis and protein expression and purification. A phylogenetic tree of these 23 MagRs from different species was also constructed using MEGA v.7.0. Evolutionary history was inferred using the neighbor-joining method and the Poisson model (Saitou & Nei, 1987). Rates among sites were calculated using the uniform rate and gaps/missing data were treated by complete deletion. The bootstrap consensus tree inferred from 1 000 replicates was taken to represent the evolutionary history of the taxa analyzed (Felsenstein, 1985). The percentage of replicate trees in which the associated taxa clustered together in the bootstrap test (1 000 replicates) is shown next to the branches (Felsenstein, 1985). The evolutionary distances were computed using the Poisson correction method (Kaur et al., 2018), expressed as the number of amino acid substitutions

per site.

**Protein expression and purification**

The DNA sequences encoding the 23 representative MagR proteins were codon-optimized and synthesized for *E. coli* expression (Songon Biotech, China). The expression vectors containing *MagR* gene sequences were constructed as described previously (Qin et al., 2016). All MagR proteins were expressed in *E. coli* strain BL21 (DE3) with a Strep-II tag fused to the N-terminal. After induction with 20 μmol/L isopropyl-D-1-thiogalactopyranoside (IPTG) at 15°C for 20 h, cells were harvested, resuspended in lysis buffer (20 mmol/L Tris, 500 mmol/L NaCl, pH 8.0), and lysed by sonication on ice. Following centrifugation at 17 500 r/min for 45 min at 4°C, the supernatants were collected and loaded onto Strep-Tactin affinity columns (IBA GmbH, Germany). The resin was washed with 50 resin volumes of washing buffer (20 mmol/L Tris, 500 mmol/L NaCl, pH 8.0) to remove unbound proteins. The target proteins were then eluted with elution buffer (20 mmol/L Tris, 500 mmol/L NaCl, 5 mmol/L desthiobiotin, pH 8.0). The purity of all purified proteins was verified with sodium dodecyl-sulfate polyacrylamide gel electrophoresis (SDS-PAGE), with PageRuler Prestained Protein Ladder (Thermo Fisher Scientific, USA) used as the molecular weight standard. Protein concentration was estimated by measuring absorption at 280 nm with a NanoDrop spectrophotometer (NanoDrop OneC, Thermo Scientific, USA).

**Electron paramagnetic resonance measurement**

X-band (9.6 GHz) electron paramagnetic resonance (EPR) spectra were recorded using an EMX plus 10/12 spectrometer (Bruker, Billerica, MA) equipped with an Oxford ESR-910 liquid helium cryostat. For oxidized protein samples, 50 μL of glycerol was added to 200 μL of 1 mmol/L sample. The protein samples were then injected into quartz EPR tubes (Wilmad 707-SQ-250 M, USA) and frozen with liquid nitrogen. The EPR signals were collected at different temperatures (10 K, 25 K, 45 K, and 60 K) under a microwave frequency of 9.40 GHz, microwave power of 2 mW, modulation amplitude of 2.0 G, and receive gain of $1.0\times10^4$.

**Ultraviolet-visible (UV-Vis) absorption analysis and circular dichroism (CD) spectroscopy**

The UV-Vis absorption spectra of MagR proteins were measured from 300 nm to 600 nm using a NanoDrop spectrophotometer (Thermo Scientific, NanoDrop OneC, USA) at room temperature. For the regular characterization of iron and iron-sulfur cluster binding, 100 μmol/L MagR proteins were used (Figures 2, 3, 4A). To compare the stability of MagR proteins, UV-Vis spectra with time-lapse experiments were collected with 200 μmol/L MagR proteins (Figure 5). Color variation of the MagR proteins from different species was compared in solution at a concentration of 500 μmol/L (Figure 4A).

The protein-bound metals and iron-sulfur clusters in the MagR proteins were measured using a CD spectrometer MOS-500 (Biologic, France) at room temperature. The purified proteins (10 μmol/L) were prepared in 20 mmol/L phosphate buffer (pH 8.0).

**Ferrozine assay**

A stable purplish-red compound was formed by the interaction of ferrous iron with ferrozine, showing a characteristic absorption peak at 562 nm (Im et al., 2013). Total iron content of the proteins was determined by quantitatively reducing $Fe^{3+}$ to $Fe^{2+}$ using hydroxylamine-HCl (10% (w/v) HAHCl in 1 mol/L HCl) and measuring absorption at 562 nm. The standard curve used for quantification was generated using a series of ferric chloride ($FeCl_3$) concentrations (0.1–1.0 mmol/L) dissolved in 1 mol/L HCl (Supplementary Figure S2). The protein samples were prepared as described previously (Zhou et al., 2023). In brief, 80 μL of hydroxylamine-HCl (10% w/v HAHCl in 1 mol/L HCl) and 20 μL of the MagR proteins (100 μmol/L) were added to a 96-well plate (Corning, USA), then mixed well and incubated at 37°C for 30 min in the dark. Then, 100 μL of ferrozine (1 g/L ferrozine in 50% w/v ammonium acetate) was added to each well. The mixtures were incubated at 37°C for an additional 5 min in the dark. Finally, the absorption of the iron-ferrozine complex in each well was measured at 562 nm using a microplate reader (Tecan Spark, Austria). Iron content in the MagR proteins was determined using linear regression analysis in comparison with standard curves. Each protein sample was tested in three independent replicates. Histograms and statistical analysis were performed using GraphPad Prism v.9.5. Two-tailed Student's *t*-test was used to test for differences in total iron between protein samples. Statistical significance is indicated in the corresponding figures with $^{****}$: $P<0.0001$.

**Size-exclusion chromatography (SEC)**

The conformational states of the 23 different MagRs were monitored and differentiated using analytical SEC. Purified proteins were injected into a Superdex 6 Increase 10/300 GL column (GE Healthcare, USA) connected to a GE AKTA FPLC purification system, operated at a flow rate of 0.5 mL/min. TBS buffer (20 mmol/L Tris, 150 mmol/L NaCl, pH 8.0) was used throughout the analysis (Supplementary Figure S3).

## RESULTS

**MagRs are highly conserved from bacteria to humans**

MagR sequences from 131 species across all major phyla were retrieved from NCBI, with some re-sequenced and confirmed in previous lab work (Qin et al., 2016). Sequence alignment of all 131 MagRs (Supplementary Figure S1) and 23 representative MagRs (Figure 1A) demonstrated high MagR conservation from bacteria to humans. A notable difference between prokaryotic IscA and eukaryotic MagR/IscA is the presence of an additional 20–30 amino acids at the N-terminal of eukaryotic MagRs. The functional roles of this N-terminal sequence, such as N25 in pigeon MagR, have been extensively studied. The sequence serves not only as a mitochondrial targeting signal but also affects iron and iron-sulfur cluster binding in MagRs and the formation of the MagR/Cry complex (Zhang et al., 2024). While the C-terminal half of MagRs is highly conserved, the N-terminal half is more variable. Three cysteine residues, which form the iron-sulfur cluster binding site (Guo et al., 2021), were 100% conserved across all species (brown stars, Supplementary Figure S1; Figure 1A). Additionally, four aromatic residues, including tyrosine and phenylalanine, were also 100% conserved (blue stars, Supplementary Figure S1; Figure 1A), which may contribute to the intermolecular electron transport chain within tetramer MagRs and between MagRs and Cry (Xie, 2022).

To explore the evolutionary trajectory of MagRs in terms of biochemical properties and functions, 23 MagRs from different species (Figure 1A), spanning from prokaryotes to Mollusca, Arthropoda, Osteichthyes, Reptilia, Aves, and mammals, were carefully selected for protein expression and purification

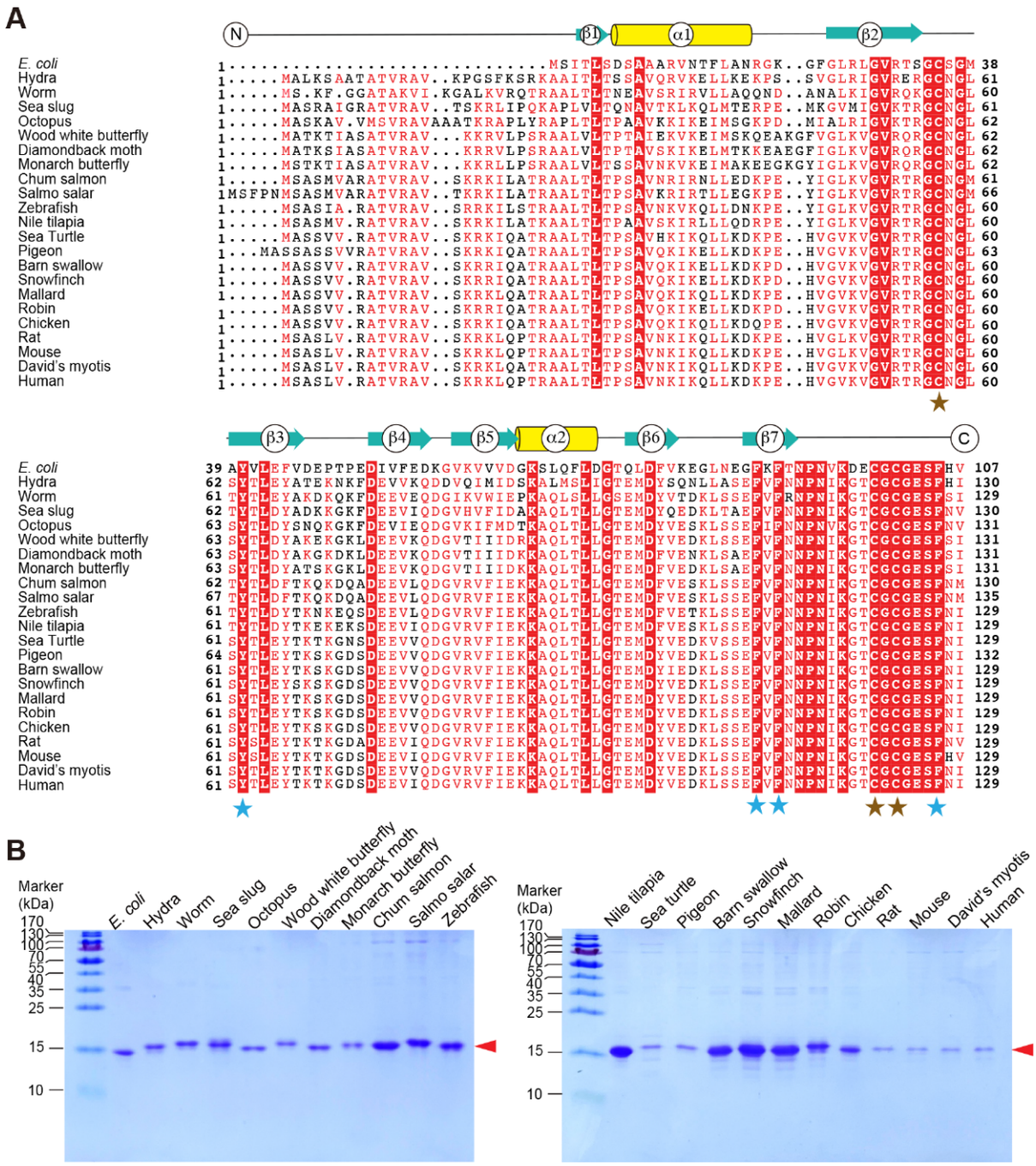



**Figure 1 Sequence alignment and purification of MagRs across species**

A: Sequence alignment of MagRs in 23 representative species. Residues with high similarity across species are shown in red. 100% conserved residues are shown in white with red background. Secondary structures are shown in upper lines, with two α-helices indicated by yellow cylinders and seven β-strands indicated by green arrows. Residues with iron-sulfur cluster binding properties are indicated by brown stars. Conserved residues with electron transfer properties are indicated by blue stars. B: SDS-PAGE of purified MagR proteins from 23 representative species.

(Figure 1B). All proteins were purified to homogeneity under aerobic conditions and appeared as single bands around 14–15 kDa in reduced SDS-PAGE.

### Iron and iron-sulfur cluster binding capacity increases during MagR evolution

Phylogenetic trees were constructed to elucidate the evolutionary relationships of MagR proteins across species (Figure 2A). Results showed that MagRs from species within the same phylum or class clustered together in the same clade, demonstrating higher sequence similarity and closer evolutionary relationships. For example, various butterfly species showed greater similarity to each other than to species from other classes. Comparable clustering patterns were observed for fish, birds, and mammals, likely due to both speciation and adaptation. Species within the same family share a more recent common ancestor than species from different families. Additionally, species within the same class or phylum often adapt to similar habitats, which may involve similar levels of iron metabolism.

A total of 23 MagR/IscA proteins from these species were purified to homogeneity. The purified proteins displayed various shades of brown, except for the purified bacterial IscA

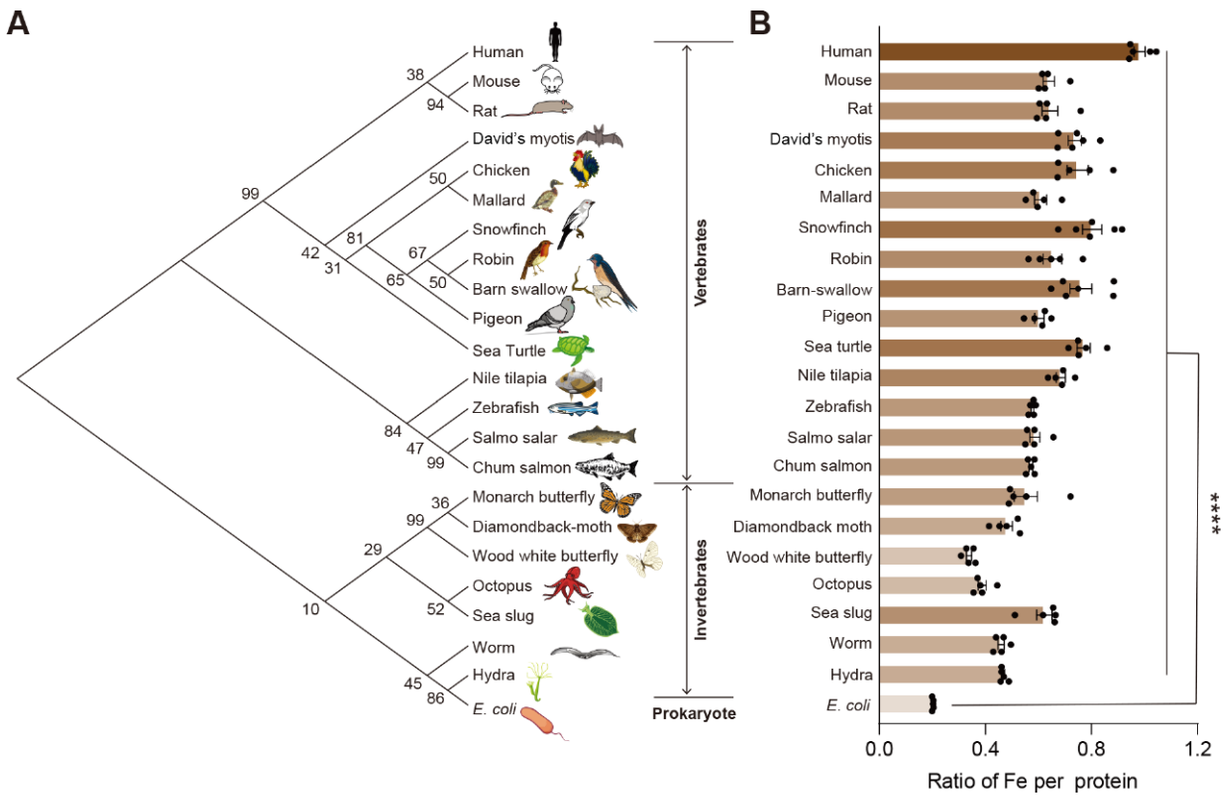



**Figure 2 Molecular phylogenetic analysis and iron binding of MagR proteins**

A: Phylogenetic trees of MagR protein sequences from 23 different species. Bootstrap values were obtained from 1 000 replicates using the neighbor-joining method in MEGA7 and are shown next to the branches. B: Total iron content in purified MagR proteins of 23 representative species measured by ferrozine assay as the ratio of iron atoms per protein monomer. Student's *t*-test, ****: $P<0.0001$.

protein, which was nearly colorless. The color of the purified MagR proteins suggests possible binding of cofactors, such as iron and/or iron-sulfur clusters, consistent with previous reports of MagRs purified from different species (Cupp-Vickery et al., 2004; Ding & Clark, 2004; Ding et al., 2007; Guo et al., 2021; Landry et al., 2013; Lu et al., 2010; Nasta et al., 2019; Ollagnier-De-Choudens et al., 2001; Wang et al., 2024; Zhou et al., 2023). Cofactor binding is essential for protein function and stability. To demonstrate the iron and iron-sulfur binding capacity of MagRs during evolution, the total iron content of each MagR was measured using the ferrozine assay and compared (Figure 2B). As expected, bacterial IscA, the ancestral protein of eukaryotic MagRs, exhibited the lowest iron content. Generally, the MagR iron content gradually increased along the evolutionary trajectory from bacteria to humans, with some exceptions. For instance, among the invertebrates tested, the sea slug (*Elysia leucolegnote*) had the highest total iron content. Among vertebrates, the sea turtle (*Dermochelys coriacea*) and white-rumped snowfinch (*Onychostruthus taczanowskii*) exhibited high iron content in MagRs compared to other fish, amphibians, reptiles, and birds tested. Conversely, MagRs from mice (*Mus musculus*) and rats (*Rattus norvegicus*) showed relatively low total iron binding. These exceptions imply potentially unique magnetoreception abilities, which warrant further investigation.

**Evolutionary biochemistry reveals evolution of three types of MagR**

MagRs can bind to both mononuclear iron and iron-sulfur clusters. As total iron content measurements cannot distinguish between these two types of binding, UV-Vis spectra, CD spectra, and EPR spectra were used to further characterize the biochemical properties of MagRs from different species.

The UV-Vis spectra of 23 purified MagR proteins from various species were measured and compared (Figure 3). In general, the UV-Vis absorption of MagRs gradually increased from bacteria to humans (Figure 3A), consistent with the color and total iron content of the purified proteins. Typically, characteristic peaks in the UV-Vis spectra at 330 nm indicate iron binding, while peaks at 330 nm, 420 nm, and 460 nm indicate iron-sulfur cluster binding of various proteins (Ding & Clark, 2004; Ding et al., 2007; Guo et al., 2021; Landry et al., 2013; Lu et al., 2010; Zhou et al., 2023).

To compare the iron-sulfur cluster binding capacity with the iron binding capacity in MagRs, the ratios of UV-Vis absorption at 420 nm or 460 nm relative to 330 nm were calculated for each MagR (Figure 3B, C). Based on the UV-Vis profiles (Figure 3A) and OD420/OD330 (Figure 3B) and OD460/OD330 (Figure 3C) absorption ratios, the 23 MagRs were classified into three different types. The first type, represented by bacterial IscA (*E. coli*, ecIscA), exhibited a single prominent peak at 330 nm (Figure 3A, D), indicating it primarily binds to iron, consistent with previous reports (Ding & Clark, 2004). The second type, including MagRs from hydras (*Hydra vulgaris*), worms (*Caenorhabditis elegans*), and sea slugs (*Elysia leucolegnote*), represented by *Caenorhabditis elegans* MagR (ceMagR), exhibited apparent peaks at 330 nm and 420 nm, with a shoulder at 460 nm (Figure 3A, E), indicating the presence of iron-sulfur cluster binding. The third type, comprising the remaining 19 MagRs, represented by *Columba livia* MagR (clMagR), showed prominent peaks at 420 nm and 460 nm (Figure 3A, F), indicating significantly enhanced iron-sulfur cluster binding. These results suggest

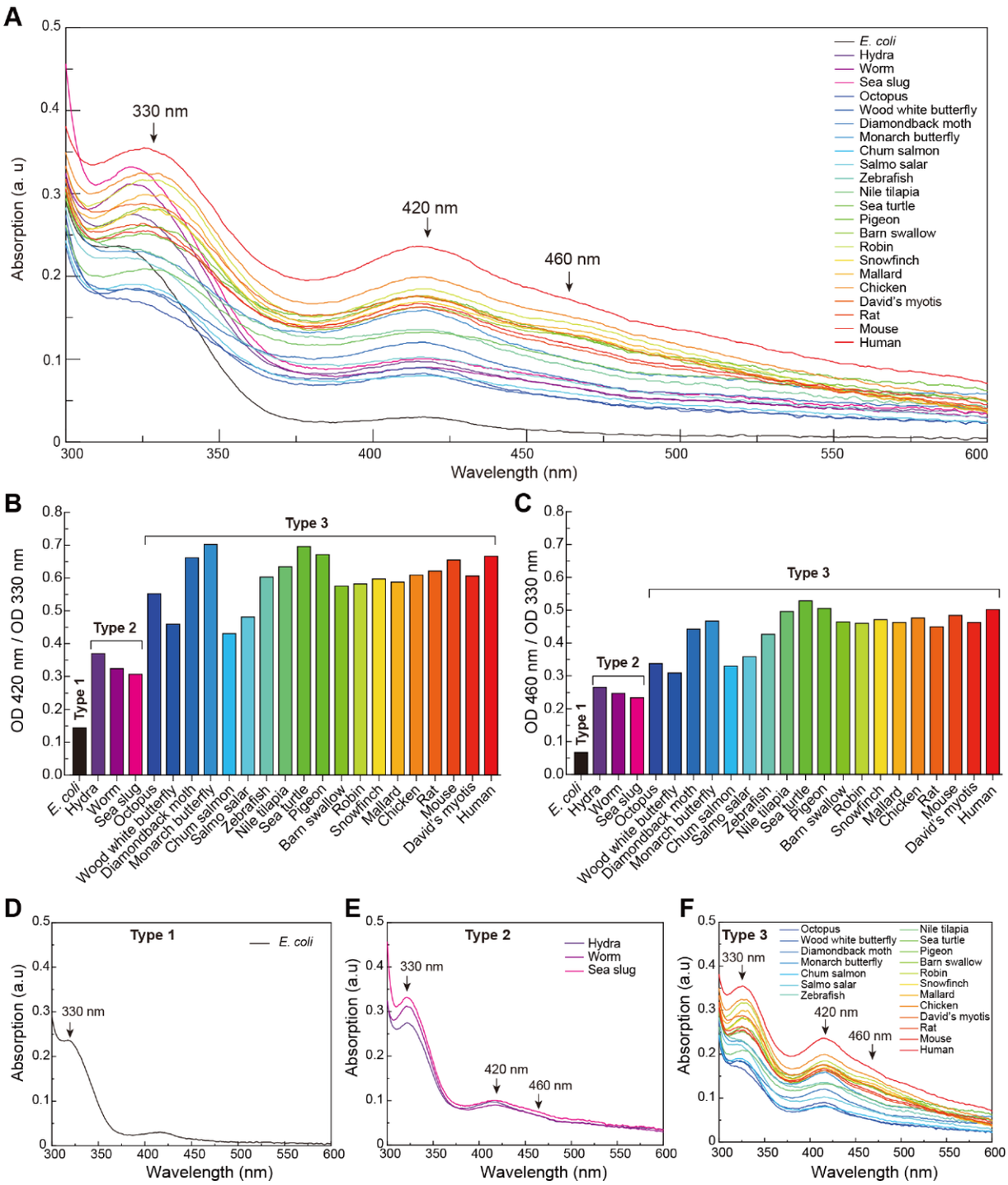



**Figure 3 MagRs from different species can be classified into three different types based on UV-Vis spectra**

A: UV−Vis absorption spectra of MagR proteins from 23 representative species. Typical peaks at 330 nm, 420 nm, and 460 nm are indicated with arrows. B, C: Comparison of iron-sulfur cluster binding in MagRs from 23 species was quantified by the ratio of absorption peaks at 420 nm (B) and 460 nm (C) relative to absorption peaks at 330 nm. Three types of MagRs were classified based on the ratio. D–F: UV-Vis spectra of 23 MagRs classified into three types. Type 1 MagR was represented by ecIscA (D), type 2 MagRs were represented by three MagRs (E), and type 3 MagRs were represented by the remaining 19 MagRs.

that over the course of evolution, the extent of iron-sulfur cluster binding in MagRs has significantly increased, evolving from no binding to partial binding, and eventually to extensive binding across different species.

**Late acquisition of iron-sulfur cluster binding in MagR evolution**

MagRs from bacteria (ecIscA), worms (ceMagR) and pigeons and humans (clMagR and hsMagR), representing the three different types, were selected to systematically characterize and compare their biochemical features during evolution. The color of these three purified proteins varied progressively from colorless to dark brown at the same concentration (Figure 4A). Type 1 bacterial ecIscA was colorless, while the worm ceMagR was light brown and the pigeon clMagR and human hsMagR were dark brown. Type 2 ceMagR displayed a very

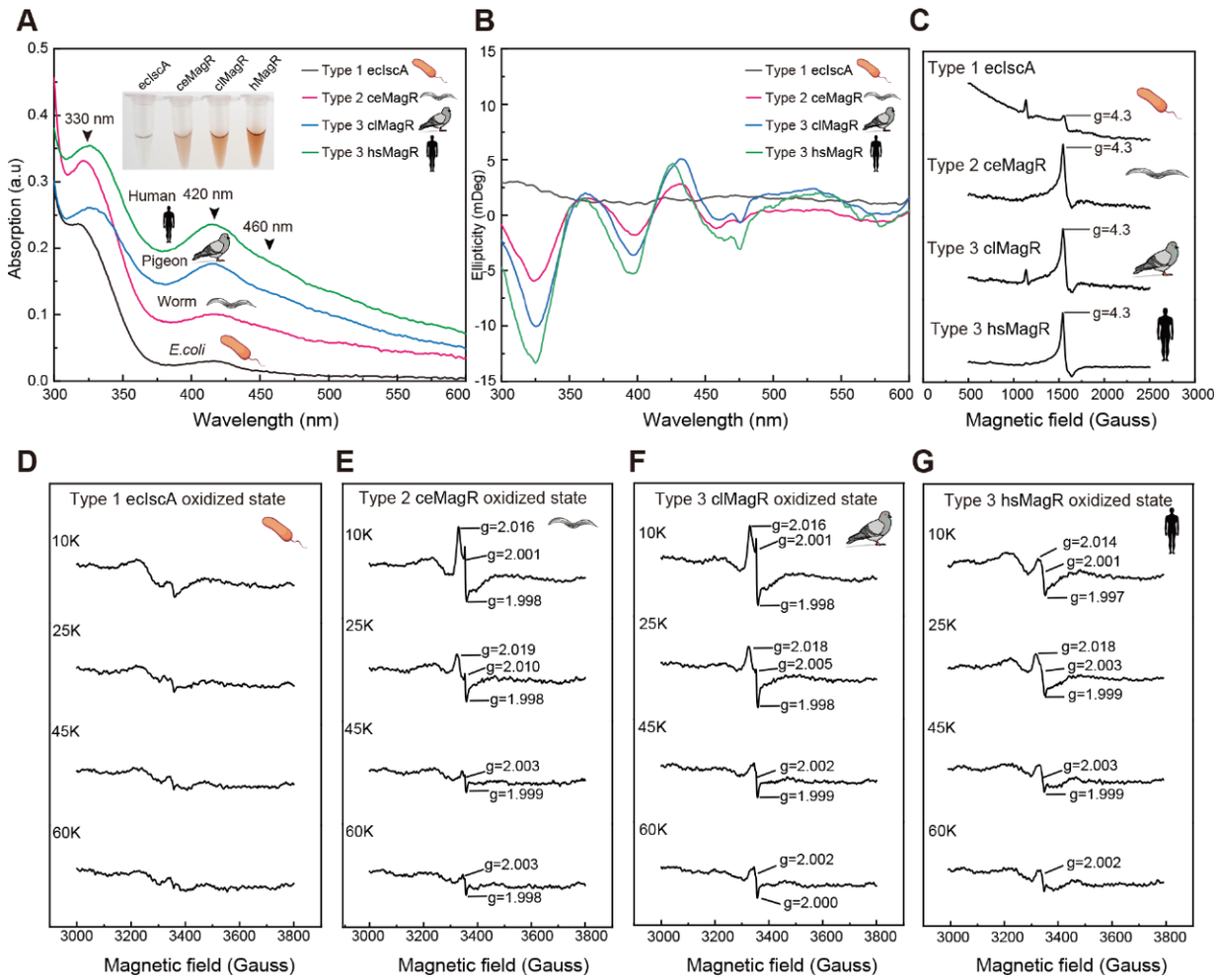



**Figure 4 Iron content and types of iron-sulfur clusters in three types of MagRs**

A: UV-Vis absorption spectra of purified MagR or IscA type proteins. Insert picture shows protein solution. B: CD spectra of purified ecIscA (black line), ceMagR (red line), and clMagR (blue line) and hsMagR (green line), representing the three types of MagR proteins, respectively. C: Comparison of EPR spectra recorded at 10 K for ecIscA, ceMagR, clMagR, and hsMagR to detect ferric iron binding in three types of MagR proteins. D–G: EPR spectra of ecIscA (D), ceMagR (E), and clMagR (F) and hsMagR (G) representing three types of MagR proteins, respectively.

high absorption peak at 330 nm, while type 3 clMagR and hsMagR exhibited significant absorption peaks at 420 nm and 460 nm, indicating stronger iron-sulfur cluster binding. These findings are consistent with the UV-Vis profiles (Figure 4A) and iron content results (Figure 2B), indicating increased binding to iron-sulfur clusters in type 3 MagRs.

CD spectroscopy was employed to characterize the types of iron-sulfur clusters and their protein environments during cluster maturation. Of note, ceMagR, clMagR, and hsMagR, but not ecIscA, showed distinct positive peaks at 371 nm and 426 nm and three negative peaks at 324 nm, 396 nm, and 463 nm, indicating the presence of [2Fe-2S] in the worm ceMagR, pigeon clMagR, and human hsMagR, but not in bacterial ecIscA (Figure 4B). To further characterize the type of iron-sulfur clusters in MagRs, EPR spectroscopy was applied as the CD spectra alone could not exclude the possible presence of [4Fe-4S] and [3Fe-4S]. The oxidized [3Fe-4S] cluster is characterized by a rhombic EPR signal with g values at g1=2.016, g2=2.002, and g3=1.96, disappearing at 45 K (Hoppe et al., 2011; Pandelia et al., 2011; Rothery et al., 2001). Consequently, two distinct iron-sulfur clusters, [2Fe-2S] and [3Fe-4S], were detected in the worm ceMagR, pigeon clMagR, and human hsMagR, but not in bacterial ecIscA, based on the EPR (Figure 4D–G) and CD spectra (Figure 4B).

EPR spectroscopy can also detect mononuclear iron binding in proteins, with a characteristic peak at g=4.3, typically due to mononuclear high-spin (S=5/2) $Fe^{3+}$ ions in sites of low symmetry (Bou-Abdallah & Chasteen, 2008; Castner et al., 1960; Drovosekov et al., 2023; Zhou et al., 2023). As shown in Figure 4C, the MagRs of all four representative species exhibited ferric iron binding.

In conclusion, all three types of MagRs from different species showed mononuclear iron binding, but only types 2 and 3 exhibited iron-sulfur cluster binding capacity. The late acquisition of iron-sulfur cluster binding in MagRs seems to have occurred only in eukaryotes during evolution.

### MagR stability increases during evolution

Cofactors such as iron-sulfur clusters are crucial for the stability and biological function of proteins. Studying the binding affinity and stability of these cofactors can provide insights into the stability of native proteins (Bushmarina et al., 2006; Mansouri et al., 2022). UV-Vis spectroscopy was applied to monitor the binding and dissociation of iron-sulfur clusters in the three different types of MagRs.

In brief, freshly purified MagR proteins from bacterial ecIscA, worm ceMagR, pigeon clMagR and human hsMagR were incubated at room temperature for 156 h (6.5 days) and

monitored by UV-Vis scanning at regular intervals (Figure 5A–D). The decay (or dissociation) curves of the iron and iron-sulfur clusters were generated by re-plotting the absorption value at 330 nm, 420 nm, and 460 nm for comparison (Figure 5E–G). A decrease in UV-Vis absorption indicates the loss of iron-sulfur clusters in the protein.

As shown in Figure 5, the UV-Vis spectra at different time points illustrated the rate at which iron or iron-sulfur clusters were dissociated from the MagR proteins. At the starting point, ceMagR had the highest absorption peak at 330 nm (Figure 5E), while hsMagR had the highest absorption peaks at 420 and 460 nm (Figure 5F, G), indicating strong iron binding in ceMagR and iron-sulfur binding in clMagR. As incubation time increased, the three types of MagRs lost their absorption at 330 nm at a similar rate, although type 2 ceMagR decreased slightly faster (Figure 5E). The dissociation rate of iron-sulfur clusters in type 2 ceMagR, as shown by the decay of absorption at 420 nm (Figure 5F) and 460 nm (Figure 5G), was much faster than in type 3 clMagR and hsMagR, suggesting that type 2 MagRs may have looser binding of iron-sulfur clusters, leading to rapid dissociation.

Taken together, our results strongly suggest that the stability of iron-sulfur clusters in MagRs had gradually increased during evolution, indicating that MagRs have become progressively more stable over time.

## DISCUSSION

MagRs are highly evolutionarily conserved from bacteria to humans (Lu et al., 2020). Initially, MagRs were identified as scaffold proteins for iron-sulfur cluster assembly and iron donors for iron-sulfur clusters involved in the synthesis of several tricarboxylic acid cycle-related enzymes (Jensen & Culotta, 2000; Krebs et al., 2001; Pelzer et al., 2000). Later research proposed that these proteins serve as a putative magnetoreceptor in the biocompass model, in complex with Cry (Qin et al., 2016), with the intermolecular electron transport chain between MagRs and Cry posited to play an essential role in magnetoreception (Qin et al., 2016; Xie, 2022). Mutation or knockout of MagRs in humans and mice results in fatal diseases or even embryonic lethality (Lebigot et al., 2020; Lee et al., 2019; Oishi et al., 2016; Sheng et al., 2023). Furthermore, knockdown of MagR expression *in vivo* abolishes orientation in the armyworm (*Mythimna separata*), validating the vital role of MagRs not only as iron-sulfur cluster assembly proteins but also as potential magnetoreceptors.

In the current study, we integrated evolutionary biology with biochemistry to gain a more complete understanding of how MagRs evolved from the prokaryotic ancestor IscA. This integration may illuminate how animal magnetoreception evolved from iron metabolism and an iron-sulfur protein. Specifically, we sought to answer the questions, “How do animal magnetoreception and navigation work?” and “How did they evolve?” (Harms & Thornton, 2013; Jayaraman et al., 2022).

We collected MagR sequences from 131 species and selected 23 representative MagRs from different species, covering prokaryotes to Mollusca, Arthropoda, Osteichthyes, Reptilia, Aves, and mammals for biochemical studies. Using these 23 purified MagR proteins, we demonstrated that total iron content in MagRs has gradually increased during evolution, suggesting that MagRs may play increasingly important roles as species evolve. All MagRs can be classified into three different types, with distinct UV-Vis absorption profiles. Type 1 MagRs were primarily found in prokaryotes, while type 2 MagRs were found in some of invertebrates, such as hydras, worms, and sea slugs, and type 3 MagRs were present in certain invertebrates, such as octopuses and insects, and in all vertebrates. Biochemical analysis revealed that type 1 MagRs only bind to mononuclear iron, while type 2

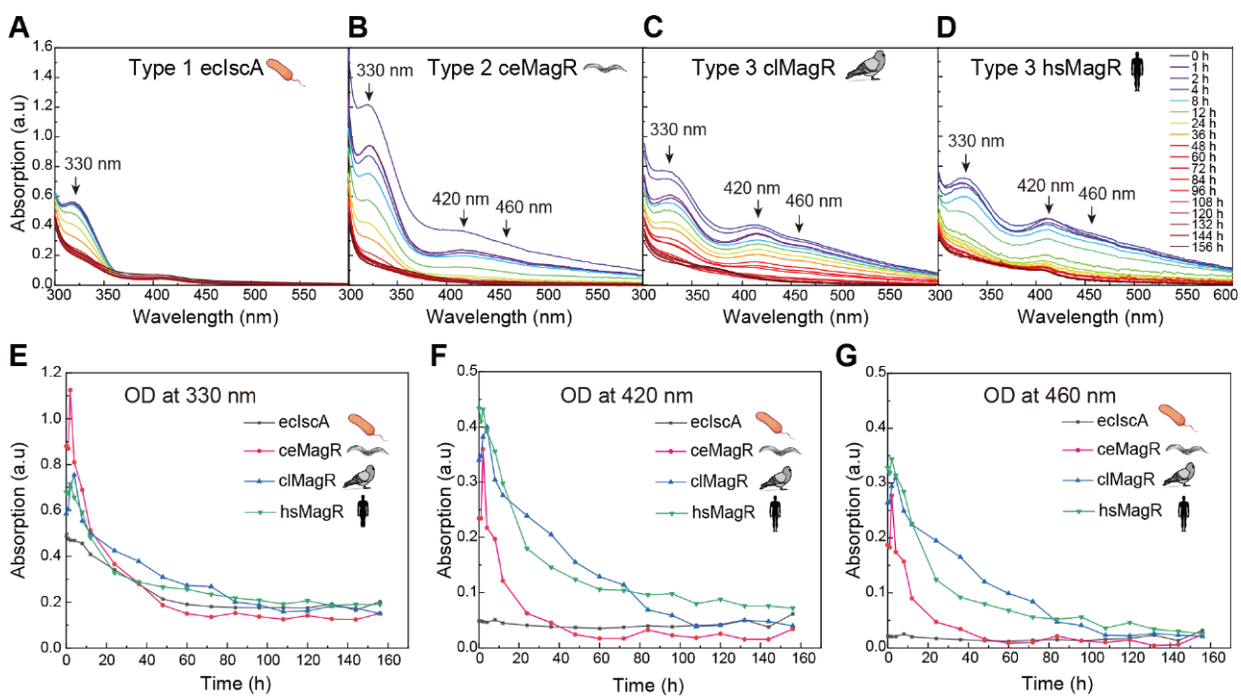



**Figure 5 Stability of iron-sulfur binding in three different types of MagRs**

A–D: UV-Vis absorption of purified ecIscA (A), ceMagR (B), clMagR (C), and hsMagR (D) recorded at room temperature for 156 h. E–G: Decay curves of UV-Vis absorption of three types of purified MagRs from four species at 330 nm (E), 420 nm (F), and 460 nm (G) during room temperature incubation. Data were derived from (A–D).

MagRs can bind to both iron and iron-sulfur clusters, although iron-sulfur cluster binding is low and unstable. In contrast, type 3 MagRs showed very high iron content, high binding affinity for both mononuclear iron and iron-sulfur clusters, and greater stability. Thus, type 2 MagRs likely represent a transitional form from type 1 in prokaryotes to type 3 in vertebrates. The few exceptions (Figure 2) may suggest selective pressure for magnetoreception and navigation during speciation, warranting further investigation.

Overall, our evolutionary biochemical studies help clarify how evolution has shaped the physiochemical properties of biological molecules such as MagRs and how these properties influence the evolutionary trajectories of MagRs.

## SUPPLEMENTARY DATA

Supplementary data to this article can be found online.

## COMPETING INTERESTS

The authors declare that they have no competing interests.

## AUTHORS' CONTRIBUTIONS

C.X. conceived the idea and designed the study. J.Z., Y.C., and C.H. carried out protein purification and CD spectroscopy. Y.Z., S.W., and M.W. helped with the EPR experiments. T.C., H.M.L., and P.Z. provided valuable suggestions on data analysis. J.Z., T.C., and C.X. wrote the paper. All authors read and approved the final version of the manuscript.

## ACKNOWLEDGMENTS

We are grateful to the Steady High Magnetic Field Facilities (High Magnetic Field Laboratory, CAS) for assistance with EPR measurements, as well as Dr. Wei Tong and Jinxing Li for their technical support. We are grateful to the core facilities of the College of Life Sciences at the University of Science and Technology of China, and core facilities of the College of Life Sciences at Anhui University for their help in CD spectral measurements.

## REFERENCES

Alerstam T, Bäckman J, Grönroos J, et al. 2019. Hypotheses and tracking results about the longest migration: The case of the arctic tern. *Ecology and Evolution*, **9**(17): 9511–9531.

Baker RR. 1980. Goal orientation by blindfolded humans after long-distance displacement: possible involvement of a magnetic sense. *Science*, **210**(4469): 555–557.

Baker RR. 1988. Human magnetoreception for navigation. *Progress in Clinical and Biological Research*, **257**: 63–80.

Begall S, Malkemper EP, Červený J, et al. 2013. Magnetic alignment in mammals and other animals. *Mammalian Biology*, **78**(1): 10–20.

Biro D. 2010. Bird navigation: a clear view of magnetoreception. *Current Biology*, **20**(14): R595–R596.

Bou-Abdallah F, Chasteen ND. 2008. Spin concentration measurements of high-spin ($g'$ = 4.3) rhombic iron(III) ions in biological samples: theory and application. *JBIC Journal of Biological Inorganic Chemistry*, **13**(1): 15–24.

Brower LP. 1996. Monarch butterfly orientation: missing pieces of a magnificent puzzle. *Journal of Experimental Biology*, **199**(Pt 1): 93–103.

Burda H, Begall S, Hart V, et al. 2020. Magnetoreception in mammals. *In*: Fritzsch B. The Senses: A Comprehensive Reference. 2nd ed. Amsterdam: Elsevier, 421–444.

Burda H, Marhold S, Westenberger T, et al. 1990. Magnetic compass orientation in the subterranean rodent*Cryptomys hottentotus* (Bathyergidae). *Experientia*, **46**(5): 528–530.

Bushmarina NA, Blanchet CE, Vernier G, et al. 2006. Cofactor effects on the protein folding reaction: acceleration of α-lactalbumin refolding by metal ions. *Protein Science*, **15**(4): 659–671.

Cadiou H, McNaughton PA. 2010. Avian magnetite-based magnetoreception: a physiologist's perspective. *Journal of the Royal Society Interface*, **7 S2**(S2): S193–S205.

Castner T Jr, Newell GS, Holton WC, et al. 1960. Note on the paramagnetic resonance of iron in glass. *The Journal of Chemical Physics*, **32**(3): 668–673.

Chae KS, Kim SC, Kwon HJ, et al. 2022. Human magnetic sense is mediated by a light and magnetic field resonance-dependent mechanism. *Scientific Reports*, **12**(1): 8997.

Cupp-Vickery JR, Silberg JJ, Ta DT, et al. 2004. Crystal structure of IscA, an iron-sulfur cluster assembly protein from *Escherichia coli. Journal of Molecular Biology*, **338**(1): 127–137.

Ding HE, Clark RJ. 2004. Characterization of iron binding in IscA, an ancient iron-sulphur cluster assembly protein. *Biochemical Journal*, **379**(Pt 2): 433–440.

Ding HE, Yang JJ, Coleman LC, et al. 2007. Distinct iron binding property of two putative iron donors for the iron-sulfur cluster assembly: IscA and the bacterial frataxin ortholog CyaY under physiological and oxidative stress conditions. *Journal of Biological Chemistry*, **282**(11): 7997–8004.

Drovosekov AB, Kreines NM, Ziganurov DA, et al. 2023. Specific features of $g \approx 4.3$ EPR line behavior in magnetic nanogranular composites. *Journal of Experimental and Theoretical Physics*, **137**(4): 562–571.

Egevang C, Stenhouse IJ, Phillips RA, et al. 2010. Tracking of Arctic terns *Sterna paradisaea* reveals longest animal migration. *Proceedings of the National Academy of Sciences of the United States of America*, **107**(5): 2078–2081.

Felsenstein J. 1985. Confidence limits on phylogenies: an approach using the bootstrap. *Evolution*, **39**(4): 783–791.

Foley LE, Gegear RJ, Reppert SM. 2011. Human cryptochrome exhibits light-dependent magnetosensitivity. *Nature Communications*, **2**: 356.

Friis I, Sjulstok E, Solov'yov IA. 2017. Computational reconstruction reveals a candidate magnetic biocompass to be likely irrelevant for magnetoreception. *Scientific Reports*, **7**(1): 13908.

Guo Z, Xu S, Chen X, et al. 2021. Modulation of MagR magnetic properties via iron–sulfur cluster binding. *Scientific Reports*, **11**(1): 23941.

Harms MJ, Thornton JW. 2013. Evolutionary biochemistry: revealing the historical and physical causes of protein properties. *Nature Reviews Genetics*, **14**(8): 559–571.

Hoppe A, Pandelia ME, Gärtner W, et al. 2011. $[Fe_4S_4]$- and $[Fe_3S_4]$-cluster formation in synthetic peptides. *Biochimica et Biophysica Acta*, **1807**(11): 1414–1422.

Hore PJ, Mouritsen H. 2016. The radical-pair mechanism of magnetoreception. *Annual Review of Biophysics*, **45**: 299–344.

Im J, Lee J, Löffler FE. 2013. Interference of ferric ions with ferrous iron quantification using the ferrozine assay. *Journal of Microbiological Methods*, **95**(3): 366–367.

Jacklyn PM, Munro U. 2002. Evidence for the use of magnetic cues in mound construction by the termite Amitermes meridionalis (Isoptera: Termitinae). *Australian Journal of Zoology*, **50**(4): 357–368.

Jayaraman V, Toledo-Patino S, Noda-García L, et al. 2022. Mechanisms of protein evolution. *Protein Science*, **31**(7): e4362.

Jensen LT, Culotta VC. 2000. Role of *Saccharomyces cerevisiae ISA1* and *ISA2* in iron homeostasis. *Molecular and Cellular Biology*, **20**(11): 3918–3927.

Johnsen S, Lohmann KJ. 2008. Magnetoreception in animals. *Physics Today*, **61**(3): 29–35.

Kaur G, Iyer LM, Subramanian S, et al. 2018. Evolutionary convergence and divergence in archaeal chromosomal proteins and Chromo-like domains from bacteria and eukaryotes. *Scientific Reports*, **8**(1): 6196.

Kimchi T, Etienne AS, Terkel J. 2004. A subterranean mammal uses the magnetic compass for path integration. *Proceedings of the National Academy of Sciences of the United States of America*, **101**(4): 1105–1109.

Kirschvink JL, Gould JL. 1981. Biogenic magnetite as a basis for magnetic field detection in animals. *Biosystems*, **13**(3): 181–201.

Kirschvink JL, Walker MM, Diebel CE. 2001. Magnetite-based magnetoreception. *Current Opinion in Neurobiology*, **11**(4): 462–467.

Krebs C, Agar JN, Smith AD, et al. 2001. IscA, an alternate scaffold for Fe-S cluster biosynthesis. *Biochemistry*, **40**(46): 14069–14080.

Landry AP, Cheng ZS, Ding HE. 2013. Iron binding activity is essential for the function of IscA in iron-sulphur cluster biogenesis. *Dalton Transactions*, **42**(9): 3100–3106.

Lebigot E, Hully M, Amazit L, et al. 2020. Expanding the phenotype of mitochondrial disease: Novel pathogenic variant in *ISCA1* leading to instability of the iron-sulfur cluster in the protein. *Mitochondrion*, **52**: 75–82.

Lee J, Ma JS, Lee K. 2019. Direct delivery of adenoviral CRISPR/Cas9 vector into the blastoderm for generation of targeted gene knockout in quail. *Proceedings of the National Academy of Sciences of the United States of America*, **116**(27): 13288–13292.

Lohmann KJ. 2016. Protein complexes: A candidate magnetoreceptor. *Nature Materials*, **15**(2): 136–138.

Lohmann KJ, Willows AOD. 1987. Lunar-modulated geomagnetic orientation by a marine mollusk. *Science*, **235**(4786): 331–334.

Lu HM, Li JD, Zhang YD, et al. 2020. The evolution history of Fe-S cluster A-type assembly protein reveals multiple gene duplication events and essential protein motifs. *Genome Biology and Evolution*, **12**(3): 160–173.

Lu JX, Bitoun JP, Tan GQ, et al. 2010. Iron-binding activity of human iron-sulfur cluster assembly protein hIscA1. *Biochemical Journal*, **428**(1): 125–131.

Maeda K, Henbest KB, Cintolesi F, et al. 2008. Chemical compass model of avian magnetoreception. *Nature*, **453**(7193): 387–390.

Mansouri HR, Carmona OG, Jodlbauer J, et al. 2022. Mutations increasing cofactor affinity, improve stability and activity of a baeyer-villiger monooxygenase. *ACS Catalysis*, **12**(19): 11761–11766.

Mouritsen H. 2018. Long-distance navigation and magnetoreception in migratory animals. *Nature*, **558**(7708): 50–59.

Mouritsen H, Ritz T. 2005. Magnetoreception and its use in bird navigation. *Current Opinion in Neurobiology*, **15**(4): 406–414.

Naisbett-Jones LC, Lohmann KJ. 2022. Magnetoreception and magnetic navigation in fishes: a half century of discovery. *Journal of Comparative Physiology A*, **208**(1): 19–40.

Nasta V, Da Vela S, Gourdoupis S, et al. 2019. Structural properties of [2Fe-2S] ISCA2-IBA57: a complex of the mitochondrial iron-sulfur cluster assembly machinery. *Scientific Reports*, **9**(1): 18986.

Oishi I, Yoshii K, Miyahara D, et al. 2016. Targeted mutagenesis in chicken using CRISPR/Cas9 system. *Scientific Reports*, **6**: 23980.

Ollagnier-De-Choudens S, Mattioli T, Takahashi Y, et al. 2001. Iron-sulfur cluster assembly: characterization of IscA and evidence for a specific and functional complex with ferredoxin. *Journal of Biological Chemistry*, **276**(25): 22604–22607.

Pandelia ME, Nitschke W, Infossi P, et al. 2011. Characterization of a unique [FeS] cluster in the electron transfer chain of the oxygen tolerant [NiFe] hydrogenase from *Aquifex aeolicus*. *Proceedings of the National Academy of Sciences of the United States of America*, **108**(15): 6097–6102.

Pelzer W, Mühlenhoff U, Diekert K, et al. 2000. Mitochondrial Isa2p plays a crucial role in the maturation of cellular iron-sulfur proteins. *FEBS Letters*, **476**(3): 134–139.

Qin SY, Yin H, Yang CL, et al. 2016. A magnetic protein biocompass. *Nature Materials*, **15**(2): 217–226.

Ritz T, Adem S, Schulten K. 2000. A model for photoreceptor-based magnetoreception in birds. *Biophysical Journal*, **78**(2): 707–718.

Rodgers CT, Hore PJ. 2009. Chemical magnetoreception in birds: the radical pair mechanism. *Proceedings of the National Academy of Sciences of the United States of America*, **106**(2): 353–360.

Rothery RA, Blasco F, Weiner JH. 2001. Electron transfer from heme $b_L$ to the [3Fe-4S] cluster of *Escherichia coli* nitrate reductase A (NarGHI). *Biochemistry*, **40**(17): 5260–5268.

Saitou N, Nei M. 1987. The neighbor-joining method: a new method for reconstructing phylogenetic trees. *Molecular Biology and Evolution*, **4**(4): 406–425.

Schulten K, Weller A. 1978. Exploring fast electron transfer processes by magnetic fields. *Biophysical Journal*, **24**(1): 295–305.

Sheng HX, Lu D, Qi XL, et al. 2023. A neuron-specific *Isca1* knockout rat developments multiple mitochondrial dysfunction syndromes. *Animal Models and Experimental Medicine*, **6**(2): 155–167.

Song DS, Tu Z, Lee FS. 2009. Human ISCA1 interacts with IOP1/NARFL and functions in both cytosolic and mitochondrial iron-sulfur protein biogenesis. *Journal of Biological Chemistry*, **284**(51): 35297–35307.

Walcott C, Gould JL, Kirschvink JL. 1979. Pigeons have magnets. *Science*, **205**(4410): 1027–1029.

Wang CX, Hilburn IA, Wu DA, et al. 2019. Transduction of the geomagnetic field as evidenced from alpha-band activity in the human brain. *eNeuro*, **6**(2): e0483–18.2019.

Wang M, Nie YG, Swaisgood RR, et al. 2023. Stable seasonal migration patterns in giant pandas. *Zoological Research*, **44**(2): 341–348.

Wang S, Zhang P, Fei F, et al. 2024. Unexpected divergence in magnetoreceptor MagR from robin and pigeon linked to two sequence variations. *Zoological Research*, **45**(1): 69–78.

Weiler BD, Bruck MC, Kothe I, et al. 2020. Mitochondrial [4Fe-4S] protein assembly involves reductive [2Fe-2S] cluster fusion on ISCA1-ISCA2 by electron flow from ferredoxin FDX2. *Proceedings of the National Academy of Sciences of the United States of America*, **117**(34): 20555–20565.

Westby GWM, Partridge KJ. 1986. Human homing: still no evidence despite geomagnetic controls. *Journal of Experimental Biology*, **120**(1): 325–331.

Wiltschko R, Wiltschko W. 1995. Magnetic Orientation in Animals. New York: Springer.

Wiltschko W, Wiltschko R. 2005. Magnetic orientation and magnetoreception in birds and other animals. *Journal of Comparative Physiology A*, **191**(8): 675–693.

Wiltschko R, Wiltschko W. 2006. Magnetoreception. *BioEssays*, **28**(2): 157–168.

Wiltschko R, Wiltschko W. 2019. Magnetoreception in birds. *Journal of the Royal Society Interface*, **16**(158): 20190295.

Xie C. 2022. Searching for unity in diversity of animal magnetoreception: from biology to quantum mechanics and back. *The Innovation*, **3**(3): 100229.

Xu JJ, Jarocha LE, Zollitsch T, et al. 2021. Magnetic sensitivity of cryptochrome 4 from a migratory songbird. *Nature*, **594**(7864): 535–540.

Zhang YQ, Zhang P, Wang JJ, et al. 2024. Mitochondrial targeting sequence of magnetoreceptor MagR: more than just targeting. *Zoological Research*, **45**(3): 468–477.

Zhou YJ, Tong TY, Wei MK, et al. 2023. Towards magnetism in pigeon MagR: Iron- and iron-sulfur binding work indispensably and synergistically. *Zoological Research*, **44**(1): 142–152.

Hore. *Zool. Res.* 2024, 45(4): 831−832
https://doi.org/10.24272/j.issn.2095-8137.2024.175

ZR | Zoological Research

Research highlight Open Access

# Proteins as nanomagnets and magnetoreceptors

It is an appealing notion that a protein molecule could act as a nanomagnet. A genetically encodable biomolecule with a permanent magnetic moment at room temperature could have a range of applications: a magnetogenetic actuator, a magnetic tag for purifying and immobilizing enzymes, a contrast agent for magnetic resonance imaging, and a basis for a biomimetic magnetic sensing device, to name just a few. A magnetic protein could perhaps also function as the sensor in the magnetic compass that enables small songbirds to navigate the huge distances between their breeding and wintering grounds. Attractive though such possibilities may be, how realistic are they?

Iron-containing nanoparticles, for example the magnetosome structures that allow magnetotactic bacteria to orient in the Earth's magnetic field, have intrinsic magnetism because they contain hundreds of thousands of iron (Fe) atoms which interact strongly with their immediate neighbours leading to a macroscopic alignment of their electron spins and hence a permanent magnetic dipole moment. Many proteins bind Fe atoms, often in the form of iron-sulphur (Fe-S) clusters, but these groupings are usually few and far between, such that the strong spin-spin coupling required for permanent magnetism would seem to be out of the question.

There was therefore some excitement in 2016 when Can Xie and his colleagues reported the discovery of a magnetic iron-containing protein complex (Qin et al., 2016). Modelling suggested a cylindrical oligomeric structure, 24 nm long and 15 nm wide, composed of 20 molecules of a homologue of the bacterial Fe-S cluster assembly protein, IscA1, adorned with 10 molecules of the flavoprotein, cryptochrome (Cry). Containing 40 Fe atoms, with the closest Fe-S centres ~1 nm apart, this ~900 kDa complex was reported to align spontaneously, like a nanoscopic compass needle, in the Earth's magnetic field. The authors suggested that the avian analogue of IscA1, dubbed MagR, in association with avian cryptochrome-4 (Cry4), could be the detector in the magnetic compass sense of migratory songbirds and other animals. Xie's proposal combines aspects of two leading hypotheses for the biophysical mechanism of animal magnetoreception. One – the radical pair mechanism – for which there is currently the most convincing evidence, is based on magnetically sensitive, light-induced electron transfer reactions in Cry4 (Hore & Mouritsen, 2016). The other relies on biogenic superparamagnetic or ferrimagnetic Fe-containing nanoparticles (e.g., magnetite, $Fe_3O_4$) coupled to mechanoreceptors or ion channels in nerve cells (Nordmann et al., 2017).

The claim that supramolecular MagR/Cry4 complexes could have an intrinsic magnetic moment sufficient to align them in a magnetic field as weak as the Earth's (25-65 μT) was initially met with blunt disbelief. In an article on the broader area of magnetogenetics, Meister estimated that one would need to cram ~$10^6$ closely packed Fe atoms into each complex before there would be any possibility of a permanent magnetic moment (Meister, 2016). Separately, Winklhofer and Mouritsen calculated that the magnetic moment would have to be $10^7$ times larger than the value Xie had measured for MagR/Cry4 to account for the reported orientation in the Earth's magnetic field (Winklhofer & Mouritsen, 2016). Nevertheless, and despite a few negative replication attempts, there have been a number of independent studies over the last few years that seem to confirm some of the properties claimed for MagR/Cry4. Three are summarized here.

First, at least three independent laboratories have had success using $Fe_3O_4$-$SiO_2$ magnetic beads to purify and immobilise catalytically active enzymes when expressed as MagR fusion proteins (Jiang et al., 2017; Kang et al., 2021; Liu et al., 2022; Wang et al., 2019). In no case was an attempt made to co-express Cry4 suggesting, perhaps, that it is not a prerequisite for MagR magnetization. However, Pekarsky et al. (2021) found that *E. coli* cells overexpressing fruit-fly MagR had no measurable permanent magnetization at low temperature and attributed their limited success at protein purification to ionic rather than magnetic interactions.

Second, the fabrication of electrochemically-based magnetic sensors has been reported by two independent research groups (Cheng et al., 2023, 2024; Xue et al., 2020). The output current of these devices, containing a layer of pigeon MagR/Cry4 immobilised on an electrode, was found to be sensitive to applied magnetic fields down to ~1 mT. The effect is thought to be due to a magnetically-induced alignment of the adsorbed MagR/Cry4 molecules which reduces the scattering of charge carriers. One of the two laboratories found that neither MagR nor Cry4 on its own showed similar effects, that the magnetic responses of the devices required light, and that MagR/Cry4 had no measurable permanent magnetic moment (Xue et al., 2020).

Third, transfection of pigeon MagR/Cry4 genes into *E. coli* cells and eukaryotic mesenchymal stem cells cultured with exogenous iron resulted in enhanced $T_2$ contrast in magnetic resonance images (MRI) of the cells (Li et al., 2023a, 2023b). The effect was not found for transfection with the MagR gene alone or in the absence of exogenous $Fe^{3+}$. It seems that MagR/Cry4 promotes the formation of intracellular paramagnetic iron oxide granules which accelerate the transverse relaxation observed by MRI. Given the failure of

This is an open-access article distributed under the terms of the Creative Commons Attribution Non-Commercial License (http://creativecommons.org/licenses/by-nc/4.0/), which permits unrestricted non-commercial use, distribution, and reproduction in any medium, provided the original work is properly cited.

Copyright ©2024 Editorial Office of Zoological Research, Kunming Institute of Zoology, Chinese Academy of Sciences

Received: 28 May 2024; Accepted: 03 June 2024; Online: 04 June 2024

several laboratories to confirm that MagR/Cry4 has a permanent magnetic moment, one wonders whether some of the other magnetic effects claimed for MagR/Cry4 could be due to the biosynthesis of (or contamination by) magnetic $Fe_3O_4$ or $Fe_2O_3$ nanoparticles.

What to make of all these articles? Either all of them, along with others not mentioned here, unwittingly report experimental artefacts or, unlikely as it may seem, MagR/Cry4 really does have unprecedented magnetic properties. The few theories have been put forward to account for these observations shed little light. Nor is it at all clear what role Cry4 might play in MagR/Cry4. Xie suggests that movement of electrons between MagR and Cry4 could be important (Qin et al., 2016; Xie, 2022). He proposes a structural model in which a central cylindrical stack of five disk-shaped MagR tetramers is surrounded by a sheath of Cry4 molecules. Within each tetramer is a ring (diameter ~1 nm) of four Fe-S clusters (one per monomer) and a concentric, perpendicular ring (diameter ~2 nm) of 16 aromatic amino acid residues (one tyrosine and three phenylalanines per monomer). It is imagined that this arrangement would provide a ~5 nm electron transfer pathway between the Cry4 chromophores (flavin adenine dinucleotide) in the periphery and the Fe-S loops in the core, via a chain of four tryptophans in Cry4, a bridge comprising two tyrosines separated by ~1 nm, and the Tyr-Phe ring in MagR within which electrons are supposed to circulate (Xie, 2022). It will be interesting to see whether this speculation is confirmed by experiment.

Clearly, more needs to be known about iron-binding in MagR/Cry4. To this end, Xie and colleagues have now completed a detailed study, published in four recent articles in *Zoological Research*, the results of which can be summarized as follows. (1) Pigeon MagR binds iron in the form of $Fe^{3+}$ and as Fe-S centres; the former requires the presence of a conserved tyrosine residue (Zhou et al., 2023). (2) The 25 N-terminal amino acid residues in pigeon MagR are essential for the stability of the MagR/Cry4 complex and enhance the Fe-binding efficiency of eukaryotic MagR relative to prokaryotic IscA (Zhang et al., 2024b). (3) There are only three sequence variations between the MagR proteins from (non-migratory) pigeon and (migratory) European robin. Two of them account for the higher $Fe^{3+}$ and Fe-S cluster affinity of the robin protein and for the different oligomeric states of pigeon (tetrameric) and robin (dimeric) MagR. Both proteins are diamagnetic at 300 K (Wang et al., 2024). (4) The stability of MagR and its affinity for $Fe^{3+}$ and Fe-S clusters have increased during the course of evolution from prokaryotes, molluscs, arthropods, bony fishes, reptiles, and birds to mammals (Zhang et al., 2024a).

Despite these new insights, fundamental questions still surround MagR/Cry4. What is the origin of any unusual intrinsic magnetism? Is the Cry4 component essential and, if so, what is its function? Does the MagR/Cry4 protein complex exist *in vivo*? And, most intriguingly of all in my view, could it be an indispensable component of the compass magnetoreceptor in birds or other animals? Whatever the answers turn out to be, they are likely to be interesting.

P. J. Hore[1,*]

[1] *Department of Chemistry, University of Oxford, OX1 3TA, UK*

*Corresponding author, E-mail: peter.hore@chem.ox.ac.uk

## REFERENCES

Cheng Q, Ge YQ, Lin B, et al. 2024. Capacitive bionic magnetic sensors based on one-step biointerface preparation. *ACS Applied Materials & Interfaces*, **16**(6): 6789–6798.

Cheng Q, Sun JF, Ge YQ, et al. 2023. Bionic magnetic sensor based on the MagR/Cry4 complex-configured graphene transistor with an integrated on-chip gate. *ACS Sensors*, **8**(2): 793–802.

Hore PJ, Mouritsen H. 2016. The radical-pair mechanism of magnetoreception. *Annual Review of Biophysics*, **45**: 299–344.

Jiang M, Zhang LJ, Wang FQ, et al. 2017. Novel application of magnetic protein: convenient one-step purification and immobilization of proteins. *Scientific Reports*, **7**: 13329.

Kang J, Kang D, Yeom G, et al. 2021. Molecular diagnostic system using engineered fusion protein-conjugated magnetic nanoparticles. *Analytical Chemistry*, **93**(50): 16804–16812.

Li N, Wang P, Xie YY, et al. 2023a. Expression of clMagR/clCry4 protein in mBMSCs provides $T_2$-contrast enhancement of MRI. *Acta Biomaterialia*, **172**: 309–320.

Li N, Xue L, Mai X, et al. 2023b. Transfection of *clMagR/clCry4* imparts MR-$T_2$ imaging contrast properties to living organisms (*E. coli*) in the presence of $Fe^{3+}$ by endogenous formation of iron oxide nanoparticles. *Frontiers in Molecular Biosciences*, **10**: 1119356.

Liu ZW, Zhao ZS, Zeng K, et al. 2022. Functional immobilization of a biofilm-releasing glycoside hydrolase dispersin B on magnetic nanoparticles. *Applied Biochemistry and Biotechnology*, **194**(2): 737–747.

Meister M. 2016. Physical limits to magnetogenetics. *Elife*, **5**: e17210.

Nordmann GC, Hochstoeger T, Keays DA. 2017. Magnetoreception - a sense without a receptor. *PLoS Biology*, **15**(10): e2003234.

Pekarsky A, Michor H, Spadiut O. 2021. Revisiting the potential functionality of the MagR protein. *Magnetochemistry*, **7**(11): 147.

Qin SY, Yin H, Yang CL, et al. 2016. A magnetic protein biocompass. *Nature Materials*, **15**(2): 217–226.

Wang L, Xu HX, Liu ZW, et al. 2019. Magnetic immobilization of a quorum sensing signal hydrolase, AiiA. *MicrobiologyOpen*, **8**(8): e00797.

Wang S, Zhang P, Fei F, et al. 2024. Unexpected divergence in magnetoreceptor MagR from robin and pigeon linked to two sequence variations. *Zoological Research*, **45**(1): 69–78.

Winklhofer M, Mouritsen H. 2016. A room-temperature ferrimagnet made of metallo-proteins?. *bioRxiv*, doi: 10.1101/094607.

Xie C. 2022. Searching for unity in diversity of animal magnetoreception: from biology to quantum mechanics and back. *The Innovation*, **3**(3): 100229.

Xue L, Hu T, Guo Z, et al. 2020. A novel biomimetic magnetosensor based on magneto-optically involved conformational variation of MagR/Cry4 complex. *Advanced Electronic Materials*, **6**(4): 1901168.

Zhang J, Chang YF, Zhang P, et al. 2024a. On the evolutionary trail of MagR. *Zoological Research*, **45**(4): 805–814.

Zhang YQ, Zhang P, Wang JJ, et al. 2024b. Mitochondrial targeting sequence of magnetoreceptor MagR: More than just targeting. *Zoological Research*, **45**(3): 468–477.

Zhou YJ, Tong TY, Wei MK, et al. 2023. Towards magnetism in pigeon MagR: Iron- and iron-sulfur binding work indispensably and synergistically. *Zoological Research*, **44**(1): 142–152.

Liu et al. *Zool. Res.* 2024, 45(4): 833−844
https://doi.org/10.24272/j.issn.2095-8137.2024.090

ZR | Zoological Research

Article Open Access

# Genetically modified pigs with CD163 point mutation are resistant to HP-PRRSV infection

Ying Liu[1,#], Lin Yang[1,#], Hong-Yong Xiang[1,#], Ming Niu[1], Jia-Cheng Deng[1], Xue-Yuan Li[1], Wen-Jie Hao[1,2], Hong-Sheng Ou-Yang[1,2,3], Tong-Yu Liu[1], Xiao-Chun Tang[1], Da-Xin Pang[1,2,3,*], Hong-Ming Yuan[1,*]

[1] *State Key Laboratory for Diagnosis and Treatment of Severe Zoonotic Infectious Diseases*, *Animal Genome Editing Technology Innovation Center*, *College of Animal Sciences*, *Jilin University*, *Changchun*, *Jilin* 130062, *China*

[2] *Chifeng Best Genetics Technology Co*., *Ltd*., *Chifeng*, *Nei Mongol* 024000, *China*

[3] *Chongqing Jitang Biotechnology Research Institute Co*., *Ltd*., *Chongqing* 400015, *China*

## ABSTRACT

Porcine reproductive and respiratory syndrome (PRRS) is a globally prevalent contagious disease caused by the positive-strand RNA PRRS virus (PRRSV), resulting in substantial economic losses in the swine industry. Modifying the CD163 SRCR5 domain, either through deletion or substitution, can eff1ectively confer resistance to PRRSV infection in pigs. However, large fragment modifications in pigs inevitably raise concerns about potential adverse effects on growth performance. Reducing the impact of genetic modifications on normal physiological functions is a promising direction for developing PRRSV-resistant pigs. In the current study, we identified a specific functional amino acid in CD163 that influences PRRSV proliferation. Viral infection experiments conducted on Marc145 and PK-15$^{CD163}$ cells illustrated that the mE535G or corresponding pE529G mutations markedly inhibited highly pathogenic PRRSV (HP-PRRSV) proliferation by preventing viral binding and entry. Furthermore, individual viral challenge tests revealed that pigs with the E529G mutation had viral loads two orders of magnitude lower than wild-type (WT) pigs, confirming effective resistance to HP-PRRSV. Examination of the physiological indicators and scavenger function of CD163 verified no significant differences between the WT and E529G pigs. These findings suggest that E529G pigs can be used for breeding PRRSV-resistant pigs, providing novel insights into controlling future PRRSV outbreaks.

**Keywords:** PRRSV; CD163; Point mutation; E529G; Pigs

This is an open-access article distributed under the terms of the Creative Commons Attribution Non-Commercial License (http://creativecommons.org/licenses/by-nc/4.0/), which permits unrestricted non-commercial use, distribution, and reproduction in any medium, provided the original work is properly cited.

Copyright ©2024 Editorial Office of Zoological Research, Kunming Institute of Zoology, Chinese Academy of Sciences

## INTRODUCTION

Porcine reproductive and respiratory syndrome (PRRS), commonly known as pig blue-ear disease, is caused by the PRRS virus (PRRSV) (Lunney et al., 2016). This contagious disease is characterized by reproductive disorders in pregnant sows and respiratory disease in pigs of all ages, particularly piglets (Ma et al., 2021b). PRRS has become one of the most economically devastating diseases affecting the swine industry worldwide (Holtkamp et al., 2013; Renken et al., 2021). While current prevention and control methods, such as vaccine immunization, are somewhat effective (Kick et al., 2023), challenges remain in overcoming the virus's immune escape mechanisms, recombination diversity, and antibody-dependent enhancement.

Research has identified CD163 as a crucial host factor for PRRSV, serving as a specific and indispensable receptor for viral entry and uncoating (Calvert et al., 2007; Van Gorp et al., 2008; Welch & Calvert, 2010; Yu et al., 2020). Advances in CRISPR/Cas9 technology have made gene editing more feasible, offering potential solutions for eradicating various diseases through genetic modification (Jiang & Doudna, 2017). Specifically, *CD163* gene knockout using the CRISPR/Cas9 system has been shown to confer complete resistance to PRRSV infection (Yang et al., 2018).

The fifth scavenger receptor cysteine-rich domain (SRCR5) of CD163 is vital for mediating PRRSV invasion into host cells by binding to viral GP2a and GP4 protein dimers (Stoian et al., 2022a). Recent studies have demonstrated that deletion or substitution of the CD163 SRCR5 domain confers resistance to PRRSV infection (Burkard et al., 2017; Prather et al., 2017; Wells et al., 2017; Whitworth et al., 2014, 2016; Xu et al., 2020). The SRCR5 domain contains four disulfide bonds necessary for PRRSV infection (Stoian et al., 2022b). Liang Guang Small Spotted and Large White pigs lacking 41 amino

Received: 20 March 2024; Accepted: 05 June 2024; Online: 06 June 2024

Foundation items: This work was supported by the Major Scientific and Technological Projects in Agricultural Biological Breeding of China (2023ZD0404302) and Youth Program of National Natural Science Foundation of China (32202754)

[#]Authors contributed equally to this work

*Corresponding authors, E-mail: pdx@jlu.edu.cn; yuanhongming@jlu.edu.cn

acids in the SRCR5 domain, including the ligand binding pocket (LBP), are not susceptible to PRRSV infection (Guo et al., 2019). Additionally, knockout of the PSTII domain of CD163 has been found to confer complete resistance to PRRSV infection (Salgado et al., 2024).

Beyond its role as a host factor for PRRSV, CD163 functions as a scavenger receptor, participating in various physiological functions (Etzerodt & Moestrup, 2013; Moestrup & Møller, 2004). For instance, the CD163 SRCR2 domain contributes to erythroblast adhesion (Fabriek et al., 2007), while the SRCR3 domain is vital for the calcium-sensitive coupling of hemoglobin (Hb)-haptoglobin (Hp) complexes (Madsen et al., 2004). Xu et al. (2020) found that pigs with SRCR5 knockout exhibited significantly higher meat color scores, increased Fe concentrations, and higher Hp content, likely due to decreased Hb metabolism and subsequent mild Fe accumulation in the meat. Consequently, large fragment modification of CD163 raises concerns regarding their potential effects on growth performance. Thus, minimizing the impact of *CD163* gene modifications on its normal physiological function, while still contributing to anti-PRRSV breeding, represents a promising direction for future research.

Previous studies have shown that PRRSV exhibits strict host specificity for swine, with an exclusive affinity for porcine primary alveolar macrophages (PAMs) (Xie et al., 2021). Additionally, artificially induced African green monkey (*Chlorocebus sabaeus*) kidney cells, such as MA-104, Marc145, and CL2621, are also susceptible to PRRSV (Shi et al., 2015), showing persistent infection in epidemiological studies. Given that CD163 performs similar biological functions *in vivo*, we hypothesized that specific amino acids in CD163 affect PRRSV proliferation. Ma et al. (2021a) discovered significant discrepancies in surface electrostatic potential among the crystal structures of the monkey CD163 SRCR5 domain, pig CD163 SRCR5 domain, and human CD163L1 SRCR8 domain, and identified several potential site mutations, including E534 (referred to as E529 in this study), that affect PRRSV proliferation in PK-15 cells.

Building upon this, we investigated the role of the pig CD163 E529 and corresponding E535 in monkeys in PRRSV proliferation. We initially verified that E535G mutation in Marc145 cells and E529G mutation in PK-15$^{CD163}$ cells inhibited PRRSV infection by preventing viral binding and entry. Subsequently, we generated genetically modified pigs with the CD163 E529G mutation, with physiological examination confirming normally maintained physiological functions. Individual PRRSV challenge experiments verified that E529G pigs were resistant to PRRSV infection, emphasizing the feasibility of the E529G mutation strategy for commercial anti-PRRSV breeding. In future research, identifying additional key amino acids in CD163 that affect PRRSV proliferation without disrupting its physiological function and developing pigs with these specific CD163 amino acid mutations may provide an effective solution to prevent PRRSV infection.

## MATERIALS AND METHODS

### Ethics statement

All animal work was approved by the Animal Welfare and Research Ethics Committee at Jilin University (Approval No. SY202403012). All procedures were conducted strictly in accordance with the Guide for the Care and Use of Laboratory Animals.

### Cells and viruses

African green monkey embryonic kidney (Marc145) cells and the porcine kidney cell line 15 (PK-15) were cultured in RPMI Medium 1640 basic (RPMI, Gibco, USA) or Dulbecco's Modified Eagle Medium (DMEM, Gibco, USA), both supplemented with 5% fetal bovine serum (FBS, Gibco, USA). The cells were incubated at 37°C in a 5% $CO_2$ atmosphere. Porcine fetal fibroblasts (PFFs) were cultured in DMEM supplemented with 10% FBS.

Highly pathogenic PRRSV (HP-PRRSV) strains JXA1, GD, and JXA1-GFP were kindly provided by Prof. Shuqi Xiao (Lanzhou Veterinary Research Institute, Lanzhou, China).

### Plasmid construction

Single-guide RNAs (sgRNAs) were designed using Zhang Lab Guide Design Resources and synthesized by Comate Bioscience (China). The plasmid pBluescriptSKII+U6-sgRNA(F+E) empty (#74707, Addgene, USA) was digested with the *Bbs*I restriction enzyme (NEB, USA) at 37°C for 1 h. The sgRNA oligonucleotides were annealed into double-stranded DNA, then inserted into the *Bbs*I site of the 74707-vector backbone. The target plasmid was named 74707-sgRNA-mE535G or 74707-sgRNA-pE529G.

Total RNA was extracted from lung tissue and reverse transcribed into cDNA. The CD163 encoding sequence was amplified from the cDNA using long-sequence polymerase chain reaction (PCR) with specific primers (CD163-CDS-F/R) and cloned into the pcDNA3.1 vector. The recombinant plasmid pcDNA3.1-CD163 and PB513B-Blastin vector were each digested with *Xba*I and *Age*I (NEB, USA), then ligated together. The constructed plasmid with a FLAG tag was named PB513B-Blastin-CD163.

The NG-ABE8e plasmid was purchased from Addgene (#138491, USA) (Jing et al., 2023).

### Construction and verification of PK-15 cells with stable CD163 expression

The PB513B-Blastin-CD163 plasmid (200 ng), used as a transposon, was mixed with transposase (20 μg) in electroporation cuvettes plus (BTX, USA) and electrotransferred into $2\times10^6$ PK-15 cells at 280 V (1 ms, three pulses) using an ECM 2001 Electro Cell Manipulator (BTX, USA). Three days after electroporation, blasticidin S was used to screen resistant cells by gradually increasing the concentration daily until it reached 15 ng/μL. Four monoclonal cells were then selected by limiting dilution. The expression of CD163 was verified by quantitative real-time polymerase chain reaction (qPCR) and western blotting (WB). Both qPCR and indirect immunofluorescence assays (IFA) were used to determine PRRSV susceptibility of the four clones.

### Mutation efficiency assessment of guide RNAs and selection of cell clones

Mutation efficiency of the guides was assessed by transfecting the 74707-sgRNA-mE535G target plasmid into $2\times10^6$ Marc145 cells or 74707-sgRNA-pE529G into PK-15$^{CD163}$ cells and PFFs, along with the NG-ABE8e base editor, using a Neon transfection system (Invitrogen, USA) (1 400 mV, one pulse, 30 ms), with a final concentration of 30 μg per component. After 72 h, one-third of the cells were collected, and genomic DNA was extracted using a TIANamp Genomic DNA Kit (Tiangen, China). The remaining cells were cultured continuously. PCR across the target sites of genomic DNA

was performed using primers (Supplementary Table S1) with 2×Taq Plus PCR Mix (Tiangen, China) to produce 1 261 bp and 1 030 bp products, respectively. Following this, 1% agarose gel electrophoresis and Sanger sequencing were conducted to analyze editing efficiency.

The reserved cells were inoculated into several 100 mm dishes after efficiency detection, with an inoculation density of 600 cells/dish for Marc145/PK-15$^{CD163}$ cells or 2 000 cells/dish for PFFs, using the limiting dilution method. Single-cell clones were selected and cultured in 24-well plates 10–12 days later. When confluence reached 80% or more, 20% of each single clone was digested and lysed with 10 μL of NP40 lysis buffer (NP40 stock solution: proteinase K: 10×standard buffer: dd$H_2O$, 1:1:10:90) for 1 h at 56°C and 10 min at 95°C. The lysate was then used as the PCR template for electrophoresis. Additionally, single point mutation events were confirmed by Sanger sequencing.

**Cell proliferation detection**

Wild-type (WT) cells and clones were inoculated into 96-well plates (*n*=3) after cell counting to ensure consistent cell numbers. Cell proliferation was detected using a CCK-8 Kit (Boster, China) and absorbance was measured at an optical density (OD) of 450 nm using an Infinite® 200 PRO Multifunctional microplate reader (TECAN, Switzerland).

**Quantification of CD163 or PRRSV mRNA**

RNA was extracted from 1×10$^5$ cells using TRNzol Universal Reagent (Tiangen, China) and RNA concentration was measured using a NanoDrop™ 1000 (Thermo Scientific, USA). Subsequently, RNA of equal quality was reverse transcribed into cDNA using a FastKing One Step RT-PCR Kit (Tiangen, China) according to the manufacturer's instructions. The mRNA levels of CD163 and PRRSV and the reference mRNA levels of GAPDH were quantified using Talent qPCR PreMix (Tiangen, China) and a fluorescence quantitative PCR detection instrument q225 (Nevogene, China) with primers (Supplementary Table S1).

**Virus titration**

Marc145 cells were inoculated into 96-well plates and infected with 10-fold serial dilutions of sample supernatants before incubation for 1 h at 37°C. The supernatants were then replaced with DMEM containing 5% FBS. The cytopathic effect (CPE) at 96 hours post-infection (hpi), characterized by clumping and shrinkage of cells, was evaluated. Viral titers were determined using the 50% tissue culture infective dose ($TCID_{50}$) and calculated following the Reed-Muench formula.

**Expression levels of CD163 and PRRSV protein by western blotting**

Approximately 1×10$^7$ cells were suspended in RIPA buffer, lysed on ice for 30 min, and centrifuged at 3 000 r/min for 20 min at 4°C. The supernatant was collected, and the protein concentration was measured using an Enhanced BCA Protein Assay Kit (Beyotime, China). Equal amounts of protein were mixed with loading buffer prior to boiling for 10 min, then subjected to electrophoresis on 10% acrylamide gels. The gels were transferred to 0.22 μm polyvinylidene fluoride (PVDF) membranes (Boster, China). Proteins were divided into several parts and separately probed with antibodies against CD163 (mouse mAb, non-reducing, Bio-Rad, China, 1 μg/mL), PRRSV-N (mouse mAb, Shandong Lvdu, China, 1:100), β-actin (mouse mAb, Proteintech, China, 1:2 000), or FLAG (Proteintech, China, 1:4 000) at 4°C for 12 h. The membranes were subsequently incubated with horseradish peroxidase (HRP)-conjugated Affinipure goat anti-mouse IgG (H+L) (Proteintech, China, 1:5 000), followed by HRP-conjugated Affinipure goat anti-rabbit IgG (H+L) (Proteintech, China, 1:5 000) for 1h at room temperature. Protein bands were visualized using a Western Blotting Visualizer C600 (Azure Biosystems, USA), according to the manufacturer's instructions.

**IFA and flow cytometry analysis**

Approximately 5×10$^4$ cells and 2×10$^6$ cells were seeded into 12- and 6-well plates, respectively. After 12 h, the cells were inoculated at a multiplicity of infection (MOI) of 0.1 with the viruses (PRRSV JXA1/GD/JXA1-GFP) or not and cultured in RPMI for 48 h at 37°C. Cells for flow cytometry (FACS) analysis were digested into individual cells and fixed in phosphate-buffered saline (PBS) with 4% formaldehyde (Boster, China) for 15 min at room temperature. Cells for IFA were directly added to 4% formaldehyde. Subsequently, all cells were permeabilized in PBS containing 0.1% Triton-X-100 (Solarbio, China) for 10 min. Cells infected with viruses were incubated overnight with antibodies against PRRSV-N or β-actin at a 1:50 dilution in PBS with 10% FBS, then incubated with fluorescein (FITC)-conjugated Affinipure goat anti-mouse IgG (H+L) (Proteintech, China, 1:500). Cells infected with viruses or not were incubated overnight with antibodies against CD163 or β-actin at a 1:50 dilution in PBS with 10% FBS, then incubated with goat anti-mouse IgG/PE antibody (Absin, China, 1:500). Three washes with PBS were performed after each step. Expression levels of viruses and CD163 were determined by antibody labeling and assessed by IFA and FACS analysis using a fluorescence microscope EVOS (AMG, USA) or a FCM SH800S (Sony, Japan) with FlowJo software.

**Binding and entry detection of PRRSV**

Approximately 5×10$^5$ cells were seeded into two 60 mm dishes for binding and entry. After 12 h, the cells were inoculated with the PRRSV GD strain at MOI=1 for 1 h at 4°C for binding. Cells were subsequently washed three times with PBS, with the binding dish stored at −80°C. Another dish was continuously cultured in RPMI 1640 for 3 h at 37°C for entry. Cells were washed three times with PBS, then dipped in an alkaline high salt solution (1 mol/L NaCl and 50 mmol/L $NaHCO_3$, pH 9.5) (Zhu et al., 2023) for 3 min, followed by washing as above. The cells were collected for RNA extraction and viral RNA was quantified by qPCR to characterize binding and entry.

**Detection of blastocyst development rate**

PFFs from Large White pigs with the E529G mutation were transplanted into enucleated oocytes by microinjection. The rate of recombinant embryo development to the blastocyst stage was examined under a micromanipulator (Nikon, Japan).

**Generation of E529G pigs**

E529G mutation PFFs were used for somatic cell nuclear transfer (SCNT), followed by embryo transplantation, as described previously (Xie et al., 2018). The genotype was identified by PCR amplification and Sanger sequencing.

**Assessment of free Hp in serum**

Blood samples from WT and E529G pigs were collected at 2 weeks of age, and serum was separated for free Hp

examination using the Porcine (Pig) ELISA Kit for Haptoglobin (Hpt) (Cloud-Clone, USA) following the manufacturer's instructions.

**Visualization and quantification of Hb-Hp uptake**

PAMs were flushed out of the lung and seeded on a 24-well plate. FITC-Hb (Ruixibio, China) and Hp (BioVISION, USA) were mixed at a 1:1 wt/wt ratio in PBS for 15 min in a centrifuge tube before experimentation. PAMs were incubated with 100 μg/mL FITC-Hb-Hp in RPMI for 4 h at 37°C, washed three times with PBS, then treated with Hoechst 33342 for 5 min followed by additional washing. Fluorescence was detected and analyzed using a fluorescence microscope EVOS (AMG, USA). The cells were also collected for quantification by FACS assay.

**Viral challenge assessment of pigs**

Both WT (*n*=3) and E529G pigs (*n*=3) (5 weeks of age) were challenged in one room with approximately $4\times10^7$ $TCID_{50}$ of JXA1. One-half of the inoculum was delivered intramuscularly and the remainder intranasally. The *in vivo* viral challenge assay was strictly performed at a designated safe place. Clinical signs, rectal temperature, and body weight gain were monitored daily. Blood samples from pigs were collected on days 0, 3, 7, 10, and 14 post injection. Serum viral load was measured by qPCR. A commercial Porcine Reproductive and Respiratory Syndrome Virus Antibody ELISA Test Kit (Jndiag, China) was used to evaluate serum virus antibody levels according to the manufacturer's instructions. The animals were then euthanized by sodium pentobarbital (100 mg/kg) at 14 days post-infection. Tissue samples from the pigs were photographed and then fixed in formalin, followed by routine paraffin sectioning, hematoxylin & eosin (H&E) staining, and Immunohistochemical (IHC) analysis. Histopathological lesions were observed under a High-Resolution Microscope Digital Camera (Olympus, Japan).

**Statistical analyses**

All data are presented as mean±standard error of the mean (SEM) from three independent experiments. Statistical analyses were performed using untailed *t*-test with GraphPad Prism software v.8.0. $P<0.05$ was considered statistically significant. *: $P<0.05$; **: $P<0.01$; ***: $P<0.001$; ****: $P<0.0001$; ns: no significance.

## RESULTS

**Preparation of Marc145 cells with E535G mutation**

To affirm the feasibility of the CD163 functional amino acid site mutation strategy, sgRNAs introducing monkey E535G and pig E529G mutations were designed and electroporated into Marc145 cells along with NG-ABE8e (Figure 1A). Ten single-cell clones were identified, and four homozygous clones (Clone-#7 referred to as E535G cells) were obtained (Supplementary Figure S1). The E535G cells grew similarly to the WT cells, with no obvious phenotypic changes or effects on cell viability, suggesting that the E535G mutation is not essential for cell growth (Figure 1B). To further ascertain whether the E535G mutation resulted in the loss of CD163 expression at the RNA and protein levels, extracts from WT and E535G mutation cells were collected and subjected to qPCR, FACS, and IFA (Figure 1C–F). Results indicated that the E535G mutation did not affect Marc145 cell viability or CD163 expression.

**E535G mutation of monkey *CD163* inhibited PRRSV proliferation in Marc145 cells**

To assess whether E535 is a key amino acid site affecting PRRSV proliferation, we inoculated cells with HP-PRRSV, including Marc145, E535G cells, and control cells (T1043A, located on *CD163* exon 13, which is not associated with the SRCR5 domain). Viral RNA levels in E535G cells post JXA1 (Figure 2A) and GD strain (Figure 2B) infection demonstrated marked inhibition, while no significant differences in T1043A cells compared with WT cells were observed. Subsequently, IFA, WB, FACS, and virus titer detection revealed a significant decrease in viral load in E535G cells (Figure 2C–E, Supplementary Figure S2A). Overall, these results suggest that the E535G mutation within *CD163* can resist HP-PRRSV infection in Marc145 cells.

As CD163 is an imperative host factor for PRRSV infection, we further analyzed whether the inhibitory effect on PRRSV in E535G cells was achieved by reducing CD163 expression. As demonstrated in Supplementary Figure S2B–D, no significant differences in the expression levels of CD163 mRNA or protein were detected. Binding and entry assays were performed (Figure 2F), with relative viral RNA expression indicating that binding and entry were significantly prevented, as expected (Figure 2G). Taken together, these results suggest that E535 is a key amino acid site that suppresses HP-PRRSV infection by inhibiting PRRSV binding and entry.

**E529G mutation inhibited PRRSV proliferation in PK-15$^{CD163}$ cells**

We confirmed that the mE535G mutation significantly inhibited PRRSV infection in Marc145 cells. Thus, we further hypothesized that the corresponding E529 site on porcine CD163 may play the same role in PRRSV infection. To better characterize the antiviral ability of the E529G mutation, we established PRRSV-permissive PK-15 cells that stably integrated pCD163. The expression of CD163 in monoclonal cells (#1-4) showed that *CD163* was successfully integrated into PK-15 cells (Figure 3A). Subsequent examination of viral RNA (Figure 3B) and protein (Figure 3C) levels in these monoclonal cells indicated that clone #4 (referred to as PK-15$^{CD163}$) was most susceptible to PRRSV. To ensure consistent CD163 copy numbers, PK-15$^{CD163}$ E529G cells (named E529G cells) were selected using NG-ABE8e (Supplementary Figure S3A). The CCK-8 assay results indicated that the E529G mutation had no impact on cell proliferation (Figure 3D). Moreover, to further investigate CD163 expression after E529G mutation, cell extracts were subjected to qPCR, WB, and FACS (Supplementary Figure S3B; Figure 3E–G), revealing no marked differences in CD163 expression between the PK-15$^{CD163}$ and E529G cells.

To evaluate whether E529G cells can resist PRRSV infection, we detected viral RNA based on qPCR. The PRRSV copy numbers at 0, 12, 36, 48, 60, and 72 h as well as viral protein levels post JXA1 and GD strain infection showed a prominent PRRSV-inhibiting effect on the E529G cells (Figure 3H–K). Simultaneously, viral protein assessment using FACS and IFA showed clear inhibition of PRRSV in E529G cells (Figure 3L, M). These findings suggest that E529G cells can effectively resist PRRSV infection. As determined above in Marc145 cells, the mE535G mutation blocked PRRSV replication by inhibiting the binding and entry of PRRSV, rather than by down-regulating CD163 expression. Consequently, we posited that resistance to PRRSV infection

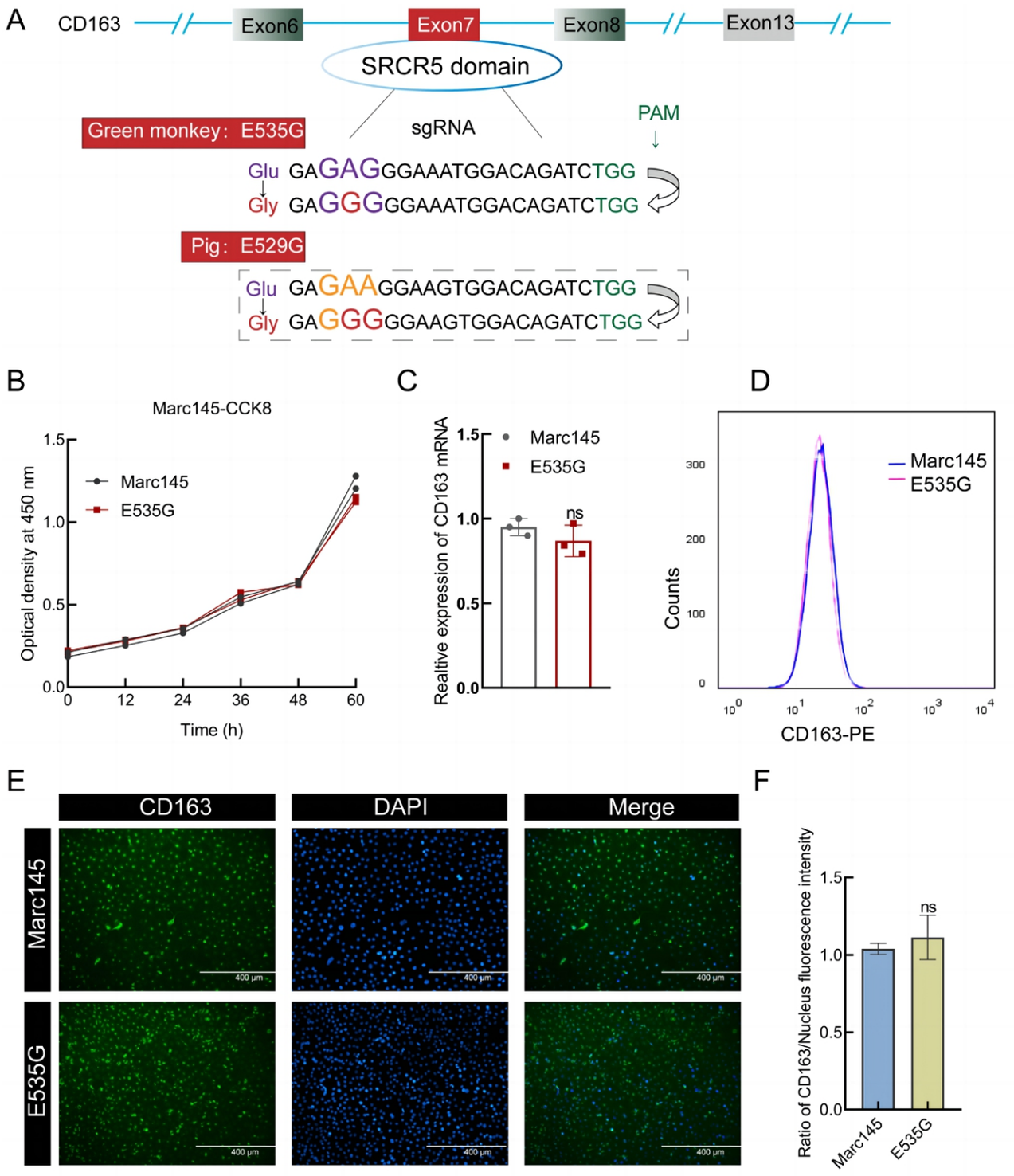



**Figure 1 Preparation of Marc145 cells with E535G mutation**

A: Schematic of sgRNA positions and sequences in green monkey and pig *CD163*. PAM and sgRNA sequences are shown in green and purple, respectively. B: CCK-8 assay of WT and E535G Marc145 cells. C: Relative expression levels of CD163 RNA were detected using qPCR with primers mCD163-F/R (Supplementary Table S1) and normalized by GAPDH. Data were analyzed using an unpaired *t*-test. Error bars represent SEM, *n*=3. Significant differences in results compared to WT are indicated as follows: ns means no significance. D, E: Expression levels of CD163 protein in WT or E535G Marc145 cells were determined by FACS (D) and IFA (E). F: Fluorescence intensity in (E) was quantified by ImageJ analysis.

in E529G cells may be achieved in the same way. As expected, qPCR analysis indicated that the E529G cells resisted PRRSV infection by suppressing the binding and entry of PRRSV (Figure 3N). We also detected CD163 expression based on qPCR, FACS, and WB after exposure of cells to HP-PRRSV. Results showed no significant differences in CD163 expression between the PK-15$^{CD163}$ and E529G cells (Supplementary Figure S3D–G). In summary, these findings substantiate that the mE535G and pE529G mutations significantly prevent PRRSV infection, highlighting the

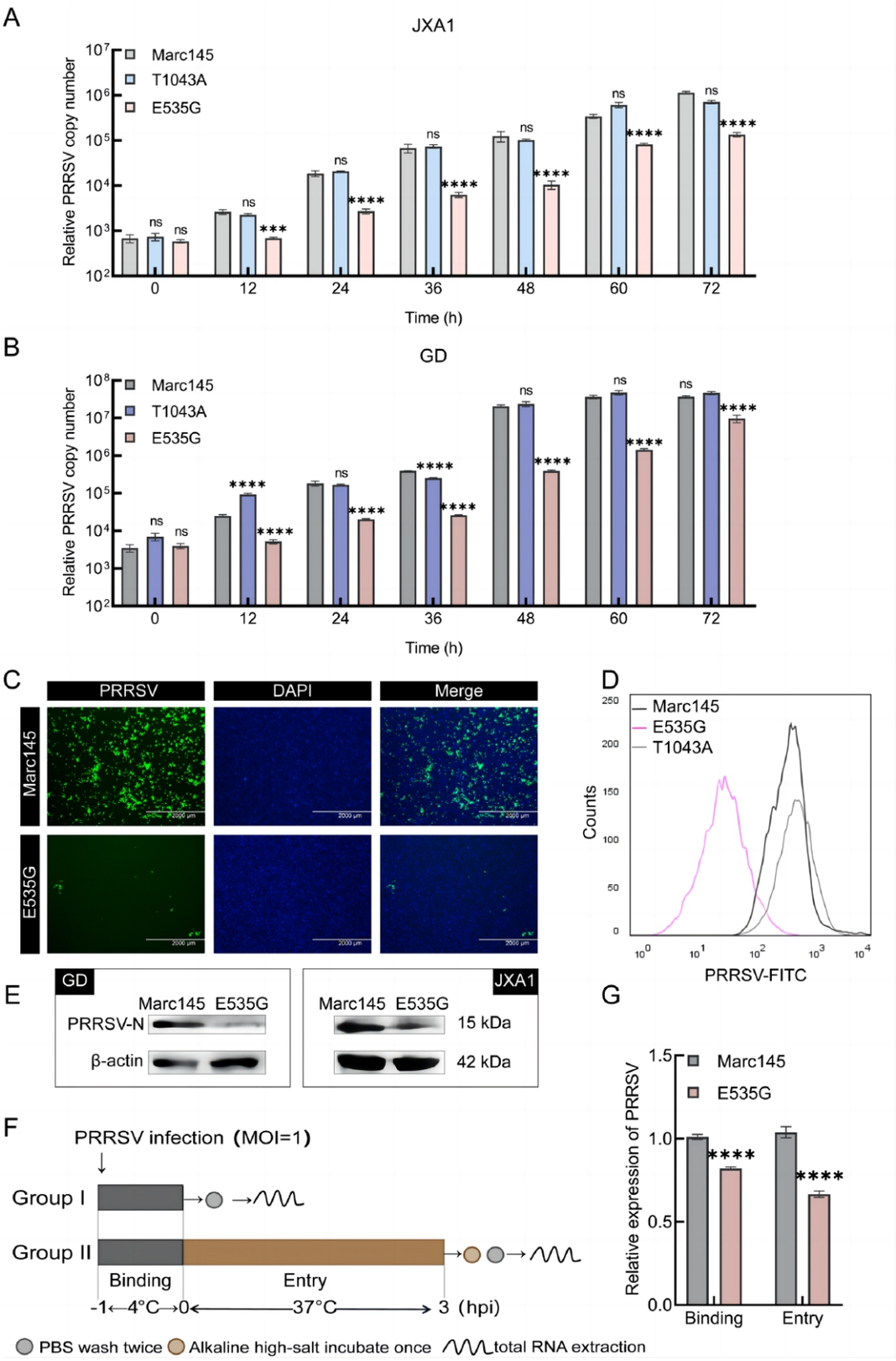



**Figure 2 E535G mutation of monkey *CD163* inhibited PRRSV proliferation in Marc145 cells**

A, B: WT or E535G Marc145 cells were seeded into 12-well plates and inoculated with JXA1 and GD strain at MOI=0.1, respectively. Cells were collected at 0, 12, 24, 36, 48, 60, and 72 hours post infection (hpi) to quantify viral RNA using qPCR with specific primers PRRSV-ORF7-F and PRRSV-ORF7-R. PRRSV copy numbers were statistically analyzed using unpaired *t*-test. C: Cells were inoculated with JXA1-GFP at MOI=0.1. PRRSV infection was characterized by IFA at 48 hpi. D: WT or E535G Marc145 cells were seeded into 60 mm dishes and inoculated with GD at MOI=0.1. PRRSV infection was assessed by FACS at 48 hpi. E: WT or E535G Marc145 cells were inoculated with GD and JXA1 strain at MOI=0.1, respectively. Viral proteins were determined using WB at 48 hpi. F: Binding and entry determination schematic of PRRSV. G: Relative expression of GD RNA was measured by qPCR for binding and entry assay. **: $P<0.01$; ****: $P<0.0001$; ns: No significance.

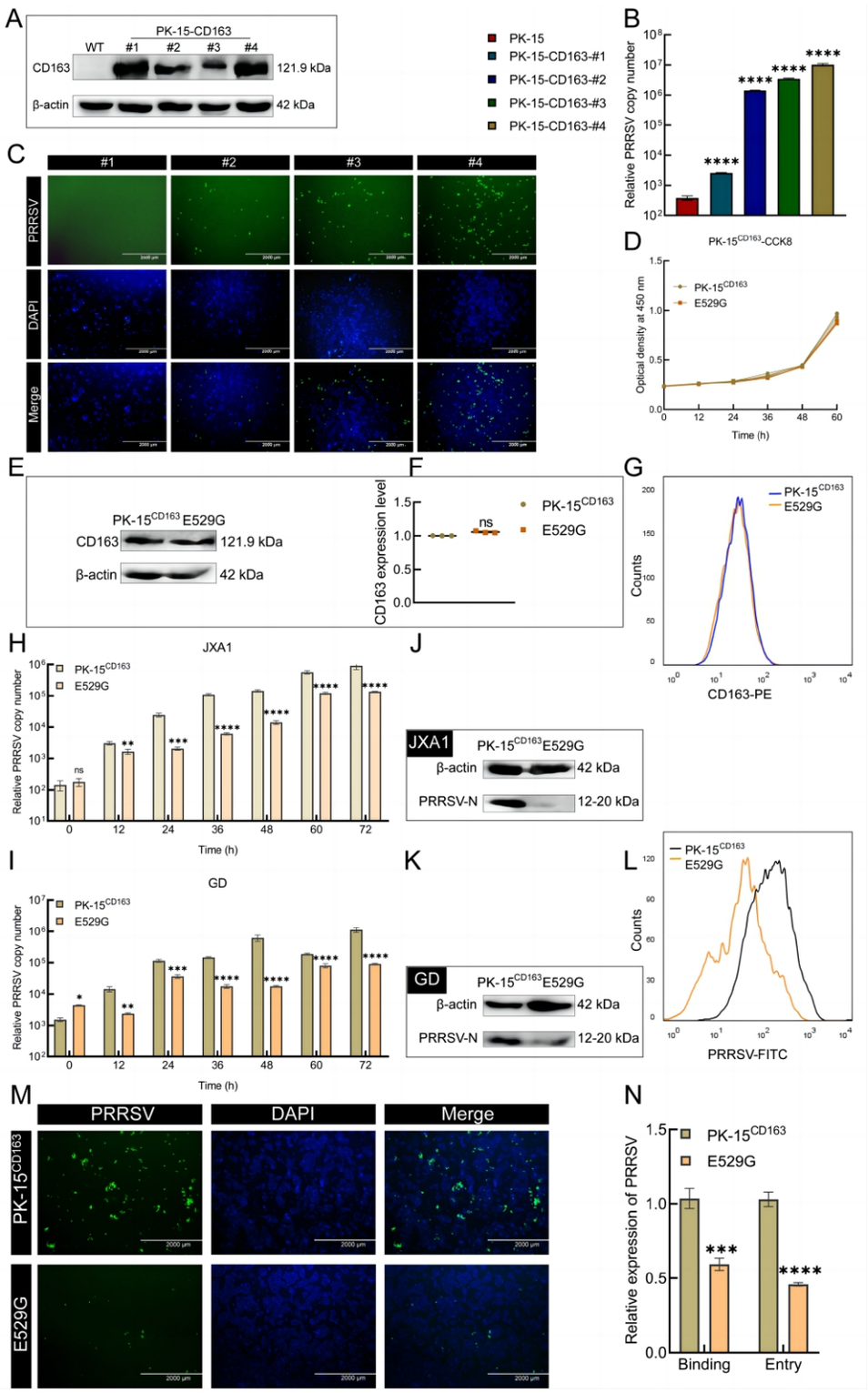



**Figure 3 E529G mutation restrained PRRSV proliferation in PK-15$^{CD163}$ cells**

A: Expression of CD163 protein in monoclonal cells (#1-4) was measured by WB with FLAG antibody. B, C: PRRSV susceptibility judging of four PK-15-CD163 cell clones was determined by JXA1-GFP proliferation using qPCR (B) and IFA (C). D: CCK-8 assay of PK-15$^{CD163}$ and E529G cells. E, F: The expression of CD163 protein was further characterized by WB with FLAG antibody (E) and quantified by ImageJ analysis (F). G: The expression levels of CD163 were texted by FACS, orange and blue lines are on behalf of PK-15$^{CD163}$ and E529G cells severally. H, I: Quantification of PRRSV mRNA were measured using qPCR at 0, 12, 36, 48, 60, and 72 hours post infection of JXA1 (H) and GD (I) strain at MOI=0.1. J, K: The cells were collected for WB assay at 48 hours post infection of JXA1 (J) and GD (K) strain (MOI=0.1) for PRRSV-N protein detecting, respectively. L: Viral protein was further determined at 48 hours post infection of GD strain at MOI=0.1 by FACS. Black line acts PK-15$^{CD163}$ cells and orange line is E529G cells. M: IFA judged viral protein expression at 72 h post JXA1-GFP infection at MOI=0.1. N: Relative expression quantity of viral RNA was examined for the process of binding and entry post infection of GD strain at MOI=1. ***: *P<0.001*; ****: *P<0.0001*; ns: No significance.

importance of these specific amino acid positions within CD163 as vital sites associated with PRRSV infection.

**Generation of *CD163*-E529G mutation pigs**

To further investigate whether the E529G mutation resists PRRSV infection *in vivo*, we generated E529G mutation pigs. Initially, PFFs from four Large White pigs with the E529G mutation (Supplementary Figure S4A) were identified and transplanted into enucleated oocytes by microinjection. Blastocyst development analysis indicated that the recombinant embryos developed normally to the blastocyst stage *in vitro* (Supplementary Table S2), substantiating that E529G PFFs may serve as SCNT donor cells. Four healthy F0 generation E529G pigs were obtained (Figure 4A). Genotype identification (Supplementary Figure S4B) revealed that all four genetically modified pigs produced the desired E529G mutation with no off-target effects (Supplementary Figure S4C).

Blood samples were collected to determine whether physiological indicators are normal in E529G pigs. Full blood counts showed that the E529G mutation had negligible impact on porcine growth (Supplementary Table S3). Concurrently, organs from both WT and E529G pigs were subjected to H&E staining, confirming the normal tissue morphology of cloned pigs (Figure 4B). Additionally, CD163 expression levels in the lung displayed no significant differences between WT and E529G pigs (Figure 4C, D). As CD163 is involved in anti-inflammatory and anti-oxidative processes via Hb-Hp complex uptake (Subramanian et al., 2013), free Hp levels in serum were measured. Results indicated no effect after E529G mutation (Figure 4E), indirectly confirming that CD163 from E529G pigs can remove free Hp normally. Furthermore, PAMs were isolated from WT and E529G pigs, and their uptake of FITC-Hb-Hp was determined using fluorescence microscopy (Figure 4F) and FACS (Figure 4G). Results indicated that PAMs from E529G pigs retained normal scavenger function. Additionally, inoculation of PAMs with HP-PRRSV-JXA1-GFP followed by fluorescence observation confirmed efficient PRRSV defense in E529G pigs (Figure 4H). Viral RNA and titer assays (Figure 4I; Supplementary Figure S4D) demonstrated that the antiviral intensity reached an order of magnitude. Overall, these *in vitro* results suggest that E529G pigs maintain normal CD163 scavenger function, exhibit healthy growth, and acquire antiviral ability against PRRSV.

***CD163*-E529G mutation pigs exhibited resistance to HP-PRRSV infection**

PRRS is a highly contagious and devastating disease affecting the pig industry. To investigate the antiviral activity of E529G pigs, three WT and three E529G pigs (5 weeks of age) were cohoused throughout the experiment and allowed to acclimate for three days prior to the initiation of the challenge. All pigs were confirmed to be PRRSV-specific antibody negative. The experiment lasted 14 days following inoculation of each pig with $4\times10^7$ $TCID_{50}$ of JXA1, with half of the inoculum delivered intramuscularly and the other half intranasally. Clinical parameters, including clinical score, percent survival, rectal temperature, and body weight gain rate, were recorded daily during the infection monitoring period and scored (Supplementary Table S4). Serum samples were collected on days 0, 3, 7, 10, and 14 to detect viral load and viral antibody levels.

During the viral challenge, WT pigs developed characteristic clinical symptoms of PRRSV infection, including respiratory disorders, high fever, slow growth, high morbidity, and mortality (Figure 5A). The average occurrence time for typical PRRSV symptoms in WT and E529G pigs was 2 dpi and 5 dpi, respectively (Figure 5A). Notably, while E529G pigs exhibited most PRRSV-related clinical signs, the symptoms were less severe compared to those in WT pigs. In addition, two of the three WT pigs died at 7 dpi and 10 dpi, respectively, whereas all E529G pigs survived until euthanasia (Figure 5B). Rectal temperatures were significantly elevated on day 4 in all challenged pigs; however, E529G pigs began to recover by 7 dpi, while WT pigs maintained a high fever throughout the monitoring period (Figure 5C). Daily body weights indicated that the E529G pigs exhibited faster weight gain than the WT pigs (Figure 5D). These findings suggest that PRRSV infection severity is mitigated in E529G pigs compared to WT pigs. Furthermore, as illustrated in Figure 5E, serum viral load in E529G pigs was two orders of magnitude lower than that in WT pigs. Concurrently, the antibody response was significantly higher in the WT pigs than in the E529G pigs (Figure 5F). Collectively, these results indicate that E529G pigs can resist PRRSV infection.

Organs were collected for histopathological analysis at the time of death for WT pigs or following euthanasia of all challenge pigs at 14 dpi. Macroscopic observation revealed significant lesions in the lung, spleen, lymph node, liver, and kidney (Figure 5G; Supplementary Figure S5A) of WT pigs (left) but not in E529G pigs (right). To further evaluate viral resistance of E529G pigs, H&E staining was conducted, which identified interstitial edema with infiltration of mononuclear cells and marked hemorrhage in lung sections of WT pigs but not in E529G pigs (Figure 5H). Pathological examination revealed significant lesions in the liver and obvious thrombi in the kidneys of WT pigs, which were absent in E529G pigs (Supplementary Figure S5B). IHC analysis of the lung indicated more severe viral infection in WT pigs than in E529G pigs (Figure 5H). Overall, these findings demonstrate significant differences in typical symptoms, mortality, viral load, viral antibody levels, and tissue lesions between WT and E529G pigs during the viral challenge.

## DISCUSSION

Genetically modified pigs with CD163 SRCR5 deletions and functional region substitutions have been shown to be resistant to PRRSV infection. However, the CD163 SRCR2 domain is implicated in erythroblast adhesion (Fabriek et al., 2007), while the SRCR3 domain is considered to be critical for the calcium-sensitive coupling of Hb-Hp complexes (Madsen et al., 2004). Xu et al. (2020) reported that SRCR5 knockout pigs exhibit significantly higher meat color scores, Fe concentrations, and Hp content than WT pigs, attributing the darker red color in SRCR5 knockout meat to decreased Hb metabolism and mild Fe-containing Hb accumulation. However, large fragment editing of *CD163* raises concerns about its impact on growth performance. PRRSV is highly specific to pigs and preferentially infects PAMs (Xie et al., 2021). Additionally, MA-104 cells and their derivatives, Marc145 and CL2621, are also susceptible to PRRSV (Shi et al., 2015). As CD163 performs similar physiological functions across species, we hypothesized that certain key amino acids in CD163 may affect PRRSV proliferation. Hence, identifying these key amino acids and establishing pigs with specific CD163 amino acid mutation may provide an effective solution to prevent PRRSV infection.

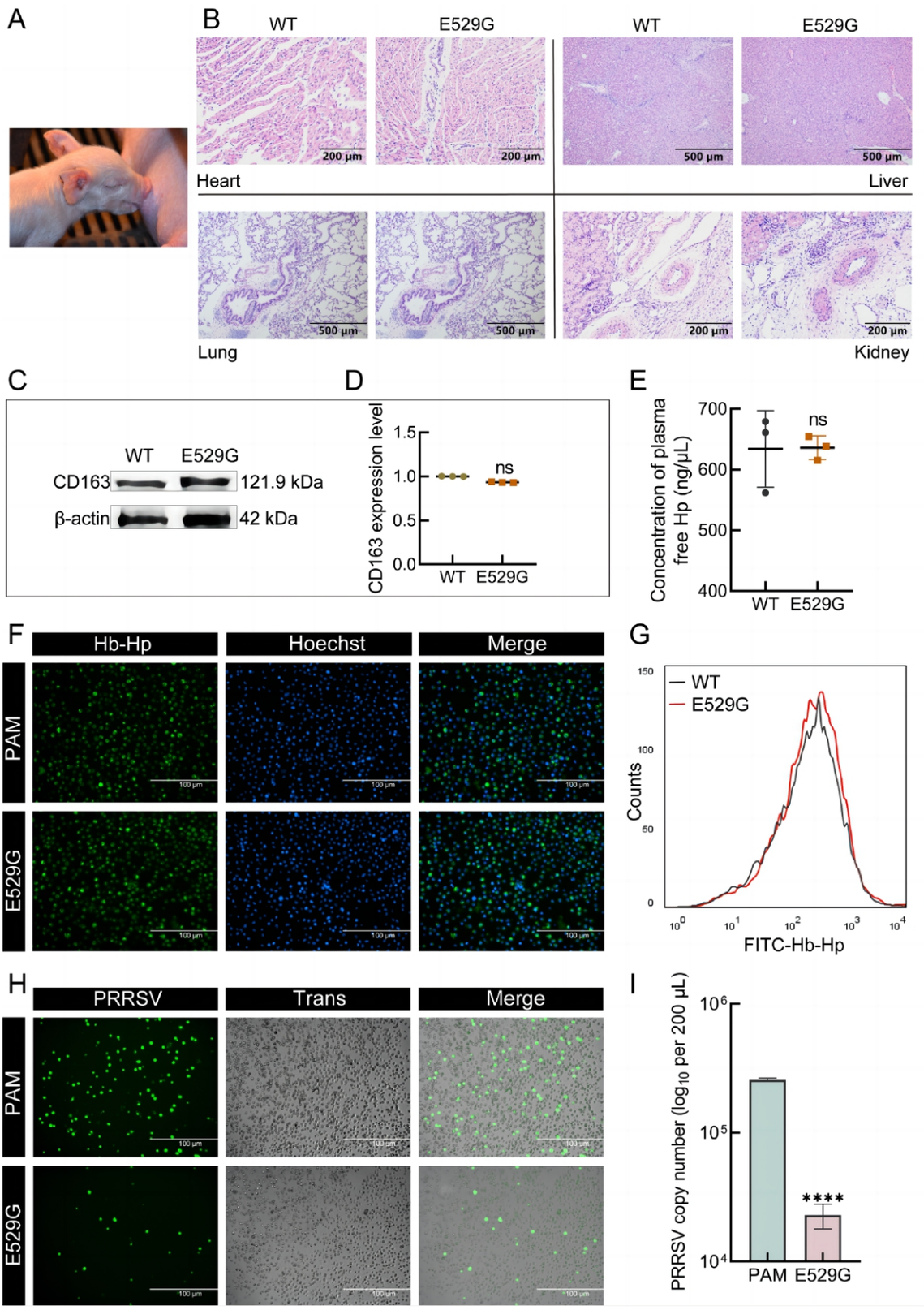



**Figure 4 Generation of *CD163*-E529G mutation pigs**

A: Picture of E529G piglets. B: H&E staining indicated normal physiological morphology of tissues from WT and E529G pigs. C: Identification of CD163 protein expression in lungs from WT and E529G pigs by WB with pCD163 antibody. D: Intensity of bands in (C) was quantified by ImageJ analysis. E: Free Hp in serum from WT and E529G pigs was detected by ELISA. SEM: WT, 634.10±63.18; E529G, 636.10±19.56, *n*=3. F, G: PAMs were separated from WT or E529G pigs and FITC-Hb-Hp complex uptake in PAMs was characterized by IFA (F) and FACS (G). H: PAMs from WT and E529G pigs were then challenged by JXA1-GFP at MOI=0.1 and viral protein expression was determined by IFA at 12 hpi. I: Viral RNA in 200 μL of supernatant in (H) was extracted for qPCR. ****: *P*<0.0001; ns: No significance. WT PAMs in F–I were from the same WT pig and E529G PAMs were from the same E529G pig.

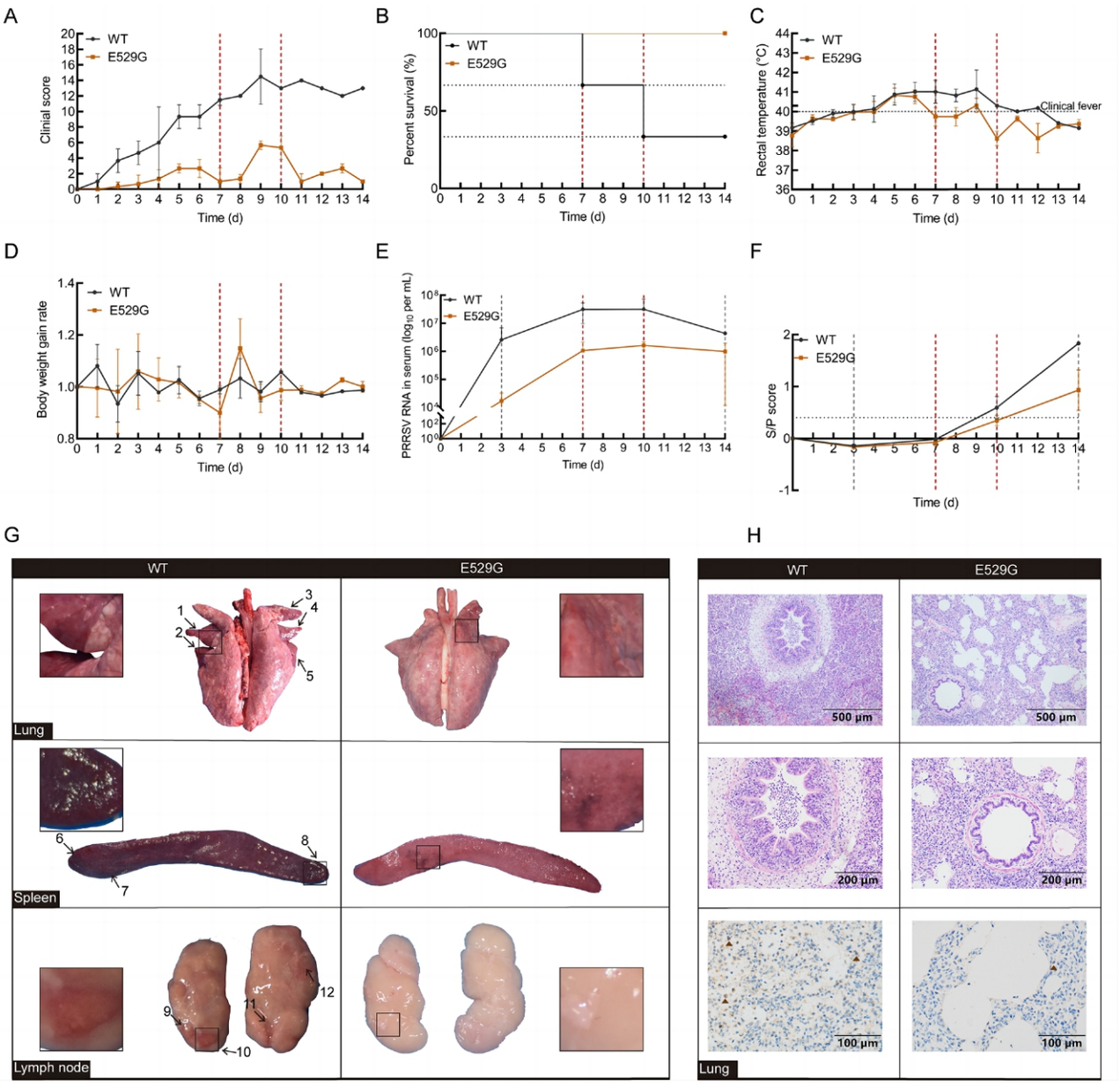



**Figure 5** ***CD163*-E529G mutation pigs were resistant to HP-PRRSV infection**

A–D: Relative clinical symptoms (A), survival rate (B), rectal temperature (C), and body weight gain rate (D) in challenged WT (black line) and E529G (brown line) pigs were monitored daily. Survival rate showed that two WT pigs died at 7 and 10 days, respectively (red dashed line). E, F: Blood samples from challenged pigs were collected on days 0, 3, 7, 10, and 14. Viral load (E) and viral antibody levels (F) in serum were separately determined by qPCR and ELISA. G: Each photo is from a single representative pig. Macroscopic observation of lung (above), spleen (medium), and lymph node (below) from WT (left) and E529G (right) pigs, and locations of tissue lesions are marked with black arrows, partial lesion locations are enlarged. H: Histopathological diagnosis in lungs between WT (left) and E529G (right) pigs was indicated by H&E staining, with 10× magnification shown above and 20× magnification shown in the middle. Viral infection in lungs from WT and E535G pigs was determined by IHC (below).

Ma et al. (2021a) suggested that E529 could be a potential site for suppressing PRRSV proliferation, although their verification was conducted only in cells, not in whole organisms. Further research is needed to determine whether the E529 point mutation affects pig growth, development, and resistance to PRRSV. Virus infection experiments on Marc145 cells demonstrated that the mE535G mutation significantly inhibited HP-PRRSV proliferation by preventing PRRSV binding and entry (Figure 2).

To exclude the influence of varying CD163 copy numbers on the assessment of cell antiviral capacity, we performed single-base editing in PK-15 cells stably integrated with *CD163* using NG-ABE8e, resulting in PK-15$^{CD163}$ cells with the pE529G mutation and consistent CD163 copy numbers (Figure 3). Similarly, virus infection experiments on PK-15$^{CD163}$ cells showed that the E529G mutation markedly inhibited PRRSV binding and entry, thereby reducing HP-PRRSV proliferation (Figure 3). Interestingly, although the inhibition trends in E535G and E529G cells were consistent, the degree of inhibition varied considerably. We hypothesize that pigs, being the only natural host of PRRSV, may possess auxiliary pathways that enhance CD163-induced virus infection in PK-15 cells stably expressing CD163. In contrast, Marc145 cells derived from monkeys, which are not natural hosts of PRRSV,

can only be infected with PRRSV following artificial induction, but lack additional mechanisms to promote virus infection. This distinction may explain the differences observed in the antiviral effects between the two types of mutations.

To further explore the effects of the *CD163* E529G mutation on individual growth and development, E529G PFF clones were screened, and blastocyst development was assessed. Results indicated that the E529G mutation did not affect the development of reconstructed embryos (Supplementary Table S2). Subsequently, four healthy F0 generation individuals were produced (Supplementary Figure S4B). Compared to the WT controls, the physiological parameters of the E529G pigs remained normal (Figure 4A, B; Supplementary Table S3). Notably, the E529G mutation did not affect the expression of the CD163 protein (Figure 4C, D), nor did it influence the ability to remove free Hp or clear Hb-Hp complexes in PAMs (Figure 4E–G). Additionally, PAMs derived from E529G pigs effectively inhibited the proliferation of HP-PRRSV *in vitro* (Figure 4H, I).

In individual challenge experiments, E529G pigs demonstrated effective defense against PRRSV infection (Figure 5). Notably, E529G pigs exhibited better anti-PRRSV efficacy than cells, likely due to the presence of both innate and acquired immunity in pigs, whereas cells only display innate immunity. None of the E529G pigs died, although the PRRSV genome was consistently detected in serum (Figure 5), which may be attributed to the high viral infective dose ($4\times10^7$ $TCID_{50}$) compared to previously reported ranges ($1\times10^5$ to $2\times10^6$ $TCID_{50}$) (Burkard et al., 2017; Prather et al., 2017; Xu et al., 2020; Yang et al., 2018).

The recent application of ABE/CBE base-editing libraries (Base Editor, ABE (A·T→G·C), CBE (C·G→T·A)) has shown promise in identifying causal mutation sites associated with disease resistance traits. Xu et al. (2021) identified several OsACC resistance loci in rice using CBE and ABE base-editing libraries. Our lab also utilized CBE base-editing libraries to identify multiple pathogenic loci in the human LDLR associated with familial hypercholesterolemia (Li et al., 2023). In the future, exploring additional key amino acids within CD163 that impact PRRSV proliferation without compromising the physiological function of CD163 via CBE and ABE base-editing libraries, with subsequent development of CD163 multi-amino acid mutant pigs, may offer an effective solution for preventing PRRSV infection.

## CONCLUSIONS

PRRS has become one of the most economically devastating diseases due to its long incubation period and multiple transmission routes, with the recombination and pathogenic diversity of PRRSV presenting additional challenges for the pig industry. Reducing the impact of *CD163* gene modification on normal physiological functions is essential for commercial anti-PRRSV breeding. In this study, we produced the first pig with a single amino acid mutation in CD163, thereby minimizing the adverse effects of *CD163* modification. Our identification of key amino acids within CD163 has established another feasible route for *CD163* gene modification, providing new insights into accelerating the development of PRRSV prevention and control.

## SUPPLEMENTARY DATA

Supplementary data to this article can be found online.

## COMPETING INTERESTS

The authors declare that they have no competing interests.

## AUTHORS' CONTRIBUTIONS

Conceived and designed the experiments: D.X.P., H.S.O.Y., and H.M.Y.; performed the experiments: Y.L., L.Y., H.Y.X., M.N., J.C.D., X.Y.L., W.J.H., T.Y.L., and X.C.T.; wrote the manuscript: Y.L., H.M.Y., and L.Y. All authors read and approved the final version of the manuscript.

## REFERENCES


Burkard C, Lillico SG, Reid E, et al. 2017. Precision engineering for PRRSV resistance in pigs: macrophages from genome edited pigs lacking CD163 SRCR5 domain are fully resistant to both PRRSV genotypes while maintaining biological function. *PLoS Pathogens*, **13**(2): e1006206.

Calvert JG, Slade DE, Shields SL, et al. 2007. CD163 expression confers susceptibility to porcine reproductive and respiratory syndrome viruses. *Journal of Virology*, **81**(14): 7371–7379.

Etzerodt A, Moestrup SK. 2013. CD163 and inflammation: biological, diagnostic, and therapeutic aspects. *Antioxidants & Redox Signaling*, **18**(17): 2352–2363.

Fabriek BO, Polfliet MMJ, Vloet RPM, et al. 2007. The macrophage CD163 surface glycoprotein is an erythroblast adhesion receptor. *Blood*, **109**(12): 5223–5229.

Guo CH, Wang M, Zhu ZB, et al. 2019. Highly efficient generation of pigs harboring a partial deletion of the CD163 SRCR5 domain, which are fully resistant to porcine reproductive and respiratory syndrome virus 2 infection. *Frontiers in Immunology*, **10**: 1846.

Holtkamp DJ, Kliebenstein JB, Neumann EJ, et al. 2013. Assessment of the economic impact of porcine reproductive and respiratory syndrome virus on United States pork producers. *Journal of Swine Health and Production*, **21**(2): 72–84.

Jiang FG, Doudna JA. 2017. CRISPR–Cas9 structures and mechanisms. *Annual Review of Biophysics*, **46**: 505–529.

Jing QQ, Liu WW, Jiang HY, et al. 2023. Highly efficient A-To-G editing in pffs via multiple abes. *Genes*, **14**(4): 908.

Kick AR, Grete AF, Crisci E, et al. 2023. Testable candidate immune correlates of protection for porcine reproductive and respiratory syndrome virus vaccination. *Vaccines*, **11**(3): 594.

Li MJ, Ma LR, Chen YW, et al. 2023. Large-scale CRISPR screen of LDLR pathogenic variants. *Research*, **6**: 0203.

Lunney JK, Fang Y, Ladinig A, et al. 2016. Porcine reproductive and respiratory syndrome virus (PRRSV): pathogenesis and interaction with the immune system. *Annual Review of Animal Biosciences*, **4**: 129–154.

Ma HF, Li R, Jiang LG, et al. 2021a. Structural comparison of CD163 SRCR5 from different species sheds some light on its involvement in porcine reproductive and respiratory syndrome virus-2 infection in vitro. *Veterinary Research*, **52**(1): 97.

Ma J, Ma LL, Yang MT, et al. 2021b. The function of the PRRSV–host interactions and their effects on viral replication and propagation in antiviral strategies. *Vaccines*, **9**(4): 364.

Madsen M, Møller HJ, Nielsen MJ, et al. 2004. Molecular characterization of the haptoglobin•hemoglobin receptor CD163: ligand binding properties of the scavenger receptor cysteine-rich domain region. *Journal of Biological Chemistry*, **279**(49): 51561–51567.

Moestrup S, Møller H. 2004. CD163: a regulated hemoglobin scavenger receptor with a role in the anti‐inflammatory response. *Annals of Medicine*, **36**(5): 347–354.

Prather RS, Wells KD, Whitworth KM, et al. 2017. Knockout of maternal *CD163* protects fetuses from infection with porcine reproductive and respiratory syndrome virus (PRRSV). *Scientific Reports*, **7**(1): 13371.

Renken C, Nathues C, Swam H, et al. 2021. Application of an economic

calculator to determine the cost of porcine reproductive and respiratory syndrome at farm-level in 21 pig herds in Germany. *Porcine Health Management*, **7**(1): 3.

Salgado B, Rivas RB, Pinto D, et al. 2024. Genetically modified pigs lacking CD163 PSTII-domain-coding exon 13 are completely resistant to PRRSV infection. *Antiviral Research*, **221**: 105793.

Shi CX, Liu YL, Ding YZ, et al. 2015. PRRSV receptors and their roles in virus infection. *Archives of Microbiology*, **197**(4): 503–512.

Stoian AMM, Rowland RRR, Brandariz-Nuñez A. 2022a. Identification of CD163 regions that are required for porcine reproductive and respiratory syndrome virus (PRRSV) infection but not for binding to viral envelope glycoproteins. *Virology*, **574**: 71–83.

Stoian AMM, Rowland RRR, Brandariz-Nuñez A. 2022b. Mutations within scavenger receptor cysteine-rich (SRCR) protein domain 5 of porcine CD163 involved in infection with porcine reproductive and respiratory syndrome virus (PRRS). *Journal of General Virology*, **103**(5): 001740.

Subramanian K, Du RJ, Tan NS, et al. 2013. CD163 and igg codefend against cytotoxic hemoglobin via autocrine and paracrine mechanisms. *The Journal of Immunology*, **190**(10): 5267–5278.

Van Gorp H, Van Breedam W, Delputte PL, et al. 2008. Sialoadhesin and CD163 join forces during entry of the porcine reproductive and respiratory syndrome virus. *Journal of General Virology*, **89**(12): 2943–2953.

Welch SKW, Calvert JG. 2010. A brief review of CD163 and its role in PRRSV infection. *Virus Research*, **154**(1-2): 98–103.

Wells KD, Bardot R, Whitworth KM, et al. 2017. Replacement of porcine CD163 scavenger receptor cysteine-rich domain 5 with a CD163-like homolog confers resistance of pigs to genotype 1 but not genotype 2 porcine reproductive and respiratory syndrome virus. *Journal of Virology*, **91**(2): e01521–16.

Whitworth KM, Lee K, Benne JA, et al. 2014. Use of the CRISPR/Cas9 system to produce genetically engineered pigs from in vitro-derived oocytes and embryos. *Biology of Reproduction*, **91**(3): 78.

Whitworth KM, Rowland RRR, Ewen CL, et al. 2016. Gene-edited pigs are protected from porcine reproductive and respiratory syndrome virus. *Nature Biotechnology*, **34**(1): 20–22.

Xie JX, Vereecke N, Theuns S, et al. 2021. Comparison of primary virus isolation in pulmonary alveolar macrophages and four different continuous cell lines for type 1 and type 2 porcine reproductive and respiratory syndrome virus. *Vaccines*, **9**(6): 594.

Xie ZC, Pang DX, Yuan HM, et al. 2018. Genetically modified pigs are protected from classical swine fever virus. *PLoS Pathogens*, **14**(12): e1007193.

Xu K, Zhou YR, Mu YL, et al. 2020. *CD163* and *pAPN* double-knockout pigs are resistant to PRRSV and TGEV and exhibit decreased susceptibility to pdcov while maintaining normal production performance. *eLife*, **9**: e57132.

Xu RF, Liu XS, Li J, et al. 2021. Identification of herbicide resistance OsACC1 mutations via in planta prime-editing-library screening in rice. *Nature Plants*, **7**(7): 888–892.

Yang HQ, Zhang J, Zhang XW, et al. 2018. CD163 knockout pigs are fully resistant to highly pathogenic porcine reproductive and respiratory syndrome virus. *Antiviral Research*, **151**: 63–70.

Yu P, Wei RP, Dong WJ, et al. 2020. CD163$^{\Delta SRCR5}$ MARC-145 cells resist PRRSV-2 infection via inhibiting virus uncoating, which requires the interaction of CD163 with calpain 1. *Frontiers in Microbiology*, **10**: 3115.

Zhu ZB, Zhang M, Yuan LL, et al. 2023. LGP2 promotes type I interferon production to inhibit PRRSV infection via enhancing MDA5-mediated signaling. *Journal of Virology*, **97**(1): e0184322.

Wang et al. *Zool. Res.* 2024, 45(4): 845−856
https://doi.org/10.24272/j.issn.2095-8137.2023.363

ZR | Zoological Research

Article Open Access

# SIL1 improves cognitive impairment in APP23/PS45 mice by regulating amyloid precursor protein processing and Aβ generation

Qunxian Wang[1], Yanshuang Jiang[1], Zijun Meng[1], Xiangjun Dong[1], Dongjie Hu[1], Liangye Ji[1], Weihui Zhou[1,*], Weihong Song[1,2,3,*]

[1] *Chongqing Key Laboratory of Child Neurodevelopment and Cognitive Disorders*, *Ministry of Education Key Laboratory of Child Development and Disorders*, *National Clinical Research Center for Child Health and Disorders*, *China International Science and Technology Cooperation Base of Child Development and Critical Disorders*, *Children's Hospital of Chongqing Medical University*, *Chongqing* 400000, *China*

[2] *Second Affiliated Hospital and Yuying Children's Hospital*, *Institute of Aging*, *Key Laboratory of Alzheimer's Disease of Zhejiang Province*, *Wenzhou Medical University*, *Wenzhou*, *Zhejiang* 325000, *China*

[3] *Oujiang Laboratory (Zhejiang Lab for Regenerative Medicine*, *Vision and Brain Health)*, *Wenzhou*, *Zhejiang* 325001, *China*

## ABSTRACT

SIL1, an endoplasmic reticulum (ER)-resident protein, is reported to play a protective role in Alzheimer's disease (AD). However, the effect of SIL1 on amyloid precursor protein (APP) processing remains unclear. In this study, the role of SIL1 in APP processing was explored both *in vitro* and *in vivo*. In the *in vitro* experiment, SIL1 was either overexpressed or knocked down in cells stably expressing the human Swedish mutant APP695. In the *in vivo* experiment, AAV-SIL1-EGFP or AAV-EGFP was microinjected into APP23/PS45 mice and their wild-type littermates. Western blotting (WB), immunohistochemistry, RNA sequencing (RNA-seq), and behavioral experiments were performed to evaluate the relevant parameters. Results indicated that SIL1 expression decreased in APP23/PS45 mice. Overexpression of SIL1 significantly decreased the protein levels of APP, presenilin-1 (PS1), and C-terminal fragments (CTFs) of APP *in vivo* and *in vitro*. Conversely, knockdown of SIL1 increased the protein levels of APP, β-site APP cleavage enzyme 1 (BACE1), PS1, and CTFs, as well as APP mRNA expression in 2EB2 cells. Furthermore, SIL1 overexpression reduced the number of senile plaques in APP23/PS45 mice. Importantly, Y-maze and Morris Water maze tests demonstrated that SIL1 overexpression improved cognitive impairment in APP23/PS45 mice. These findings indicate that SIL1 improves cognitive impairment in APP23/PS45 mice by inhibiting APP amyloidogenic processing and suggest that SIL1 is a potential therapeutic target for AD by modulating APP processing.

**Keywords:** Alzheimer's disease; SIL1; APP processing; Cognitive impairment

## INTRODUCTION

Alzheimer's disease (AD) is the leading cause of dementia in older adults, characterized by progressive learning and memory impairment. Pathological hallmarks of AD include extracellular senile plaques and intracellular neurofibrillary tangles, generated from hyperphosphorylated tau and neuronal or synaptic loss (Liao et al., 2020; Peng et al., 2022). The primary component of senile plaques is the β-amyloid peptide (Aβ), derived from amyloid precursor protein (APP) through sequential cleavage of β-secretase (BACE1) and γ-secretase in the amyloidogenic pathway (Ly et al., 2013; Zhang et al., 2017, 2020). APP, a single transmembrane protein, matures in the endoplasmic reticulum (ER) and Golgi apparatus before localizing to the plasma membrane (O'Brien & Wong, 2011). APP exists in three main isoforms: the 695-amino acid isoform, which is expressed predominantly in the central nervous system, and the 751- and 770-amino acid isoforms, which are ubiquitously expressed (Bayer et al., 1999). Under physiological conditions, APP is primarily cleaved within the Aβ domain at the $leu^{17}$ site by α-secretase, generating secreted sAPPα and C83 (CTFα83) (Esch et al., 1990), at the $Glu^{11}$ β-secretase site by BACE1, generating C89 (CTF) (Zhang et al., 2017), or at the $Phe^{20}$ θ-site by BACE2, generating C80 (Wang et al., 2019), leading to a nonamyloidogenic pathway. However, under pathological

This is an open-access article distributed under the terms of the Creative Commons Attribution Non-Commercial License (http://creativecommons.org/licenses/by-nc/4.0/), which permits unrestricted non-commercial use, distribution, and reproduction in any medium, provided the original work is properly cited.

Copyright ©2024 Editorial Office of Zoological Research, Kunming Institute of Zoology, Chinese Academy of Sciences

Received: 24 February 2024; Accepted: 07 April 2024; Online: 08 April 2024

Foundation items: The work was supported by the National Natural Science Foundation of China (82230043, 82293642)

*Corresponding authors, E-mail: zwh@hospital.cqmu.edu.cn; weihong@wmu.edu.cn

conditions, APP is initially cleaved by BACE1 at the Asp[1] site, generating secreted sAPPβ and C99 (CTFβ99), with C99 further cleaved by γ-secretase to generate CTFβ and Aβ (Deng et al., 2013; Zhang et al., 2017), leading to an amyloidogenic pathway. Early pathological deposition of Aβ in AD is believed to be a fundamental driver of AD pathology, promoting other disorders such as tau pathology (Karran & De Strooper, 2022; Selkoe & Hardy, 2016; Zhang et al., 2023b).

SIL1 nucleotide exchange factor (SIL1) is an ER-resident protein encoded by the *SIL1* gene located on chromosome 5q31.2. It functions as an adenine nucleotide exchange factor for Bip, a member of the heat shock protein 70 family, and acts as a co-chaperone of Bip by regulating its ATPase activity and facilitating the release of substrate proteins (Chung et al., 2002; Rosam et al., 2018). In 2005, SIL1 was identified by two independent research groups as the leading cause of Marinesco-Sjögren syndrome (MSS; OMIM 248800), a rare multisystem disorder in early infants (Anttonen et al., 2005; Senderek et al., 2005). Loss-of-function mutations in SIL1 disrupt the interaction between SIL1 and Bip, leading to abnormal cortical development, considered an important factor contributing to mental retardation in MSS (Inaguma et al., 2014). Additionally, SIL1 is also thought to play a role in neurodevelopment and learning through mechanisms independent of its interaction with Bip (Labisch et al., 2018; Xu et al., 2019).

Previous studies have demonstrated increased SIL1 levels in surviving neurons of patients with AD and noted alterations in the expression of proteins implicated in neurodegeneration (Labisch et al., 2018). SIL1 has also been shown to mitigate tau hyperphosphorylation associated with elevated Bip levels (Liu et al., 2016), suggesting a potential protective role in AD. Additionally, evidence indicates that SIL1 may exert beneficial effects in other neurodegenerative diseases, such as amyotrophic lateral sclerosis (ALS) (Filézac De L'Etang et al., 2015). However, whether SIL1 affects APP processing, a critical factor in AD pathology, remains unclear. To address this, the classical APP23/PS45 mouse model and cells stably transfected with the Swedish mutant APP were used to investigate the effects of SIL1 on APP processing.

## MATERIALS AND METHODS

### Animals

APP23/PS45 model mice were used as they produce visible senile plaques by 1.5 months of age and experience exacerbated deposition with age. The APP23/PS45 transgenic mice (provided by Novartis) were generated by crossing APP23 mice carrying the Swedish APP751(KM→NL) mutant transgene with PS45 mice overexpressing the human G384A mutated presenilin-1 (PS1). The mice were housed at the Children's Hospital of Chongqing Medical University Animal Care Centre under a 12 h light-dark cycle (lights on from 0700h to 1900h), with free access to food and water, in a temperature- and humidity-controlled individual ventilation cage (IVC) room. Genotypes were confirmed by polymerase chain reaction (PCR) using DNA extracted from tail tissues. All animal experiments were performed in accordance with the Guide for the Care and Use of Laboratory Animals of the Ethics Committee of Chongqing Medical University. All experimental protocols were approved by the Animal Study Committee of the Children's Hospital of Chongqing Medical University (approval number CHCMU-IACUC20221227006).

### Plasmids and siRNA

Myc-his-tagged pcDNA4 was used as the backbone to construct SIL1-myc plasmids. The cDNA extracted from HEK293 cells was used as an amplification template for PCR. Primers were synthesized by Tsingke Biotechnology (Beijing, China), with the following sequences: (forward) 5′- TTGGTACCGAGCTCGGATCCGCCACCATGGCTCCCCAGAGCCTGC-3′; (reverse) 5′-GAAGGGCCCTCTAGACTCGAGTCTCAGCTCCTTCAGCAAGCTGTTGACAG-3′. For SIL1 knockdown *in vitro*, small interfering RNA (siRNA) targeting human SIL1 and negative RNA (siNC) were synthesized by WZ Bioscience (China). The target sequences for SIL1 siRNA were: (sense) 5′-GCUGCGCUCUUUGAUCUUGAATT-3′; (anti-sense) 5′- UUCAAGAUCAAAGAGCGCAGCTT-3′.

### Cell culture and transfection

All cell lines were cultured in 90% Dulbecco's modified Eagle medium (DMEM) (Cat#C11995500BT, Gibco, USA) supplemented with 10% fetal bovine serum (FBS) (Cat#10270-106, Gibco, USA) and maintained in an incubator at 37°C with 5% $CO_2$. The $N2A^{APP}$ cell line (Du et al., 2019), consisting of mouse neuroblastoma (N2A) cells stably expressing human Swedish mutant APP695, was cultured in 90% DMEM supplemented with 10% FBS containing 50 μg/mL G418 (Cat#11811031, Gibco, USA). The 2EB2 cell line (Sun et al., 2005), comprising human embryonic kidney (HEK293) cells stably expressing human Swedish mutant APP695 and human BACE1, was maintained in 90% DMEM supplemented with 10% FBS containing 100 μg/mL zeocin (Cat#R25001, Invitrogen, USA) and 50 μg/mL G418 (Cat#11811031, Gibco, USA). The $N2A^{APP}$ and 2EB2 cells are not listed as commonly misidentified cell lines by the International Cell Line Authentication Committee. Authentication of the cell lines after treatment was performed by western blotting to confirm overexpressing bands. The maximum number of passages for each cell line was less than 50. Plasmids and siRNAs were transfected into the cells using Lipofectamine 2000 (Cat#11668019, Thermo Fisher Scientific, USA) according to the manufacturer's protocols.

### Adeno-associated virus and microinjection

The GV388 plasmid was used as a backbone for overexpressing SIL1 *in vivo*, with the following primers used to construct the SIL1-containing plasmid: (forward) 5′-GGAGGTAGTGGAATGGATCCCGCCACCATGGCTCCCCAGAGCCTGCC-3′; (reverse) 5′-TCACCATGGTGGCGGGATCAGGGCCGGGATTCTCCTCCACGTCACCGGCCTGCTTCAGCAGG-3′. The constructed plasmid was then transferred to an adeno-associated virus (AAV) to create AAV-SIL1-EGFP (Genechem Co., Ltd., Shanghai, China). The titer of AAV-SIL1-EGFP was 9.53E+12 vg/mL. Mice (6 weeks old, weighing 16–18 g) were anesthetized with an intraperitoneal (i.p.) injection of sodium pentobarbital (60 mg/kg) to minimize suffering during the procedure. Core temperature was maintained at 36.5±0.5°C. The scalp was shaved with clippers and disinfected with iodine before being mounted on a stereotaxic instrument. After the scalp was incised to expose the skull, 1 μL of AAV-SIL1-EGFP or AAV-EGFP was microinjected into each lateral ventricle via drilled holes (0.5 mm posterior, ±1.1 mm lateral, and 3 mm ventral relative to bregma). The scalp was then sutured with absorbable sutures.

After the operation, the mice were carefully relocated to a 37°C incubator to maintain their core temperature. Once they regained consciousness, they were gently transferred back to

their newly prepared cages filled with soft, clean padding. Throughout this period, their vital signs were monitored to ensure their well-being. No additional analgesics were administered to minimize the risk of adverse reactions during short-term repeated administration, prioritizing the safety and well-being of the mice. Sodium pentobarbital was chosen due to its simplicity, convenience, low cost, effectiveness, rapid induction of anesthesia, broad safe dosage range, and minimal risk of mortality and reflexes during surgery. This study was not pre-registered, and no randomization or blinding was performed. No exclusion criteria were predetermined, and no animals were excluded. Given the high mortality rate of APP23/PS45 mice, we initially microinjected negative-control AAV into 10 wild-type (WT) mice (five females and five males) and 24 APP23/PS45 mice (10 males and 14 females). Subsequently, we microinjected SIL1-containing AAV into 25 APP23/PS45 mice (10 males and 15 females).

The sample size decided for each experiment was based on our previous study (Zhang et al., 2020). All animals received AAV microinjections at 6 weeks of age, and all remaining living mice underwent behavioral tests at 5 months of age, prior to sacrifice. The mice were anesthetized with urethane (Cat#U2500, Sigma, USA; 0.8 mL/20 g, i.p.) using a 2.5 mL injection syringe. Thereafter, they received cardiac perfusion with physiological saline after complete anesthesia for subsequent extraction of brain tissues.

**Western blotting**

Cells and brain tissues of the mice were collected in RIPA lysis solution containing a protease inhibitor (Cat#4693159001, Roche, Switzerland) for 30 min. The samples were then centrifuged at 14 000 r/min for 15 min at 4°C. All supernatants were transferred to new tubes. A BCA kit (Cat#23227, Thermo Fisher Scientific, USA) was used to detect the concentration of proteins according to the manufacturer's protocols. Protein samples (30–60 μg) were diluted with 5× sample buffer and boiled at 95°C for 8 min. The samples were then separated on 12.5% tris-glycine sodium dodecyl sulfate-polyacrylamide gel electrophoresis (SDS-PAGE) or 16% tris-tricine SDS-PAGE and transferred onto well-cut, 0.22 μm aperture polyvinylidene fluoride (PVDF) membranes (CAT#SLGVR33RB, Millipore, USA). The membranes were then blocked in 5% skim milk or 5% bovine serum albumin for 1.5 h.

Aβ WB was performed following previously published methods (Liu et al., 2022). Briefly, lysates were separated on 16% tricine gel, followed by electro-transfer. The membranes were then twice boiled in phosphate-buffered saline (PBS) in a microwave for 3 min, and subsequently cooled to room temperature. The membranes were blocked in PBS containing 0.1% Tween-20 and 5% bovine serum albumin and immunoblotted with indicated primary antibodies overnight at 4°C. After incubation with goat anti-rabbit immunoglobulin G (IgG) (Cat#A0208, Beyotime, China) or anti-mouse IgG (Cat#A0216, Beyotime, China) at room temperature for 1.5 h, the proteins were detected using a Bio-Rad Imager and an ECL WB substrate (Cat#170-5061, Bio-Rad, USA). Primary antibodies SIL1 (Cat#ab228868, Abcam, UK, 1:1 000), PS1 (Cat# ab15458, Abcam, UK, 1:1 000), and BACE1 (Cat#ab108394, Abcam, UK, 1:1 000) were used to detect the SIL1, PS1, and BACE1 bands, respectively. A C20 (1:1 000–3 000) polyclonal antibody produced in our laboratory was used to detect the C-terminal fragments of APP (Zheng et al., 2022). The 6E10 antibody (Cat#SIG-39240, BioLegend, USA, 1:10 000) targeting the N-terminal of Aβ was used to detect soluble APP fragments (sAPPα and Aβ). The GAPDH (Cat#60004-1-Ig, Proteintech, China, 1:50 000–500 000), actin (Cat#ac026, ABclonal, China, 1:100 000), and tubulin (Cat# 66031-1-Ig, Proteintech, China, 1:20 000–100 000) antibodies were used to detect GAPDH, actin, and tubulin bands, respectively.

**RNA sequencing (RNA-seq)**

To explore the mechanism by which SIL1 influences APP processing, total RNA was extracted from 2EB2 cells in the siRNA and siNC groups using TRIzol (Cat#15596026, Invitrogen, USA). All samples were tested using the Illumina NovaSeq 6000 platform with the PE150 pattern at the LianChuan Company (Zhejiang, China). All raw sequence data reported in this paper were deposited in the Genome Sequence Archive (Genomics, Proteomics & Bioinformatics 2021) at the National Genomics Data Center (Nucleic Acids Res 2022), China National Center for Bioinformation/Beijing Institute of Genomics, Chinese Academy of Sciences (GSA-Human: HRA005214) and are publicly accessible at https://ngdc.cncb.ac.cn/gsa-human. The data were also deposited in the NCBI database (BioProject PRJNA1099875) and Science Data Bank database (DOI: 10.57760/sciencedb.j00139.00131). The researchers conducting the experiments were blinded to the study groups.

**Cycloheximide (CHX) treatment**

To determine the effect of SIL1 on APP degradation, 2EB2 cells were transfected with siRNA or siNC for 48 h, then seeded into 12-well plates with six wells per group. The cells were subsequently treated with 100 μg/mL CHX (Cat#C8030-100, Solarbio, China) and collected at 0, 1, 2, 4, 8, and 12 h for WB analysis.

**Dactinomycin treatment for RNA stability**

To investigate the effect of SIL1 on APP mRNA degradation, 2EB2 cells were transfected with either siRNA or siNC for 48 h, then seeded into 12-well plates with four wells per group. For RNA stability assessment, the cells were treated with 5 μg/mL dactinomycin (Cat#HY-17559, MCE, USA) to inhibit RNA synthesis. The samples were then collected at 0, 1, 2, and 4 h for subsequent RNA extraction using TRIzol reagent (Cat#15596026, Invitrogen, USA), following established protocols. The extracted RNA underwent reverse transcription to generate cDNA using PrimeScript™ RT Master Mix (Cat#RR036A, Takara, Japan), following the manufacturer's procedures. The resulting cDNA was used for quantitative PCR using a SYBR PremixExTq2007 kit (Cat#RR820A, Takara, Japan) according to the manufacturer's instructions. The APP primers for quantitative PCR were: (forward) 5′-TTGTAAGTGATGCCCTTCTCGTT-3′; (reverse) 5′-AGCAACATGCCGTAGTCATGCAA-3′. The GAPDH primers for quantitative PCR were: (forward) 5′-CTCTGCTCCTCCTGTTCGAC-3′; (reverse) 5′-GCGCCCAATACGACCAAATC-3′.

**Immunohistochemistry**

Half brain sections were fixed in freshly prepared 4% paraformaldehyde in PBS for 4–5 days, then dehydrated in a 30% sucrose solution in PBS for 2 days for sectioning into 30 μm coronal brain slices. The brain slices were washed three times with 0.3% PBST (1 L of 0.01 mol/L PBS added to 3 mL of Triton X-100) (Cat#9002-93-1, Sigma, USA) and incubated with 30% $H_2O_2$ (Cat#7722-84-1, Sigma, USA) for 30 min at

37°C. The brain slices were blocked with a 10% bovine serum albumin solution for 1 h at room temperature, then incubated with mouse monoclonal 4G8 antibody (Cat#SIG-39240, BioLegend, USA, 1:500) overnight at 4°C. The plaques on the brain slices were assayed using an ABC kit (Cat#PK6102, Vector, USA) and a DAB kit (Cat#SK4105, Vector, USA) and scanned using a full-pick scanner. The number of plaques was counted using ImageJ software.

**Immunofluorescent staining**

Mouse brain slices (30 μm thick) were washed three times using 1×PBS buffer, each lasting 10 min. Subsequently, the cleaned slices were immersed in an immunofluorescent blocking solution (Cat#P0260, Beyotime, China) for 1 h at room temperature, then incubated with SIL1 (Cat#ab228868, Abcam, UK, 1:1 000) and NeuN (Cat#ab177487, Abcam, UK, 1:1 000) primary antibodies at 4°C. After overnight incubation, the slices were incubated with donkey anti-rabbit (Cat# A11001, Invitrogen, USA, 1:1 000) or anti-mouse IgG (Cat# A11004, Invitrogen, USA, 1:1 000) for 1 h at room temperature. The slices were finally sealed with an anti-fluorescence quenching sealing solution (including DAPI) (Cat#P0131, Beyotime, China) and examined using a laser confocal microscope (Nikon, Japan) to capture immunofluorescence.

**Y-maze test**

The Y-maze test was employed to assess short-term spatial working memory in mice, as described previously (Kraeuter et al., 2019). Mice were placed at the starting point of the initial arm with their head facing the intersection of the three arms and allowed to explore freely for 8 min. Behavior and activity tracks of the mice were recorded and analyzed using ANY-maze (San Diego Instruments, USA). A successful alteration was defined as three consecutive entries into different arms. The total number of events was defined as the total number of entries into the arms minus two. Spontaneous alterations were determined by the ratio of the number of mice visiting three different arms in a row (number of successful alterations) to the total number of events.

**Morris water maze (MWM) test**

The MWM test was used to determine spatial memory and learning in mice, as described previously (Bromley-Brits et al., 2011). The test was performed in a circular pool (1.5 m diameter and 0.6 m depth) filled with opaque water. A platform (10 cm diameter) was placed in the southwest (SW), northwest (NW), northeast (NE), center, and southeast (SE) quadrants of the pool, 1 cm above the water on the first day. It was then placed in the SW quadrant 1 cm below the water on the second to fifth days and was removed on the last day. On day one, the mice were trained to find the visible platform within 60 s. On days 2–5, the mice were allowed to freely search for the hidden platform for 60 s. Each mouse underwent five trials daily from four points in the pool with an interval of 1 h. On the last day, the mice were allowed to search for the removed platform for 60 s from the same point in the pool. Behaviors were recorded and analyzed using ANY-maze (San Diego Instruments, USA). The investigators were blinded to the study groups during the experiment and data analysis.

**Statistical analysis**

All data were analyzed using SPSS v.25. GraphPad Prism was used to create quantification figures. All results are presented as mean±standard error of the mean (SEM). Replicate numbers are indicated in the figure legends. Normality was determined using the Shapiro-Wilk test. Comparisons between two groups were performed using two-tailed Student's *t*-test. Multiple comparisons were analyzed using one-way analysis of variance (ANOVA) or two-way ANOVA with *post hoc* Dunnett's multiple comparisons test. The level of statistical significance was set at $P<0.05$. No statistical tests for outliers were conducted, and no data points were excluded.

## RESULTS

**SIL1 protein was significantly decreased in APP23/PS45 mice**

Previous reports have suggested that SIL1 plays a protective role in AD. To determine the role of SIL1 in APP23/PS45 mice, WB was used to test the SIL1 protein levels in the brains of APP23/PS45 and age-matched WT mice at different ages. Results showed that SIL1 was significantly decreased in the brains of APP23/PS45 mice compared to the age-matched WT mice at 3 months (APP23/PS45 vs. WT: 0.869±0.111 vs.1.292±0.108, $P=0.044$, $n=6–7$, Figure 1A, B) and 6 months of age (APP23/PS45 vs. WT: 0.657±0.067 vs.1.407±0.204, $P=0.007$, $n=6$, Figure 1C, D). WB was also used to determine the protein level of APP. Results showed that the APP protein was significantly increased in the AD mice compared to their corresponding age-matched WT mice at 3 months (1.210±0.055 vs. 0.772±0.051, $P<0.001$, $n=6–7$) and 6 months (1.180±0.056 vs. 0.838±0.068, $P=0.004$, $n=6$; Figure 1A–D). Immunofluorescence staining was performed to investigate the localization of SIL1 in the brain. Results showed that SIL1 mainly resided in the dentate gyrus (DG), CA1, CA3, and cortical regions in both 5-month-old WT and age-matched APP23/PS45 mice (Figure 1E). Overall, SIL1 protein levels showed a significant decrease in APP23/PS45 mice, similar to previous research (Liu et al., 2016).

**Overexpression of SIL1 inhibited APP processing *in vitro***

Given the abnormal expression of SIL1 in APP23/PS45 mice, plasmids containing *SIL1* (*SIL1*-myc) or an empty vector were transfected into $N2A^{APP}$ and 2EB2 cells, respectively, to determine the effects of SIL1 on APP amyloidogenic processing. WB was used to detect the protein levels of SIL1, APP, BACE1, PS1, and APP-CTFs in the APP amyloidogenic pathway. Results showed a significant increase in SIL1 protein levels after transfection of SIL1-myc into $N2A^{APP}$ cells (SIL1 vs. vector, 0.77±0.14 vs. 0.07±0.003, $P=0.016$, $n=4$, Figure 2A, B). Conversely, the protein levels of APP (SIL1 vs. vector, 0.21±0.04 vs. 0.44±0.03, $P=0.004$, $n=4$, Figure 2A, C), PS1 (SIL1 vs. vector, 1.01±0.04 vs. 1.34±0.07, $P=0.008$, $n=4$, Figure 2A, E), CTF-99 (SIL1 vs. vector, 0.16±0.01 vs. 0.35±0.05, $P=0.012$, $n=4$, Figure 2A, F), and CTF-89 (SIL1 vs. vector, 0.17±0.03 vs. 0.28±0.04, $P=0.049$, $n=4$, Figure 2A, G) showed a significant decrease compared to the vector group, while no significant change was observed in the BACE1 protein level (SIL1 vs. vector, 0.21±0.04 vs. 0.435±0.03, $P=0.719$, $n=4$, Figure 2A, D).

To further confirm the role of SIL1 in APP processing, SIL1 was overexpressed in 2EB2 cells, followed by WB analysis. Results showed that the SIL1 protein level was markedly elevated after transfection with *SIL1*-myc (SIL1 vs. vector, 1.50±0.19 vs. 0.01±0.02, $P<0.001$, $n=5$, Figure 2H, I). In

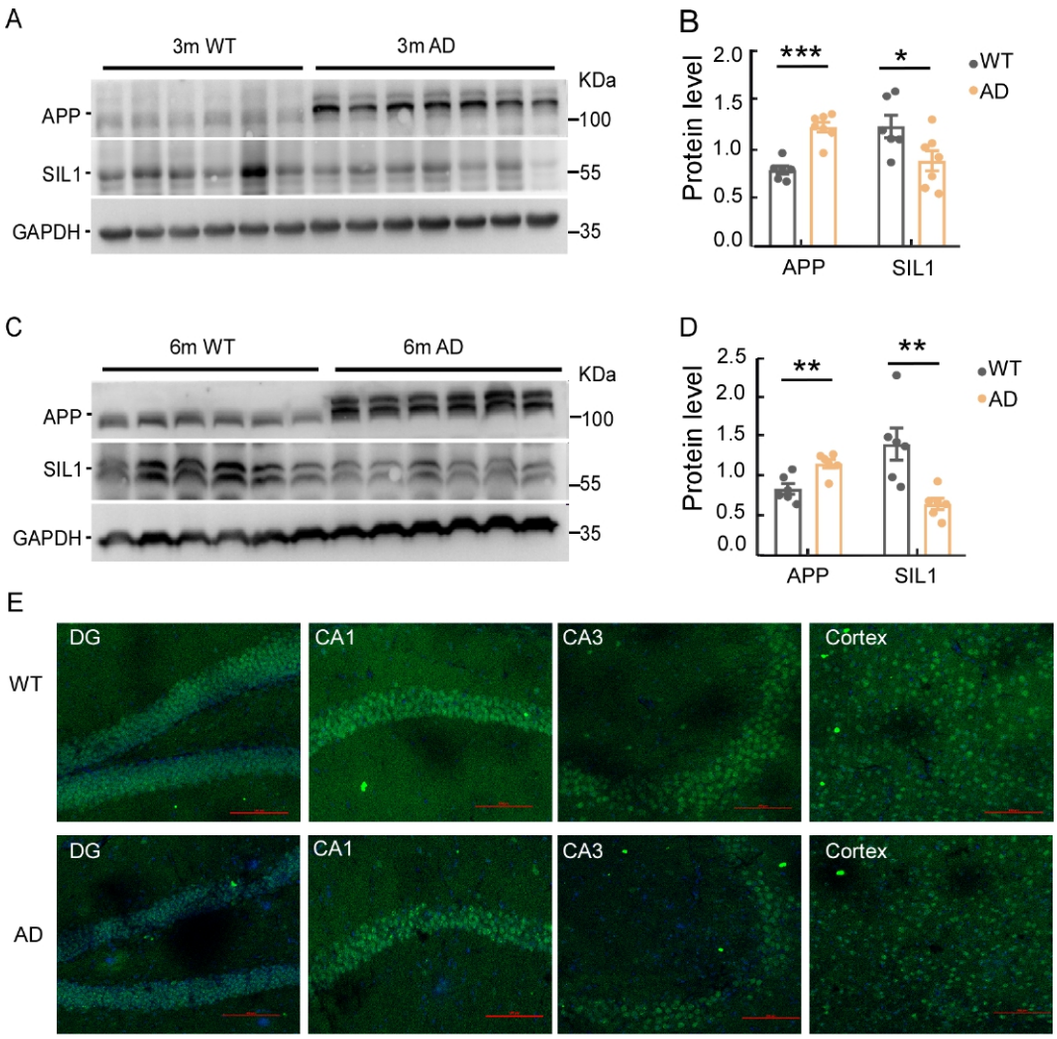



**Figure 1 Protein level of SIL1 decreased in APP23/PS45 mice**

A, B: Protein levels of SIL1 and APP in the hippocampus of 3-month-old APP23/PS45 mice and age-matched WT mice, with APP and SIL1 levels normalized to GAPDH levels for comparison. *n*=6–7 animals in each group (WT mice, *n*=6; APP23/PS45 mice, *n*=7). C, D: Protein levels of SIL1 and APP in the cortex of 6-month-old APP23/PS45 mice and age-matched WT mice, with APP and SIL1 levels normalized to GAPDH levels for comparison. *n*=6 animals in each group. E: Immunofluorescent staining of SIL1 and DAPI in DG, CA1, CA3, and cortical area of 5-month-old WT mice and age-matched APP23/PS45 mice. Scar bar: 100 μm. Data are presented as mean±SEM. *P*-values were determined by student's *t*-tests. *: $P<0.05$; **: $P<0.01$; ***: $P<0.001$.

contrast, the protein levels of APP (SIL1 vs. vector, 0.62±0.08 vs. 0.90±0.04, *P*=0.014, *n*=5, Figure 2H, J), PS1 (SIL1 vs. vector, 0.83±0.04 vs. 1.10±0.10, *P*=0.041, *n*=5, Figure 2H, L), CTF-99 (SIL1 vs. vector, 0.47±0.05 vs. 0.64±0.02, *P*=0.015, *n*=5, Figure 2H, M), and CTF-89 (SIL1 vs. vector, 0.52±0.05 vs. 0.72±0.05, *P*=0.029, *n*=5, Figure 2H, N) were significantly decreased compared to the vector group, while the protein levels of BACE1 were not significantly affected (SIL1 vs. vector, 0.99±0.11 vs. 1.07±0.06, *P*=0.495, *n*=5, Figure 2H, K). Thus, SIL1 overexpression significantly suppressed APP processing *in vitro*.

**Knockdown of SIL1 enhanced APP processing by increasing APP expression *in vitro***

Given that SIL1 expression was decreased in APP23/PS45 mice, and SIL1 overexpression significantly suppressed APP amyloidogenic processing, we further explored the effects of SIL1 on APP amyloidogenic processing using siRNA to target and knockdown SIL1 in 2EB2 cells. Results showed that SIL1 knockdown in 2EB2 cells led to a significant decrease in the protein level of SIL1 (siSIL1 vs. siNC, 0.73±0.07 vs. 1.27±0.15, *P*=0.018, *n*=4, Figure 3A, B), as well as a significant increase in the protein levels of APP (siSIL1 vs. siNC, 1.11±0.03 vs. 0.89±0.06, *P*=0.021, *n*=4, Figure 3A, C), PS1 (siSIL1 vs. siNC, 1.14±0.02 vs. 0.86±0.05, *P*=0.002, *n*=4, Figure 3A, D), BACE1 (siSIL1 vs. siNC, 1.08±0.05 vs. 0.918±0.03, *P*=0.022, *n*=4, Figure 3A, G), C99 (siSIL1 vs. siNC, 0.63±0.06 vs. 0.39±0.05, *P*=0.023, *n*=4, Figure 3A, E), and C89 (siSIL1 vs. siNC, 0.60±0.05 vs. 0.37±0.03, *P*=0.01, *n*=4, Figure 3A, F) compared to the control group. These findings demonstrate that SIL1 knockdown enhanced APP amyloidogenic processing.

To elucidate the effect of SIL1 knockdown on APP amyloidogenic processing, RNA-seq was performed to identify differentially expressed genes (DEGs) after SIL1 knockdown in 2EB2 cells. Genes exhibiting a $\log_2$(fold-change) exceeding 0.5 were categorized as DEGs. Results indicated that multiple genes were altered following SIL1 knockdown, including down-regulated genes such as *TEME245*, *TMEM109*, *RNF11*, *EIF4G2*, *EFTUD2*, and *SIL1*, and up-regulated genes such as *TPM4*, *NACC1*, *PPP1R14B*, *APP*, *KIF1C*, and *VIM*. The *SIL1*

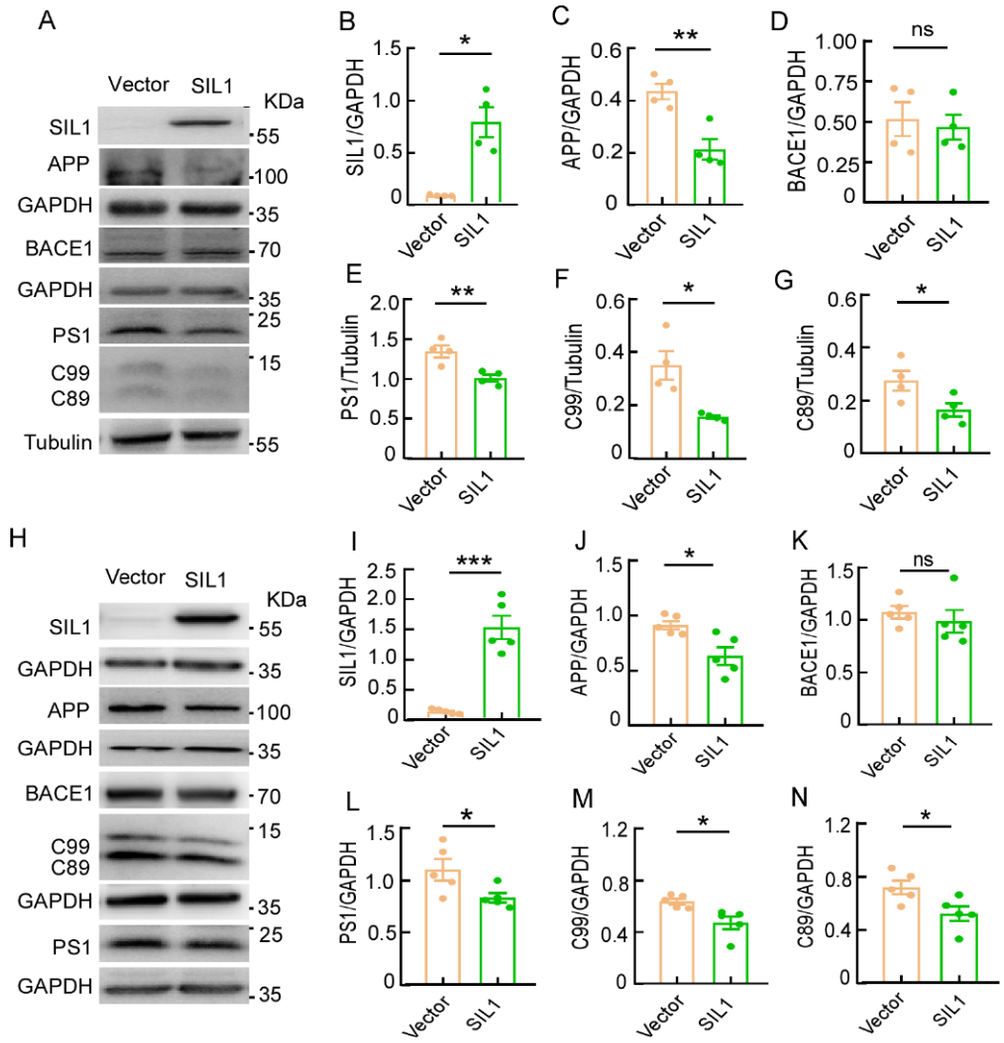



**Figure 2 Overexpression of SIL1 significantly reduced APP processing in N2A$^{APP}$ and 2EB2 cells**

A: SIL1 overexpression significantly reduced APP processing in N2A$^{APP}$ cells. N2A$^{APP}$ cells were transfected with SIL1-myc plasmids or empty vector, then harvested for western blot analysis after transfection for 24 h. A, C: APP, A, E: PS1, A, F: C99, and A, G: C89 were decreased in the SIL1 overexpression group compared to the empty vector group, with APP, PS1, C99, and C89 levels normalized to their corresponding GAPDH levels for comparison. A, D: BACE1 showed no significant change between SIL1 overexpression and empty vector, with BACE1 levels normalized to GAPDH levels for comparison. *n*=4 of independent cell culture preparations. H: SIL1 overexpression significantly reduced APP processing in 2EB2 cells. 2EB2 cells were also transfected with SIL1-myc plasmids and empty vector, followed by western blot analysis after 24 h of transfection. H, J: APP, H, L: PS1, H, M: C99, and H, M: C89 were significantly decreased in SIL1 overexpression group compared to empty vector group, with APP, PS1, C99, and C89 levels normalized to their corresponding GAPDH or tubulin levels for comparison. H, K: BACE1 showed no significant change between the two groups, with BACE1 levels normalized to GAPDH levels for comparison. *n*=5 of independent cell culture preparations. Data are presented as mean±SEM. *P*-values were determined by student's *t*-tests. ns: Not significant; *: *P*<0.05; **: *P*<0.01.

gene was significantly down-regulated, with SIL1 read counts significantly decreased in the siSIL1 group compared to the siNC group (*P*=0.003, *n*=3, Figure 3H, I). The read count, typically calculated based on original sequencing data (FASTQ files) by comparing reads to the reference genome or transcriptome, represents the number of reads per gene in the sample; that is, the number of sequenced reads mapped to each gene in the sequencing data, directly measuring gene expression and reflecting gene abundance. Simultaneously, the *APP* gene was significantly up-regulated, with APP read counts significantly increased in the siSIL1 group compared to the siNC group (*P*=0.001, *n*=3, Figure 3H, J), also normalized to the reference genome. Furthermore, changes in expression extended to genes associated with membrane integrity, transcriptional regulation processes, and other physiological functions. This complex web of gene expression changes strongly suggests that SIL1 knockdown enhanced APP amyloidogenic processing by influencing APP transcriptional regulation.

Next, to determine the effect of SIL1 on APP protein degradation, 2EB2 cells were treated with 100 μg/mL CHX after transfection with siSIL1 or siNC for 48 h. The cells were then collected at 0, 1, 2, 4, 8, and 12 h for WB analysis. Results showed that SIL1 did not affect APP protein degradation (*P*>0.05, *n*=5, Figure 3K, L).

To further determine the effect of SIL1 on the APP mRNA level, 2EB2 cells were treated with 5 μg/mL dactinomycin to inhibit RNA synthesis after transfection with siSIL1 or siNC for 48 h. The cells were collected at 0, 1, 2, and 4 h for quantitative PCR analysis. Results demonstrated that after SIL1 knockdown, the degradation rate of APP mRNA did not change significantly (*P*=0.258, *n*=6, Figure 3M). These

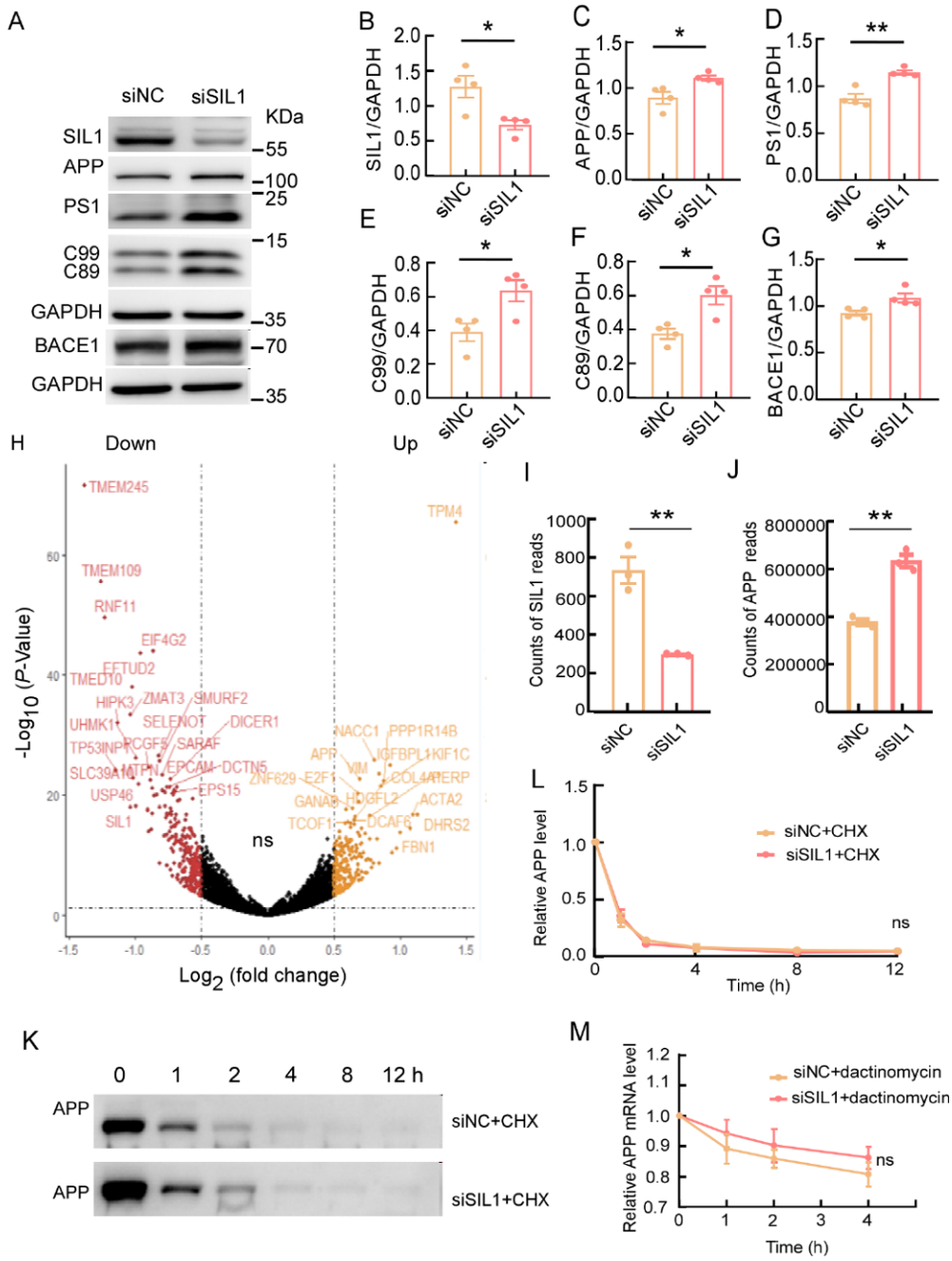



**Figure 3 Knockdown of SIL1 increased APP processing in 2EB2 cells**

A: WB was used to determine effects of SIL1 knockdown on APP processing in 2EB2 cells. 2EB2 cells were transfected with siRNA to knockdown SIL1 (siSIL1) or negative siRNA (siNC), then harvested for western blot analysis after transfection for 48 h. Protein levels of A, B: APP, A, D: PS1, A, E: C99, A, F: C89, and A, G: BACE1 were significantly increased in the siSIL1 group compared to the siNC group, with protein levels normalized to their corresponding GAPDH levels for comparison. $n$=4 of independent cell culture preparations. H: Volcanic map of differentially expressed genes in 2EB2 cells after transfection with siSIL1 and siNC, as determined using RNA-seq. SIL1 was down-regulated, and APP gene was up-regulated. I, J: Relative qualification of mRNA expression level of SIL1 and APP in 2EB2 cells after transfection with siSIL1 and siNC, with counts of SIL1 and APP reads normalized to the reference genome. $n$=3 of independent cell culture preparations. K, L: APP protein level after treatment with CHX at 0, 1, 2, 4, 8, and 12 h, with APP levels at 1, 2, 4, 8, and 12 h normalized to APP levels at 0 h. $n$=5 of independent cell culture preparations. M: APP mRNA level after treatment with dactinomycin at 0, 1, 2, and 4 h, with APP mRNA levels normalized to GAPDH mRNA levels. $n$=6 of independent cell culture preparations. Data are presented as mean±SEM. $P$-values were determined using student's $t$-tests in (B–G, I, J) and two-way ANOVA with Dunnett's *post hoc* analysis in (M, L). ns: Not significant; *: $P$<0.05; **: $P$<0.01; ***: $P$<0.001.

findings suggest that SIL1 knockdown in 2EB2 cells may affect transcription regulation but not post-transcriptional gene regulation.

In summary, our results suggest that SIL1 knockdown enhanced APP amyloidogenic processing, likely by regulating transcription under pathological conditions.

**Overexpression of SIL1 improved cognitive impairments in APP23/PS45 mice**

As SIL1 was significantly decreased in APP23/PS45 mice,

and SIL1 overexpression *in vitro* significantly suppressed APP processing, we next assessed whether the elevation of SIL1 would improve APP23/PS45 mouse behavior. Firstly, AAV carrying SIL1-cDNA and control AAV were microinjected into the lateral ventricle of mice at 1.5 months of age. After microinjection for 3 months, all living mice underwent the Y-maze test. Results showed that AD-EGFP mice (APP23/PS45 mice microinjected with control AAV) had a lower autonomic alteration rate than WT-EGFP mice (WT mice microinjected with control AAV) ($P$=0.013, $n$=10–17, Figure 4B), suggesting that APP23/PS45 mice had short-term memory impairment. The overexpression of SIL1 significantly increased the autonomic alteration rate in APP23/PS45 mice (AD-SIL1-EGFP, APP23/PS45 mice microinjected with SIL1 AAV) (AD-SIL1-EGFP vs. AD-EGFP, $P$=0.009, $n$=17–20, Figure 4B). This suggests that SIL1 overexpression rescued short-term spatial memory impairment in AD mice.

The MWM test was also applied to determine impacts on spatial learning and memory in mice. Results showed that AD-EGFP mice had a similar escape latency ($P$=0.085, $n$=10–17, Figure 4D) and swimming distance as WT-EGFP mice ($P$=0.670, $n$=10–17, Figure 4E) on the visible platform day (first day). Moreover, AD mice infected with SIL1-AAV (AD-SIL1-EGFP) showed a similar escape latency ($P$=0.452, $n$=17–20, Figure 4D) and swimming distance ($P$=0.925, $n$=17–20, Figure 4E) as AD-EGFP mice on the visible platform day. These findings suggest that SIL1 elevation did not affect the visual and motor abilities of AD mice. Results also demonstrated that AD-EGFP mice had a significantly longer escape latency on the hidden platform days compared to WT-EGFP mice ($P$=0.008, $n$=10–17, Figure 4F). AD-SIL1-EGFP mice showed a shorter escape latency than AD-EGFP mice, but no significant differences were observed ($P$=0.081, $n$=17–20, Figure 4F). On the final day, AD-EGFP mice spent significantly shorter time crossing the platform zone in the targeted quadrant compared to WT-EGFP mice ($P$=0.001,

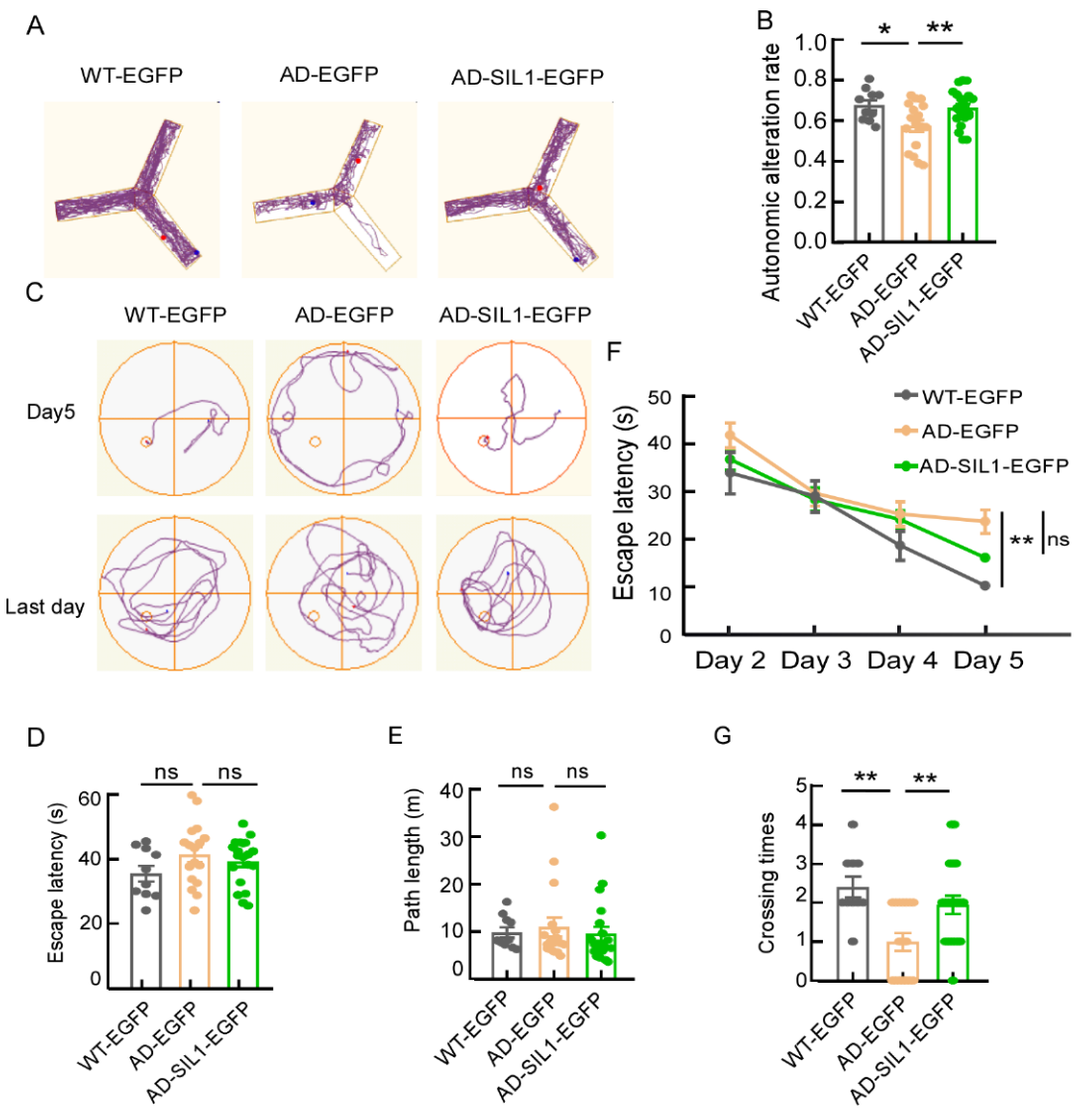



**Figure 4 Overexpression of SIL1 improved learning and memory in APP23/PS45 mice**

A: Activity tracks of mice in the Y-maze test. B: Spontaneous alteration rate of mice was detected by the Y-maze test. C: Activity track of mice on day 5 and final day in the MWM test. D: Escape latencies of mice on visible platform. E: Path distance of mice on visible platform. F: Escape latencies of mice on hidden platform. G: Time crossing the platform located in target quadrant. $n$=10–20 animals in each group (WT-EGFP, $n$=10; AD-EGFP, $n$=17; AD-SIL1-EGFP, $n$=20). Data are presented as mean±SEM. $P$-values were determined by one-way ANOVA with Dunnett's *post hoc* analysis in B, D, E, G and by two-way ANOVA with Dunnett's *post hoc* analysis in F. ns: Not significant, *: $P$<0.05; **: $P$<0.01.

*n*=10–17, Figure 4G). Moreover, mice overexpressing SIL1 (AD-SIL1-EGFP) spent significantly longer time crossing the platform zone in the targeted quadrant compared to AD-EGFP mice (*P*=0.005, *n*=17–20, Figure 4G). These findings suggest that SIL1 overexpression significantly rescued spatial memory in AD mice.

**Overexpression of SIL1 significantly decreased APP processing *in vivo***

To determine whether SIL1 overexpression improved cognitive impairment in APP23/PS45 mice by inhibiting APP amyloidogenic processing, WB was performed to determine the protein levels of SIL1, APP, BACE1, PS1, CTFs, sAPPα, and Aβ. Results showed that the protein level of SIL1 was significantly decreased in AD-EGFP mice (0.40±0.04 vs. 0.58±0.05, *P*=0.032, *n*=4, Figure 5A, B), while the protein levels of APP (1.38±0.09 vs. 0.67±0.02, *P*<0.001, *n*=4, Figure 5A, C), PS1 (1.41±0.09 vs. 0.92±0.05, *P*<0.001, *n*=4, Figure 5A, D), C99 (0.84±0.04 vs. 0.00±0.00, *P*<0.001, *n*=4, Figure 5A, E), C89 (0.92±0.04 vs. 0.00±0.00, *P*<0.001, *n*=4, Figure 5A, F), BACE1 (2.33±0.32 vs. 0.97±0.15, *P*=0.024, *n*=4, Figure 5A, G), sAPPα (1.39±0.07 vs. 0.44±0.01, *P*<0.001, *n*=4, Figure 5A, H), and Aβ (1.36±0.03 vs. 0.00±0.00, *P*<0.001, *n*=4, Figure 5A, I) were significantly increased in AD-EGFP mice compared to WT-EGFP mice. After overexpressing SIL1 (AD-SIL1-EGFP) in AD mice, the protein level of SIL1 was significantly increased (0.87±0.05 vs. 0.40±0.04, *P*=0.002, *n*=4–5, Figure 5A, B), while the protein levels of APP (1.00±0.04 vs. 1.38±0.09, *P*=0.002, *n*=4–5, Figure 5A, C), PS1 (0.77±0.05 vs. 1.41±0.09, *P*<0.001, *n*=4–5, Figure 5A, D), C99 (0.41±0.02 vs. 0.84±0.04, *P*<0.001, *n*=4–5, Figure 5A, E), C89 (0.47±0.03 vs. 0.92±0.04, *P*<0.001, *n*=4–5, Figure 5A, F), sAPPα (1.08±0.23 vs. 1.39±0.07, *P*=0.02, *n*=4–5, Figure 5A, H), and Aβ (1.22±0.06 vs. 1.36±0.03, *P*=0.046, *n*=4–5, Figure 5A, I) were significantly decreased. The protein level of BACE1 (1.66±0.43 vs. 2.33±0.32, *P*=0.263, *n*=4–5, Figure 5A, G) showed a non-significant decreasing trend. The WB results suggest that SIL1 overexpression significantly decreased APP amyloidogenic processing *in vivo*.

To further determine the effect of SIL1 on APP amyloidogenic processing, immunohistochemical staining was used to assess senile plaque deposition by Aβ. Results showed that plaque number significantly decreased in AD-SIL1-EGFP mice compared to AD-EGFP mice (88.47±6.28 vs. 107.17±4.63, *P*=0.034, *n*=7, Figure 5J, K). To determine the effectiveness of intracerebroventricular injection, brain slices (30 μm) from the three groups were washed with PBS (three times, 5 min each time) and sealed with an anti-fluorescence quenching sealing solution containing DAPI for confocal laser scanning. Results showed that the AAVs carrying EGFP in each group were mainly distributed in the hippocampus (Figure 5L), strongly suggesting successful microinjection into the lateral ventricle. Collectively, our results indicate that SIL1 overexpression significantly suppressed APP amyloidogenic processing.

## DISCUSSION

Studies have shown that SIL1 is highly expressed in the hippocampus and is closely associated with neurodevelopment, memory, and learning (Inaguma et al., 2014; Xu et al., 2019). Moreover, SIL1 has been shown to play a protective role in AD. In this study, SIL1 expression was significantly decreased in the brains of APP23/PS45 mice, suggesting its potential involvement in the pathogenesis of AD, although the mechanism remains unclear. To investigate the role of SIL1 in APP processing, we overexpressed SIL1-myc in $N2A^{APP}$ and 2EB2 cells, resulting in a significant decrease in the protein levels of APP, PS1, C99, and C89, while the protein level of BACE1 remained unchanged. Conversely, SIL1 knockdown in 2EB2 cells not only reversed the protein levels of APP, PS1, C99, and C89, but also increased the protein level of BACE1. These findings imply that the effects of overexpression and knockdown were not completely opposite. Notably, endogenous SIL1 may not directly interact with BACE1, as introducing exogenous SIL1 into the cells did not result in a significant change in BACE1 levels. Furthermore, we microinjected AAV carrying SIL1 into the lateral ventricles of APP23/PS45 mice. This elevation of SIL1 significantly reduced the APP processing and Aβ deposition and improved both short-term and long-term spatial memory based on the Y-maze and MWM tests, respectively. Collectively, these findings suggest that SIL1 plays a protective role in APP23/PS45 mice by decreasing APP processing and Aβ deposition.

AD is characterized by the accumulation of Aβ in the brain with hyperphosphorylated microtubule-associated tau. Previous studies assessing genetic, biochemical, and behavioral components suggest that the generation of neurotoxic Aβ from sequential APP proteolysis is a crucial step in AD development (Boerwinkle et al., 2023; Elangovan et al., 2023; Masters et al., 2015; O'Brien & Wong, 2011; Selkoe & Hardy, 2016). Chaperone-mediated autophagy (Bourdenx et al., 2021; Zhang et al., 2023a) plays an important role in AD pathogenesis by regulating Aβ and tau metabolism. However, the impact of SIL1, a co-chaperone, on APP processing related to autophagy remains unclear. In this study, we observed a significant increase in APP mRNA expression after SIL1 knockdown in 2EB2 cells. However, the degradation rates of APP protein and mRNA were not significantly altered, as shown by WB analysis and quantitative PCR, implying that SIL1 decreases APP processing by reducing APP transcription under pathological conditions. Consequently, the reduction in APP expression levels leads to decreased APP processing. However, further studies are required to fully elucidate the mechanism by which SIL1 affects APP mRNA expression.

Recent studies have shown that SIL1 may function as an oncogene, showing up-regulation in certain types of cancer, such as breast cancer (Li et al., 2020) and glioblastoma multiforme (Xu et al., 2018). SIL1 suppression has been found to inhibit cancer cell proliferation and induce apoptosis by activating caspase-3/7 or inhibiting the AKT-mTOR pathway. These findings raise concerns regarding the safety of SIL1 overexpression. However, in the context of AD, SIL1 may play a beneficial role in reducing neuronal loss and synaptic impairment, thereby improving cognitive function in APP23/PS45 mice. Previous research has shown that SIL1 primarily accumulates in the postsynaptic density (PSD) fraction of neurons and directly interacts with proteins such as GluN2A. Moreover, SIL1 knockdown results in the inactivation of Reelin signaling and impedes synaptic NMDA receptor maturation in young mice at 3 weeks of age (Xu et al., 2019). Nevertheless, the specific mechanism of action of SIL1 in adult APP23/PS45 mice remains unknown. A recent report highlighted the involvement of many genes in synaptic

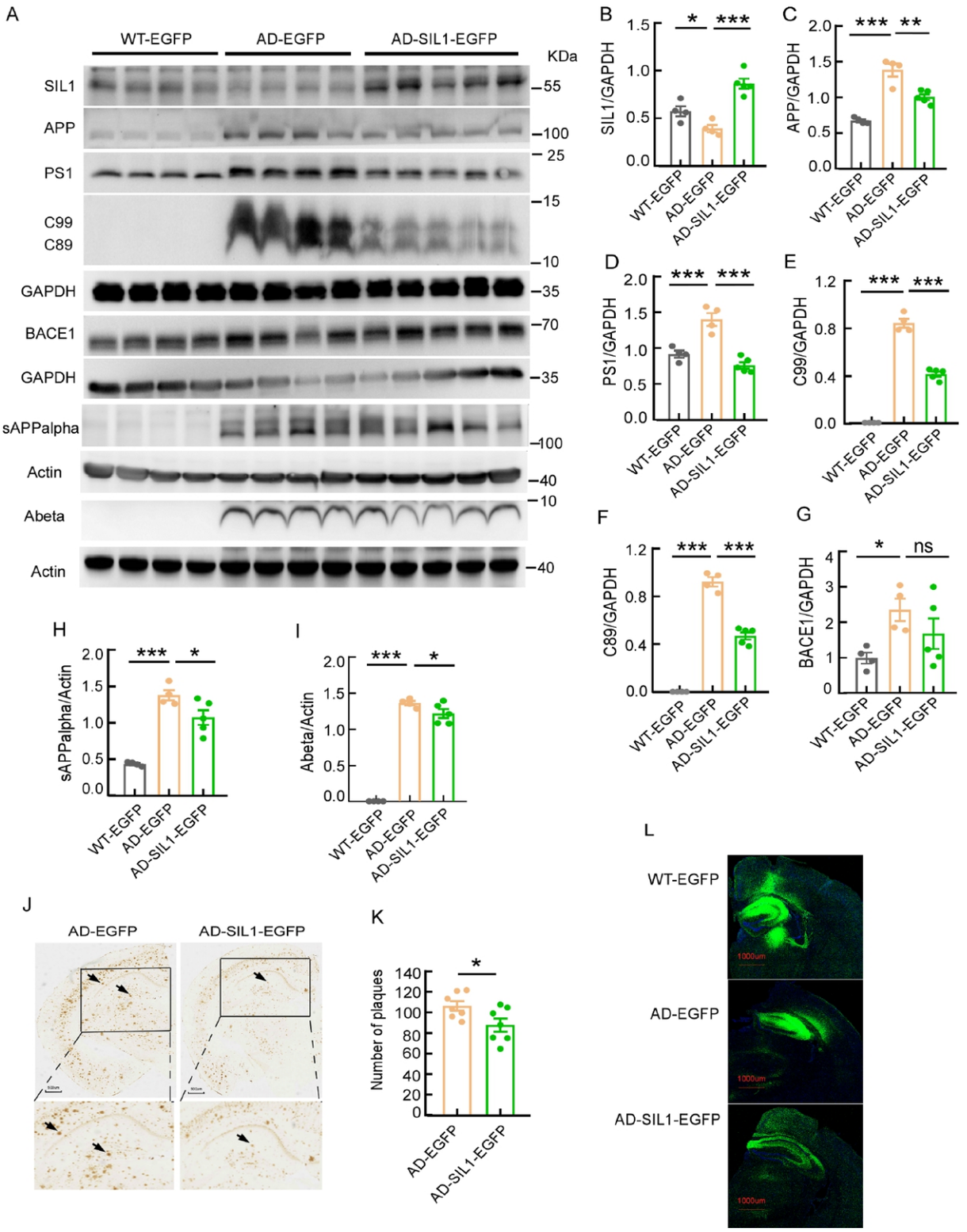



**Figure 5 Overexpression of SIL1 significantly reduced APP processing and number of plaques in APP23/PS45 mice**

SIL1 decreased APP processing *in vivo*. All mice were sacrificed, with half the hippocampus extracted for WB analysis after behavioral experiments. A: Protein levels of SIL1, APP, PS1, C99, C89, sAPPα, Aβ, and BACE1 were detected by WB among WT-EGFP (WT mice microinjected with negative-control AAV), AD-EGFP (APP23/PS45 mice microinjected with negative-control AAV), and AD-SIL1-EGFP mice (APP23/PS45 mice microinjected with SIL1-overexpression AAV). *n*=4–5 mice in each group (WT-EGFP, *n*=4; AD-EGFP, *n*=4; AD-SIL1-EGFP, *n*=5). Qualification of B: SIL1, C: APP, D: PS1, E: C99, F: C89, G: BACE1, H: sAPPα, and I: Aβ, with protein levels normalized to their corresponding GAPDH or actin levels for comparison. L: Immunofluorescent staining showed distribution of AAVs carrying EGFP distributed in the hippocampus of mice in three groups. Scale bar: 1 000 μm. J: Plaques in AD-SIL1-EGFP and AD-EGFP groups by immunohistochemical staining. Scale bar: 500 μm. K: Quantification of plaques between AD-EGFP and AD-SIL1-EGFP mice. *n*=7 animals in each group. Data are presented as mean±SEM. *P*-values were determined by one-way ANOVA with Dunnett's *post hoc* analysis. ns: Not significant; *: *P*<0.05; **: *P*<0.01; ***: *P*<0.001.

plasticity in AD (Wang et al., 2023), suggesting that further research is needed to determine whether SIL1 cooperates with these genes to influence AD progression. Furthermore, APP23/PS45 mice exhibit early-onset familial AD, which accounts for less than one percent of AD cases in human patients (Chen & Zhang, 2022). Thus, focusing solely on SIL1 in this model may present limitations. Whether SIL1 levels decrease in AD patients and contribute to Aβ clearance rather than its generation requires further study.

In conclusion, this study demonstrated that SIL1 levels were decreased in APP23/PS45 mice and that its overexpression improved cognitive impairment by inhibiting APP amyloidogenic processing to reduce Aβ deposition. These findings suggest that SIL1 may be a potential therapeutic target for AD. However, additional research is required to elucidate the mechanisms by which SIL1 influences APP processing and to evaluate its safety in therapeutic applications.

## DATA AVAILABILITY

The raw RNA-seq data reported in this study are available from the NCBI database (BioProjectID PRJNA1099875), China National Center for Bioinformation database (GSA-Human: HRA005214), and Science Data Bank database (DOI: 10.57760/sciencedb.j00139.00131).

## COMPETING INTERESTS

The authors declare that they have no competing interests.

## AUTHORS' CONTRIBUTIONS

Q.W. and W.S. conceived and designed the research. Q.W., Y.J., Z.M., X.D., D.H., and L.J. conducted the experiments. W.Z. and W.S. contributed reagents, materials, and analytical tools. W.S. and W.Z. supervised the project. Q.W., W.Z., and W.S. wrote the manuscript and revised manuscript. All authors read and approved the final version of the manuscript.

## REFERENCES


Anttonen AK, Mahjneh I, Hämäläinen RH, et al. 2005. The gene disrupted in Marinesco-Sjögren syndrome encodes SIL1, an HSPA5 cochaperone. *Nature Genetics*, **37**(12): 1309–1311.

Bayer TA, Cappai R, Masters CL, et al. 1999. It all sticks together—the APP-related family of proteins and Alzheimer's disease. *Molecular Psychiatry*, **4**(6): 524–528.

Boerwinkle AH, Gordon BA, Wisch J, et al. 2023. Comparison of amyloid burden in individuals with down syndrome versus autosomal dominant Alzheimer's disease: a cross-sectional study. *The Lancet Neurology*, **22**(1): 55–65.

Bourdenx M, Martín-Segura A, Scrivo A, et al. 2021. Chaperone-mediated autophagy prevents collapse of the neuronal metastable proteome. *Cell*, **184**(10): 2696–2714. e25.

Bromley-Brits K, Deng Y, Song WH. 2011. Morris water maze test for learning and memory deficits in Alzheimer's disease model mice. *Journal of Visualized Experiments*, (53): 2920.

Chen ZY, Zhang Y. 2022. Animal models of Alzheimer's disease: applications, evaluation, and perspectives. *Zoological Research*, **43**(6): 1026–1040.

Chung KT, Shen Y, Hendershot LM. 2002. BAP, a mammalian BiP-associated protein, is a nucleotide exchange factor that regulates the ATPase activity of BiP. *Journal of Biological Chemistry*, **277**(49): 47557–47563.

Deng Y, Wang Z, Wang RT, et al. 2013. Amyloid-β protein (Aβ) Glu11 is the major β-secretase site of β-site amyloid-β precursor protein-cleaving enzyme 1(BACE1), and shifting the cleavage site to Aβ Asp1 contributes to Alzheimer pathogenesis. *European Journal of Neuroscience*, **37**(12): 1962–1969.

Du YH, Du YX, Zhang Y, et al. 2019. MKP-1 reduces Aβ generation and alleviates cognitive impairments in Alzheimer's disease models. *Signal Transduction and Targeted Therapy*, **4**: 58.

Elangovan A, Babu HWS, Iyer M, et al. 2023. Untangle the mystery behind DS-associated AD - Is APP the main protagonist?. *Ageing Research Reviews*, **87**: 101930.

Esch FS, Keim PS, Beattie EC, et al. 1990. Cleavage of amyloid β peptide during constitutive processing of its precursor. *Science*, **248**(4959): 1122–1124.

Filézac De L'Etang A, Maharjan N, Cordeiro Braña M, et al. 2015. Marinesco-Sjögren syndrome protein SIL1 regulates motor neuron subtype-selective ER stress in ALS. *Nature Neuroscience*, **18**(2): 227–238.

Inaguma Y, Hamada N, Tabata H, et al. 2014. *SIL1*, a causative cochaperone gene of Marinesco-Sjögren syndrome, plays an essential role in establishing the architecture of the developing cerebral cortex. *EMBO Molecular Medicine*, **6**(3): 414–429.

Karran E, De Strooper B. 2022. The amyloid hypothesis in Alzheimer disease: new insights from new therapeutics. *Nature Reviews Drug Discovery*, **21**(4): 306–318.

Kraeuter AK, Guest PC, Sarnyai Z. 2019. The Y-maze for assessment of spatial working and reference memory in mice. *In*: Guest OC. Pre-Clinical Models: Techniques and Protocols. New York: Humana, 105–111.

Labisch T, Buchkremer S, Phan V, et al. 2018. Tracking effects of SIL1 increase: taking a closer look beyond the consequences of elevated expression level. *Molecular Neurobiology*, **55**(3): 2524–2546.

Li ZF, Xu WW, Li JD, et al. 2020. Nucleotide exchange factor SIL1 promotes the progress of breast cancer cells via regulating the cell cycle and apoptosis. *Science Progress*, **103**(1): 36850419891046.

Liao XX, Cai F, Sun ZF, et al. 2020. Identification of Alzheimer's disease-associated rare coding variants in the *ECE2* gene. *JCI Insight*, **5**(4): e135119.

Liu X, Che RB, Liang WP, et al. 2022. Clusterin transduces Alzheimer-risk signals to amyloidogenesis. *Signal Transduction and Targeted Therapy*, **7**(1): 325.

Liu ZC, Chu J, Lin L, et al. 2016. SIL1 rescued bip elevation-related tau hyperphosphorylation in ER stress. *Molecular Neurobiology*, **53**(2): 983–994.

Ly PTT, Wu YL, Zou HY, et al. 2013. Inhibition of GSK3β-mediated BACE1 expression reduces Alzheimer-associated phenotypes. *The Journal of Clinical Investigation*, **123**(1): 224–235.

Masters CL, Bateman R, Blennow K, et al. 2015. Alzheimer's disease. *Nature Reviews Disease Primers*, **1**: 15056.

O'Brien RJ, Wong PC. 2011. Amyloid precursor protein processing and Alzheimer's disease. *Annual Review of Neuroscience*, **34**: 185–204.

Peng L, Bestard-Lorigados I, Song W. 2022. The synapse as a treatment avenue for Alzheimer's disease. *Molecular Psychiatry*, **27**(7): 2940–2949.

Rosam M, Krader D, Nickels C, et al. 2018. Bap (Sil1) regulates the molecular chaperone BiP by coupling release of nucleotide and substrate. *Nature Structural & Molecular Biology*, **25**(1): 90–100.

Selkoe DJ, Hardy J. 2016. The amyloid hypothesis of Alzheimer's disease at 25 years. *EMBO Molecular Medicine*, **8**(6): 595–608.

Senderek J, Krieger M, Stendel C, et al. 2005. Mutations in *SIL1* cause Marinesco-Sjögren syndrome, a cerebellar ataxia with cataract and myopathy. *Nature Genetics*, **37**(12): 1312–1314.

Sun XL, Wang YC, Qing H, et al. 2005. Distinct transcriptional regulation and function of the human *BACE2* and *BACE1* genes. *The FASEB Journal*, **19**(7): 739–749.

Wang T, Zhou YQ, Wang Y, et al. 2023. Long-term potentiation-based screening identifies neuronal PYGM as a synaptic plasticity regulator participating in Alzheimer's disease. *Zoological Research*, **44**(5): 867–881.

Wang Z, Xu Q, Cai F, et al. 2019. BACE2, a conditional β-secretase, contributes to Alzheimer's disease pathogenesis. *JCI Insight*, **4**(1): e123431.

Xu H, Xu SC, Zhang R, et al. 2018. SIL1 functions as an oncogene in glioma by AKT/mTOR signaling pathway. *OncoTargets and Therapy*, **11**: 3775–3783.

Xu SL, Zhu J, Mi K, et al. 2019. Functional role of SIL1 in neurodevelopment and learning. *Neural Plasticity*, **2019**: 9653024.

Zhang ST, Cai F, Wu YL, et al. 2020. A presenilin-1 mutation causes Alzheimer disease without affecting Notch signaling. *Molecular Psychiatry*, **25**(3): 603–613.

Zhang ST, Wang Z, Cai F, et al. 2017. BACE1 cleavage site selection critical for amyloidogenesis and Alzheimer's pathogenesis. *Journal of Neuroscience*, **37**(29): 6915–6925.

Zhang XW, Zhu XX, Tang DS, et al. 2023a. Targeting autophagy in Alzheimer's disease: Animal models and mechanisms. *Zoological Research*, **44**(6): 1132–1145.

Zhang Y, Chen HQ, Li R, et al. 2023b. Amyloid β-based therapy for Alzheimer's disease: challenges, successes and future. *Signal Transduction and Targeted Therapy*, **8**(1): 248.

Zheng QY, Song BB, Li GL, et al. 2022. USP25 inhibition ameliorates Alzheimer's pathology through the regulation of APP processing and Aβ generation. *The Journal of Clinical Investigation*, **132**(5): e152170.

Zhao et al. *Zool. Res.* 2024, 45(4): 857−874
https://doi.org/10.24272/j.issn.2095-8137.2024.085

ZR | Zoological Research

Article Open Access

# NLRP3-mediated autophagy dysfunction links gut microbiota dysbiosis to tau pathology in chronic sleep deprivation

Na Zhao[1,#], Xiu Chen[1,#], Qiu-Gu Chen[1], Xue-Ting Liu[1], Fan Geng[1], Meng-Meng Zhu[1], Fu-Ling Yan[1], Zhi-Jun Zhang[1], Qing-Guo Ren[1,2,*]

[1] *Department of Neurology*, *School of Medicine*, *Southeast University*, *Nanjing*, *Jiangsu* 210009, *China*
[2] *Department of Neurology*, *Affiliated Zhongda Hospital*, *Southeast University*, *Nanjing*, *Jiangsu* 210009, *China*

## ABSTRACT

Emerging evidence indicates that sleep deprivation (SD) can lead to Alzheimer's disease (AD)-related pathological changes and cognitive decline. However, the underlying mechanisms remain obscure. In the present study, we identified the existence of a microbiota-gut-brain axis in cognitive deficits resulting from chronic SD and revealed a potential pathway by which gut microbiota affects cognitive functioning in chronic SD. Our findings demonstrated that chronic SD in mice not only led to cognitive decline but also induced gut microbiota dysbiosis, elevated NLRP3 inflammasome expression, GSK-3β activation, autophagy dysfunction, and tau hyperphosphorylation in the hippocampus. Colonization with the "SD microbiota" replicated the pathological and behavioral abnormalities observed in chronic sleep-deprived mice. Remarkably, both the deletion of NLRP3 in *NLRP3*$^{-/-}$ mice and specific knockdown of NLRP3 in the hippocampus restored autophagic flux, suppressed tau hyperphosphorylation, and ameliorated cognitive deficits induced by chronic SD, while GSK-3β activity was not regulated by the NLRP3 inflammasome in chronic SD. Notably, deletion of NLRP3 reversed NLRP3 inflammasome activation, autophagy deficits, and tau hyperphosphorylation induced by GSK-3β activation in primary hippocampal neurons, suggesting that GSK-3β, as a regulator of NLRP3-mediated autophagy dysfunction, plays a significant role in promoting tau hyperphosphorylation. Thus, gut microbiota dysbiosis was identified as a contributor to chronic SD-induced tau pathology via NLRP3-mediated autophagy dysfunction, ultimately leading to cognitive deficits. Overall, these findings highlight GSK-3β as a regulator of NLRP3-mediated autophagy dysfunction, playing a critical role in promoting tau hyperphosphorylation.

This is an open-access article distributed under the terms of the Creative Commons Attribution Non-Commercial License (http://creativecommons.org/licenses/by-nc/4.0/), which permits unrestricted non-commercial use, distribution, and reproduction in any medium, provided the original work is properly cited.

Copyright ©2024 Editorial Office of Zoological Research, Kunming Institute of Zoology, Chinese Academy of Sciences

**Keywords:** Chronic sleep deprivation; Tau pathology; NLRP3 inflammasome; Autophagy; GSK-3β; Microbiota-gut-brain axis

## INTRODUCTION

Adequate sleep is essential for optimal cognitive functioning, including decision-making, attention, learning, and memory (Donlea, 2019; Krueger et al., 2016). Both experimental and clinical studies have shown that sleep deprivation (SD) can increase the risk and progression of Alzheimer's disease (AD) (Lucey et al., 2021; Shi et al., 2018). Epidemiological data have also indicated that sleeping less than 5 h per night is associated with a two-fold increase in the incidence of dementia compared to sleeping for 7–8 h (Robbins et al., 2021). Experimental SD has been shown to impair learning and memory in both humans and mice (Lo et al., 2016; Wadhwa et al., 2019; Yin et al., 2017). Intracellular accumulation of hyperphosphorylated tau forming neurofibrillary tangles (NFTs) is a pathological hallmark of AD (Scheltens et al., 2021). Several studies have demonstrated that the sleep-wake cycle regulates tau levels in the cerebrospinal fluid (CSF) of humans and brain interstitial fluid (ISF) of mice, with SD increasing tau levels in both fluids and promoting the spread of tau pathology in the brain (Barthélemy et al., 2020; Holth et al., 2019). Despite strong evidence suggesting that SD can lead to AD-related pathological changes and impair cognitive functioning, the underlying mechanisms remain largely unknown.

The gut microbiota plays a crucial role in mediating the bidirectional interactions between the brain and gut, known as the microbiota-gut-brain axis (Mayer et al., 2022). This axis is closely related to human health, influencing neural development, neurotransmission, and behavior, with disruptions in the gut microbial community and composition linked to various neurological disorders, including both AD patients and mouse models (Morais et al., 2021; Vuotto et al., 2020; Zhang et al., 2017; Zhuang et al., 2018). Colonization with fecal microbiota from healthy wild-type (WT) mice has

Received: 18 March 2024; Accepted: 27 May 2024; Online: 28 May 2024
Foundation items: This study was supported by the National Natural Science Foundation of China (81870850) and Postgraduate Research & Practice Innovation Program of Jiangsu Province (KYCX23_0322)
[#]Authors contributed equally to this work
*Corresponding author, E-mail: renqingguo1976@163.com

been shown to improve tau-associated pathology, beta-amyloid plaque deposition, and cognitive decline in transgenic AD mice (Kim et al., 2020). Likewise, changes in gut microbial communities have been observed in animal models and humans with sleep disorders. Various sleep disruption protocols, including acute sleep restriction (Benedict et al., 2016; El Aidy et al., 2020), acute sleep-wake cycle shifts (Liu et al., 2020), chronic sleep fragmentation (Poroyko et al., 2016), and repeated sleep disruption (Bowers et al., 2020), have been shown to alter gut microbiota composition. However, further research is needed to determine whether the gut microbiota plays a critical role in cognitive deficits resulting from chronic SD and to elucidate the mechanisms of the microbiota-gut-brain axis in this process.

Interactions between the gut microbiota and brain primarily involve three parallel or interconnecting routes, including the endocrine system, immune system, and nerve pathways, all of which involve microbial products and metabolites (Cryan et al., 2019). In particular, microbial-immune interactions are key factors in the microbiota-gut-brain axis (Agirman et al., 2021; Pellegrini et al., 2020). Various studies have indicated that the gut microbiota can shape peripheral inflammatory responses, which may lead to neuroinflammation and neurodegeneration (Pearson-Leary et al., 2020; Pellegrini et al., 2018). Both our and previous studies have demonstrated that SD can disrupt the gut microbiota, contributing to both peripheral and central inflammatory responses and ultimately causing cognitive deficits, supporting the existence of a microbiota-gut-inflammation-brain axis (Wang et al., 2021; Zhao et al., 2023). NOD-like receptor family pyrin domain containing 3 (NLRP3) inflammasome-mediated neuroinflammation is considered a contributor to the pathogenesis and progression of AD (Feng et al., 2020). Therefore, it is plausible that the NLRP3 inflammasome serves as a crucial intersection in the microbiota-gut-brain axis related to cognitive deficits resulting from chronic SD.

Pathological aggregation of tau, a microtubule-associated protein that stabilizes neuronal microtubules and promotes axonal outgrowth, plays a major role in AD and other neurodegenerative disorders (Avila et al., 2004). Several factors contribute to tau aggregation, including imbalances between tau kinase and phosphatase activities, neuroinflammation, oxidative stress, and impaired tau clearance (Spillantini & Goedert, 2013). The autophagy-lysosome system, responsible for tau clearance, is essential for preventing the excessive accumulation of aggregated tau. Autophagy (macroautophagy) is a key conserved intracellular clearance process that delivers cytoplasmic contents to lysosomes for degradation (Levine & Kroemer, 2019). This process is vital for maintaining protein homeostasis by eliminating misfolded proteins, impaired organelles, and aggregated proteins (Kaushik & Cuervo, 2015). Compromised autophagy can lead to AD pathogenesis, especially tau pathology (Hamano et al., 2021; Zhang et al., 2021), with *in vitro* studies showing that inhibiting autophagic flux hampers tau clearance and subsequently induces aggregation of insoluble tau proteins (Hamano et al., 2008). Additionally, activation of the autophagy-lysosome pathway in tauopathy mouse models has a robust impact on attenuating tau pathology (Lachance et al., 2019; Polito et al., 2014). It is becoming increasingly clear that autophagy and the NLRP3 inflammasome are interconnected through reciprocal regulation (Biasizzo & Kopitar-Jerala, 2020; Tang et al., 2021). Many studies have shown that autophagy dysfunction can result in excessive NLRP3 inflammasome activation (Wang et al., 2017). Conversely, the NLRP3 inflammasome has also been shown to negatively regulate autophagy (Cosin-Roger et al., 2017; Wu et al., 2021). However, the interaction between autophagy and the NLRP3 inflammasome is complex and controversial, and their roles in the gut-brain crosstalk involved in cognitive deficits due to chronic SD remain underexplored and require further clarification.

Based on these observations, we hypothesize that the microbiota-gut-brain axis is involved in cognitive deficits resulting from chronic SD. Thus, we explored how the gut microbiota influences AD-related pathology and cognitive functioning in chronic SD. Our findings provide persuasive evidence that gut microbiota dysbiosis, driven by chronic SD, contributes to tau pathology via NLRP3-mediated autophagy dysfunction, ultimately leading to cognitive deficits. Additionally, we determined that GSK-3β, beyond acting as a tau kinase, serves as a regulator of NLRP3-mediated autophagy dysfunction, significantly promoting tau hyperphosphorylation and aggregation. This study enhances our understanding of the microbiota-gut-brain axis in cognitive deficits resulting from chronic SD and provides new perspectives for developing microbiome-based treatments for cognitive impairment caused by SD as well as insights into the interaction between AD and sleep disorders.

## MATERIALS AND METHODS

### Experimental design

This study was divided into four phases. Details on the experimental design are shown in Supplementary Figure S1.

### Animals

Male C57BL/6J mice (6–8 weeks) were obtained from the Nanjing University Model Animal Research Center (Nanjing, China), while male *NLRP3*$^{-/-}$ mice (6–8 weeks) with a C57BL/6 background were obtained from the Jackson Laboratory. The animals were housed at the Southeast University Laboratory Animal Center (China) under specific pathogen-free conditions at a temperature of 22±2℃, humidity of 50%±5%, and standard 12:12 h light-dark cycle (lights on from 0700h to 1900h). All animal groups in the same batch were housed under identical conditions, including the same type of cage, bedding materials, and nestlets, all located in the same vivarium room. The mice were provided with the same autoclaved drinking water and food (Teklab certified global 18% protein rodent diet; cat. number T2018SC.15) *ad libitum*. Each mouse consumed approximately 4.0 mL of water per day, with no significant difference in water or food consumption among groups. The study employed a sterilized diet, sterilized cages, bedding, and water bottles, all autoclaved as a unit prior to cage changes, and cages were only opened within a HEPA-filtered animal transfer station when changing cages or collecting samples. All animal experiments were conducted in compliance with animal ethics and authorized by the Southeast University Institutional Animal Care and Use Committee (approval No. 20200418020). All efforts were made to minimize animal suffering and reduce the number of animals used.

### Chronic SD procedures

Before conducting chronic SD (Bowers et al., 2020), all mice were raised for 1 week in chronic SD cages to acclimate to the

devices. The chronic SD cage consisted of an autoclaved, ventilated, transparent, microisolator chamber (height of 14 cm, diameter of 32 cm) with sterile bedding and standard laboratory food/water. A 30 cm long metal rod was fixed in the center at the bottom of the chamber. Throughout the chronic SD period, the metal rod was set up to spin at a steady speed (five revolutions per min) to keep the mice awake for 20 h each day (Zeitgeber time (ZT) 6–ZT2) for 21 consecutive days. Experimenters visually inspected mice at regular intervals during the SD windows to ensure that the metal rods were functioning properly and that the SD mice were awake. From ZT2 to ZT6, the metal rod remained stationary, allowing mice subjected to chronic SD to rest. ZT was defined as the number of hours after the onset of the light period (ZT0). Control mice allowed to sleep regularly were raised in identical SD devices in which the metal rod remained stationary during the chronic SD period.

**Antibiotic treatment protocol**

According to previously published protocols (Zhang et al., 2019), drinking water mixed with several antibiotics, including ciprofloxacin (Macklin, China, 200 mg/L), ampicillin (Meryer, China, 1 g/L), vancomycin (Macklin, China, 500 mg/L), metronidazole (Aladdin, China, 1 g/L), and imipenem plus cilastatin (MSD, USA, 250 mg/L), was administered to C57BL/6J mice for substantial depletion of the gut microbiota. The antibiotic solution was changed every 2–3 days, and the water bottles containing antibiotic solution were turned over every day. Antibiotic treatment was continued for 7 weeks. Finally, the antibiotic solution was replaced with sterile tap water 3 days before fecal microbiota transplantation.

**Fecal sample collection**

Before collecting fecal samples, mice were moved to autoclaved, ventilated, microisolator cages and provided with standard laboratory food and water (one mouse/cage). The mice were maintained in the cages under careful observation until 3–4 fresh fecal pellets (each mouse) were excreted. The mice were then removed from the cages and fresh fecal pellets from each animal were collected directly in sterile 1.5 mL centrifuge tubes using sterile cotton swabs. The fresh fecal samples were immediately stored at –80°C until fecal microbiota transplantation or microbiome analysis. All fecal samples were obtained between ZT8 and ZT12 to minimize circadian rhythm effects.

**Fecal microbiota transplantation (FMT)**

The FMT procedures followed previous published protocols (Liao et al., 2019), with some modifications. In brief, 200 μL of fecal dilution was transferred to recipient antibiotic-treated mice for 7 days via oral gavage. To prepare the dilution, fresh fecal samples were collected from chronic SD mice (SD group) and normal sleep mice (CON group). The fecal pellets from two groups were pooled and homogenized in anaerobic phosphate-buffered saline (PBS), respectively (25 mg stool/100 μL PBS). The samples were then vortexed for 5 min, followed by gentle centrifugation at 50 ×*g* for 3 min to precipitate the larger fecal particles. The supernatants of the two groups were then collected and diluted with sterile PBS (1:1). Finally, the antibiotic-treated mice were randomly divided into two groups and treated with 200 μL of fecal suspension from the CON and chronic SD groups, respectively, by oral gavage for 1 week. To determine whether differences in microbiota community structure between chronic SD and CON mice were maintained in the recipient mice, stools were harvested from recipient mice colonized with fecal microbiota from normal sleep mice (FMT-CON group) and chronic SD mice (FMT-SD group) 1 week post-FMT. Subsequently, 16S rRNA gene sequencing was performed on fecal samples from the CON, SD, FMT-CON, and FMT-SD groups. Principal coordinate analysis (PCoA) showed an obvious separation in the gut microbiota composition between the normal sleep donor mice and chronic SD donor mice. Likewise, the normal sleep microbiota recipient mice and chronic SD microbiota recipient mice exhibited a clear difference in gut microbial communities. In contrast, similarities were observed between the corresponding recipient and donor mice (Supplementary Figure S2). These results validated the fidelity of FMT.

**Behavioral tests**

The Morris water maze (MWM) and novel object recognition (NOR) tests were used to evaluate cognitive functioning in mice.

**MWM test:** The MWM test was applied to assess spatial learning and memory abilities of the research animals. The water maze consisted of a cylindrical water tank (diameter of 120 cm and height of 40 cm) with four quadrants. During the MWM test, the water tank was filled with water (depth of 30 cm and temperature of 21±1°C). During the acquisition trials, a platform (diameter of 10 cm) hidden 1.0 cm below the water surface was placed in the set quadrant and mice were trained to find the hidden platform with 60 s for 5 consecutive days. Each day, mice facing the tank wall were gently placed in the water from pseudo-random quadrants. If the mice did not locate the platform within 60 s, they were manually guided to the platform and required to remain on the platform for 30 s. The escape latencies of the mice were recorded. On day 6, the spatial probe trial was performed to determine memory retention. The mice were allowed to swim freely in the water tank for 60 s with the platform removed. Time spent in the target quadrant, number of platform crossings, and swimming paths were recorded using a video capture system.

**NOR test:** The NOR test was conducted to assess the tendency of mice to distinguish between a novel and familiar object, consisting of habituation, training, and testing stages. The mice were first individually conditioned to an open-field box for 10 min. One day later, two identical objects were placed into the two opposing corners of the open-field box. The mice were then allowed to explore the area and objects for 5 min. Time spent exploring the identical objects was recorded to determine any object preferences. During the testing phase, mice were placed in the same area with one familiar object and one novel object, then allowed to freely explore the objects for 5 min. Time spent exploring the familiar object (TF) and novel object (TN) was recorded. Exploration was recognized as orbiting, sniffing, and pawing the object. Recordings were ceased when the mice moved their heads 1 cm away from the object. After each trial, all objects and apparatus were cleaned using 70% ethanol to eliminate residual odor. A recognition index (RI) was calculated as RI=(TN/(TN+TF))×100%.

**Tissue collection**

One day after completing all behavior tests, the mice were sacrificed under deep anesthesia and brain tissues were promptly removed. Hippocampal samples were dissected from the brain tissues and stored at –80°C for subsequent

detection. Brain tissues were also fixed, dehydrated, embedded, and sectioned for immunofluorescence and immunohistochemical staining.

**16S rRNA gene sequencing analysis**

Cetyltrimethylammonium bromide (CTAB)/sodium dodecyl sulfate (SDS) was used to extract whole genome DNA from the fecal samples of both the chronic SD and control mice. The V3–V4 variable regions of the 16S rRNA gene were amplified and sequenced using the Illumina MiSeq/HiSeq2500 platform. The UPARSE package was employed to perform sequence analysis using the UPARSE-OTUref and UPARSE-OTU algorithms. We selected a representative sequence for each operational taxonomic unit (OTU) and annotated taxonomic information for each representative sequence using the RDP classifier. Sequences with a similarity of more than 97% were categorized as the same OTU. To investigate alpha-diversity (within samples) and beta-diversity (across samples), internal Perl scripts were utilized. Krona plots were used to display the relative abundance of bacterial diversity from phylum to species. Principal component analysis (PCA) was performed using QIIME before cluster analysis to minimize the dimension of original variables. PCoA facilitated the extraction and visualization of principal coordinates from multidimensional, complicated data. Both unweighted and weighted-UniFrac distance, known as the phylogenetic measures of beta-diversity, were calculated using QIIME to explore differences in community composition between different groups. STAMP was used to verify dissimilarities in the abundance of individual taxonomies between the chronic SD and control groups.

**Immunohistochemical and immunofluorescence staining**

Brain tissues were fixed in 4% paraformaldehyde for 24 h, then transferred to ascending grades of ethyl alcohol for dehydration, followed by immersion in xylene and embedding in paraffin. The paraffin-embedded blocks were cut into sections (5 μm thick) for immunohistochemical and immunofluorescence staining.

For immunofluorescence staining, the paraffin-embedded brain sections were baked at 60°C for 2 h, dewaxed in xylene three times, sequentially placed in a gradient ethanol, and rinsed with distilled water twice. The sections were then immersed in sodium citrate solution (pH=6.0) for antigen retrieval by microwave for 20 min. After cooling down to room temperature, the sections were washed with PBS three times and blocked with 3% bovine serum albumin (BSA) at room temperature for 30 min, followed by incubation with monoclonal antibodies, including anti-phospho-tau (Ser396) (1:1 000, Abcam, UK) and anti-NLRP3 (1:200, AdipoGen, USA) at 4°C overnight in a wet box. The following day, the sections were washed with PBS three times (5 min each) and incubated with appropriate secondary antibodies (1:1 000, Abcam, UK) for 1 h in a wet box. After washing with PBS for 3×5 min, nuclei were counterstained with 4',6-diamidino-2-phenylindole (DAPI) mounting medium at room temperature for 20 min. The stained sections were observed and imaged using a confocal microscope (Zeiss, Germany).

For immunohistochemical staining, the paraffin-embedded brain sections were deparaffinized, rehydrated, and heated in a microwave oven for 20 min in Tris-EDTA (pH 9.0) for antigen retrieval. Endogenous peroxidase activity was blocked with 0.3% $H_2O_2$ in absolute methanol for 30 min and nonspecific sites were blocked with 3% BSA for 30 min at room temperature. The sections were then incubated with primary antibodies at optimized dilutions at 4°C overnight. The next day, the sections were washed twice with PBS and subsequently incubated with biotin-labeled secondary antibodies for 1 h at 37°C. The immunoreaction was developed using a Histostain TM-SP kit (ThermoFisher Scientific, USA). An enzyme substrate 3,3'-diaminobenzidine (DAB) Substrate-Kit (Vector) was used to visualize the signal, with the sections then counterstained with hematoxylin. The sections were imaged using a microscope (Olympus BX60, Japan).

**Western blotting**

Hippocampal tissues were collected and lysed on ice for 30 min with RIPA lysis buffer consisting of 50 mmol/L Tris-HCl (pH 7.0), 1 mmol/L EDTA, 0.1 mmol/L phenylmethylsulfonyl fluoride (PMSF), 1 mmol/L benzamidine, 0.5 mmol/L isobutylmethylxanthine, and multiple inhibitors. The samples were then homogenized, with the homogenates then centrifuged at 12 000 r/min for 15 min at 4°C. The resulting supernatants were collected, and the protein concentrations of the supernatants were determined using a bicinchoninic acid (BCA) protein assay kit (Beyotime, China). Protein samples diluted with loading buffer (6×concentrate; Beyotime, China) were boiled for 8 min, then stored at –20°C.

To separate proteins, equal amounts of protein samples were subjected to 7.5%–12.5% sodium dodecyl sulfate-polyacrylamide gel electrophoresis (SDS-PAGE), then transferred to polyvinylidene difluoride (PVDF) membranes (Immobilon Transfer Membrane, Millipore, USA) at 300 mA for 0.5–2 h and blocked with 5% (w/v) nonfat milk for 2 h at room temperature. The membranes were incubated with primary antibodies in 5% (w/v) BSA at 4°C overnight, then washed with TBST for 8 min three times and incubated with appropriate goat anti-rabbit or goat anti-mouse peroxidase-conjugated secondary antibodies (1:5 000, Pierce, USA) for 1 h at room temperature. The blots were visualized using an enhanced chemiluminescence substrate (ECL, Millipore, USA) and integral optical density values (IOD) were measured by Image Pro-Plus v.6.0 software. The β-actin protein level was used as the internal control. Primary antibodies used included: anti-phospho-tau (Thr231) (1:1 000, Abcam, UK), anti-phospho-tau (Ser396) (1:5 000, Abcam, UK), anti-tau-1 (1:1 000, Merck Millipore, USA), anti-tau-5 (1:1 000, Abcam, UK), anti-total-GSK-3β (GSK-3β) (1:1 000, Cell Signaling Technology, USA), anti-phospho-GSK-3β (Ser9) (1:1 000, Cell Signaling Technology, USA), anti-NLRP3 (1:2 000, AdipoGen, USA), anti-IL-1β (1:1 000, Abcam, UK), anti-IBA-1 (1:1 000, Wako, Japan), anti-Beclin-1 (1:1 000, Cell Signaling Technology, USA), anti-LC3B (1:1 000, Cell Signaling Technology, USA), anti-SQSTM1/p62 (1:1 000, Merck Millipore, USA), and anti-β-actin (1:1 000, Abcam, UK).

**Reverse transcription-quantitative real-time polymerase chain reaction (RT-qPCR)**

Total RNA was isolated from hippocampal tissues using TRIzol reagent (ThermoFisher Scientific, USA). The purity, quantity, and integrity of RNA were measured using a Nano-Drop 8000 Spectrophotometer (ThermoFisher Scientific, USA). The Omniscript Reverse Transcription Kit (Qiagen, Japan) was applied in accordance with the manufacturer's instructions to generate cDNA from a total of 1 μg of RNA. Fast SYBR GreenER Master Mix (ThermoFisher Scientific, USA) was utilized according to the manufacturer's

recommendations for qPCR assembly using a Real-Time PCR System (Applied Biosystems 7300). The $2^{-\Delta\Delta CT}$ method, which calculates the relative quantification of a target gene normalized to the GAPDH gene, was used to determine mRNA expression. The PCR primers used included: mouse total tau: forward 5'-GAA CCA CCA AAA TCC GGA GA-3'; reverse 5'-CTC TTA CTA GCT GAT GGT GAC-3'; GAPDH: forward 5'-ACA ACT TTG GTA TCG TGG AAG G-3'; reverse 5'-GCC ATC ACG CCA CAG TTT C-3'.

**Knockdown of NLRP3 using adeno-associated virus (AAV) delivery**

AAV vectors containing a non-specific sequence (CGC TGA GTA CTT CGA AAT GTC) or short hairpin RNA targeting NLRP3 (CCA GGA TCC TCT TCC TCA TA) were designed and obtained from GeneChem (China). Mice received a microinjection of AAV vectors carrying green fluorescent protein (GFP) (AAV-GFP) or targeting NLRP3 (AAV-NLRP3) into the hippocampus. In brief, mice were anesthetized with 4% chloral hydrate (intraperitoneal injection), then immobilized in a stereotaxic apparatus (David Kopf Instruments, USA). Two small holes (diameter of 1 mm) were then drilled in precise sites of the bared skull (AP: −2.0 mm, ML: ±2.0 mm, DV: −2.0 mm), followed by microinjection of 2.0 μL of AAV vectors (AAV-GFP: $11.4\times10^{12}$ vg/mL or AAV-NLRP3: $8.33\times10^{12}$ vg/mL) into the bilateral hippocampus with a microsyringe (1.0 μL per side, 0.2 μL/min), which was kept in place for 10 min following injection to avoid viral particle backflow. Vectors encoded with enhanced GFP help verify successful infusion via fluorescence microscopy. Western blotting was also carried out to confirm the effects of transfection.

**Cell culture**

Primary hippocampal neurons were obtained from embryonic day 18 (E18) WT mice and *NLRP3*$^{-/-}$ mice. The neurons were grown in 6-well or 12-well plates covered with Poly-D-Lysine/Laminin (Sigma-Aldrich, USA) for 3 h to allow neurons to attach to the plates. Neurobasal medium with 25 mmol/L glutamate, 2% B27, and 0.5 mmol/L glutamine (ThermoFisher Scientific, USA) was applied to the culture neurons. Every 3 days, half of the culture medium was replaced with fresh neurobasal medium. All neurons were kept in $CO_2$ incubators (temperature 37℃, $CO_2$ 5%, humidity 95%). After 7 days of culture, the primary hippocampal neurons were treated with Akt inhibitor MK-2206 (Selleckchem, USA). Finally, primary neurons subjected to western blotting and immunofluorescence staining. Each condition was conducted in three biological replicates.

**Statistical analysis**

All collected data were shown as mean±standard error of the mean (SEM) and statistical analyses were conducted using GraphPad Prism v.9.0 (GraphPad Software, USA). Differences between two individual groups were compared using unpaired Student's *t*-test. The Mann-Whitney *U* test was employed for non-normally distributed data, while Welch's *t*-test was used for data with unequal variances. One-way analysis of variance (ANOVA), coupled with Tukey's *post hoc* test for multiple comparisons was used to determine statistical differences among three or more groups. Data from different groups at different time points, such as escape latencies during 5 day MWM spatial training, were compared using repeated measures two-way ANOVA. Differences were regarded as statistically significant at $P<0.05$. Each experiment was carried out with at least three replicates.

## RESULTS

**Chronic SD induced cognitive deficits and altered gut microbiota composition in mice**

The MWM test is typically applied to assess cognitive functioning. In the training trials, the mice subjected to chronic SD exhibited longer escape latencies than the mice allowed to sleep regularly, especially on days 4 and 5 (group: $F_{(1,16)}=16.004$, $P=0.0013$, $\eta_p^2=0.533$; day: $F_{(4,56)}=152.721$, $P<0.0001$, $\eta_p^2=0.916$; interaction: $F_{(4,56)}=3.063$, $P=0.0237$, $\eta_p^2=0.180$; day 4: $P=0.0158$; day 5: $P=0.0029$, Figure 1A). In the spatial probe trial, the chronic SD mice exhibited poorer performance compared to control mice, as evidenced by the lower percentage of time spent in the target quadrant ($t_{14}=3.945$, $P=0.0015$, Cohen's d=1.988, Figure 1B) and fewer platform crossings ($t_{14}=3.024$, $P=0.0091$, Cohen's d=1.525, Figure 1C). The heatmaps of swimming paths indicated that, compared to mice in the chronic SD group, the control group mice swam more frequently in the platform and surrounding areas (Figure 1D). These findings suggest that chronic SD impairs spatial learning and memory ability in mice.

Our previous study revealed distinct differences in the gut microbial communities between the chronic SD and control groups (Zhao et al., 2023). Sequences were annotated into OTUs. As depicted in the Venn diagram, the two groups shared 1 101 OTUs, with 298 OTUs unique to the control group and 203 OTUs unique to the chronic SD group (Supplementary Figure S3A). PCoA based on the weighted-UniFrac index exhibited a clear difference in gut microbiota composition between the two groups (Supplementary Figure S3B). At the phylum level, Proteobacteria, Bacteroidetes, and Firmicutes were the dominant bacteria, comprising most of the gut microbiota community. Compared to the control group, the chronic SD group exhibited a marked increase in the relative abundance of Bacteroidetes from 56% to 71%, while the relative abundances of Proteobacteria and Firmicutes decreased (Supplementary Figure S3C). Additionally, at the genus level, the chronic SD group showed an increased relative abundance of *Odoribacter* and a concomitant reduction in *Lactobacillus* (Supplementary Figure S3D). Overall, these findings indicate that chronic SD alters the composition of gut microbiota in mice.

**Chronic SD induced tau hyperphosphorylation and GSK-3β activation in the hippocampus of mice**

Next, we investigated the influence of chronic SD on tau phosphorylation. Compared to control mice, the levels of tau phosphorylation at the Thr231 (pT231) and Ser396 (pS396) sites were significantly up-regulated in the hippocampus of chronic SD mice (pT231: $t_4=3.940$, $P=0.0170$; pS396: $t_4=4.896$, $P=0.0081$, Figure 2A), as verified by immunofluorescence staining (Figure 2C). In addition, the level of Tau-1 was decreased in the hippocampus of chronic SD mice (Tau-1: $t_4=4.890$, $P=0.0081$, Figure 2A). Lower expression of Tau-1, a non-phosphorylated tau located at the Ser198/199/202 sites, reflected an increase in tau phosphorylation. Interestingly, the level of total tau (Tau-5) in the chronic SD group was higher than that in the control group (Tau-5: $t_4=4.902$, $P=0.0080$, Figure 2A). However, no significant difference in the mRNA level of tau was observed

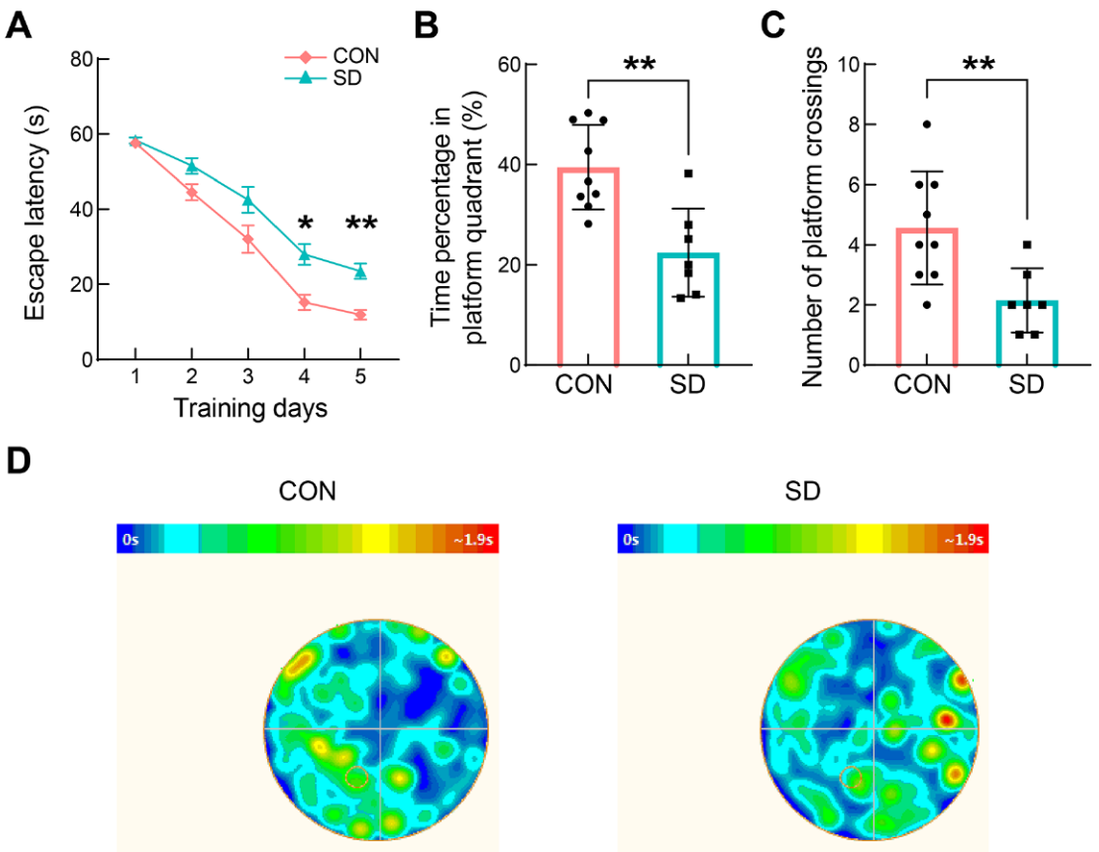



**Figure 1 Chronic SD induced cognitive deficits in mice**

A: Escape latency of chronic SD mice and controls for five consecutive training days in the MWM test. B: Percentage of time spent in platform quadrant in spatial probe trial of the MWM test. C: Number of platform crossings in spatial probe trial of the MWM test. D: Representative heatmaps of swimming paths in spatial probe trial of the MWM test. All data are expressed as mean±SEM. CON $n$=9 mice/group; SD $n$=7 mice/group. Data were considered significant at $^{*}$: $P$<0.05, $^{**}$: $P$<0.01, $^{***}$: $P$<0.001, $^{****}$: $P$<0.0001. ns: Not significant. Means were compared using two-way repeated measures ANOVA with Bonferroni *post hoc* comparison in panel A and Student's *t*-test in panel B, C. SD: Chronic sleep-deprived mice; CON: Normal sleep littermate controls,

between the two groups ($t_6$=0.285, $P$=0.7852, Figure 2B).

The activity of GSK-3β, known to act as an important tau kinase, was measured by western blotting. The chronic SD mice exhibited a down-regulation in phosphorylated GSK-3β at the Ser9 site compared to the control mice, resulting in the activation of GSK-3β (pS9-GSK-3β: $t_4$=7.390, $P$=0.0018, Figure 2D). In addition, no differences were found in the level of total GSK-3β (t-GSK-3β: $t_4$=0.8703, $P$=0.4332, Figure 2D). These findings suggest that chronic SD can induce intracellular tau hyperphosphorylation and excessive activation of GSK-3β in the hippocampus of mice.

**Chronic SD activated NLRP3 inflammasome and inhibited autophagy in the hippocampus of mice**

The levels of interleukin-1β (IL-1β) and NLRP3 in the hippocampus of mice were measured by western blot analysis. Results indicated that the expression levels of IL-1β and NLRP3 were significantly elevated in the hippocampus of the chronic SD group compared to the control group (NLRP3: $t_4$=5.292, $P$=0.0061; IL-1β: $t_4$=7.049, $P$=0.0021, Figure 3A). Up-regulation of NLRP3 expression in the hippocampus of the chronic SD group was also confirmed through immunofluorescence staining (Figure 3B). The expression level of IBA-1, indicative of microglial activation, was also elevated in the hippocampus of chronic SD mice (IBA-1: $t_4$=3.570, $P$=0.0234, Figure 3A). Based on detection of autophagy activity, the levels of several autophagosome markers, including Beclin-1, microtubule-associated protein light chain 3 (LC3)-II, and conversion of LC3-I to LC3-II, were decreased in the hippocampus of chronic SD mice compared to control mice (Beclin-1: $t_4$=4.277, $P$=0.0129; LC3-II: $t_4$=5.094, $P$=0.0070; LC3-II/I: $t_4$=4.643, $P$=0.0097, Figure 3C). In addition, the expression of SQSTM1/p62 was significantly increased in the chronic SD group (p62: $t_4$=5.002, $P$=0.0075, Figure 3C). These findings indicate that chronic SD induces NLRP3 inflammasome activation and blocks autophagic flux in the hippocampus of mice.

**SD microbiota transplantation impaired cognitive function, increased tau phosphorylation, and activated GSK-3β in mice**

FMT was performed to examine whether changes in gut microbiota from chronic SD mice contribute to pathological brain abnormalities and behavioral alterations. Gut microbiota from normal sleep mice or chronic SD mice were transplanted into healthy WT mice via oral gavage for 1 week. Notably, FMT from chronic SD mice, but not from normal sleep mice, resulted in a significant reduction in the RI of the NOR test, indicating cognitive decline in the chronic SD microbiota recipient mice ($t_{15}$=3.057, $P$=0.0080, Cohen's d=1.485, Figure 4A, B). Western blot analysis revealed increased levels of phosphorylated tau (pS396-tau and pT231-tau) and

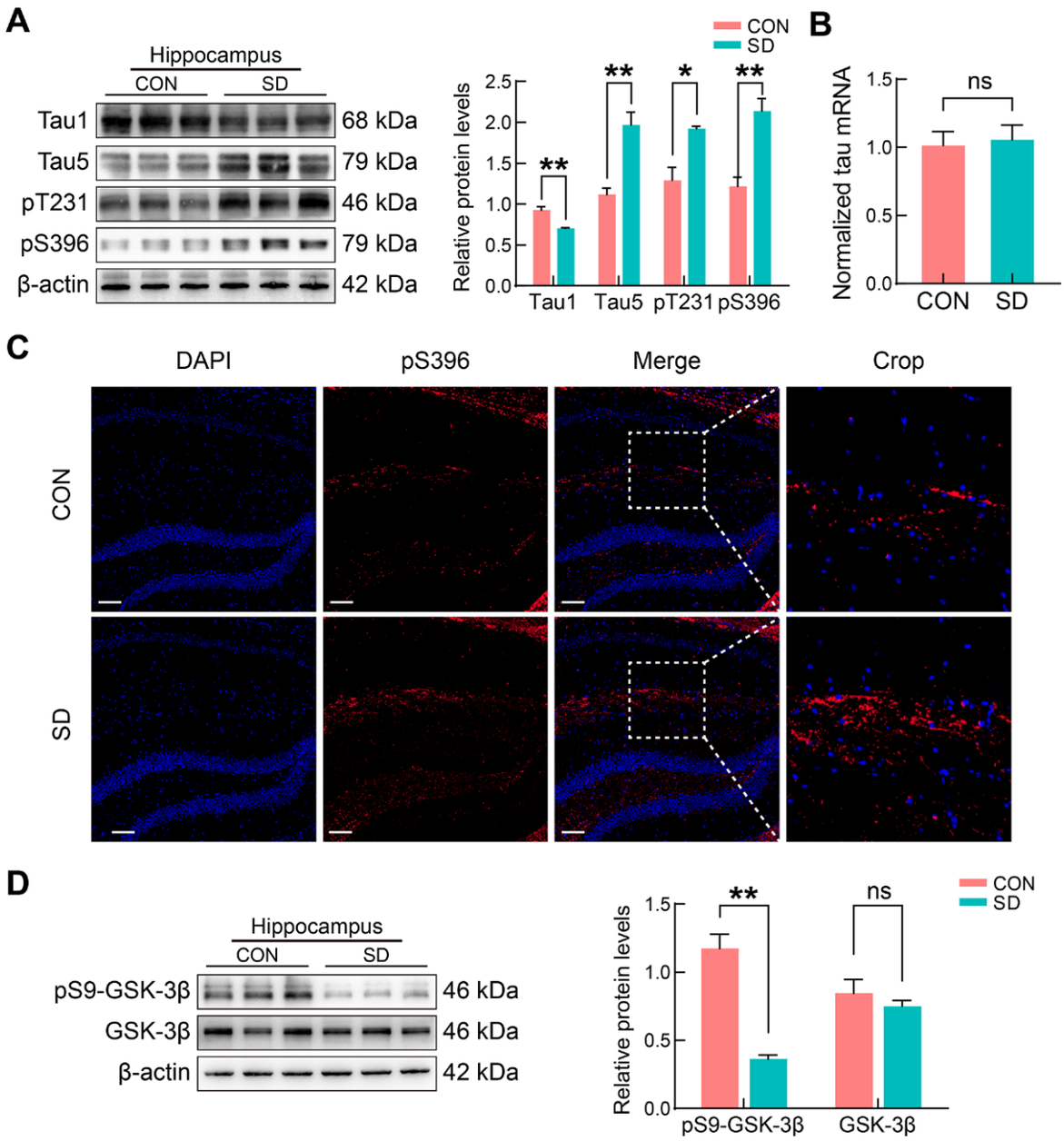



**Figure 2 Chronic SD induced tau hyperphosphorylation and GSK-3β activation in the hippocampus of mice**

A: Protein levels of Tau-1, Tau-5, pS396-tau, and pT231-tau were determined by western blotting in hippocampus of chronic SD mice and controls. B: mRNA level of tau measured by qPCR in hippocampus of chronic SD mice and controls. C: Representative immunofluorescence staining against pS396-tau in hippocampal regions (CA1, CA3, and DG). Magnification ×10, Scale bar: 100 μm. D: Protein levels of p-GSK-3β (Ser9) and total GSK-3β were determined by western blotting in hippocampus of chronic SD mice and controls. All data are expressed as mean±SEM. $n$=3 mice/group. β-actin was used as the loading control in western blot analysis. Data were considered significant at $^{*}$: $P$<0.05, $^{**}$: $P$<0.01, $^{***}$: $P$<0.001, $^{****}$: $P$<0.0001 by Student's $t$-test. ns: Not significant. SD: Chronic sleep-deprived mice; CON: Normal sleep littermate controls.

reduced levels of non-phosphorylated tau (Tau-1) in the hippocampus of chronic SD microbiota recipient mice compared to control recipient mice (pT231: $t_4$=3.079, $P$=0.0370; pS396: $t_4$=8.546, $P$=0.0010; Tau-1: $t_4$=5.932, $P$=0.0040, Figure 4C). Immunofluorescence staining against pS396-tau also demonstrated that colonization with chronic SD microbiota increased tau phosphorylation at the Ser396 site in the hippocampus of recipient mice (Figure 4D). Additionally, the expression of total tau (Tau-5) was enhanced in the hippocampus of chronic SD microbiota recipient mice (Tau-5: $t_4$=3.964, $P$=0.0166, Figure 4C). Further, an obvious decrease in the phosphorylation of GSK-3β at the Ser9 site, with no change in total GSK-3β levels, was observed in the hippocampus of recipient mice treated with chronic SD microbiota, suggesting pronounced activation of GSK-3β (pS9-GSK-3β: $t_4$=4.533, $P$=0.0106; t-GSK-3β: $t_4$=0.4500, $P$=0.6760, Figure 4E).

**SD microbiota transplantation inhibited autophagic flux and enhanced NLRP3 inflammasome activity**

As shown in western blot analysis, the transfer of gut microbiota derived from chronic SD mice resulted in the inhibition of autophagy, as indicated by the down-regulation of LC3-II, Beclin-1, and the LC3-II/LC3-I ratio, and up-regulation of SQSTM1/p62 in the hippocampus of chronic SD microbiota recipient mice (Beclin-1: $t_4$=4.370, $P$=0.0120; LC3-II: $t_4$=3.782,

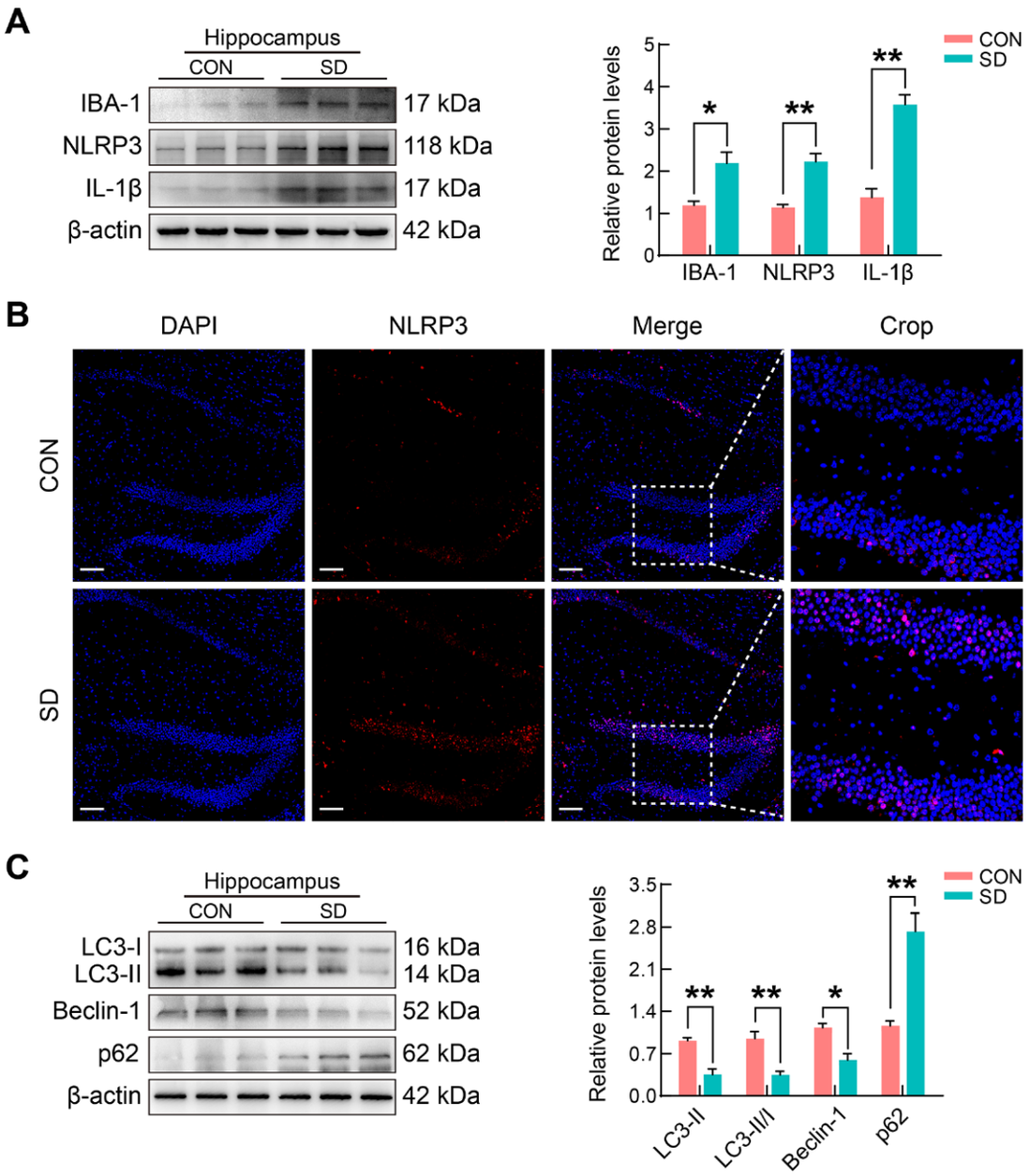



**Figure 3 Chronic SD induced NLRP3 inflammasome activation and autophagy inhibition in the hippocampus of mice**

A: Protein levels of IBA-1, NLRP3, and IL-1β were determined by western blotting in hippocampus of chronic SD mice and controls. B: Representative immunofluorescence staining against NLRP3 was performed on hippocampal regions (CA1, CA3, and DG). Magnification ×10, Scale bar: 100 μm. C: Protein levels of Beclin-1, LC3-II, SQSTM1/p62 and LC3-II/LC3-I ratio were determined by western blotting in hippocampus of chronic SD mice and controls. All data are expressed as mean±SEM. *n*=3 mice/group. β-actin was used as the loading control in western blot analysis. Data were considered significant at *: $P<0.05$, **: $P<0.01$, ***: $P<0.001$, ****: $P<0.0001$ by Student's *t*-test. ns: Not significant. SD: Chronic sleep-deprived mice; CON: Normal sleep littermate controls.

$P$=0.0194; LC3-II/I: $t_4$=4.054, $P$=0.0154; p62: $t_4$=4.464, $P$=0.0111, Figure 5A). Concomitantly, compared to the normal sleep microbiota recipient mice, the chronic SD microbiota recipient mice displayed higher expression levels of IL-1β, NLRP3, and IBA-1 in the hippocampus (IBA-1: $t_4$=4.465, $P$=0.0111; NLRP3: $t_4$=3.358, $P$=0.0284; IL-1β: $t_4$=4.298, $P$=0.0127, Figure 5B, C).

**Pathological and behavioral changes from chronic SD were nearly reversed in *NLRP3*$^{-/-}$ mice**

Next, we explored the role of the NLRP3 inflammasome in chronic SD. Different from WT mice, *NLRP3*$^{-/-}$ mice showed no NLRP3 expression and very low IL-1β and IBA-1 expression in the hippocampus, regardless of their exposure to chronic SD or normal sleep (IBA-1: $F_{(3,8)}$=26.273, $P$=0.0002; WT/CON vs. WT/SD: $P$=0.0011; *NLRP3*$^{-/-}$/CON vs. *NLRP3*$^{-/-}$/SD: $P$=0.9502; WT/CON vs. *NLRP3*$^{-/-}$/CON: $P$=0.4410; WT/SD vs. *NLRP3*$^{-/-}$/SD: $P$=0.0004, NLRP3: $F_{(3,8)}$=61.374, $P$<0.0001; WT/CON vs. WT/SD: $P$=0.0002; *NLRP3*$^{-/-}$/CON vs. *NLRP3*$^{-/-}$/SD: $P$=0.9995; WT/CON vs. *NLRP3*$^{-/-}$/CON: $P$=0.0255; WT/SD vs. *NLRP3*$^{-/-}$/SD: $P$=0.0001, IL-1β: $F_{(3,8)}$=20.457, $P$=0.0004; WT/CON vs. WT/SD: $P$=0.0036; *NLRP3*$^{-/-}$/CON vs. *NLRP3*$^{-/-}$/SD: $P$=0.9329; WT/CON vs. *NLRP3*$^{-/-}$/CON: $P$=0.3386; WT/SD vs. *NLRP3*$^{-/-}$/SD: $P$=0.0009, Figure 6F).

Cognitive performance was evaluated using the NOR test. After chronic SD, cognitive functioning was markedly disrupted

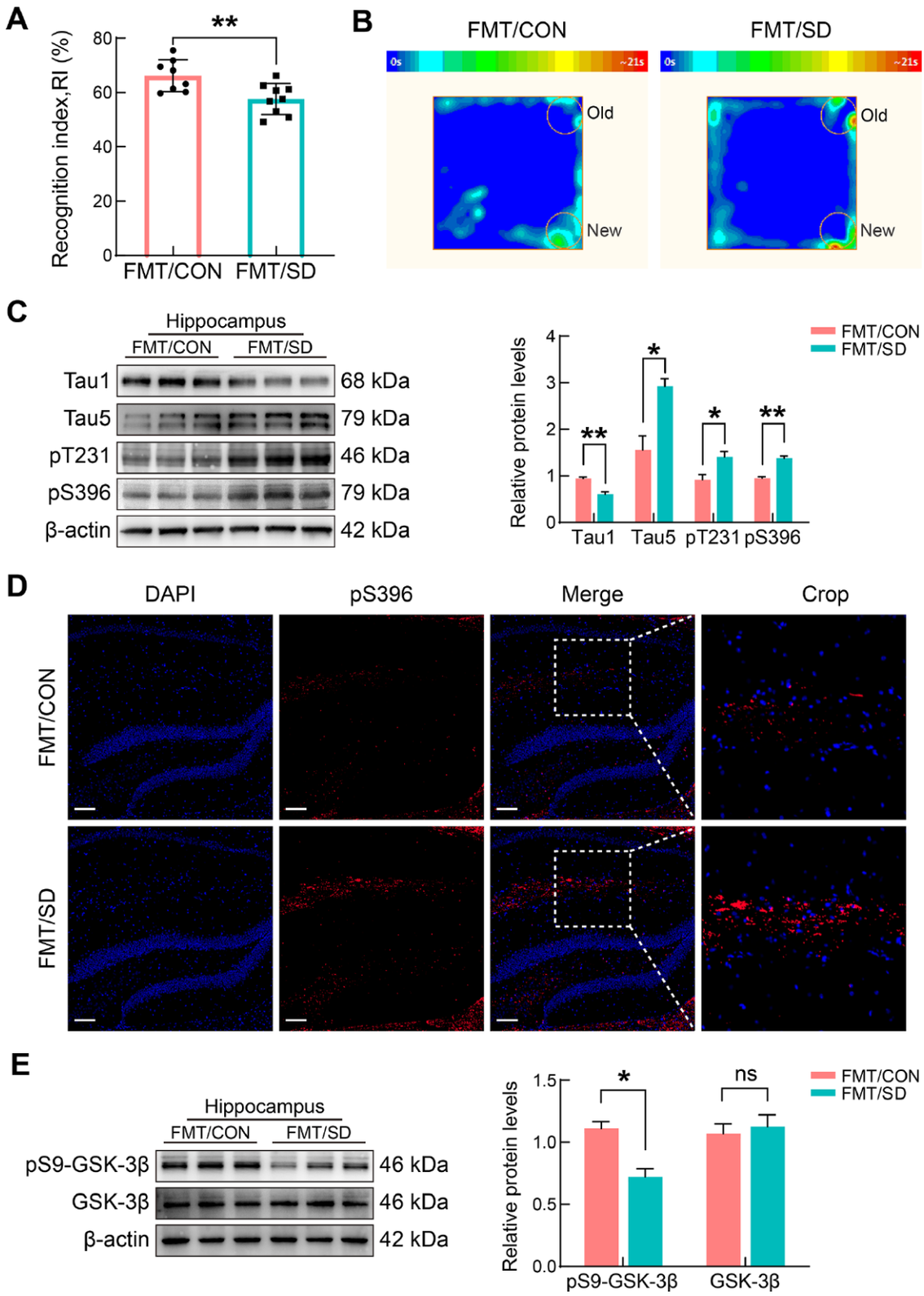



**Figure 4 SD microbiota transplantation impaired cognitive function, increased tau phosphorylation, and activated GSK-3β**

A, B: Recognition index (A) and map of trajectory (B) in the novel object recognition test. C: Protein levels of Tau-1, Tau-5, pS396-tau, and pT231-tau were determined by western blotting in hippocampus of chronic SD microbiota recipient mice and control microbiota recipient mice. D: Representative immunofluorescence staining against pS396-tau was performed on hippocampal regions (CA1, CA3, and DG). Magnification ×10, Scale bar: 100 μm. E: Protein levels of p-GSK-3β (Ser9) and total GSK-3β were determined by western blotting in hippocampus of chronic SD microbiota recipient mice and controls. All data are expressed as mean±SEM. A, B: FMT/CON $n$=8 mice/group; FMT/SD $n$=9 mice/group. C–E: $n$=3 mice/group. β-actin was used as the loading control in western blot analysis. Data were considered significant at $^{*}$: $P$<0.05, $^{**}$: $P$<0.01, $^{***}$: $P$<0.001, $^{****}$: $P$<0.0001 by Student's $t$-test. ns: Not significant. FMT-SD: Fecal microbiota transplantation (FMT) of chronic sleep-deprived mice; FMT-CON: Fecal microbiota transplantation (FMT) of control normal sleep mice.

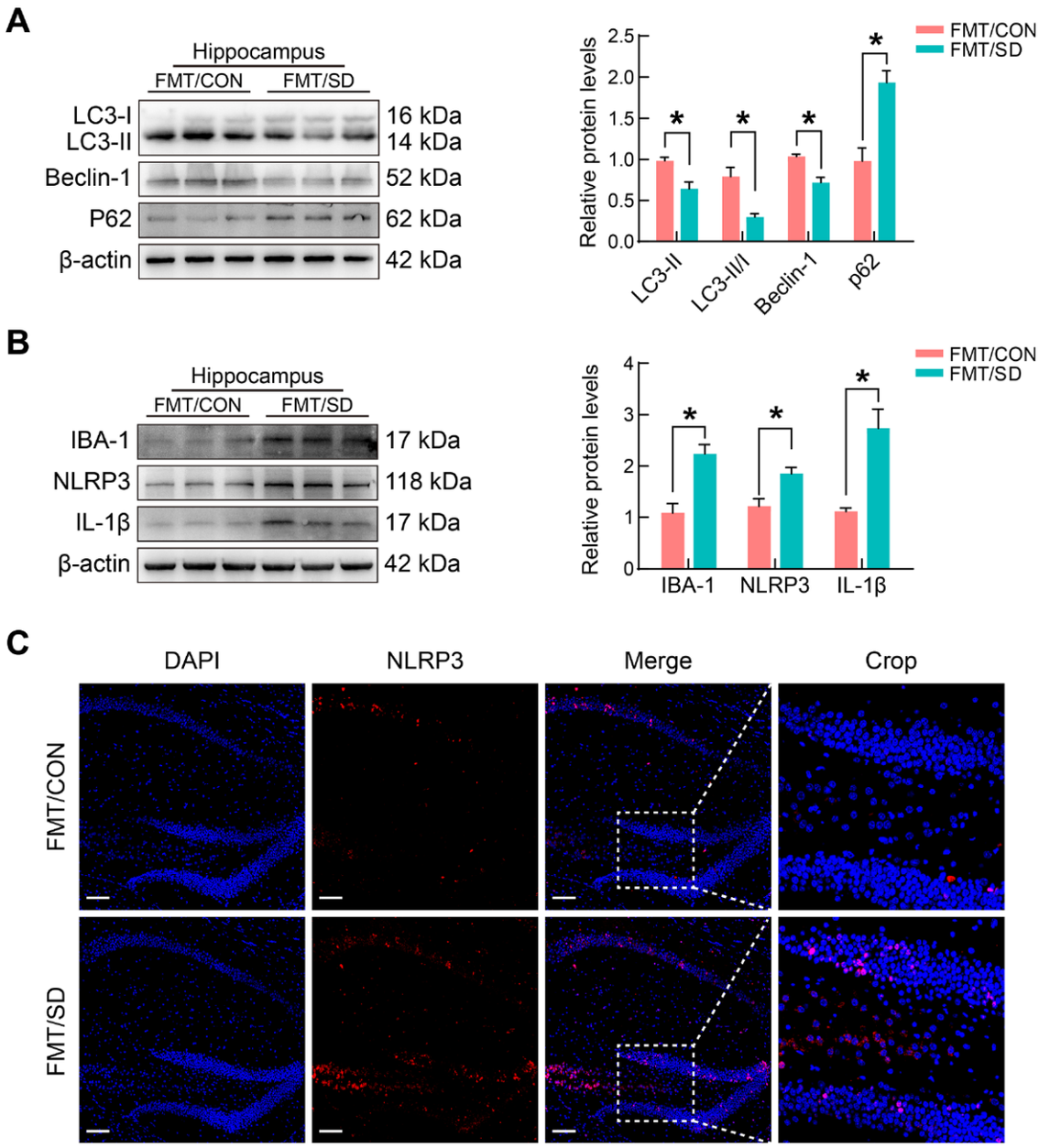
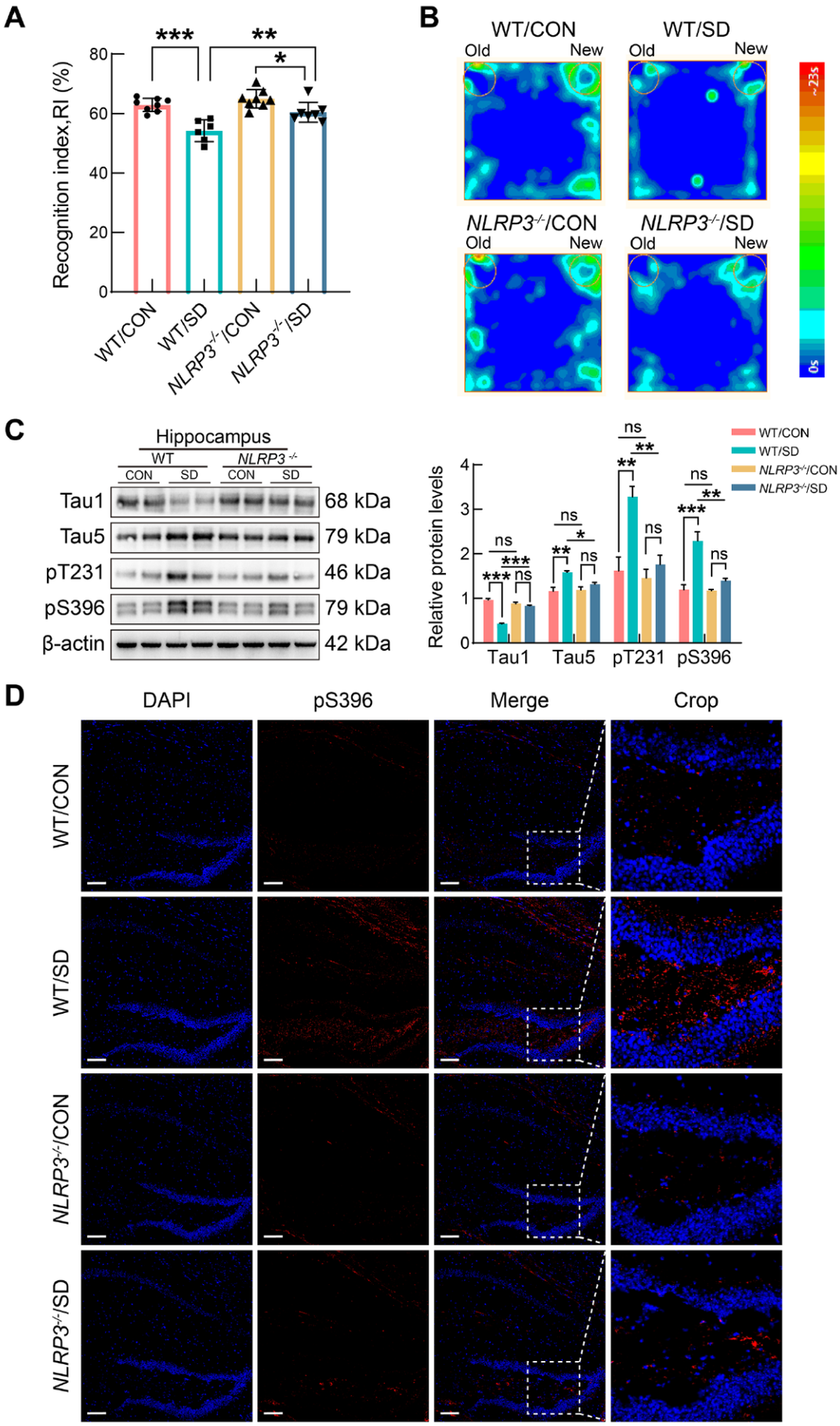



**Figure 5 SD microbiota transplantation inhibited autophagic flux and enhanced NLRP3 inflammasome activity**

A: Protein levels of Beclin-1, LC3-II, SQSTM1/p62, and the LC3-II/LC3-I ratio were determined by western blotting in hippocampus of chronic SD microbiota recipient mice and control microbiota recipient mice. B: Protein levels of IBA-1, NLRP3, and IL-1β were determined by western blotting in hippocampus of chronic SD microbiota recipient mice and controls. C: Representative immunofluorescence staining against NLRP3 was performed on hippocampal regions (CA1, CA3, and DG). Magnification ×10, Scale bar: 100 μm. All data are expressed as mean±SEM. *n*=3 mice/group. β-actin was used as the loading control in western blot analysis. Data were considered significant at *: $P<0.05$, **: $P<0.01$, ***: $P<0.001$, ****: $P<0.0001$ by Student's *t*-test. ns: Not significant. FMT-SD: Fecal microbiota transplantation (FMT) of chronic sleep-deprived mice; FMT-CON: Fecal microbiota transplantation (FMT) of control normal sleep mice.

in WT mice but not in *NLRP3*$^{-/-}$ mice. Chronic SD resulted in an obvious decline in the RI, which improved by NLRP3 inflammasome deficiency ($F_{(3,25)}$=15.191, $P$<0.0001; WT/CON vs. WT/SD: $P$=0.0001; *NLRP3*$^{-/-}$/CON vs. *NLRP3*$^{-/-}$/SD: $P$=0.0424; WT/CON vs. *NLRP3*$^{-/-}$/CON: $P$=0.5513; WT/SD vs. *NLRP3*$^{-/-}$/SD: $P$=0.0064, Figure 6A, B). Correspondingly, chronic SD decreased the level of Tau-1 and elevated the levels of pT231-tau, pS396-tau, and Tau-5 in the hippocampus of WT mice, which were not observed in the hippocampus of *NLRP3*$^{-/-}$ mice (Tau-1: $F_{(3,8)}$=31.399, $P$<0.0001; WT/CON vs. WT/SD: $P$=0.0002; *NLRP3*$^{-/-}$/CON vs. *NLRP3*$^{-/-}$/SD: $P$=0.7797; WT/CON vs. *NLRP3*$^{-/-}$/CON: $P$=0.9999; WT/SD vs. *NLRP3*$^{-/-}$/SD: $P$=0.0004, Tau-5: $F_{(3,8)}$=12.070, $P$=0.0024; WT/CON vs. WT/SD: $P$=0.0036; *NLRP3*$^{-/-}$/CON vs. *NLRP3*$^{-/-}$/SD: $P$=0.4571; WT/CON vs. *NLRP3*$^{-/-}$/CON: $P$=0.9768; WT/SD vs. *NLRP3*$^{-/-}$/SD: $P$=0.0453, pT231: $F_{(3,8)}$=12.048, $P$=0.0025; WT/CON vs. WT/SD: $P$=0.0056; *NLRP3*$^{-/-}$/CON vs. *NLRP3*$^{-/-}$/SD: $P$=0.8212; WT/CON vs. *NLRP3*$^{-/-}$/CON: $P$=0.9661; WT/SD vs. *NLRP3*$^{-/-}$/SD: $P$=0.0094, pS396: $F_{(3,8)}$=19.367, $P$=0.0005; WT/CON vs. WT/SD: $P$=0.0009; *NLRP3*$^{-/-}$/CON vs. *NLRP3*$^{-/-}$/SD: $P$=0.5685; WT/CON vs. *NLRP3*$^{-/-}$/CON: $P$=0.9988; WT/SD vs. *NLRP3*$^{-/-}$/SD: $P$=0.0034, Figure 6C, D). In contrast to WT mice, no significant differences in the expression levels of LC3-II,


A
Recognition index,RI (%)
WT/CON
WT/SD
NLRP3-/-/CON
NLRP3-/-/SD
B
WT/CON
WT/SD
NLRP3-/-/CON
NLRP3-/-/SD
Old
New
~23s
0s
C
Hippocampus
WT
NLRP3-/-
CON
SD
Tau1
Tau5
pT231
pS396
β-actin
68 kDa
79 kDa
46 kDa
79 kDa
42 kDa
Relative protein levels
D
DAPI
pS396
Merge
Crop

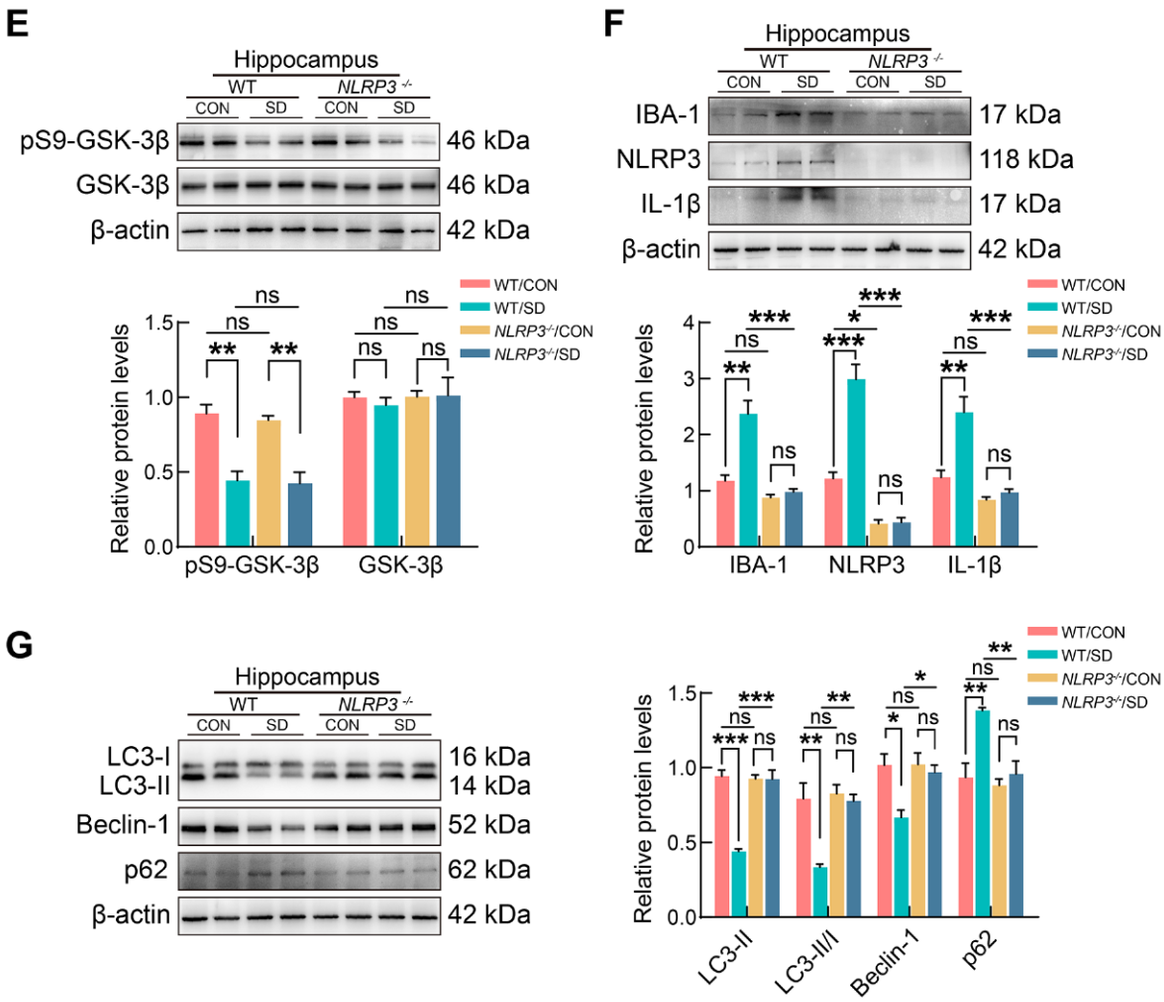



**Figure 6 Behavioral and pathological changes induced by chronic SD were reversed in *NLRP3*$^{-/-}$ mice**

A, B: Recognition index (A) and trajectory map (B) of WT/CON, WT/SD, *NLRP3*$^{-/-}$/CON, and *NLRP3*$^{-/-}$/SD mice in novel object recognition test. C: Protein levels of Tau-1, Tau-5, pS396-tau, and pT231-tau were determined by western blotting in hippocampus of WT/CON, WT/SD, *NLRP3*$^{-/-}$/CON, and *NLRP3*$^{-/-}$/SD mice. D: Representative immunofluorescence staining against pS396-tau was performed on hippocampal regions (CA1, CA3, and DG). Magnification ×10, Scale bar: 100 μm. E: Protein levels of p-GSK-3β (Ser9) and total GSK-3β were determined by western blotting in hippocampus. F: Protein levels of IBA-1, NLRP3, and IL-1β were determined by western blotting in hippocampus. G: Protein levels of Beclin-1, LC3-II, SQSTM1/p62, and LC3-II/LC3-I ratio were determined by western blotting in hippocampus. All data are expressed as mean±SEM. A, B: WT/CON $n$=8 mice/group; WT/SD $n$=6 mice/group; *NLRP3*$^{-/-}$/CON $n$=8 mice/group; *NLRP3*$^{-/-}$/SD $n$=7 mice/group. C–G: $n$=3 mice/group. β-actin was used as loading control in western blot analysis. Data were considered significant at $^{*}$: $P$<0.05, $^{**}$: $P$<0.01, $^{***}$: $P$<0.001, $^{****}$: $P$<0.0001. ns: Not significant. Means were compared using one-way ANOVA with Tukey's *post hoc* test. WT/CON: Normal sleep wild-type mice; WT/SD: Chronic sleep-deprived wild-type mice; *NLRP3*$^{-/-}$/CON: Normal sleep NLRP3 knockout mice; *NLRP3*$^{-/-}$/SD: Chronic sleep-deprived NLRP3 knockout mice.

Beclin-1, and SQSTM1/p62, or the ratio of LC3-II/LC3-I, were found in the hippocampus of *NLRP3*$^{-/-}$ mice following exposure to chronic SD (LC3-II: $F_{(3,8)}$=39.800, $P$<0.0001; WT/CON vs. WT/SD: $P$=0.0001; *NLRP3*$^{-/-}$/CON vs. *NLRP3*$^{-/-}$/SD: $P$>0.9999; WT/CON vs. *NLRP3*$^{-/-}$/CON: $P$=0.9887; WT/SD vs. *NLRP3*$^{-/-}$/SD: $P$=0.0001, LC3-II/I: $F_{(3,8)}$=13.451, $P$=0.0017; WT/CON vs. WT/SD: $P$=0.0041; *NLRP3*$^{-/-}$/CON vs. *NLRP3*$^{-/-}$/SD: $P$=0.9461; WT/CON vs. *NLRP3*$^{-/-}$/CON: $P$=0.9801; WT/SD vs. *NLRP3*$^{-/-}$/SD: $P$=0.0050, Beclin-1: $F_{(3,8)}$=5.130, $P$=0.0287; WT/CON vs. WT/SD: $P$=0.0192; *NLRP3*$^{-/-}$/CON vs. *NLRP3*$^{-/-}$/SD: $P$=0.9303; WT/CON vs. *NLRP3*$^{-/-}$/CON: $P$>0.9999; WT/SD vs. *NLRP3*$^{-/-}$/SD: $P$=0.0408, p62: $F_{(3,8)}$=11.600, $P$=0.0028; WT/CON vs. WT/SD: $P$=0.0069; *NLRP3*$^{-/-}$/CON vs. *NLRP3*$^{-/-}$/SD: $P$=0.8559; WT/CON vs. *NLRP3*$^{-/-}$/CON: $P$=0.9468; WT/SD vs. *NLRP3*$^{-/-}$/SD: $P$=0.0095, Figure 6G). Interestingly, the down-regulation of phosphorylated GSK-3β at the Ser9 site induced by chronic SD, which was observed in WT mice, reappeared in *NLRP3*$^{-/-}$ mice, suggesting that deletion of NLRP3 did not influence GSK-3β activation due to chronic SD (pS9-GSK-3β: $F_{(3,8)}$=19.091, $P$=0.0005; WT/CON vs. WT/SD: $P$=0.0026; *NLRP3*$^{-/-}$/CON vs. *NLRP3*$^{-/-}$/SD: $P$=0.0038; WT/CON vs. *NLRP3*$^{-/-}$/CON: $P$=0.9425; WT/SD vs. *NLRP3*$^{-/-}$/SD: $P$=0.9953, Figure 6E). In addition, chronic SD had no effect on the expression level of total GSK-3β in either WT or *NLRP3*$^{-/-}$ mice (t-GSK-3β: $F_{(3,8)}$=0.183, $P$=0.9051; WT/CON vs. WT/SD: $P$=0.9455; *NLRP3*$^{-/-}$/CON vs. *NLRP3*$^{-/-}$/SD: $P$=0.9999; WT/CON vs. *NLRP3*$^{-/-}$/CON: $P$>0.9999; WT/SD vs. *NLRP3*$^{-/-}$/SD: $P$=0.9093, Figure 6E).

**Knockdown of NLRP3 in the hippocampus restored autophagic flux, suppressed tau hyperphosphorylation, and ameliorated cognitive deficits in chronic SD mice**

To investigate the role of the NLRP3 inflammasome in the

brains of chronic SD mice, AAV-NLRP3 was stereotaxically microinjected into the hippocampus to achieve regional knockdown of NLRP3 expression.

Chronic SD mice injected with AAV-NLRP3 exhibited lower levels of IL-1β, NLRP3, and IBA-1 expression in the hippocampus than the chronic SD mice injected with AAV-GFP (IBA-1: $t_4$=7.323, $P$=0.0018; NLRP3: $t_4$=5.793, $P$=0.0044; IL-1β: $t_4$=8.199, $P$=0.0012, Figure 7A). Notably, a marked increase in the levels of Beclin-1, LC3-II, and the LC3-II/LC3-I ratio and a marked decrease in the level of SQSTM1/p62 were observed in the hippocampus of chronic SD mice injected with AAV-NLRP3 (Beclin-1: $t_4$=6.778, $P$=0.0025; LC3-II: $t_4$=5.719, $P$=0.0046; LC3-II/I: $t_4$=3.265, $P$=0.0309; p62: $t_4$=3.159, $P$=0.0342, Figure 7C). However, no differences were observed in the levels of phosphorylated GSK-3β at the Ser9 site and total GSK-3β between the chronic SD mice injected with AAV-NLRP3 and AAV-GFP, suggesting that hippocampal knockdown of NLRP3 had no influence on GSK-3β activity in chronic SD (pS9-GSK-3β: $t_4$=0.663, $P$=0.5436; t-GSK-3β: $t_4$=0.3517, $P$=0.7428, Figure 7B). Interestingly, AAV-NLRP3 microinjection significantly inhibited the chronic SD-induced increase in the expression of pT231-tau, pS396-tau, and Tau-5 and decrease in the expression of Tau-1 in the hippocampus of mice (pT231: $t_4$=4.336, $P$=0.0123; pS396: $t_4$=6.042, $P$=0.0038; Tau-1: $t_4$=8.420, $P$=0.0011; Tau-5: $t_4$=6.846, $P$=0.0024, Figure 7D, E). In addition, chronic SD mice injected with AAV-NLRP3 performed better in the discrimination test between familiar and novel objects compared to the chronic SD mice injected with AAV-GFP, as reflected by the significant increase in RI ($t_{18}$=3.426, $P$=0.0030, Cohen's d=1.532, Figure 7F, G).

**Deletion of NLRP3 reversed NLRP3 inflammasome activation, autophagy deficits, and tau hyperphosphorylation caused by Akt inhibitor-induced activation of GSK-3β in primary hippocampal neurons**

To determine the suitable dose and duration of the Akt inhibitor MK-2206, primary hippocampal neurons were treated with MK-2206 (250 nmol/L, 500 nmol/L, and 750 nmol/L) or 0.1% dimethyl sulfoxide (DMSO) and collected after 12, 24, and 48 h. Following MK-2206 treatment, a dose-dependent decrease was observed in the phosphorylation of the Akt downstream target GSK-3β (Ser9) at multiple time points (Figure 8A). A MK-2206 concentration of 250 nmol/L for 48 h was applied to treat primary hippocampal neurons derived from *NLRP3*$^{-/-}$ and WT mice in the following experiments.

The Akt inhibitor MK-2206 contributed to the pronounced activation of GSK-3β in primary hippocampal neurons, whether derived from *NLRP3*$^{-/-}$ or WT mice, as confirmed by the reduction in GSK-3β (Ser9) phosphorylation (pS9-GSK-3β: $F_{(3,8)}$=31.740, $P$<0.0001; t-GSK-3β: $F_{(3,8)}$=0.436, $P$=0.7335, Figure 8B). We next investigated the impact of MK-2206 treatment on the NLRP3 inflammasome. Of note, western blot analysis indicated that the NLRP3 and IL-1β protein expression levels were increased in the primary hippocampal neurons derived from WT mice after MK-2206 treatment, but were absent in the primary hippocampal neurons derived from *NLRP3*$^{-/-}$ mice, whether treated with vehicle or MK-2206 (NLRP3: $F_{(3,8)}$=46.752, $P$<0.0001; IL-1β: $F_{(3,8)}$=31.813, $P$=0.0004, Figure 8C). MK-2206 administration down-regulated the Beclin-1 and LC3-II protein expression levels, as well as the LC3-II/LC3-I ratio, and up-regulated the SQSTM1/p62 expression level in the primary hippocampal neurons derived from WT mice, with these effects inhibited in the primary hippocampal neurons derived from *NLRP3*$^{-/-}$ mice (LC3-II: $F_{(3,8)}$=19.462, $P$=0.0005; LC3-II/I: $F_{(3,8)}$=15.534, $P$=0.0011; Beclin-1: $F_{(3,8)}$=9.586, $P$=0.0050; p62: $F_{(3,8)}$=7.727, $P$=0.0095, Figure 8D). In addition, increased pT231-tau, pS396-tau, and Tau-5 expression and decreased Tau-1 expression were observed in the primary hippocampal neurons derived from WT mice after MK-2206 treatment, but were not found in the primary hippocampal neurons derived from *NLRP3*$^{-/-}$ mice (Tau-1: $F_{(3,8)}$=8.774, $P$=0.0065; Tau-5: $F_{(3,8)}$=8.656, $P$=0.0068; pT231: $F_{(3,8)}$=7.225, $P$=0.0115; pS396: $F_{(3,8)}$=6.263, $P$=0.0171, Figure 8E, F).

In summary, these results indicate that GSK-3β activation, induced by an Akt inhibitor, contributed to NLRP3 inflammasome activation, autophagy inhibition, and tau hyperphosphorylation in the primary hippocampal neurons derived from WT mice. However, those phenomena were reversed in the primary hippocampal neurons derived from *NLRP3*$^{-/-}$ mice.

## DISCUSSION

Sleep is essential for maintaining homeostasis of the central nervous system. During sleep, the brain clears metabolic waste, processes information, and consolidates memories, allowing for optimal cognitive function (Fultz et al., 2019). Conversely, SD has been shown to impair cognitive function and heighten the risk of neurological disorders, such as AD. At present, however, the potential mechanisms linking SD to cognitive impairment remain poorly understood. In this study, we found that the gut microbiota composition in chronic SD mice differed markedly from that in WT controls. Specifically, gut microbiota derived from chronic SD mice exhibited significant alterations in the phyla Firmicutes, Bacteroidetes, and Proteobacteria, as well as in the genera *Lactobacillus* and *Odoribacter*. The Firmicutes-to-Bacteroidetes ratio, a key indicator of gut microbiota dysbiosis (Yang et al., 2015), was significantly reduced in chronic SD mice, similar to findings in the gut microbiota of AD mice and patients (Harach et al., 2017; Vogt et al., 2017), suggesting that an increased relative abundance of Bacteroidetes and a decreased relative abundance of Firmicutes may link chronic SD with AD. In addition, tau hyperphosphorylation and cognitive impairment were also observed in chronic SD mice. Interestingly, transferring gut microbiota derived from chronic SD mice led to tau aggregation and hyperphosphorylation and cognitive impairment in recipient mice. These findings indicate that the detrimental effects of chronic SD can be transmitted via gut microbiota, suggesting that changes in gut microbiota composition are secondary to chronic SD and play a direct pathogenetic role in tau hyperphosphorylation and cognitive impairment.

Tau is a microtubule-associated protein that promotes microtubule assembly and stability (Weingarten et al., 1975). Evidence indicates that overexpression of phosphorylated tau can damage neuronal synaptic plasticity and cause memory deficits (Li et al., 2019; Yin et al., 2016). In this study, phosphorylated tau at multiple sites, including Thr231 and Ser396, was markedly up-regulated and non-phosphorylated tau (Tau-1) was significantly down-regulated in the hippocampus of chronic SD mice. The aberrant aggregation of hyperphosphorylated tau can be attributed to two main factors: overexpression of tau kinases, especially GSK-3β, and disruption of tau clearance. Various studies on tau

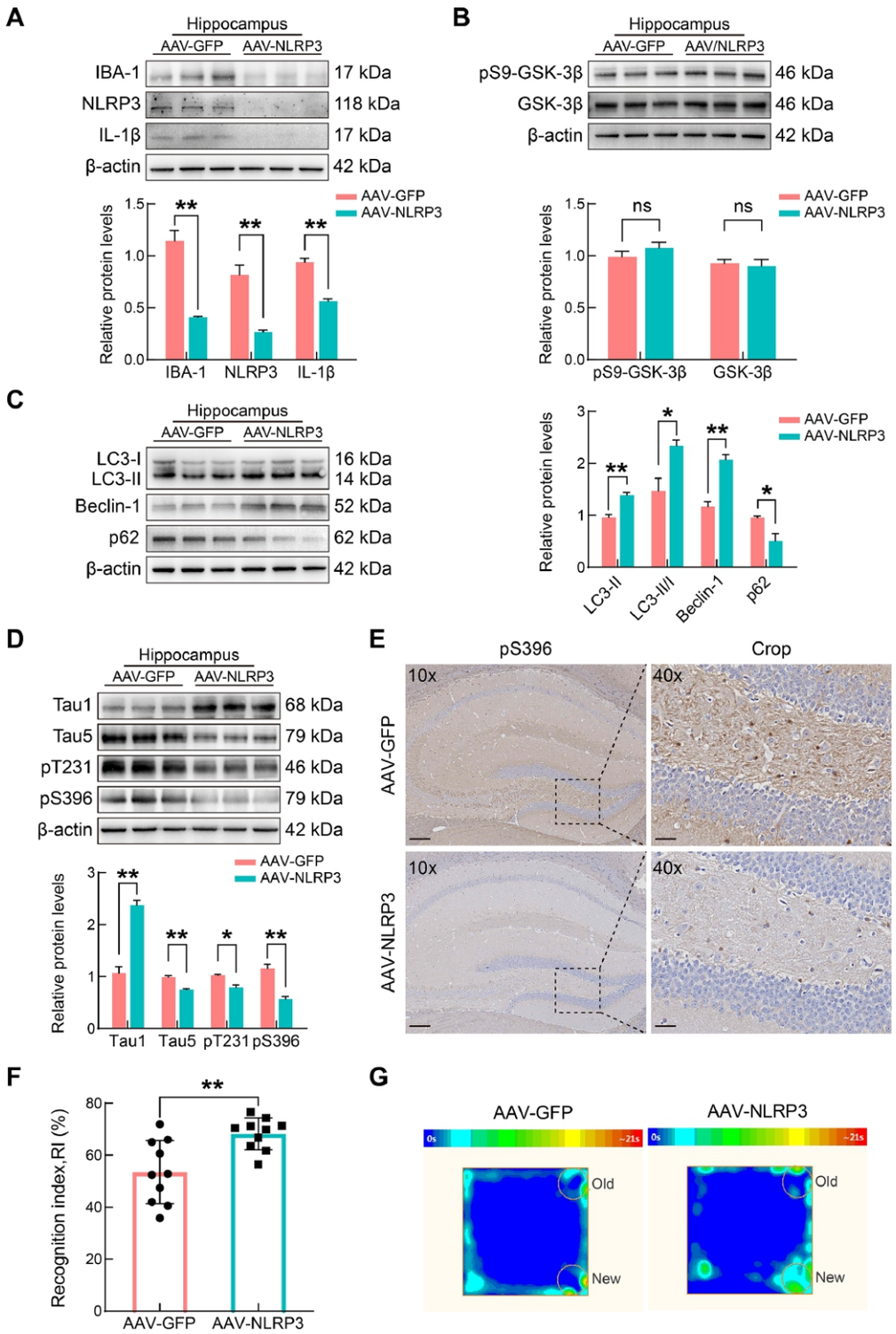



**Figure 7 Knockdown of NLRP3 in the hippocampus restored autophagic flux, suppressed tau hyperphosphorylation, and ameliorated cognitive deficits**

A: Protein levels of IBA-1, NLRP3, and IL-1β were determined by western blotting in hippocampus of chronic SD mice injected with AAV-GFP and chronic SD mice injected with AAV-NLRP3. B: Protein levels of p-GSK-3β (Ser9) and total GSK-3β were determined by western blotting in hippocampus of AAV-GFP and AAV-NLRP3 mice. C: Protein levels of Beclin-1, LC3-II, SQSTM1/p62, and LC3-II/LC3-I ratio were determined by western blotting in hippocampus of AAV-GFP and AAV-NLRP3 mice. D: Protein levels of Tau-1, Tau-5, pS396-tau, and pT231-tau were determined by western blotting in hippocampus of AAV-GFP and AAV-NLRP3 mice. E: Representative immunohistochemical staining against pS396-tau were performed on hippocampal regions (CA1, CA3, and DG). Magnification ×10, Scale bar: 100 μm. Magnification ×40, Scale bar: 25 μm. F, G: Recognition index (F) and trajectory map (G) of AAV-GFP and AAV-NLRP3 mice in novel object recognition test. All data are expressed as mean±SEM. A–E: $n$=3 mice/group. F, G: $n$=10 mice/group. β-actin was used as loading control in western blot analysis. Data are considered significant at $^{*}$: $P$<0.05, $^{**}$: $P$<0.01, $^{***}$: $P$<0.001, $^{****}$: $P$<0.0001. ns: Not significant. Means were compared using Student's $t$-test. AAV-GFP: Chronic sleep-deprived mice injected with AAV-GFP; AAV-NLRP3: Chronic sleep-deprived mice injected with AAV-NLRP3.

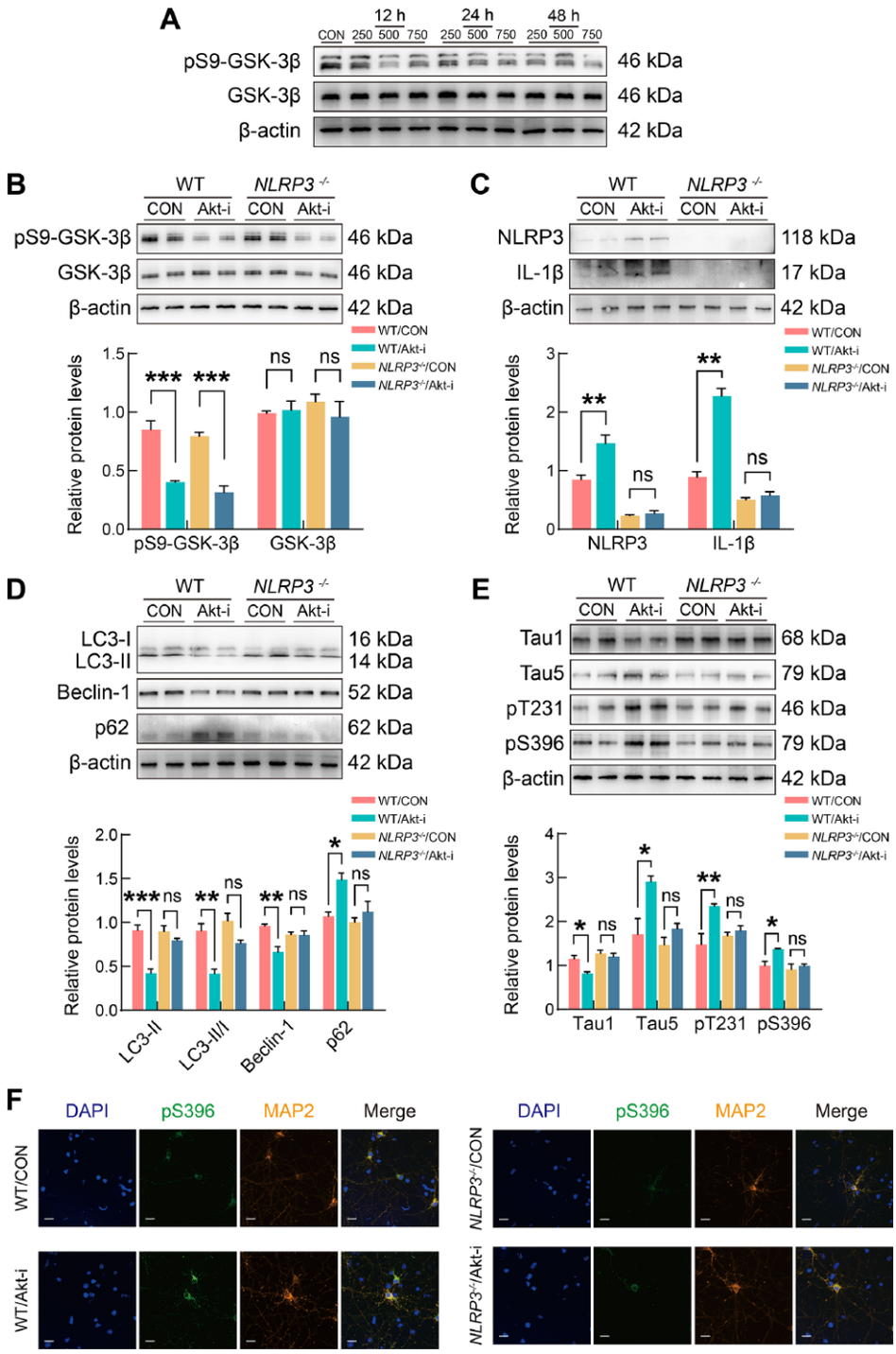



**Figure 8 Deletion of NLRP3 reversed NLRP3 inflammasome activation, autophagy deficits, and tau hyperphosphorylation caused by Akt inhibitor-induced activation of GSK-3β in primary hippocampal neurons**

A: Primary hippocampal neurons were treated with Akt inhibitor MK-2206 (250 nmol/L, 500 nmol/L, and 750 nmol/L) or 0.1% dimethyl sulfoxide (DMSO) and collected after 12, 24, and 48 h. Western blotting was conducted to assess expression levels of p-GSK-3β (Ser9) and total GSK-3β. B: Protein levels of p-GSK-3β (Ser9) and total GSK-3β were determined by western blotting in primary hippocampal neurons obtained from WT and *NLRP3*$^{-/-}$ mice with or without Akt inhibitor treatment. C: Protein levels of IBA-1, NLRP3, and IL-1β were determined by western blotting in four groups. D: Protein levels of Beclin-1, LC3-II, SQSTM1/p62, and LC3-II/LC3-I ratio were determined by western blotting in four groups. E: Protein levels of Tau-1, Tau-5, pS396-tau, and pT231-tau were determined by western blotting in four groups. F: Representative immunofluorescence staining against pS396-tau was performed on primary hippocampal neurons. Magnification ×60, Scale bar: 20 μm. All data are expressed as mean±SEM. *n*=3 independent experiments for each group. β-actin was used as loading control in western blot analysis. Data are considered significant at $^{*}$: $P$<0.05, $^{**}$: $P$<0.01, $^{***}$: $P$<0.001, $^{****}$: $P$<0.0001. ns: Not significant. Means were compared using one-way ANOVA with Tukey's *post hoc* test. WT/CON: Primary hippocampal neurons obtained from WT mice without Akt inhibitor treatment; WT/Akt-i: Primary hippocampal neurons obtained from WT mice with Akt inhibitor treatment; *NLRP3*$^{-/-}$/CON: Primary hippocampal neurons obtained from *NLRP3*$^{-/-}$ mice without Akt inhibitor treatment; *NLRP3*$^{-/-}$/Akt-i: Primary hippocampal neurons obtained from *NLRP3*$^{-/-}$ mice with Akt inhibitor treatment.

hyperphosphorylation have identified GSK-3β as a key kinase in tau hyperphosphorylation, as GSK-3β-mediated tau phosphorylation promotes toxic self-aggregation (L'episcopo et al., 2016; Martin et al., 2013). The autophagy-lysosome system is also a crucial mechanism for tau clearance. Both *in vitro* and *in vivo* findings have shown that inhibition of autophagic flux impedes tau clearance, leading to the aggregation of insoluble tau proteins (Hamano et al., 2021). Interestingly, chronic SD increased the level of total tau without affecting its mRNA level, suggesting that chronic SD disturbs tau clearance. We found that chronic SD inhibited autophagic flux and activated GSK-3β in the brain. Similarly, colonization with "SD microbiota" led to autophagy dysfunction and GSK-3β activation in the hippocampus of recipient mice. These findings suggest that GSK-3β activation and autophagy dysfunction are involved in gut microbiota dysbiosis-mediated tau pathology in chronic SD.

The gut microbiota produces a significant amount of harmful microbial products and metabolites, which trigger peripheral and central inflammatory responses (Blander et al., 2017). The NLRP3 inflammasome is considered an important signaling interface that mediates inflammation upon recognition of microbial or danger-associated molecular stimuli (Liao et al., 2019; Sendler et al., 2020). Activation of the NLRP3 inflammasome leads to the autocleavage and activation of caspase-1, which induces the maturation and release of IL-1β (Paik et al., 2021). IL-1β, a proinflammatory cytokine, is regulated by NLRP3 inflammasome activation, and its production is markedly inhibited in *NLRP3*$^{-/-}$ mice (Fujimura et al., 2023). When NLRP3/IL-1β signaling is inappropriately activated or overactivated, it creates a chronic inflammatory environment that drives the pathogenesis and progression of many diseases, including age-related diseases, Parkinson's disease, and AD. Overactivation of the NLRP3 inflammasome and subsequent secretion of IL-1β in microglia mediates neuroinflammation, which drives the hyperphosphorylation and aggregation of tau, accelerating AD progression (Ising et al., 2019). Thus, we hypothesize that the NLRP3 inflammasome is a crucial node linking gut microbiota dysbiosis to tau pathology and cognitive deficits in chronic SD. In this study, we found that chronic SD enhanced NLRP3 inflammasome activity. Similarly, colonization with "SD microbiota" led to the overexpression of the NLRP3 inflammasome. To investigate whether the NLRP3 inflammasome is a crucial node linking gut microbiota dysbiosis to tau pathology and cognitive impairment in chronic SD, we used *NLRP3*$^{-/-}$ mice. Results showed that, following chronic SD, cognitive function was significantly impaired in WT mice but not in *NLRP3*$^{-/-}$ mice. Additionally, autophagy dysfunction and tau hyperphosphorylation observed in WT mice following chronic SD were reversed in *NLRP3*$^{-/-}$ mice. Consistently, specific knockdown of NLRP3 in the hippocampus restored autophagic flux, suppressed tau hyperphosphorylation, and ameliorated cognitive deficits in chronic SD mice. These findings demonstrate that the NLRP3 inflammasome is a core regulator of autophagy, which, in turn, regulates the aggregation and phosphorylation of tau in cognitive deficits resulting from chronic SD. Taken together, these results indicate that alterations in gut microbiota exposed to chronic SD can lead to tau aggregation and hyperphosphorylation primarily by triggering NLRP3-mediated autophagy dysfunction, ultimately causing cognitive impairment.

Interestingly, the deletion of NLRP3 in *NLRP3*$^{-/-}$ mice and the regional knockdown of NLRP3 in the hippocampus had no effect on GSK-3β activation due to chronic SD, suggesting that GSK-3β activity is not regulated by the NLRP3 inflammasome under chronic SD conditions. Recent evidence has highlighted the role of GSK-3β as a regulator of adaptive and innate immune responses (Beurel et al., 2010). GSK-3β modulates the Toll-like receptor-mediated inflammatory response and differentially regulates the production of pro-inflammatory and anti-inflammatory cytokines (Martin et al., 2005; Rehani et al., 2009). Furthermore, GSK-3β activation promotes the migration and activation of microglia and astrocytes, with its up-regulation in these cells increasing several proinflammatory cytokines, including IL-1, IL-6, and tumor necrosis factor α (TNF-α) (Beurel & Jope, 2009; Renault-Mihara et al., 2011; Wang et al., 2010). In addition, accumulating evidence indicates that GSK-3β may be involved in NLRP3 inflammasome activation in various diseases, including lupus nephritis, myocardial infarction, and cerebral ischemia/reperfusion injury (Arumugam et al., 2022; Wang et al., 2020, 2022). This suggests that GSK-3β may be the upstream regulator of the NLRP3 inflammasome, triggering its activation in chronic SD. To explore the potential connections between GSK-3β and the NLRP3 inflammasome, we treated primary hippocampal neurons derived from WT and *NLRP3*$^{-/-}$ mice with the Akt inhibitor MK-2206. The serine/threonine kinase Akt, also known as protein kinase B (PKB), is a central node in many signaling pathways and modulates the function of many downstream proteins (Tsai et al., 2022). GSK-3β is a critical downstream target of Akt. When Akt is activated, it phosphorylates GSK-3β at the Ser9 site, resulting in GSK-3β inhibition (Manning & Toker, 2017). Given the lack of a direct GSK-3β agonist, we used the Akt inhibitor MK-2206 to achieve GSK-3β activation. As expected, MK-2206 administration down-regulated the phosphorylation of GSK-3β (Ser9), resulting in its activation. GSK-3β activation via Akt inhibition contributed to NLRP3 inflammasome activation, autophagy inhibition, and tau hyperphosphorylation in primary hippocampal neurons derived from WT mice. However, those effects were reversed in primary hippocampal neurons derived from *NLRP3*$^{-/-}$ mice. These findings indicate that GSK-3β is not only a tau kinase but also a regulator of the NLRP3 inflammasome, triggering its activation under chronic SD conditions. GSK-3β also acts as a tau kinase and regulator of NLRP3-mediated autophagy dysfunction, co-promoting tau hyperphosphorylation. Although GSK-3β remained activated, the improved autophagy induced by NLRP3 deficiency was sufficient to suppress tau hyperphosphorylation. Thus, GSK-3β plays a significant role in promoting tau hyperphosphorylation and aggregation by regulating NLRP3-mediated autophagy dysfunction.

In summary, chronic SD leads to gut microbiota dysbiosis, which subsequently triggers GSK-3β activation in the brain. Activated GSK-3β functions as both a tau kinase and a regulator of NLRP3-mediated autophagy dysfunction, promoting tau hyperphosphorylation and aggregation, ultimately resulting in cognitive impairment. To the best of our knowledge, this study is the first to identify gut microbiota dysbiosis as a key driver of tau pathology via NLRP3-mediated autophagy dysfunction in chronic SD, contributing to cognitive deficits. Future research should explore intervention strategies targeting gut microbiota composition, NLRP3 inflammasome activation, and tau pathology to mitigate the

detrimental consequences of chronic SD. Our study highlights the role of GSK-3β as a regulator of NLRP3-mediated autophagy dysfunction, which promotes tau hyperphosphorylation and aggregation.

This study also has some limitations. First, we only investigated the effects of chronic SD on gut microbiota using animal models. However, it would be beneficial to include human subjects for clinical validation. Additionally, while our research focused on the molecular mechanisms in the brain regulated by gut microbiota dysbiosis in chronic SD, we did not examine the peripheral pathways through which gut microbiota affects the brain, which warrants further investigation.

## SUPPLEMENTARY DATA

Supplementary data to this article can be found online.

## COMPETING INTERESTS

The authors declare that they have no competing interests.

## AUTHORS' CONTRIBUTIONS

N.Z. designed the research, conducted the experiments, acquired and analyzed the data, and wrote the manuscript. X.C. conducted the experiments and acquired and analyzed the data. Q.G.C. conducted the experiments. X.T.L. and F.G. analyzed the data. M.M.Z. acquired the reagents. F.L.Y. and Z.J.Z. reviewed the manuscript. Q.G.R designed the research and reviewed the manuscript. All authors read and approved the final version of the manuscript.

## ACKNOWLEDGMENTS

We thank Hai-Long Zhao for technical support.

## REFERENCES

Agirman G, Yu KB, Hsiao EY. 2021. Signaling inflammation across the gut-brain axis. *Science*, **374**(6571): 1087–1092.

Arumugam S, Qin YQ, Liang ZW, et al. 2022. GSK3β mediates the spatiotemporal dynamics of NLRP3 inflammasome activation. *Cell Death & Differentiation*, **29**(10): 2060–2069.

Avila J, Lucas JJ, Pérez M, et al. 2004. Role of tau protein in both physiological and pathological conditions. *Physiological Reviews*, **84**(2): 361–384.

Barthélemy NR, Liu HY, Lu W, et al. 2020. Sleep deprivation affects tau phosphorylation in human cerebrospinal fluid. *Annals of Neurology*, **87**(5): 700–709.

Benedict C, Vogel H, Jonas W, et al. 2016. Gut microbiota and glucometabolic alterations in response to recurrent partial sleep deprivation in normal-weight young individuals. *Molecular Metabolism*, **5**(12): 1175–1186.

Beurel E, Jope RS. 2009. Lipopolysaccharide-induced interleukin-6 production is controlled by glycogen synthase kinase-3 and STAT3 in the brain. *Journal of Neuroinflammation*, **6**: 9.

Beurel E, Michalek SM, Jope RS. 2010. Innate and adaptive immune responses regulated by glycogen synthase kinase-3 (GSK3). *Trends in Immunology*, **31**(1): 24–31.

Biasizzo M, Kopitar-Jerala N. 2020. Interplay between NLRP3 inflammasome and autophagy. *Frontiers in Immunology*, **11**: 591803.

Blander JM, Longman RS, Iliev ID, et al. 2017. Regulation of inflammation by microbiota interactions with the host. *Nature Immunology*, **18**(8): 851–860.

Bowers SJ, Vargas F, González A, et al. 2020. Repeated sleep disruption in mice leads to persistent shifts in the fecal microbiome and metabolome. *PLoS One*, **15**(2): e0229001.

Cosin-Roger J, Simmen S, Melhem H, et al. 2017. Hypoxia ameliorates intestinal inflammation through NLRP3/mTOR downregulation and autophagy activation. *Nature Communications*, **8**(1): 98.

Cryan JF, O'riordan KJ, Cowan CSM, et al. 2019. The microbiota-gut-brain axis. *Physiological Reviews*, **99**(4): 1877–2013.

Donlea JM. 2019. Roles for sleep in memory: insights from the fly. *Current Opinion in Neurobiology*, **54**: 120–126.

El Aidy S, Bolsius YG, Raven F, et al. 2020. A brief period of sleep deprivation leads to subtle changes in mouse gut microbiota. *Journal of Sleep Research*, **29**(6): e12920.

Feng YS, Tan ZX, Wu LY, et al. 2020. The involvement of NLRP3 inflammasome in the treatment of Alzheimer's disease. *Ageing Research Reviews*, **64**: 101192.

Fujimura K, Karasawa T, Komada T, et al. 2023. NLRP3 inflammasome-driven IL-1β and IL-18 contribute to lipopolysaccharide-induced septic cardiomyopathy. *Journal of Molecular and Cellular Cardiology*, **180**: 58–68.

Fultz NE, Bonmassar G, Setsompop K, et al. 2019. Coupled electrophysiological, hemodynamic, and cerebrospinal fluid oscillations in human sleep. *Science*, **366**(6465): 628–631.

Hamano T, Enomoto S, Shirafuji N, et al. 2021. Autophagy and Tau protein. *International Journal of Molecular Sciences*, **22**(14): 7475.

Hamano T, Gendron TF, Causevic E, et al. 2008. Autophagic-lysosomal perturbation enhances tau aggregation in transfectants with induced wild-type tau expression. *European Journal of Neuroscience*, **27**(5): 1119–1130.

Harach T, Marungruang N, Duthilleul N, et al. 2017. Reduction of Abeta amyloid pathology in APPPS1 transgenic mice in the absence of gut microbiota. *Scientific Reports*, **7**: 41802.

Holth JK, Fritschi SK, Wang C, et al. 2019. The sleep-wake cycle regulates brain interstitial fluid tau in mice and CSF tau in humans. *Science*, **363**(6429): 880–884.

Ising C, Venegas C, Zhang SS, et al. 2019. NLRP3 inflammasome activation drives tau pathology. *Nature*, **575**(7784): 669–673.

Kaushik S, Cuervo AM. 2015. Proteostasis and aging. *Nature Medicine*, **21**(12): 1406–1415.

Kim MS, Kim Y, Choi H, et al. 2020. Transfer of a healthy microbiota reduces amyloid and tau pathology in an Alzheimer's disease animal model. *Gut*, **69**(2): 283–294.

Krueger JM, Frank MG, Wisor JP, et al. 2016. Sleep function: toward elucidating an enigma. *Sleep Medicine Reviews*, **28**: 46–54.

Lachance V, Wang Q, Sweet E, et al. 2019. Autophagy protein NRBF2 has reduced expression in Alzheimer's brains and modulates memory and amyloid-beta homeostasis in mice. *Molecular Neurodegeneration*, **14**(1): 43.

L'episcopo F, Drouin-Ouellet J, Tirolo C, et al. 2016. GSK-3*β*-induced Tau pathology drives hippocampal neuronal cell death in Huntington's disease: involvement of astrocyte-neuron interactions. *Cell Death & Disease*, **7**: e2206.

Levine B, Kroemer G. 2019. Biological functions of autophagy genes: a disease perspective. *Cell*, **176**(1-2): 11–42.

Li XG, Hong XY, Wang YL, et al. 2019. Tau accumulation triggers STAT1-dependent memory deficits by suppressing NMDA receptor expression. *EMBO Reports*, **20**(6): e47202.

Liao LJ, Schneider KM, Galvez EJC, et al. 2019. Intestinal dysbiosis augments liver disease progression via NLRP3 in a murine model of primary sclerosing cholangitis. *Gut*, **68**(8): 1477–1492.

Liu Z, Wei ZY, Chen JY, et al. 2020. Acute sleep-wake cycle shift results in community alteration of human gut microbiome. *mSphere*, **5**(1): e00914–19.

Lo JC, Ong JL, Leong RLF, et al. 2016. Cognitive performance, sleepiness, and mood in partially sleep deprived adolescents: the need for sleep study. *Sleep*, **39**(3): 687–698.

Lucey BP, Wisch J, Boerwinkle AH, et al. 2021. Sleep and longitudinal cognitive performance in preclinical and early symptomatic Alzheimer's disease. *Brain*, **144**(9): 2852–2862.

Manning BD, Toker A. 2017. AKT/PKB signaling: navigating the network. *Cell*, **169**(3): 381–405.

Martin L, Latypova X, Wilson CM, et al. 2013. Tau protein kinases: involvement in Alzheimer's disease. *Ageing Research Reviews*, **12**(1): 289–309.

Martin M, Rehani K, Jope RS, et al. 2005. Toll-like receptor-mediated cytokine production is differentially regulated by glycogen synthase kinase 3. *Nature Immunology*, **6**(8): 777–784.

Mayer EA, Nance K, Chen S. 2022. The gut-brain axis. *Annual Review of Medicine*, **73**: 439–453.

Morais LH, Schreiber HL, Mazmanian SK. 2021. The gut microbiota-brain axis in behaviour and brain disorders. *Nature Reviews Microbiology*, **19**(4): 241–255.

Paik S, Kim JK, Silwal P, et al. 2021. An update on the regulatory mechanisms of NLRP3 inflammasome activation. *Cellular & Molecular Immunology*, **18**(5): 1141–1160.

Pearson-Leary J, Zhao CY, Bittinger K, et al. 2020. The gut microbiome regulates the increases in depressive-type behaviors and in inflammatory processes in the ventral hippocampus of stress vulnerable rats. *Molecular Psychiatry*, **25**(5): 1068–1079.

Pellegrini C, Antonioli L, Calderone V, et al. 2020. Microbiota-gut-brain axis in health and disease: is NLRP3 inflammasome at the crossroads of microbiota-gut-brain communications?. *Progress in Neurobiology*, **191**: 101806.

Pellegrini C, Antonioli L, Colucci R, et al. 2018. Interplay among gut microbiota, intestinal mucosal barrier and enteric neuro-immune system: a common path to neurodegenerative diseases?. *Acta Neuropathologica*, **136**(3): 345–361.

Polito VA, Li HM, Martini-Stoica H, et al. 2014. Selective clearance of aberrant tau proteins and rescue of neurotoxicity by transcription factor EB. *EMBO Molecular Medicine*, **6**(9): 1142–1160.

Poroyko VA, Carreras A, Khalyfa A, et al. 2016. Chronic sleep disruption alters gut microbiota, induces systemic and adipose tissue inflammation and insulin resistance in mice. *Scientific Reports*, **6**: 35405.

Rehani K, Wang HZ, Garcia CA, et al. 2009. Toll-like receptor-mediated production of IL-1Ra is negatively regulated by $GSK_3$ via the MAPK ERK1/2. *The Journal of Immunology*, **182**(1): 547–553.

Renault-Mihara F, Katoh H, Ikegami T, et al. 2011. Beneficial compaction of spinal cord lesion by migrating astrocytes through glycogen synthase kinase-3 inhibition. *EMBO Molecular Medicine*, **3**(11): 682–696.

Robbins R, Quan SF, Weaver MD, et al. 2021. Examining sleep deficiency and disturbance and their risk for incident dementia and all-cause mortality in older adults across 5 years in the United States. *Aging*, **13**(3): 3254–3268.

Scheltens P, De Strooper B, Kivipelto M, et al. 2021. Alzheimer's disease. *The Lancet*, **397**(10284): 1577–1590.

Sendler M, Van Den Brandt C, Glaubitz J, et al. 2020. NLRP3 inflammasome regulates development of systemic inflammatory response and compensatory anti-inflammatory response syndromes in mice with acute pancreatitis. *Gastroenterology*, **158**(1): 253–269. e14.

Shi L, Chen SJ, Ma MY, et al. 2018. Sleep disturbances increase the risk of dementia: a systematic review and meta-analysis. *Sleep Medicine Reviews*, **40**: 4–16.

Spillantini MG, Goedert M. 2013. Tau pathology and neurodegeneration. *The Lancet Neurology*, **12**(6): 609–622.

Tang MM, Liu T, Jiang P, et al. 2021. The interaction between autophagy and neuroinflammation in major depressive disorder: from pathophysiology to therapeutic implications. *Pharmacological Research*, **168**: 105586.

Tsai PJ, Lai YH, Manne RK, et al. 2022. Akt: a key transducer in cancer. *Journal of Biomedical Science*, **29**(1): 76.

Vogt NM, Kerby RL, Dill-Mcfarland KA, et al. 2017. Gut microbiome alterations in Alzheimer's disease. *Scientific Reports*, **7**(1): 13537.

Vuotto C, Battistini L, Caltagirone C, et al. 2020. Gut microbiota and disorders of the central nervous system. *The Neuroscientist*, **26**(5-6): 487–502.

Wadhwa M, Prabhakar A, Anand JP, et al. 2019. Complement activation sustains neuroinflammation and deteriorates adult neurogenesis and spatial memory impairment in rat hippocampus following sleep deprivation. *Brain, Behavior, and Immunity*, **82**: 129–144.

Wang DY, Zhang JB, Jiang WK, et al. 2017. The role of NLRP3-CASP1 in inflammasome-mediated neuroinflammation and autophagy dysfunction in manganese-induced, hippocampal-dependent impairment of learning and memory ability. *Autophagy*, **13**(5): 914–927.

Wang MJ, Huang HY, Chen WF, et al. 2010. Glycogen synthase kinase-3β inactivation inhibits tumor necrosis factor-α production in microglia by modulating nuclear factor κB and MLK3/JNK signaling cascades. *Journal of Neuroinflammation*, **7**: 99.

Wang SH, Cui LG, Su XL, et al. 2022. GSK-3β-mediated activation of NLRP3 inflammasome leads to pyroptosis and apoptosis of rat cardiomyocytes and fibroblasts. *European Journal of Pharmacology*, **920**: 174830.

Wang SH, Su XL, Xu LN, et al. 2020. Glycogen synthase kinase-3β inhibition alleviates activation of the NLRP3 inflammasome in myocardial infarction. *Journal of Molecular and Cellular Cardiology*, **149**: 82–94.

Wang Z, Chen WH, Li SX, et al. 2021. Gut microbiota modulates the inflammatory response and cognitive impairment induced by sleep deprivation. *Molecular Psychiatry*, **26**(11): 6277–6292.

Weingarten MD, Lockwood AH, Hwo SY, et al. 1975. A protein factor essential for microtubule assembly. *Proceedings of the National Academy of Sciences of the United States of America*, **72**(5): 1858–1862.

Wu AG, Zhou XG, Qiao G, et al. 2021. Targeting microglial autophagic degradation in NLRP3 inflammasome-mediated neurodegenerative diseases. *Ageing Research Reviews*, **65**: 101202.

Yang T, Santisteban MM, Rodriguez V, et al. 2015. Gut dysbiosis is linked to hypertension. *Hypertension*, **65**(6): 1331–1340.

Yin MM, Chen YL, Zheng H, et al. 2017. Assessment of mouse cognitive and anxiety-like behaviors and hippocampal inflammation following a repeated and intermittent paradoxical sleep deprivation procedure. *Behavioural Brain Research*, **321**: 69–78.

Yin YL, Gao D, Wang YL, et al. 2016. Tau accumulation induces synaptic impairment and memory deficit by calcineurin-mediated inactivation of nuclear CaMKIV/CREB signaling. *Proceedings of the National Academy of Sciences of the United States of America*, **113**(26): E3773–E3781.

Zhang L, Wang Y, Xia XY, et al. 2017. Altered gut microbiota in a mouse model of Alzheimer's disease. *Journal of Alzheimers Disease*, **60**(4): 1241–1257.

Zhang Y, Huang RR, Cheng MJ, et al. 2019. Gut microbiota from NLRP3-deficient mice ameliorates depressive-like behaviors by regulating astrocyte dysfunction via circHIPK2. *Microbiome*, **7**(1): 116.

Zhang ZG, Yang XF, Song YQ, et al. 2021. Autophagy in Alzheimer's disease pathogenesis: therapeutic potential and future perspectives. *Ageing Research Reviews*, **72**: 101464.

Zhao N, Chen QG, Chen X, et al. 2023. Intestinal dysbiosis mediates cognitive impairment via the intestine and brain NLRP3 inflammasome activation in chronic sleep deprivation. *Brain, Behavior, and Immunity*, **108**: 98–117.

Zhuang ZQ, Shen LL, Li WW, et al. 2018. Gut microbiota is altered in patients with Alzheimer's disease. *Journal of Alzheimers Disease*, **63**(4): 1337–1346.

Cao & Zhang. *Zool. Res.* 2024, 45(4): 875−876
https://doi.org/10.24272/j.issn.2095-8137.2024.183

ZR | Zoological Research

News Open Access

# Targeting synaptic pathology in Alzheimer's disease

Alzheimer's disease (AD) is a neurodegenerative disorder characterized by memory and cognitive impairments. The two primary pathological hallmarks of AD include the accumulation of β-amyloid (Aβ) plaques and formation of neurofibrillary tangles (NFTs) composed predominantly of hyperphosphorylated tau protein (Zhang et al., 2023). Moreover, synaptic dysfunction is considered another crucial factor in AD pathogenesis and is closely associated with cognitive decline. Notably, synaptic damage, loss, and dysfunction manifest earlier than the pathological features of Aβ plaques and NFTs (Knopman et al., 2021). Therefore, understanding the mechanisms underlying synaptic dysfunction in AD is vital for providing insights into disease mechanisms and developing novel therapeutic strategies.

Synapses are the fundamental structures for memory storage and information transmission within the central nervous system (CNS). The number and structure of synapses undergo dynamic changes to optimize neuronal connections associated with cognitive functions. This process, known as synaptic plasticity, plays a crucial role in shaping the neural circuits that underlie learning and memory (Yu et al., 2024). Pathogenic Aβ and tau proteins induce synaptic defects in AD by interacting with specific synaptic proteins and mitochondria. These interactions result in alterations in the composition of synaptic proteins, oxidative stress, chronic inflammatory responses, and excessive activation of glial cells (Tzioras et al., 2022). Consequently, synapses are excessively eliminated, leading to axonal degeneration and, ultimately, neuronal loss.

Aβ is generated through the sequential cleavage of amyloid precursor protein (APP) by β- and γ-secretases. At low concentrations, Aβ facilitates neuronal survival and axonal branching, regulates potassium ion channel function, and maintains normal neuronal activity. Aβ can exist as monomers, soluble oligomers, and fibrillar deposits. Compared to monomers and protofibrils, Aβ oligomers are strongly associated with synaptic loss and progressive cognitive decline in patients with AD. In the early stages of AD, Aβ oligomers aggregate around neurons and bind tightly to multiple receptors at excitatory synapses (Tu et al., 2014). The Aβ-receptor complexes can lead to enhanced synaptic toxicity as well as structural, compositional, and functional changes in synapses.

Tau is a principal microtubule-associated protein that binds to and stabilizes microtubules in neurons. Hyperphosphorylated, misfolded, and oligomeric tau proteins accumulate at both presynaptic and postsynaptic terminals, eventually forming NFTs. Tau accumulation at presynaptic sites reduces cytoskeleton stability, enlarges synaptic terminals, depletes the synaptic vesicle pool, impairs synaptic transmission, and disrupts synaptic plasticity. Hyperphosphorylated tau induces an increase in the release of cytosolic calcium ($Ca^{2+}$) from the endoplasmic reticulum, leading to transient elevations in spontaneous neurotransmitter release and defects in exocytosis (Moreno et al., 2016). Similar to Aβ oligomers, tau oligomers exhibit synaptotoxicity. Extracellular tau oligomers are internalized by neurons and mislocalized within postsynaptic dendritic compartments during disease progression. They interact with complexes formed by postsynaptic protein FYN, PSD95, and N-methyl-D-aspartate (NMDA) receptors, thereby interfering with glutamate receptor signaling and trafficking (Shen et al., 2023). Ultimately, this results in decreased expression of these receptors on the cell surface, leading to subsequent changes in dendritic spine morphology and synaptic loss.

Aβ and tau may synergistically disrupt critical molecular signaling pathways for presynaptic and postsynaptic plasticity in the AD brain, exacerbating disease progression. Both Aβ and tau inhibit the activity of the transcription factor cAMP response element-binding protein (CREB) and its upstream regulator $Ca^{2+}$/calmodulin-dependent protein kinase II (CaMKII), which are essential for synaptic plasticity and memory formation. Mitochondria-generated cellular energy is vital for maintaining various synaptic functions, such as mobilizing synaptic vesicles from reserve pools to release sites, supporting vesicle release/recycling, facilitating synaptic assembly/plasticity, and regulating intracellular $Ca^{2+}$ concentration. Dysregulation of proteins mediating mitochondrial energy metabolism, such as muscle glycogen phosphorylase, compromises energy production and has been observed in AD (Wang et al., 2023). Both Aβ and tau can trigger mitochondrial alterations, resulting in reduced adenosine triphosphate (ATP) production, disrupted mitophagy, and increased oxidative stress/reactive oxygen species (ROS) generation, ultimately leading to progressive synaptic loss, axonal changes, and neuronal degeneration.

Synaptic degeneration and AD pathology propagation are also influenced by glial cells in the brain. Variations in the triggering receptor expressed on myeloid cells 2, predominantly expressed in microglia, and astrocyte-derived apolipoprotein E4 are closely associated with the risk and severity of AD. Abnormally activated microglia and astrocytes are common pathological features in AD. Microglia are primary immune cells in the CNS, and activated microglia can release pro-inflammatory cytokines such as tumor necrosis factor (TNF) and interleukin 1 (IL-1), which can damage synapses. Moreover, activated microglia excessively phagocytose and prune synapses through a complement-dependent

This is an open-access article distributed under the terms of the Creative Commons Attribution Non-Commercial License (http://creativecommons.org/licenses/by-nc/4.0/), which permits unrestricted non-commercial use, distribution, and reproduction in any medium, provided the original work is properly cited.

Copyright ©2024 Editorial Office of Zoological Research, Kunming Institute of Zoology, Chinese Academy of Sciences

Received: 28 May 2024; Accepted: 05 July 2024; Online: 10 July 2024

mechanism, leading to synaptic loss in AD animal models (Tzioras et al., 2022). Astrocytes are crucial for maintaining the blood-brain barrier, supporting neurons, recycling neurotransmitters, and regulating synaptic function. Reactive astrocytes in AD models impair synaptic function by reducing phagocytic ability and disrupting glutamate transport and signaling, thereby contributing to synaptic loss (Brandebura et al., 2023).

The clearance of toxic proteins is essential for maintaining synaptic homeostasis. Autophagy plays a pivotal role in modulating Aβ metabolism and tau pathology by influencing their production, secretion, and clearance (Zhao et al., 2024). Local autophagic activity at synapses is also crucial for regulating memory formation (Zhang et al., 2023). Dysregulation of autophagy has been observed in AD, and interventions that stimulate autophagy can reverse impairments in synaptic plasticity and enhance cognitive function in AD models.

Changes in synaptic function can impact the integrity of downstream neural circuits. In animal models, disruption of the entorhinal-hippocampal circuitry results in a compensatory increase in synaptogenesis in the hippocampus, similar to changes observed in AD patients (Kim et al., 2022). Adult hippocampal neurogenesis (AHN), representing a significant form of neuroplasticity, is substantially decreased during the early stages of AD, potentially contributing to memory and cognitive impairments. Enriched environments can enhance AHN in AD mice, concurrently reducing Aβ accumulation and tau phosphorylation within the hippocampus. Furthermore, genetic and pharmacological stimulation of AHN, combined with brain-derived neurotrophic factor administration, can potentially improve cognitive function in AD mice (Kim et al., 2022; Li et al., 2023). Therefore, targeting AHN in adult AD patients and AD animal models may provide a novel strategy for treating AD.

As Aβ and tau are the primary pathogenic factors in AD, most therapeutic developments have focused on reducing their aggregation and accumulation. At present, the US Food and Drug Administration (FDA) has approved several Aβ monoclonal antibodies, including aducanumab and lecanemab, for AD treatment, while therapies targeting tau are still under investigation (Zhang et al., 2023). Given the importance of synaptic dysfunction in AD pathogenesis, exploring new treatments targeting synapses represents another promising avenue. Indeed, other major FDA-approved AD drugs, such as cholinesterase inhibitors (donepezil, galantamine, and rivastigmine) and NMDA receptor antagonists (memantine), target synaptic receptors. However, the therapeutic effects of these available drugs are limited. A complete elucidation of synaptic pathology in AD will not only enhance our understanding of disease pathogenesis but also reveal new treatment strategies.

## COMPTING INTERESTS

The authors declare that they have no competing interests.

## AUTHORS' CONTRIBUTIONS

J.C. and Y.W.Z. conceived the review and wrote the manuscript. All authors read and approved the final version of the manuscript.

Jing Cao[1,*], Yun-Wu Zhang[1,*]

[1] *Fujian Provincial Key Laboratory of Neurodegenerative Disease and Aging Research*, *Institute of Neuroscience*, *School of Medicine*, *Xiamen University*, *Xiamen*, *Fujian* 361102, *China*

*Corresponding authors, E-mail: caojing21@stu.xmu.edu.cn; yunzhang@xmu.edu.cn

## REFERENCES

Brandebura AN, Paumier A, Onur TS, et al. 2023. Astrocyte contribution to dysfunction, risk and progression in neurodegenerative disorders. *Nature Reviews Neuroscience*, **24**(1): 23–39.

Kim TA, Syty MD, Wu K, et al. 2022. Adult hippocampal neurogenesis and its impairment in Alzheimer's disease. *Zoological Research*, **43**(3): 481–496.

Knopman DS, Amieva H, Petersen RC, et al. 2021. Alzheimer disease. *Nature Reviews Disease Primers*, **7**(1): 33.

Li Y, Xu NN, Hao ZZ, et al. 2023. Adult neurogenesis in the primate hippocampus. *Zoological Research*, **44**(2): 315–322.

Moreno H, Morfini G, Buitrago L, et al. 2016. Tau pathology-mediated presynaptic dysfunction. *Neuroscience*, **325**: 30–38.

Shen Z, Sun DX, Savastano A, et al. 2023. Multivalent Tau/PSD-95 interactions arrest in vitro condensates and clusters mimicking the postsynaptic density. *Nature Communications*, **14**(1): 6839.

Tu SC, Okamoto SI, Lipton SA, et al. 2014. Oligomeric Aβ-induced synaptic dysfunction in Alzheimer's disease. *Molecular Neurodegeneration*, **9**: 48.

Tzioras M, McGeachan RI, Durrant CS, et al. 2022. Synaptic degeneration in Alzheimer disease. *Nature Reviews Neurology*, **19**(1): 19–38.

Wang T, Zhou YQ, Wang Y, et al. 2023. Long-term potentiation-based screening identifies neuronal PYGM as a synaptic plasticity regulator participating in Alzheimer's disease. *Zoological Research*, **44**(5): 867–881.

Yu LD, Zeng FF, Fan MS, et al. 2024. PCDH17 restricts dendritic spine morphogenesis by regulating ROCK2-dependent control of the actin cytoskeleton, modulating emotional behavior. *Zoological Research*, **45**(3): 535–550.

Zhang XW, Zhu XX, Tang DS, et al. 2023. Targeting autophagy in Alzheimer's disease: animal models and mechanisms. *Zoological Research*, **44**(6): 1132–1145.

Zhao N, Chen X, Chen QG, et al. 2024. NLRP3-mediated autophagy dysfunction links gut microbiota dysbiosis to tau pathology in chronic sleep deprivation. *Zoological Research*, **45**(4): 857–874.

Yao et al. *Zool. Res.* 2024, 45(4): 877−909
https://doi.org/10.24272/j.issn.2095-8137.2024.199

ZR | Zoological Research

Review Open Access

# Study of tree shrew biology and models: A booming and prosperous field for biomedical research

Yong-Gang Yao[1,2,3,4,*], Li Lu[1,2,3,4], Rong-Jun Ni[5,6], Rui Bi[1,2,3,4,§], Ceshi Chen[1], Jia-Qi Chen[2], Eberhard Fuchs[7], Marina Gorbatyuk[8], Hao Lei[9,10], Hongli Li[1,2,3], Chunyu Liu[11], Long-Bao Lv[2], Kyoko Tsukiyama-Kohara[12], Michinori Kohara[13], Claudia Perez-Cruz[14], Gregor Rainer[15], Bao-Ci Shan[16,17], Fang Shen[18,19], An-Zhou Tang[20,21], Jing Wang[22], Wei Xia[20,21], Xueshan Xia[23], Ling Xu[1,2,3,4], Dandan Yu[1,2,3,4], Feng Zhang[11], Ping Zheng[1,2,3,4], Yong-Tang Zheng[1,2,3,4], Jumin Zhou[1], Jiang-Ning Zhou[24,25]

[1] *Key Laboratory of Genetic Evolution and Animal Models*, *Yunnan Key Laboratory of Animal Models and Human Disease Mechanisms*, *Kunming Institute of Zoology*, *Chinese Academy of Sciences*, *Kunming*, *Yunnan* 650204, *China*
[2] *National Research Facility for Phenotypic & Genetic Analysis of Model Animals (Primate Facility)*, *and National Resource Center for Non-Human Primates*, *Kunming Institute of Zoology*, *Chinese Academy of Sciences*, *Kunming*, *Yunnan* 650107, *China*
[3] *KIZ-CUHK Joint Laboratory of Bioresources and Molecular Research in Common Diseases*, *Kunming Institute of Zoology*, *Chinese Academy of Sciences*, *Kunming*, *Yunnan* 650204, *China*
[4] *Kunming College of Life Science*, *University of Chinese Academy of Sciences*, *Kunming*, *Yunnan* 650204, *China*
[5] *Mental Health Center and Psychiatric Laboratory*, *West China Hospital*, *Sichuan University*, *Chengdu*, *Sichuan* 610041, *China*
[6] *Sichuan Clinical Medical Research Center for Mental Disorders*, *Chengdu*, *Sichuan* 610044, *China*
[7] *German Primate Center*, *Leibniz Institute of Primate Research*, *Göttingen* 37077, *Germany*
[8] *Department of Optometry and Vision Science*, *School of Optometry*, *University of Alabama at Birmingham*, *Birmingham*, *AL* 35294, *USA*
[9] *State Key Laboratory of Magnetic Resonance and Atomic and Molecular Physics*, *Innovation Academy for Precision Measurement Science and Technology*, *Chinese Academy of Sciences*, *Wuhan*, *Hubei* 430071, *China*
[10] *Wuhan National Laboratory for Optoelectronics*, *Huazhong University of Science and Technology*, *Wuhan*, *Hubei* 430074, *China*
[11] *Soong Ching Ling Institute of Maternity and Child Health*, *International Peace Maternity and Child Health Hospital*, *Shanghai Jiao Tong University School of Medicine*, *Shanghai* 200030, *China*
[12] *Transboundary Animal Diseases Center*, *Joint Faculty of Veterinary Medicine*, *Kagoshima University*, *Kagoshima-city*, *Kagoshima* 890-8580, *Japan*
[13] *Department of Microbiology and Cell Biology*, *Tokyo Metropolitan Institute of Medical Science*, *Tokyo* 156-8506, *Japan*
[14] *Pharmacology Department*, *Cinvestav*, *Mexico City* 07360, *Mexico*
[15] *Department of Medicine*, *University of Fribourg*, *Fribourg CH*-1700, *Switzerland*
[16] *Beijing Engineering Research Center of Radiographic Techniques and Equipment*, *Institute of High Energy Physics*, *Chinese Academy of Sciences*, *Beijing* 100049, *China*
[17] *School of Nuclear Science and Technology*, *University of Chinese Academy of Sciences*, *Beijing* 100049, *China*
[18] *CAS Key Laboratory of Mental Health*, *Institute of Psychology*, *Chinese Academy of Sciences*, *Beijing* 100101, *China*
[19] *Department of Psychology*, *University of Chinese Academy of Sciences*, *Beijing* 100101, *China*
[20] *Department of Otorhinolaryngology Head and Neck Surgery*, *First Affiliated Hospital of Guangxi Medical University*, *Nanning*, *Guangxi* 530000, *China*
[21] *Key Laboratory of Early Prevention and Treatment for Regional High Frequency Tumor (Guangxi Medical University)*, *Ministry of Education*, *Nanning*, *Guangxi* 530000, *China*
[22] *Department of Neurobiology*, *School of Basic Medical Sciences*, *Nanjing Medical University*, *Nanjing*, *Jiangsu* 211166, *China*
[23] *School of Public Health*, *Kunming Medical University*, *Kunming*, *Yunnan* 650500, *China*
[24] *CAS Key Laboratory of Brain Function and Diseases*, *Division of Life Sciences and Medicine*, *University of Science and Technology of China*, *Hefei*, *Anhui* 230027, *China*
[25] *Institute of Brain Science*, *First Affiliated Hospital of Anhui Medical University*, *Hefei*, *Anhui* 230022, *China*

This is an open-access article distributed under the terms of the Creative Commons Attribution Non-Commercial License (http://creativecommons.org/licenses/by-nc/4.0/), which permits unrestricted non-commercial use, distribution, and reproduction in any medium, provided the original work is properly cited.
Copyright ©2024 Editorial Office of Zoological Research, Kunming Institute of Zoology, Chinese Academy of Sciences

Received: 17 June 2024; Accepted: 03 July 2024; Online: 05 July 2024
Foundation items: This work was supported by the STI2030-Major Projects (2021ZD0200900 to Y.G.Y.) and "Light of West China" Program of the Chinese Academy of Sciences (xbzg-zdsys-202302 to Y.G.Y.)
*Corresponding author, E-mail: yaoyg@mail.kiz.ac.cn
§Authors are listed in alphabetic order from the fourth author onwards

**ABSTRACT**

The tree shrew (*Tupaia belangeri*) has long been proposed as a suitable alternative to non-human primates (NHPs) in biomedical and laboratory research due to its close evolutionary relationship with primates. In recent years, significant advances have facilitated tree shrew studies, including the determination of the tree shrew genome, genetic manipulation using spermatogonial stem cells, viral vector-mediated gene delivery, and mapping of the tree shrew brain atlas. However, the limited availability of tree shrews globally remains a substantial challenge in the field. Additionally, determining the key questions best answered using tree shrews constitutes another difficulty. Tree shrew models have historically been used to study hepatitis B virus (HBV) and hepatitis C virus (HCV) infection, myopia, and psychosocial stress-induced depression, with more recent studies focusing on developing animal models for infectious and neurodegenerative diseases. Despite these efforts, the impact of tree shrew models has not yet matched that of rodent or NHP models in biomedical research. This review summarizes the prominent advancements in tree shrew research and reflects on the key biological questions addressed using this model. We emphasize that intensive dedication and robust international collaboration are essential for achieving breakthroughs in tree shrew studies. The use of tree shrews as a unique resource is expected to gain considerable attention with the application of advanced techniques and the development of viable animal models, meeting the increasing demands of life science and biomedical research.

**Keywords:** Tree shrew; Animal model; Neurodegenerative diseases; Infectious diseases; Neuroscience; Phenome

**INTRODUCTION**

Human economic and societal development over recent decades has substantially shifted the burden of diseases (Achoki et al., 2022; GBD 2019 Diseases and Injuries Collaborators, 2020; Zhou et al., 2019). In China, for example, an analysis of the Global Burden of Diseases, Injuries, and Risk Factors Study (GBD) from 1990 to 2017 revealed marked changes in health patterns, including mortality, disability, and risk factors (GBD 2019 Cancer Risk Factors Collaborators, 2022; Zhou et al., 2019). Notably, although overall disease burden decreased, the top causes of death and disability-adjusted life-years differed significantly between 1990 and 2017, shifting from lower respiratory infections and neonatal disorders to stroke and ischemic heart disease (Zhou et al., 2019). The evolving global burden of diseases and injuries presents difficulties for biomedical research and underscores the urgent need for effective prophylactics. Consequently, establishing and applying valid disease models is essential to gain a deeper understanding of disease pathobiology and combating human diseases. Rodents, such as mice and rats, have traditionally served as the primary animal models in research. However, the genetic differences between rodents and humans, as well as disparities in comparative anatomy and disease model phenotyping and biases affecting internal and external validity, pose considerable challenges for translating murine models to human diseases (Justice & Dhillon, 2016; McGonigle & Ruggeri, 2014; Ruberte et al., 2023; van der Worp et al., 2010). Identifying experimental animals with anatomical structures and functional units similar to humans is essential for the reproducibility and translatability of human disease models. Non-human primates (NHPs) are considered the optimal models for studying human diseases and advancing biomedical research due to their high genetic, anatomical, physiological, pathological, and brain function similarities to humans (National Academies of Sciences, Engineering, and Medicine et al., 2023; Phillips et al., 2014; Roelfsema & Treue, 2014; Tarantal et al., 2022; Yao & Construction Team of the KIZ Primate Facility, 2022). The value of NHPs in biomedical research is well-established (National Academies of Sciences, Engineering, and Medicine et al., 2023), especially in modeling neurodegenerative and infectious diseases such as Alzheimer's disease (AD; Arnsten et al., 2021; Haque & Levey, 2019; Pan et al., 2024) and COVID-19 (Ma et al., 2022; Saturday & van Doremalen, 2023; Song et al., 2020), as well as in understanding human biology (Estrada et al., 2017; Guo et al., 2023b; Wu et al., 2022; Zhang et al., 2022). However, bioethical concerns and high maintenance costs limit the widespread use of NHPs compared to rodents.

Tree shrews are genetically closer to NHPs than rodents, as evidenced by cross-species anatomical ontology, transcriptomic profiling, and comparative physiology (Dimanico et al., 2021; Fan et al., 2013, 2019; Ni et al., 2018a, 2018b; Ye et al., 2021; Zhang et al., 2020a) (Figure 1). They also offer several advantages as experimental animals, including small adult body size, brief reproductive cycle, short life span, and lower maintenance costs (Yao, 2017), with the recently launched Tree Shrew User Meeting underscoring the progress and promising future of tree shrews as animal models in neuroscience research (Savier et al., 2021). Recent reviews have highlighted the use of tree shrews in modeling human viral infections and cancer research (Kayesh et al., 2021; Li et al., 2018b; Lu et al., 2021), while earlier reviews emphasized their role as an emerging model for various human diseases (Cao et al., 2003; Xiao et al., 2017; Yao, 2017). However, research using tree shrews has not flourished as expected, as evidenced by a PubMed search using "tree shrew or Tupaia" as keywords, which yielded only 1 777 entries from 1958 to March 2024 (Figure 2). Most studies involving tree shrews over the past decades have focused on vision and neurobiology, with their use as infection models gaining increasingly attention in recent years. It is evident that fostering a larger research community dedicated to use the tree shrews as a model organism is desirable. A timely summation of recent tree shrew studies, with a comprehensive discussion of the benefits, limitations, and future directions of this animal in biomedical research, is necessary to meet the growing needs of the field and address the global burden of diseases.

**BIOLOGICAL OVERVIEW AND TAXONOMY OF TREE SHREWS**

The tree shrew is a small rat-sized mammal with a high brain-to-body mass ratio, large eyes, and high mobility. It reaches sexual maturity at around 5 months and has a short gestation period of approximately 6 weeks, typically producing a litter of

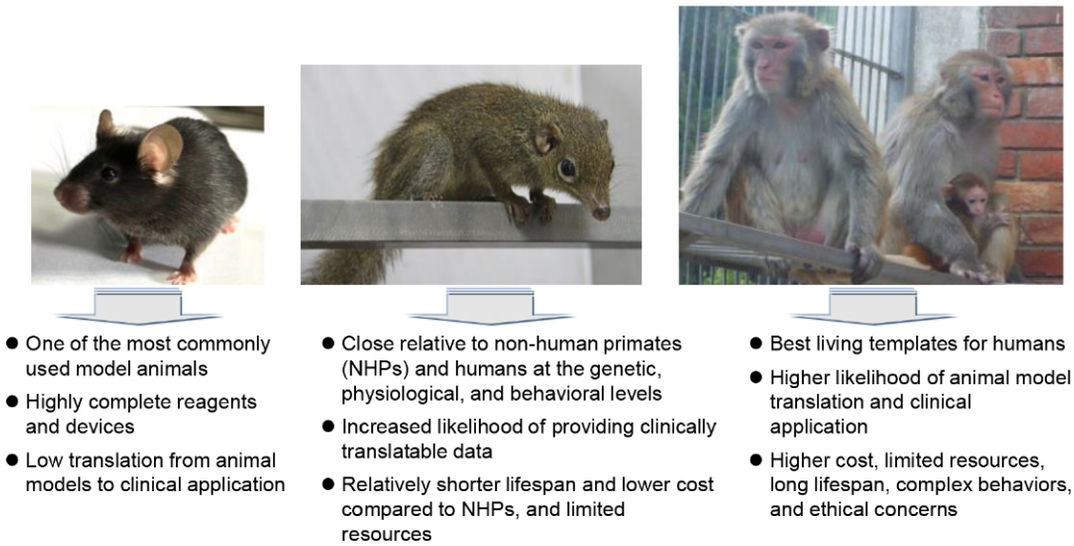



**Figure 1 Advantages and disadvantages of tree shrews as experimental models compared to rodents and non-human primates**

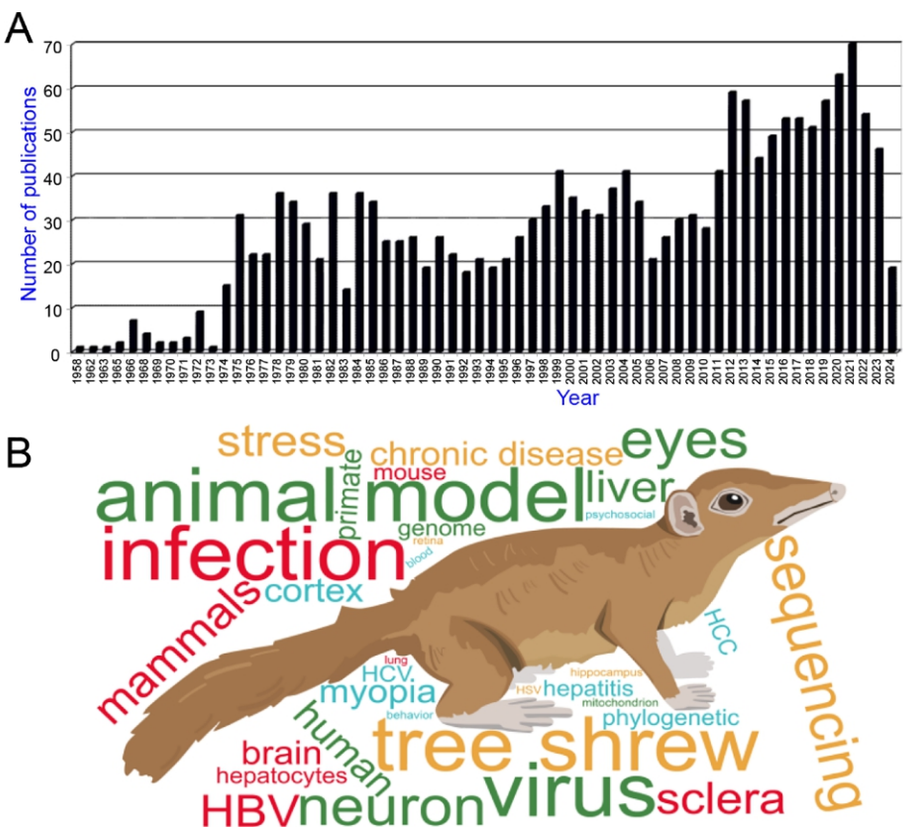



**Figure 2 Number of tree shrew publications in the field**

A: Distribution of tree shrew publications since the 1950s according to a PubMed search ("tree shrews or Tupaia") on 26 March 2024 (1 777 publications). B: Word-frequency based on abstracts of tree shrew publications in (A).

one to five offspring. In our Kunming breeding center (China), tree shrews have a lifespan of six to eight years. They are relatively inexpensive to maintain compared to larger experimental animals, such as monkeys and dogs. Tree shrews are widely distributed in South and Southwest China, as well as in adjacent regions of South and Southeast Asia (Fuchs & Corbach-Söhle, 2010; Peng et al., 1991). In the most recent edition of *The UFAW Handbook on the Care and Management of Laboratory and Other Research Animals* (Ninth Edition), Fuchs (2024) provides an excellent biological overview of tree shrews.

Currently, the tree shrew is classified within the Order Scandentia, which comprises two recognized families, Ptilocercidae and Tupaiidae (Helgen, 2005; Xu et al., 2013). Historically, resolving the phylogeny of tree shrew species has been difficult due to limited specimens and samples from critical taxa (Roberts et al., 2011; Wang, 1987). While 15 tree shrew species are currently recognized within the genus *Tupaia* (Helgen, 2005), the species status of *T. moellendorffi* and *T. palawanensis* has been questioned due to their small genetic distance (Roberts et al., 2011). Tree shrews used in early biomedical research were introduced from China,

Thailand, Malaysia, and nearby regions, and were likely *T. belangeri* and *T. glis*. However, confusion arose in published reports due to the differing views of taxonomists, with some regarding both species as one and others considering *T. belangeri* as a subspecies of *T. glis* (Wang, 1987), leading to the use of *T. glis belangeri* in some publications (e.g., McCollum & Roberts, 2014; Norton et al., 2010; Romero-Herrera & Lehmann, 1974; Siegwart & Norton, 1998). Based on the original sources and common names, both *T. belangeri* (e.g., Collins & Tsang, 1987; Darai et al., 1978; Fuchs & Schumacher, 1990; McBrien & Norton, 1992) and *T. glis* common tree shrew, e.g., (Chunhabundit et al., 1993; Kurohmaru et al., 1996; Sherman et al., 1977) have been used in biomedical studies, leading to potential ambiguity in the reproducibility of animal models when different species are not clearly identified. The NCBI taxonomy for *Tupaia* (ID 9394; https://www.ncbi.nlm.nih.gov/datasets/taxonomy/9394/) lists a total of 17 species. The Chinese tree shrew, initially named *T. chinensis* in 1879, was later reclassified as *T. belangeri* (Wang, 1987). The proposed reclassification of the Chinese tree shrew (*T. belangeri chinensis*) as a distinct species (*T. chinensis*) was supported by its significant genetic distance from the northern tree shrew (*T. belangeri*), as evidenced by our previous phylogenetic tree based on 2 117 single-copy genes (Fan et al., 2013). However, it has also been suggested that Chinese tree shrews could be classified in six subspecies of *T. belangeri* (*T. b. chinensis*, *T. b. gaoligongensis*, *T. b. modesta*, *T. b. tonquinia*, *T. b. yunalis*, *T. b. yaoshanensis*) based on morphological characters and body hair color (Wang, 1987). Different subspecies of Chinese tree shrews have been used to create animal models. For instance, *T. b. yunalis* adults have been used to establish a human rotavirus infection model (Pang et al., 1983) and test the efficacy of *Valeriana jatamansi* treatment (Pang et al., 1984). This subspecies has also been used to establish an infection model of *Mycobacterium leprae*, supporting the proliferation of this pathogen of leprosy (Wang et al., 1990). The *T. b. chinensis* subspecies has been used to characterize the potential roles of *Tupaia* immune genes in viral infection (Gu et al., 2021a, 2021b; Xu et al., 2016, 2020b) and to test aging effects on cognitive impairment and the potential for developing animal models of AD (Fan et al., 2018; Li et al., 2024). The genetic background of different tree shrew species from different geographic regions may affect their susceptibility to certain pathogens and/or naturally occurring diseases. As such, attention should be paid to the original source when selecting animals for testing.

## AVAILABLE EXPERIMENTAL TREE SHREW COLONIES AND CELL LINE RESOURCES

Currently, several tree shrew colonies exist worldwide, each with specific maintenance purposes and research goals. Two primary tree shrew colonies are maintained in the United States. Of note, the University of Alabama at Birmingham (UAB) (https://www.uab.edu/research/administration/Centers Cores/Pages/Tree-Shrew-Core.aspx) maintains a colony that produces 80–130 young tree shrews annually, primarily for eye and vision research as well as other studies within the United States (e.g., KhalafAllah et al., 2024; Khanal et al., 2023; Norton et al., 2010; Siegwart & Norton, 1998). The Max Planck Florida Institute for Neuroscience maintains a smaller colony of about 80–100 animals, generating young tree shrews for internal research purposes and colony maintenance.

The German Primate Center (Deutsches Primatenzentrum, DPZ) at Göttingen maintained a tree shrew colony for nearly 30 years, supplying animals to research institutes across Germany and Europe, with a peak of 200–300 animals between 2004 and 2009 (Fuchs, 2015). However, this colony was closed following the retirement of Prof. Eberhard Fuchs, and the animals were transferred to the Department of Behavioral Physiology at the Center for Behavior and Neurosciences, University of Groningen, in the Netherlands (Fuchs, 2015). Additionally, the University of Fribourg Platform for Translational Neuroscience in Switzerland maintains a tree shrew breeding facility, producing up to 40 animals per year for internal research and external users.

The largest tree shrew colony in China is maintained by the experimental animal center of the Kunming Institute of Zoology, Chinese Academy of Sciences. Established in the 1970s, this colony has faced interruptions over the past decades. Currently, it houses approximately 2 000–3 000 individuals, depending on the needs for colony expansion, and supplies around 1 000 animals annually to various institutes and universities in China and abroad. Additionally, the experimental animal centers of the Kunming Medical University and the Institute of Medical Biology of the Chinese Academy of Medical Sciences host two large colonies for research purposes, further highlighting the ample tree shrew resources in China.

The tree shrew colonies in the United States and Germany were originally sourced from Thailand. However, following the export ban of these animals from Thailand, China and Malaysia emerged as primary global suppliers. Limited access to tree shrew resources worldwide has posed a significant challenge to their widespread use in biomedical research. It is essential to introduce new tree shrews into existing colonies to prevent inbreeding and support colony expansion. However, animal rights activists have also impeded the transportation of these animals and hindered research activities involving tree shrews. It is crucial for scientists working with tree shrews to advocate for their research and emphasize the benefits of using this animal model. The tree shrew center at the Kunming Institute of Zoology is prepared to provide tree shrews to researchers globally for scientific purposes.

To minimize the use of living tree shrews and adhere to the 3Rs (replacement, reduction, and refinement) in experimental animal biology (MacArthur Clark, 2018; Sneddon et al., 2017), it is essential to develop immortalized tree shrew cells, induced pluripotent stem cells (iPSCs), and organoids. Currently, only a few immortalized tree shrew cell lines exist (e.g., Gu et al., 2019b; Yin et al., 2019; Zhang et al., 2020c), while there are no reports of iPSCs or organoids for tree shrews. The establishment of iPSCs and iPSC-derived neurons from hibernating thirteen-lined ground squirrels (Ou et al., 2018) serves as an excellent example for research on non-model organisms, including tree shrews. Developing iPSC-derived organ-on-a-chip platforms and three-dimensional (3D) organoid culture systems (Augustyniak et al., 2019; Palasantzas et al., 2023; Rauth et al., 2021; Teli et al., 2023) for tree shrews would significantly advance comparative physiology, disease modeling, and pharmacological research. To maximize the potential of tree shrew resources, it is crucial to foster international collaborations, share living tree shrews and associated cell lines, and develop innovative techniques.

## DO WE NEED AN INBRED STRAIN OF TREE SHREW?

Advances in sequencing technologies (De Coster et al., 2021; Hook & Timp, 2023; Zhang et al., 2011) now allow researchers to determine the genome sequences of wild animals and non-model organisms, providing crucial insights into their genetic backgrounds, which is essential for their use as experimental animals. The application of cutting-edge gene editing techniques (Badon et al., 2024; Li et al., 2019; Luo et al., 2016; Ma et al., 1998; Pfeiffer & Stafforst, 2023; Villiger et al., 2024), especially adeno-associated virus (AAV) vector-mediated gene delivery or genome editing (Challis et al., 2022; Taha et al., 2022; Wang et al., 2019a, 2020a), has greatly accelerated the creation of genetically modified animals and gene therapy applications. These advancements in sequencing and gene editing have revolutionized the study of non-model animals. Theoretically, any wild animal could be used as an experimental animal with appropriate ethical approval, and research on non-model organisms can significantly facilitate biomedical research and our understanding of life and evolution (Cusick et al., 2021; Guo et al., 2023b; Meadows & Lindblad-Toh, 2017; Zhao et al., 2021a). However, for drug screening and other tests of new prophylactics and treatments, inbred experimental animals are preferred to ensure consistent and comparable results. This key advantage of model animals highlights the necessity of developing an inbred tree shrew strain.

In 2011, we began efforts to establish an inbred Chinese tree shrew strain at the Kunming Institute of Zoology (Chen et al., 2022a) to facilitate broader application in research, but progress has been limited. Despite over a decade of effort, we have only managed to obtain a small number of inbred offspring to the ninth filial generation (F9) (unpublished data). A significant issue is infanticide during sibling mating, which was excessively high in our inbred colonies, in contrast to regular tree shrew colonies (either closed colonies or hybrids) under the same conditions, which successfully produce offspring. The exact cause for this cannibalistic behavior is unknown (Chen et al., 2022a). Given the suggested efficacy of oxytocin in preventing infanticide (Lezama-García et al., 2019; McCarthy, 1990; Olazábal & Alsina-Llanes, 2016), we administered oxytocin to tree shrew mothers to potentially mitigate this issue. Due to the prevalence of cannibalistic behavior, we resorted to artificial rearing for inbred tree shrew pups, despite it being time-consuming. After extensive efforts, we discovered that commercially available milk substitutes for guinea pigs (Wombaroo Food Products, Australia) effectively supported the survival and growth of Chinese tree shrew pups (Chen et al., 2022a). This milk replacer simplifies the process for laboratories needing to artificially rear Chinese tree shrew pups.

As anticipated, we observed various spontaneous diseases in the inbred tree shrews, including fetal death, idiopathic short stature, spontaneous cataracts, and spontaneous skin, breast, and liver cancers (Figure 3). Positively, the occurrence of these spontaneous diseases is currently low in our inbred tree shrew colony, suggesting that once the infanticide issue is resolved, it will not hinder the expansion of the inbred tree shrew colony. The availability of inbred tree shrew families provides a valuable resource for investigating key genetic questions, such as mutation rates in pedigrees (Bergeron et al., 2023; Wu et al., 2024), inbreeding depression (Charlesworth & Willis, 2009; Hedrick & Garcia-Dorado, 2016), and mechanisms of spontaneous disease models.

## BEHAVIORAL TESTS FOR TREE SHREWS

Tree shrews exhibit skittish and agile behavior, which complicates cognitive assessments. Early behavioral tests compared learning set formation among rodents, tree shrews, and primates (Leonard et al., 1966; Ohta, 1983; Ohta et al., 1984, 1985). Correct task rates indicate the ability of an animal to learn rules, enabling intelligence comparisons across species under standardized conditions. The performance of tree shrews was intermediate between that of rodents and primates, reflecting their evolutionary phylogeny. In further comparative research, Takahashi et al. (2008) examined transitive inference, a higher-order cognitive function for logical deduction, through a spatial discrimination task involving rats and tree shrews, while Mustafar et al. (2018) compared visual cue-based decision-making discrimination tasks involving humans, monkeys, tree shrews, and rats. Both studies found that tree shrews performed better than rats, highlighting their cognitive potential. Li et al. (2022) established a response-time perceptual decision-making paradigm for tree shrews, involving a contrast-discrimination perceptual decision task to generate informative choice and response time data. Analyses suggested that in addition to choice-related evidence accumulation, time-tracking mechanisms may influence decision-making, especially when trial delays follow incorrect responses (Li et al., 2022). Tree shrews were also used as a model for analyzing cognitive flexibility (Pan et al., 2022).

At present, the repertoire of behavioral assays tailored for tree shrews is limited, often adapted from rodent-based paradigms. Ohl et al. (1998) developed a modified hole-board test for tree shrews, incorporating an associative visual task and a memory-dependent spatial task. Tree shrews rapidly learned the associative task compared to the spatial task, with their performance significantly influenced by age and chronic stress (Li et al., 2024; Keuker et al., 2004; Ohl & Fuchs, 1999). Previous object recognition tasks assessing novelty preference found that tree shrews exhibited a pronounced exploratory bias towards novel or displaced objects (Khani & Rainer, 2012; Nair et al., 2014). Shang et al. (2015) demonstrated that tree shrews effectively associated an aversive stimulus (foot shock) with lighting conditions within a light/dark box. These findings validate the suitability of tree shrews in cognitive tasks originally designed for rodents and highlight the modulatory influence of age and health status on task performance, relevant for modeling cognitive disorders.

Deficits in spatial cognition are common among patients with early AD (Coughlan et al., 2018). As such, the development of sensitive behavioral assays is imperative for evaluating AD model validity. Li et al. (2023b) subjected tree shrews to a series of rodent-derived spatial cognitive tasks, including the radial-arm maze, cheese-board maze, and water maze, to assess the sensitivity of these tasks to hippocampal lesion-induced spatial memory impairment. Their findings revealed that bilateral hippocampal lesions significantly impaired performance in all tasks, with the cheeseboard task emerging as the most sensitive indicator of spatial memory loss, potentially serving as a valuable tool for monitoring progressive cognitive decline in aging and AD models.

Furthermore, with proper equipment and behavioral paradigms, complex behaviors such as cooperation (Nowak, 2006, 2012; West et al., 2021) and social avoidance (Gellner et al., 2021; Toth & Neumann, 2013), as reported in other species, can also be investigated in tree shrews. Jiang et al.

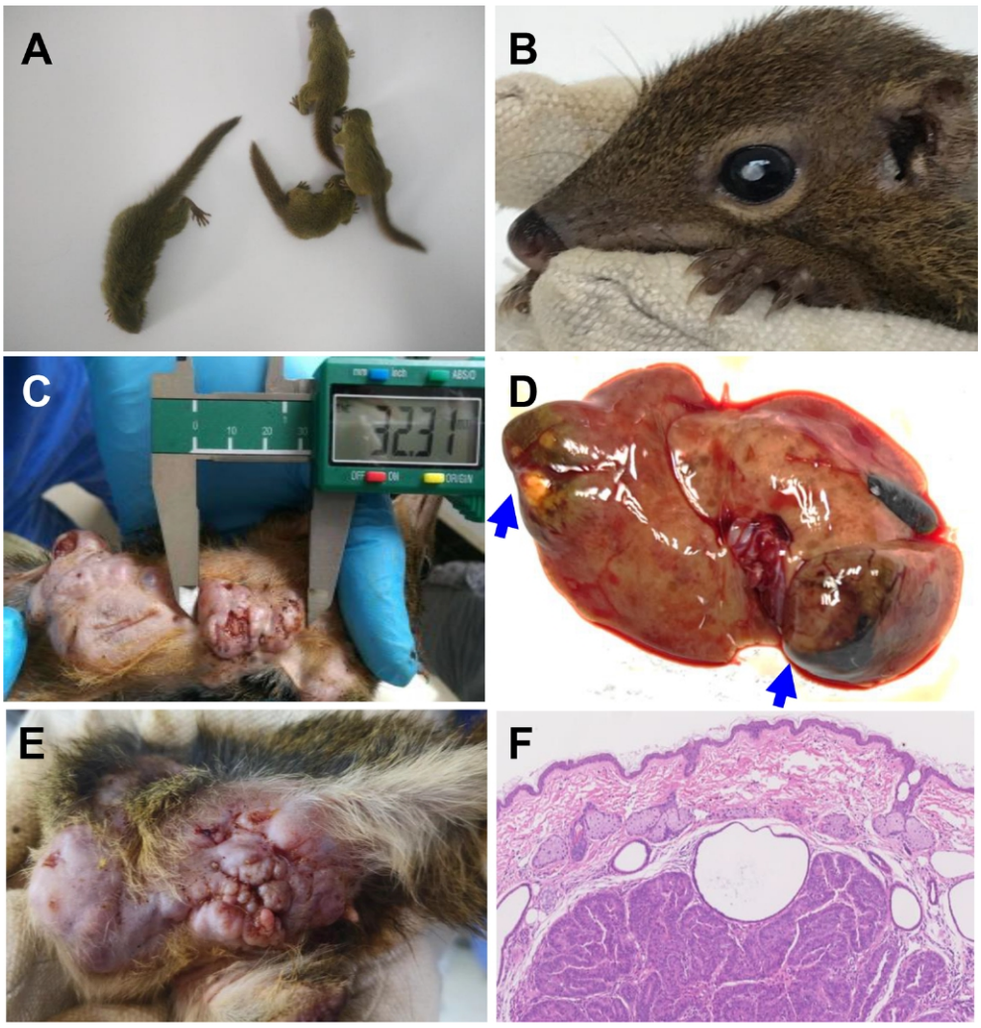



**Figure 3 Spontaneous diseases in inbred tree shrew populations**

A: Idiopathic short stature (ISS). Four tree shrews reached an age of 27 days. Tree shrew on the left is a normal individual, while three individuals on the right exhibit ISS. B: Spontaneous cataracts. C: Spontaneous breast cancer. D: Spontaneous liver cancer. Tumors are indicated by blue arrows. E: Spontaneous skin cancer. F: Histological hematoxylin & eosin-stained skin section of an individual with spontaneous apocrine carcinoma cancer.

(2021b) recently designed a temporal coordination task to quantitatively assess cooperative behavior in mice, rats, and tree shrews and found that tree shrews exhibited the best cooperative abilities and strategies among the three species in the automated behavioral paradigm. Additionally, Ni et al. (2020) employed a modified social preference-avoidance test to assess social behavior towards unfamiliar conspecifics and found that male tree shrews showed social avoidance behavior while male mice showed prosocial behavior. These studies demonstrate the capability of tree shrews to serve as animal models for research on social avoidance and prosocial behaviors.

Reports on the behavioral activities of wild tree shrews remain scarce, limiting our understanding of this animal and its use in disease models. Despite having non-opposable thumbs, tree shrews are capable of grasping objects. Notably, based on forced-food grasping experiments, Maille et al. (2013) found that tree shrews exhibit paw preference at an individual level, but not at a population level, and that paw laterality can be learned. We observed an unusual restricted walking behavior in tree shrews during training sessions for various tasks (unpublished data; Supplementary Material: Video), the significance of which is unknown. By introducing artificial intelligence (AI) and deep learning-based action recognition techniques, similar to those used for NHPs and mice (Bala et al., 2020; Huang et al., 2021; Li et al., 2023c; Marks et al., 2022; Zhang et al., 2023b), and optimizing automated behavior classification systems for tree shrews, we expect to achieve better quantification of behaviors, thereby enhancing our understanding of pose estimation, inference, and behavior classification in this species.

## TREE SHREW BRAIN ATLAS

Understanding the morphological structure, projections, circuits, and neural cell types of the brain is crucial for unraveling the behavioral, neural, and molecular mechanisms underlying normal brain function and neurological disorders (Qiu et al., 2024; Tian et al., 2022). With their high brain-to-body ratio, tree shrews have received considerable attention in recent decades.

### Development of tree shrew brain atlas

The tree shrew nervous system has been extensively investigated, focusing on the anatomy and stereotactic

localization of the brainstem, spinal cord, cortex, and thalamus (Diamond et al., 1970; Marrocco et al., 1970; Shriver & Noback, 1967; Snyder et al., 1969; Tigges & Shantha, 1969). The first version of the tree shrew brain atlas, published in the late 1970s, represented a significant milestone in neurobiological research on tree shrews (Marrocco et al., 1970; Tigges & Shantha, 1969). Marrocco et al. (1970) provided brain outlines and subfields at 10 levels using the Horsley-Clarke system of coordinates, with the horizontal zero plane passing through the ear bars and infraorbital ridge and the vertical zero plane running perpendicular to the horizontal zero and passing through the interaural line. This atlas had a profound impact on subsequent neurobiological research on tree shrews. The second version of the tree shrew brain atlas in stereotaxic coordinates, developed by Yang et al. (1990), has been crucial for studying Chinese tree shrew neurobiology. This atlas, which contains 37 brain drawings and stained figures at approximately 500 μm intervals, features the horizontal zero plane running parallel to the plane that passes through the ear bars and incisor bar at 4 mm above the interaural line, while the vertical zero plane runs perpendicular to the horizontal zero plane and passes through the interaural line.

We developed the third version of tree shrew brain atlas, providing the first systematic nomenclature and detailed mapping of the tree shrew brain, including stained sections in the coronal, sagittal, and horizontal planes using the interaural and bregma reference systems (Zhou & Ni, 2016). The atlas also features coronal, sagittal, and horizontal planes of the whole brain obtained using 9.4T magnetic resonance imaging (MRI). This version has facilitated the experiments involving tree shrew brain stereotaxic injections, tracing projections among different brain regions, and recognizing specific nuclei. Researchers have also provided detailed descriptions of the localization and comparative anatomy of various brain regions, including the amygdala, hypothalamus, thalamus, cerebellar nucleus, and piriform cortex (Airaksinen et al., 1989; Flügge et al., 1994; Maher et al., 2021; McCollum & Roberts, 2014; Ni et al., 2014; Parra et al., 2019; Rice et al., 2011). These studies have identified more than 328 subregions and clarified the boundaries between subregions, such as the olfactory bulb, basal ganglia, septal region, preoptic region, striatum, hypothalamus, thalamus, hippocampus, mesencephalon, metencephalon, and myelencephalon.

We and other researchers later characterized the distribution and anatomical localization of key proteins in different cell types within the brains of tree shrews, rats, and mice, including vasopressin, oxytocin, vasoactive intestinal polypeptide (Ni et al., 2014), neuropeptide Y (Ni et al., 2015), glutamate transporter (Balaram et al., 2015), monoamine receptor (Palchaudhuri & Flügge, 2005), corticotropin-releasing factor (Shu et al., 2015), calbindin (Ni et al., 2018a), parvalbumin (Ni et al., 2018b), nitric oxide synthase, calretinin (Rice et al., 2011), and tyrosine hydroxylase (Huang et al., 2020; Ni et al., 2021). Studies on neurotransmitters and their receptors in stress-related tree shrew brain regions during stress responses have also provided insights into the structural plasticity of the hippocampus (Fuchs & Flügge, 1998; Magariños et al., 1996), dynamic levels of serotonin receptors and adrenergic receptors (Flügge, 1995, 1996; Flügge et al., 1997), changes in glucocorticoid and mineralocorticoid receptors in the hippocampus (Meyer et al., 2001), corticotropin-releasing factor in the paraventricular nucleus of the hypothalamus and central extended amygdala (Kozicz et al., 2008), and the regulation of corticotrophin-releasing-hormone upon acute stress (Fang et al., 2016). Comparative anatomical studies have also identified differences in neuropeptide Y and its receptors in response to stress between tree shrews and rats (Zambello et al., 2010).

Doublecortin is primarily and transiently expressed in newly born neurons in the subventricular zone (SVZ) and subgranular zone (SGZ), playing a crucial role in neurogenesis within the olfactory bulb and hippocampus. In tree shrews, doublecortin-immunoreactive neurons in the SVZ and SGZ display a mix of rodent and primate-like topographic characteristics (Ai et al., 2021). Most neural progenitors in the SVZ of the tree shrew neocortex are self-amplifying intermediate progenitor cells, which contribute to brain volume expansion and the generation of a six-layered neocortex (Yin et al., 2020). Additionally, the basal radial glia and other neural stem and progenitor cells involved in tree shrew neocortex development have been identified and characterized, showing a closer relationship to NHPs than to rodents (Römer et al., 2018). Neural stem cells from tree shrews also exhibit distinct characteristics that differ from those of rats (Hu et al., 2018).

Application of single-cell and spatially resolved transcriptomics (Piwecka et al., 2023; Vandereyken et al., 2023; Wu & Zhang, 2020) in the tree shrew brain will enhance our understanding of the diversity of neural cell types and provided a comprehensive profile of their generation during brain development. Recent research on the single-cell transcriptomes of two tree shrew fetal whole brains identified 20 cell clusters, potentially comprising 14 cell types, through integrated analysis of tree shrew, rhesus macaque, and human brains (Zhuang et al., 2023). Another recent study created an integrated single-cell transcriptomic atlas of the retina from tree shrews and representative vertebrates, offering insights into the evolution and innovation of neuronal cell classes and types (Hahn et al., 2023). Furthermore, ongoing efforts are in the process of developing a fine-grained single-cell transcriptomic atlas of the tree shrew brain.

**Afferent and efferent connections in tree shrew brains**

Whole-brain mapping in tree shrews has revealed afferent projections to the 5th cerebellar lobule and paramedian lobule of the cerebellum (Ni et al., 2018a). Dye tracing and viral tracing have provided details into the neural circuit connections in tree shrews, highlighting the structural and functional connections between various brain regions, such as the suprachiasmatic nucleus, caudate nucleus, putamen, accumbens nucleus (Ni et al., 2021), bed nucleus of the stria terminalis (Ni et al., 2016), visual cortex (Lyon et al., 2003; Petry & Bickford, 2019), pulvinar (Day-Brown et al., 2010), temporal cortex (Chomsung et al., 2010), striate cortex (Bosking et al., 1997; Muly & Fitzpatrick, 1992), hypothalamus, and raphe (Reuss & Fuchs, 2000). These identified connections offer valuable insights into the conservation of neural pathways during mammalian brain evolution. The MRI atlas of the tree shrew provides high spatial resolution and detailed *in situ* brain structure data, facilitating the analysis of neuroimaging data in tree shrews (Dai et al., 2017, 2018; Huang et al., 2018; Wang et al., 2013). Additionally, the Allen Mouse Brain Common Coordinate Framework (CCF) was introduced to support the mapping and visualization of brain-wide gene expression and mesoscale connectivity (Wang et al., 2020d). Developing a standard 3D

reference atlas of the tree shrew brain will be very useful for mapping and visualizing individual subregions, cell types, molecular distributions, and connections.

Currently, whole-brain imaging datasets with anatomical annotation at single-neuron resolution have been achieved in mice (Gong et al., 2016; Qiu et al., 2024) and zebrafish (Kunst et al., 2019). Recent advances in spatially resolved single-cell RNA sequencing have enabled the whole-brain mapping of molecularly defined cell types in mice (Zhang et al., 2023a), which could also be applied to the tree shrew brain. Combining single-cell tracings with detailed annotation of whole-brain regions in tree shrews will allow for the generation of a mesoscale connectome, crucial for understanding brain function and structure. Of note, current advancements provide an ideal opportunity to map large brains at subcellular resolution (Shen et al., 2022), thereby helping to uncover the intricacies of the tree shrew brain.

## TREE SHREW VISUAL SYSTEM AND VISUAL CORTEX

The visual system of the tree shrew has been extensively studied over the past few decades, providing valuable insights into the anatomy, projections, circuits, and functions of the visual cortex and subcortical regions as well as the complexity of brain function (Baldwin et al., 2013; Bosking et al., 1997; Chomsung et al., 2010; Fitzpatrick, 1996; Kaas et al., 1972; Norton et al., 1985; Rockland & Lund, 1982; Ungersböck et al., 1991). Fitzpatrick (1996) reviewed the functional organization of local circuits in the visual cortex, focusing on the striate cortex, while Petry & Bickford (2019) provided a comprehensive review of the second visual system of the tree shrew. New approaches have further refined our understanding of the visual system in tree shrews.

Using intrinsic signal optical imaging and electrophysiology, Bosking et al. (2002) elucidated the spatial distribution patterns of population activity in the primary visual cortex (V1), demonstrating that thin line stimuli activate large populations of neurons in the V1, with significant overlap in activity from stimuli presented in nearby visual space. Mooser et al. (2004) depicted the morphological basis for orientation tuning in the V1 of tree shrews, revealing that the anisotropic arrangement of axon terminals is the principal source of orientation bias from feedforward connections. Further research into cross-orientation suppression has indicated that superimposed gratings affect V1 population responses through precise divisive suppression, supporting population coding in this region (MacEvoy et al., 2009). Comparisons of functional maps of orientation preference across species, including tree shrews, have shown a universal pattern in the evolution of orientation columns in the visual cortex (Kaschube et al., 2010). These orientation maps, established via moiré interference of regularly spaced ON (light-responsive)- and OFF (dark-responsive)-center retinal ganglion cell mosaics, provide a blueprint for the early development of cortical maps and receptive fields in the visual cortex of tree shrews (Paik & Ringach, 2011, 2012). Using two-photon imaging of GCaMP6 calcium signals, Lee et al. (2016) mapped the receptive fields of layer 2/3 neurons in the tree shrew visual cortex, identifying novel features of ON-OFF input convergence that support an invariant columnar architecture tailored to specific topographic constraints. Veit et al. (2014) examined receptive field structure, stimulus selectivity, response modulation, and orientation tuning for single neurons in the V1 of tree shrews, providing further evidence for the conservation of V1 functional organization between tree shrews and NHPs, and highlighting the role of intracortical recurrent processing in shaping V1 response properties (Veit et al., 2014).

Recent studies have provided more fine-grained details into neural coding in the tree shrew visual cortex. Sedigh-Sarvestani et al. (2021), using a chronic *in vivo* two-photon calcium imaging approach, identified a sinusoidal transformation of the visual field that forms the basis for periodic maps in the secondary visual area (V2) in the tree shrew, suggesting that cortical circuits can flexibly implement solutions for sensory surface representation. Similarly, Schumacher et al. (2022) used the same calcium imaging method to monitor V1 neurons in tree shrews during a Go/No-Go fine orientation discrimination task and observed selective and persistent learning-induced plasticity in the V1, supporting the notion that visual discrimination improves with training. Tanabe et al. (2022) discovered that tree shrew V1 neurons exhibit strong tuning to binocular disparity, comparable to that in primates, with computational modeling further suggesting that orientation-specific recurrent circuitry in the tree shrew V1 may underlie the observed tuning. These findings underscore the value of using tree shrews in studying binocular vision and demonstrating the role of cortical columns in computing stereoscopic depth.

Listing all findings from previous studies on the visual system and visual cortex of tree shrews is beyond the scope of this review. Nonetheless, research has significantly advanced our understanding of key questions about the visual system and helped reconstruct functional maps and connections. The introduction of more quantitative behavioral tests and neural modulation via optogenetic stimulation (Huang et al., 2014; Savier et al., 2021; Wang et al., 2023a) is expected to uncover the mechanisms of visual perception at multiple levels. Indeed, Wang et al. (2023a) demonstrated that optogenetic activation of CamKII projection neurons in the visual thalamus can be perceived by tree shrews. The transition from visual to optogenetic stimulus detection suggests that visual thalamus activation triggers visual percepts, paving the way for a new generation of visual prostheses based on thalamic optogenetics.

## GENETIC CHARACTERIZATION OF TREE SHREW IMMUNE SYSTEM

Before the completion of tree shrew genome sequencing (e.g., Fan et al., 2013), the cloning and characterization of immune genes in the tree shrew were rather uncommon due to the lack of genetic information, with amplification primer pairs typically designed based on other species. These earlier studies provided a glimpse into tree shrew immune genes. For instance, Oppelt et al. (2010) performed the first characterization of major histocompatibility complex (MHC) class II DRB genes in tree shrews, identifying 14 DRB haplotypes in 230 individuals. Zhang et al. (2013) analyzed the genomic organization of tree shrew MHC class I genes, finding high homology between tree shrews and primates. Mu et al. (2014) characterized the tree shrew TRIM5 family, discovering that tree shrew TRIM5-cyclophilin A (*TRIMCyp*) fusion gene represents a new paradigm of novel gene origination.

With the release of assembled tree shrew genomes using second-generation (Fan et al., 2013) and third-generation sequencing technology (Fan et al., 2019), retrieving specific gene sequences has become more accessible via public

databases, such as treeshrewDB (www.treeshrewdb.org; Fan et al., 2014; Ye et al., 2021) and TupaiaBase (http://tupaiabase.org; Sanada et al., 2019a). This genomic information has facilitated the characterization of tree shrew genes and gene families. Zhang et al. (2020b) studied the heavy chain constant region of immunoglobulin (Ig) in tree shrews and found that tree shrews possess only four classes of antibodies (IgM, IgG, IgE, and IgA), lacking IgD, with the oldest IgM antibody showing high homology with that of primates and recombinant IgG showing effective immuno-protective effects against HSV-1 infection and superior bactericidal effects compared to mouse IgG (Zhang et al., 2020b). We characterized the tree shrew guanylate-binding protein (GBP) family, which belongs to IFN-inducible GTPases and defends the host against invading pathogens, revealing five *GBP* genes (*tGBP1*, tGBP2, *tGBP4*, *tGBP5*, and *tGBP7*) that are ubiquitously expressed in a variety of tissues (Gu et al., 2019a). All the *tGBP* genes can be inducible by IFN-γ treatment or viral infections, with *tGBP1* exhibiting antiviral activity against vesicular stomatitis virus (VSV) and HSV-1 (Gu et al., 2019a). Mechanistically, tGBP1 interacts with STING to initiate autophagy and restrict HSV-1 infection (Gu et al., 2021a), while it interacts with the VSV phosphoprotein and represses primary transcription of the viral genome (Gu et al., 2021b).

We also characterized 2',5'-oligoadenylate synthetase (OAS), a member of the ISG family that synthesizes 2',5'-oligoadenylate (2-5A) in tree shrews (Yao et al., 2019). Results indicated that tree shrews contain four putative OASs (tOASs, including tOAS1, tOAS2, tOASL1, and tOASL2, but no tOAS3) constitutively expressed in various tissues. These tOASs are up-regulated upon viral infection, leading to the inhibition of DNA and RNA viral replication in renal cells (Yao et al., 2019). Notably, tOASL1 knockdown impairs antiviral immune response, while its overexpression potentiates RNA virus-triggered antiviral responses (Yao et al., 2020). Mechanistically, tOASL1 promotes cellular antiviral immune responses by recruiting melanoma differentiation-associated gene 5 (MDA5), a cytoplasmic dsRNA sensor, to mitochondrial antiviral signaling gene (MAVS), and immune signaling adaptor, enhancing their interaction (Yao et al., 2020). Additionally, the tree shrew genome contains multiple copies of cyclooxygenase and lipoxygenase genes (ALOX isoforms), including four copies of *ALOX15* (*tupALOX15a-d*), compared to the single copy found in humans and mice (Schäfer et al., 2020). The enzymatic properties of tupALOX15a and tupALOX15c show subtle differences and adhere to the “Triad Concept and Evolutionary Hypothesis of ALOX15 specificity” (Schäfer et al., 2020). Further characterization of these ALOX isoforms in tree shrews has important biological implications due to their role in the biosynthesis of inflammatory mediators.

A deeper understanding of the functions of tree shrew immune genes will provide valuable insights into their susceptibility to viral infections and their innate and adaptive immunity. Our previous research showed that the tree shrew *TRIMCyp* lacks antiviral activity against human immunodeficiency virus 1 (HIV-1), macaque simian immunodeficiency virus (SIVmac), and N-tropic murine leukemia virus (N-MLV) infections due to a mutation in the RING, B-box, and coiled-coil (RBCC) motif, a signature motif of the TRIM family (Mu et al., 2014). This may explain the susceptibility of tree shrews to many human viruses. We also characterized the apolipoprotein B mRNA-editing enzyme catalytic polypeptide-like 3 (APOBEC3) family, which contains several antiviral factors that inhibit the replication of various human viruses, including HIV-1 and hepatitis B virus (HBV) (Sadeghpour et al., 2021; Stavrou & Ross, 2015), in tree shrews. Notably, we identified five APOBEC3 members (tsAPOBEC3s) highly expressed in immune-related tissues, which can be up-regulated by interferon-α2β treatment and edit both strands of HIV-1 DNA via deaminase-dependent mechanisms (Luo et al., 2018). The tsAPOBEC3 proteins have been shown to restrict HBV replication, possibly explaining the failure to establish a persistent HBV infection model using tree shrews (Luo & Zheng, 2020). Using tree shrew primary cells from a variety of tissues, Luo et al. (2021) showed that these cells are permissive to pseudotyped HIV-1. Tree shrew lung fibroblasts with transduction of retroviral vectors for human CD4 and CCR5 support HIV-1 entry and replication, but viral infectivity is suppressed by tsAPOBEC3 proteins, especially tsA3Z2c-Z1b (Luo et al., 2021). Similarly, the natural loss of the retinoic acid-inducible gene I (RIG-I) in tree shrews (Fan et al., 2013) results in functional replacement by MDA5, another key cytoplasmic sensor of viral pathogen-associated molecular patterns (Xu et al., 2016). The change in the RIG-I-like receptor (RLR)-mediated signaling pathway (Onomoto et al., 2021; Rehwinkel & Gack, 2020; Zheng et al., 2023) in tree shrews is accompanied by alternative splicing of tree shrew STING, with short and long STING isoforms playing different roles in modulating anti-RNA virus responses (Xu et al., 2020b). In addition, although tree shrew MAVS (tMAVS) is generally evolutionarily and functionally conserved (Xu et al., 2015), the cleavage pattern of tMAVS by the NS3/4A protease of the hepatitis C virus (HCV) differs from that of humans, leading to impaired IRF3-mediated induction of IFN-β but maintained NF-κB signaling in tree shrew primary hepatocytes upon HCV infection (Xu et al., 2020c). Consequently, tMAVS serves as a dual target for innate immune evasion and restriction of viral replication via NF-κB in tree shrew hepatocytes during HCV infection, potentially explaining why tree shrews can be acutely infected by HCV but do not develop persistent infections (Xu et al., 2020c).

Characterizing the genetic and functional aspects of tree shrew immune genes has not only enhanced our understanding of the uniqueness and evolutionary conservation of the tree shrew immune system but has also helped clarify the susceptibility of tree shrews to specific viral infections and the difficulties in establishing persistent infection models (e.g., HBV and HCV). By identifying potential restriction factors and utilizing genetic modification of target genes, it is anticipated that better tree shrew infection models will be established in the future.

## GENETIC MODIFICATION OF TREE SHREWS

Unlike NHPs, tree shrews do not exhibit a menstrual cycle. Additionally, female tree shrews do not display vaginal plugs after mating, which are commonly produced by males after mating to physically obstruct the female genital tract and prevent remating (Fromhage, 2012; Stockley et al., 2020). As such, the *in vitro* fertilization techniques used for NHPs (e.g., Sun et al., 2008) cannot be applied to tree shrews, nor can the standard genetic modification procedures used for rats (Hirabayashi et al., 2019), mice (El Marjou et al., 2021), rhesus monkeys, and crab-eating monkeys (Luo et al., 2016; Niu et al., 2010; Sasaki et al., 2009; Zhao et al., 2019).

Spermatogonial stem cells (SSCs) continuously produce spermatozoa in the testes (Kubota & Brinster, 2018) and are utilized for generating genetically modified animals (Feng et al., 2002; Wu et al., 2015). Given the difficulties of collecting tree shrew embryos (Yan et al., 2016) to establish embryonic stem cells, or the difficulties in collecting tree shrew oocytes and sperm for *in vitro* fertilization, we established an SSC line for successful genetic manipulation of tree shrews. We developed a culture system for tree shrew SSC expansion and created transgenic tree shrews using lentiviral transduction (Li et al., 2017). This SSC-based gene editing approach paves the way for further genome manipulation of tree shrews. To date, we have generated transgenic tree shrews overexpressing causal genes for familiar AD, such as amyloid-beta precursor protein (APP) and presenilin 1 (PSEN1) mutants (Knopman et al., 2021; Zhang et al., 2019a), with preliminary analyses, including cognitive and pathological tests, revealing neuroinflammation in brain tissues and cognitive impairment at an early age (unpublished data).

The successful culture of tree shrew SSCs also established a basis for precise genome editing using advanced gene editing techniques such as base editing (Pfeiffer & Stafforst, 2023). However, two significant obstacles remain regarding genetic modifications using SSCs. Firstly, the efficient delivery of genome editors into tree shrew SSCs has proven to be more challenging than anticipated. We are currently optimizing the vector and RNA delivery systems via electroporation. Promising *in vivo* delivery systems for gene therapy, especially for AAV and lipid nanoparticles (Madigan et al., 2023; Taha et al., 2022), are being evaluated for their application potential in tree shrew SSCs. Secondly, long-term culture of tree shrew SSCs (>50 passages) leads to a loss of spermatogenesis ability due to DNA damage accumulation and mitochondrial dysfunction (Li et al., 2023a). Supplementation with nicotinamide riboside has shown beneficial effects on the long-term culture of tree shrew SSCs (Li et al., 2023a). Thus, limiting culture passages should help minimize the deleterious effects of prolonged culture on gene editing.

To date, few studies have reported on the transient delivery of exogenous genes into tree shrew organs and tissues. We tested several types of AAVs and achieved consistent expression of exogenous genes in adult tree shrew brain tissues using AAV9 and AAV8 (unpublished data). Knockdown of the X-linked primate-specific gene SSX family member 1 (*SSX1*) in tree shrews, using *Ssx1*-shRNA-containing and EGFP-expressing AAV9 vectors delivered via injection into the seminiferous tubules, successfully mimics asthenoteratozoospermia phenotypes observed in human patients with *SSX1* deleterious variants, providing a model for studying testis-enriched primate specific genes in spermatogenesis (Liu et al., 2023). Xu et al. (2017) explored genetic manipulation in the developing tree shrew brain using *in utero* electroporation (IUE) and retroviral delivery of short-hairpin RNAs, demonstrating the feasibility of gene manipulation using these methods for establishing tree shrew models of neurodevelopmental diseases.

Given the differing time and cost requirements for genetic modifications at the germline level using the SSC procedure (Li et al., 2017) versus the tissue level using transient exogenous gene delivery, researchers must balance these approaches. We advocate for the use of AAV- or lipid nanoparticle-mediated delivery of certain genes or gene editors into tree shrew tissues to create disease models due to the shorter timeframe and relatively lower cost. Nonetheless, the choice of procedure depends on the research goals and tree shrews should only be used following the 3R principles. In addition to generating genetically modified tree shrews, the establishment of SSCs and related culture systems (Li et al., 2017) provides a rapid platform for characterizing pathogenic genes causing idiopathic male infertility, including oligozoospermia, teratozoospermia, and asthenozoospermia, especially for primate-specific genes (Shao et al., 2019). Testing semen samples and testis tissues after transplantation and recovery of genetically modified SSCs with pathogenic mutations can elucidate the pathogenesis of male infertility and create valid disease models, as had been demonstrated by Liu et al. (2023).

## WHY HAVE RECENT TREE SHREW DISEASE MODELS NOT LED TO BREAKTHROUGHS?

In recent years, tree shrews have been increasingly used to create animal models for different diseases, particularly infectious diseases (Kayesh et al., 2021; Li et al., 2018b; Xia et al., 2022; Xu et al., 2020a; Wang et al., 2023b; Zhang et al., 2019b; Zhao et al., 2020b) and cancer research (Jiang et al., 2017; Tu et al., 2019; Zeng et al., 2023). Various studies have also explored the effects of aging on tree shrew brains (Li et al., 2024; Rodriguez-Callejas et al., 2020; Wei et al., 2017) and the potential efficacy of natural products against AD (Wang et al., 2020c; Yang et al., 2022). Parkinson's disease models of tree shrew were also induced by using 1-methyl-4-phenyl-1,2,3,6-tetrahydropyridine (MPTP; Ma et al., 2013) and its oxidized product 1-methyl-4-phenylpyridinium (MPP+; Li et al., 2023d). We have provided a summary of these tree shrew models in the context of face validity, predictive validity, and construct validity (Table 1), as several excellent review papers have already been published. For instance, Cao et al. (2003) and Xiao et al. (2017) provided summaries of tree shrew models reported before 2017; Li et al. (2018b) and Kayesh et al. (2021) provided comprehensive reviews of the use of tree shrews in establishing human viral infection models; and Lu et al. (2021) reviewed tree shrew tumor models and their clinical manifestations. These reviews consistently concluded that tree shrews hold considerable promise as powerful animal models for studying human diseases.

Based on the disease models listed in Table 1, most recently reported tree shrew models pertain to infectious diseases, including Epstein Barr virus (Xia et al., 2022, 2024), Zika virus (Baloch et al., 2021; Zhang et al., 2019b, 2019c), human, avian, and swine influenza viruses (Li et al., 2018a; Sanada et al., 2019c; Wang et al., 2023b, 2024c; Xu et al., 2019; Yuan et al., 2019), human adenovirus species B (Li et al., 2021c; Liu et al., 2024), HBV (Kayesh et al., 2017a; Li et al., 2021b; Sanada et al., 2019a), HCV (Feng et al., 2017; Kayesh et al., 2017b; Lu et al., 2020), and severe acute respiratory syndrome coronavirus 2 (SARS-CoV-2; Xu et al., 2020a; Zhao et al., 2020b). The successful establishment of these viral infection models in tree shrews offers a valuable platform for studying host-virus interactions, cross-species infection mechanisms (Wang et al., 2023b), and testing multiple anti-viral treatments, including neutralizing monoclonal antibodies (Liu et al., 2024), ionizable lipid SM-102-based CRISPR nanoparticles (Yi et al., 2023), and hepatitis B surface-small antigen and hepatitis B core antigen

**Table 1 Summary of recent tree shrew models for human diseases**

| Disease / intervention | Modeling methods | Phenotypes and symptoms | Potential mechanism, drug efficacy, and limitations | References |
|---|---|---|---|---|
| Naturally aging | Adult (mean age 3.8 years), old (mean age 6 years), and aged (mean age 7.5 years) tree shrews | Aged tree shrews showed increased activated microglia labeled with ferritin and dystrophic microglia labeled with Iba1, increased oxidative RNA damage, as revealed by 8-hydroxyguanine (8-OHG) staining in all hippocampal regions, enhanced Tau hyperphosphorylation in dentate gyrus (DG), CA3, and subiculum (SUB) subregions, and phagocytic inclusions of cellular debris or neurons containing tau aggregates and/or damaged RNA in activated M2 microglia. Adult and old tree shrews harbored increased hypertrophic astrocytes in hippocampal region, while aged animals contained significant atrophic astrocytes compared to younger animals. | *Mechanism:* Aged tree shrews showed increased oxidative stress, phosphorylated tau, and dystrophic microglia in hippocampus; S100A10, a protein overexpressed by neuroprotective-type astrocytes, occurred in the nucleus of hypertrophic astrocytes of young animals, but in the cytoplasmic compartment of atrophic astrocytes in aged animals. Aged tree shrews could be used to study brain and microglial alterations during aging process. *Limitations:* Only histochemical and immunofluorescence assays were performed, with no characterization of molecular mechanisms and potential targets. | Rodriguez-Callejas et al., 2020; 2024 |
| | Adult (about 1 year old) and aged (6 years old or older) tree shrews | Aged tree shrews showed impaired cognitive performance, as revealed by pole-board and novel object recognition tests, increased Aβ accumulation and phosphorylated Tau protein, synaptic degeneration, neuronal loss, and gliosis in cortical and hippocampal tissues. | *Mechanism:* Aged tree shrews showed increased levels of Aβ40, Aβ42, total-Aβ, and phosphorylation of Tau at Ser202/Thr205 and Thr231, decreased levels of PSD95 and NeuN, and increased levels of GFAP and Iba1 in cortical and hippocampal tissues. *Limitations:* No characterization of natural aging pattern was performed at omics and single-cell levels. | Li et al., 2024 |
| Alzheimer's disease (AD) | Adult male tree shrews (15 months old) received an intracerebroventricular (icv) injection of $A\beta_{1\text{-}40}$ | $A\beta_{1\text{-}40}$-treated tree shrews showed cognitive impairments, hippocampal atrophy, increased apparent diffusion coefficient (ADC) and fractional anisotropy (FA) based on diffusion tensor magnetic resonance imaging (DTI) analysis, thinner and smaller cells in hippocampal CA3 and DG subregions and reduced number of cells in DG, neurotic plaques and neurofibrillary tangles (NFTs) in hippocampus, and cell apoptosis. | *Mechanism:* Expression levels of apoptosis related genes, including *Bad*, *IAP*, and *Cytochrome c*, were down-regulated, expression level of *TNF-R1* was up-regulated, differentially expressed genes were enriched in AD pathways and other biological processes. *Limitations:* Sample size was too small for robust conclusions and interpretation of molecular mechanism may be biased based on transcriptome analysis alone. | Lin et al., 2016 |
| AD and donepezil | Adult male tree shrews (1–1.5 years old) received icv injection of $A\beta_{1\text{-}40}$, followed by daily treatment with donepezil (1 mg/kg) | $A\beta_{1\text{-}40}$-treated tree shrews showed spatial cognitive deficits, body weight loss, hippocampal atrophy with lateral ventricle enlargement, enlarged temporal horn and increased ADC in DTI analysis, Aβ deposits, neuronal loss, and glial activation. Donepezil ameliorated all symptoms. | *Mechanism:* Expression of choline acetyl transferase (ChAT) and BDNF and phosphorylation of TrkB were decreased, acetylcholinesterase (AChE) activity and fibrillary acid protein (GFAP) expression were increased, $A\beta_{1\text{-}40}$ injection affected cholinergic system and BDNF/TrkB-signaling pathway. *Drug efficacy:* Donepezil rescued gene expression abnormalities caused by $A\beta_{1\text{-}40}$, and showed a protective effect. *Limitations:* Detailed description of data analyses lacking, and independent validation still required. | Zheng et al., 2018 |
| AD and Ginsenoside Rg1 (GRg1) | Adult male tree shrews (6 months old) received an $A\beta_{25\text{–}35}$ injection in both hippocampal regions, with daily dose of D-galactose (D-gal) at 125 mg/kg; treatment groups included intragastric (ig) administration of donepezil daily (3 mg/kg) and GRg1 | $A\beta_{25\text{–}35}$-injected group showed impaired learning and memory in Morris water maze test, increased Tau expression in hippocampal and cortical tissues, altered bacterial communities, increased oxidative stress damage, microglial activation, inflammation, and apoptosis in hippocampal and cortical tissues. Donepezil and high concentrations of GRg1 ameliorated impaired learning and memory ability and related abnormalities in tree shrews treated with $A\beta_{25\text{–}35}$ and D-gal. High concentrations of GRg1 reduced Tau-positive cells and changed abundances of *Proteobacteria*, *Verrucomicrobia*, and *Lactobacillus* in gut microbiota | *Mechanism:* Tree shrews treated with $A\beta_{25\text{–}35}$ and D-gal showed increased tau expression and altered gut microbiota composition and abundance, increased Aβ1-42, BACE1, and phosphorylated Tau levels, enhanced oxidative stress injury, as revealed by increased nitrotyrosine and 8-OHG levels and decreased expression of SOD1, increased expression of Iba1 and IL-1, and decreased levels of MAP2, NeuN, β-catenin, and phosphorylated GSK-3β. *Drug efficacy:* Donepezil and high concentrations of GRg1 decreased Tau expression, reversed altered levels of related proteins, exerted a neuroprotective effect, and altered gut microbiota. *Limitations:* No detailed targets or mechanisms were tested. | Wang et al., 2020c; Yang et al., 2022 |

**Continued**

| Disease / intervention | Modeling methods | Phenotypes and symptoms | Potential mechanism, drug efficacy, and limitations | References |
|---|---|---|---|---|
| Parkinson's disease (PD) induced by $MPP^+$ | Male tree shrews (1.5 years old) received a unilateral nigral injection of 50 μg $MPP^+$ | $MPP^+$-treated tree shrews manifested PD clinical symptoms, including motor deficits (difficulties in forelimb use, loss of balance, stooped posture), bradykinesia, rest tremor, gait abnormalities, postural instability, and apomorphine-induced rotations; increased PD score based on improved Kurlan scale; marked dopaminergic neuron loss (up to 95%) in substantia nigra on lesioned side of the brain | *Mechanism:* Precise injection of $MPP^+$ into substantia nigral region depleted local dopaminergic neurons and resulted in PD-like symptoms in tree shrews.<br>*Limitations:* No test for Lewy body-like pathology and related changes in circuit; no test for treatments such as stem cell transplantation and related drugs. | Li et al., 2023d |
| Cerebral ischemia (CI) | Adult male tree shrews (6-months old) received permanent distal middle cerebral artery occlusion after anesthesia | Tree shrews in CI group exhibited a decline in aggressive behavior, seeking behavior, and voluntary activity, and showed no response to stimuli and increased neural behavior scores (higher scores represent more severe damage). Magnetic resonance imaging showed high signals at infarct area. 2,3,5-triphenyltetrazolium chloride (TTC) staining revealed a marked white infarction. Defective cortical structure and deep-stained nuclei were observed in cortex of CI group. Most neurons shrank in size, with a reduced number of NeuN- and GFAP-positive cells around lesion epicenter in the CI group relative to the sham group. | *Mechanism:* Cerebral ischemia in tree shrews was demonstrated by alterations in neural behavior score and pathological analyses for neural cell morphology and infarct area.<br>*Limitations:* Drug efficacy was not tested and no molecular target was identified. | Wang et al., 2019c |
| Depression and clomipramine | Adult male tree shrews were subjected to chronic psychosocial stress induced by social defeat between dominant and subordinate animals | Socially defeated tree shrews exhibited a decrease in sucrose preference, exploration behaviors, locomotion distance, and social interaction.<br>Oral clomipramine administration reversed almost all depression-like behaviors, but not motivational reduction. | *Mechanism:* Chronic social defeat induced a broad spectrum of behavioral changes, including anhedonia, motivation reduction, and social avoidance, with no report of potential mechanism.<br>*Drug efficacy:* Clomipramine had a therapeutic effect on socially defeated animals, but no effect on rescuing motivational reduction.<br>*Limitations:* No detailed target for clomipramine was analyzed and no molecular mechanism regarding why clomipramine had no effect on reversing reduced motivation in socially defeated tree shrews was provided. | Shen et al., 2018 |
| Cocaine motivation | Adult male tree shrews were subjected to cocaine self-administration (SA) | Tree shrews were trained to acquire cocaine SA. Cocaine craving (as measured by number of active nose-pokes) gradually increased, then declined along cocaine withdrawal timeline; incubation of cue-induced cocaine craving occurred on withdrawal day (WD) 45. Knockdown of Cav1.2 inhibited cocaine craving on WD45. | *Mechanism:* Striatal dopamine D1 receptor (D1R), but not D2R, mediated up-regulation of Cav1.2, showing a time-dependent increase in nucleus accumbens (NAc) during incubation of cocaine craving.<br>*Drug efficacy:* Injection of L-type calcium channels antagonist verapamil in NAc decreased cocaine-seeking behaviors.<br>*Limitations:* D1R-Cav1.2 signaling underlying incubation of cocaine craving needs validation, especially in the context of cocaine relapse. | Duan et al., 2021 |
| Cocaine-seeking habit | Adult male tree shrews were subjected to cocaine and sucrose SA, compared to sucrose-habitual behavior and cocaine-seeking habitual behavior | Habitual cocaine-seeking behaviors (HCSB) and habitual sucrose-seeking behaviors (HSSB) were established in tree shrews. | *Mechanism:* Animals with HCSB exhibited higher D1Rs and $Ca_v1.2$ expression but lower D2Rs and $Ca_v1.3$ expression in the putamen, while animals with HSSB exhibited lower membrane expression of D2R in the putamen than animals with non-habitual behavior.<br>*Limitations:* Imbalanced function between putamen and nucleus caudate and the neural circuits need to be further determined. | Duan et al., 2022 |

**Continued**

| Disease / intervention | Modeling methods | Phenotypes and symptoms | Potential mechanism, drug efficacy, and limitations | References |
|---|---|---|---|---|
| Glaucoma / ocular hypertension | Adult tree shrews (1.7-7.7 years old) were injected with ferromagnetic beads (50 μL of a 25 mg/mL solution) into anterior chamber, which were then directed into iridocorneal angle by a magnet to block aqueous outflow | Tree shrews injected with ferromagnetic beads (treated group) showed significantly increased intraocular pressure (IOP) relative to control group during 12-week follow-up period, average of 22.7±3.6 mm Hg. Significant retinal nerve fiber layer (RNFL) was thinner and optic nerve axon counts and density were reduced in treated group, along with progressive bowing of lamina cribrosa and posterior displacement of anterior laminar surface in tree shrews with increasing severity of experimental glaucoma | *Mechanism:* Reductions in RNFL thickness and optic nerve axon counts and density were associated with IOP elevation. Optic nerves in the treated group showed histopathology consistent with glaucomatous optic neuropathy<br>*Limitations:* No drug efficacy was tested | Samuels et al., 2018 |
| Hyperopia | Starting at 24±1 days of visual experience, juvenile tree shrews (6 weeks old) received light treatment through amber filters (BPI 500/550 dyed acrylic) either atop cage (Filter group, 300–400 lux) or through amber-dyed lenses fitted into a goggle frame (Goggle group). Age-matched animals raised in standard lighting (100–300 lux) were used as the control group | Animals in Filter group became progressively more hyperopic, whereas animals in the Goggle and control groups showed continued normal emmetropization during 11-day treatment period. Significant hyperopia (mean [SE] = 3.5 [0.6] D) was observed in Filter group compared to Goggle (0.2 [0.8] D) and control groups (1.0 [0.2] D). Filter group had significantly thicker choroid at the end of 11-day treatment. Vitreous chamber depth in Filter group decreased with increasing hyperopia, whereas that in the Goggle and control groups was similar. End-of-treatment vitreous chamber depth was significantly smaller than that in the other two groups. | *Mechanism:* Exposure to ambient amber light caused substantial hyperopia in tree shrews but had no effect on refractive error in Goggle group.<br>*Limitations:* No drug efficacy or prophylactics was tested. | Khanal et al., 2021 |
| Choroidal neovascularization (CNV) | Adult tree shrews (2 years old) were subjected to CNV by laser photocoagulation | Retinal edema and damaged Haller's layer in choroid occurred 7 days after photocoagulation; after day 14, neovascularization in retina destroyed ganglion cell layer, disrupted nerve fiber layer, loosened Haller's and Sattler's layers, with neovascularization surrounded by neutrophils, macrophages, and fibroblasts; microvessel density increased. | *Mechanism:* Choroid and retinal transcriptomic data were used to identify differentially expressed genes during CNV; signaling pathways, including fatty acid metabolic pathway and cell adhesion molecular signaling, and genes in ribosomal protein family and complement system were involved in tree shrew CNV.<br>*Limitations:* No drug efficacy was tested and no molecular target was verified. | Jia et al., 2021 |
| Chronic experimental autoimmune uveitis (EAU) | Adult tree shrews (4–8 months old) were subcutaneously immunized at tail base and both thighs with six inter-photoreceptor retinoid-binding proteins (IRBPs) of tree shrews (R14, $IRBP_{1197-1211}$, R16 and $IRBP_{1041-1071}$) and bovines (R14 and R16) | $IRBP_{1197–1211}$ and R14 induced ocular inflammation and chronic EAU (including conjunctival hyperemia, ciliary injections, whitish hypopyon spots, and corneal ulcers and edema), with subretinal deposits and retinal damage. Inflammatory infiltration of innate immune cells and adaptive immune cells into conjunctiva, cornea, anterior chamber, ciliary processes, choroid, and retina, and retinal lesions were main histopathological changes. Subretinal deposits positively expressed Aβ, CD8, and P2RY12. RGS4 inhibitor CCG203769 and dihydroartemisinin significantly alleviated retinal pathological damage of $IRBP_{1197-1211}$-induced EAU by decreasing expression of CD4 T-cells. | *Mechanism:* Chronic EAU in tree shrews was elicited by bovine R14 and tree shrew $IRBP_{1197-1211}$, characterized by retinal degeneration, retinal damage with subretinal Aβ deposits and microglial/macrophage infiltration, and T-cell response, likely by altering multiple signaling pathways including mitogen-activated protein kinase (MAPK) signaling.<br>*Limitations:* No molecular target was experimentally verified. | Hu et al., 2022 |
| Diabetic retinopathy | Male adult tree shrews received a single intraperitoneal injection of streptozotocin (STZ; 175 mg/kg) | In total, 75% of animals developed type 1 diabetes with sustained hyperglycemia; islet β cells were almost lost in the pancreas of diabetic animals; serum levels of glycated hemoglobin, free fatty acids, total cholesterol, high- and low-density lipoproteins, and triglycerides were increased; cone photoreceptor function was compromised as shown by diminished A- and B-wave photopic electroretinogram amplitudes; retinal function was lost; retinal ganglion cell (RGC) function was compromised, with loss of RGCs and peripheral short-wave sensitivity (SWS) cones. | *Mechanism:* SWS cones and RGCs were lost after STZ injection, with increased expression of TRIB3, VEGF, and p-AKT/p-mTOR axis, but reduced levels of ISR-1 protein in diabetic retinas.<br>*Limitations:* No drug efficacy was tested. | Gorbatyuk et al., 2022 |

**Continued**

| Disease / intervention | Modeling methods | Phenotypes and symptoms | Potential mechanism, drug efficacy, and limitations | References |
|---|---|---|---|---|
| Diabetic cerebral ischemia | Adult male tree shrews fed a high-fat diet for 8 weeks received an intravenous injection of 2% STZ (100 mg/kg body weight), with photochemically induced cortical thrombotic cerebral ischemia | STZ application resulted in a relatively high ratio (up to 77%) of successful diabetes modeling. Diabetic animals showed polydipsia, polyphagia, polyuria, thinned retina layers with disordered structures, with pathological retinal changes aggravated after cerebral ischemia. Ischemic postconditioning reduced pathological changes in diabetic retinopathy and alleviated retinopathy. | *Mechanism:* Diabetes and cerebral ischemia increased retinal VEGF expression, which was reduced by ischemic postconditioning. *Limitations:* No drug efficacy was tested for diabetic retinopathy; molecular mechanisms of the ameliorating effects of ischemic postconditioning were not determined. | Zhao et al., 2020a |
| Ischemia stroke and diabetes mellitus | Adult male tree shrews were treated with STZ (Zhao et al., 2020a), and thrombotic cerebral ischemic stroke was induced using photochemical treatment | Tree shrews with diabetes mellitus (DM) and DM ischemic stroke (DMIS) showed increased water intake, urine volume, serum glucose levels, altered biochemical indicators, and abnormal ultrastructure of cellular organelles; DMIS group exhibited a larger infarct size. Transcriptomic analysis of infarct tissues identified differentially expressed genes and enriched pathways. | *Mechanism:* DM tree shrews showed increased *IL-8* expression and activation of inflammatory status relative to healthy controls; DMIS group showed increased expression of *CCL7*, ATP-binding cassette sub-family A member 12, and adhesion G protein-coupled receptor E2 relative to DM group. *Limitations:* No drug efficacy was tested and no molecular target was verified. | Zhao et al., 2021b |
| | | Ischemic postconditioning reduced infarct size and reduced nerve cell injury in tree shrews with DMIS. Transcriptomic analysis of ischemic cerebral tissues identified differentially expressed genes and enriched pathways. | *Mechanism:* Ischemic postconditioning reduced inflammation and stress responses by decreasing activity of TNF and NF-κB signaling, and Fc gamma R-mediated phagocytosis. *Limitations:* No drug efficacy was tested and no molecular target was experimentally verified. | Zhao et al., 2021c |
| Diabetes and regeneration of islet β-cells | Male tree shrews (8 weeks old) were intraperitoneally injected with STZ (150 mg/kg) | Increased fasting blood glucose and mean serum insulin levels after STZ treatment for 3 days; islets were smaller and deformed, with visible cell necrosis and degeneration, and number of islets was reduced; intra-islet cell regeneration was only scattered at day 7 after STZ treatment, with no regeneration of centroacinar cells | *Mechanism:* Proportion and expression of insulin-positive cells in islets were decreased after STZ treatment; positive PDX-1 expression was observed in pancreatic interstitial cells and dendritic cells of pancreatic lymph; repair mechanism of STZ-injured islet β-cells in tree shrews was similar to that of humans. *Limitations:* No drug efficacy or stem cell transplantation therapy was tested. | Zhao et al., 2018 |
| Diabetes mellitus and mesenchymal stem cell (MSC) transplantation | Male tree shrews were intraperitoneally injected (lower right quadrant of abdomen) with STZ (170 mg/kg), with intraportal transplantation of insulin-producing cells (IPCs) derived from human MSCs | Tree shrews showed increased blood glucose levels, loss of body weight, and no intact islets in the pancreas after STZ treatment; after IPC transplantation (which expressed islet-related genes and secreted high levels of insulin) one week after STZ treatment, blood glucose levels decreased to normal levels in diabetic animals and body weight recovered; liver tissues of diabetic animals with IPC transplantation showed extensive and diffuse edema and scattered insulin-positive cells in hepatic sinusoids. | *Mechanism:* Transplantation of IPCs expressing insulin, NGN3, and PDX1, derived from MSCs, reversed hyperglycemia and weight loss in diabetic tree shrews induced by STZ. *Limitations:* Recovery of pancreatic islets in STZ-induced diabetes model was not examined, with a different mechanism compared to human diabetes; no follow-up study was conducted to monitor the fate and potential risk of malignancy of transplanted cells. | Zhu et al., 2023 |
| Chronic stomach mucosal injury | Adult tree shrews (2-3 years old) were administered a daily intraperitoneal injection of MPTP (2 mg/kg/day) for 13 weeks | Tree shrews showed local congestion or diffuse hemorrhagic spots on the gastric mucosa, multiple regions of redness and bleeding on inner wall covered with white moss, or partial slight shedding of gastric mucosa; H&E staining of gastric mucosa showed immune cell infiltrations. | *Mechanism:* Integration of transcriptomic and proteomic data revealed changes in mRNA and proteins in gastric mucosa, and identified several genes (e.g., *RPL4*, *ANXA1, GAST*, and *DDC*) involved in MPTP-induced mucosal injury. *Limitations:* No experimental assays to characterize the highlighted genes in MPTP-induced mucosal injury and affected signaling pathways were conducted. | Wang et al., 2024a |

**Continued**

| Disease / intervention | Modeling methods | Phenotypes and symptoms | Potential mechanism, drug efficacy, and limitations | References |
|---|---|---|---|---|
| Asthenoteratozoospermia | Adult male tree shrews (6 months old or older) were injected with TR-AAV9-*Ssx1*-shRNA (each 80 μL, dose of $1.5\times10^{12}$ vector genome/mL) into seminiferous tubules of bilateral testes via rete testis for 60 days | Levels of *Ssx1* mRNA and protein were significantly reduced in the testes of tree shrews with TR-AAV9-*Ssx1*-shRNA injection. Tree shrews with *Ssx1* knockdown displayed reduced testis weight, impaired spermatogenesis or loss of germ cells in seminiferous tubules, abnormal sperm morphologies (absent, coiled, or angulated flagella; absence of peripheral or central microtubules at midpiece and principal piece of sperm flagella), and reduced sperm motility. | *Mechanism:* Expression of multiple spermatogenesis-associated factors was dysregulated in testes of tree shrews with *Ssx1* deficiency, and these factors were enriched in multiple biological processes involved in spermatogenesis<br>*Limitations:* No detailed mechanism regarding SSX1 deficiency in spermatogenesis was determined and no drug efficacy was tested. | Liu et al., 2023 |
| Breast cancer | Female tree shrews (6 months to 1 year old) were administered an intraductal injection of *PI3KCA-H1047R* or *H-RAS-Q61L* lentiviruses at different titers ($3\times10^{7}$ TU/mL and $1.4\times10^{6}$ TU/mL, respectively) into 3rd pair of mammary glands | Incidence of breast tumor in tree shrews injected with *PI3KCA-H1047R* lentivirus was 41.7%–58.3% within 3–10 weeks after infection, but no breast tumors were detected in animals injected with *H-RAS-Q61L* lentivirus within 10 weeks. Dominant pathological type was intraductal papilloma and atypical hyperplasia, with only one case of invasive ductal carcinoma. Tumor sections were positive for progesterone receptor (PR) but negative for human epidermal growth factor receptor-2 (HER-2) staining and had weak or no staining for estrogen receptor-α (ERα). PI3K inhibitor alpelisib inhibited growth of transplanted tumors in NOD-SCID mice. | *Mechanism:* Common *PI3KCA-H1047R* mutation caused a high incidence of breast tumor in tree shrews, which were hormone receptor-positive and HER2 negative. PI3K pathway was involved in development of breast tumors.<br>*Limitations:* Precise reason why *PI3KCA-H1047R* and *H-RAS-Q61L* lentiviruses behaved differently in mammary tumor induction in tree shrews and FVB mice was not determined, with this species-specific pattern having important implications regarding development of breast cancer in humans. | Zeng et al., 2023 |
| | Female tree shrews (10–12-months old) were injected with DMBA (10 mg/kg) in one side of lumbar mammary fatty pad four times (once per week for 2 weeks and suspended for one week), with or without intramuscularly injection of MPA (100 mg/kg) once per 2 weeks five times from 1st DMBA injection | Around 10% of tree shrews with DMBA treatment and 50% of tree shrews with DMPA and MPA developed breast lesions. All induced breast lesions were intraductal papilloma and atypical ductal hyperplasia, with almost equal incidence. Breast lesions were highly vascular and had regular morphology, clear margins, and heterogeneous enhancement. Breast lesions were positive for ERα, PR, and cytokeratin 5/6 (CK5/6) staining, but negative for HER-2 staining. | *Mechanism*: Combination of DMBA and MPA effectively established breast precancerous lesions including intraductal papilloma and atypical ductal hyperplasia in tree shrews. Tissues of atypical ductal hyperplasia showed a higher expression of B cell lymphoma-extra-large (Bcl-xl) and lower expression of B cell lymphoma 2 associated X protein (Bax) than those with intraductal papilloma.<br>*Limitations*: No detailed mechanism was studied for induced breast lesions and no drug effects were tested. | Chen et al., 2019 |
| Spontaneous mammary gland tumor | Female tree shrews of different ages | Spontaneous mammary tumors usually occurred in virgin tree shrews at 2–3 years old, with an incidence rate of 24.6% (15/61). Simultaneous or metachronous multiplex tumor rate was 60%. Familial mammary gland tumor incidence was observed for some pedigrees. Intraductal papillary adenomas were predominant and tubulopapillary carcinomas were also found but at a lower frequency. All tumors were PR-positive, nearly all were negative for HER-2 staining (4.3%), and 91.3% were positive for ERα staining. | *Mechanism*: No PTEN and PIK3CA mutations were observed in mammary tumors after sequencing. Most simultaneous or metachronous multiplex tumors exhibited possible origins from multiple sites. More than 25% of mammary tumor cells expressed Nectin-4.<br>*Limitations*: Genetic aspects of familial inheritance of mammary tumors were not determined and no drug effects were tested. | Chi et al., 2020 |
| Glioblastoma | Adult tree shrews (1–2 years old) were intracranially injected with pTomo-H-RasV12-shp53 lentivirus ($3\times10^{11}$/ml titer, expressing HRasV12 and shRNA targeting tree shrew *Tp53*) into hippocampus | Tree shrews showed slight neurological symptoms, including ataxia, imbalance, and emaciation after lentivirus delivery for 4 weeks. Induced gliomas exhibited aggressive behavior and relatively short latency, with reduced animal survival. Gliomas showed increased cell density, necrosis and pseudopalisades, vascular hyperplasia, and active cellular proliferation, and resembled human high-grade gliomas. | *Mechanism*: Transcriptomic profiling of tree shrew gliomas indicated that tumors belonged to mesenchymal subgroup of human glioblastoma multiforme.<br>*Limitations*: No drug effects were tested. | Tong et al., 2017 |

**Continued**

| Disease / intervention | Modeling methods | Phenotypes and symptoms | Potential mechanism, drug efficacy, and limitations | References |
|---|---|---|---|---|
| Pancreatic cancer | Adult male tree shrews (2–3 years old) were injected with lentiviral vectors containing mutant oncogene $KRAS^{G12D}$ and shRNAs targeting *Tp53*, *Cdkn2a*, *Cdkn2b*, and *Cdkn2a/b* in head of pancreas | Pancreatic tumors with full penetrance were observed at 3–7 weeks after lentivirus injection. Tumors were moderately differentiated ductal adenocarcinomas and expressed several well-established markers of human pancreatic cancer, including CK19, Muc5, MMP7, and Hes1. Tree shrews showed gross morphological changes associated with pancreatic cancer, including intestinal darkening, colorectal inflation, gall bladder dilatation, and blockage of bile overflow. Induced pancreatic cancer originated from malignant transformation of acinar cells. | *Mechanism*: Induced pancreatic cancer resembled human pancreatic ductal adenocarcinoma based on transcriptomic profiling; expression of oncogenic *Kras* along with loss of *Tp53*, *Cdkn2a*, and *Cdkn2b* expression were essential for transformation of acinar cells and induction of tree shrew pancreatic cancer. Rb1 signaling pathway was actively involved in this process.<br>*Limitations*: No drug effects were tested. | Tu et al., 2019 |
| Basal cell carcinoma (BCC) | Adult male tree shrews were intracutaneously injected with pCDH-mSmoA1 lentivirus ($5.6\times10^5$ TU) and shRNA targeting tree shrew *Tp53* lentivirus (shp53, $2\times10^5$ TU) in dorsum and tail skin | Tree shrews with pCDH-SmoA1 lentivirus injection exhibited human BCC-like pathological characteristics, including hyperplasia of skin cells with hair follicle disruption, pigmentation, and nuclear explosion expansion. Around 40% of tree shrews presented with BCC-like phenotypes after 4 weeks following delivery of pCDH-SmoA1 lentivirus, which reached 60% after 6–8 weeks. Injection of pCDH-mSmoA1 and shp53 lentiviruses resulted in BCC-like phenotypes in 70% of tree shrews at 2 weeks, which reached 100% after 4 weeks. | *Mechanism*: Activation of Hh signaling pathway by SmoA1 overexpression induced tree shrew BCC, which was further accelerated by knockdown of tumor suppressor *p53.*<br>*Limitations*: No characterization of related molecular markers of BCC was conducted and no drug effects were tested. | Jiang et al., 2017 |
| Acute respiratory distress syndrome (ARDS) | Lipopolysaccharide (LPS, 180–200 mg/kg) was administered to tree shrews via intratracheal instillation | LPS-treated tree shrews demonstrated symptoms of respiratory failure between days 3 and 5, and exhibited behavioral abnormalities (less activity, piloerection, and tachypnea) from day 3. LPS-treated animals showed a $PaO_2$ to $FiO_2$ (P/F) ratio of 160–200 mmHg, suggesting moderate ARDS. LPS treatment caused bilateral patchy infiltrates, typical diffuse alveolar damage, pulmonary inflammation, and lung tissue injury (e.g., thickened alveolar septum, hemorrhage, edema, proteinaceous debris, massive neutrophils accumulation, and infiltration). | *Mechanism*: One-hit intratracheal instillation of LPS led to symptoms resembling acute phase of human ARDS.<br>*Limitations*: No detailed mechanism of this LPS-induced model was determined and no drug effects were tested. | He et al., 2024 |
| Chronic pulmonary inflammation (CPI) | Adult male tree shrews (4–6 months old) were subcutaneously injected with 0.25 mL of solution (2 mg/mL of bovine type II collagen, 0.1 mol/L acetic acid, emulsified in complete Freund's adjuvant) to induce arthritis | Joint inflammation severity worsened over two weeks and peaked at day 21, followed by remission and slow recovery. Swollen soft tissue, narrowed joint spaces, marginal erosions, denser and abnormal lymphoid infiltrates, and cartilage damage were observed in bone joints, including forelimb joint. Diffused lymphoid infiltrates in lung tissue were detected at day 21. Typical CPI but no fibrosis developed pathologically in the collagen-induced arthritis associated CPI model. | *Mechanism*: Abnormal up-regulation of pulmonary chemokine CXCL10 was associated with lung damage, and CXCL10-CXCR3 chemotaxis mediated joint inflammation in this model. Treatment with CXCR3 antagonist NBI74330 down-regulated inflammatory infiltrates and expression of inflammatory factors and chemokines.<br>*Limitations*: No experimental assays were conducted to reveal the initiation and role of CXCL10-CXCR3 chemotaxis. | Gao et al., 2018 |
| Idiopathic pulmonary fibrosis | Tree shrews (3–5 months old) were administered bleomycin (1.75 U/kg body weight) via intratracheal catheter | After bleomycin exposure for 21 days, fibrotic responses were observed in a significant portion of the lungs, with increased levels of fibrotic collagen area and hydroxyproline relative to control animals. Bleomycin exposure induced myofibroblast differentiation, increased extracellular matrix proteins, and activated FAK signaling in lung tissues, indicating increased pro-fibrotic responses and fibrotic remodeling. During fibrosis, monocyte-derived macrophages were significantly recruited and polarized to a profibrotic phenotype. Macrophage-derived profibrotic mediators from bleomycin-exposed tree shrews promoted fibroblast activation. | *Mechanism*: FAK signaling was actively mediated pro-fibrotic responses in lungs of bleomycin-exposed tree shrews. Monocyte-derived macrophage-fibroblast crosstalk induced fibrosis.<br>*Limitations*: No drug effects were tested. | Che et al., 2021; Larson-Casey et al., 2020 |

**Continued**

| Disease / intervention | Modeling methods | Phenotypes and symptoms | Potential mechanism, drug efficacy, and limitations | References |
|---|---|---|---|---|
| Systemic sclerosis | Adult tree shrews (10–12 months old) were subcutaneously injected with different doses of bleomycin (0.4, 2, and 4 ng/mL; 100 μL of solution) for 21 days | Long-term injection of bleomycin caused ulcers in the skin injection site of tree shrews and induced inflammation and/or fibrosis in skin and internal organs. Medium to high doses of bleomycin caused markedly thickened dermis, infiltration of inflammatory cells, increased collagen fibers and collagen volume fraction in skin, pulmonary septal thickening, and fibrosis and inflammatory cells infiltration in the lung. Increased expression of α-SMA in skin and presence of serum autoantibodies (antinuclear antibodies and anti-scleroderma-70) were observed in bleomycin-treated animals. | *Mechanism*: Bleomycin-treated tree shrews showed similar pathological and serological changes to human systemic sclerosis. Ten hub genes (*KIF20A*, *KIF11*, *UBE2C*, *BUB1B*, *CDK1*, *CCNB2*, *AURKB*, *TOP2A*, *PLK1*, and *NCAPG*) were identified based on transcriptomic profiling; immune cell infiltrations in the skin may play a key role. *Limitations*: No drug effects were tested. | Zheng et al., 2024 |
| Periodontitis | Adult male tree shrews (2–6 months old) were modeled using a 2-0 ligature through the mandibular space between the first and second molars, with tightening on the subgingival surface of first molar crown | Tree shrews showed ligature-induced inflammatory reactions, e.g., swelling, redness, and tissue softening in the gingiva at week 2. Redness and swelling of the gums continued in weeks 3 and 4, and spontaneous bleeding of the gingiva was observed at week 4, followed by gradual reduction of swelling and redness and disappearance of hemorrhaging at weeks 5–8. Severe bone destruction and significantly increased molar root exposure were observed after induction of periodontitis, along with substantial inflammatory infiltrates, apical migration of junctional epithelium, and alveolar bone loss. | *Mechanism*: Inflammatory infiltrates and transition from acute to chronic inflammation were involved in development of gingival swelling, redness, spontaneous bleeding, and bone loss after induction of periodontitis *Limitations*: No drug effects were tested. | Ma et al., 2023 |
| Osteonecrosis | Adult male tree shrews (6 months old) were intravenously injected with LPS (300 μg/kg), followed by three intraperitoneal injections of methylprednisolone (MPS; 130 mg/kg) over a 24 h interval, with subsequent delivery of MPS two times per week until 12 weeks | Treated tree shrews showed increased levels of bone alkaline phosphatase, bone GLA protein, N-terminal propeptide of type I collagen, and C-terminal propeptide of type I collagen relative to control animals, with subchondral trabecular bone deterioration of femoral heads, including cortical bone partial collapse, trabecular fracture, trabecular sparseness, thinning, and increased intercellular spacing. Increased cell apoptosis and fused adipose cells into vacuoles, and decreased bone quality were observed. | *Mechanism:* Administration of low-dose LPS combined with high-dose MPS resulted in femoral head necrosis in tree shrews. *Limitations:* No drug efficacy was tested and no detailed target or mechanism was studied. | Chen et al., 2020 |
| Osteoporosis | Bilateral ovaries were removed in healthy female tree shrews (6 months old; ovariectomy (OVX) group) after anesthesia, with animals euthanized at 6 months after surgery | Animals in the OVX group showed a significantly low level of serum estradiol, high bone turnover and bone loss, increased body weight, and reduced uterus weight and uterus coefficient compared to the sham group. OVX group exhibited a decreased in number and connections of trabeculae in the third lumbar vertebra, decreased structural stiffness, and fewer osteoblasts but more osteoclasts relative to the sham group. | *Mechanism:* Osteoporosis was induced in tree shrews by ovariectomy. Transcriptomic analysis of first lumbar vertebra identified several differentially expressed genes associated with osteoporosis. *Limitations:* No drug efficacy was tested and no detailed target or mechanism was studied. | Wang et al., 2019b |
| SARS-CoV-2 infection | Adult (1-year old) and aged (5–6 years old) tree shrews were infected with $10^7$ $TCID_{50}$ SARS-CoV-2 strain 107 by oral, intranasal, and ocular routes | Lung infiltrates were visible from 3 days post-infection (dpi) in 85% of infected animals. Most lung lobes had high viral RNA copies, which peaked at 3 dpi and decreased to undetectable levels at 14 dpi. Sporadic or massive pulmonary punctate hemorrhage, thickened alveolar septa, and interstitial hemorrhage were observed. Viral antigens were present in a small number of pneumocytes in infected lung tissues. Elevated white blood cell, lymphocyte, monocyte, and granulocyte counts were detected, as well as increased aspartate aminotransferase after infection in the adult group and decreased monocytes in the old group. | *Mechanism:* Tree shrews were susceptible to SARS-CoV-2 infection, displaying viral shedding, lung lesions, and alterations in blood biochemical indices. *Limitations:* No vaccine or drug efficacy was tested, no data about host immune response were provided, and no intra- or inter-species transmission study was performed. | Xu et al., 2020a |

**Continued**

| Disease / intervention | Modeling methods | Phenotypes and symptoms | Potential mechanism, drug efficacy, and limitations | References |
|---|---|---|---|---|
| | Young (6–12 months old), adult (2–4 years old), and old (5–7 years old) tree shrews were infected nasally with $10^6$ PFU SARS-CoV-2 | Some infected animals showed an increased body temperature. Low viral shedding and replication in tissues occurred in all three groups. Pathological changes included pulmonary abnormalities, widened pulmonary septum, interstitial hyperemia, airway obstruction, consolidation of lung margin, local hemorrhagic necrosis, and infiltration of inflammatory cells. Mild histopathological changes were observed in brain, heart, liver, and pancreas. | *Mechanism:* Tree shrews were less susceptible to SARS-CoV-2 infection but may be a potential intermediate host. *Limitations:* No data about host immune response were provided and no intra- or inter-species transmission study was performed. | Zhao et al., 2020b |
| Zika virus (ZIKV) infection | Tree shrews (5 months old) were infected with $10^5$ or $10^6$ PFU of ZIKV strain GZ01 via subcutaneous injection; neonatal tree shrews (1-day old) were inoculated via the intracerebral route with $10^5$ PFU of ZIKV | Tree shrews showed ZIKV infection and replication in primary kidney, testis, and peripheral blood cells. ZIKV-infected tree shrews developed transient viremia and skin rash at 2 dpi (which disappeared at 3 dpi), with the abdomen and chest being the main sites of dermatological manifestations. Apparent cutaneous lesions characterized by massive hemorrhage and inflammatory cell infiltration were observed in the hypodermis, along with *in situ* viral replication. ZIKV caused systemic infection involving multiple organs, including the brain. Testes had the highest viral load. ZIKV infection had a protection against secondary homologous infection. ZIKV was neurovirulent and replicated in neonatal animals, leading to a 75% mortality rate within 21 dpi. | *Mechanism:* Genes with antiviral immunity and inflammatory response were up-regulated by ZIKV infection in tree shrews. Both innate and adaptive immune responses were induced by ZIKV infection. *Limitations:* Exact mechanism underlying dermatological manifestations was not examined and no vaccine or drug efficacy was tested. | Zhang et al., 2019b |
| | Sexually mature tree shrews were infected with $10^5$ or $10^6$ PFU ZIKV GZ01 strain via the vaginal route | No dermatological manifestations were observed in tree shrews after ZIKV vaginal infection. Viral RNA loads were detected in blood, saliva, urine, and vaginal douching, with ZIKV viremia in vaginal lavage peaking at 1 dpi and persisting until 10 dpi in several animals. ZIKV vaginal infection led to systemic multi-tissue and multi-organ infections. | *Mechanism:* Female tree shrews were infected with ZIKV via the vaginal route. Expression levels of key inflammatory genes, including *IL6*, *IL8*, *TNFα*, *CCL5*, and *CXCL9*, were increased in the spleen of ZIKV-infected tree shrews. *Limitations:* No vaccine or drug efficacy was tested. | Baloch et al., 2021 |
| Dengue virus (DENV) infection | Adult tree shrews were infected with $1\times10^4$ PFU DENV-2 or DENV-3 through intravenous injection or multisite subcutaneous injection | DENV-3 productively proliferated in tree shrew bone marrow mesenchymal stem cells at 4 dpi. Half of the animals presented with viremia, and most presented with high neutralizing antibody titers at 7 and 15 dpi. Alterations in some hematological and biochemical parameters, including modest thrombocytopenia, slight decrease in white blood cell count, and increased levels of aspartate transaminase, alanine aminotransferase, and alkaline phosphatase were observed in tree shrews after DENV infection. Viral RNA was barely detectable in the liver at 48 dpi but was detectable in the brain. Intra-brain bleeding lesions were more severe in animals with an intravenous injection of DENV than those with subcutaneous infection. | *Mechanism:* Tree shrews displayed fever, viremia, abnormal aminotransferase levels, and death after DENV infection, resembling clinical manifestations in humans. *Limitations:* Potential mechanism regarding vascular leakage and central nervous system impairment after DENV infection was not determined and no drug efficacy was tested. | Jiang et al., 2021a |
| | Tree shrew fibroblast cells were infected with DENV-1, DENV-2, DENV-3, and DENV-4 | DENV serotypes 1–4 replicated in tree shrew fibroblast cells, with a linear increase in viral load at 24–96 h post-infection in both cells and culture supernatants. DENV-2 had the highest viral growth among all serotypes. Different DENV serotypes showed variable viral replication kinetics and TLR and cytokine expression profiles in fibroblast cells. | *Mechanism: TLR8* mRNA was induced during DENV infection. Knockdown of *TLR8* led to an increase in DENV-1 viral load. *Limitations:* No drug efficacy was tested, no detailed mechanism was studied, and no *in vivo* infection of DENV was performed. | Kayesh et al., 2017c |

**Continued**

| Disease / intervention | Modeling methods | Phenotypes and symptoms | Potential mechanism, drug efficacy, and limitations | References |
|---|---|---|---|---|
| Kaposi's sarcoma-associated herpesvirus (KSHV) | Tree shrews (4–5 months old) were infected with $5\times10^7$ GFU rKSHV.219 via the intravenous route | Tree shrew kidney epithelial cells were the most susceptible cells to KSHV infection, with KSHV genomic DNA, mRNA, and KSHV-specific proteins detected in this cell type up to 32 dpi. KSHV DNA and mRNA were detected in peripheral blood mononuclear cells and various tissues of KSHV-infected tree shrews. Lymphocyte infiltration, lymphoid tissue focal aggregation, alveolar wall thickening, hepatocyte edema, and hepatic necrosis were observed in the spleen, lung, and liver of a certain proportion of KSHV-infected animals. | *Mechanism:* Tree shrews exhibited a robust innate immune response against KSHV infection.<br>*Limitations:* No transcriptomic profiling was performed in tissues upon KSHV infection and no drug efficacy was tested. | Li et al., 2021a |
| Herpes simplex virus-1 (HSV-1) | Adult female tree shrews (6 months old) were infected with $10^6$ PFU HSV-1 strain McKrae by dropping on each eye without ocular scarification (McKrae group) and HSV-1 17+ strain with ocular scarification (17+ group). Trigeminal ganglia (TG) were collected from 17+ group at 58 dpi | Herpes simplex keratitis was induced in McKrae group, and eyes recovered at 33 dpi. The 17+ group exhibited more pronounced scarring and opaqueness in cornea and inflammation in eye lids during acute infection stage between 5 and 15 dpi compared to McKrae group. Thickening cornea, inflammatory infiltration, weakened luminousness, rough cornea surface, and deciduous corneal epithelial cells were observed during weeks 1 and 3 post-infection, with corneas showing recovery by 33 dpi. Titer of active virus peaked at 5 and 10 dpi, then reduced to the lowest level at 13 dpi, with persistent infection or spontaneous reactivation. Viral protein was detected in the cornea epithelial layer and retina neuronal ganglion cells at 5–20 dpi. Cornea supernatants and ciliary ganglion homogenates from the McKrae group at 46 dpi induced a cytopathic effect at 3 days post co-cultivation in RS1 cells. HSV-1 efficiently infected tree shrew eyes and persisted during latency period. | *Mechanism:* Decreased transcript levels of *ICP0*, *ICP4*, and *LAT* were detected after the acute infection stage, but *LAT* increased at 46 dpi, indicating latency of HSV-1 in tree shrew eyes (ciliary ganglion). Comparison of transcriptomes of infected TGs from tree shrews, mice, and humans showed that HSV-1 transcription in acutely infected TGs differed dramatically between mice and tree shrews. HSV-1 transcripts were detected in mouse TGs during acute infection but had an abortive infectious cycle in tree shrew TGs. During latency, LAT was detected in mouse, tree shrew, and human TGs but ICP0 transcripts were only found in tree shrew and human TGs. Infected human and tree shrew TGs exhibited a more similar LAT region transcription peak.<br>*Limitations:* No detailed molecular mechanism regarding HSV-1 latency in tree shrews was uncovered and no drug efficacy was tested. | Li et al., 2020; Wang et al., 2020b |
| Influenza A viruses (IAVs) | Healthy adult tree shrews were infected with $10^5$ $TCID_{50}$/mL swine influenza virus subtype H3N2 (SW2783 group) and avian influenza virus subtype H6N6 (ZZ346 group) through nasal drip, conjunctiva drip, and pharyngeal tonsil drip | Tree shrews presented with decreased appetite, reduced activity, and increased nasopharyngeal secretions at 1 dpi which lasted 8 days, with severe symptoms in the SW2783 group. Both viruses replicated and spread, with SW2783 showing stronger replication capacity than ZZ346. Infection was restricted to the upper respiratory tract, and nucleoprotein expression peaked at 3–5 dpi and gradually recovered at 7–14 dpi. Various histopathological changes were observed in respiratory tract tissues, with limited cell necrosis and infiltration of inflammatory cells in mucosal epithelium of nasal turbinate. Both viruses were transmissible in tree shrews, and SW2783 could transmit from tree shrews to guinea pigs. | *Mechanism:* Swine SW2783 and avian ZZ346 strains infected tree shrews, induced effective innate and adaptive immune responses, and regulated response degrees. In total, 14 differentially expressed miRNAs were identified in turbinate tissues from SW2783-infected tree shrews, including some miRNAs involved in viral replication and proliferation by regulating signal transduction, and others playing an antiviral role via regulating immune response.<br>*Limitations:* No vaccine or drug efficacy was tested. | Wang et al., 2023b, 2024c |
| | Adult tree shrews were infected with $10^6$ PFU avian H5N1 (highly virulent) and H7N9 (lowly pathogenic) into nostrils and trachea by aerosolized administration and onto tonsils and conjunctivae with pipette | H5N1 group showed elevated body temperature, body weight loss, and decreased locomotor activity starting from 2 dpi, with one of four infected animals dying. Tree shrews infected with H7N9 exhibited no clinical symptoms. Both viruses were continuously detected in nasal, oral, tracheal, and conjunctival swab samples and lung tissues, peaking at 1–2 dpi and replicating in lung tissues. Animals infected with H5N1, but not H7N9, displayed severe diffuse pneumonia, with focal inflammation around bronchioles. Antibody responses were detected in infected animals. | *Mechanism:* H5N1-infected tree shrews had higher expression levels of cytokine genes (*IFNG*, *IL6*, *TNFA*) compared to those without infection or with H7N9 infection, and severity of pneumonia was correlated with mRNA expression of proinflammatory cytokines.<br>*Limitations:* Reasons for significant differences in symptoms between H5N1 infection and H7N9 infection were not determined and no vaccine or drug efficacy was tested. | Sanada et al., 2019c |

**Continued**

| Disease / intervention | Modeling methods | Phenotypes and symptoms | Potential mechanism, drug efficacy, and limitations | References |
|---|---|---|---|---|
| | Tree shrews were infected intranasally with $10^6$ $TCID_{50}$ H9N2 viruses (Y280-wt and Y280 virus with mammalian adaptation mutation PB2-E627K). For ex vivo cultures of nasal turbinate, trachea, and lung tissues, tissue blocks were infected with $10^6$ $TCID_{50}$ H9N2 (Y280-wt and Y280-PB2-E627K) for 2 h, then cultured with fresh medium to 72 h dpi | Viral shedding was found in nasal washes of tree shrews, with longer persistence of PB2-E627K mutant virus up to 6 dpi. Tree shrews infected by PB2-E627K exhibited increased body temperature and body weight loss. H9N2 virus replicated in nasal turbinate and lungs. Animals with Y208-wt infection showed infiltration of inflammatory cells and focal edema on submucosal layer of nasal turbinate at 2 dpi, while those infected with PB2-E627K showed increased severity of lesions characterized by necrotic and sloughed epithelial cells and increased lymphocytic infiltration. Lung tissues showed similar lesion patterns. PB2-E627K virus replicated more efficiently than Y280-wt virus in *ex vivo* culture model of nasal turbinate, trachea, and lung tissues. | *Mechanism:* mRNA expression levels of cytokines, including TNF-α, IFN-β, IL-8, IL-13, and IL-6, were increased in infected tree shrews and respiratory tissues. PB2-E627K virus mutant had a higher induction effect than Y280-wt virus.<br>*Limitations:* No transcriptomic profiling was performed for tissues infected with two viruses of different virulence and no vaccine or drug efficacy was tested. | Li et al., 2018a |
| | Tree shrews (1–4 months old) were infected intranasally with $10^6$ EID50 pandemic H1N1 (pdmH1N1), avian H5N1, and human H7N9, respectively. Contact infection between tree shrews and guinea pigs was also tested | Three influenza viruses efficiently replicated in tree shrew primary renal cells and lung cells, and induced expression of *IFNβ*, *IFIT2*, and *OASL*. Tree shrews showed subclinical symptoms after infection with three viruses, with viral tropism in respiratory tract. Lung lesions, including obvious alveolar edema, interstitial edema, hemorrhage, and inflammatory cell infiltration, were observed at 3 dpi, with pdmH1N1 infection showing more severe lesions than H5N1 and G7N9. Influenza viruses induced protective responses against homologous challenge in tree shrews. PdmH1N1 and H7N9, but not H5N1, were transmissible in tree shrews. H7N9, but not pdmH1N1, was transmissible from tree shrews to guinea pigs. | *Mechanism:* Tree shrews were infected by different subtypes of influenza viruses, which induced a humoral immune response upon infection.<br>*Limitations:* No detailed mechanisms were studied and no vaccine or drug efficacy was tested. | Xu et al., 2019 |
| Influenza B viruses (IBVs) | Male tree shrews were intranasally inoculated with $10^6$ $TCID_{50}$ IBV V0215 or Y12. Infected tree shrews were compared with infected ferrets and mice | IBVs replicated in the respiratory tract of tree shrews, ferrets, and mice, with peak viral titers in nasal washes at 2 dpi. Infected tree shrews, but not ferrets, exhibited weight loss. Seroconversion was observed in tree shrews, with higher antibody titer in animals inoculated with V0215 compared to Y12. Clinical signs and pathological changes were mild. Elevated levels of cytokines and inflammation were detected in respiratory tract of all three infected animals. Infected tree shrews presented with rhinitis and pneumonia, and Y12 infection caused more disease severity relative to V0215 infection in tree shrews. | *Mechanism:* Peak and period of respiratory IBV viral shedding in tree shrews was similar to those in humans. IBV infection led to elevated levels of cytokines in respiratory tract of tree shrews.<br>*Limitations:* No mechanism was reported for different virulence and tissue tropism of V0215 and Y12 in tree shrews and between tree shrews and ferrets or mice. No intra- or inter-species transmission was performed and no vaccine or drug efficacy was tested. | Yuan et al., 2019 |
| Human adenovirus (HAdV) species B | Male tree shrews were intranasally infected with $5\times10^6$ $TCID_{50}$ HAdV-55. For HAdV-55 vaccine evaluation, tree shrews were intramuscularly vaccinated with $2\times10^{10}$ of inactivated HAdV-55 VPs, and two booster vaccinations on days 14 and 28 | HAdV species B (HAdV-55, HAdV-7, HAdV-14) replicated in tree shrew primary cells from the kidney, lung, and trachea and caused the cytopathic effect (CPE). HAdV-55 infection led to rapid weight loss and increased body temperature. HAdV-55 was detected in respiratory tract and lung of infected tree shrews with interstitial pneumonia. Pre-vaccination provided a protective effect against homologous infection. HAdV-55 transmitted among tree shrews. | *Mechanism:* HAdV-55 infection induced cytokine gene expression in peripheral blood mononuclear cells (PBMCs) of tree shrews. Pre-vaccination inhibited HAdV-55 replication *in vivo*.<br>*Limitations:* No mechanisms for pathological alterations and HAdV-55 distribution in respiratory tract and other organs were investigated. | Li et al., 2021c |

**Continued**

| Disease / intervention | Modeling methods | Phenotypes and symptoms | Potential mechanism, drug efficacy, and limitations | References |
|---|---|---|---|---|
| Epstein-Barr virus (EBV) | Adult tree shrews (1–1.5 years old) were inoculated with $3.9\times10^8$ copies of EBV by intravenous injection | Most tree shrews (8/10) showed evidence of EBV infection, with intermittent or transient increases in EBV copy number and expression of EBV genes in PBMCs post-infection. Anti-EBV capsid antigen IgG increased by varying degrees in tree shrews with increasing EBV copy number. Splenic corpuscle hyperplasia, inflammatory cell infiltration in liver, and extensive lymphocyte proliferation in mesenteric lymph node enlargement were observed in some infected animals, but none had obvious abnormalities in lungs or nasopharynx. | *Mechanism*: Tree shrews were infected by EBV via intravenous infusion and presented with different patterns concerning EBV copy number. EBV-related gene expression was detected after infection. Lymphocytes and spleen were primary targets of EBV infection<br>*Limitations*: No study on the mechanisms of EBV entry into the nasopharynx was conducted and no drug or vaccine efficacy was tested. | Wang et al., 2017 |
| | Primary tree shrew PBMCs were infected with $1\times10^7$ copies of EBV. Adult tree shrews were injected with $2\times10^7$ copies of EBV via femoral vein. Daily intraperitoneal injection of cyclosporine A (CsA, 25 mg/kg) was used for immunosuppression at 5 weeks post-infection after two consecutive negative results of EBV-DNA | Tree shrew PBMCs supported EBV replication and proliferation. EBV-infected tree shrews displayed fever and weight loss, increased white blood cell count and total cell counts, and decreased neutrophils after infection. Immune organs (spleen and lymph nodes) had higher viral loads. Tree shrews acted as asymptomatic carriers of EBV, with viral protein detectable in blood and tissues. EBV infection increased percentage of immature neutrophils (rod-shaped nucleus) and neutrophils containing specific cytoplasmic intoxication particles. EBV infection altered gut microflora in composition and metabolome profile, peaking at 7 dpi. Autophagy and ferroptosis signaling pathways were activated by EBV infection, along with alterations in the competing endogenous RNA (ceRNA) network that regulates EBV-host interactions. CsA increased the proliferation ability of EBV-infected PBMCs, promoted transformation into immortalized cells, and caused EBV reactivation in infected animals. | *Mechanism*: Tree shrews possessed the same key residues in the complement C3d receptor 2 (CR2) that binds to the gp350 protein as humans, which facilitates viral entry. EBV infection led to dynamic transcriptomic changes in tree shrew blood cells. Neutropenia in EBV-infected animals at early infection may affect EBV immune escape and long-term latency. Changes in gut microflora during EBV infection were correlated with fecal metabolic profile. EBV infection caused alterations in ceRNA networks that remodel the immune microenvironment. Immunosuppression caused EBV reactivation in latency.<br>*Limitations*: No study on the mechanisms underlying the proposed neutrophil suppression hypothesis or alterations in gut microbiota and ceRNA network during EBV infection was conducted and no drug or vaccine efficacy was tested. | Xia et al., 2022, 2023, 2024; Shi et al., 2023 |
| Hepatitis B virus (HBV) | Adult tree shrews (>2 months old) were treated with triamcinolone steroid (5 mg/kg) for 2 days, followed by intraperitoneal inoculation with $10^8$ copies of HBV in 1 mL of human serum | Infected animals displayed enhanced serum HBV and viral proteins were synthesized *de novo* in hepatocytes, with hepatitis B surface antigen (HBsAg) and hepatitis Be antigen (HBeAg) titers, and HBV DNA and covalently closed circular DNA (cccDNA) copies peaking at day 9, declining at days 15 and 21, and becoming undetectable at day 42. HBV infection led to elevated alanine transaminase levels and inflammatory infiltration and hepatocyte ballooning degeneration in liver. | *Mechanism*: A complete and natural process from HBV infection, replication, to elimination was modulated in tree shrews, with a noncytopathic-mediated control of cccDNA content during acute viral hepatitis<br>*Limitations*: No characterization for host immune response during HBV infection and elimination was performed and no vaccine efficacy was tested. | Li et al., 2021b |
| | Newborn tree shrews were subcutaneously administered with $10^6$ copies of HBV genotype A (HBV-A) or C (HBV-C) per animal; Adult tree shrews (1-year old) were intraperitoneally injected with $10^{6\text{-}7}$ copies of HBV-A | HBV-A showed higher intrahepatic replication than HBV-C in newborn tree shrews, leading to abnormal architecture of liver cell cords and mitotic figures at 8 dpi. HBV-DNA and HBsAg were detected in liver tissues of adult animals at 28 dpi. HBV infection caused expression alterations in IFN-β, TLR1, TLR3, TLR9, and cGAS, and suppression of NTCP expression during chronic phase of infection. | *Mechanism*: Suppression of IFN-β may have contributed to establishment of chronic HBV infection in tree shrews.<br>*Limitations*: No precise mechanisms for signaling pathways activated by HBVinfection and host immune response during chronic HBV infection were determined and no vaccine efficacy was tested. | Kayesh et al., 2017a |
| Hepatitis C virus (HCV) | Tree shrew bone marrow-derived mesenchymal stem cells (BM-MSCs) overexpressing human CD81, OCLN, and miR-122 were infected with 0.5 MOI HCVcc derived from J6/JFH1 (HCV2a) | HCV viral copies and core protein were detected in culture supernatants of infected BM-MSCs overexpressing human CD81/OCLN or CD81/OCLN/miR-122. VEGF treatment increased BM-MSC infectivity to HCV. | *Mechanism*: BM-MSCs overexpressing human CD81, OCLN, and miR-122 supported HCV replication and infectious virus production, and VEGF enhanced HCV infectivity in these cells.<br>*Limitations*: No data on host immune response or the exact mechanisms underlying HCV replication and production of infectious particles were provided and no drug efficacy was tested. | Lu et al., 2020 |

**Continued**

| Disease / intervention | Modeling methods | Phenotypes and symptoms | Potential mechanism, drug efficacy, and limitations | References |
|---|---|---|---|---|
| | Adult tree shrews (1-year old) were infected intraperitoneally with HCV (genotypes 1a, 1b, 4a, and 2a (JFH1)) for 41 weeks | All HCV genotypes established infections and showed intermittent HCV propagation. Infected animals produced anti-core and anti-NS3 antibodies and had increased levels of reactive oxygen species (ROS) in serum and liver. Pathological changes, including lymphocytic infiltration, disturbance of hepatic cords, and initiation of fibrosis, were observed in livers of infected tree shrews. | *Mechanism*: Intrahepatic levels of TLR3, TLR7, and TLR9 were significantly increased upon HCV infection. Increased levels of IFNβ in tree shrews with HCV genotypes 1a and 2a infection were detected, along with a decrease in NTCP. Humoral and innate immune responses and ROS were involved in HCV infection. *Limitations*: No detailed mechanism was studied and no drug or vaccine efficacy was tested. | Kayesh et al., 2017b |
| | Tree shrews (6 months old) were infected intravenously with $1\times10^7$ copies of HCVcc (J6/JFH1) in the tail | Nearly half of the tree shrews were infected, with intermittent HCV viremia and mild hepatitis. HCV-specific proteins (Core, E2, NS3/4, and NS5A) were detected in hepatocytes of infected tree shrews. Various degrees of microvesicular fat accumulation, vacuolar degeneration, hepatic edema, and lymphocytic infiltration were observed in the livers of infected animals. | *Mechanism*: HCV infection led to mild hepatitis in tree shrews. *Limitations*: No validation for sample infectivity of infected tree shrews was conducted, no data on host immune response was provided, and no drug or vaccine efficacy was tested. | Feng et al., 2017 |

We only compiled publications from January 2017 to May 2024, and summarized the main symptoms of each tree shrew model. Please refer to the original publication for additional details.

vaccinations (Sanada et al., 2019b). With advancements in detecting viruses carried by tree shrews using meta-transcriptomic sequencing and other high-throughput cutting-edge techniques, it may be possible to identify natural viral infections in wild and artificially reared tree shrews (Zhou et al., 2024), thereby broadening our knowledge about the susceptibility of tree shrews to viral infections and aiding the establishment of tree shrew infection models.

Tree shrews can be used to model lung lesions during viral infections (Li et al., 2021c; Xu et al., 2020a), as well as pulmonary fibrosis induced by bleomycin and pro-fibrotic mediators (Che et al., 2021) and acute respiratory distress syndrome induced by intratracheal instillation of lipopolysaccharide (He et al., 2024). These tree shrew lung disease models provide a valuable opportunity for understanding the pathogenesis of lung diseases and for preclinical drug development. Several studies have also reported the development of spontaneous breast tumors (Elliot et al., 1966; Sun et al., 2021; Xia et al., 2012) and mammary gland cancer (Chi et al., 2020) in tree shrews, suggesting their potential as a valid model for breast cancer research. Indeed, intraductal injection of lentivirus expressing the PIK3CA p.H1047R mutation has been shown to induce a high incidence of breast cancer in tree shrews (Zeng et al., 2023), while administration of 7,12-dimethylbenz(a)anthracene (DMBA) and medroxyprogesterone acetate (MPA) in combination can also induce breast tumor (Xia et al., 2014) and precancerous lesions (Chen et al., 2019).

Tree shrews have also been used to develop models for various other human diseases, such as systemic sclerosis induced by subcutaneous injection of bleomycin (Zheng et al., 2024), periodontitis induced by nylon thread ligatures around the lower first molars (Ma et al., 2023), steroid-associated osteonecrosis induced by low-dose lipopolysaccharide combined with high-dose methylprednisolone (Chen et al., 2020), radiation (20-Gy)-induced tensor veli palatini muscle injury (Zhao et al., 2022), kidney oxalate calculi disease induced by intraperitoneal injection of glyoxylic acid (Wang et al., 2024b), chronic autoimmune uveitis with subretinal deposits and retinal damage induced by immunization with inter-photoreceptor retinoid-binding proteins (Hu et al., 2022), diabetic retinopathy induced by sustained hyperglycemia following a single streptozotocin dose (Gorbatyuk et al., 2022), and cocaine-seeking (Duan et al., 2021). Although the therapeutic and prophylactic applications of these models await further validation, the existing data are promising, demonstrating a high degree of similarity between tree shrew pathobiology and human diseases.

The characterization of spontaneous disease models in tree shrew breeding colonies offers crucial insights into the establishment of related disease models. For instance, Klein et al. (2022) reported a high prevalence of AA-amyloidosis (up to 72%) in their tree shrew colony. Combined with previous reports of age-related accumulation of amyloid deposits in the brain (Fan et al., 2018; Li et al., 2024; Yamashita et al., 2012), this suggests that tree shrews may possess genetic and physiological predispositions to developing AD, although further validation is needed. Intracerebroventricular injection of Aβ1-40 has been shown to induce cognitive impairment and neuronal apoptosis in tree shrews, resembling AD symptoms (Lin et al., 2016), with donepezil providing a protective effect in this model (Zheng et al., 2018). Similarly, Yang et al. (2022) claimed that intracerebral injection of Aβ25-35 can lead to AD-like symptoms, which can be ameliorated by ginsenoside Rg1 treatment through regulation of oxidative stress, apoptosis, and neuroinflammation. These studies again highlight the potential of using tree shrews to create AD models.

With their large eyes and high structural similarity to human eyes, tree shrews are an excellent model for studying eye diseases, such as refractive development (Gawne et al., 2017; Norton & McBrien, 1992), myopia (Abbott et al., 2011; Khanal et al., 2023; Marsh-Tootle & Norton, 1989; Norton et al., 2006), and glaucoma (Samuels et al., 2018). Noninvasive *in vivo* imaging techniques, such as optical coherence tomography (OCT) and scanning laser ophthalmoscopy, allow for detailed examination of the anatomical features of the tree shrew retina (Abbott et al., 2011; Grannonico et al., 2024; Miller et al., 2024; Sajdak et al., 2019; Samuels et al., 2018), facilitating the study of related diseases. For instance, Samuels et al. (2018) injected ferromagnetic beads into the

anterior chamber of tree shrews, inducing sustained elevation of intraocular pressure and optic nerve damage akin to human glaucoma, and monitored changes in retinal nerve fiber layer thickness using near-infrared OCT. Researchers optimized visible-light OCT fibergraphy (vis-OCTF) (Grannonico et al., 2021; Miller et al., 2020) to non-invasively visualize individual retinal ganglion cell axon bundles and their surrounding microvasculature in living tree shrew retinas, demonstrating a dense retinal nerve fiber layer, a thick ganglion cell layer, and distinct sublayer structures within the inner plexiform layer (Grannonico et al., 2024; Miller et al., 2024). These studies provide direct evidence for the use of tree shrews in investigating optic neuropathies and retinal ganglion cell injury. Similarly, tree shrews have also been utilized as models for myopia. Notably, limited bandwidth short-wavelength light can produce slowly developing myopia in tree shrews, resembling human juvenile-onset myopia (Khanal et al., 2023). She et al. (2023) explored the therapeutic effects of ambient narrowband long-wavelength light on myopia in lens-induced and form-deprivation myopia tree shrew models and found that repeated red light can reduce myopia, providing a potential reference for red-light therapy in humans. In contrast to rodents, tree shrews are diurnal, and their sleeping patterns are similar to humans (Coolen et al., 2012; Dimanico et al., 2021), making them a suitable model for studying sleep regulation and function, e.g., cold exposure effects on rapid-eye-movement sleep (van Hasselt et al., 2023).

The genome-based approach for creating animal models (Yao, 2017) is particularly beneficial for tree shrews, especially for characterizing primate-specific genes also found in tree shrews, as exemplified by the study on the primate-specific *SSX1* gene in asthenoteratozoospermia (Liu et al., 2023). As we deepen our understanding of the tree shrew's unique genetic features and common genes and pathways at the genome and transcriptome levels (Fan et al., 2018; Ye et al., 2021), we will gain better insights into the validity and feasibility of using tree shrews to model certain human diseases.

However, it must be acknowledged that, compared to earlier studies on the susceptibility of tree shrews to HBV (Su et al., 1987; Walter et al., 1996; Yan et al., 1996), HCV (Amako et al., 2010; Xie et al., 1998; Xu et al., 2007; Zhao et al., 2002), HDV (Li et al., 1995), and HEV (Yu et al., 2016) infections, many recent reports on tree shrew disease models have not garnered sufficient attention and have rarely been replicated in multiple research groups. This lack of interest and replication limits their use in evaluating drug efficacy and new treatments. One reason for limited global interest is the inaccessibility of tree shrew resources. Another reason is the challenge of meeting all three types of validity for certain human diseases with a tree shrew model. The utility of these models is limited because they have not yet led to landmark discoveries, such as the identification of sodium taurocholate cotransporting polypeptide (NTCP) as the HBV receptor (Yan et al., 2012), nor have they been used successfully to test potential drugs and vaccines. Despite the challenges in making important progress, scientific discovery is a gradual process, and multidisciplinary perspectives and international collaborations can enhance the translational potential of these models. To increase awareness and use of tree shrews in research, tree shrew studies should be promoted at scientific meetings through workshops, posters, and lectures. In addition, training courses, videos, guidelines, and protocols (e.g., housing, handling, substance application, blood collection, anesthesia) should be made available to ensure new users can rapidly learn how to handle these experimental animals.

## KEY QUESTIONS FOR FUTURE TREE SHREW STUDIES

The study of tree shrew biology is driven by both curiosity about the animal and the demands of biomedical research. From an evolutionary perspective, every species is unique, providing insights into natural history and evolution. For instance, investigating paw preference (Maille et al., 2013) and cooperation (Jiang et al., 2021b) in tree shrews has deepened our understanding of the evolution of manual laterality and cooperative behavior. The functional dissection of spatial coding, orientation maps, and visual learning in the tree shrew V1 system (Bosking et al., 2002; MacEvoy et al., 2009; Schumacher et al., 2022; Tanabe et al., 2022) has helped clarify the fundamental activities and mechanisms of the visual cortex. Due to the homology between their visual system and that of primates, tree shrews are a valuable model for testing and refining novel therapeutic approaches for visual disorders, with their similar eye structure to humans also facilitating our understanding of myopia (Abbott et al., 2011; Khanal et al., 2023; Marsh-Tootle & Norton, 1989; Norton et al., 2006). Creating tree shrew models of human diseases is highly desirable (Table 1) and a primary reason for securing financial support for their study. We believe that addressing the following key questions with tree shrews in biomedical research is crucial for understanding the scientific value of this species in the long term. These questions are not limited to tree shrew studies but have broader implications in the era of big data.

### Question #1. Can the main biological traits of tree shrews be genetically decoded?

Our current knowledge of tree shrew phenotypes, including reproduction, physiology, behavior, and aging, are quite limited. To fully decode the biological traits of tree shrews and establish disease models, comprehensive data on their complete phenome, transcriptome, epigenome, and genome are needed. This data-driven personalized approach has been proposed for human populations (Yurkovich et al., 2024), which integrates genetics and environmental factors to elucidate the development of various phenotypes, including normal traits and diseases. Longitudinal measurements of related phenotypes during growth and ageing are critical for precisely defining life status, necessitating the use of multiple phenomic profiling technologies. Notably, templates established for human populations (c.f. Liu & Crawford, 2022; Yurkovich et al., 2024; and references therein) and model animals such as mice (Bogue et al., 2023; Brown et al., 2018) and rats (Zinski et al., 2021) can be adapted for tree shrew genome-phenome studies. Algorithms and software programs developed for rodent behavioral tests should also be optimized to accommodate the specific characteristics of tree shrews. A user-friendly and publicly available integrated databank and biobank would also help attract researchers to this field. By gaining a deeper understanding of tree shrews, we can fully leverage this experimental resource.

### Question #2. Can a digitized tree shrew life be created through precise modeling?

The recent advancements in AI have opened new avenues for basic sciences and biomedical research, significantly

benefiting health management and clinical practices (Agu & Obulose, 2024; Ong et al., 2024; Thirunavukarasu et al., 2023; Voigtlaender et al., 2024; Zhang et al., 2023b). With the application of large language models and the accumulation of big data on tree shrews at the cellular level—including DNA alterations, RNA regulation and expression, protein expression and degradation, and metabolite production—alongside meso- and macro-scale phenotypic data and longitudinal phenome dynamics, it may be possible to reconstruct a digitized life of tree shrews. Such an approach would integrate computational models linking the genome, epigenome, environment, and lifestyle with phenotypic information, including behaviors. This may provide predictive information regarding the development and onset of diseases in tree shrews, enhancing their use in modeling human diseases.

**Question #3. Can an ideal tree shrew model be established for human disease prediction and precision medicine?**

Our understanding of human diseases has significantly evolved over the past decades. In addition to common diseases, such as diabetes, stroke, hypertension, and AD, there are more than 7 000 rare diseases in humans (100,000 Genomes Project Pilot Investigators et al., 2021; Kernohan & Boycott, 2024; Tambuyzer et al., 2020; Zhu et al., 2022). The pathobiology of these rare diseases is highly complex, requiring long-term efforts to establish models using appropriate experimental animals. Similar to rodents, tree shrews will not be the sole solution for this problem. Identifying which common or rare diseases can be best modeled in tree shrews remains an open question. While existing studies (e.g., Table 1) are promising, they have not yet provided sufficient evidence that an ideal tree shrew model for certain human disease can be established. Answers from the previous two questions will hopefully guide future efforts in developing valid tree shrew disease models. Genetically modified tree shrews or viral vector-mediated gene delivery offer excellent approaches for characterizing gene functions and mechanisms. However, this requires detailed analyses at the levels of specific cell types, cell clusters, cell communications, and networks. In tree shrew brain research, it is critical to accurately define neuronal cell types, connections, circuits, and projections. Researchers must fully consider the unique and dominant position of tree shrews in terms of behavior or face validity when establishing disease models. This also applies to cross-species studies, as tree shrews offer distinct advantages compared to rodents, such as their visual system and social attributes. An equally important question is how studying the tree shrew brain can enhance our knowledge of the human brain and related disorders. Under these conditions, tree shrews may serve as a useful tool to verify the effectiveness and safety of related disease research. The high face validity and predictive validity of tree shrews in certain disease models are crucial for analyzing disease mechanisms. Addressing the lack of specific research reagents and toolkits, common to all non-model organisms, remains an urgent need. To solve these issues, we must undergo a paradigm shift now and, in the future, utilizing cutting-edge technologies.

## CONCLUSIONS

Due to the urgent need for animal models to meet the changing global burden of diseases, ethical considerations, cost efficiency, resource availability, and suitability as viable animal models, tree shrews have emerged as a promising model in the field. Tree shrews, being more closely related to humans than mice and rats, are more likely to yield translational insights to humans (Yao, 2017). Indeed, over the past decades, several key findings in tree shrews have broadened our knowledge about life and health. Notably, the discovery of tree shrew susceptibility to HBV (Su et al., 1987; Walter et al., 1996; Yan et al., 1996) and HCV infections (Amako et al., 2010; Xie et al., 1998; Xu et al., 2007; Zhao et al., 2002) led to the identification of NTCP as a functional receptor for HBV and HDV (Li, 2015; Yan et al., 2012). This landmark discovery resolved a long-standing mystery regarding HBV entry, spurring subsequent studies to characterize the NTCP structure (Qi & Li, 2022; and references therein), establish *in vitro* HBV infection models (Guo et al., 2023a), and develop potent and selective inhibitors (Chen et al., 2022b; Liu et al., 2021), all contributing to the prevention and treatment of these infections. Similarly, the initial establishment of the tree shrew model for myopia (Marsh-Tootle & Norton, 1989; Norton et al., 2006; Sherman et al., 1977) opened new avenues for studying the pathobiology of myopia and evaluating prophylactics. The use of tree shrews in visual cortex research has also yielded rich insights regarding the working theory of the visual system (Fitzpatrick, 1996; Lee et al., 2016; MacEvoy et al., 2009; Sedigh-Sarvestani et al., 2021; Tanabe et al., 2022). The development of a chronic psychosocial stress model in tree shrews (Fuchs, 2005; Fuchs & Flügge, 2002; Kramer et al., 1999; Magariños et al., 1996) has also facilitated the discovery of potential treatments (Czéh et al., 2001; Fuchs et al., 1996; Parésys et al., 2016; Schmelting et al., 2014; van der Hart et al., 2002). The decoding of the tree shrew genome (Fan et al., 2013, 2019; Ye et al., 2021) and genetic modifications using SSCs (Li et al., 2017) have further paved the way for uncovering more secrets of this animal and broadening its applications in biomedical research.

By summarizing the key findings and animal models, we believe that tree shrews can serve as an adjunct and alternative to NHPs (Cao et al., 2003; Savier et al., 2021; Xiao et al., 2017; Yao, 2017), and as an essential complement to studies of model organisms for both basic and biomedical research (Lehner, 2013; Yamamoto et al., 2024). Researchers have consistently endeavored to establish tree shrews as viable laboratory animals, focusing on resource sharing, inbred strain development, and behavioral, genetic, and animal model optimization. Tree shrews are particularly appealing to investigators seeking models for testing potential drug therapies for infectious and neurodegenerative diseases, given their close relationship to NHPs and lower cost. Addressing the longstanding low acceptance of tree shrews in biomedical research is crucial. A bright future for tree shrew research is anticipated, especially with increased international collaborations and the sharing of resources and technologies.

## COMPETING INTERESTS

The authors declare that they have no competing interests.

## AUTHORS' CONTRIBUTIONS

Y.G.Y. conceived the idea and designed the study. Y.G.Y. wrote the entire draft, L.L. wrote the draft section "Behavioral tests for tree shrews", and R.J.N. and J.N.Z. wrote the draft section "Tree shrew brain atlas". Y.G.Y., H.L., L.X., and D.Y. compiled Table 1. All authors provided valuable

discussion, edited the manuscript, and read and approved the final version of the manuscript.


## ACKNOWLEDGMENTS

We thank Prof. Jianhua JC Cang and Dr. Xiaorong Liu from the University of Virginia, and Prof. David Fitzpatrick from the Max Planck Florida Institute for Neuroscience for their helpful comments. We thank Mr. Weibo Kang for help with the preparation of Figure 2 and Prof. Xiaoyong Man for making Figure 3H.


## REFERENCES


100, 000 Genomes Project Pilot Investigators, Smedley D, Smith KR, et al. 2021. 100, 000 genomes pilot on rare-disease diagnosis in health care - preliminary report. *The New England Journal of Medicine*, **385**(20): 1868–1880.

Abbott CJ, Grünert U, Pianta MJ, et al. 2011. Retinal thinning in tree shrews with induced high myopia: optical coherence tomography and histological assessment. *Vision Research*, **51**(3): 376–385.

Achoki T, Sartorius B, Watkins D, et al. 2022. Health trends, inequalities and opportunities in South Africa's provinces, 1990–2019: findings from the Global Burden of Disease 2019 Study. *Journal of Epidemiology & Community Health*, **76**(5): 471–481.

Agu PC, Obulose CN. 2024. Piquing artificial intelligence towards drug discovery: tools, techniques, and applications. *Drug Development Research*, **85**(2): e22159.

Ai JQ, Luo RC, Tu T, et al. 2021. Doublecortin-expressing neurons in Chinese tree shrew forebrain exhibit mixed rodent and primate-like topographic characteristics. *Frontiers in Neuroanatomy*, **15**: 727883.

Airaksinen MS, Flügge G, Fuchs E, et al. 1989. Histaminergic system in the tree shrew brain. *The Journal of Comparative Neurology*, **286**(3): 289–310.

Amako Y, Tsukiyama-Kohara K, Katsume A, et al. 2010. Pathogenesis of hepatitis C virus infection in *Tupaia belangeri. Journal of Virology*, **84**(1): 303–311.

Arnsten AFT, Datta D, Preuss TM. 2021. Studies of aging nonhuman primates illuminate the etiology of early-stage Alzheimer's-like neuropathology: an evolutionary perspective. *American Journal of Primatology*, **83**(11): e23254.

Augustyniak J, Bertero A, Coccini T, et al. 2019. Organoids are promising tools for species-specific in vitro toxicological studies. *Journal of Applied Toxicology*, **39**(12): 1610–1622.

Badon IW, Oh Y, Kim HJ, et al. 2024. Recent application of CRISPR-Cas12 and OMEGA system for genome editing. *Molecular Therapy*, **32**(1): 32–43.

Bala PC, Eisenreich BR, Yoo SBM, et al. 2020. Automated markerless pose estimation in freely moving macaques with OpenMonkeyStudio. *Nature Communications*, **11**(1): 4560.

Balaram P, Isaamullah M, Petry HM, et al. 2015. Distributions of vesicular glutamate transporters 1 and 2 in the visual system of tree shrews (*Tupaia belangeri*). *The Journal of Comparative Neurology*, **523**(12): 1792–1808.

Baldwin MKL, Wei HY, Reed JL, et al. 2013. Cortical projections to the superior colliculus in tree shrews (*Tupaia belangeri*). *The Journal of Comparative Neurology*, **521**(7): 1614–1632.

Baloch Z, Shen ZL, Zhang L, et al. 2021. Recapitulating Zika virus infection in vagina of tree shrew (*Tupaia belangeri*). *Frontiers in Cellular and Infection Microbiology*, **11**: 687338.

Bergeron LA, Besenbacher S, Zheng J, et al. 2023. Evolution of the germline mutation rate across vertebrates. *Nature*, **615**(7951): 285–291.

Bogue MA, Ball RL, Walton DO, et al. 2023. Mouse phenome database: curated data repository with interactive multi-population and multi-trait analyses. *Mammalian Genome*, **34**(4): 509–519.

Bosking WH, Crowley JC, Fitzpatrick D. 2002. Spatial coding of position and orientation in primary visual cortex. *Nature Neuroscience*, **5**(9): 874–882.

Bosking WH, Zhang Y, Schofield B, et al. 1997. Orientation selectivity and the arrangement of horizontal connections in tree shrew striate cortex. *Journal of Neuroscience*, **17**(6): 2112–2127.

Brown SDM, Holmes CC, Mallon AM, et al. 2018. High-throughput mouse phenomics for characterizing mammalian gene function. *Nature Reviews Genetics*, **19**(6): 357–370.

Cao J, Yang EB, Su JJ, et al. 2003. The tree shrews: adjuncts and alternatives to primates as models for biomedical research. *Journal of Medical Primatology*, **32**(3): 123–130.

Challis RC, Ravindra Kumar S, Chen XH, et al. 2022. Adeno-associated virus toolkit to target diverse brain cells. *Annual Review of Neuroscience*, **45**: 447–469.

Charlesworth D, Willis JH. 2009. The genetics of inbreeding depression. *Nature Reviews Genetics*, **10**(11): 783–796.

Che PL, Wang MM, Larson-Casey JL, et al. 2021. A novel tree shrew model of pulmonary fibrosis. *Laboratory Investigation*, **101**(1): 116–124.

Chen JQ, Zhang QY, Yu DD, et al. 2022a. Optimization of milk substitutes for the artificial rearing of Chinese tree shrews (*Tupaia belangeri chinensis*). *Animals*, **12**(13): 1655.

Chen MJ, Ou C, Yang C, et al. 2019. A novel animal model of induced breast precancerous lesion in tree shrew. *Biological and Pharmaceutical Bulletin*, **42**(4): 580–585.

Chen Q, Ma ZX, Xia LB, et al. 2020. A tree shrew model for steroid-associated osteonecrosis. *Zoological Research*, **41**(5): 564–568.

Chen SW, Zhang L, Chen Y, et al. 2022b. Inhibiting sodium taurocholate cotransporting polypeptide in HBV-related diseases: from biological function to therapeutic potential. *Journal of Medicinal Chemistry*, **65**(19): 12546–12561.

Chi HY, Tanaka Y, Hifumi T, et al. 2020. Pathological and genetic aspects of spontaneous mammary gland tumor in *Tupaia belangeri* (tree shrew). *PLoS One*, **15**(5): e0233232.

Chomsung RD, Wei HY, Day-Brown JD, et al. 2010. Synaptic organization of connections between the temporal cortex and pulvinar nucleus of the tree shrew. *Cerebral Cortex*, **20**(4): 997–1011.

Chunhabundit P, Thongpila S, Mingsakul T, et al. 1993. Microvascularization of the common tree shrew (*Tupaia glis*) superior cervical ganglion studied by vascular corrosion cast with scanning electron microscopy. *Acta Anatomica*, **148**(1): 49–56.

Collins PM, Tsang WN. 1987. Growth and reproductive development in the male tree shrew (*Tupaia belangeri*) from birth to sexual maturity. *Biology of Reproduction*, **37**(2): 261–267.

Coolen A, Hoffmann K, Barf RP, et al. 2012. Telemetric study of sleep architecture and sleep homeostasis in the day-active tree shrew *Tupaia belangeri. Sleep*, **35**(6): 879–888.

Coughlan G, Laczó J, Hort J, et al. 2018. Spatial navigation deficits-overlooked cognitive marker for preclinical Alzheimer disease?. *Nature Reviews Neurology*, **14**(8): 496–506.

Cusick JA, Wellman CL, Demas GE. 2021. The call of the wild: using non-model systems to investigate microbiome-behaviour relationships. *Journal of Experimental Biology*, **224**(10): jeb224485.

Czéh B, Michaelis T, Watanabe T, et al. 2001. Stress-induced changes in cerebral metabolites, hippocampal volume, and cell proliferation are prevented by antidepressant treatment with tianeptine. *Proceedings of the National Academy of Sciences of the United States of America*, **98**(22): 12796–12801.

Dai JK, Wang SX, Shan D, et al. 2017. A diffusion tensor imaging atlas of white matter in tree shrew. *Brain Structure and Function*, **222**(4): 1733–1751.

Dai JK, Wang SX, Shan D, et al. 2018. Super-resolution track-density imaging reveals fine anatomical features in tree shrew primary visual cortex and hippocampus. *Neuroscience Bulletin*, **34**(3): 438–448.

Darai G, Schwaier A, Komitowski D, et al. 1978. Experimental infection of

*Tupaia belangeri* (tree shrews) with herpes simplex virus types 1 and 2. *The Journal of Infectious Diseases*, **137**(3): 221–226.

Day-Brown JD, Wei H, Chomsung RD, et al. 2010. Pulvinar projections to the striatum and amygdala in the tree shrew. *Frontiers in Neuroanatomy*, **4**: 143.

De Coster W, Weissensteiner MH, Sedlazeck FJ. 2021. Towards population-scale long-read sequencing. *Nature Reviews Genetics*, **22**(9): 572–587.

Diamond IT, Snyder M, Killackey H, et al. 1970. Thalamo-cortical projections in the tree shrew (*Tupaia glis*). *The Journal of Comparative Neurology*, **139**(3): 273–306.

Dimanico MM, Klaassen AL, Wang J, et al. 2021. Aspects of tree shrew consolidated sleep structure resemble human sleep. *Communications Biology*, **4**(1): 722.

Duan Y, Jin LT, Du WJ, et al. 2022. Alterations of dopamine receptors and the adaptive changes of L-type calcium channel subtypes regulate cocaine-seeking habit in tree shrew. *Life*, **12**(7): 984.

Duan Y, Meng YM, Du WJ, et al. 2021. Increased cocaine motivation in tree shrews is modulated by striatal dopamine D1 receptor-mediated upregulation of $Ca_V$ 1.2. *Addiction Biology*, **26**(6): e13053.

El Marjou F, Jouhanneau C, Krndija D. 2021. Targeted transgenic mice using CRISPR/Cas9 technology. *Methods in Molecular Biology*, **2214**: 125–141.

Elliot OS, Elliot MW, Lisco H. 1966. Breast cancer in a tree shrew (*Tupaia glis*). *Nature*, **211**(5053): 1105.

Estrada A, Garber PA, Rylands AB, et al. 2017. Impending extinction crisis of the world's primates: why primates matter. *Science Advances*, **3**(1): e1600946.

Fan Y, Huang ZY, Cao CC, et al. 2013. Genome of the Chinese tree shrew. *Nature Communications*, **4**: 1426.

Fan Y, Luo RC, Su LY, et al. 2018. Does the Genetic feature of the Chinese tree shrew (*Tupaia belangeri chinensis*) support its potential as a viable model for Alzheimer's disease research?. *Journal of Alzheimer's Disease*, **61**(3): 1015–1028.

Fan Y, Ye MS, Zhang JY, et al. 2019. Chromosomal level assembly and population sequencing of the Chinese tree shrew genome. *Zoological Research*, **40**(6): 506–521.

Fan Y, Yu DD, Yao YG. 2014. Tree shrew database (TreeshrewDB): a genomic knowledge base for the Chinese tree shrew. *Scientific Reports*, **4**: 7145.

Fang H, Sun YJ, Lv YH, et al. 2016. High activity of the stress promoter contributes to susceptibility to stress in the tree shrew. *Scientific Reports*, **6**: 24905.

Feng LX, Chen YL, Dettin L, et al. 2002. Generation and in vitro differentiation of a spermatogonial cell line. *Science*, **297**(5580): 392–395.

Feng Y, Feng YM, Lu CX, et al. 2017. Tree shrew, a potential animal model for hepatitis C, supports the infection and replication of HCV *in vitro* and *in vivo*. *Journal of General Virology*, **98**(8): 2069–2078.

Fitzpatrick D. 1996. The functional organization of local circuits in visual cortex: insights from the study of tree shrew striate cortex. *Cerebral Cortex*, **6**(3): 329–341.

Flügge G. 1995. Dynamics of central nervous 5-HT1A-receptors under psychosocial stress. *Journal of Neuroscience*, **15**(11): 7132–7140.

Flügge G. 1996. Alterations in the central nervous alpha 2-adrenoceptor system under chronic psychosocial stress. *Neuroscience*, **75**(1): 187–196.

Flügge G, Ahrens O, Fuchs E. 1994. Monoamine receptors in the amygdaloid complex of the tree shrew (*Tupaia belangeri*). *The Journal of Comparative Neurology*, **343**(4): 597–608.

Flügge G, Ahrens O, Fuchs E. 1997. β-adrenoceptors in the tree shrew brain. II. Time-dependent effects of chronic psychosocial stress on [$^{125}$I]iodocyanopindolol binding sites. *Cellular and Molecular Neurobiology*, **17**(4): 417–432.

Fromhage L. 2012. Mating unplugged: a model for the evolution of mating plug (dis-)placement. *Evolution*, **66**(1): 31–39.

Fuchs E. 2005. Social stress in tree shrews as an animal model of depression: an example of a behavioral model of a CNS disorder. *CNS Spectrums*, **10**(3): 182–190.

Fuchs E. 2015. Tree shrews at the German Primate Center. *Primate Biology*, **2**(1): 111–118.

Fuchs E. 2024. Tree shrews. *In*: Golledge H, Richardson C. The UFAW Handbook on the Care and Management of Laboratory and Other Research Animals. 9th ed. Chichester: Wiley-Blackwell, 324–339.

Fuchs E, Corbach-Söhle S. 2010. Tree shrews. *In*: Hubrecht R, Kirkwood J. The UFAW Handbook on the Care and Management of Laboratory and Other Research Animals. 8th ed. Chichester: Wiley-Blackwell, 262–275.

Fuchs E, Flügge G. 1998. Stress, glucocorticoids and structural plasticity of the hippocampus. *Neuroscience & Biobehavioral Reviews*, **23**(2): 295–300.

Fuchs E, Flügge G. 2002. Social stress in tree shrews: effects on physiology, brain function, and behavior of subordinate individuals. *Pharmacology, Biochemistry & Behavior*, **73**(1): 247–258.

Fuchs E, Kramer M, Hermes B, et al. 1996. Psychosocial stress in tree shrews: clomipramine counteracts behavioral and endocrine changes. *Pharmacology, Biochemistry & Behavior*, **54**(1): 219–228.

Fuchs E, Schumacher M. 1990. Psychosocial stress affects pineal function in the tree shrew (*Tupaia belangeri*). *Physiology & Behavior*, **47**(4): 713–717.

Gao B, Lin J, Jiang ZM, et al. 2018. Upregulation of chemokine CXCL10 enhances chronic pulmonary inflammation in tree shrew collagen-induced arthritis. *Scientific Reports*, **8**(1): 9993.

Gawne TJ, Siegwart JT Jr, Ward AH, et al. 2017. The wavelength composition and temporal modulation of ambient lighting strongly affect refractive development in young tree shrews. *Experimental Eye Research*, **155**: 75–84.

GBD 2019 Cancer Risk Factors Collaborators. 2022. The global burden of cancer attributable to risk factors, 2010–19: a systematic analysis for the Global Burden of Disease Study 2019. *The Lancet*, **400**(10352): 563–591.

GBD 2019 Diseases and Injuries Collaborators. 2020. Global burden of 369 diseases and injuries in 204 countries and territories, 1990–2019: a systematic analysis for the Global Burden of Disease Study 2019. *The Lancet*, **396**(10258): 1204–1222.

Gellner AK, Voelter J, Schmidt U, et al. 2021. Molecular and neurocircuitry mechanisms of social avoidance. *Cellular and Molecular Life Sciences*, **78**(4): 1163–1189.

Gong H, Xu DL, Yuan J, et al. 2016. High-throughput dual-colour precision imaging for brain-wide connectome with cytoarchitectonic landmarks at the cellular level. *Nature Communications*, **7**: 12142.

Gorbatyuk OS, Pitale PM, Saltykova IV, et al. 2022. A novel tree shrew model of diabetic retinopathy. *Frontiers in Endocrinology*, **12**: 799711.

Grannonico M, Miller DA, Liu MN, et al. 2021. Global and regional damages in retinal ganglion cell axon bundles monitored non-invasively by visible-light optical coherence tomography fibergraphy. *Journal of Neuroscience*, **41**(49): 10179–10193.

Grannonico M, Miller DA, Liu MN, et al. 2024. Comparative in vivo imaging of retinal structures in tree shrews, humans, and mice. *eNeuro*, **11**(3): ENEURO.0373–23.2024.

Gu TL, Yu DD, Fan Y, et al. 2019a. Molecular identification and antiviral function of the guanylate-binding protein (GBP) genes in the Chinese tree shrew (*Tupaia belangeri chinesis*). *Developmental & Comparative Immunology*, **96**: 27–36.

Gu TL, Yu DD, Li Y, et al. 2019b. Establishment and characterization of an immortalized renal cell line of the Chinese tree shrew (*Tupaia belangeri chinesis*). *Applied Microbiology and Biotechnology*, **103**(5): 2171–2180.

Gu TL, Yu DD, Xu L, et al. 2021a. *Tupaia* GBP1 interacts with STING to initiate autophagy and restrict herpes simplex virus type 1 infection. *The*

*Journal of Immunology*, **207**(11): 2673–2680.

Gu TL, Yu DD, Xu L, et al. 2021b. *Tupaia* guanylate-binding protein 1 interacts with vesicular stomatitis virus phosphoprotein and represses primary transcription of the viral genome. *Cytokine*, **138**: 155388.

Guo HB, Urban S, Wang WS. 2023a. *In vitro* cell culture models to study hepatitis B and D virus infection. *Frontiers in Microbiology*, **14**: 1169770.

Guo YT, Shao Y, Bi XP, et al. 2023b. Harvesting the fruits of the first stage of the Primate Genome Project. *Zoological Research*, **44**(4): 725–728.

Hahn J, Monavarfeshani A, Qiao M, et al. 2023. Evolution of neuronal cell classes and types in the vertebrate retina. *Nature*, **624**(7991): 415–424.

Haque RU, Levey AI. 2019. Alzheimer's disease: a clinical perspective and future nonhuman primate research opportunities. *Proceedings of the National Academy of Sciences of the United States of America*, **116**(52): 26224–26229.

He J, Zhao Y, Fu ZL, et al. 2024. A novel tree shrew model of lipopolysaccharide-induced acute respiratory distress syndrome. *Journal of Advanced Research*, **56**: 157–165.

Hedrick PW, Garcia-Dorado A. 2016. Understanding inbreeding depression, purging, and genetic rescue. *Trends in Ecology & Evolution*, **31**(12): 940–952.

Helgen KM. 2005. Order scandentia. *In*: Wilson DE, Reeder DM. Mammal Species of the World: A Taxonomic and Geographic Reference. 3rd ed. Baltimore: John Hopkins University Press, 104–109.

Hirabayashi M, Takizawa A, Hochi S. 2019. Embryonic stem cells and gene manipulation in rat. *Methods in Molecular Biology*, **2018**: 115–130.

Hook PW, Timp W. 2023. Beyond assembly: the increasing flexibility of single-molecule sequencing technology. *Nature Reviews Genetics*, **24**(9): 627–641.

Hu KJ, Lv LB, Huang H, et al. 2022. A novel tree shrew model of chronic experimental autoimmune uveitis and its disruptive application. *Frontiers in Immunology*, **13**: 889596.

Hu YD, Zhao Q, Zhang XR, et al. 2018. Comparison of the properties of neural stem cells of the hippocampus in the tree shrew and rat *in vitro*. *Molecular Medicine Reports*, **17**(4): 5676–5683.

Huang K, Han YN, Chen K, et al. 2021. A hierarchical 3D-motion learning framework for animal spontaneous behavior mapping. *Nature Communications*, **12**(1): 2784.

Huang Q, Nie BB, Ma C, et al. 2018. Stereotaxic $^{18}$F-FDG PET and MRI templates with three-dimensional digital atlas for statistical parametric mapping analysis of tree shrew brain. *Journal of Neuroscience Methods*, **293**: 105–116.

Huang XY, Elyada YM, Bosking WH, et al. 2014. Optogenetic assessment of horizontal interactions in primary visual cortex. *Journal of Neuroscience*, **34**(14): 4976–4990.

Huang ZH, Ni RJ, Luo PH, et al. 2020. Distribution of tyrosine-hydroxylase-immunoreactive neurons in the hypothalamus of tree shrews. *The Journal of Comparative Neurology*, **528**(6): 935–952.

Jia J, Qiu DD, Lu CX, et al. 2021. Transcriptome analysis of choroid and retina from tree shrew with choroidal neovascularization reveals key signaling moieties. *Frontiers in Genetics*, **12**: 654955.

Jiang LM, Lu CX, Sun QM. 2021a. Tree shrew as a new animal model for the study of Dengue virus. *Frontiers in Immunology*, **12**: 621164.

Jiang LP, Shen QS, Yang CP, et al. 2017. Establishment of basal cell carcinoma animal model in Chinese tree shrew (*Tupaia belangeri chinensis*). *Zoological Research*, **38**(4): 180–190.

Jiang MP, Wang MYX, Shi QQ, et al. 2021b. Evolution and neural representation of mammalian cooperative behavior. *Cell Reports*, **37**(7): 110029.

Justice MJ, Dhillon P. 2016. Using the mouse to model human disease: increasing validity and reproducibility. *Disease Models & Mechanisms*, **9**(2): 101–103.

Kaas JH, Hall WC, Killackey H, et al. 1972. Visual cortex of the tree shrew (*Tupaia glis*): architectonic subdivisions and representations of the visual field. *Brain Research*, **42**(2): 491–496.

Kaschube M, Schnabel M, Löwel S, et al. 2010. Universality in the evolution of orientation columns in the visual cortex. *Science*, **330**(6007): 1113–1116.

Kayesh MEH, Ezzikouri S, Chi HY, et al. 2017a. Interferon-β response is impaired by hepatitis B virus infection in *Tupaia belangeri*. *Virus Research*, **237**: 47–57.

Kayesh MEH, Ezzikouri S, Sanada T, et al. 2017b. Oxidative stress and immune responses during hepatitis C virus infection in *Tupaia belangeri*. *Scientific Reports*, **7**(1): 9848.

Kayesh MEH, Kitab B, Sanada T, et al. 2017c. Susceptibility and initial immune response of *Tupaia belangeri* cells to dengue virus infection. *Infection, Genetics and Evolution*, **51**: 203–210.

Kayesh MEH, Sanada T, Kohara M, et al. 2021. Tree shrew as an emerging small animal model for human viral infection: a recent overview. *Viruses*, **13**(8): 1641.

Kernohan KD, Boycott KM. 2024. The expanding diagnostic toolbox for rare genetic diseases. *Nature Reviews Genetics*, **25**(6): 401–415.

Keuker JIH, de Biurrun G, Luiten PGM, et al. 2004. Preservation of hippocampal neuron numbers and hippocampal subfield volumes in behaviorally characterized aged tree shrews. *The Journal of Comparative Neurology*, **468**(4): 509–517.

KhalafAllah MT, Fuchs PA, Nugen F, et al. 2024. Heterogenous thinning of peripapillary tissues occurs early during high myopia development in juvenile tree shrews. *Experimental Eye Research*, **240**: 109824.

Khanal S, Norton TT, Gawne TJ. 2021. Amber light treatment produces hyperopia in tree shrews. *Ophthalmic & Physiological Optics*, **41**(5): 1076–1086.

Khanal S, Norton TT, Gawne TJ. 2023. Limited bandwidth short-wavelength light produces slowly-developing myopia in tree shrews similar to human juvenile-onset myopia. *Vision Research*, **204**: 108161.

Khani A, Rainer G. 2012. Recognition memory in tree shrew (*Tupaia belangeri*) after repeated familiarization sessions. *Behavioural Processes*, **90**(3): 364–371.

Klein A, Radespiel U, Felmy F, et al. 2022. AA-amyloidosis in captive northern tree shrews (*Tupaia belangeri*). *Veterinary Pathology*, **59**(2): 340–347.

Knopman DS, Amieva H, Petersen RC, et al. 2021. Alzheimer disease. *Nature Reviews Disease Primers*, **7**(1): 33.

Kozicz T, Bordewin LAP, Czéh B, et al. 2008. Chronic psychosocial stress affects corticotropin-releasing factor in the paraventricular nucleus and central extended amygdala as well as urocortin 1 in the non-preganglionic Edinger-Westphal nucleus of the tree shrew. *Psychoneuroendocrinology*, **33**(6): 741–754.

Kramer M, Hiemke C, Fuchs E. 1999. Chronic psychosocial stress and antidepressant treatment in tree shrews: time-dependent behavioral and endocrine effects. *Neuroscience & Biobehavioral Reviews*, **23**(7): 937–947.

Kubota H, Brinster RL. 2018. Spermatogonial stem cells. *Biology of Reproduction*, **99**(1): 52–74.

Kunst M, Laurell E, Mokayes N, et al. 2019. A cellular-resolution atlas of the larval zebrafish brain. *Neuron*, **103**(1): 21–38. e5.

Kurohmaru M, Maeda S, Suda A, et al. 1996. An ultrastructural and lectin-histochemical study on the seminiferous epithelium of the common tree shrew (*Tupaia glis*). *Journal of Anatomy*, **189**(Pt 1): 87–95.

Larson-Casey JL, He C, Che PL, et al. 2020. Technical advance: the use of tree shrews as a model of pulmonary fibrosis. *PLoS One*, **15**(11): e0241323.

Lee KS, Huang XY, Fitzpatrick D. 2016. Topology of ON and OFF inputs in visual cortex enables an invariant columnar architecture. *Nature*, **533**(7601): 90–94.

Lehner B. 2013. Genotype to phenotype: lessons from model organisms for human genetics. *Nature Reviews Genetics*, **14**(3): 168–178.

Leonard C, Schneider GE, Gross CG. 1966. Performance on learning set and delayed-response tasks by tree shrews (*Tupaia glis*). *Journal of Comparative and Psychology*, **62**(3): 501–504.

Lezama-García K, Mariti C, Mota-Rojas D, et al. 2019. Maternal behaviour in domestic dogs. *International Journal of Veterinary Science and Medicine*, **7**(1): 20–30.

Li C, Bi R, Wang L, et al. 2023a. Characterization of long-term *ex vivo* expansion of tree shrew spermatogonial stem cells. *Zoological Research*, **44**(6): 1080–1094.

Li CH, Yan LZ, Ban WZ, et al. 2017. Long-term propagation of tree shrew spermatogonial stem cells in culture and successful generation of transgenic offspring. *Cell Research*, **27**(2): 241–252.

Li CJ, Hui YQ, Zhang R, et al. 2023b. A comparison of behavioral paradigms assessing spatial memory in tree shrews. *Cerebral Cortex*, **33**(19): 10303–10321.

Li CW, McHaney KM, Sederberg PB, et al. 2022. Tree shrews as an animal model for studying perceptual decision-making reveal a critical role of stimulus-independent processes in guiding behavior. *eNeuro*, **9**(6): ENEURO.0419–22.2022.

Li CX, Xiao ZF, Li YR, et al. 2023c. Deep learning-based activity recognition and fine motor identification using 2D skeletons of cynomolgus monkeys. *Zoological Research*, **44**(5): 967–980.

Li DQ, Baloch Z, Zhao Y, et al. 2021a. Establishment of tree shrew animal model for Kaposi's sarcoma-associated herpesvirus (HHV-8) infection. *Frontiers in Microbiology*, **12**: 710067.

Li H, Mei LY, Nie XP, et al. 2023d. New tree shrew Parkinson's model: a cost-effective alternative to monkey models. *bioRxiv*, doi: https://doi.org/10.1101/2023.09.01.555918.

Li HL, Xiang BL, Li X, et al. 2024. Cognitive deficits and Alzheimer's disease-like pathologies in the aged Chinese tree shrew. *Molecular Neurobiology*, **61**(4): 1892–1906.

Li J, Shi TD, Han JF, et al. 2021b. A systematic study of *Tupaia* as a model for human acute hepatitis B infection. *The Journal of Veterinary Medical Science*, **83**(6): 1004–1011.

Li JJ, Hong SY, Chen WJ, et al. 2019. Advances in detecting and reducing off-target effects generated by CRISPR-mediated genome editing. *Journal of Genetics and Genomics*, **46**(11): 513–521.

Li LH, Li Y, Li X, et al. 2020. HSV-1 infection and pathogenesis in the tree shrew eye following corneal inoculation. *Journal of Neurovirology*, **26**(3): 391–403.

Li QF, Ding MQ, Wang H, et al. 1995. The infection of hepatitis D virus in adult tupaia. *National Medical Journal of China*, **75**(10): 611–613. (in Chinese)

Li RF, Yuan B, Xia XS, et al. 2018a. Tree shrew as a new animal model to study the pathogenesis of avian influenza (H9N2) virus infection. *Emerging Microbes & Infections*, **7**(1): 166.

Li RF, Zanin M, Xia XS, et al. 2018b. The tree shrew as a model for infectious diseases research. *Journal of Thoracic Disease*, **10**(S19): S2272–S2279.

Li WH. 2015. The hepatitis B virus receptor. *Annual Review of Cell and Developmental Biology*, **31**: 125–147.

Li X, Zhou ZC, Liu WK, et al. 2021c. Chinese tree shrew: a permissive model for in vitro and in vivo replication of human adenovirus species B. *Emerging Microbes & Infections*, **10**(1): 424–438.

Lin N, Xiong LL, Zhang RP, et al. 2016. Injection of Aβ1–40 into hippocampus induced cognitive lesion associated with neuronal apoptosis and multiple gene expressions in the tree shrew. *Apoptosis*, **21**(5): 621–640.

Liu CY, Si W, Tu CF, et al. 2023. Deficiency of primate-specific *SSX1* induced asthenoteratozoospermia in infertile men and cynomolgus monkey and tree shrew models. *The American Journal of Human Genetics*, **110**(3): 516–530.

Liu SY, Crawford DC. 2022. Maturation and application of phenome-wide association studies. *Trends in Genetics*, **38**(4): 353–363.

Liu XL, Li ZF, Li X, et al. 2024. Neutralizing monoclonal antibodies protect against human adenovirus type 55 infection in transgenic mice and tree shrews. *Emerging Microbes & Infections*, **13**(1): 2307513.

Liu Y, Zhang L, Yan H, et al. 2021. Design of dimeric bile acid derivatives as potent and selective human NTCP inhibitors. *Journal of Medicinal Chemistry*, **64**(9): 5973–6007.

Lu CX, Feng Y, Sun XM, et al. 2020. Tree shrew bone marrow-derived mesenchymal stem cells express CD81, OCLN, and miR-122, facilitating the entire hepatitis C virus life cycle. *Journal of Medical Virology*, **92**(12): 3465–3474.

Lu T, Peng HM, Zhong LP, et al. 2021. The tree shrew as a model for cancer research. *Frontiers in Oncology*, **11**: 653236.

Luo MT, Fan Y, Mu D, et al. 2018. Molecular cloning and characterization of *APOBEC3* family in tree shrew. *Gene*, **646**: 143–152.

Luo MT, Mu D, Yang X, et al. 2021. Tree shrew cells transduced with human CD4 and CCR5 support early steps of HIV-1 replication, but viral infectivity is restricted by APOBEC3. *Journal of Virology*, **95**(16): e0002021.

Luo MT, Zheng YT. 2020. The tsAPOBEC3 proteins restrict HBV replication and may limit the establishment of persistent infection in tree shrews. *Cellular & Molecular Immunology*, **17**(10): 1107–1108.

Luo X, Li M, Su B. 2016. Application of the genome editing tool CRISPR/Cas9 in non-human primates. *Zoological Research*, **37**(4): 214–219.

Lyon DC, Jain N, Kaas JH. 2003. The visual pulvinar in tree shrews II. Projections of four nuclei to areas of visual cortex. *The Journal of Comparative Neurology*, **467**(4): 607–627.

Ma KL, Gao JH, Huang ZQ, et al. 2013. Motor function in MPTP-treated tree shrews (*Tupaia belangeri chinensis*). *Neurochemical Research*, **38**(9): 1935–1940.

Ma LY, Chen R, Zhang YL, et al. 2023. The tree shrew as a new animal model for the study of periodontitis. *Journal of Clinical Periodontology*, **50**(8): 1075–1088.

Ma Q, Ma WJ, Song TZ, et al. 2022. Single-nucleus transcriptomic profiling of multiple organs in a rhesus macaque model of SARS-CoV-2 infection. *Zoological Research*, **43**(6): 1041–1062.

Ma X, Wong ASY, Tam HY, et al. 1998. *In vivo* genome editing thrives with diversified CRISPR technologies. *Zoological Research*, **39**(2): 58–71.

MacArthur Clark J. 2018. The 3Rs in research: a contemporary approach to replacement, reduction and refinement. *British Journal of Nutrition*, **120**(S1): S1–S7.

MacEvoy SP, Tucker TR, Fitzpatrick D. 2009. A precise form of divisive suppression supports population coding in the primary visual cortex. *Nature Neuroscience*, **12**(5): 637–645.

Madigan V, Zhang F, Dahlman JE. 2023. Drug delivery systems for CRISPR-based genome editors. *Nature Reviews Drug Discovery*, **22**(11): 875–894.

Magariños AM, McEwen BS, Flügge G, et al. 1996. Chronic psychosocial stress causes apical dendritic atrophy of hippocampal CA3 pyramidal neurons in subordinate tree shrews. *Journal of Neuroscience*, **16**(10): 3534–3540.

Maher EE, Prillaman ME, Keskinoz EN, et al. 2021. Immunocytochemical and ultrastructural organization of the taste thalamus of the tree shrew (*Tupaia belangeri*). *The Journal of Comparative Neurology*, **529**(10): 2558–2575.

Maille A, Jäschke N, Joly M, et al. 2013. Does a nonprimate mammal, the northern tree shrew (*Tupaia belangeri*), exhibit paw preference in two forms of a grasping task?. *Journal of Comparative Psychology*, **127**(1): 14–23.

Marks M, Jin QH, Sturman O, et al. 2022. Deep-learning based identification, tracking, pose estimation, and behavior classification of interacting primates and mice in complex environments. *Nature Machine*

*Intelligence*, **4**(4): 331–340.
Marrocco RT, De Valois RL, Boles JI. 1970. A stereotaxic atlas of the brain of the tree shrew (*Tupaia glis*). *Journal für Hirnforschung*, **12**(4): 307–312.
Marsh-Tootle WL, Norton TT. 1989. Refractive and structural measures of lid-suture myopia in tree shrew. *Investigative Ophthalmology & Visual Science*, **30**(10): 2245–2257.
McBrien NA, Norton TT. 1992. The development of experimental myopia and ocular component dimensions in monocularly lid-sutured tree shrews (*Tupaia belangeri*). *Vision Research*, **32**(5): 843–852.
McCarthy MM. 1990. Oxytocin inhibits infanticide in female house mice (*Mus domesticus*). *Hormones and Behavior*, **24**(3): 365–375.
McCollum LA, Roberts RC. 2014. Ultrastructural localization of tyrosine hydroxylase in tree shrew nucleus accumbens core and shell. *Neuroscience*, **271**: 23–34.
McGonigle P, Ruggeri B. 2014. Animal models of human disease: challenges in enabling translation. *Biochemical Pharmacology*, **87**(1): 162–171.
Meadows JRS, Lindblad-Toh K. 2017. Dissecting evolution and disease using comparative vertebrate genomics. *Nature Reviews Genetics*, **18**(10): 624–636.
Meyer U, van Kampen M, Isovich E, et al. 2001. Chronic psychosocial stress regulates the expression of both GR and MR mRNA in the hippocampal formation of tree shrews. *Hippocampus*, **11**(3): 329–336.
Miller DA, Grannonico M, Liu MN, et al. 2020. Visible-light optical coherence tomography fibergraphy for quantitative imaging of retinal ganglion cell axon bundles. *Translational Vision Science & Technology*, **9**(11): 11.
Miller DA, Grannonico M, Liu MN, et al. 2024. Visible-light optical coherence tomography fibergraphy of the tree shrew retinal ganglion cell axon bundles. *IEEE Transactions on Medical Imaging*, doi: 10.1109/TMI.2024.3380530.
Mooser F, Bosking WH, Fitzpatrick D. 2004. A morphological basis for orientation tuning in primary visual cortex. *Nature Neuroscience*, **7**(8): 872–879.
Mu D, Yang H, Zhu JW, et al. 2014. Independent birth of a novel *TRIMCyp* in *Tupaia belangeri* with a divergent function from its paralog *TRIM5*. *Molecular Biology and Evolution*, **31**(11): 2985–2997.
Muly EC, Fitzpatrick D. 1992. The morphological basis for binocular and ON/OFF convergence in tree shrew striate cortex. *Journal of Neuroscience*, **12**(4): 1319–1334.
Mustafar F, Harvey MA, Khani A, et al. 2018. Divergent solutions to visual problem solving across mammalian species. *eNeuro*, **5**(4): ENEURO.0167–18.2018.
Nair J, Topka M, Khani A, et al. 2014. Tree shrews (*Tupaia belangeri*) exhibit novelty preference in the novel location memory task with 24-h retention periods. *Frontiers in Psychology*, **5**: 303.
National Academies of Sciences, Engineering, and Medicine, Division on Earth and Life Studies, Health and Medicine Division, et al. 2023. Nonhuman Primate Models in Biomedical Research: State of the Science and Future Needs. Washington: National Academies Press.
Ni RJ, Huang ZH, Luo PH, et al. 2018a. The tree shrew cerebellum atlas: systematic nomenclature, neurochemical characterization, and afferent projections. *The Journal of Comparative Neurology*, **526**(17): 2744–2775.
Ni RJ, Huang ZH, Shu YM, et al. 2018b. Atlas of the striatum and Globus pallidus in the tree shrew: comparison with rat and mouse. *Neuroscience Bulletin*, **34**(3): 405–418.
Ni RJ, Luo PH, Shu YM, et al. 2016. Whole-brain mapping of afferent projections to the bed nucleus of the stria terminalis in tree shrews. *Neuroscience*, **333**: 162–180.
Ni RJ, Shu YM, Li T, et al. 2021. Whole-brain afferent inputs to the caudate nucleus, putamen, and accumbens nucleus in the tree shrew striatum. *Frontiers in Neuroanatomy*, **15**: 763298.
Ni RJ, Shu YM, Luo PH, et al. 2015. Immunohistochemical mapping of neuropeptide Y in the tree shrew brain. *The Journal of Comparative Neurology*, **523**(3): 495–529.
Ni RJ, Shu YM, Wang J, et al. 2014. Distribution of vasopressin, oxytocin and vasoactive intestinal polypeptide in the hypothalamus and extrahypothalamic regions of tree shrews. *Neuroscience*, **265**: 124–136.
Ni RJ, Tian Y, Dai XY, et al. 2020. Social avoidance behavior in male tree shrews and prosocial behavior in male mice toward unfamiliar conspecifics in the laboratory. *Zoological Research*, **41**(3): 258–272.
Niu YY, Yu Y, Bernat A, et al. 2010. Transgenic rhesus monkeys produced by gene transfer into early-cleavage-stage embryos using a simian immunodeficiency virus-based vector. *Proceedings of the National Academy of Sciences of the United States of America*, **107**(41): 17663–17667.
Norton TT, Amedo AO, Siegwart JT Jr. 2006. Darkness causes myopia in visually experienced tree shrews. *Investigative Ophthalmology & Visual Science*, **47**(11): 4700–4707.
Norton TT, Amedo AO, Siegwart JT Jr. 2010. The effect of age on compensation for a negative lens and recovery from lens-induced myopia in tree shrews (*Tupaia glis belangeri*). *Vision Research*, **50**(6): 564–576.
Norton TT, McBrien NA. 1992. Normal development of refractive state and ocular component dimensions in the tree shrew (*Tupaia belangeri*). *Vision Research*, **32**(5): 833–842.
Norton TT, Rager G, Kretz R. 1985. ON and OFF regions in layer IV of striate cortex. *Brain Research*, **327**(1-2): 319–323.
Nowak MA. 2006. Five rules for the evolution of cooperation. *Science*, **314**(5805): 1560–1563.
Nowak MA. 2012. Evolving cooperation. *Journal of Theoretical Biology*, **299**: 1–8.
Ohl F, Fuchs E. 1999. Differential effects of chronic stress on memory processes in the tree shrew. *Cognitive Brain Research*, **7**(3): 379–387.
Ohl F, Oitzl MS, Fuchs E. 1998. Assessing cognitive functions in tree shrews: visuo-spatial and spatial learning in the home cage. *Journal of Neuroscience Methods*, **81**(1-2): 35–40.
Ohta H. 1983. Learning set formation in slow lorises *(Nycticebus coucang*). *Folia Primatologica*, **40**(4): 256–267.
Ohta H, Ishida H, Matano S. 1984. Learning set formation in ring-tailed lemurs (*Lemur catta*). *Folia Primatologica*, **43**(1): 53–58.
Ohta H, Matsutani S, Ishida H, et al. 1985. Learning set formation in common tree shrews (*Tupaia glis*). *Folia Primatologica*, **44**(3-4): 204–209.
Olazábal DE, Alsina-Llanes M. 2016. Are age and sex differences in brain oxytocin receptors related to maternal and infanticidal behavior in naïve mice?. *Hormones and Behavior*, **77**: 132–140.
Ong JCL, Seng BJJ, Law JZF, et al. 2024. Artificial intelligence, ChatGPT, and other large language models for social determinants of health: current state and future directions. *Cell Reports Medicine*, **5**(1): 101356.
Onomoto K, Onoguchi K, Yoneyama M. 2021. Regulation of RIG-I-like receptor-mediated signaling: interaction between host and viral factors. *Cellular & Molecular Immunology*, **18**(3): 539–555.
Oppelt C, Wutzler R, von Holst D. 2010. Characterisation of MHC class II DRB genes in the northern tree shrew (*Tupaia belangeri*). *Immunogenetics*, **62**(9): 613–622.
Ou JX, Ball JM, Luan YZ, et al. 2018. iPSCs from a hibernator provide a platform for studying cold adaptation and its potential medical applications. *Cell*, **173**(4): 851–863. e16.
Paik SB, Ringach DL. 2011. Retinal origin of orientation maps in visual cortex. *Nature Neuroscience*, **14**(7): 919–925.
Paik SB, Ringach DL. 2012. Link between orientation and retinotopic maps in primary visual cortex. *Proceedings of the National Academy of Sciences of the United States of America*, **109**(18): 7091–7096.
Palasantzas VEJM, Tamargo-Rubio I, Le K, et al. 2023. iPSC-derived organ-on-a-chip models for personalized human genetics and pharmacogenomics studies. *Trends in Genetics*, **39**(4): 268–284.

Palchaudhuri M, Flügge G. 2005. 5-$HT_{1A}$ receptor expression in pyramidal neurons of cortical and limbic brain regions. *Cell and Tissue Research*, **321**(2): 159–172.

Pan MT, Zhang H, Li XJ, et al. 2024. Genetically modified non-human primate models for research on neurodegenerative diseases. *Zoological Research*, **45**(2): 263–274.

Pan TT, Liu C, Li DM, et al. 2022. Nucleus accumbens-linked executive control networks mediating reversal learning in tree shrew brain. *Zoological Research*, **43**(4): 528–531.

Pang QF, Liu JC, Wan XB, et al. 1983. Experimental infection of adult *Tupaia belangeri yunalis* with human rotavirus. *Chinese Medical Journal*, **96**(2): 85–94.

Pang QF, Wan XB, Chen SD, et al. 1984. Treatment of rotavirus infection in tree shrews (*Tupaia belangeri yunalis*) with herbal *Valeriana jatamansi* (VJ). *Journal of Traditional Chinese Medicine*, **4**(4): 301–306.

Parésys L, Hoffmann K, Froger N, et al. 2016. Effects of the synthetic neurosteroid: 3β-methoxypregnenolone (MAP4343) on behavioral and physiological alterations provoked by chronic psychosocial stress in tree shrews. *International Journal of Neuropsychopharmacology*, **19**(4): pyv119.

Parra A, Baker CA, Bolton MM. 2019. Regional specialization of pyramidal neuron morphology and physiology in the tree shrew neocortex. *Cerebral Cortex*, **29**(11): 4488–4505.

Peng YZ, Ye ZZ, Zou RJ, et al. 1991. Biology of Chinese Tree Shrews. Kunming: Yunnan Science and Technology Press. (in Chinese)

Petry HM, Bickford ME. 2019. The second visual system of the tree shrew. *The Journal of Comparative Neurology*, **527**(3): 679–693.

Pfeiffer LS, Stafforst T. 2023. Precision RNA base editing with engineered and endogenous effectors. *Nature Biotechnology*, **41**(11): 1526–1542.

Phillips KA, Bales KL, Capitanio JP, et al. 2014. Why primate models matter. *American Journal of Primatology*, **76**(9): 801–827.

Piwecka M, Rajewsky N, Rybak-Wolf A. 2023. Single-cell and spatial transcriptomics: deciphering brain complexity in health and disease. *Nature Reviews Neurology*, **19**(6): 346–362.

Qi XB, Li WH. 2022. Unlocking the secrets to human NTCP structure. *The Innovation*, **3**(5): 100294.

Qiu S, Hu YC, Huang YM, et al. 2024. Whole-brain spatial organization of hippocampal single-neuron projectomes. *Science*, **383**(6682): eadj9198.

Rauth S, Karmakar S, Batra SK, et al. 2021. Recent advances in organoid development and applications in disease modeling. *Biochimica et Biophysica Acta* (*BBA*) - *Reviews on Cancer*, **1875**(2): 188527.

Rehwinkel J, Gack MU. 2020. RIG-I-like receptors: their regulation and roles in RNA sensing. *Nature Reviews Immunology*, **20**(9): 537–551.

Reuss S, Fuchs E. 2000. Anterograde tracing of retinal afferents to the tree shrew hypothalamus and raphe. *Brain Research*, **874**(1): 66–74.

Rice MW, Roberts RC, Melendez-Ferro M, et al. 2011. Neurochemical characterization of the tree shrew dorsal striatum. *Frontiers in Neuroanatomy*, **5**: 53.

Roberts TE, Lanier HC, Sargis EJ, et al. 2011. Molecular phylogeny of treeshrews (Mammalia: Scandentia) and the timescale of diversification in Southeast Asia. *Molecular Phylogenetics and Evolution*, **60**(3): 358–372.

Rockland KS, Lund JS. 1982. Widespread periodic intrinsic connections in the tree shrew visual cortex. *Science*, **215**(4539): 1532–1534.

Rodriguez-Callejas JD, Fuchs E, Perez-Cruz C. 2020. Increased oxidative stress, hyperphosphorylation of tau, and dystrophic microglia in the hippocampus of aged *Tupaia belangeri. Glia*, **68**(9): 1775–1793.

Rodriguez-Callejas JD, Irene-Fierro M, Aguilar-Navarro S, et al. 2024. Astroglial atrophy associates with loss of nuclear S100A10 in the hippocampus of aged male tree shrews. *bioRxiv*, doi: https://doi.org/10.1101/2024.07.04.602113.

Roelfsema PR, Treue S. 2014. Basic neuroscience research with nonhuman primates: a small but indispensable component of biomedical research. *Neuron*, **82**(6): 1200–1204.

Römer S, Bender H, Knabe W, et al. 2018. Neural progenitors in the developing neocortex of the northern tree shrew (*Tupaia belangeri*) show a closer relationship to gyrencephalic primates than to lissencephalic rodents. *Frontiers in Neuroanatomy*, **12**: 29.

Romero-Herrera AE, Lehmann H. 1974. The myoglobin of primates: VI. *Tupaia glis belangeri* (Common treeshrew). *Biochimica et Biophysica Acta* (*BBA*) - *Protein Structure*, **359**(2): 236–241.

Ruberte J, Schofield PN, Sundberg JP, et al. 2023. Bridging mouse and human anatomies; a knowledge-based approach to comparative anatomy for disease model phenotyping. *Mammalian Genome*, **34**(3): 389–407.

Sadeghpour S, Khodaee S, Rahnama M, et al. 2021. Human APOBEC3 variations and viral infection. *Viruses*, **13**(7): 1366.

Sajdak BS, Salmon AE, Cava JA, et al. 2019. Noninvasive imaging of the tree shrew eye: wavefront analysis and retinal imaging with correlative histology. *Experimental Eye Research*, **185**: 107683.

Samuels BC, Siegwart JT, Zhan WJ, et al. 2018. A novel tree shrew (*Tupaia belangeri*) model of glaucoma. *Investigative Ophthalmology & Visual Science*, **59**(7): 3136–3143.

Sanada T, Tsukiyama-Kohara K, Shin-I T, et al. 2019a. Construction of complete *Tupaia belangeri* transcriptome database by whole-genome and comprehensive RNA sequencing. *Scientific Reports*, **9**(1): 12372.

Sanada T, Yamamoto N, Kayesh MEH, et al. 2019b. Intranasal vaccination with HBs and HBc protein combined with carboxyl vinyl polymer induces strong neutralizing antibody, anti-HBs IgA, and IFNG response. *Biochemical and Biophysical Research Communications*, **520**(1): 86–92.

Sanada T, Yasui F, Honda T, et al. 2019c. Avian H5N1 influenza virus infection causes severe pneumonia in the Northern tree shrew (*Tupaia belangeri*). *Virology*, **529**: 101–110.

Sasaki E, Suemizu H, Shimada A, et al. 2009. Generation of transgenic non-human primates with germline transmission. *Nature*, **459**(7246): 523–527.

Saturday T, van Doremalen N. 2023. Pathogenesis of severe acute respiratory syndrome coronavirus-2 in nonhuman primates. *Current Opinion in Virology*, **63**: 101375.

Savier E, Sedigh-Sarvestani M, Wimmer R, et al. 2021. A bright future for the tree shrew in neuroscience research: summary from the inaugural Tree Shrew Users Meeting. *Zoological Research*, **42**(4): 478–481.

Schäfer M, Fan Y, Gu TL, et al. 2020. The lipoxygenase pathway of *Tupaia belangeri* representing *Scandentia*. Genomic multiplicity and functional characterization of the ALOX15 orthologs in the tree shrew. *Biochimica et Biophysica Acta* (*BBA*) - *Molecular and Cell Biology of Lipids*, **1865**(2): 158550.

Schmelting B, Corbach-Söhle S, Kohlhause S, et al. 2014. Agomelatine in the tree shrew model of depression: effects on stress-induced nocturnal hyperthermia and hormonal status. *European Neuropsychopharmacology*, **24**(3): 437–447.

Schumacher JW, McCann MK, Maximov KJ, et al. 2022. Selective enhancement of neural coding in V1 underlies fine-discrimination learning in tree shrew. *Current Biology*, **32**(15): 3245–3260. e5.

Sedigh-Sarvestani M, Lee KS, Jaepel J, et al. 2021. A sinusoidal transformation of the visual field is the basis for periodic maps in area V2. *Neuron*, **109**(24): 4068–4079. e6.

Shang SJ, Wang C, Guo CB, et al. 2015. The formation and extinction of fear memory in tree shrews. *Frontiers in Behavioral Neuroscience*, **9**: 204.

Shao Y, Chen CY, Shen H, et al. 2019. GenTree, an integrated resource for analyzing the evolution and function of primate-specific coding genes. *Genome Research*, **29**(4): 682–696.

She ZH, Ward AH, Gawne TJ. 2023. The effects of ambient narrowband long-wavelength light on lens-induced myopia and form-deprivation myopia in tree shrews. *Experimental Eye Research*, **234**: 109593.

Shen F, Qi KK, Duan Y, et al. 2018. Differential effects of clomipramine on depression-like behaviors induced by the chronic social defeat paradigm in tree shrews. *Journal of Psychopharmacology*, **32**(10): 1141–1149.

Shen Y, Ding LF, Yang CY, et al. 2022. Mapping big brains at subcellular resolution in the era of big data in zoology. *Zoological Research*, **43**(4): 597–599.

Sherman SM, Norton TT, Casagrande VA. 1977. Myopia in the lid-sutured tree shrew (*Tupaia glis*). *Brain Research*, **124**(1): 154–157.

Shi N, Chen HL, Lai YJ, et al. 2023. Cyclosporine A induces Epstein-Barr virus reactivation in tree shrew (*Tupaia belangeri chinensis*) model. *Microbes and Infection*, **25**(8): 105212.

Shriver JE, Noback CR. 1967. Cortical projections to the lower brain stem and spinal cord in the tree shrew (*Tupaia glis*). *The Journal of Comparative Neurology*, **130**(1): 25–53.

Shu YM, Ni RJ, Sun YJ, et al. 2015. Distribution of corticotropin-releasing factor in the tree shrew brain. *Brain Research*, **1618**: 270–285.

Siegwart JT Jr, Norton TT. 1998. The susceptible period for deprivation-induced myopia in tree shrew. *Vision Research*, **38**(22): 3505–3515.

Sneddon LU, Halsey LG, Bury NR. 2017. Considering aspects of the 3Rs principles within experimental animal biology. *Journal of Experimental Biology*, **220**(Pt 17): 3007–3016.

Snyder M, Killackey H, Diamond IT. 1969. Color vision in the tree shrew after removal of posterior neocortex. *Journal of Neurophysiology*, **32**(4): 554–563.

Song TZ, Zheng HY, Han JB, et al. 2020. Delayed severe cytokine storm and immune cell infiltration in SARS-CoV-2-infected aged Chinese rhesus macaques. *Zoological Research*, **41**(5): 503–516.

Stavrou S, Ross SR. 2015. APOBEC3 proteins in viral immunity. *The Journal of Immunology*, **195**(10): 4565–4570.

Stockley P, Franco C, Claydon AJ, et al. 2020. Revealing mechanisms of mating plug function under sexual selection. *Proceedings of the National Academy of Sciences of the United States of America*, **117**(44): 27465–27473.

Su JJ, Yan RQ, Gan YQ, et al. 1987. Experimental infection of human hepatitis B virus (HBV) in adult tree shrews. *Chinese Journal of Pathology*, **16**(2): 103–106,166. (in Chinese)

Sun J, Liu WJ, Guo YB, et al. 2021. Characterization of tree shrew telomeres and telomerase. *Journal of Genetics and Genomics*, **48**(7): 631–639.

Sun Q, Dong J, Yang WT, et al. 2008. Efficient reproduction of cynomolgus monkey using pronuclear embryo transfer technique. *Proceedings of the National Academy of Sciences of the United States of America*, **105**(35): 12956–12960.

Taha EA, Lee J, Hotta A. 2022. Delivery of CRISPR-Cas tools for *in vivo* genome editing therapy: trends and challenges. *Journal of Controlled Release*, **342**: 345–361.

Takahashi M, Ushitani T, Fujita K. 2008. Inference based on transitive relation in tree shrews (*Tupaia belangeri*) and rats (*Rattus norvegicus*) on a spatial discrimination task. *The Psychological Record*, **58**(2): 215–227.

Tambuyzer E, Vandendriessche B, Austin CP, et al. 2020. Therapies for rare diseases: therapeutic modalities, progress and challenges ahead. *Nature Reviews Drug Discovery*, **19**(2): 93–111.

Tanabe S, Fu JM, Cang JH. 2022. Strong tuning for stereoscopic depth indicates orientation-specific recurrent circuitry in tree shrew V1. *Current Biology*, **32**(24): 5274–5284. e6.

Tarantal AF, Noctor SC, Hartigan-O'Connor DJ. 2022. Nonhuman primates in translational research. *Annual Review of Animal Biosciences*, **10**: 441–468.

Teli P, Kale V, Vaidya A. 2023. Beyond animal models: revolutionizing neurodegenerative disease modeling using 3D in vitro organoids, microfluidic chips, and bioprinting. *Cell and Tissue Research*, **394**(1): 75–91.

Thirunavukarasu AJ, Ting DSJ, Elangovan K, et al. 2023. Large language models in medicine. *Nature Medicine*, **29**(8): 1930–1940.

Tian JJ, Ren M, Zhao PL, et al. 2022. Dissection of the long-range projections of specific neurons at the synaptic level in the whole mouse brain. *Proceedings of the National Academy of Sciences of the United States of America*, **119**(40): e2202536119.

Tigges J, Shantha TR. 1969. A Stereotaxic Brain Atlas of the Tree Shrew: (*Tupaia glis*). Baltimore: Williams & Wilkins Co.

Tong Y, Hao J, Tu Q, et al. 2017. A tree shrew glioblastoma model recapitulates features of human glioblastoma. *Oncotarget*, **8**(11): 17897–17907.

Toth I, Neumann ID. 2013. Animal models of social avoidance and social fear. *Cell and Tissue Research*, **354**(1): 107–118.

Tu Q, Yang D, Zhang XN, et al. 2019. A novel pancreatic cancer model originated from transformation of acinar cells in adult tree shrew, a primate-like animal. *Disease Models & Mechanisms*, **12**(4): dmm038703.

Ungersböck A, Kretz R, Rager G. 1991. Synaptogenesis in the primary visual cortex of the tree shrew (*Tupaia belangeri*). *The Journal of Comparative Neurology*, **308**(3): 491–504.

van der Hart MGC, Czéh B, de Biurrun G, et al. 2002. Substance P receptor antagonist and clomipramine prevent stress-induced alterations in cerebral metabolites, cytogenesis in the dentate gyrus and hippocampal volume. *Molecular Psychiatry*, **7**(9): 933–941.

van der Worp HB, Howells DW, Sena ES, et al. 2010. Can animal models of disease reliably inform human studies?. *PLoS Medicine*, **7**(3): e1000245.

van Hasselt SJ, Epifani L, Zantinge D, et al. 2023. A study on REM sleep homeostasis in the day-active tree shrew (*Tupaia belangeri*): cold-induced suppression of REM sleep is not followed by a rebound. *Biology*, **12**(4): 614.

Vandereyken K, Sifrim A, Thienpont B, et al. 2023. Methods and applications for single-cell and spatial multi-omics. *Nature Reviews Genetics*, **24**(8): 494–515.

Veit J, Bhattacharyya A, Kretz R, et al. 2014. On the relation between receptive field structure and stimulus selectivity in the tree shrew primary visual cortex. *Cerebral Cortex*, **24**(10): 2761–2771.

Villiger L, Joung J, Koblan L, et al. 2024. CRISPR technologies for genome, epigenome and transcriptome editing. *Nature Reviews Molecular Cell Biology*, **25**(6): 464–487.

Voigtlaender S, Pawelczyk J, Geiger M, et al. 2024. Artificial intelligence in neurology: opportunities, challenges, and policy implications. *Journal of Neurology*, **271**(5): 2258–2273.

Walter E, Keist R, Niederöst B, et al. 1996. Hepatitis B virus infection of tupaia hepatocytes *in vitro* and *in vivo*. *Hepatology*, **24**(1): 1–5.

Wang CY, Ye YS, Long WH, et al. 2024a. RNA sequencing and proteomic profiling reveal alterations by MPTP in chronic stomach mucosal injury in tree shrew Chinese (*Tupaia belangeri chinensis*). *Scientific Reports*, **14**(1): 74.

Wang D, Tai PWL, Gao GP. 2019a. Adeno-associated virus vector as a platform for gene therapy delivery. *Nature Reviews Drug Discovery*, **18**(5): 358–378.

Wang D, Zhang F, Gao GP. 2020a. CRISPR-based therapeutic genome editing: strategies and *in vivo* delivery by AAV vectors. *Cell*, **181**(1): 136–150.

Wang EL, Ye YS, Zhang K, et al. 2020b. Longitudinal transcriptomic characterization of viral genes in HSV-1 infected tree shrew trigeminal ganglia. *Virology Journal*, **17**(1): 95.

Wang G, Huang ZY, Wu YY, et al. 2024b. Primate-like tree shrew will be the preferred animal for investigating nephrolithiasis. *Urolithiasis*, **52**(1): 3.

Wang HY, Liu JH, Ye SZ, et al. 1990. Preliminary observations on experimental leprosy in tupaias (*Tupaia belangeri yunalis*). *Leprosy Review*, **61**(1): 12–18.

Wang J, Azimi H, Zhao YL, et al. 2023a. Optogenetic activation of visual thalamus generates artificial visual percepts. *eLife*, **12**: e90431.

Wang LM, Lu JL, Zeng YQ, et al. 2020c. Improving Alzheimer's disease by altering gut microbiota in tree shrews with ginsenoside Rg1. *FEMS Microbiology Letters*, **367**(4): fnaa011.

Wang QH, Liu ZH, Zeng X, et al. 2024c. Integrated analysis of miRNA-mRNA expression of newly emerging swine H3N2 influenza virus cross-species infection with tree shrews. *Virology Journal*, **21**(1): 4.

Wang QH, Zeng X, Tang S, et al. 2023b. Pathogenicity and anti-infection immunity of animal H3N2 and H6N6 subtype influenza virus cross-species infection with tree shrews. *Virus Research*, **324**: 199027.

Wang QX, Ding SL, Li Y, et al. 2020d. The Allen mouse brain common coordinate framework: a 3D reference atlas. *Cell*, **181**(4): 936–953. e20.

Wang SX, Shan D, Dai JK, et al. 2013. Anatomical MRI templates of tree shrew brain for volumetric analysis and voxel-based morphometry. *Journal of Neuroscience Methods*, **220**(1): 9–17.

Wang YL, Ma ZX, Zheng YY, et al. 2019b. Establishment of an osteoporosis model in tree shrews by bilateral ovariectomy and comprehensive evaluation. *Experimental and Therapeutic Medicine*, **17**(5): 3644–3654.

Wang YX. 1987. Taxonomic research on Burma-Chinese tree shrew, *Tupaia belangeri* (Wagner), from Southern China. *Zoological Research*, **8**(3): 213–230. (in Chinese)

Wang YY, Niu RZ, Wang JD, et al. 2019c. Establishment of brain ischemia model in tree shrew. *Brain Research*, **1718**: 194–200.

Wang Z, Yi X, Du L, et al. 2017. A study of Epstein-Barr virus infection in the Chinese tree shrew (*Tupaia belangeri chinensis*). *Virology Journal*, **14**(1): 193.

Wei S, Hua HR, Chen QQ, et al. 2017. Dynamic changes in DNA demethylation in the tree shrew (*Tupaia belangeri chinensis*) brain during postnatal development and aging. *Zoological Research*, **38**(2): 96–102.

West SA, Cooper GA, Ghoul MB, et al. 2021. Ten recent insights for our understanding of cooperation. *Nature Ecology & Evolution*, **5**(4): 419–430.

Wu DD, Qi XG, Yu L, et al. 2022. Initiation of the primate genome project. *Zoological Research*, **43**(2): 147–149.

Wu K, Qin D, Qian Y, et al. 2024. A new era of mutation rate analyses: concepts and methods. *Zoological Research*, **45**(4): 767–780.

Wu Y, Zhang K. 2020. Tools for the analysis of high-dimensional single-cell RNA sequencing data. *Nature Reviews Nephrology*, **16**(7): 408–421.

Wu YX, Zhou H, Fan XY, et al. 2015. Correction of a genetic disease by CRISPR-Cas9-mediated gene editing in mouse spermatogonial stem cells. *Cell Research*, **25**(1): 67–79.

Xia HJ, He BL, Wang CY, et al. 2014. *PTEN/PIK3CA* genes are frequently mutated in spontaneous and medroxyprogesterone acetate-accelerated 7, 12-dimethylbenz(a)anthracene-induced mammary tumours of tree shrews. *European Journal of Cancer*, **50**(18): 3230–3242.

Xia HJ, Wang CY, Zhang HL, et al. 2012. Characterization of spontaneous breast tumor in tree shrews (*Tupaia belangeri chinenesis*). *Zoological Research*, **33**(1): 55–59.

Xia W, Chen HL, Feng YW, et al. 2022. Tree shrew is a suitable animal model for the study of Epstein Barr virus. *Frontiers in Immunology*, **12**: 789604.

Xia W, Liu L, Shi N, et al. 2023. Epstein Barr virus infection in tree shrews alters the composition of gut microbiota and metabolome profile. *Virology Journal*, **20**(1): 177.

Xia W, Shi N, Li CQ, et al. 2024. RNA-Seq and miRNA-Seq data from Epstein-Barr virus-infected tree shrews reveal a ceRNA network contributing to immune microenvironment regulation. *Virulence*, **15**(1): 2306795.

Xiao J, Liu R, Chen CS. 2017. Tree shrew (*Tupaia belangeri*) as a novel laboratory disease animal model. *Zoological Research*, **38**(3): 127–137.

Xie ZC, Riezu-Boj JI, Lasarte JJ, et al. 1998. Transmission of hepatitis C virus infection to tree shrews. *Virology*, **244**(2): 513–520.

Xu D, Zhu YG, Xu ZH. 2017. Efficient genetic manipulation in the developing brain of tree shrew using *in utero* electroporation and virus infection. *Journal of Genetics and Genomics*, **44**(10): 507–509.

Xu L, Fan Y, Jiang XL, et al. 2013. Molecular evidence on the phylogenetic position of tree shrews. *Zoological Research*, **34**(2): 70–76. (in Chinese)

Xu L, Yu DD, Fan Y, et al. 2016. Loss of RIG-I leads to a functional replacement with MDA5 in the Chinese tree shrew. *Proceedings of the National Academy of Sciences of the United States of America*, **113**(39): 10950–10955.

Xu L, Yu DD, Ma YH, et al. 2020a. COVID-19-like symptoms observed in Chinese tree shrews infected with SARS-CoV-2. *Zoological Research*, **41**(5): 517–526.

Xu L, Yu DD, Peng L, et al. 2015. Characterization of a *MAVS* ortholog from the Chinese tree shrew (*Tupaia belangeri chinensis*). *Developmental & Comparative Immunology*, **52**(1): 58–68.

Xu L, Yu DD, Peng L, et al. 2020b. An alternative splicing of *Tupaia* STING modulated anti-RNA virus responses by targeting MDA5-LGP2 and IRF3. *The Journal of Immunology*, **204**(12): 3191–3204.

Xu L, Yu DD, Yao YL, et al. 2020c. *Tupaia* MAVS is a dual target during hepatitis C virus infection for innate immune evasion and viral replication via NF-κB. *The Journal of Immunology*, **205**(8): 2091–2099.

Xu S, Li XY, Yang JY, et al. 2019. Comparative pathogenicity and transmissibility of pandemic H1N1, avian H5N1, and human H7N9 influenza viruses in tree shrews. *Frontiers in Microbiology*, **10**: 2955.

Xu XP, Chen HB, Cao XM, et al. 2007. Efficient infection of tree shrew (*Tupaia belangeri*) with hepatitis C virus grown in cell culture or from patient plasma. *Journal of General Virology*, **88**(Pt 9): 2504–2512.

Yamamoto S, Kanca O, Wangler MF, et al. 2024. Integrating non-mammalian model organisms in the diagnosis of rare genetic diseases in humans. *Nature Reviews Genetics*, **25**(1): 46–60.

Yamashita A, Fuchs E, Taira M, et al. 2012. Somatostatin-immunoreactive senile plaque-like structures in the frontal cortex and nucleus accumbens of aged tree shrews and Japanese macaques. *Journal of Medical Primatology*, **41**(3): 147–157.

Yan H, Zhong GC, Xu GW, et al. 2012. Sodium taurocholate cotransporting polypeptide is a functional receptor for human hepatitis B and D virus. *eLife*, **1**: e00049.

Yan LZ, Sun B, Lyu LB, et al. 2016. Early embryonic development and transplantation in tree shrews. *Zoological Research*, **37**(4): 252–258.

Yan RQ, Su JJ, Huang DR, et al. 1996. Human hepatitis B virus and hepatocellular carcinoma I. Experimental infection of tree shrews with hepatitis B virus. *Journal of Cancer Research and Clinical Oncology*, **122**(5): 283–288.

Yang WG, Liu JL, Luo YQ, et al. 1990. A stereotaxic atlas of the brain of *Tupaia belangeri* and macaque monkey living in Guangxi. Nanning: Guangxi Science & Technology Publishing House. (in Chinese)

Yang Y, Wang LM, Zhang CJ, et al. 2022. Ginsenoside Rg1 improves Alzheimer's disease by regulating oxidative stress, apoptosis, and neuroinflammation through Wnt/GSK-3β/β-catenin signaling pathway. *Chemical Biology & Drug Design*, **99**(6): 884–896.

Yao YG. 2017. Creating animal models, why not use the Chinese tree shrew (*Tupaia belangeri chinensis*)?. *Zoological Research*, **38**(3): 118–126.

Yao YG, Construction Team of the KIZ Primate Facility. 2022. Towards the peak: the 10-year journey of the National Research Facility for Phenotypic and Genetic Analysis of Model Animals (Primate Facility) and a call for international collaboration in non-human primate research. *Zoological Research*, **43**(2): 237–240.

Yao YL, Yu DD, Xu L, et al. 2019. Molecular characterization of the 2', 5'-oligoadenylate synthetase family in the Chinese tree shrew (*Tupaia*

*belangeri chinensis*). *Cytokine*, **114**: 106–114.

Yao YL, Yu DD, Xu L, et al. 2020. *Tupaia* OASL1 promotes cellular antiviral immune responses by recruiting MDA5 to MAVS. *The Journal of Immunology*, **205**(12): 3419–3428.

Ye MS, Zhang JY, Yu DD, et al. 2021. Comprehensive annotation of the Chinese tree shrew genome by large-scale RNA sequencing and long-read isoform sequencing. *Zoological Research*, **42**(6): 692–709.

Yi JZ, Lei XL, Guo FT, et al. 2023. Co-delivery of Cas9 mRNA and guide RNAs edits hepatitis B virus episomal and integration DNA in mouse and tree shrew models. *Antiviral Research*, **215**: 105618.

Yin BW, Song QK, Chen LX, et al. 2019. Establishment of an immortalized intestinal epithelial cell line from tree shrews by lentivirus-mediated *hTERT* gene transduction. *Cytotechnology*, **71**(1): 107–116.

Yin CH, Zhou X, Yao YG, et al. 2020. Abundant self-amplifying intermediate progenitors in the subventricular zone of the Chinese tree shrew neocortex. *Cerebral Cortex*, **30**(5): 3370–3380.

Yu WH, Yang CC, Bi YH, et al. 2016. Characterization of hepatitis E virus infection in tree shrew (*Tupaia belangeri chinensis*). *BMC Infectious Diseases*, **16**: 80.

Yuan B, Yang CG, Xia XS, et al. 2019. The tree shrew is a promising model for the study of influenza B virus infection. *Virology Journal*, **16**(1): 77.

Yurkovich JT, Evans SJ, Rappaport N, et al. 2024. The transition from genomics to phenomics in personalized population health. *Nature Reviews Genetics*, **25**(4): 286–302.

Zambello E, Fuchs E, Abumaria N, et al. 2010. Chronic psychosocial stress alters NPY system: different effects in rat and tree shrew. *Progress in Neuro-Psychopharmacology and Biological Psychiatry*, **34**(1): 122–130.

Zeng L, Zhang HY, Yang CY, et al. 2023. Generation of a tree shrew breast cancer model using lentivirus expressing *PIK3CA-H1047R*. *Zoological Research*, **44**(1): 94–97.

Zhang DF, Xu M, Bi R, et al. 2019a. Genetic analyses of Alzheimer's disease in China: achievements and perspectives. *ACS Chemical Neuroscience*, **10**(2): 890–901.

Zhang J, Chiodini R, Badr A, et al. 2011. The impact of next-generation sequencing on genomics. *Journal of Genetics and Genomics*, **38**(3): 95–109.

Zhang J, Luo RC, Man XY, et al. 2020a. The anatomy of the skin of the Chinese tree shrew is very similar to that of human skin. *Zoological Research*, **41**(2): 208–212.

Zhang JJ, Xiao HJ, Bi YW, et al. 2020b. Characteristics of the tree shrew humoral immune system. *Molecular Immunology*, **127**: 175–185.

Zhang L, Shen ZL, Feng Y, et al. 2019b. Infectivity of Zika virus on primary cells support tree shrew as animal model. *Emerging Microbes & Infections*, **8**(1): 232–241.

Zhang M, Pan XJ, Jung W, et al. 2023a. Molecularly defined and spatially resolved cell atlas of the whole mouse brain. *Nature*, **624**(7991): 343–354.

Zhang NN, Zhang L, Deng YQ, et al. 2019c. Zika virus infection in *Tupaia belangeri* causes dermatological manifestations and confers protection against secondary infection. *Journal of Virology*, **93**(8): e01982–18.

Zhang X, Lai GY, Volpe G, et al. 2022. Towards a primate single-cell atlas. *Zoological Research*, **43**(4): 691–694.

Zhang XH, Dai ZX, Zhang GH, et al. 2013. Molecular characterization, balancing selection, and genomic organization of the tree shrew (*Tupaia belangeri*) MHC class I gene. *Gene*, **522**(2): 147–155.

Zhang XM, Yu DD, Wu Y, et al. 2020c. Establishment and transcriptomic features of an immortalized hepatic cell line of the Chinese tree shrew. *Applied Microbiology and Biotechnology*, **104**(20): 8813–8823.

Zhang YJ, Luo ZY, Sun YW, et al. 2023b. From beasts to bytes: revolutionizing zoological research with artificial intelligence. *Zoological Research*, **44**(6): 1115–1131.

Zhao JG, Lai LX, Ji WZ, et al. 2019. Genome editing in large animals: current status and future prospects. *National Science Review*, **6**(3): 402–420.

Zhao L, Gao F, Gao S, et al. 2021a. Biodiversity-based development and evolution: the emerging research systems in model and non-model organisms. *Science China Life Sciences*, **64**(8): 1236–1280.

Zhao L, Huang SY, Liao QW, et al. 2021b. RNA-seq analysis of ischemia stroke and normal brain in a tree shrew model with or without type 2 diabetes mellitus. *Metabolic Brain Disease*, **36**(7): 1889–1901.

Zhao L, Liao QW, Zhang YT, et al. 2020a. Ischemic postconditioning mitigates retinopathy in tree shrews with diabetic cerebral ischemia. *Journal of Diabetes Research*, **2020**: 6286571.

Zhao L, Tan SF, Liao QW, et al. 2021c. The neuroprotective effect and RNA-sequence analysis of postconditioning on the ischemic stroke with diabetes mellitus tree shrew model. *Brain and Behavior*, **11**(11): e2354.

Zhao PC, Xia W, Wei JL, et al. 2022. An investigation of the mechanisms of radiation-induced muscle injury in a tree shrew (*Tupaia belangeri*) model. *Dose-Response*, **20**(1): 15593258221082878.

Zhao XP, Tang ZY, Klumpp B, et al. 2002. Primary hepatocytes of *Tupaia belangeri* as a potential model for hepatitis C virus infection. *Journal of Clinical Investigation*, **109**(2): 221–232.

Zhao Y, Wang JB, Kuang DX, et al. 2020b. Susceptibility of tree shrew to SARS-CoV-2 infection. *Scientific Reports*, **10**(1): 16007.

Zhao YQ, Liu YQ, Yuan JF, et al. 2018. Regeneration of islet β-cells in tree shrews and rats. *Animal Models and Experimental Medicine*, **1**(2): 152–161.

Zheng H, Niu SW, Zhao HB, et al. 2018. Donepezil improves the cognitive impairment in a tree shrew model of Alzheimer's disease induced by amyloid-$\beta_{1-40}$ via activating the BDNF/TrkB signal pathway. *Metabolic Brain Disease*, **33**(6): 1961–1974.

Zheng J, Shi WJ, Yang ZQ, et al. 2023. RIG-I-like receptors: molecular mechanism of activation and signaling. *Advances in Immunology*, **158**: 1–74.

Zheng LT, Chen SY, Wu QL, et al. 2024. Tree shrews as a new animal model for systemic sclerosis research. *Frontiers in Immunology*, **15**: 1315198.

Zhou H, Tian RR, Wang XR, et al. 2024. Identification of novel mammalian viruses in tree shrews (*Tupaia belangeri chinensis*). *Zoological Research*, **45**(2): 429–438.

Zhou JN, Ni RJ. 2016. The tree shrew (*Tupaia belangeri chinensis*) brain in stereotaxic coordinates. Singapore: Springer.

Zhou MG, Wang HD, Zeng XY, et al. 2019. Mortality, morbidity, and risk factors in China and its provinces, 1990–2017: a systematic analysis for the Global Burden of Disease Study 2017. *The Lancet*, **394**(10204): 1145–1158.

Zhu CY, Hong W, Wang L, et al. 2022. Towards key scientific questions in the diagnosis and treatment of rare diseases: summary from the 297th Meeting of the Shuangqing Forum. *Zoological Research*, **43**(2): 234–236.

Zhu ZJ, Feng BZ, Yang YW, et al. 2023. Transplantation of insulin-producing cells derived from human MSCs to treat diabetes in a non-human primate model. *Artificial Organs*, **47**(8): 1298–1308.

Zhuang XL, Zhang JJ, Shao Y, et al. 2023. Integrative omics reveals rapidly evolving regulatory sequences driving primate brain evolution. *Molecular Biology and Evolution*, **40**(8): msad173.

Zinski AL, Carrion S, Michal JJ, et al. 2021. Genome-to-phenome research in rats: progress and perspectives. *International Journal of Biological Sciences*, **17**(1): 119–133.

Xiong et al. *Zool. Res.* 2024, 45(4): 910−923
https://doi.org/10.24272/j.issn.2095-8137.2024.158

ZR | Zoological Research

Review Open Access

# Updated roles of the gut microbiota in exploring shrimp etiology, polymicrobial pathogens, and disease incidence

Jin-Bo Xiong[1,2,*], Hao-Nan Sha[1,2], Jiong Chen[1,2,3,*]

[1] *State Key Laboratory for Managing Biotic and Chemical Threats to the Quality and Safety of Agro-products*, *School of Marine Sciences*, *Ningbo University*, *Ningbo*, *Zhejiang* 315211, *China*

[2] *Key Laboratory of Aquacultural Biotechnology*, *Ministry of Education*, *School of Marine Sciences*, *Ningbo University*, *Ningbo*, *Zhejiang* 315211, *China*

[3] *Laboratory of Biochemistry and Molecular Biology*, *School of Marine Sciences*, *Ningbo University*, *Ningbo*, *Zhejiang* 315211, *China*

## ABSTRACT

*Litopenaeus vannamei* is the most extensively cultured shrimp species globally, recognized for its scale, production, and economic value. However, its aquaculture is plagued by frequent disease outbreaks, resulting in rapid and massive mortality. etiological research often lags behind the emergence of new diseases, leaving the causal agents of some shrimp diseases unidentified and leading to nomenclature based on symptomatic presentations, especially in cases involving co- and polymicrobial pathogens. Comprehensive data on shrimp disease statuses remain limited. In this review, we summarize current knowledge on shrimp diseases and their effects on the gut microbiome. Furthermore, we also propose a workflow integrating primary colonizers, “driver” taxa in gut networks from healthy to diseased states, disease-discriminatory taxa, and virulence genes to identify potential polymicrobial pathogens. We examine both abiotic and biotic factors (e.g., external and internal sources and specific-disease effects) that influence shrimp gut microbiota, with an emphasis on the “holobiome” concept and common features of gut microbiota response to diverse diseases. After excluding the effects of confounding factors, we provide a diagnosis model for quantitatively predicting shrimp disease incidence using disease common-discriminatory taxa, irrespective of the causal agents. Due to the conservation of functional genes used in designing specific primers, we propose a practical strategy applying qPCR-assayed abundances of disease common-discriminatory functional genes. This review updates the roles of the gut microbiota in exploring shrimp etiology, polymicrobial pathogens, and disease incidence, offering a refined perspective for advancing shrimp aquaculture health management.

**Keywords:** Shrimp disease; Gut microbiota; Polymicrobial pathogens; Diagnosis model; Disease common-discriminatory taxa; Disease prediction

## INTRODUCTION

*Litopenaeus vannamei* has emerged as one of the most successful aquaculture species due to its low food conversion ratio, contributing significantly to the “Blue Revolution”. Over the past 40 years, its production has increased from less than 0.075 million tons in 1980 to over 7.3 million tons in 2021 (FAO, 2023). This remarkable achievement is partially attributed to the development of large-scale production facilities, high-density farming practices, and intensive feeding regimens, which have also created stressful conditions that facilitate the frequent occurrence and rapid spread of diverse infectious diseases (Table 1). Although antibiotics are commonly applied as prophylactic and therapeutic agents, their overuse and abuse has led to bacterial resistance, increased disease susceptibility, and the emergence of new diseases (Lu et al., 2021; Rodgers & Furones, 2009; Sha et al., 2024a; Zhou et al., 2019a). Vaccination represents an alternative strategy for controlling infectious diseases; however, its efficacy is often limited in juvenile shrimp due to their inability to develop long-term acquired immunity (Falaise et al., 2016). Importantly, shrimp diseases cause rapid and massive mortality within days, often without noticeable symptoms at onset stage of disease (Kumar et al., 2020; Thitamadee et al., 2016; Xiong et al., 2017a). Several methods are currently used to evaluate disease risk in shrimp

This is an open-access article distributed under the terms of the Creative Commons Attribution Non-Commercial License (http://creativecommons.org/licenses/by-nc/4.0/), which permits unrestricted non-commercial use, distribution, and reproduction in any medium, provided the original work is properly cited.

Copyright ©2024 Editorial Office of Zoological Research, Kunming Institute of Zoology, Chinese Academy of Sciences

Received: 12 May 2024; Accepted: 17 June 2024; Online: 18 June 2024

Foundation items: This work was supported by the National Natural Science Foundation of China (32371596, 32071549), Key Research and Development Project of Zhejiang Province (2021C02062), Key Scientific and Technological Grant of Zhejiang for Breeding New Agricultural Varieties (2021C02069-5-2), Key Project of Ningbo Science and Technology Bureau (2023S003), and One Health Interdisciplinary Research Project of Ningbo University (HZ202404)

*Corresponding authors, E-mail: xiongjinbo@nbu.edu.cn; jchen1975@163.com

**Table 1 Summary of shrimp diseases, potential causative agents, and typical symptoms**

| Disease name | Causative agent | Typical symptoms | References |
|---|---|---|---|
| White spot disease | White spot syndrome virus | Sharp reduction in food consumption, listlessness, loose cuticle, white spots 0.5–2.0 mm in diameter | Liu et al., 2009 |
| Taura syndrome | Taura syndrome virus | Soft cuticle, empty guts, extreme lethargy, and expansion of reddish chromatophores | Brock, 1997 |
| Yellow head disease | Yellow head virus | Nuclear pyknosis and heterokaryosis, bleached or pale-yellow cephalothorax, discoloration of underlying hepatopancreas | Boonyaratpalin et al., 1993 |
| Tetrahedral baculovirosis | *Baculovirus penaei* | Whitish midguts in severe infections. Polyhedral occlusion bodies | Couch, 1974 |
| Spherical baculovirosis | Monodon baculovirus | Hypertrophied nuclei with single or multiple eosinophilic occlusion bodies, chromatin diminution and margination | Chen et al., 1989 |
| Infectious hypodermal and hematopoietic necrosis (IHHN) | IHHN virus | Buff-colored spots at carapace and abdominal plates, bluish, necrotic, melanized cuticle in serious disease | Lightner et al., 1983 |
| Infectious myonecrosis (IMN) | IMN virus | Opaque skeletal muscle | Lightner et al., 1983 |
| White tail disease | *Macrobrachium* nodavirus | Tails exhibiting white lesions | Arcier et al., 1999 |
| Hepatopancreatic parvovirus disease | Hepatopancreatic parvovirus | Slowed growth rate | Chong & Loh, 1984 |
| Hemocyte iridescent virus disease | Hemocyte iridescent virus | Hepatopancreatic atrophy with color fading, empty stomach and guts, and soft shell | Qiu et al., 2017 |
| Running mortality syndrome | Nodavirus | Enlarged nuclei in hepatopancreas, coagulative muscle necrosis, whitening muscle, slow growth and softening shell | Zhang et al., 2014 |
| Abdominal segment deformity disease | Unknown retrovirus-like agent | Enlarged or twisted abdominal segments, either laterally and/or dorsoventrally, sometimes opaque muscles | Sakaew et al., 2008 |
| Slow growth syndrome | Laem Singh virus and a cryptic integrase containing element | Slow growth and coefficients of size variation > 35% | Chayaburakul et al., 2004 |
| Acute hepatopancreatic necrosis disease | *Vibrio anguillarum*, *Vibrio parahaemolyticus* | Sloughing tubule epithelial cells, pale hepatopancreas, massive and rapid mortality | Tran et al., 2013 |
| Necrotizing hepatopancreatitis | *Rickettsia*-like bacterium | Reduced feeding activity, empty guts, pale hepatopancreas | Chayaburakul et al., 2004 |
| “Bright-red” syndrome | *Vibrio harveyi* | Lethargy, anorexia, flaccid body, multifocal reddish discoloration spots on abdominal cuticle, melanized erosions around spots | Soto-Rodriguez et al., 2010 |
| Luminous vibriosis | *Vibrio campbellii* | Symptoms include fluorescent, less food consumption and high mortality | Wang et al., 2015 |
| White feces syndrome | Uncertain *Vibrio* | White-golden gut contents and white fecal strings | Durai et al., 2015 |
| Black gill disease | *Fusarium solani, Fusarium moniliforme*, *Aspergillus awamori* | Changes from “gill discoloration” to “blackened gill” with disease progression, with subsequent death | Hatai & Egusa, 1978 |
| Balantidiasis | *Zoothamnium* | Reduction in feeding and growth. Increased risk of secondary bacterial infections and massive mortality | Nurlatiffah et al., 2018 |
| Hepatopancreatic microsporidiosis | *Enterocytozoon hepatopenaei* | Severely stunted growth | Chayaburakul et al., 2004 |
| Amoebic gill disease | Amphizoic amoeba | Reduced appetite, lethargy, respiratory distress, eroded carapace, and blackened gill | Han, 2019 |
| “Cotton shrimp-like” disease | Uncertain fungi | Reduced growth, atrophic hepatopancreas, empty digestive tract, and inactivity. Soft shell with slightly white, opaque muscle | Zhou et al., 2019b |
| Blue body syndrome | Unknown | Slow growth, reduced or no feed intake, thin, partially or fully blue bodies | Liang et al., 2020 |

aquaculture, including water quality indices, *Vibrio* species density, pathogen diagnostics, as well as artificial intelligence and machine learning techniques (Bohara et al., 2024; Ferreira et al., 2011; MacAulay et al., 2022). However, these approaches are predominantly qualitative, rather than quantitative, and lag behind the detection of early stages of disease onset stage. Therefore, there is an urgent need to establish quantitative strategies for predicting the incidence of shrimp disease.

The gut microbiota plays an indispensable role in maintaining shrimp fitness and health by aiding in digestion, vitamin synthesis, immunity regulation, toxin degradation, and pathogen suppression (Cornejo-Granados et al., 2018; Holt et al., 2021; Sha et al., 2024b; Xiong, 2018). As such, the gut microbiota acts as a central hub, integrating environmental exposure with genetic and immune signals to influence shrimp fitness. In healthy shrimp, optimal balance of gut symbionts provides numerous benefits, while an imbalanced gut microbiota increases disease risk (Holt et al., 2021; Xiong, 2018). Researches on human and terrestrial animal microbiomes have established cause-and-effect relationships, demonstrating that a healthy gut microbiome influences the colonization, growth, and virulence of pathogens, thereby affecting disease outcomes (Bäumler & Sperandio, 2016; Kamada et al., 2013). However, comparable studies on the causal roles of the gut microbiota in aquatic invertebrates such as shrimp are scarce (Sha et al., 2024b). High-throughput sequencing (HTS) and metagenomics have provided increasing evidence that the gut microbiomes of diseased shrimp differ significantly from those of healthy individuals (Holt et al., 2021; Mao et al., 2023; Sha et al., 2022b), a condition known as “dysbiosis”. This suggests that sensitive gut commensals could serve as reliable indicators for diagnosing shrimp health. Growing evidence suggests that the extent of deviation from the healthy gut microbiota may be linearly correlated with the severity of shrimp disease (Chen et al., 2017; Lu et al., 2023; Xiong et al., 2017a). Consequently, gut bacterial indicators could be used to diagnose the onset and severity of shrimp diseases.

The causal links between gut microbiota and shrimp health

remain relatively unexplored compared to the extensive research conducted on humans. Advances in sequencing technologies have significantly enhanced our understanding of the interactions between shrimp health and their gut microbiota. Nevertheless, much remains to be discovered regarding the shared and unique responses of the gut microbiome to diverse shrimp diseases. Recent reviews have highlighted external factors influencing shrimp microbiota (Cornejo-Granados et al., 2018; Holt et al., 2021) and diagnostic approaches ranging from traditional visual inspection and histopathology to portable sequencing and artificial intelligence for early disease detection (Bohara et al., 2024; MacAulay et al., 2022). In contrast, this review focuses on the current state of shrimp diseases and their effects on the gut microbiota. Going a step further, we conclude the common features of gut microbiota responses to diverse shrimp diseases and their potential applications in predicting disease incidence. While the concept of co- and polymicrobial pathogens is accepted in human and veterinary medicine (Frisan, 2021), it has received little attention in aquaculture. Given the challenges of identifying polymicrobial pathogens using Koch's postulates, we propose an integrated workflow that incorporates diverse ecological features to identify potential polymicrobial pathogens.

## CURRENT STATE OF SHRIMP DISEASES

One of the primary challenges in shrimp aquaculture is the frequent occurrence of disease outbreaks, leading to rapid and massive mortality (Seibert & Pinto, 2012; Thitamadee et al., 2016). Over the past two decades, scientific research on shrimp diseases has intensified in response to the global expansion of shrimp production. Shrimp are susceptible to infections from a wide range of pathogens across microbial kingdoms, including viruses, bacteria, fungi, and parasites, throughout the entire aquaculture cycle (Table 1). Despite periodic updates from the World Organization for Animal Health (WOAH) on the status on shrimp diseases, a comprehensive understanding is still lacking. The following section provides a brief summary of current knowledge on shrimp diseases and their impact on the gut microbiome.

### Viral pathogens

Approximately 20 viruses have been identified as causative agents of shrimp diseases, including members of the Parvoviruses, Baculoviruses, Picornaviruses, Toga-like viruses, as well as several newly identified viral families (Arulmoorthy et al., 2020). Among these, white spot syndrome virus (WSSV) poses the most significant threat to shrimp health globally, leading to substantial production losses (Flegel, 2006; Liu et al., 2009). WSSV, an ovaloid, double-stranded DNA virus with a lipid envelope (120–150 nm×270–290 nm), infects the nuclei of mesodermal- and ectodermal-derived tissues, resulting in reduced food intake and lethargy in infected shrimp (Pradeep et al., 2012). Intriguingly, WSSV can attach to abiotic microplastics, thereby prolonging their survival and virulence under varying water pH and temperatures (Shan et al., 2023). This persistence in abiotic hosts may contribute to the recurrence of WSSV infections. Since its first report in the early 1990s, global economic losses attributed to WSSV have been established at approximately $15 billion USD, increasing at an alarming rate of $1 billion USD per year and accounting for a 10% loss in global shrimp production (Panchal et al., 2021). Currently, there is no effective strategy to prevent and control this disease. WSSV infection significantly alters the composition of the shrimp gut microbiota, leading to enrichment in Proteobacteria and Fusobacteria phyla, as well as pathogenic bacteria belonging to the *Arcobacter* and *Flavobacterium* genera (Wang et al., 2019). While gut bacterial diversity and richness remain unaffected, WSSV infection increases the heterogeneity of gut bacterial communities (de Souza Valente et al., 2020). Additionally, prior WSSV infection predisposes shrimp to subsequent *Vibrio campbellii* infections, resulting in more rapid and severe mortality compared to *V. campbellii* alone (Phuoc et al., 2008).

In addition to WSSV, yellow head virus (YHV), specifically genotype one among six genetically related genotypes, is a rod-shaped, enveloped positive-sense single-stranded RNA virus (40–60 nm×150–200 nm). YHV induces persistent and severe disease in shrimp (Boonyaratpalin et al., 1993), although major outbreaks have not been reported in recent years. YHV has been detected exclusively in outdoor ponds, but not in covered ponds, suggesting an airborne mode of transmission (Thitamadee et al., 2016). However, potential carriers and non-aquatic insects have tested negative for YHV, casting doubt on the airborne vector hypothesis. The rapid dissemination of YHV may be attributed to the cannibalistic behavior of YHV-infected individuals (Tuyen et al., 2014). The initial source of YHV infection remains unclear, but the close genetic relationship among YHV genotypes suggests that it may naturally infect wild penaeid or palemonid shrimp (Wijegoonawardane et al., 2008). Surprisingly, limited research has been conducted on the response of the shrimp gut microbiota to YHV infection.

Decapod iridescent virus 1 (DIV1), a recently identified icosahedral linear double-stranded DNA virus, induces stunted growth and 100% cumulative mortality in shrimp (Qiu et al., 2017). DIV1 infection reduces the abundance of potentially beneficial populations of Bacteroidetes, Firmicutes, and Actinobacteria, while significantly enriching pathogenic bacteria such as *Vibrio* and *Photobacterium*. These microbial shifts elevate the risk of secondary bacterial infections. Furthermore, the proliferation of pathogenic bacteria triggers the expression of NF-κB inhibitors, which suppress the TLR-mediated immune response, exacerbating DIV1 infection (Liao et al., 2023).

In summary, viral infections frequently disrupt the composition of shrimp gut microbiota, increasing susceptibility to secondary bacterial infections (Liao et al., 2023; Shan et al., 2023). However, the specific alterations in bacterial populations appear to be dependent on the viral pathogen involved.

### Bacterial pathogens

Vibriosis is the most prevalent and severe bacterial disease endangering shrimp aquaculture, caused by gram-negative *Vibrio* bacteria such as *V. harveyi*, *V. parahaemolyticus*, *V. vulnificus*, and *V. anguillarum* (Kumar et al., 2020; Li et al., 2022; Shen et al., 2021a). These diseases are typically elicited by external stressors and, if left untreated, can result in rapid and extensive mortality. Although many *Vibrio* species are opportunistic pathogens, certain strains, such as *V. harveyi* and *V. parahaemolyticus*, can act as acute pathogens (Dhar et al., 2019; Zhou et al., 2012). The *V. harveyi* clade comprises luminous bacteria commonly detected in coastal and marine waters, as well as in the skin and gut of aquatic

organisms (Ina- Salwany et al., 2019; Vandenberghe et al., 2003). *Vibrio harveyi* infections can cause multiple shrimp diseases, including “bright-red syndrome” (Soto-Rodriguez et al., 2010), “bacterial white tail disease” (Zhou et al., 2012), and luminescent vibriosis (Mandal & Das, 2018; Wang et al., 2015). In addition, *V. parahaemolyticus* carrying the *pirAB* gene can cause acute hepatopancreatic necrosis disease (AHPND) (Han et al., 2015; Tran et al., 2013) and red disease in shrimp (Jayasree et al., 2006). In addition to *Vibrio*, other pathogenic genera have been reported, such as *Shewanella algae*, which causes black spot disease (Cao et al., 2018), *Acinetobacter venetianus*, which causes red leg disease (Huang et al., 2020a), and *Streptocephalus sirindhornae* and *Branchinella thailandensis*, which cause black disease (Saejung et al., 2011). Notably, some *Vibrio* species, such as *V. hepatarius* and *V. diabolicus*, are non-pathogenic and serve as probiotics that protect shrimp from infection (Ramirez et al., 2022; Restrepo et al., 2021). Consequently, traditional monitoring of *Vibrio* species density may erroneously suggest an elevation of disease risk.

Gut bacterial communities in shrimp are disrupted upon exposure to *V. harveyi*, with amplicon sequence variants (ASVs) from the Harveyi and Vulnificus clades becoming enriched (Angthong et al., 2023). Interestingly, the resilience of the gut microbiota can mitigate shrimp mortality during *V. harveyi* infection (Rungrassamee et al., 2016). *Vibrio* strains carrying the pVA1 plasmid, which encodes the binary *pirAB* toxin genes, are the causal agents of shrimp AHPND (Han et al., 2015). The virulent plasmid pVA1 harbors a post-segregational killing system, enabling its stable inheritance and dissemination among *Vibrio* species (Kumar et al., 2020) and non-*Vibrio* and non-pathogenic strains, such as *Algoriphagus* species, via conjugative transfer (Muthukrishnan et al., 2019). These molecular characteristics partially explain the difficulty in controlling shrimp AHPND. Indeed, AHPND poses a serious threat to the shrimp industry worldwide, often causing extensive or complete mortality within days (Kumar et al., 2020). The occurrence of AHPND substantially reduces α-diversity and the stability of the gut bacterial community, while increasing the variation coefficient and ecological dysbiosis indices compared to healthy shrimp (Dong et al., 2021). Of note, the gut microbiota exhibits different responses to infection by AHPND-causing *V. parahaemolyticus* (Vp) compared to common pathogenic Vp. Specifically, AHPND-causing Vp infection results in rapid shifts in the gut bacterial community, with enrichment of *Photobacterium* and *Vibrio* genera. In contrast, common Vp infection increases the abundance of gut *Motilimonas* and *Ruegeria* genera (Chang et al., 2023). Furthermore, variations in the bacterioplankton community in rearing water correlate with the virulence of Vp (Aguilar-Rendón et al., 2022). Similarly, elevated nutrient levels enhance the virulence of AHPND-causing Vp (Li et al., 2022), leading to quicker dysbiosis in the gut microbiota and earlier and higher mortality in shrimp compared to AHPND-causing Vp precultured at oligotrophic condition (Sha et al., 2022a). Intriguingly, the gut microbiota responds linearly to increasing shrimp AHPND severity, enabling accurate diagnosis of progressed stages of AHPND using gut indicators (Lu et al., 2023; Shen et al., 2021a).

**Fungal pathogens**

Fungi are prevalent in aquatic environments, with approximately 500 species isolated from marine and estuarine habitats, including several that act as opportunistic pathogens of shrimp (Karunasagar et al., 2004). Fungal infections typically result in chronic and steady losses, causing lower mortality rates compared to viral and bacterial infections (Paulraj et al., 2016). Common pathogenic fungi include *Lagenidium callinectes* and *Sirolpidium* species (Karunasagar et al., 2004), which preferentially infect larval shrimp. These pathogens enter larvae through antennae, eyestalks, and body tissues, ultimately causing death. Fungal spores and mycelia are detectable in targeted tissues, particularly the gills and appendages, rather than in the shrimp gut and hepatopancreas (Karunasagar et al., 2004). Endophytic *Fusarium* species, known plant pathogens producing fumonisins and trichothecenes that affect human and animal health (Munkvold, 2017), are also causal agents of shrimp black gill disease (BG), leading to chronic mortality over prolonged infections (Khoa et al., 2004). Research on the effects of fungal pathogens on the shrimp gut microbiota is limited compared to studies on viral and bacterial infections. Some studies indicate that fungal infections alter gut microbiota composition. For example, shrimp with BG harbor higher levels of the pathogenic fungus *Candida*, and reduced abundances of *Didymella* and *Filobasidium* in the gut (Li et al., 2019). However, gut microbial diversity remains comparable between healthy and BG-affected cohorts (Song et al., 2022). Although many fungi are saprophytic or parasitic, certain strains, such as *Aspergillus niger* and *A. fumigatus* are beneficial for shrimp growth, health, and antifungal immunity (Brzezinska & Jankiewicz, 2012; Li et al., 2012; Zhang et al., 2023).

**Parasitic pathogens**

Parasites are detrimental to their hosts as they exploit host nutrients for their own utilization, adversely affecting host immunity and growth. Various parasites, particularly protozoa, impact shrimp at different developmental stages (Table 1). Among these, *Enterocytozoon hepatopenaei* (EHP) has emerged as an important pathogen in shrimp aquaculture (Aranguren et al., 2017). EHP is an intracellular and microsporidian parasite that causes shrimp hepatopancreatic microsporidiosis, leading to stunted growth (Chayaburakul et al., 2004). Shrimp size is inversely associated with EHP load (Shen et al., 2021b). Environmental reservoirs can harbor EHP, resulting in recurrent infections in shrimp populations (Raj et al., 2023). EHP infection follows a cyclic pattern, where shrimp with severe infections can regress to milder infection, but never fully recover. This parasite-host interaction impairs shrimp health, leading to stunted growth and low mortality (López-Carvallo et al., 2022). Although EHP infection does not cause acute mortality, it increases shrimp susceptibility to subsequent microbial infections, including *Vibrio* species (Shen et al., 2021a), and WSSV (Suryakodi et al., 2022). The impact of EHP on the shrimp gut microbiota is less understood compared to bacterial and viral pathogens. The gut microbiota is affected by EHP infection severity, with enrichment of *Vibrio*, *Pseudomonas*, and *Bradyrhizobium* species (Shen et al., 2021a). EHP infection progression displaces beneficial microbes with opportunistic/pathogenic bacteria and fungi, depleting energy reserves. Specifically, the late stages of EHP infection are marked by an increase in gut bacterial genera such as *Leadbetterella*, *Aquimarina*, and *Vibrio*, and the fungal genus *Malassezia* (López-Carvallo et al., 2022). EHP infection causes greater dispersion, lower modularity, and a decrease in the proportion of negative associations and keystone taxa within the gut network, resulting in an unstable gut microbiota

(Shen et al., 2022). These alterations, in turn, compromise the capacity of shrimp to combat invading pathogens (Xiong, 2018). Chronic EHP infection progressively disrupts the bacterial communities in the gut and hepatopancreas (López-Carvallo et al., 2022; Shen et al., 2022). Consequently, gut EHP-discriminatory taxa can accurately distinguish healthy shrimp from EHP-infected individuals with infection progression (Shen et al., 2022). It is important to note that not all parasitic protozoa are harmful; some, such as certain phagotrophs, can be commensal or beneficial to shrimp health. For example, gut phagotrophs can directly prey on bacterial pathogens, thereby supporting shrimp health through interkingdom predator-prey interactions (Lu et al., 2022).

**Emerging and syndromic diseases**

Given the lag in etiological studies, the causal agents of various shrimp diseases are unknown. In such cases, the emerging and syndromic diseases are named based on typical symptoms, such as white feces syndrome (WFS) (Durai et al., 2015), "blue body syndrome" (Liang et al., 2020), and "cotton shrimp-like" disease (Zhou et al., 2019b) (Table 1).

Shrimp WFS typically manifests 50 to 60 days post-inoculation, causing persistent mortality, reducing survival rates by 20% to 30% and decreasing yield by up to 60% (Durai et al., 2015). WFS is characterized by white-golden gut contents and white fecal strings, but its complex etiology remains inconclusive. In this context, efforts devoted to the exploration of the etiological factors of WFS could significantly contribute to the current paradigm. The etiology of WFS has been proposed as a co-infection involving EHP and opportunistic marine pathogens, including *Vibrio* and *Propionigenium* species (Sriurairatana et al., 2014; Subash et al., 2023). Nevertheless, experimental challenges using these pathogens have failed to satisfy Koch's postulates (Aranguren Caro et al., 2021; Munkongwongsiri et al., 2022). Transplantation of gut microbiota from WFS-affected shrimp to healthy subjects induces WFS in recipients, suggesting a causal role for gut dysbiosis in WFS (Huang et al., 2020b). Shrimp infected with WFS show enrichment of various gut bacteria, such as *Candidatus Bacilloplasma*, *Phascolarctobacterium*, and *Vibrio*, but decreased levels of *Paracoccus* and *Lactococcus* based on field and microcosm studies (Boopathi et al., 2023; Hou et al., 2018; Huang et al., 2020b). Both gut bacterial and microeukaryotic disease-discriminatory taxa indicate the progression of WFS in shrimp (Dai et al., 2019a; Xiong et al., 2017a). While these findings collectively suggest that gut microbiota dysbiosis is implicated in WFS etiology, the causal pathogens involved in WFS remain uncertain. Recent studies integrating primary colonizers, "driver" taxa in gut networks from healthy and WFS-affected shrimp, WFS-discriminatory taxa, and encoding virulence genes have identified *V. fluvialis*, *V. coralliilyticus*, and *V. tubiashii* as potential WFS pathogens (Dai et al., 2018; Lu et al., 2020). The causal roles of the three pathogens in shrimp WFS have been further validated through pure culture experiments (Sha et al., 2024b). Given ongoing debates, other pathogens implicated in shrimp WFS cannot be ruled out, meriting further corroborative research.

Based on previous studies, we propose a workflow for identifying potential polymicrobial pathogens (Figure 1). Initially, the taxonomies of the microbial community are assigned by blasting against an up-to-date pathogen database with strict criteria, including 100% similarity (Lo et al., 2023). Due to the high temporal dynamics of the gut microbiota as shrimp age (Figure 2A) (Xiong et al., 2020), age-discriminatory taxa are excluded to account for host age effects (Figure 2B). After this optimization, primary responders, which are absent from healthy individuals and show linear enrichment during disease progression, are extracted from the community. Next, keystone taxa are identified using a causal inference algorithm integrated with dynamic intervention simulation (Wu et al., 2022). The removal of these keystone taxa results in network fragmentation (Dai et al., 2019b). These potential pathogens can serve as biomarkers for accurately diagnosing shrimp health status. Finally, candidate polymicrobial pathogens are confirmed using molecular approaches, such as pathogen-specific virulence genes. The infection order and ratio of the polymicrobial pathogens can be inferred by tracing back to the gut microbiota in disease-progressed individuals (Figure 1). This workflow provides a robust solution for identifying

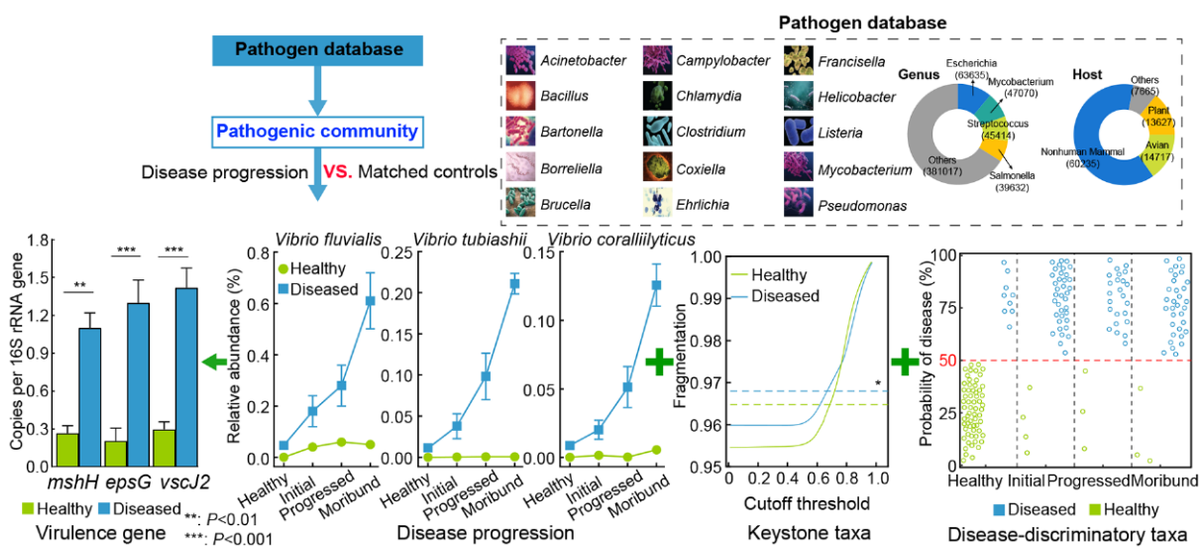



**Figure 1 Proposed workflow for identifying potential polymicrobial pathogens**

Polymicrobial pathogens are identified based on high similarity with pathogens, linear enrichment over disease progression, keystone taxa, disease-discriminatory taxa, and pathogen-specific virulence genes.

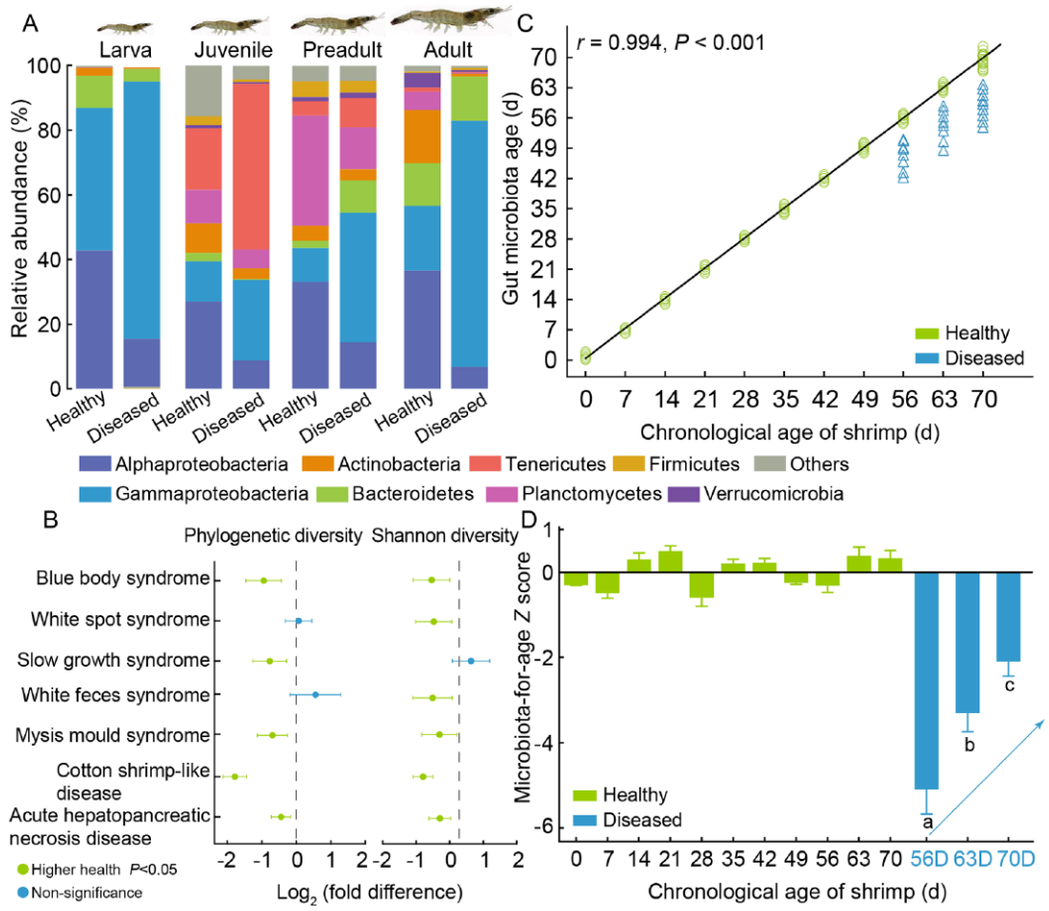



**Figure 2 Gut microbiota between shrimp health status and over life stages**

A: Comparison of dominant gut bacterial phyla or classes between healthy and diseased shrimp at each life stage. B: Gut microbial diversity showing no consistent change between shrimp health status. C: Regression between actual age of healthy shrimp against predicted age using age-discriminatory taxa profiles. Predicted age of diseased shrimp significantly deviated from linear fit. D: Microbiota maturity expressed as a microbiota-for-age *Z* score, with mean ± standard deviation. Differences in microbiota maturity at different ages between healthy (green bar) and diseased (blue bar) shrimp based on *post-hoc* Tukey's multiple comparison.

polymicrobial pathogens (Dai et al. 2018; Lu et al. 2020). The efficacy of this workflow is exemplified in our recent work, which identified *V. fluvialis*, *V. coralliilyticus*, and *V. tubiashii* as the causative pathogens of shrimp WFS (Sha et al., 2024b).

Running mortality syndrome (RMS) leads to persistent low-level mortality throughout the shrimp culture period (Zhang et al., 2014). RMS-affected shrimp are negative for all major WOAH-listed pathogens as well as common pathogens, such as WSSV, YHV, and *Vibrio* species. Moreover, cohabitation of healthy and RMS-affected shrimp does not result in RMS transmission (Alavandi et al., 2019). The incidence of RMS is positively associated with high stocking density, elevated nitrite levels, and increased turbidity, indicating that RMS may be related to pond ecosystem conditions rather than being infectious in nature. However, recent research has identified covert mortality nodavirus (CMNV) as the causal agent of RMS. CMNV infection suppresses the expression of genes involved in digestion, absorption, and growth hormones, which is consistent with the stunted growth observed in shrimp infected with CMNV (Liu et al., 2022).

The two aforementioned diseases reinforce that our understanding of the etiology of newly emerging shrimp diseases is still lacking. Given deteriorating water quality, increasing stocking density, and extreme weather events, this knowledge gap is likely to persist. However, the identification of causal agents for emerging and syndromic diseases can be achieved through the dedicated efforts of aquatic scientists and the advancement of new technologies.

## OVERVIEW OF FACTORS AFFECTING GUT MICROBIOTA OF SHRIMP

Bacterioplankton and shrimp coexist in their rearing environments, forming a mutually beneficial equilibrium characterized by synergistic interactions. The most significant association occurs in the gut, where the microbiota begins to establish from the egg stage, acquiring microbes from the surrounding water, initial feed, and younger individuals (Xiong, 2018; Zhang et al., 2021a). It is increasingly clear that the gut microbiota plays indispensable roles in shrimp fitness, immunity, and health (Holt et al., 2021; Xiong et al., 2019a). Regulating the gut microbiome offers a promising strategy for disease prevention in shrimp aquaculture. However, developing effective approaches requires knowledge of the factors influencing the shrimp gut microbiota. Extensive research has identified various factors affecting the shrimp gut microbiota, including diet (Arce et al., 2021), rearing water salinity (Deris et al., 2022; Hou et al., 2020), temperature (Xiong et al., 2015), nitrite exposure (Huang et al., 2020c), chronic hypoxia (Sun et al., 2020), and stock density (Deng

et al., 2019). In addition to these abiotic variables, biotic factors also strongly influence the gut microbiota, including life stage (Xiong et al., 2020), pathogen exposure (Angthong et al., 2023), disease severity (Xiong et al., 2017a), causal agents (Song et al., 2022), and interkingdom predator-prey interactions (Lu et al., 2022). Meta-analysis has shown that water type (seawater or freshwater) is the primary factor shaping the shrimp gut microbiota, followed by lifestyle (wild-type, farm, or laboratory), life stage, diet, and health status (Cornejo-Granados et al., 2018). Correspondingly, our recent research on marine-cultured shrimp highlighted the impact of life stage and different diseases on shaping the gut microbiota (Mao et al., 2023). While it has been suggested that microbial communities exhibit functional redundancy due to their high diversity (Miki et al., 2014), this redundancy diminishes when disturbances, such as abrupt changes in geochemical variables or host diseases, exceed the buffer capacity of the gut microbiome (Lu et al., 2022; Zhu et al., 2016). Thus, the gut microbiome is frequently altered by disturbances, leading to physiological disorders in shrimp and increased susceptibility to infections (Chen et al., 2017; Holt et al., 2021; Huang et al., 2021; Xiong et al., 2015). These lines of evidence, among others, demonstrate that the shrimp gut microbiota is highly dynamic, rather than static, and is consistently governed by both biotic and abiotic variables.

Koch's postulates have been updated and reformulated to encompass pathogens, local milieu, and susceptible individuals as collective contributors to disease (Sultana et al., 2017; Xiong & Shi, 2024). Under this scenario, it is necessary to consider the shrimp farming system holistically, using the "holobiome" concept, which includes microbiomes in rearing water, sediment, feed, and host, along with their interactions (Gutiérrez-Pérez et al., 2022). Following this logic, disease occurrence can be attributed to an imbalance among pathogens, hosts, and the environment, with the gut microbiota serving as a critical link between the host and the whole system (Engering et al., 2013). Recent research on the shrimp microbiome has thus focused on optimizing the gut microbiome through dietary supplements, probiotics, and prebiotics (Goh et al., 2022). To date, however, available approaches have proven inefficient and unsustainable in the field, despite promising results in microcosm and mesocosm studies. A plausible explanation is that healthy shrimp also exert strong selection on external taxa (Kamada et al., 2013; Xiong, 2018; Xiong et al., 2019a), hindering the successful establishment of applied probiotics. Additionally, as diseases cause a gradual deviation from a healthy state, the pathobiome is expected to evolve, leading to specific symbiont profiles (pathobiomes) at the onset, progression, and moribund stages of shrimp diseases (Lu et al., 2023; Shen et al., 2021a; Xiong et al., 2017a). Addressing this challenge requires the design of therapeutic strategies tailored to shrimp age and disease stage (Xiong et al., 2016). From this perspective, integrative experimental designs are essential to identify the "holobiome" components that significantly influence the shrimp gut microbiome and drive disease progression. Understanding these factors will enable the development of targeted strategies to optimize shrimp cultivation through effective gut microbiome management.

## SOURCES OF SHRIMP GUT MICROBIOTA

Aquatic animals are continuously exposed to their rearing water, and shrimp, being filter feeders, are assumed to acquire their gut commensals primarily from bacterioplankton communities in rearing water (De Schryver & Vadstein, 2014). However, research indicates that the microbial communities in rearing water and shrimp gut are distinct (Chen et al., 2017; Cornejo-Granados et al., 2017; Xiong et al., 2019b). As benthic animals, shrimp also interact with sediment microbial communities, which serve as an important external species pool for the gut microbiota. Compared to rearing water, sediment bacterial communities are more similar to those in the shrimp gut (Cornejo-Granados et al., 2017; Fan et al., 2019; Huang et al., 2021), contributing 36% and 75% of gut symbionts in juveniles and adults, respectively (Zhang et al., 2021a). Interestingly, the gut microbiota in adult shrimp is primarily inherited from the gut commensals of juveniles, forming an internal species pool (Zhang et al., 2021a, 2021b). Indeed, the shrimp gut microbiota is only weakly influenced by the geochemical variables and microbial communities in the rearing water (Xiong et al., 2019b; Zhang et al., 2021b). One possible explanation is that shifts in the gut microbiota lag behind shifts in the bacterioplankton community and geochemical variables. Alternatively, healthy shrimp may be resilient to mild stressors, with their gut microbiota primarily affected by host physiological parameters (Huang et al., 2018). This assertion is supported by observations that the proportion of gut commensals sourced from the ambient bacterioplankton community increases gradually during disease progression, due to compromised selection on surrounding taxa over the same timeframe (Lu et al., 2023; Xiong et al., 2018). Given the open circulatory system of invertebrates, shrimp gut symbionts may also disperse from other organs, such as the hepatopancreas. A high proportion of bacterial taxa are shared between the shrimp gut and hepatopancreas, serving as species pools for each other (Bao et al., 2024). Notably, dramatic changes in rearing conditions, such as elevated temperature and eutrophication, can markedly enhance pathogen virulence, resulting in earlier and higher shrimp mortality (Li et al., 2022; Sha et al., 2022a). Considering that disease results from an imbalance among the host, environmental variables, and ambient microbes (Mallon et al., 2015; Xiong, 2018), it is crucial to systematically explore the microbiomes across rearing water, sediment, and gut in relation to shrimp health status. Such exploration is essential for understanding pathogen transmission and etiological mechanisms.

## DIVERSITY AS A BIOMARKER OF DISEASE

Ecologically, a diversity-poor community is more susceptible to invasion by external species compared to a diversity-rich community, known as the diversity-stability relationship (Wang & Loreau, 2014). The rationale behind a positive diversity-stability relationship is that a diverse community confers an insurance effect, where high diversity increases the presence of functionally versatile and redundant species against disturbances, and a negative covariance effect, where losses in some taxa due to disturbance are compensated by gains in others (Cadotte et al., 2012). Given the crucial role of the gut microbiota in antagonizing invading pathogens, numerous studies have compared the gut microbial diversity between healthy and diseased shrimp, revealing a decrease in alpha-diversity in infected shrimp (Shen et al., 2021a; Song et al., 2022; Yao et al., 2018). However, a reduction in diversity is not universally observed in diseased individuals, with some studies reporting comparable (Wang et al., 2019; Xiong et al.,

2017b) or significantly increased diversity in infected shrimp (Zhou et al., 2019b) (Figure 2C). These discrepancies can be attributed to the type (e.g., causal agents) and strength (e.g., disease severity) of disturbance and the metrics used to measure diversity (e.g., weighted Shannon diversity, unweighted observed species). For example, we recently found that gut bacterial diversity is comparable between healthy and diseased shrimp at the disease onset stage (Chen et al., 2017; Lu et al., 2020; Xiong et al., 2017a). As the disease progresses, pathogen colonization outcompetes resident gut microbes, resulting in reduced microbial diversity. However, some resident species may benefit from the ecological niches created by the infection. In addition, diseased shrimp may attenuate their selective effect on external taxa, allowing for the random establishment of surrounding species (Mao et al., 2023; Sha et al., 2022b). Consequently, there is no consistent pattern of decreased gut microbial diversity in diseased shrimp (Figure 2C). Moreover, diversity is strongly affected by sequencing depth, making it challenging to compare diversity across studies. Therefore, declining gut microbial diversity is not a reliable indicator of shrimp health.

## COMMON FEATURES OF GUT MICROBIOTA IN RESPONSE TO SHRIMP DISEASES

A growing body of evidence indicates that shrimp diseases significantly alter the gut microbiota, supporting the notion that gut dysbiosis may be a causal agent of shrimp diseases (Angthong et al., 2023; Chen et al., 2017; Cornejo-Granados et al., 2017; Huang et al., 2020b). However, this "chicken-and-egg" dilemma requires sophisticated experiments to disentangle the causes and mechanisms. According to the Anna Karenina principle, all healthy microbiomes are alike, whereas each disease-associated microbiome is unique to the diseased individual (Zaneveld et al., 2017). This principle suggests that host diseases induce heterogeneity and stochasticity in the gut microbiota. Following this logic, extensive studies have compared the heterogeneity of gut microbiota between healthy and diseased shrimp. Generally, shrimp diseases increase beta-dispersion, average variation degree, temporal turnover rate, and dysbiosis indices of the gut microbiota (Lu et al., 2023; Mao et al., 2023; Yao et al., 2018). However, the consistency of these signatures remains controversial. Shrimp with severe disease appear to exhibit a more stable gut microbiota over time compared to healthy controls (Lu et al., 2020; Xiong et al., 2017a). A plausible explanation is that the gut microbiota is not resilient to intense disturbance, such as severe disease.

According to the holobiont theory, hosts selectively acquire gut commensals from their surrounding environments to improve their fitness (Bordenstein & Theis, 2015). This suggests that the gut microbiota of healthy shrimp is predominantly shaped by deterministic processes, including selection pressures from abiotic environmental variables, biotic host filtering, and interspecies interactions (Cavender-Bares et al., 2009; Nemergut et al., 2013), leading to predictable community structures over space and time. Accordingly, the gut microbiota exhibits a time-similarity decay relationship throughout shrimp development (Xiong et al., 2020). This pattern is fundamental, as deviations from the temporally defined trend are positively associated with disease severity. Conversely, the occurrence of shrimp diseases weakens the relative importance of deterministic processes governing the gut microbiota, regardless of the causal pathogens (Mao et al., 2023; Sha et al., 2022b). Diseased shrimp typically exhibit a sharp reduction in food consumption (Table 1) and may redirect energy towards immune responses. Consequently, the ability of diseased shrimp to selectively filter external taxa becomes compromised, resulting in increased inter-individual variation and a more stochastic assembly of the gut microbiota.

Although extensive studies have illustrated the effect of environmental and host selection on the gut microbiota, few have explored the role of interspecies interactions during shrimp disease progression (Bäumler & Sperandio, 2016; Lu et al., 2023; Xiong et al., 2018). Characterizing these interactions is critical, as resident gut microbes can directly compete for nutrients or facilitate resistance against invading pathogens (Coyte et al., 2015). The strength of these interspecies interactions is a good predictor of susceptibility to pathogenic disease (Banerjee et al., 2018). In general, gut network stability and complexity are disrupted by shrimp diseases, as evidenced by diverse topological properties, including reduced robustness, modularity and proportion of negative associations, as well as increased vulnerability (Sha et al., 2024b; Xiong et al., 2018; Yao et al., 2018). Among network nodes, gut keystone species exert disproportional roles in sustaining the stability, dynamics, and function of the gut microbiota, making them excellent candidate targets for gut microbiota-based interventions (Dai et al., 2019b; Shetty et al., 2017; Wu et al., 2022). Case studies have shown that one keystone strain can effectively inhibit or eliminate one pathogen, such as *Clostridium scindens* against *C. difficile* (Buffie et al., 2015) and *Bacillus subtilis* against *Staphylococcus aureus* (Piewngam et al., 2018) in humans. Inspired by these findings, we recently designs a probiotic consortium that efficiently antagonizes the casual pathogens of shrimp WFS (Sha et al., 2024b). Nevertheless, comparable work in aquaculture species is still limited, warranting further study.

In conclusion, shrimp diseases typically induce dysbiosis, elevated heterogeneity, and stochasticity in the gut microbiota, although the causal relationships require rigorous validation. In addition, shrimp diseases disrupt the stability of the gut microbial network, potentially increasing susceptibility to invading pathogens. These common features across diverse diseases highlight the potential of sensitive gut microbial markers as indicators of shrimp health, irrespective of the causal agents. Early detection of these adverse changes in the gut microbiota is important for predicting and managing the risk of shrimp diseases.

## COMMON DISEASE-DISCRIMINATORY TAXA PREDICTING SHRIMP HEALTH STATUS

As discussed above, the shrimp gut microbiota displays common features in response to diverse diseases. The underlying mechanism involves pathogenic infections triggering the production of reactive oxygen species, which facilitate aerobic respiration. Facultative anaerobic bacteria can utilize nonfermentable substrates as carbon sources, enabling them to outcompete obligate anaerobic Bacteroidia for fermentable nutrients (Winter & Bäumler, 2014). Consistent with this mechanism, shrimp diseases frequently increase the abundance of facultative anaerobic Proteobacteria in the gut, while reducing obligate anaerobic Bacteroidia (Mao et al., 2023; Sha et al., 2022b). It is important to note that the shrimp

gut microbiota is affected by diverse biotic and abiotic variables, including shrimp life stage (Xiong et al., 2020), different diseases (Yu et al., 2018a), hypervariable regions (Mao et al., 2023), health status (Angthong et al., 2023; Chen et al., 2017), aquaculture location, and sequencing platform (Cornejo-Granados et al., 2018; Mao et al., 2023) (Figure 3A).

Shrimp age is a robust predictor of variance in the gut microbiota, leading to a predictable microbial assembly as shrimp age (Xiong et al., 2020). The profiles of age-discriminatory taxa in the gut accurately diagnose the chronological age of healthy shrimp. However, the onset of disease can disrupt this defined trend (Figure 2B). Specifically, the microbiota-for-age *Z* (MAZ) score quantifies the variance in predicted microbiota age across different host age ranges and remains relatively stable in healthy shrimp. In contrast, the MAZ value sharply decreases with the onset of shrimp disease (Figure 2D) (Xiong et al., 2017a). A key challenge is distinguishing gut microbiota features between healthy and diseased shrimp, considering life stage and other confounding variables (Figure 3). To address this, we propose a workflow for identifying disease common-discriminatory taxa. Initially, a parametric permutational multivariate analysis of variance quantitatively evaluates the effect of various factors on gut microbiota variance, ranking them based on their relative contributions. Subsequently, a random forest model or comparable method, such as statistical logistic regression, identifies indicators characterizing the most influential driving factors, with aquaculture location often being paramount (Figure 3A). To minimize the location effect, the identified location-discriminatory taxa are excluded from the gut microbiota. This process is repeated for subsequent factors until shrimp health status is the primary focus. Finally, disease common-discriminatory taxa serve as biomarkers for diagnosing shrimp health status, independent of the causal agents (Figure 3C). It is also possible to infer potential disease or causal pathogens through disease specific-discriminatory

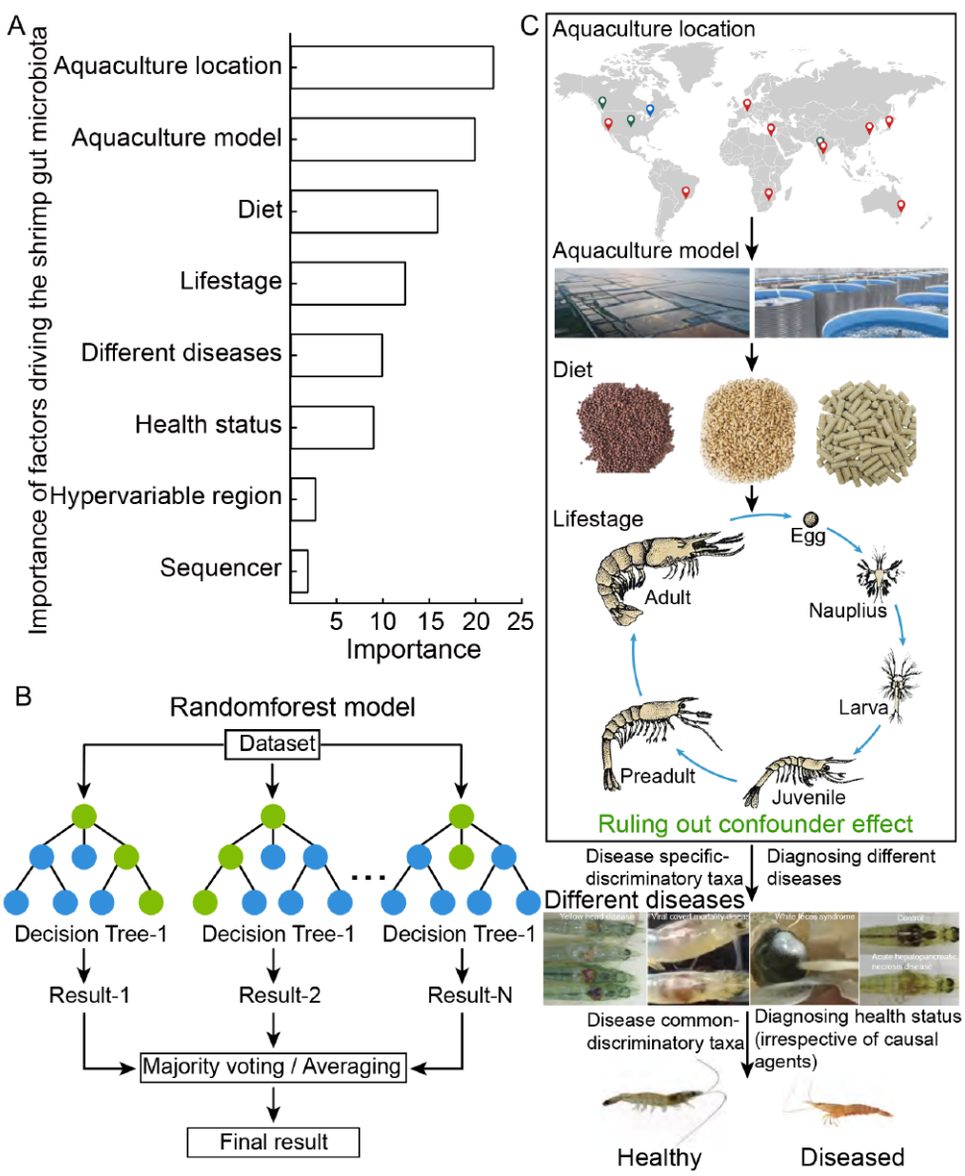



**Figure 3 Flowchart screening disease common-discriminatory taxa for diagnosing shrimp health status**

A: Quantifying relative importance of factors governing shrimp gut microbiota in descending order. B: Identifying discriminatory taxa for each factor using a random forest model. C: Identifying disease common-discriminatory taxa after progressive removal of effects of factors more important than health status in governing gut microbiota.

taxa, dependent on the causal agents. These optimized procedures can significantly improve diagnostic accuracy, as demonstrated in our recent studies (Mao et al., 2023; Sha et al., 2022b). Current research often compares gut microbiotas between healthy and severely diseased cohorts, leaving uncertainty about whether disease common-discriminatory taxa can predict disease onset. However, case studies provide supportive evidence for this potential (Lu et al., 2023; Shen et al., 2021a; Xiong et al., 2017a), although further validation is needed before practical application.

Disease common-discriminatory taxa are predominantly identified using high-throughput sequencing (HTS), which is time-consuming, expensive, and technically demanding, limiting its application in routine rapid-turnaround disease monitoring and early warning. An attractive solution to these limitations is proposed using quantitative real-time polymerase chain reaction (qPCR) to detect the relative abundances of gut microbial indicators (Yu et al. 2018b). In this case study, using disease-discriminatory phyla, diagnostic accuracy (93.2%) slightly lower than disease-discriminatory taxa (95.1%) and designed specific primers for these phyla for qPCR analysis, showing high consistency between qPCR and HTS assays in diagnosing shrimp WFS (Yu et al., 2018b). Nevertheless, subsequent meta-analyses have reported bacterial taxonomic effects on the diagnostic model, demonstrating that disease biomarkers at the bacterial species level provide the highest diagnostic accuracy (Mao et al., 2023; Sha et al., 2022b). However, due to confounding variables among studies, the identified gut disease-discriminatory taxa rarely overlap. Additionally, the bacterial 16S rDNA gene is insufficient to distinguish bacteria at the species level, except for a few well-studied pathogens. In contrast, functional genes are more conserved than 16S rDNA genes among phylogenic species that encode specific traits (Yang, 2021). Genes encoding a functional trait share conserved regions for maintaining topological structures and active sites, enabling the design of specific primers, such as those used in qPCR-based SmartChip assays. Following this logic, detecting disease-discriminatory functional genes using qPCR is a promising approach. Considering the rapid decrease in the cost of metagenomic sequencing, researchers can explore the gut functional structures across different shrimp health statuses and during disease progression. Importantly, gut microbiome data should be deposited into publicly accessible databases, allowing researchers to screen for common disease-discriminatory functional genes using meta-analysis in an unbiased manner.

## CONCLUSIONS AND PERSPECTIVES

Due to increasing stocking densities and deteriorating water quality, the emergence of new and frequent shrimp diseases is expected. The etiological and molecular mechanisms of these newly emerged diseases remain poorly understood (Table 1), posing significant challenges to shrimp production. It is now recognized that certain infectious diseases are caused by co-infections with polymicrobial pathogens that synergistically disrupt host homeostasis, rather than by a single pathogen. This complexity challenges the traditional “one pathogen, one disease” concept, especially as uncultivable bacteria may significantly contribute to pathogenicity. In addition, Koch’s postulates are difficult to satisfy when the composition and ratios of polymicrobial pathogens are unknown. In this context, ecological approaches that integrate primary colonizers, keystone taxa, and disease-discriminatory taxa offer a promising alternative for inferring polymicrobial pathogens (Figure 1). Candidate pathogens can be selectively isolated using inferred conditions for subsequent validation (Oberhardt et al., 2015). Shrimp diseases, such as AHPND, generally cause rapid and massive mortality, making early disease prediction crucial for preventing disease progression. Disease common-discriminatory taxa and disease specific-discriminatory taxa hold potentials for predicting disease incidence and inferring causal agents (Figure 2), guiding timely and allopathic treatments. However, current studies typically use static comparisons between diseased and healthy shrimp, resulting in limited data on gut microbiota over the course of the disease and limited confidence in diagnosing disease onset (Yu et al., 2018b). Additionally, abiotic and biotic information is often insufficient when depositing shrimp disease research data into public databases. To address these issues, we propose that detailed relevant data should be collected throughout the course of the disease to construct reliable models for early disease prediction. As our understanding of the gut microbiome and shrimp diseases advances, it becomes increasingly clear that innovative solutions, such as antagonistic probiotic consortia and biomarkers, can be systematically developed to enhance the sustainability of shrimp aquaculture.

## COMPETING INTERESTS

The authors declare that they have no competing interests.

## AUTHORS’ CONTRIBUTIONS

J.C. and J.B.X. conceptualized the manuscript. J.B.X. and H.N.S. wrote the manuscript. H.N.S. and J.B.X. collected the references and prepared the figures. All authors read and approved the final version of the manuscript.

## REFERENCES


Aguilar-Rendón KG, Soto-Rodriguez SA, Gomez-Gil B, et al. 2022. Water microbiome dynamics of pacific white shrimp *Penaeus vannamei* infected with *Vibrio parahaemolyticus* strains responsible for acute hepatopancreatic necrosis disease. *Aquaculture*, **551**: 737871.

Alavandi SV, Muralidhar M, Syama Dayal J, et al. 2019. Investigation on the infectious nature of running mortality syndrome (RMS) of farmed Pacific white leg shrimp, *Penaeus vannamei* in shrimp farms of India. *Aquaculture*, **500**: 278–289.

Angthong P, Uengwetwanit T, Uawisetwathana U, et al. 2023. Investigating host-gut microbial relationship in *Penaeus monodon* upon exposure to *Vibrio harveyi*. *Aquaculture*, **567**: 739252.

Aranguren Caro LF, Mai HN, Cruz-Florez R, et al. 2021. Experimental reproduction of white feces syndrome in whiteleg shrimp. *Penaeus vannamei*. *PLoS One*, **16**(12): e0261289.

Aranguren LF, Han JE, Tang KFJ. 2017. *Enterocytozoon hepatopenaei* (EHP) is a risk factor for acute hepatopancreatic necrosis disease (AHPND) and septic hepatopancreatic necrosis (SHPN) in the Pacific white shrimp *Penaeus vannamei*. *Aquaculture*, **471**: 37–42.

Arce KS, de Souza Valente C, do Vale Pereira G, et al. 2021. Modulation of the gut microbiota of Pacific white shrimp (*Penaeus vannamei* boone, 1931) by dietary inclusion of a functional yeast cell wall‐based additive. *Aquaculture Nutrition*, **27**(4): 1114–1127.

Arcier JM, Herman F, Lightner DV, et al. 1999. A viral disease associated with mortalities in hatchery-reared postlarvae of the giant freshwater prawn *Macrobrachium rosenbergii*. *Diseases of Aquatic Organisms*, **38**(3): 177–181.

Arulmoorthy MP, Anandajothi E, Vasudevan S, et al. 2020. Major viral

diseases in culturable penaeid shrimps: a review. *Aquaculture International*, **28**(5): 1939–1967.

Banerjee S, Schlaeppi K, van der Heijden MG. 2018. Keystone taxa as drivers of microbiome structure and functioning. *Nature Reviews Microbiology*, **16**(9): 567–576.

Bao SC, Wang WJ, Deng ZX, et al. 2024. Changes of bacterial communities and bile acid metabolism reveal the potential "intestine-hepatopancreas axis" in shrimp. *Science of the Total Environment*, **938**: 173384.

Bäumler AJ, Sperandio V. 2016. Interactions between the microbiota and pathogenic bacteria in the gut. *Nature*, **535**(7610): 85–93.

Bohara K, Joshi P, Acharya KP, et al. 2024. Emerging technologies revolutionising disease diagnosis and monitoring in aquatic animal health. *Reviews in Aquaculture*, **16**(2): 836–854.

Boonyaratpalin S, Supamattaya K, Kasornchandra J, et al. 1993. Non-occluded baculo-like virus, the causative agent of yellow head disease in the black tiger shrimp (*Penaeus monodon*). *Fish Pathology*, **28**(3): 103–109.

Boopathi S, Meenatchi R, Brindangnanam P, et al. 2023. Microbiome analysis of *Litopenaeus vannamei* reveals *Vibrio* as main risk factor of white faeces syndrome. *Aquaculture*, **576**: 739829.

Bordenstein SR, Theis KR. 2015. Host biology in light of the microbiome: ten principles of holobionts and hologenomes. *PLoS Biology*, **13**(8): e1002226.

Brock JA. 1997. Taura syndrome, a disease important to shrimp farms in the americas. *World Journal of Microbiology & Biotechnology*, **13**(4): 415–418.

Brzezinska MS, Jankiewicz U. 2012. Production of antifungal chitinase by *Aspergillus niger* LOCK 62 and its potential role in the biological control. *Current Microbiology*, **65**(6): 666–672.

Buffie CG, Bucci V, Stein RR, et al. 2015. Precision microbiome reconstitution restores bile acid mediated resistance to *Clostridium difficile. Nature*, **517**(7533): 205–208.

Cadotte MW, Dinnage R, Tilman D. 2012. Phylogenetic diversity promotes ecosystem stability. *Ecology*, **93**(sp8): S223–S233.

Cao HP, Chen SJ, Lu LQ, et al. 2018. *Shewanella algae*: an emerging pathogen of black spot disease in freshwater-cultured whiteleg shrimp (*Penaeus vannamei*). *The Israeli Journal of Aquaculture-Bamidgeh*, **70**: 1472.

Cavender-Bares J, Kozak KH, Fine PVA, et al. 2009. The merging of community ecology and phylogenetic biology. *Ecology Letters*, **12**(7): 693–715.

Chang YT, Ko HT, Wu PL, et al. 2023. Gut microbiota of Pacific white shrimp (*Litopenaeus vannamei*) exhibits distinct responses to pathogenic and non-pathogenic *Vibrio parahaemolyticus. Microbiology Spectrum*, **11**(5): e01180-23.

Chayaburakul K, Nash G, Pratanpipat P, et al. 2004. Multiple pathogens found in growth-retarded black tiger shrimp *Penaeus monodon* cultivated in thailand. *Diseases of Aquatic Organisms*, **60**(2): 89–96.

Chen SN, Chang PS, Kou GH, et al. 1989. Studies on virogenesis and cytopathology of penaeus monodon baculovirus (MBV) in the giant tiger prawn (*Penaeus monodon*) and the red tail prawn (*Penaeus penicillatus*). *Fish Pathology*, **24**(2): 89–100.

Chen WY, Ng TH, Wu JH, et al. 2017. Microbiome dynamics in a shrimp grow-out pond with possible outbreak of acute hepatopancreatic necrosis disease. *Scientific Reports*, **7**(1): 9395.

Chong Y, Loh H. 1984. Hepatopancreas clamydial and parvoviral infections of farmed marine prawns in Singapore. *Singapore Veterinary Journal*, **9**: 51–56.

Cornejo-Granados F, Gallardo-Becerra L, Leonardo-Reza M, et al. 2018. A meta-analysis reveals the environmental and host factors shaping the structure and function of the shrimp microbiota. *PeerJ*, **6**: e5382.

Cornejo-Granados F, Lopez-Zavala AA, Gallardo-Becerra L, et al. 2017. Microbiome of Pacific whiteleg shrimp reveals differential bacterial community composition between wild, aquacultured and AHPND/EMS outbreak conditions. *Scientific Reports*, **7**(1): 11783.

Couch JA. 1974. An enzootic nuclear polyhedrosis virus of pink shrimp: ultrastructure, prevalence, and enhancement. *Journal of Invertebrate Pathology*, **24**(3): 311–331.

Coyte KZ, Schluter J, Foster KR. 2015. The ecology of the microbiome: networks, competition, and stability. *Science*, **350**(6261): 663–666.

Dai WF, Qiu QF, Chen J, et al. 2019a. Gut eukaryotic disease-discriminatory taxa are indicative of Pacific white shrimp (*Litopenaeus vannamei*) white feces syndrome. *Aquaculture*, **506**: 154–160.

Dai WF, Chen J, Xiong JB. 2019b. Concept of microbial gatekeepers: positive guys?. *Applied Microbiology & Biotechnology*, **103**(2): 633–641.

Dai WF, Yu WN, Xuan LX, et al. 2018. Integrating molecular and ecological approaches to identify potential polymicrobial pathogens over a shrimp disease progression. *Applied Microbiology & Biotechnology*, **102**(8): 3755–3764.

De Schryver P, Vadstein O. 2014. Ecological theory as a foundation to control pathogenic invasion in aquaculture. *The ISME Journal*, **8**(12): 2360–2368.

de Souza Valente C, Rodiles A, Marques MRF, et al. 2020. White spot syndrome virus (WSSV) disturbs the intestinal microbiota of shrimp (*Penaeus vannamei*) reared in biofloc and clear seawater. *Applied Microbiology & Biotechnology*, **104**(18): 8007–8023.

Deng YL, Xu XY, Yin XW, et al. 2019. Effect of stock density on the microbial community in biofloc water and Pacific white shrimp (*Litopenaeus vannamei*) gut microbiota. *Applied Microbiology & Biotechnology*, **103**(10): 4241–4252.

Deris ZM, Iehata S, Gan HM, et al. 2022. Understanding the effects of salinity and *Vibrio harveyi* on the gut microbiota profiles of *Litopenaeus vannamei. Frontiers in Marine Science*, **9**: 974217.

Dhar AK, Piamsomboon P, Caro LFA, et al. 2019. First report of acute hepatopancreatic necrosis disease (AHPND) occurring in the USA. *Diseases of Aquatic Organisms*, **132**(3): 241–247.

Dong PS, Guo HP, Wang YT, et al. 2021. Gastrointestinal microbiota imbalance is triggered by the enrichment of *Vibrio* in subadult *Litopenaeus vannamei* with acute hepatopancreatic necrosis disease. *Aquaculture*, **533**: 736199.

Durai V, Gunalan B, Johnson PM, et al. 2015. Effect on white gut and white feces disease in semi intensive *Litopenaeus vannamei* shrimp culture system in south Indian state of Tamilnadu. *International Journal of Marine Science*, **5**(14): 1–5.

Engering A, Hogerwerf L, Slingenbergh J. 2013. Pathogen-host-environment interplay and disease emergence. *Emerging Microbes & Infections*, **2**(1): e5.

Falaise C, François C, Travers MA, et al. 2016. Antimicrobial compounds from eukaryotic microalgae against human pathogens and diseases in aquaculture. *Marine Drugs*, **14**(9): 159.

Fan LF, Wang ZL, Chen MS, et al. 2019. Microbiota comparison of Pacific white shrimp intestine and sediment at freshwater and marine cultured environment. *Science of the Total Environment*, **657**: 1194–1204.

FAO. 2023. Global aquaculture production data. Rome: FAO.

Ferreira NC, Bonetti C, Seiffert WQ. 2011. Hydrological and water quality indices as management tools in marine shrimp culture. *Aquaculture*, **318**(3-4): 425–433.

Flegel TW. 2006. Detection of major penaeid shrimp viruses in asia, a historical perspective with emphasis on thailand. *Aquaculture*, **258**(1-4): 1–33.

Frisan T. 2021. Co‐ and polymicrobial infections in the gut mucosa: the host–microbiota–pathogen perspective. *Cellular Microbiology*, **23**(2):

e13279.
Goh JXH, Tan LTH, Law JWF, et al. 2022. Harnessing the potentialities of probiotics, prebiotics, synbiotics, paraprobiotics, and postbiotics for shrimp farming. *Reviews in Aquaculture*, **14**(3): 1478–1557.
Gutiérrez-Pérez ED, Vázquez-Juárez R, Magallón-Barajas F, et al. 2022. How a holobiome perspective could promote intensification, biosecurity and eco-efficiency in the shrimp aquaculture industry. *Frontiers in Marine Science*, **9**: 975042.
Han JE. 2019. Detection of the amoebic parasite (order Dactylopodida) in cultured Pacific white shrimp (*Litopenaeus vannamei*). *Aquaculture*, **507**: 246–250.
Han JE, Tang KFJ, Tran LH, et al. 2015. *Photorhabdus* insect-related (Pir) toxin-like genes in a plasmid of *Vibrio parahaemolyticus*, the causative agent of acute hepatopancreatic necrosis disease (AHPND) of shrimp. *Diseases of Aquatic Organisms*, **113**(1): 33–40.
Hatai K, Egusa S. 1978. Studies on the pathogenic fungus associated with black gill disease of kuruma prawn, *Penaeus japonicus*-II: some of the note on the BG-Fusarium. *Fish Pathology*, **12**(4): 225–231.
Holt CC, Bass D, Stentiford GD, et al. 2021. Understanding the role of the shrimp gut microbiome in health and disease. *Journal of Invertebrate Pathology*, **186**: 107387.
Hou DW, Huang ZJ, Zeng SZ, et al. 2018. Intestinal bacterial signatures of white feces syndrome in shrimp. *Applied Microbiology & Biotechnology*, **102**(8): 3701–3709.
Hou DW, Zhou RJ, Zeng SZ, et al. 2020. Intestine bacterial community composition of shrimp varies under low-and high-salinity culture conditions. *Frontiers in Microbiology*, **11**: 589164.
Huang F, Pan LQ, Song MS, et al. 2018. Microbiota assemblages of water, sediment, and intestine and their associations with environmental factors and shrimp physiological health. *Applied Microbiology & Biotechnology*, **102**(19): 8585–8598.
Huang MX, Xie J, Yu QR, et al. 2020c. Toxic effect of chronic nitrite exposure on growth and health in Pacific white shrimp *Litopenaeus vannamei. Aquaculture*, **529**: 735664.
Huang XD, Gu Y, Zhou HH, et al. 2020a. *Acinetobacter venetianus*, a potential pathogen of red leg disease in freshwater-cultured whiteleg shrimp *Penaeus vannamei. Aquaculture Reports*, **18**: 100543.
Huang ZJ, Hou DW, Zhou RJ, et al. 2021. Environmental water and sediment microbial communities shape intestine microbiota for host health: the central dogma in an anthropogenic aquaculture ecosystem. *Frontiers in Microbiology*, **12**: 772149.
Huang ZJ, Zeng SZ, Xiong JB, et al. 2020b. Microecological Koch's postulates reveal that intestinal microbiota dysbiosis contributes to shrimp white feces syndrome. *Microbiome*, **8**(1): 32.
Ina‐Salwany MY, Al‐Saari N, Mohamad A, et al. 2019. Vibriosis in fish: a review on disease development and prevention. *Journal of Aquatic Animal Health*, **31**(1): 3–22.
Jayasree L, Janakiram P, Madhavi R. 2006. Characterization of *Vibrio* spp. Associated with diseased shrimp from culture ponds of Andhra Pradesh (India). *Journal of the World Aquaculture Society*, **37**(4): 523–532.
Kamada N, Chen GY, Inohara N, et al. 2013. Control of pathogens and pathobionts by the gut microbiota. *Nature Immunology*, **14**(7): 685–690.
Karunasagar I, Karunasagar I, Umesha RK. 2004. Microbial diseases in shrimp aquaculture. Goa, India: National Institute of Oceanography.
Khoa LV, Hatai K, Aoki T. 2004. *Fusarium incarnatum* isolated from black tiger shrimp, *Penaeus monodon* fabricius, with black gill disease cultured in Vietnam. *Journal of Fish Diseases*, **27**(9): 507–515.
Kumar R, Ng TH, Wang HC. 2020. Acute hepatopancreatic necrosis disease in penaeid shrimp. *Reviews in Aquaculture*, **12**(3): 1867–1880.
Li J, Jiang HY, Li LM, et al. 2019. The effect of disease and season to hepatopancreas and intestinal mycobiota of *Litopenaeus vannamei. Frontiers in Microbiology*, **10**: 889.
Li LY, Lu JQ, Zhan PP, et al. 2022. RNA-seq analysis unveils temperature and nutrient adaptation mechanisms relevant for pathogenicity in *Vibrio parahaemolyticus. Aquaculture*, **558**: 738397.
Li XJ, Zhang Q, Zhang AL, et al. 2012. Metabolites from *Aspergillus fumigatus*, an endophytic fungus associated with *Melia azedarach*, and their antifungal, antifeedant, and toxic activities. *Journal of Agricultural & Food Chemistry*, **60**(13): 3424–3431.
Liang QJ, Li ZH, Ou MF, et al. 2020. Hypoimmunity and intestinal bacterial imbalance are closely associated with blue body syndrome in cultured *Penaeus vannamei. Aquaculture*, **522**: 735118.
Liao MZ, Liao XZ, Long XX, et al. 2023. Host-microbiota interactions and responses of *Metapenaeus ensis* infected with decapod iridescent virus 1. *Frontiers in Microbiology*, **13**: 1097931.
Lightner DV, Redman RM, Bell TA. 1983. Infectious hypodermal and hematopoietic necrosis, a newly recognized virus disease of penaeid shrimp. *Journal of Invertebrate Pathology*, **42**(1): 62–70.
Liu KF, Liu WJ, Kou GH, et al. 2009. Shrimp white spot syndrome-from pathology to pathogenomics. *Fish Pathology*, **44**(2): 55–58.
Liu S, Xia JT, Tian Y, et al. 2022. Investigation of pathogenic mechanism of covert mortality nodavirus infection in *Penaeus vannamei. Frontiers in Microbiology*, **13**: 904358.
Lo LSH, Liu X, Liu HB, et al. 2023. Aquaculture bacterial pathogen database: pathogen monitoring and screening in coastal waters using environmental DNA. *Water Research*, **20**: 100194.
López-Carvallo JA, Cruz-Flores R, Dhar AK. 2022. The emerging pathogen *Enterocytozoon hepatopenaei* drives a degenerative cyclic pattern in the hepatopancreas microbiome of the shrimp (*Penaeus vannamei*). *Scientific Reports*, **12**(1): 14766.
Lu JQ, Li XH, Qiu QF, et al. 2022. Gut interkingdom predator-prey interactions are key determinants of shrimp health. *Aquaculture*, **546**: 737304.
Lu JQ, Mao JN, Qi XJ, et al. 2023. The assembly of gut microbiota implicates shrimp acute hepatopancreas necrosis disease progression. *Applied Microbiology & Biotechnology*, **107**(24): 7489–7500.
Lu JQ, Zhang XC, Qiu QF, et al. 2020. Identifying potential polymicrobial pathogens: moving beyond differential abundance to driver taxa. *Microbial Ecology*, **80**(2): 447–458.
Lu JQ, Zhang XX, Wang CH, et al. 2021. Responses of sediment resistome, virulence factors and potential pathogens to decades of antibiotics pollution in a shrimp aquafarm. *Science of the Total Environment*, **794**: 148760.
MacAulay S, Ellison AR, Kille P, et al. 2022. Moving towards improved surveillance and earlier diagnosis of aquatic pathogens: from traditional methods to emerging technologies. *Reviews in Aquaculture*, **14**(4): 1813–1829.
Mallon CA, van Elsas JD, Salles JF. 2015. Microbial invasions: the process, patterns, and mechanisms. *Trends in Microbiology*, **23**(11): 719–729.
Mandal A, Das SK. 2018. Comparative efficacy of neem (*Azadirachta indica*) and non-neem supplemented biofloc media in controlling the harmful luminescent bacteria in natural pond culture of *Litopenaeus vannaemei. Aquaculture*, **492**: 157–163.
Mao JN, Lu JQ, Chen J, et al. 2023. Consistent features of the gut microbiota in response to diverse shrimp *Litopenaeus vannamei* diseases: a meta‐analysis. *Fish & Fisheries*, **24**(6): 1103–1117.
Miki T, Yokokawa T, Matsui K. 2014. Biodiversity and multifunctionality in a microbial community: a novel theoretical approach to quantify functional redundancy. *Proceedings of the Royal Society B: Biological Sciences*, **281**(1776): 20132498.
Munkongwongsiri N, Prachumwat A, Eamsaard W, et al. 2022. *Propionigenium* and *Vibrio* species identified as possible component causes

of shrimp white feces syndrome (WFS) associated with the microsporidian *Enterocytozoon hepatopenaei. Journal of Invertebrate Pathology*, **192**: 107784.

Munkvold GP. 2017. Fusarium species and their associated mycotoxins. *Methods in Molecular Biology*, **1542**: 51–106.

Muthukrishnan S, Defoirdt T, Shariff M, et al. 2019. Horizontal gene transfer of the *pirAB* genes responsible for acute hepatopancreatic necrosis disease (AHPND) turns a non-*Vibrio* strain into an AHPND-positive pathogen. *BioRxiv*, doi: https://doi.org/10.1101/2019.12.20.884320.

Nemergut DR, Schmidt SK, Fukami T, et al. 2013. Patterns and processes of microbial community assembly. *Microbiology & Molecular Biology Reviews*, **77**(3): 342–356.

Nurlatiffah N, Kismiyati I, Ulkhaq MF. 2018. Value of prevalence and intensity of ectoparasite infesting *Litopenaeus vannamei. Journal of Fisheries & LIife Science*, **3**(2): 17–19.

Oberhardt MA, Zarecki R, Gronow S, et al. 2015. Harnessing the landscape of microbial culture media to predict new organism–media pairings. *Nature Communications*, **6**: 8493.

Panchal V, Kumar S, Hossain SN, et al. 2021. Structure analysis of thymidylate synthase from white spot syndrome virus reveals WSSV-specific structural elements. *International Journal of Biological Macromolecules*, **167**: 1168–1175.

Paulraj A, Musthafa MS, Altaff K, et al. 2016. Chytrid *Batrachochytrium dendrobatidis* fungal infection in freshwater prawn, *Macrobrachium rosenbergii* (de Man)-A new report. *Aquaculture*, **464**: 521–528.

Phuoc LH, Corteel M, Nauwynck HJ, et al. 2008. Increased susceptibility of white spot syndrome virus-infected *Litopenaeus vannamei* to *Vibrio campbellii. Environmental Microbiology*, **10**(10): 2718–2727.

Piewngam P, Zheng Y, Nguyen TH, et al. 2018. Pathogen elimination by probiotic *Bacillus via* signalling interference. *Nature*, **562**(7728): 532–537.

Pradeep B, Rai P, Mohan SA, et al. 2012. Biology, host range, pathogenesis and diagnosis of *White spot syndrome virus. Indian Journal of Virology*, **23**(2): 161–174.

Qiu L, Chen MM, Wan XY, et al. 2017. Characterization of a new member of *Iridoviridae*, Shrimp hemocyte iridescent virus (SHIV), found in white leg shrimp (*Litopenaeus vannamei*). *Scientific Reports*, **7**(1): 11834.

Raj M, Sathiyaraj G, Narayanan B, et al. 2023. Characterization of *Enterocytozoon hepatopenaei* causing hepatopancreatic microsporidiosis in *L. vannamei* and a new molecular method for its detection in shrimps, and other environmental samples. *Journal of Invertebrate Pathology*, **199**: 107951.

Ramirez M, Domínguez-Borbor C, Salazar L, et al. 2022. The probiotics *Vibrio diabolicus* (Ili), *Vibrio hepatarius* (P62), and *Bacillus cereus sensu stricto* (P64) colonize internal and external surfaces of *Penaeus vannamei* shrimp larvae and protect it against *Vibrio parahaemolyticus. Aquaculture*, **549**: 737826.

Restrepo L, Domínguez-Borbor C, Bajaña L, et al. 2021. Microbial community characterization of shrimp survivors to AHPND challenge test treated with an effective shrimp probiotic (*Vibrio diabolicus*). *Microbiome*, **9**(1): 88.

Rodgers CJ, Furones MD. 2009. Antimicrobial agents in aquaculture: practice, needs and issues. *In*: Rogers C, Basurco B. The use of veterinary drugs and vaccines in mediterranean aquaculture. Zaragoza: CIHEAM, 41–59.

Rungrassamee W, Klanchui A, Maibunkaew S, et al. 2016. Bacterial dynamics in intestines of the black tiger shrimp and the Pacific white shrimp during *Vibrio harveyi* exposure. *Journal of Invertebrate Pathology*, **133**: 12–19.

Saejung C, Hatai K, Wada S, et al. 2011. Clinical observations of black disease in fairy shrimps, *Streptocephalus sirindhornae* and *Branchinella thailandensis*, from Thailand and pathogen verification. *Journal of Fish Diseases*, **34**(12): 911–920.

Sakaew W, Pratoomthai B, Anantasomboon G, et al. 2008. Abdominal segment deformity disease (ASDD) of the whiteleg shrimp *Penaeus vannamei* reared in Thailand. *Aquaculture*, **284**(1-4): 46–52.

Seibert CH, Pinto AR. 2012. Challenges in shrimp aquaculture due to viral diseases: distribution and biology of the five major penaeid viruses and interventions to avoid viral incidence and dispersion. *Brazilian Journal of Microbiology*, **43**(3): 857–864.

Sha HN, Li LY, Lu JQ, et al. 2022a. High nutrient induces virulence in the AHPND-causing *Vibrio parahaemolyticus*, interpretation from the ecological assembly of shrimp gut microbiota. *Fish & Shellfish Immunology*, **127**: 758–765.

Sha HN, Lu JQ, Chen J, et al. 2022b. A meta‐analysis study of the robustness and universality of gut microbiota–shrimp diseases relationship. *Environmental Microbiology*, **24**(9): 3924–3938.

Sha HN, Song TT, Zhan PP, et al. 2024a. Sarafloxacin hydrochloride exposure disrupts gut microbiota and increases shrimp susceptibility to *Vibrio anguillarum* infection. *Aquaculture*, **586**: 740810.

Sha HN, Lu JQ, Chen J, et al. 2024b. Rationally designed probiotics prevent shrimp white feces syndrome via the probiotics–gut microbiome–immunity axis. *npj Biofilms & Microbiomes*, **10**(1): 40.

Shan LP, Hu Y, Hu L, et al. 2023. Involvement of microplastics in the conflict between host immunity defense and viral virulence: promoting the susceptibility of shrimp to WSSV infection. *Environmental Science & Technology*, **57**(31): 11634–11642.

Shen HY, Song TT, Lu JQ, et al. 2021a. Shrimp AHPND causing *Vibrio anguillarum* infection: quantitative diagnosis and identifying antagonistic bacteria. *Marine Biotechnology*, **23**(6): 964–975.

Shen H, Fan XP, Qiao Y, et al. 2021b. The links among *Enterocytozoon hepatopenaei* infection, growth retardation and intestinal microbiota in different sized shrimp *Penaeus vannamei. Aquaculture Reports*, **21**: 100888.

Shen HY, Zhang XC, Qian D, et al. 2022. Pathobiology of *Enterocytozoon hepatopenaei* (EHP) in shrimp: diagnosis and interpretation from the gut bacterial community. *Aquaculture*, **554**: 738169.

Shetty SA, Hugenholtz F, Lahti L, et al. 2017. Intestinal microbiome landscaping: insight in community assemblage and implications for microbial modulation strategies. *FEMS Microbiology Reviews*, **41**(2): 182–199.

Song TT, Sha HN, Qiu QF, et al. 2022. Common disease-discriminatory fungal taxa accurately diagnose shrimp white feces syndrome, black gills, and retardation diseases. *Aquaculture*, **561**: 738643.

Soto-Rodriguez SA, Gomez-Gil B, Lozano R. 2010. 'Bright-red'syndrome in Pacific white shrimp *Litopenaeus vannamei* is caused by *Vibrio harveyi. Diseases of Aquatic Organisms*, **92**(1): 11–19.

Sriurairatana S, Boonyawiwat V, Gangnonngiw W, et al. 2014. White feces syndrome of shrimp arises from transformation, sloughing and aggregation of hepatopancreatic microvilli into vermiform bodies superficially resembling gregarines. *PLoS One*, **9**(6): e99170.

Subash P, Chrisolite B, Sivasankar P, et al. 2023. White feces syndrome in *Penaeus vannamei* is potentially an *Enterocytozoon hepatopenaei* (EHP) associated pathobiome origin of *Vibrio* spp. *Journal of Invertebrate Pathology*, **198**: 107932.

Sultana S, Sarker SA, Brüssow H. 2017. What happened to koch's postulates in diarrhoea?. *Environmental Microbiology*, **19**(8): 2926–2934.

Sun SM, Yang M, Fu HT, et al. 2020. Altered intestinal microbiota induced by chronic hypoxia drives the effects on lipid metabolism and the immune response of oriental river prawn *Macrobrachium nipponense. Aquaculture*, **526**: 735431.

Suryakodi S, Ahmed AN, Badhusha A, et al. 2022. First report on the occurrence of white spot syndrome virus, infectious myonecrosis virus and

*Enterocytozoon hepatopenaei* in *Penaeus vannamei* reared in freshwater systems. *Journal of Fish Diseases*, **45**(5): 699–706.

Thitamadee S, Prachumwat A, Srisala J, et al. 2016. Review of current disease threats for cultivated penaeid shrimp in Asia. *Aquaculture*, **452**: 69–87.

Tran L, Nunan L, Redman RM, et al. 2013. Determination of the infectious nature of the agent of acute hepatopancreatic necrosis syndrome affecting penaeid shrimp. *Diseases of Aquatic Organisms*, **105**(1): 45–55

Tuyen NX, Verreth J, Vlak JM, et al. 2014. Horizontal transmission dynamics of white spot syndrome virus by cohabitation trials in juvenile *Penaeus monodon* and *P. vannamei. Preventive Veterinary Medicine*, **117**(1): 286–294.

Vandenberghe J, Thompson FL, Gomez-Gil B, et al. 2003. Phenotypic diversity amongst *Vibrio* isolates from marine aquaculture systems. *Aquaculture*, **219**(1-4): 9–20.

Wang J, Huang YJ, Xu KH, et al. 2019. White spot syndrome virus (WSSV) infection impacts intestinal microbiota composition and function in *Litopenaeus vannamei. Fish & Shellfish Immunology*, **84**: 130–137.

Wang LP, Chen YW, Huang H, et al. 2015. Isolation and identification of *Vibrio campbellii* as a bacterial pathogen for luminous vibriosis of *Litopenaeus vannamei. Aquaculture Research*, **46**(2): 395–404.

Wang SP, Loreau M. 2014. Ecosystem stability in space: α, β and γ variability. *Ecology Letters*, **17**(8): 891–901.

Wijegoonawardane PKM, Cowley JA, Phan T, et al. 2008. Genetic diversity in the yellow head nidovirus complex. *Virology*, **380**(2): 213–225.

Winter SE, Bäumler AJ. 2014. Why related bacterial species bloom simultaneously in the gut: principles underlying the 'like will to like' concept. *Cellular Microbiology*, **16**(2): 179–184.

Wu DF, Liu L, Jiao N, et al. 2022. Targeting keystone species helps restore the dysbiosis of butyrate‐producing bacteria in nonalcoholic fatty liver disease. *iMeta*, **1**(4): e61.

Xiong JB, Wang K, Wu JF, et al. 2015. Changes in intestinal bacterial communities are closely associated with shrimp disease severity. *Applied Microbiology & Biotechnology*, **99**(16): 6911–6919.

Xiong JB, Dai WF, Li CH. 2016. Advances, challenges, and directions in shrimp disease control: the guidelines from an ecological perspective. *Applied Microbiology & Biotechnology*, **100**(16): 6947–6954.

Xiong JB, Zhu JY, Dai WF, et al. 2017a. Integrating gut microbiota immaturity and disease‐discriminatory taxa to diagnose the initiation and severity of shrimp disease. *Environmental Microbiology*, **19**(4): 1490–1501.

Xiong JB, Dai WF, Zhu JY, et al. 2017b. The underlying ecological processes of gut microbiota among cohabitating retarded, overgrown and normal shrimp. *Microbial Ecology*, **73**(4): 988–999.

Xiong JB. 2018. Progress in the gut microbiota in exploring shrimp disease pathogenesis and incidence. *Applied Microbiology & Biotechnology*, **102**(17): 7343–7350.

Xiong JB, Dai WF, Qiu QF, et al. 2018. Response of host–bacterial colonization in shrimp to developmental stage, environment and disease. *Molecular Ecology*, **27**(18): 3686–3699.

Xiong JB, Nie L, Chen J. 2019a. Current understanding on the roles of gut microbiota in fish disease and immunity. *Zoological Research*, **40**(2): 70–76.

Xiong JB, Xuan LX, Yu WN, et al. 2019b. Spatiotemporal successions of shrimp gut microbial colonization: high consistency despite distinct species pool. *Environmental Microbiology*, **21**(4): 1383–1394.

Xiong JB, Li XH, Yan MC, et al. 2020. Comparable ecological processes govern the temporal succession of gut bacteria and microeukaryotes as shrimp aged. *Microbial Ecology*, **80**(4): 935–945.

Xiong JB, Shi ZJ. 2024. Editorial: environments-pathogens-the gut microbiota and host diseases. *Frontiers in Microbiology* **14**: 1357125.

Yang YF. 2021. Emerging patterns of microbial functional traits. *Trends in Microbiology*, **29**(10): 874–882.

Yao ZY, Yang KJ, Huang L, et al. 2018. Disease outbreak accompanies the dispersive structure of shrimp gut bacterial community with a simple core microbiota. *AMB Express*, **8**(1): 120.

Yu WN, Wu JH, Zhang JJ, et al. 2018a. A meta-analysis reveals universal gut bacterial signatures for diagnosing the incidence of shrimp disease. *FEMS Microbiology Ecology*, **94**(10): fiy147.

Yu WN, Cao JX, Dai WF, et al. 2018b. Quantitative PCR analysis of gut disease-discriminatory phyla for diagnosing shrimp disease incidence. *Applied & Environmental Microbiology*, **84**(18): e01387–18.

Zaneveld JR, McMinds R, Thurber RV. 2017. Stress and stability: applying the anna karenina principle to animal microbiomes. *Nature Microbiology*, **2**: 17121.

Zhang M, Liang HF, Lei YF, et al. 2023. *Aspergillus niger* confers health benefits and modulates the gut microbiota of juvenile Pacific white shrimp (*Penaeus vannamei*) under farming conditions. *Frontiers in Marine Science*, **10**: 1211993.

Zhang QL, Liu Q, Liu S, et al. 2014. A new nodavirus is associated with covert mortality disease of shrimp. *Journal of General Virology*, **95**(12): 2700–2709.

Zhang XC, Li XH, Lu JQ, et al. 2021a. Quantifying the importance of external and internal sources to the gut microbiota in juvenile and adult shrimp. *Aquaculture*, **531**: 735910.

Zhang WQ, Zhu ZD, Chen J, et al. 2021b. Quantifying the importance of abiotic and biotic factors governing the succession of gut microbiota over shrimp ontogeny. *Frontiers in Microbiology*, **12**: 752750.

Zhou JF, Fang WH, Yang XL, et al. 2012. A nonluminescent and highly virulent *Vibrio harveyi* strain is associated with "bacterial white tail disease" of *Litopenaeus vannamei* shrimp. *PLoS One*, **7**(2): e29961.

Zhou L, Chen CZ, Xie J, et al. 2019b. Intestinal bacterial signatures of the "cotton shrimp-like" disease explain the change of growth performance and immune responses in Pacific white shrimp (*Litopenaeus vannamei*). *Fish & Shellfish Immunology*, **92**: 629–636.

Zhou RJ, Zeng SZ, Hou DW, et al. 2019a. Occurrence of human pathogenic bacteria carrying antibiotic resistance genes revealed by metagenomic approach: a case study from an aquatic environment. *Journal of Environmental Sciences*, **80**: 248–256.

Zhu JY, Dai WF, Qiu QF, et al. 2016. Contrasting ecological processes and functional compositions between intestinal bacterial community in healthy and diseased shrimp. *Microbial Ecology*, **72**(4): 975–985.

Guo et al. *Zool. Res.* 2024, 45(4): 924−936
https://doi.org/10.24272/j.issn.2095-8137.2024.034

ZR | Zoological Research

Article Open Access

# Rotating magnetic field inhibits Aβ protein aggregation and alleviates cognitive impairment in Alzheimer's disease mice

Ruo-Wen Guo[1,2], Wen-Jing Xie[1,3], Biao Yu[1], Chao Song[1], Xin-Miao Ji[1], Xin-Yu Wang[1,3], Mei Zhang[4], Xin Zhang[1,2,3,*]

[1] *High Magnetic Field Laboratory*, *CAS Key Laboratory of High Magnetic Field and Ion Beam Physical Biology*, *Hefei Institutes of Physical Science*, *Chinese Academy of Sciences*, *Hefei*, *Anhui* 230031, *China*

[2] *Science Island Branch of Graduate School*, *University of Science and Technology of China*, *Hefei*, *Anhui* 230036, *China*

[3] *Institutes of Physical Science and Information Technology*, *Anhui University*, *Hefei*, *Anhui* 230601, *China*

[4] *School of Life Sciences*, *Division of Life Sciences and Medicine*, *University of Science and Technology of China*, *Hefei*, *Anhui* 230026, *China*

## ABSTRACT

Amyloid beta (Aβ) monomers aggregate to form fibrils and amyloid plaques, which are critical mechanisms in the pathogenesis of Alzheimer's disease (AD). Given the important role of Aβ1-42 aggregation in plaque formation, leading to brain lesions and cognitive impairment, numerous studies have aimed to reduce Aβ aggregation and slow AD progression. The diphenylalanine (FF) sequence is critical for amyloid aggregation, and magnetic fields can affect peptide alignment due to the diamagnetic anisotropy of aromatic rings. In this study, we examined the effects of a moderate-intensity rotating magnetic field (RMF) on Aβ aggregation and AD pathogenesis. Results indicated that the RMF directly inhibited Aβ amyloid fibril formation and reduced Aβ-induced cytotoxicity in neural cells *in vitro*. Using the AD mouse model APP/PS1, RMF restored motor abilities to healthy control levels and significantly alleviated cognitive impairments, including exploration and spatial and non-spatial memory abilities. Tissue examinations demonstrated that RMF reduced amyloid plaque accumulation, attenuated microglial activation, and reduced oxidative stress in the APP/PS1 mouse brain. These findings suggest that RMF holds considerable potential as a non-invasive, high-penetration physical approach for AD treatment.

**Keywords:** Alzheimer's disease; Rotating magnetic field; Amyloid-β; Cognitive function; Alzheimer's disease animal models

## INTRODUCTION

Alzheimer's disease (AD) is a chronic, incurable neurodegenerative condition and the most prevalent form of dementia worldwide, predominantly afflicting the elderly. Its primary clinical manifestations include cognitive and behavioral decline, memory recall impairments, and spatial perception difficulties, as well as changes in personality and disposition (Ballard et al., 2011; Graff-Radford et al., 2021). Advances in modern medicine have extended human lifespans, leading to a notable increase in age-related neurodegenerative disorders. At present, more than 55 million individuals worldwide are affected by AD and other types of dementia, with projections estimating a rise to 152 million by 2050 (Gauthier et al., 2021). This trend presents an increasingly critical public health challenge, imposing substantial socioeconomic and personal burdens on sufferers and their families (2023 Alzheimer's disease facts and figures, 2023).

The pathogenesis of AD is characterized by the presence of senile plaques and neurofibrillary tangles. These pathological changes are driven by the deposition of beta-amyloid protein and the entanglement of hyperphosphorylated tau (Blennow et al., 2006). Amyloid beta peptide (Aβ) is the primary cause of senile plaque formation, generated by the cleavage of amyloid precursor protein (APP) into peptide fragments predominantly composed of Aβ1-40 and Aβ1-42, which aggregate to form oligomers or fibrils (Bayer et al., 1999; Chen et al., 2017; Iwatsubo et al., 1995; Selkoe, 2001). Notably, Aβ oligomers exert neurotoxic effects that ultimately lead to neuronal cell death (Tiwari et al., 2019). Inhibition of Aβ accumulation within the central nervous system has been shown to effectively ameliorate cognitive deficits in mouse models of AD (Companys-Alemany et al., 2022; Fu et al., 2016; Zhang et al., 2019), demonstrating the therapeutic potential of reducing Aβ accumulation in AD treatment.

Magnetic fields possess the advantage of high penetration,

This is an open-access article distributed under the terms of the Creative Commons Attribution Non-Commercial License (http://creativecommons.org/licenses/by-nc/4.0/), which permits unrestricted non-commercial use, distribution, and reproduction in any medium, provided the original work is properly cited.

Copyright ©2024 Editorial Office of Zoological Research, Kunming Institute of Zoology, Chinese Academy of Sciences

Received: 05 April 2024; Accepted: 25 April 2024; Online: 26 April 2024

Foundation items: This study was supported by the National Key R&D Program of China (2023YFB3507004), National Natural Science Foundation of China (U21A20148), International Partnership Program of Chinese Academy of Sciences (116134KYSB20210052), Heye Health Technology Chong Ming Project (HYCMP2021010), and CASHIPS Director's Fund (BJPY2021A06)

*Corresponding author, E-mail: xinzhang@hmfl.ac.cn

allowing them to penetrate the whole body, including the brain. *In vitro* experiments have demonstrated that magnetic fields can affect the alignment of peptide dipoles, resulting in a reduction of the inherent beta-folding conformation (Todorova et al., 2016), considered an intermediate state in amyloid-like protein formation (Michaels et al., 2018; Todorova et al., 2016). The diphenylalanine (FF) sequence within KLVFF is critical for Aβ assembly and amyloid aggregation (Castelletto et al., 2017). The self-assembled tubular structures of FF align in high static magnetic fields due to the magnetic moments arising from the anisotropy of aromatic rings in peptide fragments (Hill et al., 2007). A moderate-intensity rotating magnetic field (RMF) generated by a pair of permanent magnets has been shown to agitate self-assembled β-peptide foldamers (Kwon et al., 2015). Thus, we hypothesize that applying a similar RMF may disrupt the Aβ assembly process, thereby reducing senile plaque formation.

In this study, we performed both *in vivo* and *in vitro* experiments to explore the potential application of RMF in AD. Our findings demonstrated that RMF significantly inhibited Aβ amyloid fibril formation and reduced cellular cytotoxicity *in vitro.* Moreover, *in vivo* animal behavior assessments and pathological examinations revealed the substantial potential of RMF in AD treatment.

## MATERIALS AND METHODS

### Preparation of Aβ peptide monomers

Aβ1-42 peptide (Sangon Biotech, China) was dissolved in 1,1,1,3,3,3-hexafluoro-2-propanol (HFIP) (1 mg/mL) and thoroughly dried under a nitrogen stream to obtain peptide films. The films were then dissolved in 10 mmol/L sodium hydroxide and further diluted with phosphate-buffered saline (PBS) to the desired experimental concentration. Control groups for all experiments were treated with PBS containing the same concentration of sodium hydroxide.

### Cell culture

Neuroblastoma SH-SY5Y cells (ATCC) were cultured in a mixture of Minimum Essential Medium (MEM, Gibco, 2193264, USA) and Nutrient Mixture F12 (F12, Gibco, 2276977, USA) containing 10% fetal bovine serum (FBS) (CLARK Bioscience, FB 25015, USA). The cells were grown at 37°C under 5% $CO_2$ conditions and passaged every 3–4 days.

### Animals

APP/PS1 mice are double transgenic mice expressing a chimeric mouse/human amyloid precursor protein (Mo/HuAPP695swe) and a mutant human presenilin 1 (PS1-dE9). All experimental mice were obtained from Nanjing GemPharmatech Co., Ltd. (China). The APP/PS1 mice were divided into sham and 0.4 T RMF groups, with age-matched C57 mice used as wild-type (WT) controls. Starting at 2 months of age, the APP/PS1 mice were exposed to 0.4 T RMF or sham treatment for 3–6 h/day, 5 days/week (Monday–Friday, 2–11 months old, 3 h/day; 11–14 months old, 6 h/day). The WT mice were raised in individual ventilated cages (IVC).

The study was conducted according to the National Institutes of Health Guide for the Care and Use of Laboratory Animals (NIH publication, 8th Edition, 2011). All procedures were approved by the Association of Laboratory Animal Sciences at Anhui Medical University (No. LLSC20232243).

### RMF setup

The RMF equipment setup has been described previously (Ji et al., 2023). Briefly, the apparatus consisted of two assembled permanent magnets (N42M neodymium) fixed on a rotor, with the North and South poles oriented upwards. The magnets exhibited surface magnetic flux densities of approximately 1 T, and the rotor operated at a clockwise frequency of 4.2 Hz. For the sham group, two non-magnetized neodymium assemblies were used, rotating at the same frequency. The entire assembly was placed inside a square wooden box (44 cm×41 cm×52 cm (length×width×height)).

For cellular and protein assays, both the magnetic field exposure and sham group samples were positioned on the surface of the wooden box, enclosed in customized 37°C incubators with a water bath, with or without a 5% $CO_2$ supply (Figure 1A). The maximum magnetic field intensity at the sample location was 0.4 T.

In animal experiments, cages for both the magnetic field exposure and the sham groups (two cages per group) were placed above the wooden boxes. The mice were then exposed to magnetic field or sham conditions for 3–6 h/day, 5 days/week over a period of 12 months. The maximum magnetic field intensity at the position of the mouse feet was 0.4 T.

### Thioflavin T (ThT) assay

ThT powder (1.3 mg) was added to 15 mL of PBS solution to prepare a 275 μmol/L ThT stock solution. Aβ1-42 monomer solution (10 μmol/L) was mixed with ThT solution (25 μmol/L) to a final volume of 200 μL in a 96-well plate. After 24 h of treatment at 37°C with either 0.4 T RMF or sham, fluorescence intensity was measured using a SpectraMax i3x plate reader (Molecular Devices, USA) with excitation and emission wavelengths of 440 nm and 480 nm, respectively (Liu et al., 2020).

### Circular dichroism (CD) spectroscopy

Aβ1-42 solution (50 μmol/L) was treated with 0.4 T RMF or sham at 37°C for 24 h. The sample was then placed in a quartz cuvette and measured at room temperature using a J1 700 circular dichroism spectrometer (JASCO, Japan). Wavelengths were scanned from 190 nm to 260 nm at 1 nm intervals, with spectra averaged over three scans. CD curves were smoothed using GraphPad Prism v9.0 and analyzed using Spectra Manager v.2.0.

### Dynamic light scattering (DLS)

Aβ1-42 solution (50 μmol/L) treated with 0.4 T RMF or sham (24 h, 37°C) was analyzed using a Zetasizer Nano-ZSE particle analyzer (Malvern Instrument, UK) with a laser source at λ=633 nm and a scattering angle of θ=173 degrees. Each sample was measured 10 times, and size distribution was plotted using GraphPad Prism v.9.0.

### Dot blotting assay

Nitrocellulose membranes were cut into 1 cm pieces, onto which was spotted 2 μL of Aβ1-42 solution (50 μmol/L, treated with 0.4 T RMF or sham at 24 h and 37°C). The membranes were air-dried, and incubated with 5% bovine serum albumin for 30 min at room temperature, followed by incubation with A11 (Thermo Fisher, AHB0052, USA) (1:1 000) and 6E10 (Covance, SIG-39320, USA) antibodies (1:1 000) overnight at 4°C. The A11 antibody is specific to soluble oligomers (Pujadas et al., 2014) and the 6E10 antibody can detect all types of Aβ proteins (Yang et al., 2017). After washing with

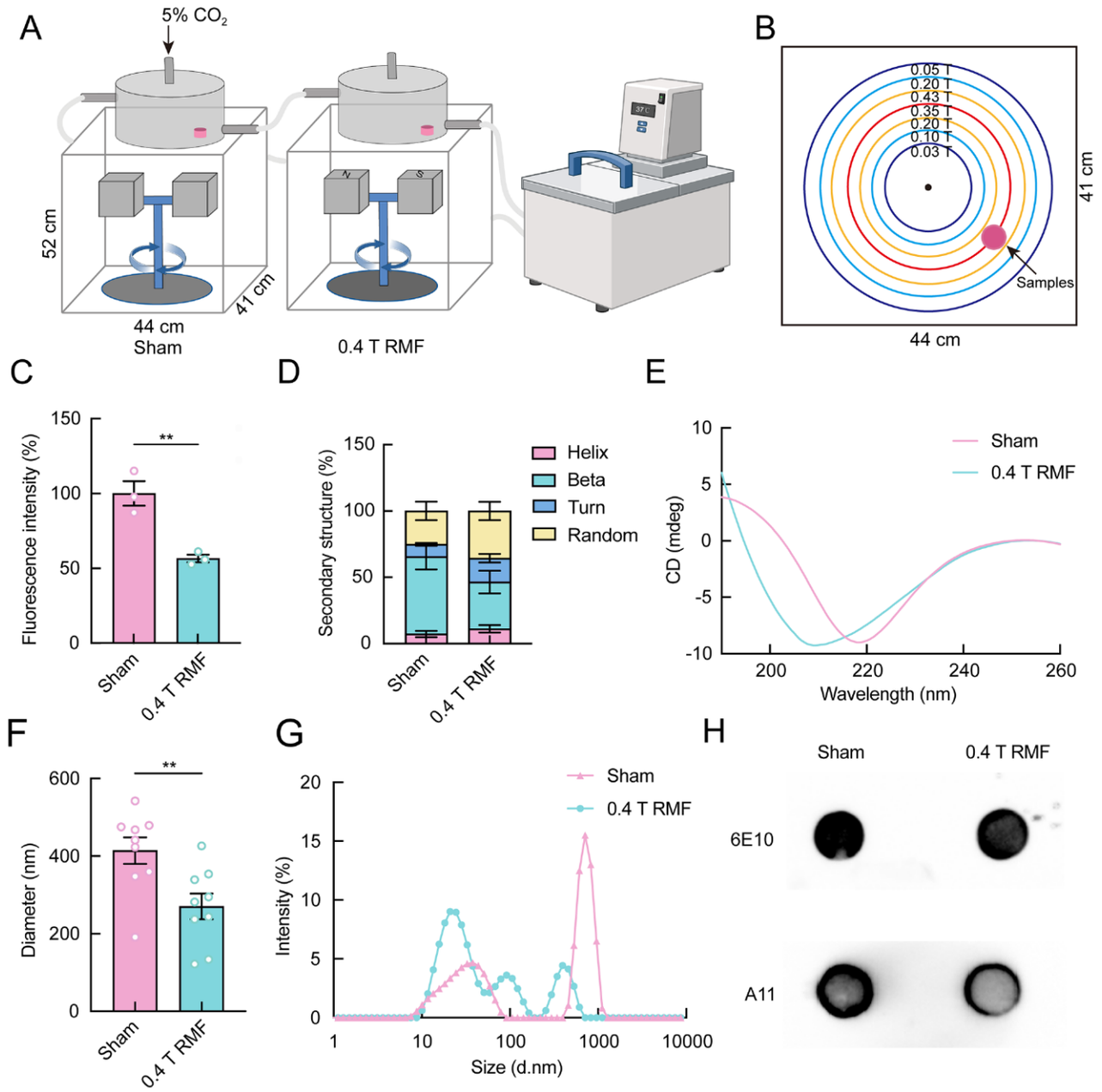



**Figure 1 RMF inhibits Aβ amyloid fibril formation *in vitro***

A: Illustration of experimental setup for peptide and cellular experiments. Non-magnetized and magnetized neodymium were used to construct the sham and RMF instruments, respectively. Surface intensity of the magnetized neodymium for RMF was ~1 T, while the intensity at the experimental samples was ~0.4 T Max. B: Measured magnetic flux density distribution on the surface of the instrument. Cells and peptides were placed at the 0.4 T position for most experiments. C: Aβ1-42 aggregation was monitored by ThT fluorescence assay with and without 0.4 T RMF treatment. D: Distribution ratio of different protein structures in Aβ1-42 solution after 24 h of sham or 0.4 T RMF treatment. Data are mean±SEM, $n$=3. E: Circular dichroism spectra of Aβ1-42 solution treated with sham or 0.4 T RMF for 24 h. F: DLS measurement the Aβ1-42 particle size after 24 h of treatment with and without 0.4 T RMF. Data are mean±SEM, $n$=9. G: DLS showing particle size distribution of Aβ1-42 after sham or 0.4 T RMF treatment for 24 h. H: Representative dot blot bands of Aβ monomers and oligomers. $^{*}$: $P$<0.05; $^{**}$: $P$<0.01.

TBST, the membranes were incubated with secondary antibodies (1:1 000) for 40 min at room temperature. The membranes were then washed and exposed for chemiluminescent detection using an imaging system.

**Cell viability assay**

SH-SY5Y cells were seeded at a density of $1\times10^4$ cells/well in a 96-well plate overnight. After adhering, the medium was replaced with Aβ1-42 solution at different concentrations, and the cells were treated with 0.4 T RMF and sham for 24 h. Cell viability was detected using a Cell Counting Kit-8 (CCK-8) (MedChemExpress, HY-K0301, USA). After incubating each well with 10 μL of CCK-8 solution for 1 h, absorbance was measured at 450 nm using a SpectraMax i3x plate reader (Molecular Devices, USA).

**Cell live/dead staining**

Cells were seeded in small culture plates (0.8 cm diameter) and treated with or without Aβ1-42. After RMF treatment for different durations, the cells were collected and centrifuged at

1 000 ×*g* for 5 min at room temperature. An appropriate volume of calcein acetoxymethyl ester (calcein AM)/propidium iodide (PI) detection working solution was then added according to the manufacturer's instructions. The samples were then incubated at 37°C in the dark for 30 min before analysis using a fluorescence microscope (Olympus, SZX10, Japan).

**Flow cytometry apoptosis analysis**

SH-SY5Y cells were seeded at a density of $3\times10^5$ cells/dish in a cell culture dish (3 cm diameter) and incubated overnight at 37°C. After adhering, the medium was replaced with Aβ1-42 solution (20 μmol/L) and the cells were treated with 0.4 T RMF or sham for 24 h. Apoptosis was detected using an Annexin V-FITC Apoptosis Detection Kit (BD Biosciences, 0076884, USA). Flow cytometry was performed using a Cyto FLEX flow cytometer (Beckman Coulter, USA).

**Open field test (OFT)**

Mice were placed in a white polyvinyl chloride (PVC) open field apparatus (SA215, SANS, China), consisting of a square area divided into four equal zones (40 cm×40 cm×40 cm (length×width×height)), with a central area (30 cm×30 cm (length×width)) and a peripheral area. The apparatus was cleaned before each trial, and the mice were placed in the center of the square. The ANY-Maze Video Tracking System (Stoelting, USA) was used to record the movement trajectories of mice within the central area for 5 min, measuring movement distance, average movement speed, and time spent in the central area.

**Novel object recognition test (NORT)**

After a 24 h interval following the OFT, the mice were returned to the same square area. Two identical objects in shape and color were placed within the area, and the mice were allowed to explore these objects for 10 min. After 2 h, one of the objects was replaced with a new object (different shape and color), and the mice were again allowed 10 min to explore. During training, the time spent exploring the familiar object was denoted as T1, and the time spent exploring the novel object was denoted as T2. The recognition index (RI) was calculated using the formula to assess the cognitive level of the mice:

$$RI = T2/(T1+T2)\times 100\% \quad (1)$$

**Morris water maze (MWM) experiment**

The experiment was conducted in a circular water pool (SA201, SANS, China) filled with non-toxic water containing white dye, maintained at 25°C, with a diameter of 120 cm. A movable circular platform (8 cm diameter) was submerged 1.5 cm beneath the surface of the water within the target quadrant. During the initial training phase, mice were placed randomly into the pool from four different directions and given 60 s to locate the hidden platform. If a mouse failed to find the platform within the allotted time, it was guided to the platform and allowed to remain there for around 15 s. This training was conducted over 5 days, with time taken to find the platform, swimming speed, and swimming path recorded. On day 6, the platform was removed, and the mice were placed in the pool from the opposite direction to the original platform location and given 60 s to find the original platform position. Movement, time taken to reach the target quadrant, and former location of the platform were recorded within 60 s. The ANY-Maze Video Tracking System (Stoelting, USA) was used to record data during the test period. Movement paths were analyzed using Pathfinder (Cooke et al., 2019).

**Immunofluorescence**

Following anesthesia, mice were perfused with saline, followed by 4% paraformaldehyde (PFA). Organ tissues were placed in 4% PFA at 4°C overnight. A semi-automatic microtome (Leica Biosystems RM2245, Germany) was used to section the tissues into 5 μm slices for subsequent experiments. Mouse brain tissue sections were permeabilized with 0.5% Triton X-100 for 10 min at room temperature. After blocking, the sections were incubated overnight at 4°C with antibodies 6E10 (1:500) and IBA1 (1:500). The following day, the sections were incubated with secondary antibodies (1:1 000 ) for 1 h at room temperature, and 4',6-diamidino-2-phenylindole (DAPI) was used to stain the cell nuclei. Finally, the sections were examined under a Nikon TS100 microscope (Nikon, Japan).

**Thioflavin S (Thio S) staining**

After dewaxing, brain tissue sections were washed, incubated with 0.5% Thio S dissolved in 50% ethanol for 20 min at room temperature, washed twice in 80% ethanol (10 s each time), and finally rinsed with $ddH_2O$. After mounting, the sections were examined under a Nikon TS100 microscope (Nikon, Japan).

**Hematoxylin and eosin (H&E) staining**

After dewaxing, mouse organ sections were stained with H&E, decolorized with alcohol, rinsed with water, and subjected to ethanol dehydration. Finally, the sections were mounted and examined under a Nikon TS100 microscope (Nikon, Japan).

**Nonalcoholic fatty liver disease (NAFLD) activity score (NAS)**

The NAS was used to assess NAFLD severity, providing a semiquantitative assessment of four histological features: steatosis (0–3), lobular inflammation (0–2), hepatocyte ballooning (0–2), and fibrosis (0–4) (Kleiner et al., 2005).

**Oil red O staining**

Mouse liver tissues were embedded in optical coherence tomography (OCT) compound, and frozen slices (5 μm) were prepared at −20°C. A saturated Oil Red O solution was dissolved in isopropyl alcohol and distilled water at a ratio of 3:2 (v:v). After filtration, frozen sections were stained in dilute Oil Red O solution for 6 h at room temperature. The sections were then rinsed with 60% isopropyl alcohol aqueous solution three times and running water once. The frozen sections were counterstained with hematoxylin solution for 1–2 min and washed with water. The stained sections were sealed with neutral gelatin and photographed using a Nikon TS100 microscope (Nikon, Japan).

**Enzyme linked immunosorbent assay (ELISA)**

Malondialdehyde (MDA) and superoxide dismutase (SOD) levels in the mouse hippocampus and medial prefrontal cortex (mPFC) were determined according to the manufacturer's instructions (Aimeng Youning, China). Absorbance was measured at 450 nm using a SpectraMax i3x plate reader (Molecular Devices, USA).

**RNA sequencing (RNA-seq) analysis**

After anesthesia, the mice were perfused with saline, and hippocampal tissue was isolated and stored at −80°C. Total RNA was extracted using Trizol (15596018, Thermo Fisher,

USA). Transcriptomic analysis was conducted by LC-BioTechnology (China). The generated transcriptome data were processed using StringTie and Ballgown to calculate fragments per kilobase million (FPKM) values for assessing gene expression levels. Gene Ontology (GO) enrichment analysis of differentially expressed genes (DEGs) was also conducted by LC-BioTechnology Co., Ltd. (https://www.omicstudio.cn/tool).

**Statistical analysis**

All statistical analyses were performed using GraphPad Prism v.9.0. Experimental data are presented as mean±standard error of the mean (SEM). One-way or two-way analysis of variance (ANOVA) or two-tailed unpaired *t*-tests were used to calculate *P*-values for comparisons. $P<0.05$ was considered statistically significant.

## RESULTS

**0.4 T RMF inhibits Aβ amyloid fibril formation *in vitro***

To elucidate the impact of RMF on Aβ amyloid aggregation, we used RMF instruments consisting of a pair of neodymium magnets, with non-magnetized neodymium serving as a sham control, and equipped with a temperature and gas control system (Figure 1A) (Ji et al., 2023). The Aβ1-42 solution was placed in the instrument, with a magnetic field intensity of approximately 0.4 T in the RMF group (Figure 1B). The presence of β-folded structures, characteristic of amyloid proteins, was assessed using ThT fluorescence analysis, a widely adopted method for amyloid fibril identification (Abeyawardhane et al., 2018; Younan & Viles, 2015). Results showed that the ThT fluorescence intensity of the Aβ1-42 solution treated with 0.4 T RMF decreased by about 43% compared to the sham group (Figure 1C). Given that the progression of Aβ aggregation from soluble monomers to insoluble fibrils involves a conformational shift from α-helices to β-sheets (Ding et al., 2003), CD spectra were employed to examine the distribution of protein secondary structures in Aβ1-42 monomer solutions (100 μmol/L). The sham group primarily exhibited β-sheets as the secondary structure, accounting for approximately 58.3%. In contrast, the β-sheets content of the Aβ1-42 monomer solution treated with 0.4 T RMF decreased by 25.2% compared to the sham group (Figure 1D, E). The DLS experiments revealed that the average particle diameter of the Aβ1-42 solution (100 μmol/L) treated with 0.4 T RMF was smaller than that of the sham group (Figure 1F). Additionally, the sham group exhibited a higher percentage of protein distribution in the large diameter area (Figure 1G). Dot blotting revealed a higher A11 level in the sham group compared to the 0.4 T RMF group (Figure 1H). These findings demonstrate the ability of 0.4 T RMF to inhibit the aggregation of Aβ1-42 monomeric protein under *in vitro* conditions at 37°C.

**0.4 T RMF mitigates Aβ-induced cytotoxicity *in vitro***

We conducted *in vitro* experiments using the human neuroblastoma cell line SH-SY5Y to evaluate the effects of RMF on Aβ1-42-induced cytotoxicity, as depicted in Figure 1A.

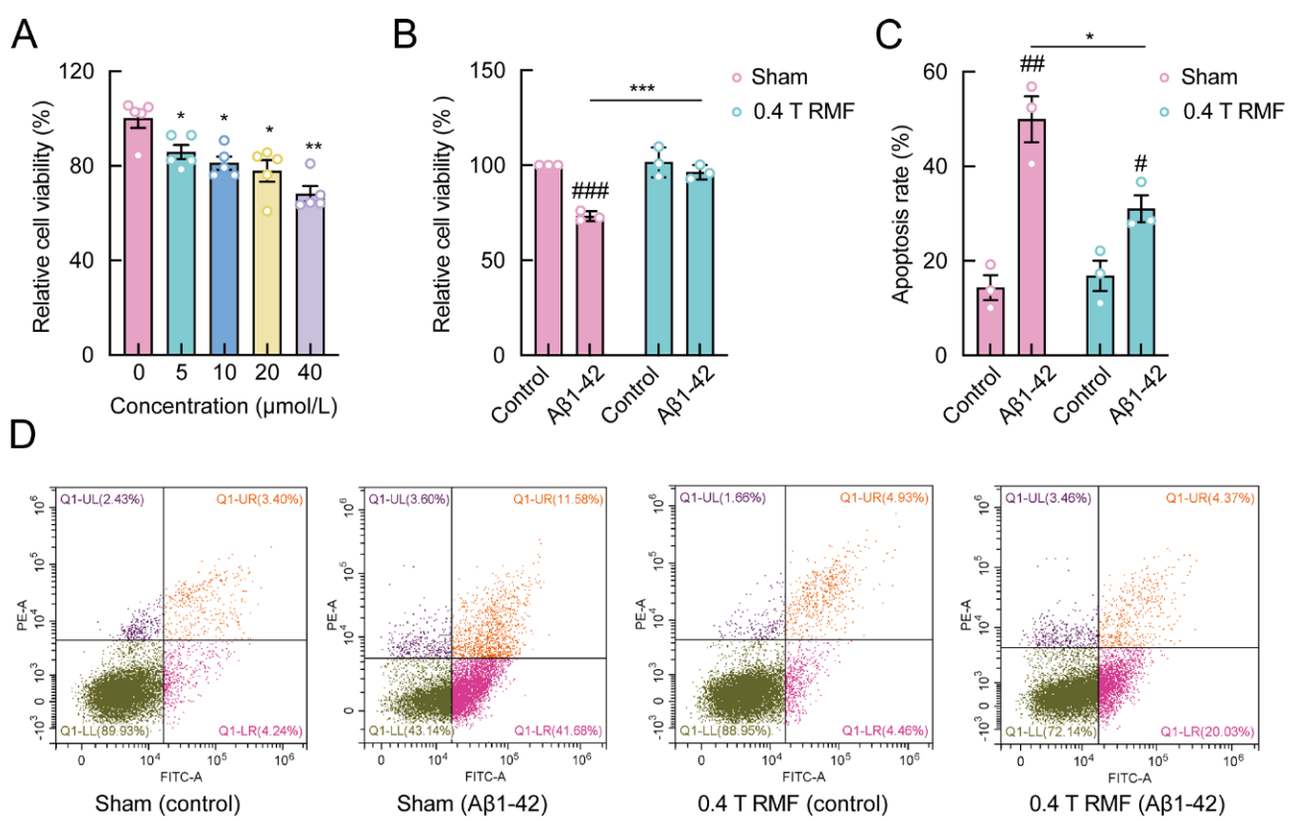



**Figure 2 RMF reduces Aβ-induced cytotoxicity *in vitro***

A: Cell viability of SH-SY5Y cells treated with different concentrations of Aβ1-42 solution after 24 h. Data are mean±SEM, $n=5$. $^{*}$: $P<0.05$; $^{**}$: $P<0.01$. B: Viability of SH-SY5Y cells treated with or without Aβ1-42 solution (20 μm) after treatment with sham or 0.4 T RMF for 24 h. C: Apoptosis rate of SH-SY5Y cells treated with or without Aβ1-42 solution (20 μm) after treatment with sham or 0.4 T RMF for 24 h. Data are mean±SEM, $n=3$. $^{*}$: $P<0.05$; $^{**}$: $P<0.01$; $^{\#}$: $P<0.05$, and $^{\#\#}$: $P<0.01$ compared to control group. D: Representative flow cytometry images of sham and 0.4 T RMF-treated Aβ1-42 solution after 24 h.

Before RMF exposure, the SH-SY5Y cells were treated with different concentrations of Aβ1-42 protein monomer solution, and relative cell viability was determined after 24 h of incubation at 37°C. Results show that the relative cell viability decreased with increasing concentrations of Aβ1-42 monomer solution: 85.85% (5 μmol/L), 81.17% (10 μmol/L), 77.90% (20 μmol/L), and 68.17% (40 μmol/L) (Figure 2A). A concentration of 20 μmol/L was selected for subsequent experiments. Live/dead staining with calcein-AM and PI was performed to differentiate between live and dead cells. SH-SY5Y cells treated with Aβ1-42 and exposed to 0.1 T or 0.4 T RMF exhibited higher cell viability compared to the sham group, consistently observed across all three timepoints tested (24, 48, and 72 h). Notably, the 0.4 T RMF group showed greater cell viability than the 0.1 T RMF group (Supplementary Figure S1). Specifically, treatment with 0.4 T RMF increased SH-SY5Y cell viability by 23.1% compared to the sham group (Figure 2B). Additionally, flow cytometry revealed a 19.6% reduction in apoptosis in cells treated with 20 μmol/L Aβ monomer solution and exposed to 0.4 T RMF (Figure 2C, D). These results indicate that 0.4 T RMF can reduce Aβ1-42 aggregate-induced cytotoxicity in SH-SY5Y cells.

**0.4 T RMF improves motor and exploration abilities in APP/PS1 mice**

We further examined the impact of RMF on reducing Aβ1-42 aggregation in the brains of 2-month-old male APP/PS1 mice based on *in vivo* experiments (Figure 3A). The mouse cages were positioned on the RMF and sham instruments, as described previously (Ji et al., 2023). After 12 months of RMF exposure, no significant differences in body weight were observed (Supplementary Figure S2A). The APP/PS1 mice consumed slightly more food and water compared to the WT group (Supplementary Figures S2B, C). In the OFT and NORT (Figure 3B) experiments, no significant differences were detected in motor, exploratory, or non-spatial memory abilities among the three groups at 2 months of age. However, the APP/PS1 mice appeared more active than the WT healthy mice (Supplementary Figure S3A–D), possibly due to aggressive behavior (Pugh et al., 2007). At 6 months of age, no obvious differences in behavioral tests were observed among the three groups (Supplementary Figure S3E–H). At 11 months of age, there was a non-significant trend towards improved motor, exploratory, and non-spatial memory abilities in the RMF group compared to the sham group (Supplementary Figure S3I–L). Therefore, we increased the RMF exposure time from 3 h/day to 6 h/day (5 days/week). At 14 months, the RMF-treated mice exhibited restored motor, exploration, and non-spatial memory abilities, similar to the WT healthy group (Figure 3C, D). In the OFT, the RMF group showed significantly higher time in the center area, total distance traveled, and mean speed compared to the sham group (Figure 3E–G). Based on the NORT, the cognitive index of the RMF group reached levels similar to the WT healthy group, with significantly improved recognition memory compared to the sham group (Figure 3H).

**0.4 T RMF significantly alleviates spatial memory impairments in APP/PS1 mice**

We employed the MWM to assess the spatial learning and memory abilities of the APP/PS1 mice (Figure 4A). Following RMF exposure, the 14-month-old APP/PS1 mice exhibited improved escape latency compared to the sham group (Figure 4B). During the learning phase (days 1–5), no significant differences were observed in swimming speed or distance among the three groups (Figure 4C, D). However, the RMF group exhibited significantly restored memory and spatial learning abilities on day 6 (Figure 4E–H). The MWM trajectories are shown in Figure 4J. We performed subsequent analysis of the search strategies of mice after the learning phase (days 1–5). Using Pathfinder, we categorized all mouse movements into nine search strategies (Figure 4I) (Brody & Holtzman, 2006). Analysis revealed a daily increase in effective strategies in the WT and RMF groups over the five training days, whereas the sham group demonstrated a decline in effective training strategies on days 4 and 5 (Figure 4K). These findings indicate that after 12 months of RMF treatment, spatial memory and learning abilities were restored in APP/PS1 mice, suggesting the potential of RMF in alleviating cognitive impairments in AD mice.

**0.4 T RMF reduces amyloid plaque deposition and microglial activation in the brains of APP/PS1 mice**

We performed Thio S staining to examine amyloid plaques in the brains of APP/PS1 mice. Results revealed reduced deposition of Aβ1-42 protein in both the mPFC (Figure 5A, B) and hippocampus (Figure 5C, D) of APP/PS1 mice treated with RMF. Given that abnormal morphology and proliferation of microglia are characteristic of AD histopathology (Hansen et al., 2018; Hickman et al., 2008), we used specific antibodies for Iba-1 to label microglia and 6E10 to label amyloid plaques. In the sham group, the mPFC and hippocampus of APP/PS1 mice exhibited extensive microglial activation and Aβ protein accumulation. In contrast, RMF treatment significantly reduced 1ba1 activation and Aβ protein aggregation in these brain regions (Figure 5E–H, Supplementary Figures S4A–D). In summary, treatment of APP/PS1 mice with RMF for 12 months reduced the deposition of Aβ protein and decreased microglial activation in the brains of APP/PS1 mice.

**0.4 T RMF reduces oxidative stress in APP/PS1 mouse brains and lipid deposition in the liver**

To explore the mechanisms underlying the reduction of Aβ aggregation in the brains of AD mice, we isolated hippocampal tissue from APP/PS1 mice and conducted RNA-seq analysis. Results identified 564 up-regulated and 700 down-regulated DEGs in the hippocampal tissue after RMF treatment compared to the sham group (Figure 6A). GO enrichment analysis indicated that RMF treatment was associated with signaling pathways related to apoptosis, consistent with our previous experimental results. Moreover, GO pathway analysis suggested that RMF affected signaling pathways related to oxidative stress and lipid metabolism (Figure 6B). The gene heatmap indicated significant differences in genes related to these pathways (Figure 6C–E). Furthermore, several differences in the expression of genes associated with AD were detected (Figure 6F).

To investigate the association between oxidative stress and RMF, we quantified oxidative stress levels in the hippocampus of mice using ELISA. Results showed that MDA levels were higher in the hippocampus of the sham group compared to the WT group, while the RMF-treated APP/PS1 mice showed reduced MDA levels (Figure 6G). Conversely, SOD levels were lower in the sham group compared to the WT group, while the RMF-treated group displayed an ascending trend (Figure 6H).

Additionally, lipid accumulation and ballooning degeneration were prominent in the livers of APP/PS1 mice in the sham

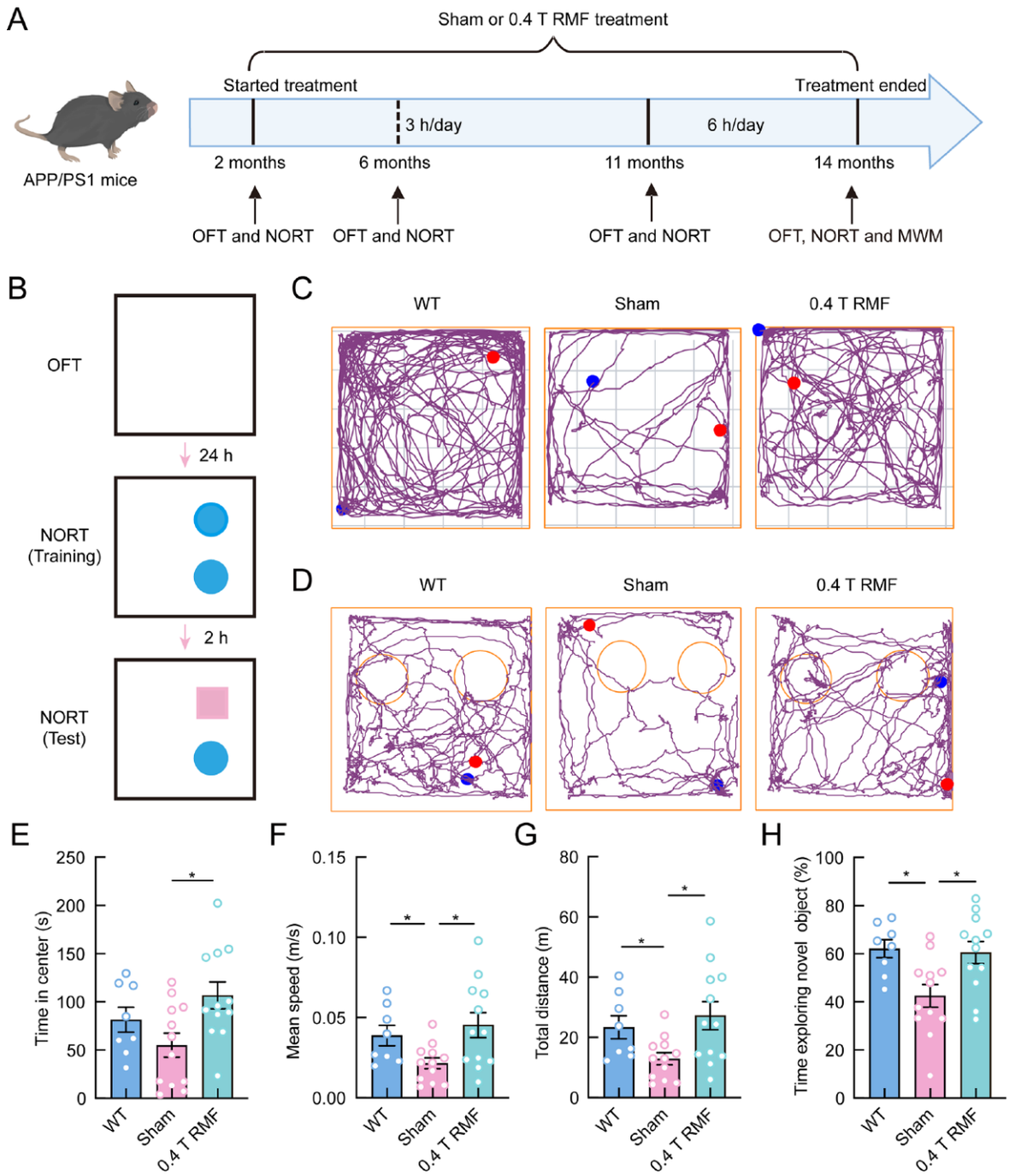



**Figure 3 RMF improves motor and exploration abilities in APP/PS1 mice**

A: Experimental design. APP/PS1 mice were exposed to a sham or RMF device for 12 months, with magnetic field exposure of 3 h/day (weekdays) from 2–11-months-old and 6 h/day (weekdays) from 11–14-months-old. Behavioral experiments were conducted at 2-, 11-, and 14-months-old. B: Illustration of OFT and NORT device. C: Representative mouse trajectories in OFT. D: Representative mouse trajectories in NORT. E–H: Behavioral tests at 14-months-old. E: Time spent by mice exploring central area in OFT. F: Average movement speed of mice in OFT. G: Total movement distance of mice in OFT. H: Percentage of time spent exploring novel objects in NORT. Data are mean±SEM, WT group, $n$=8; Sham and RMF group, $n$=12). $^{*}$: $P$<0.05; $^{**}$: $P$<0.01.

group. Interestingly, RMF-treated mice exhibited significantly reduced lipid accumulation, nearly reaching levels observed in healthy mice. Evaluation of NAS revealed significantly higher scores in the sham group, while RMF-treated mice exhibited scores similar to the WT group (Figure 6I, K). Additionally, oil red O staining confirmed the substantial reduction of lipid accumulation in the livers of RMF-treated APP/PS1 mice (Figure 6J, L). No significant differences were observed in the heart, spleen, or lung tissues among the three groups of mice (Supplementary Figure S5). This suggests that treatment with RMF may alleviate damage in the liver, brain and kidney tissues of APP/PS1 mice.

## DISCUSSION

AD is one of the most prevalent neurodegenerative ailments linked with aging (Singh, 2020) and has been a focal point for diverse therapeutic strategies in clinical contexts spanning

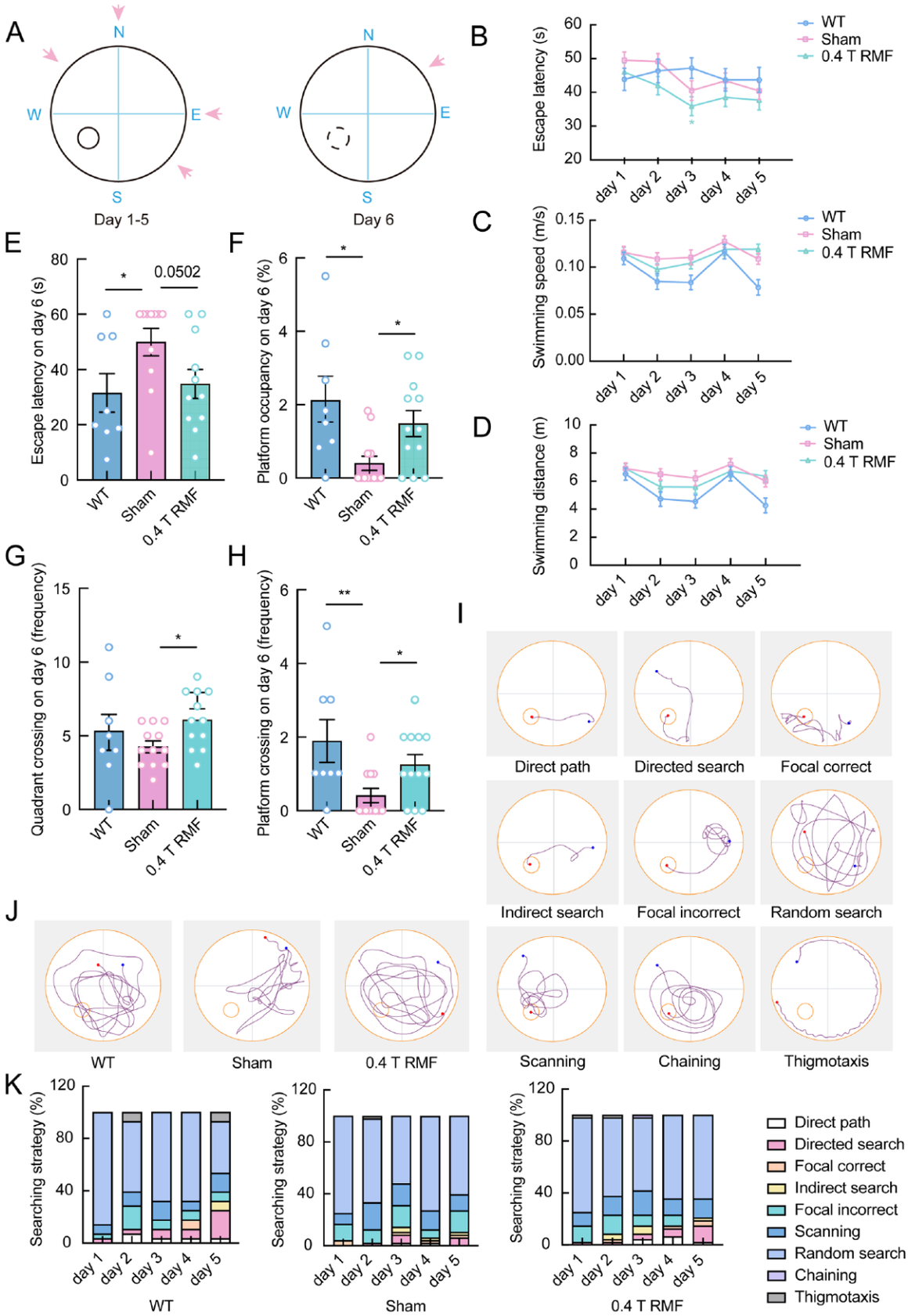



**Figure 4 RMF significantly alleviates spatial memory impairments in APP/PS1 mice**

A: Illustration of MWM device. B: Escape latency during training days. C: Swimming speed during training days. D: Swimming distance during training days. E: Escape latency during probe trial. F: Percentage of time spent on platform during probe trial. G: Number of platform crossings during probe trial. H: Number of target quadrant crossings during probe trial. I: Different types of search strategies during training days. J: Representative mouse trajectories in MWM. K: Percentage of different search strategies. Data are mean±SEM, WT group, $n$=8; Sham and RMF group, $n$=12). $^{*}$: $P$<0.05, $^{**}$: $P$<0.01.

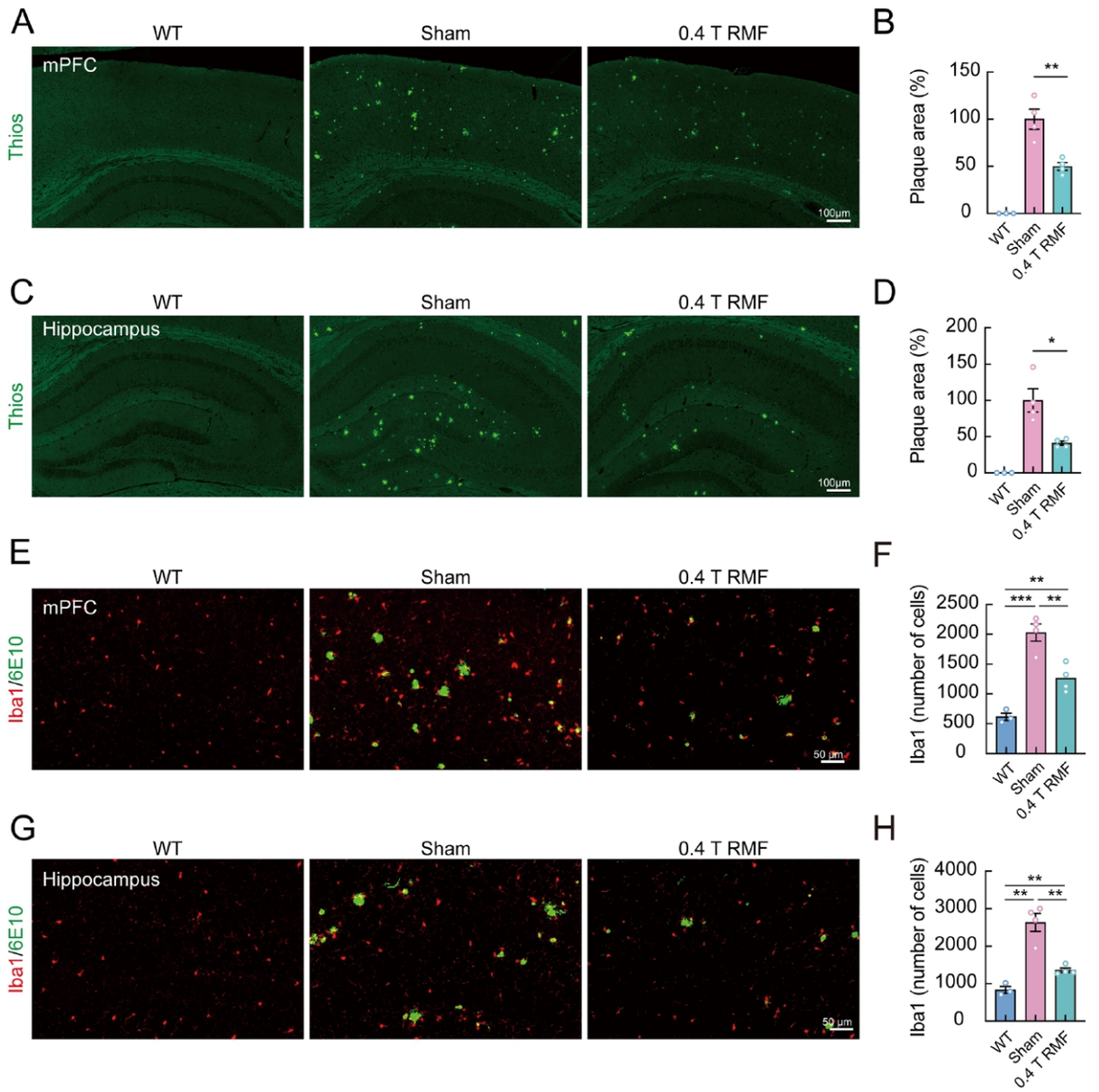



**Figure 5 RMF reduces amyloid plaque deposition and microglial activation in APP/PS1 mouse brain**

A: Thio S staining in mPFC of WT, sham, and 0.4 T RMF-treated groups. B: Relative area of Aβ plaque in mPFC of WT, sham, and 0.4 T RMF-treated groups. C: Thio S staining in hippocampus of WT, sham, and 0.4 T RMF-treated groups. D: Relative area of Aβ plaque in hippocampus of WT, sham, and 0.4 T RMF-treated groups. E: Immunofluorescence with anti-Iba1 (red) and E610 (green) antibody in mPFC of WT, sham, and 0.4 T RMF-treated groups. F: Number of Iba1-positive microglia in mPFC of WT, sham, and 0.4 T RMF-treated groups. G: Immunofluorescence with anti-Iba1 (red) and E610 (green) antibodies in hippocampus of WT, sham, and 0.4 T RMF-treated groups. H: Number of Iba1-positive microglia in hippocampus of WT, sham, and 0.4 T RMF-treated groups. Data are mean±SEM, WT group, $n$=3; Sham and RMF group, $n$=4). *: $P$<0.05; **: $P$<0.01.

several decades (Andrieu et al., 2015; Fish et al., 2019). Most drugs approved by the US Food and Drug Administration (FDA) for treating AD aim to alleviate symptoms without altering disease progression and are accompanied by side effects such as headaches and nausea (2023 Alzheimer's disease facts and figures, 2023). Additionally, their effectiveness is limited by issues such as poor solubility and difficulty in crossing the blood-brain barrier (BBB) (Karthivashan et al., 2018). Nonpharmacological interventions are commonly used to alleviate agitation and aggressive behavior in AD patients, often proving more effective and safer than pharmacological interventions (2023 Alzheimer's disease facts and figures, 2023). Research has shown that magnetic fields, such as electromagnetic fields and transcranial magnetic stimulation, may reduce neuronal damage and cognitive impairment in AD (Arendash et al., 2010; Huang et al., 2017). Although prolonged exposure to high-gradient magnetic fields has been shown to have adverse effects on severely diabetic mice (Yu et al., 2023), moderate-intensity RMF is not associated with any reported side effects. Based on *in vivo* and *in vitro* experiments, we discovered that RMF can disrupt Aβ assembly and reduce amyloid plaque deposition in the brains of AD mice, which restored motor ability and significantly alleviated cognitive impairment (Figure 7).

We propose two primary mechanisms by which RMF affects

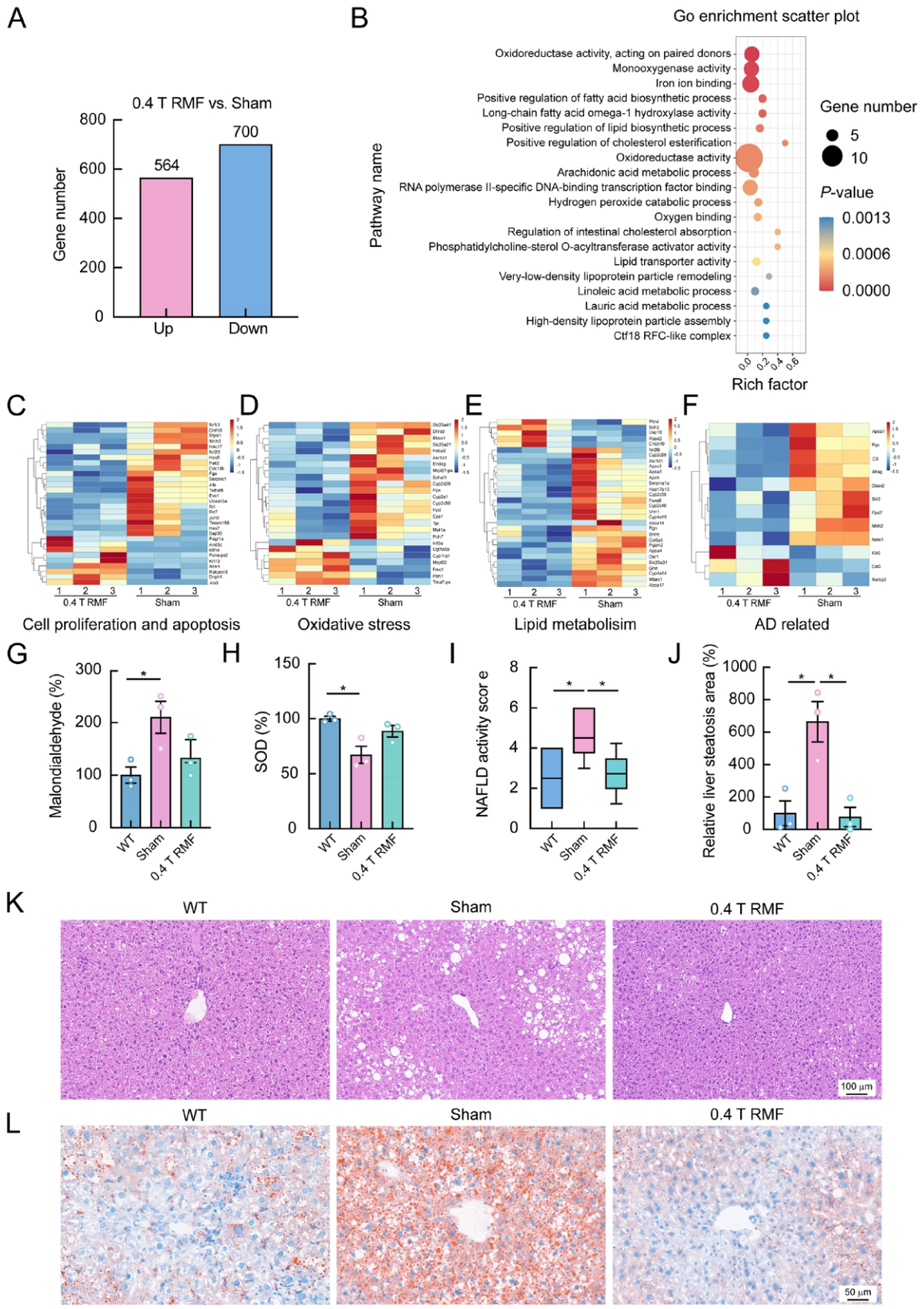



**Figure 6 RMF reduces oxidative stress in APP/PS1 mouse brain and lipid deposition in the liver**

A–F: Gene number, GO term, and heatmap of differentially expressed genes (DEGs) in the hippocampus of 14-month-old APP/PS1 mice after treatment with sham or RMF, revealed by RNA-seq. G, H: ELISA measurement of MDA and SOD levels. I, J: NAS and relative steatosis area in the liver of WT, sham, and RMF-treated mice. K: Representative images of H&E staining of liver of WT, sham, and RMF-treated mice. L: Representative images of oil red O staining of liver of WT, sham, and RMF-treated mice. Data are mean±SEM, $n$=3. $^{*}$: $P$<0.05; $^{**}$: $P$<0.01.

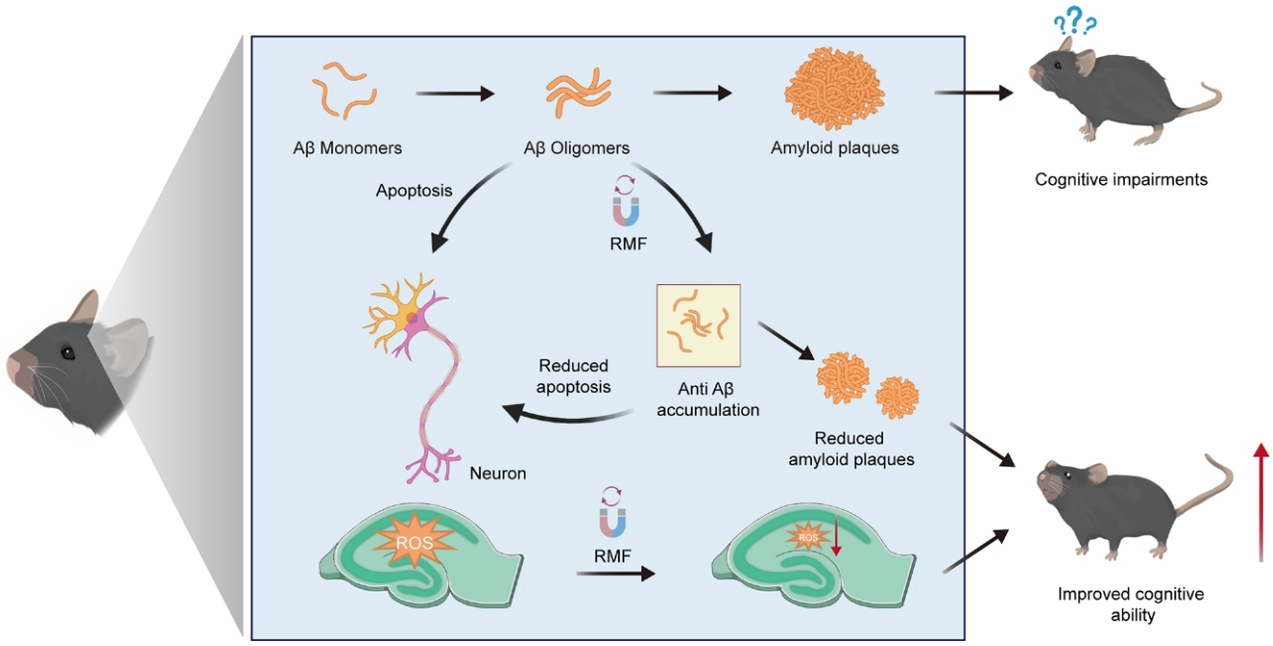



**Figure 7 RMF reduces Aβ protein aggregation and alleviates cognitive impairment in AD mice**

Aβ assembly. The first mechanism involves diamagnetic anisotropy of the peptide. Aβ1-42 monomers, comprising 42 amino acid residues, feature two α-helix segments linked by a regular type I β-turn structure (Kaur et al., 2020). Peptide bonds exhibit inherent diamagnetic anisotropy, generating torque that align proteins within a magnetic field. When peptide bonds are organized within a uniform structural feature (α-helix or β-sheet), the cumulative anisotropy reflects the diamagnetic magnetization of each peptide bond (Pauling, 1979). These factors may induce shifts in the arrangement and orientation of Aβ protein monomers under RMF, ultimately impeding their aggregation.

The second mechanism involves the induced electric field. Saikia et al. (2019) proposed that low-intensity electric fields can suppress peptide aggregation without affecting their natural structure, whereas static magnetic fields of approximately 0.8 T show minimal ability to induce conformational changes. Furthermore, they stated that electromagnetic fields can align large molecules or dipoles along the axis of the applied field (Saikia et al., 2019). Our preliminary studies using the same set of devices demonstrated that RMF can hinder F-actin assembly via induced electric fields, effectively inhibiting breast cancer cell adhesion, migration, and metastasis in mice (Ji et al., 2023). This observation sparked our curiosity in determining whether RMF can also impede Aβ aggregation, a self-assembling protein. We hypothesize that RMF-induced electric fields can directly interact with molecular dipole moments to disrupt Aβ aggregation.

Furthermore, we propose that the alleviating effects of RMF on AD mice may be caused by multiple reasons, not limited to Aβ assembly. Firstly, our results indicated that RMF treatment reduced oxidative stress levels in the hippocampus of APP/PS1 mice. Aggregation of Aβ protein can cause oxidative stress and promote cell apoptosis. Oxidative stress accelerates AD progression by damaging intracellular macromolecules and regulating the post-translational modification of APP protein and the activity of its secreted enzymes (Lehtinen & Bonni, 2006; Schieber & Chandel, 2014). Several studies have shown that magnetic fields can lower oxidative stress levels in cells and mouse tissues (Feng et al., 2022; Frachini et al., 2024). Thus, the reduction of oxidative stress likely contributes significantly to the positive effects of RMF on AD mice. Secondly, our results also showed that RMF affected lipid metabolism, leading to notable changes in the liver. However, the primary effect of RMF on AD mice seems to be the inhibition of Aβ protein aggregation, as shown by both *in vivo* and *in vitro* experiments, rather than changes in lipid metabolism. Despite this, we cannot exclude the potential contribution of lipid metabolism in AD. Future studies using more specialized devices are necessary to dissect the relative contributions of the brain versus the liver.

Our study has some limitations. Firstly, due to the constraints with the RMF instruments, we were unable to test other RMF parameters. Future research should explore whether different field strengths and frequencies, combined with shorter treatment durations, could enhance therapeutic effects. We hope this will encourage further investigation into the use of magnetic fields for treating neurodegenerative diseases, exploring a variety of intensities and frequencies for potential clinical applications. Secondly, space limitations in the animal facility restricted our study to a single AD model (APP/PS1 mice). Future studies should include more mouse models, such as five familial AD (5×FAD) mice, which express human APP and PSEN1 transgenes with a total of five AD-linked mutations. Thirdly, our study only included male mice. Given the higher incidence of AD in females, it is crucial to examine sex-specific differences in responses to RMF treatment.

In conclusion, our findings suggest that intermittent exposure to moderate-intensity RMF holds promise as a non-invasive, high-penetration physical therapy for AD, capable of alleviating neuronal damage and cognitive impairment. While multiple factors contribute to the development of AD, we are optimistic that this “incurable” disease may eventually become preventable or manageable. RMF, either alone or in combination with other pharmaceutical or dietary interventions, could represent a novel treatment strategy worth

exploring in future studies.

## DATA AVAILABILITY

The data presented in the study have been deposited in the National Genomics Data Center (NGDC) (accession number: CRA016912), Science Data Bank (https://doi.org/10.57760/sciencedb.07903), and NCBI database (accession number: GSE269222).

## SUPPLEMENTARY DATA

Supplementary data to this article can be found online.

## COMPETING INTERESTS

The authors declare that they have no competing interests.

## AUTHORS' CONTRIBUTIONS

X.Z. and R.W.G. designed the experiments. R.W.G., W.J.X., B.Y., S.C., X.M.J., X.Y.W., and M.Z. performed the experiments. X.Z. and R.W.G. wrote the manuscript with editing by all authors. All authors read and approved the final version of the manuscript.

## ACKNOWLEDGMENTS

We thank Ding Joe Wang for cartoon illustrations.

## REFERENCES

[Anonymous]. 2023. 2023 Alzheimer's disease facts and figures. *Alzheimer's & Dementia*, **19**(4): 1598–1695.

Abeyawardhane DL, Fernández RD, Murgas CJ, et al. 2018. Iron redox chemistry promotes antiparallel oligomerization of α-synuclein. *Journal of the American Chemical Society*, **140**(15): 5028–5032.

Andrieu S, Coley N, Lovestone S, et al. 2015. Prevention of sporadic Alzheimer's disease: lessons learned from clinical trials and future directions. *The Lancet Neurology*, **14**(9): 926–944.

Arendash GW, Sanchez-Ramos J, Mori T, et al. 2010. Electromagnetic field treatment protects against and reverses cognitive impairment in Alzheimer's disease mice. *Journal of Alzheimer's Disease*, **19**(1): 191–210.

Ballard C, Gauthier S, Corbett A, et al. 2011. Alzheimer's disease. *The Lancet*, **377**(9770): 1019–1031.

Bayer TA, Cappai R, Masters CL, et al. 1999. It all sticks together—the APP-related family of proteins and Alzheimer's disease. *Molecular Psychiatry*, **4**(6): 524–528.

Blennow K, De Leon MJ, Zetterberg H. 2006. Alzheimer's disease. *The Lancet*, **368**(9533): 387–403.

Brody DL, Holtzman DM. 2006. Morris water maze search strategy analysis in PDAPP mice before and after experimental traumatic brain injury. *Experimental Neurology*, **197**(2): 330–340.

Castelletto V, Ryumin P, Cramer R, et al. 2017. Self-assembly and anti-amyloid cytotoxicity activity of amyloid beta peptide derivatives. *Scientific Reports*, **7**: 43637.

Chen GF, Xu TH, Yan Y, et al. 2017. Amyloid beta: structure, biology and structure-based therapeutic development. *Acta Pharmacologica Sinica*, **38**(9): 1205–1235.

Companys-Alemany J, Turcu AL, Schneider M, et al. 2022. NMDA receptor antagonists reduce amyloid-*β* deposition by modulating calpain-1 signaling and autophagy, rescuing cognitive impairment in 5XFAD mice. *Cellular and Molecular Life Sciences*, **79**(8): 408.

Cooke MB, O'leary TP, Harris P, et al. 2019. Pathfinder: open source software for analyzing spatial navigation search strategies. *F1000Research*, **8**: 1521.

Ding F, Borreguero JM, Buldyrey SV, et al. 2003. Mechanism for the α-helix to β-hairpin transition. *Proteins: Structure, Function, and Bioinformatics*, **53**(2): 220–228.

Feng CL, Yu B, Song C, et al. 2022. Static magnetic fields reduce oxidative stress to improve wound healing and alleviate diabetic complications. *Cells*, **11**(3): 443.

Fish PV, Steadman D, Bayle ED, et al. 2019. New approaches for the treatment of Alzheimer's disease. *Bioorganic & Medicinal Chemistry Letters*, **29**(2): 125–133.

Frachini ECG, Silva JB, Fornaciari B, et al. 2024. Static magnetic field reduces intracellular ROS levels and protects cells against peroxide-induced damage: suggested roles for catalase. *Neurotoxicity Research*, **42**(1): 2.

Fu AKY, Hung KW, Yuen MYF, et al. 2016. IL-33 ameliorates Alzheimer's disease-like pathology and cognitive decline. *Proceedings of the National Academy of Sciences of the United States of America*, **113**(19): E2705–E2713.

Gauthier S, Rosa-Neto P, Morais JA, et al. 2021. World Alzheimer Report 2021: Journey through the Diagnosis of Dementia. London: Alzheimer's Disease International.

Graff-Radford J, Yong KXX, Apostolova LG, et al. 2021. New insights into atypical Alzheimer's disease in the era of biomarkers. *The Lancet Neurology*, **20**(3): 222–234.

Hansen DV, Hanson JE, Sheng M. 2018. Microglia in Alzheimer's disease. *Journal of Cell Biology*, **217**(2): 459–472.

Hickman SE, Allison EK, El Khoury J. 2008. Microglial dysfunction and defective β-amyloid clearance pathways in aging Alzheimer's disease mice. *Journal of Neuroscience*, **28**(33): 8354–8360.

Hill RJA, Sedman VL, Allen S, et al. 2007. Alignment of aromatic peptide tubes in strong magnetic fields. *Advanced Materials*, **19**(24): 4474–4479.

Huang ZL, Tan T, Du YH, et al. 2017. Low-frequency repetitive transcranial magnetic stimulation ameliorates cognitive function and synaptic plasticity in APP23/PS45 mouse model of Alzheimer's disease. *Frontiers in Aging Neuroscience*, **9**: 292.

Iwatsubo T, Mann DMA, Odaka A, et al. 1995. Amyloid β protein (Aβ) deposition: Aβ42(43) precedes Aβ40 in down syndrome. *Annals of Neurology*, **37**(3): 294–299.

Ji XM, Tian XF, Feng SA, et al. 2023. Intermittent F-actin perturbations by magnetic fields inhibit breast cancer metastasis. *Research*, **6**: 0080.

Karthivashan G, Ganesan P, Park SY, et al. 2018. Therapeutic strategies and nano-drug delivery applications in management of ageing Alzheimer's disease. *Drug Delivery*, **25**(1): 307–320.

Kaur A, Kaur A, Goyal D, et al. 2020. How does the mono-triazole derivative modulate $A\beta_{42}$ aggregation and disrupt a protofibril structure: insights from molecular dynamics simulations. *ACS Omega*, **5**(25): 15606–15619.

Kleiner DE, Brunt EM, Van Natta M, et al. 2005. Design and validation of a histological scoring system for nonalcoholic fatty liver disease. *Hepatology*, **41**(6): 1313–1321.

Kwon S, Kim BJ, Lim HK, et al. 2015. Magnetotactic molecular architectures from self-assembly of β-peptide foldamers. *Nature Communications*, **6**(1): 8747.

Lehtinen MK, Bonni A. 2006. Modeling oxidative stress in the central nervous system. *Current Molecular Medicine*, **6**(8): 871–881.

Liu FF, Zhao WP, Zhao F, et al. 2020. Dual effect of the acidic polysaccharose ulvan on the inhibition of Amyloid-β protein fibrillation and disintegration of mature fibrils. *ACS Applied Materials & Interfaces*, **12**(37): 41167–41176.

Michaels TCT, Šarić A, Habchi J, et al. 2018. Chemical kinetics for bridging molecular mechanisms and macroscopic measurements of amyloid fibril formation. *Annual Review of Physical Chemistry*, **69**: 273–298.

Pauling L. 1979. Diamagnetic anisotropy of the peptide group. *Proceedings of the National Academy of Sciences of the United States of America*, **76**(5): 2293–2294.

Pugh PL, Richardson JC, Bate ST, et al. 2007. Non-cognitive behaviours in an APP/PS1 transgenic model of Alzheimer's disease. *Behavioural Brain Research*, **178**(1): 18–28.

Pujadas L, Rossi D, Andrés R, et al. 2014. Reelin delays amyloid-beta fibril formation and rescues cognitive deficits in a model of Alzheimer's disease. *Nature Communications*, **5**: 3443.

Saikia J, Pandey G, Sasidharan S, et al. 2019. Electric field disruption of amyloid aggregation: potential noninvasive therapy for Alzheimer's disease. *ACS Chemical Neuroscience*, **10**(5): 2250–2262.

Schieber M, Chandel NS. 2014. ROS function in redox signaling and oxidative stress. *Current Biology*, **24**(10): R453–R462.

Selkoe DJ. 2001. Alzheimer's disease: genes, proteins, and therapy. *Physiological Reviews*, **81**(2): 741–766.

Singh RK. 2020. Recent trends in the management of Alzheimer's disease: current therapeutic options and drug repurposing approaches. *Current Neuropharmacology*, **18**(9): 868–882.

Tiwari S, Atluri V, Kaushik A, et al. 2019. Alzheimer's disease: pathogenesis, diagnostics, and therapeutics. *International Journal of Nanomedicine*, **14**: 5541–5554.

Todorova N, Bentvelzen A, English NJ, et al. 2016. Electromagnetic-field effects on structure and dynamics of amyloidogenic peptides. *The Journal of Chemical Physics*, **144**(8): 085101.

Yang SH, Lee DK, Shin J, et al. 2017. Nec-1 alleviates cognitive impairment with reduction of Aβ and tau abnormalities in APP/PS1 mice. *EMBO Molecular Medicine*, **9**(1): 61–77.

Younan ND, Viles JH. 2015. A comparison of three fluorophores for the detection of amyloid fibers and prefibrillar oligomeric assemblies. ThT (Thioflavin T); ANS (1-Anilinonaphthalene-8-sulfonic Acid); and bisANS (4, 4'-Dianilino-1, 1'-binaphthyl-5, 5'-disulfonic acid). *Biochemistry*, **54**(28): 4297–4306.

Yu B, Song C, Feng CL, et al. 2023. Effects of gradient high-field static magnetic fields on diabetic mice. *Zoological Research*, **44**(2): 249–258.

Zhang PS, Kishimoto Y, Grammatikakis I, et al. 2019. Senolytic therapy alleviates Aβ-associated oligodendrocyte progenitor cell senescence and cognitive deficits in an Alzheimer's disease model. *Nature Neuroscience*, **22**(5): 719–728.

Zhu et al. *Zool. Res.* 2024, 45(4): 937−950
https://doi.org/10.24272/j.issn.2095-8137.2024.021

ZR | Zoological Research

Article Open Access

# TAX1BP1 and FIP200 orchestrate non-canonical autophagy of p62 aggregates for mouse neural stem cell maintenance

Yi-Fu Zhu[1,#], Rong-Hua Yu[2,#], Shuai Zhou[2], Pei-Pei Tang[3], Rui Zhang[2], Yu-Xin Wu[2], Ran Xu[6], Jia-Ming Wei[3], Ying-Ying Wang[2], Jia-Li Zhang[2], Meng-Ke Li[2], Xiao-Jing Shi[4], Yu-Wei Zhang[5], Guang-Zhi Liu[5], Rick F. Thorne[2], Xu Dong Zhang[2,6], Mian Wu[1,2,5,*], Song Chen[2,3,5,*]

[1] *School of Life Sciences*, *Division of Life Sciences and Medicine*, *University of Science and Technology of China*, *Hefei*, *Anhui* 230001, *China*

[2] *Translational Research Institute of Henan Provincial People's Hospital and People''s Hospital of Zhengzhou University*, *Tianjian Laboratory of Advanced Biomedical Sciences*, *Academy of Medical Sciences*, *Zhengzhou University*, *Zhengzhou*, *Henan* 450053, *China*

[3] *Institute of Medicinal Biotechnology*, *Jiangsu College of Nursing*, *Huai'an*, *Jiangsu* 223300, *China*

[4] *Laboratory Animal Center*, *Academy of Medical Science*, *Zhengzhou University*, *Zhengzhou*, *Henan* 450052, *China*

[5] *Henan Key Laboratory of Stem cell Differentiation and Modification*, *Henan Provincial People's Hospital*, *Henan University*, *Zhengzhou*, *Henan* 450053, *China*

[6] *School of Biomedical Sciences and Pharmacy*, *The University of Newcastle*, *NSW* 2308, *Australia*

## ABSTRACT

Autophagy plays a pivotal role in diverse biological processes, including the maintenance and differentiation of neural stem cells (NSCs). Interestingly, while complete deletion of *Fip200* severely impairs NSC maintenance and differentiation, inhibiting canonical autophagy via deletion of core genes, such as *Atg5*, *Atg16l1*, and *Atg7*, or blockade of canonical interactions between FIP200 and ATG13 (designated as FIP200-4A mutant or FIP200 KI) does not produce comparable detrimental effects. This highlights the likely critical involvement of the non-canonical functions of FIP200, the mechanisms of which have remained elusive. Here, utilizing genetic mouse models, we demonstrated that FIP200 mediates non-canonical autophagic degradation of p62/sequestome1, primarily via TAX1BP1 in NSCs. Conditional deletion of *Tax1bp1* in *fip200*$^{hGFAP}$ conditional knock-in (cKI) mice led to NSC deficiency, resembling the *fip200*$^{hGFAP}$ conditional knockout (cKO) mouse phenotype. Notably, reintroducing wild-type TAX1BP1 not only restored the maintenance of NSCs derived from *tax1bp1*-knockout *fip200*$^{hGFAP}$ cKI mice but also led to a marked reduction in p62 aggregate accumulation. Conversely, a TAX1BP1 mutant incapable of binding to FIP200 or NBR1/p62 failed to achieve this restoration. Furthermore, conditional deletion of *Tax1bp1* in *fip200*$^{hGFAP}$ cKO mice exacerbated NSC deficiency and p62 aggregate accumulation compared to *fip200*$^{hGFAP}$ cKO mice. Collectively, these findings illustrate the essential role of the FIP200-TAX1BP1 axis in mediating the non-canonical autophagic degradation of p62 aggregates towards NSC maintenance and function, presenting novel therapeutic targets for neurodegenerative diseases.

**Keywords:** Non-canonical autophagy; TAX1BP1; FIP200; p62; Aggregates; Neural stem cell

## INTRODUCTION

Neurogenesis, responsible for producing all neuronal lineages in the central nervous system (CNS) —including neurons, astrocytes, and oligodendrocytes —is primarily active during development but persists into adulthood to maintain tissue homeostasis. Analogous to hematopoiesis, neurogenesis constitutes a hierarchical differentiation cascade involving multipotent progenitors termed neural stem cells (NSCs) (Casares-Crespo et al., 2018; Fleming & Rubinsztein, 2020; Zhao et al., 2008). Rodent research has established that adult neurogenesis occurs in the subventricular zone (SVZ) of the lateral ventricle and within the dentate gyrus (DG) subgranular zone (SGZ) of the hippocampus (Doetsch et al., 1999; Gage, 2000; Palmer et al., 1997). However, the debate on whether adult NSCs have specific locational functions persists (Becher & Holland, 2010), with some studies suggesting that adult

This is an open-access article distributed under the terms of the Creative Commons Attribution Non-Commercial License (http://creativecommons.org/licenses/by-nc/4.0/), which permits unrestricted non-commercial use, distribution, and reproduction in any medium, provided the original work is properly cited.

Copyright ©2024 Editorial Office of Zoological Research, Kunming Institute of Zoology, Chinese Academy of Sciences

Received: 22 January 2024; Accepted: 30 April 2024; Online: 01 May 2024

Foundation items: This work was supported by the National Natural Science Foundation of China (U2004138, 81773132, 81820108021), University Excellent Teaching Team of "Qinglan Project" in Jiangsu Province (2022-25), Henan Province Key Research and Development Project (232102521028), and Excellent Youth Foundation of Henan Scientific Committee (21230040016)

[#]Authors contributed equally to this work

*Corresponding authors, E-mail: wumian@ustc.edu.cn; schen@zzu.edu.cn

neurogenesis contributes to olfaction in the SVZ but to learning and memory in the hippocampus (Liu et al., 2013). Disruptions in NSC maintenance and neurogenesis can contribute to developmental abnormalities and neurodegenerative conditions, such as Alzheimer's, Parkinson's, and Huntington's diseases (Huang & Klionsky, 2007). Thus, elucidating the cellular and molecular mechanisms governing NSC functionality could pave the way for novel therapeutic interventions.

Autophagy is a highly conserved degradation pathway essential for the removal of damaged organelles and protein aggregates. This lysosome-dependent process is critical in the etiology of various diseases, including neurodegeneration, cancer, and autoimmunity (Guo & Zhao, 2020; Klionsky et al., 2021; Thorburn, 2018). Canonical autophagy, orchestrated by autophagy-related genes (ATGs), is crucial for the initiation and maturation of autophagosomes to facilitate degradation (Bhutia et al., 2018). Notably, while deletion of canonical ATGs in neuronal lineages, such as *Atg5*, *Atg7*, and *Atg16l1*, results in protein aggregate accumulation and subsequent neurodegeneration, these manipulations do not influence NSC maintenance or differentiation (Donde et al., 2020; Liang et al., 2010; Vázquez et al., 2012; Wang et al., 2014; Xi et al., 2016). Similarly, deletion of the autophagy activator protein *Fip200/Rb1cc1* (RB1 inducible coiled-coil 1) in the central and peripheral nervous system leads to characteristic neuropathies, including progressive axonopathy and spongiform degeneration associated with the accumulation of ubiquitinated protein aggregates (Liang et al., 2010). However, subsequent studies have demonstrated that eliminating FIP200 expression severely impacts NSC homeostasis through the progressive depletion of NSCs (Wang et al., 2013, 2016). These contrasting observations provide valuable insights into the potential mechanisms regulating NSC fitness during adult neurogenesis.

FIP200 is traditionally recognized for initiating canonical autophagy through complex formation with ATG13-ULK1-ATG101. However, research has revealed that FIP200 has more expansive roles, interacting with a range of autophagy-related proteins such as calcium binding and coiled-coil domain 2 (CALCOCO2/NDP52), cell cycle progression 1 (CCPG1), 5-azacytidine induced 2 (AZI2/NAP1), and sequestome1 (SQSTM1/p62) and key regulators such as p53 and TSC complex subunit 1 (TSC1), thereby modulating diverse cellular functions via non-canonical autophagy (Yeo et al., 2020). As a multifunctional adaptor protein, p62 acts as a major receptor for the degradation of ubiquitinated protein aggregates (Bjørkøy et al., 2006; Lyu et al., 2022; Pankiv et al., 2007). Deletion and mutations in p62 are associated with neurodegenerative diseases such as Alzheimer's disease (Schaeffer & Goedert, 2012; Zheng et al., 2012), Parkinson's disease (Friesen et al., 2020; Oh et al., 2022), Huntington's disease (Rué et al., 2013; Yang et al., 2021), amyotrophic lateral sclerosis (ALS) (Majcher et al., 2015), and frontotemporal lobar degeneration (FTLD) (Deng et al., 2020; Ma et al., 2019). Notably, p62 was the first selective autophagy receptor implicated in macroautophagy (also termed aggrephagy) (Bjørkøy et al., 2006; Pankiv et al., 2007). Subsequent research has identified several other aggrephagy receptors, including next to BRCA1 gene 1 protein (NBR1), nuclear dot protein 52 (NDP52), optineurin (OPTN), tax1 binding protein 1 (TAX1BP1), toll interacting protein (TOLLIP), and chaperonin containing TCP1 subunit 2 (CCT2) (Gibertini et al., 2023; Ma et al., 2022; Sarraf et al., 2020; Trapannone et al., 2023). Despite these discoveries, the function of aggrephagy in NSCs remains unclear. We previously showed that *Fip200* deletion in NSCs, but not knockout of *Atg5*, *Atg7*, or *Atg16l1*, leads to the accumulation of p62, NBR1, and TAX1BP1 along with p62/ubiquitinated protein aggregates (Wang et al., 2016). Of note, deletion of *p62* rescues *fip200*$^{hGFAP}$ conditional knockout (cKO) NSCs, highlighting the pivotal role of aggrephagy in NSC maintenance and neurogenesis (Gibertini et al., 2023; Ma et al., 2022; Sarraf et al., 2020; Trapannone et al., 2023).

Here, we elucidated the discrete functions of three aggrephagy receptors —TAX1BP1, p62, and NBR1 —during NSC maintenance using a mouse model with conditional gene deletions in NSCs and reconstitution with functionally deficient mutants. Similar to *fip200*$^{hGFAP}$ cKO mice, conditional deletion of *Tax1bp1* in *fip200* conditional knock-in (cKI) mice resulted in the aggregation of NBR1 and p62, resulting in NSC deficiency. Conditional deletion of *Tax1bp1* in *fip200* cKO mice exacerbated p62/NBR1 aggregation and NSC deficiency compared to *fip200* cKO mice. Identification of the underlying non-canonical autophagic mechanism indicated that NBR1 promotes interactions between TAX1BP1 and p62 aggregates. Overall, our study revealed a mechanism by which FIP200 regulates NSC maintenance and differentiation via non-canonical autophagy of p62/aggregates, principally via TAX1BP1.

## MATERIALS AND METHODS

### Mouse experiments

The *fip200* cKO mice, with *Fip200* conditionally deleted in postnatal NSCs (Wang et al., 2013, 2016), were generated by crossing *hGFAP*-Cre transgenic mice, expressing Cre in postnatal NSCs (Wang et al., 2009, 2013), with *fip200* F/F mice. The *fip200* cKI mice, carrying *fip200* F/KI alleles (Chen et al., 2016), were crossed with *hGFAP*-Cre mice. The *tax1bp1* F/F mice, bearing two flox alleles with exon 4 flanked by two loxP sequences, were newly generated. The *tax1bp1* cKO mice, carrying *tax1bp1* F/F alleles, were crossed with *hGFAP*-Cre mice. The *fip200* cKI; *tax1bp1* cKO mice, carrying *fip200* F/KI and *tax1bp1* F/F alleles, were crossed with *hGFAP*-Cre mice. The *fip200* cKO; *tax1bp1* cKO (*2* cKO) mice, carrying the *fip200* F/F and *tax1bp1* F/F alleles, were crossed with *hGFAP*-Cre mice. All mice were maintained on FVB backgrounds. Age- and littermate-matched control and mutant mice were used for analysis to minimize the impact of modifier genes. All animal experiments and procedures were carried out in accordance with the guidelines of the Institutional Animal Care and were approved by Animal Research Ethics Committee of the Laboratory Animal Center of Zhengzhou University (ZZU-LAC20210702[17]). Genotyping for *Fip200* F/F, *Fip200* +/KI, *Tax1bp1* F/F, and *Cre* alleles was performed by polymerase chain reaction (PCR) analysis of tail DNA.

### Reagents and antibodies

Plasmid transfections were carried out using Lipo8000 transfection reagent (Beyotime, China). Small interfering RNA (siRNA) transfections were carried out using Lipofectamine RNAiMAX transfection reagent (Invitrogen, USA).

Primary antibodies included mouse anti-b-ACTIN (Sigma, USA, 1:5 000 dilution), rabbit anti-FIP200 (Proteintech, China, 1:2 000 dilution), rabbit anti-p62 (Cell Signaling Technology,

USA, 1:1 000 dilution), mouse anti-NBR1 (Santa Cru Biotechnology, USA, 1:500 dilution), rabbit anti-TAX1BP1 (Proteintech, China, 1:1 000 dilution), rabbit anti-OPTN (Proteintech, China, 1:1 000 dilution), rabbit anti-TOLLIP (Proteintech, China, 1:1 000 dilution), rabbit anti-CCT2 (Proteintech, China, 1:1 000 dilution), mouse anti-HA (Sigma, USA , 1:5 000 dilution), mouse anti-Flag (Sigma, USA, 1:5 000 dilution), mouse anti-GFP (Santa Cru Biotechnology, USA, 1:1 000 dilution), mouse anti-GFAP (Proteintech, China, 1:1 000 dilution), rabbit anti-NESTIN (Proteintech, China, 1:1 000 dilution), rabbit anti-SOX2 (Proteintech, China, 1:1 000 dilution), rabbit anti-DOUBLECORTIN (Servicebio, China, 1:1 000 dilution), rabbit anti-KI67 (Servicebio, China, 1:1 000 dilution). Secondary antibodies included goat anti-rabbit IgG (H+L), horseradish peroxidase (HRP) (Invitrogen, USA, 1:50 000 dilution), goat anti-mouse IgG (H+L) horseradish peroxidase (HRP) (Invitrogen, USA, 1:50 000 dilution), chicken anti-mouse IgG (H+L) cross-adsorbed, Alexa Fluor 488 (Invitrogen, USA, 1:1 000 dilution), goat anti-rabbit IgG (H+L) cross-adsorbed, and Alexa Fluor 594 (Invitrogen, USA, 1:1 000 dilution).

**Cell culture and treatment**

Mouse SVZ tissues at postnatal day 0 (P0) and P28 were isolated under a dissection microscope and cut into 1 $mm^3$ cubes. The tissues were digested in 0.2% trypsin to obtain single-cell suspensions. The cells were cultured in neurobasal medium (Gibco, USA) supplemented with B27 without vitamin A (Gibco, USA), 10 ng/mL basic fibroblast growth factor (bFGF, Novoprotein, China), and 20 ng/mL epidermal growth factor (EGF, Novoprotein, China) in ultra-low attachment multiple well plates (Corning, USA). The medium was supplemented on days 3, 6, and 9. Neurospheres with diameters larger than 50 μm were counted 9 d after culturing. For passaging, primary neurospheres were collected and incubated in 0.2% trypsin at 37°C for 10 min with pipetting 50 times. After the addition of trypsin inhibitor (Sigma, Germany) supplemented with DNase I (Beyotime, China) to stop digestion, dispersed cells were collected by centrifugation at 400 ×*g* for 10 min at room temperature, counted and cultured for secondary neurosphere formation, with quantification conducted in the same way as primary neurosphere formation. HEK293T cells (ATCC) were cultured in Dulbecco's Modified Eagle Medium (DMEM) supplemented with 10% fetal bovine serum (FBS), L-glutamine (2 mmol/L), penicillin (10 Units/mL), and streptomycin (0.1 mg/mL).

For siRNA treatment, NSCs were seeded in 24-well plates (100 000 cells/well). After 24 h, the cells were transfected with siRNA (25 nmol/L final concentration) using Lipofectamine™ RNAiMAX transfection reagent in OptiMEM medium. At 8 h after transfection, the NSCs were cultured in 6-well plates (20 000 cells/well) for 5 days. The siRNA sequences were: Tax1bp1, 5'-GUCUCCUAUGCCUGAACAU-3'; Nbr1, 5'-GCCACUUGCACAUUAUUCU-3'; and p62, 5'-GCUGAAACAUGGACACUUU-3'.

Stable expression of full-length or mutant forms of TAX1BP1 was achieved using lentiviral-mediated transduction. The indicated epitope-tagged constructs were cloned into the Lenti-EFS-Flag-puro vector and transfected with psPAX2 and pmd2.g in HEK293T cells to derive lentiviral particles. After centrifugation at 3 000 ×*g* for 10 min at room temperature and filtration through 0.45 μm filter (Beyotime, China), lentiviral supernatants were added to NSCs. The infected neurospheres were selected with 1 μg/mL puromycin in neurosphere media to obtain pools stably expressing Tax1bp1 mutants.

**Western blotting**

Mouse SVZ tissues were microdissected from brains and extracted in sodium dodecyl sulfate (SDS)-lysis buffer containing 2% SDS, 62.5 mmol/L Tris pH 6.8, 10% glycerol, and 5% β-mercaptoethanol.

Lysates were boiled for 10 min and analyzed by sodium dodecyl-sulfate polyacrylamide gel electrophoresis (SDS-PAGE) on 4%–20% gels (160 V, 45 min) (BioRad Laboratories, USA), followed by immunoblotting on nitrocellulose membranes using a wet blotting system (400 mA, 30 min) (BioRad Laboratories, USA). Membranes were incubated with primary and secondary antibodies diluted in 5% milk/TBST solutions, and immunocomplexes were developed using SuperSignal™ West Pico PLUS (Thermo Fisher, USA) and visualized using an Azure c600 Western Blot Imager (Azure Biosystems, USA).

**Immunoprecipitation**

At 24 h post-transfection, HEK293FT cells were lysed in immunoprecipitation buffer (50 mmol/L Tris-HCl, pH 8.0, 150 mmol/L NaCl, 0.5 mmol/L ethylenediaminetetraacetic acid (EDTA), 0.5% NP-40, 10% glycerol) containing EDTA-free protease inhibitor cocktail (MCE, China) for 30 min at 4°C. The lysates were centrifuged at 12 000 ×*g* for 10 min at 4°C, and the soluble supernatant fractions were subjected to immunoprecipitation with Pierce™Anti-DYKDDDDK Magnetic Agarose (Invitrogen, USA) or Pierce Anti-HA Magnetic Beads (Invitrogen, USA). After incubation for 4 h at 4°C, the beads were washed three times with TBST and boiled with SDS-lysis buffer for 10 min.

**Histology and immunofluorescence**

Mice were euthanized using $CO_2$, and whole brains were collected after perfusion. Fixation was performed for 16 h at 4°C using 4% (wt/vol) freshly made, prechilled phosphate-buffered saline (PBS)-buffered paraformaldehyde (PFA). Brain tissues were sagittally sectioned, embedded in paraffin, and cut into 5 μm slices using a Leica 2125 Microtome (Leica, Germany). Slides from histologically comparable positions (triangular lateral ventricle with intact rostral migratory stream (RMS)) were subjected to hematoxylin and eosin (H&E) and immunofluorescence (IF) staining. For routine histological examination, sections were stained with H&E. For IF analysis of brain tissue, sections were washed in xylene three times (5 min each), rehydrated in graded ethanol solutions (100%, 95%, 85%, and 75%, 2 min each). After heat-activated antigen retrieval in Tris-EDTA pH 9.0 buffer, 6% bovine serum albumin (BSA)/TBST solution was used to block the sections at room temperature for 30 min. Sections were incubated with primary antibodies at 4°C for 16 h in an immunohistochemical wet box, washed in PBS three times (5 min each), and incubated with 1:1 000 Alexa Fluor™ 488 or Alexa Fluor™ 594 secondary antibodies for 1 h at room temperature. After washing three times (5 min each) in PBS, sections were stained with antifade mounting medium with 4',6-diamidino-2-phenylindole (DAPI, Beyotime, China) and visualized using epifluorescence or confocal microscopy (Nikon, Japan). For IF, NSCs were fixed in cold methanol for 10 min, blocked in 3% BSA/TBST solution for 30 min, then incubated with primary and secondary antibodies as described as above.

**Statistical analysis**

Statistical significance was determined using GraphPad Prism v.6, using unpaired Student's two-tailed *t*-test for one-way comparisons and one-way analysis of variance (ANOVA) for multiple comparisons. No statistical methods were used to determine sample sizes. Unless expressly noted, experiments were not randomized, and the investigators were not blinded to group allocations or outcome assessments. Data are presented as mean±standard error of the mean (SEM) (error bars). $^{*}$: $P<0.05$; $^{**}$: $P<0.01$; $^{***}$: $P<0.001$; and $^{****}$: $P<0.0001$.

## RESULTS

### Self-renewal of *fip200* cKI NSCs *in vitro* is impaired by *TAX1BP1* knockdown

Prior studies have demonstrated that reconstitution of *fip200* KO mice with an ATG13-binding mutant, denoted FIP200-4A (Chen et al., 2016), is sufficient to sustain murine NSC maintenance and neurogenesis *in vivo* (Liu et al., 2021). However, the specific mechanisms by which the FIP200-4A mutant supports NSC homeostasis in the context of the *fip200* KI mice remain unclear.

To further explore this paradigm, we generated *fip200* cKO mice and *fip200* cKI mice. By P28, the *fip200* cKI mice exhibited normal physical development and hindlimb motor abilities compared to the *fip200* cKO mice (Supplementary Figure S1A, B). Consistent with earlier research (Liu et al., 2021), histological analysis revealed that *fip200* cKI mice displayed restored SVZ cellularity and DG area measures compared to the *fip200* cKO mice (Supplementary Figure S1C, D). Additionally, a marked accumulation of p62 was observed in the SVZ and DG of *fip200* cKO mice, but not in wild-type (WT) or *fip200* cKI mice (Figure 1A; Supplementary Figure S1E). The presence of unresolved p62 aggregates suggests that differences between the *fip200* cKO and *fip200* cKI mice involve disruptions in NSC maintenance resulting from defective non-canonical autophagy of protein aggregates (or aggrephagy).

In addition to p62, previous studies have reported the accumulation of autophagy receptors TAX1BP1 and NBR1 in *fip200*$^{hGFAP}$ cKO NSCs (Wang et al., 2016), necessitating the identification of specific aggrephagy receptors utilized in NSCs. To gain further mechanistic insights, we evaluated six reported aggrephagy receptors —TAX1BP1, NBR1, p62, OPTN, TOLLIP, and CCT2—in SVZ tissues of different *Fip200* genotypes. Western blotting revealed significant elevations in the TAX1BP1, NBR1, and p62 protein levels in *fip200* cKO mice, while the levels of OPTN, TOLLIP, and CCT2 showed no detectable changes (Figure 1B; Supplementary Figure S1F). Consistent with these *in vivo* observations, the protein levels of TAX1BP1, NBR1, and p62 were significantly increased in *fip200* cKO NSCs (Figure 1C; Supplementary Figure S1G).

To explore functional relationships, TAX1BP1, NBR1, and p62 were knocked down in P28-derived NSCs from different experimental backgrounds. Depleting TAX1BP1 led to a significant increase in p62 and NBR1 protein levels in *fip200* cKI NSCs but not in *fip200* cKO NSCs. In contrast, NBR1 knockdown did not significantly affect TAX1BP1 or p62 levels (Figure 1D; Supplementary Figure S1H). Neurosphere assays used to assess NSC self-renewal showed that individual knockdown of TAX1BP1, NBR1, and p62 did not impact the self-renewal capacity of WT NSCs. However, p62 knockdown largely restored the diminished self-renewal capability of *fip200* cKO NSCs. In contrast, TAX1BP1 knockdown further reduced neurosphere formation in *fip200* cKO NSCs, with similar impairment observed in *fip200* cKI NSCs. NBR1 knockdown exerted negligible effects on *fip200* cKO NSCs, with only a modest reduction in neurosphere formation observed in *fip200* cKI NSCs (Figure 1E, F). Strikingly, similar to *fip200* cKO NSCs, TAX1BP1 knockdown led to a significant accumulation of p62 aggregates in *fip200* cKI NSCs (Figure 1G, H). These results suggest that the degradation of p62 aggregates via the FIP200-4A mutant primarily relies on TAX1BP1 as an essential intermediary, with its loss inducing p62 aggregate accumulation in NSCs (Figure 1I).

### TAX1BP1 ablation in *fip200* cKI mice causes SVZ degeneration via NSC deficiency

To further investigate the role of TAX1BP1 in maintaining NSC homeostasis *in vivo*, we generated cKO mice with exon 4 of the *Tax1bp1* allele flanked by loxP sites. These mice were crossed with *hGFAP*-Cre transgenic mice to produce NSC-specific *tax1bp1* cKO mice (Supplementary Figure S2A–D). Founder mice were also used to generate *tax1bp1* cKO mice on a *fip200* cKI background (*fip200* cKI; *tax1bp1* cKO mice).

Initial evaluation of SVZ tissues at P28 among the genotypes showed a significant increase in p62 protein levels in the *fip200* cKI; *tax1bp1* cKO mice relative to their WT, *fip200* cKI, and *tax1bp1* cKO littermates (Figure 2A; Supplementary Figure S2E), suggesting considerable blockade of p62 aggregate degradation. Neurosphere assays confirmed marked reductions in neurosphere formation in both primary and secondary SVZ cultures derived from P28 *fip200* cKI; *tax1bp1* cKO mice (Figure 2B, C). H&E staining showed significant reductions in both SVZ and DG width and cellularity in *fip200* cKI; *tax1bp1* cKO mice, whereas these parameters in *fip200* cKI and *tax1bp1* cKO mice were similar to those in WT mice (Figure 2D, E). These phenotypes, together with the *in vitro* results, imply that TAX1BP1 is necessary to maintain normal NSCs in *fip200* cKI mice.

To conclusively establish the role of TAX1BP1, we analyzed the NSC populations in the SVZ and DG using GFAP$^{+}$NESTIN$^{+}$ and GFAP$^{+}$SOX2$^{+}$ markers. Results revealed significant reductions in the NSC population in *fip200* cKI; *tax1bp1* cKO mice compared to their *fip200* cKI and *tax1bp1* cKO counterparts (Figure 2F–I; Supplementary Figure S2F–I). Furthermore, *fip200* cKI; *tax1bp1* cKO mice exhibited decreased proliferation and differentiation and increased apoptosis and microglial infiltration (Figure 2J–M; Supplementary Figure S2J–O). These findings underscore the critical role of TAX1BP1 in the maintenance and differentiation of postnatal NSCs in *fip200* cKI mice.

### TAX1BP1 ablation in *fip200* cKI mice leads to NSC deficiency through p62/NBR1 aggregation

Given that TAX1BP1 ablation increased p62 levels in the SVZ of *fip200* cKI mice, we next investigated its involvement in the formation of p62/NBR1 aggregates and consequent impact on the NSC pool. We first explored how manipulating TAX1BP1 affected NBR1 and p62 protein levels in SVZ tissues across different experimental backgrounds. Results showed a marked up-regulation of NBR1 and p62 in the SVZ of *fip200* cKI; *tax1bp1* cKO mice, while their levels in *fip200* cKI and *tax1bp1* cKO mice remained comparable to that in WT mice (Figure 3A; Supplementary Figure S3A). Moreover, increased NBR1 and p62 aggregates were found in the SVZ and DG regions of *fip200* cKI; *tax1bp1* cKO mice (Figure 3B–E),

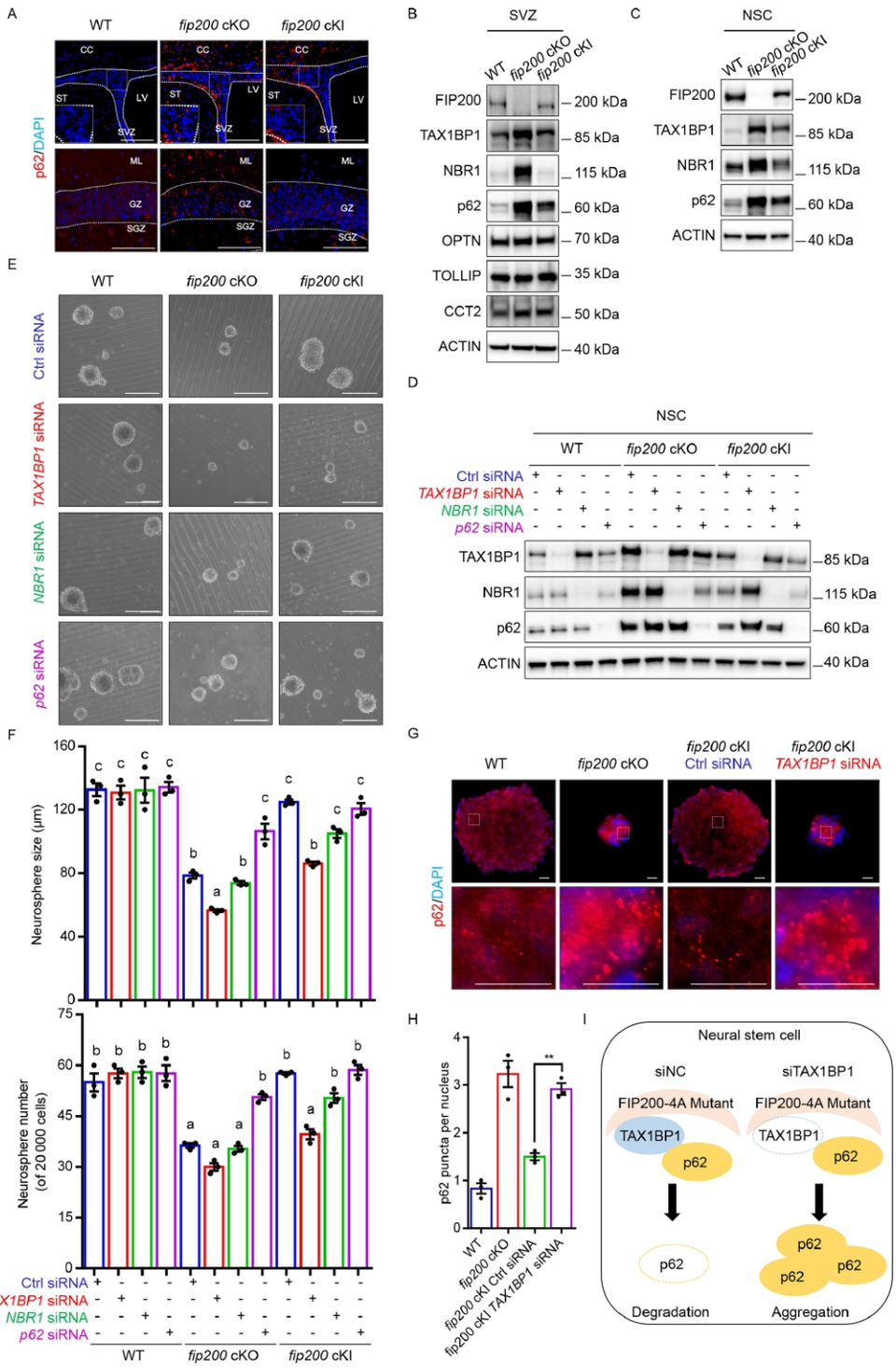



**Figure 1 Sufficient self-renewal of *fip200* cKI NSCs *in vitro* is impaired by TAX1BP1 knockdown**

A: Immunofluorescence of p62 puncta and DAPI in SVZ and SGZ from WT, *fip200* cKO, *fip200* cKI mice at P28. Dotted lines indicate boundaries of SVZ and DG. Scale bar: 100 μm. B: Lysates were extracted from the SVZ of P28 WT, *fip200* cKO, and *fip200* cKI mice, with aggrephagy receptor protein levels analyzed by western blotting. ACTIN was used as a loading control. C: Lysates were extracted from NSCs of P28 WT, *fip200* cKO, and *fip200* cKI mice, with TAX1BP1, NBR1, and p62 protein levels analyzed by western blotting. ACTIN was used as a loading control. D: Western blotting of FIP200, TAX1BP1, NBR1, and p62 protein levels in WT, *fip200* cKO, and *fip200* cKI NSCs with or without *TAX1BP1*, *NBR1*, or *p62* siRNA transfection. ACTIN was used as a loading control. E: Neurosphere formation from WT, *fip200* cKO, and *fip200* cKI NSCs with or without *TAX1BP1*, *NBR1* or *p62* siRNA transfection. Representative phase contrast images. Scale bar: 200 μm. F: Mean±SEM of number and size of neurospheres ($n$=3 independent samples). Same character means not significant, different character means $P$<0.05 (one-way ANOVA with Tukey's multiple comparisons test). G: Immunofluorescence of p62 puncta and DAPI in WT, *fip200* cKO, *fip200* cKI Ctrl siRNA, and *fip200* cKI *TAX1BP1* siRNA neurospheres. Scale bar: 20 μm. H: Mean±SEM of p62 puncta per neurosphere ($n$=3 independent samples). **: $P$<0.01 (one-way ANOVA with Dunnett's multiple comparisons test). I: Schematic of FIP200 4A-mutant, TAX1BP1 and p62 status in Ctrl siRNA or *TAX1BP1* siRNA *fip200* cKI NSC conditions.

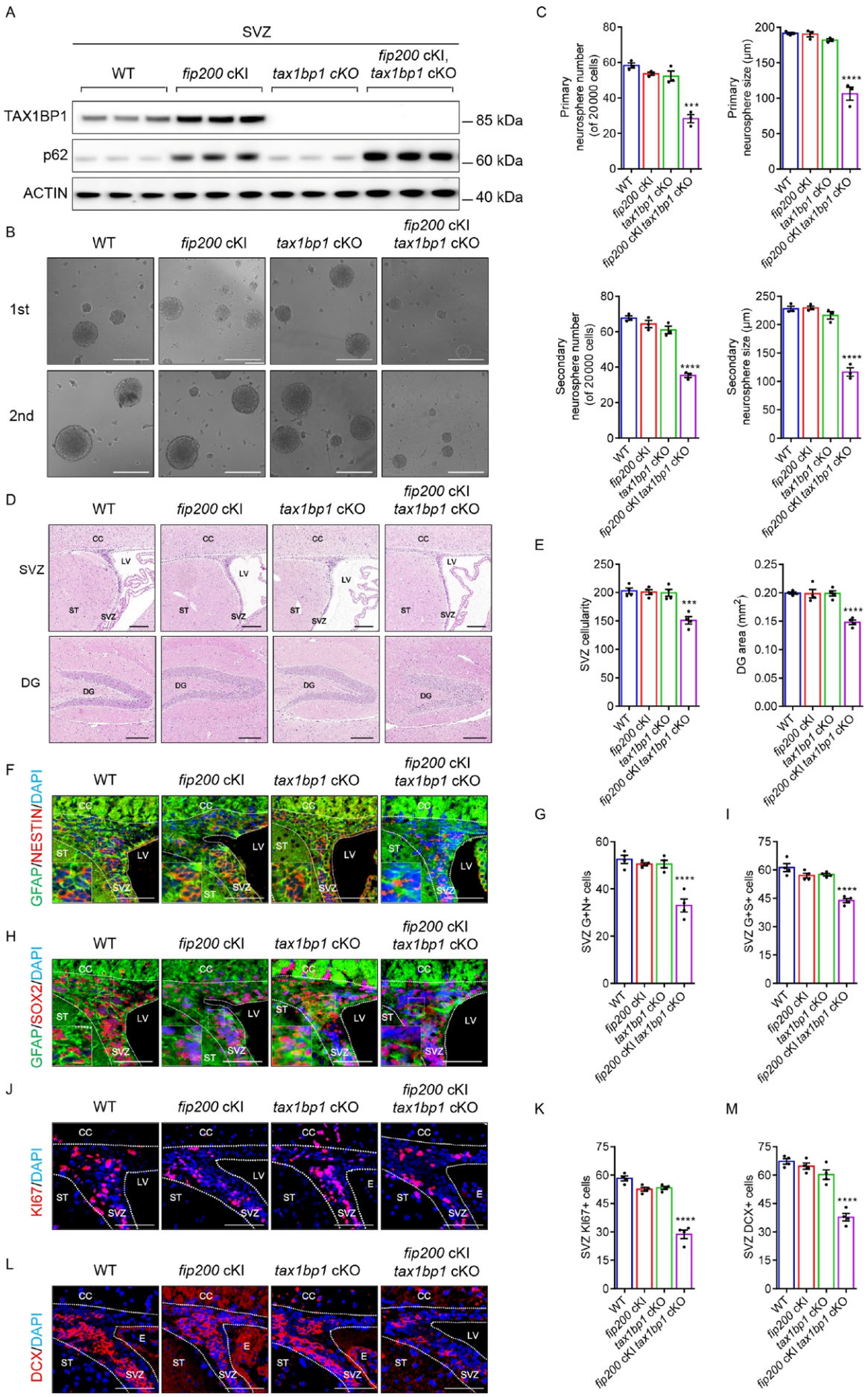

A
SVZ
WT
fip200 cKI
tax1bp1 cKO
fip200 cKI, tax1bp1 cKO
TAX1BP1
p62
ACTIN
85 kDa
60 kDa
40 kDa
B
1st
2nd
C
Primary neurosphere number (of 20000 cells)
Primary neurosphere size (μm)
Secondary neurosphere number (of 20000 cells)
Secondary neurosphere size (μm)
D
SVZ
DG
E
SVZ cellularity
DG area (mm²)
F
GFAP/NESTIN/DAPI
G
SVZ G+N+ cells
H
GFAP/SOX2/DAPI
I
SVZ G+S+ cells
J
KI67/DAPI
K
SVZ KI67+ cells
L
DCX/DAPI
M
SVZ DCX+ cells
CC
LV
ST
SVZ
DG
E

**Figure 2 TAX1BP1 ablation in *fip200* cKI mice causes degeneration of SVZ due to NSC deficiency**

A: Lysates were extracted from the SVZ of P28 WT, *fip200* cKI, *tax1bp1* cKO, and *fip200* cKI; *tax1bp1* cKO mice and analyzed by western blotting. ACTIN was used as a loading control. B: Primary (first) and secondary (second) neurosphere formation in WT, *fip200* cKI, *tax1bp1* cKO, and *fip200* cKI; *tax1bp1* cKO mice at P28. Representative phase contrast images. Scale bar: 200 μm. C: Mean±SEM of number and size of primary and secondary neurospheres ($n$=3 independent samples). ***: $P$<0.001; ****: $P$<0.0001 (one-way ANOVA with Dunnett's multiple comparisons test). D: Histological analysis of sagittal sections of SVZ and DG from WT, *fip200* cKI, *tax1bp1* cKO, and *fip200* cKI; *tax1bp1* cKO mice at P28. Dotted lines indicate boundaries of SVZ and DG. Scale bar: 200 μm. E: Mean±SEM of SVZ cellularity and DG area per section from WT ($n$=4), *fip200* cKI ($n$=4), *tax1bp1* cKO ($n$=4), and *fip200* cKI; *tax1bp1* cKO mice ($n$=4) at P28. ***: $P$<0.001; ****: $P$<0.0001 (one-way ANOVA with Dunnett's multiple comparisons test). F: Immunofluorescence of GFAP, NESTIN, and DAPI in SVZ from WT, *fip200* cKI, *tax1bp1* cKO, and *fip200* cKI; *tax1bp1* cKO mice at P28. Dotted lines indicate boundaries of SVZ. Scale bar: 50 μm. G: Mean±SEM of GFAP and NESTIN positive cells per SVZ section from WT ($n$=4), *fip200* cKI ($n$=4), *tax1bp1* cKO ($n$=4), and *fip200* cKI; *tax1bp1* cKO mice ($n$=4) at P28. ****: $P$<0.0001 (one-way ANOVA with Dunnett's multiple comparisons test). H: Immunofluorescence of GFAP, SOX2, and DAPI in SVZ from WT, *fip200* cKI, *tax1bp1* cKO, and *fip200* cKI; *tax1bp1* cKO mice at P28. Dotted lines indicate boundaries of SVZ. Scale bar: 50 μm. I: Mean±SEM of GFAP and SOX2 positive cells per SVZ section from WT ($n$=4), *fip200* cKI ($n$=4), *tax1bp1* cKO ($n$=4) and *fip200* cKI; *tax1bp1* cKO mice ($n$=4) at P28. ****: $P$<0.0001 (one-way ANOVA with Dunnett's multiple comparisons test). J: Immunofluorescence of KI67 and DAPI in SVZ from WT, *fip200* cKI, *tax1bp1* cKO, and *fip200* cKI; *tax1bp1* cKO mice at P28. Dotted lines indicate boundaries of SVZ. Scale bar: 50 μm. K: Mean±SEM of KI67 positive cells per SVZ section from WT ($n$=4), *fip200* cKI ($n$=4), *tax1bp1* cKO ($n$=4), and *fip200* cKI; *tax1bp1* cKO mice ($n$=4) at P28. ****: $P$<0.0001 (one-way ANOVA with Dunnett's multiple comparisons test). L: Immunofluorescence of DCX and DAPI in SVZ from WT, *fip200* cKI, *tax1bp1* cKO, and *fip200* cKI; *tax1bp1* cKO mice at P28. Dotted lines indicate boundaries of SVZ. Scale bar: 50 μm. M: Mean±SEM of DCX positive cells per SVZ section from WT ($n$=4), *fip200* cKI ($n$=4), *tax1bp1* cKO ($n$=4), and *fip200* cKI; *tax1bp1* cKO mice ($n$=4) at P28. ****: $P$<0.0001 (one-way ANOVA with Dunnett's multiple comparisons test).

correlating with NSC deficiency (Figure 2F–M; Supplementary Figure S2F–M). These findings were further validated *in vitro*, where elevated levels and aggregation of NBR1 and p62 were confirmed in *fip200* cKI; *tax1bp1* cKO neurospheres (Figure 3F–J; Supplementary Figure S3B). Collectively, these results indicate that the ablation of TAX1BP1 in *fip200* cKI mice leads to NSC deficiency primarily through the formation of p62/NBR1 aggregates, highlighting the essential role of TAX1BP1 in maintaining postnatal NSC health via aggrephagy.

**FIP200-4A mutant elicits p62 aggregation via interactions with TAX1BP1 and NBR1**

To identify the protein-protein interaction hierarchies required for p62 aggregate degradation via FIP200, we first evaluated the binding between recombinant epitope-tagged versions of FIP200-4A, NBR1, TAX1BP1, OPTN, and p62 proteins using immunoprecipitation-based assays. Interestingly, FIP200-4A co-immunoprecipitated with TAX1BP1 and NBR1 but not with p62 (Supplementary Figure S4A), implicating TAX1BP1 and NBR1 as potential enhancers of FIP200-p62 interactions. Consistent with this, our previous mass spectrometry analysis of mouse embryonic fibroblasts (MEFs) identified TAX1BP1 as the only aggrephagy receptor among the top 50 candidates regulating the FIP200-ATG13-ULK1 complex (Yang et al., 2022). Subsequent experiments revealed that NBR1 binds to TAX1BP1 along with forming self-interactions (Supplementary Figure S4B, C), while p62 interacts with itself, as well as NBR1, TAX1BP1, and OPTN to varying extents (Supplementary Figure S4D). Notably, associations between TAX1BP1 and NBR1 substantially enhanced the binding between FIP200 and p62 (Figure 4A). However, while NBR1 enhanced the binding between TAX1BP1 and p62, TAX1BP1 did not affect the NBR1-p62 association (Figure 4B; Supplementary Figure S4E). These findings establish the functional significance of TAX1BP1-NBR1 interactions, with TAX1BP1 directing the binding of FIP200-4A to p62 for subsequent degradation.

Next, we sought to identify the regions in TAX1BP1 essential for enabling p62 degradation via the FIP200-4A mutant. Using Flag-tagged TAX1BP1 truncation (Δ) constructs, reciprocal immunoprecipitation assays revealed that the NBR1 interaction region of TAX1BP1 existed within the 449–470 amino acid (aa) sequence (Supplementary Figure S4F), consistent with recent research identifying the interaction region between 420–506 aa (Ohnstad et al., 2020). To further refine the binding sites, we analyzed overlapping TAX1BP1Δ mutants lacking residues across the 449–470 aa sequence, which narrowed the binding region to between 449 and 463 aa (Supplementary Figure S4G). Alanine-scanning mutagenesis, where each set of four residues between 449 and 463 in TAX1BP1 was substituted with Ala (i.e., 449–452, 453–456, 457–460, and 461–464), was then employed to reconstruct interactions between TAX1BP1, NBR1, and p62 in HEK293T cells. Results revealed that only the 449–452 TAX1BP1 mutant (YREK to AAAA) failed to coprecipitate NBR1 and p62, while other alanine mutants showed enhanced TAX1BP1/p62 binding compared to intact TAX1BP1 (Figure 4C). Of note, the TAX1BP1$^{\text{YREK449-452AAAA}}$ mutant maintained its binding affinity for FIP200 and LC3B (Supplementary Figure S4H, I). These findings highlight YREK as an essential motif required for NBR1 binding, allowing the selective disruption of TAX1BP1-NBR1 interactions using a YREK mutant construct that preserves other relevant binding interactions.

**TAX1BP1 mediates p62 aggrephagy by recruiting FIP200 and NBR1**

To gain deeper mechanistic insights into how the non-canonical autophagy function of FIP200 maintains NSCs, we utilized the Flag-TAX1BP1$^{\text{YREK449-452AAAA}}$ mutant together with previously characterized TAX1BP1 constructs, including the V143S mutant, which disrupts binding to LC3 (Flag-TAX1BP1$^{\text{V143S}}$) (Sarraf et al., 2020) and the A114Q mutant, which disrupts TAX1BP1 binding to FIP200 (Flag-TAX1BP1$^{\text{A114Q}}$) (Ohnstad et al., 2020). WT TAX1BP1 (Flag-WT TAX1BP1) and these mutants were reintroduced into NSCs derived at P28 from *fip200* cKI; *tax1bp1* cKO mice. Notably, re-expression of Flag-WT TAX1BP1 and Flag-TAX1BP1$^{\text{V143S}}$ but not Flag-TAX1BP1$^{\text{YREK449-452AAAA}}$ or Flag-TAX1BP1$^{\text{A114Q}}$, resulted in diminished p62 and NBR1 levels (Figure 4D; Supplementary Figure S4J). This pattern was also reflected in the levels of accumulated p62 aggregates within the cells (Figure 4E, F), indicating that the YREK449-

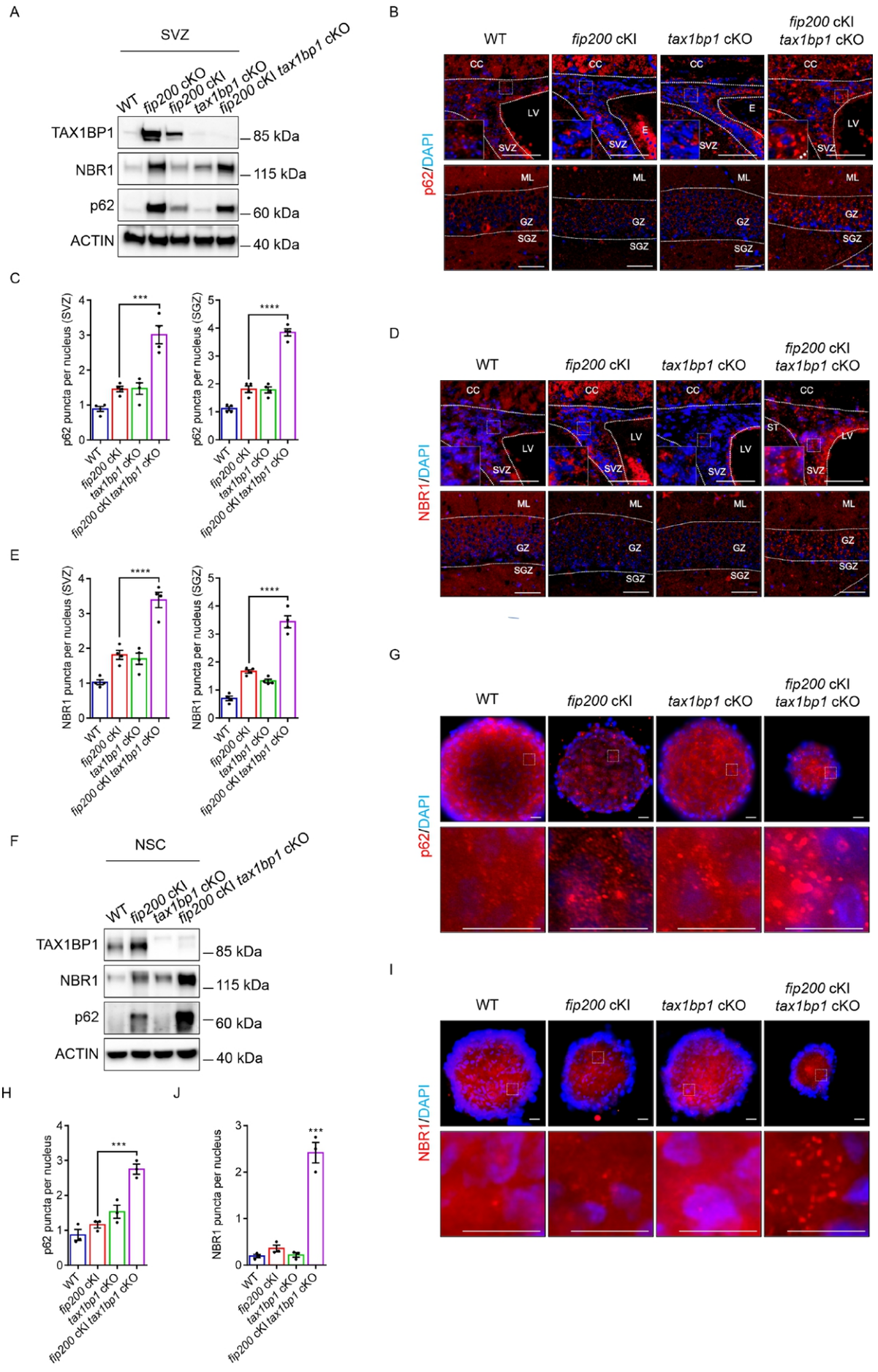

A
SVZ
WT
fip200 cKO
fip200 cKI
tax1bp1 cKO
fip200 cKI tax1bp1 cKO
TAX1BP1
NBR1
p62
ACTIN
85 kDa
115 kDa
60 kDa
40 kDa
B
WT
fip200 cKI
tax1bp1 cKO
fip200 cKI tax1bp1 cKO
p62/DAPI
CC
LV
SVZ
E
ML
GZ
SGZ
C
p62 puncta per nucleus (SVZ)
p62 puncta per nucleus (SGZ)
***
****
D
NBR1/DAPI
ST
E
NBR1 puncta per nucleus (SVZ)
NBR1 puncta per nucleus (SGZ)
F
NSC
G
I
H
J
p62 puncta per nucleus
NBR1 puncta per nucleus

**Figure 3 TAX1BP1 ablation in *fip200* cKI mice causes p62 and NBR1 aggregation**

A: Lysates were extracted from the SVZ of P28 WT, *fip200* cKI, *tax1bp1* cKO, and *fip200* cKI; *tax1bp1* cKO mice, with TAX1BP1, NBR1, and p62 protein levels analyzed by western blotting. ACTIN was used as a loading control. B: Immunofluorescence of p62 puncta and DAPI in SVZ and SGZ from WT, *fip200* cKI, *tax1bp1* cKO, and *fip200* cKI; *tax1bp1* cKO mice at P28. Dotted lines indicate boundaries of SVZ and DG. Scale bar: 50 μm. C: Mean±SEM of p62 puncta per SVZ and SGZ section from WT (*n*=4), *fip200* cKI (*n*=4), *tax1bp1* cKO (*n*=4), and *fip200* cKI; *tax1bp1* cKO mice (*n*=4) at P28. ***: *P*<0.001; ****: *P*<0.0001 (one-way ANOVA with Dunnett's multiple comparisons test). D: Immunofluorescence of NBR1 puncta and DAPI in SVZ and SGZ from WT, *fip200* cKI, *tax1bp1* cKO, and *fip200* cKI; *tax1bp1* cKO mice at P28. Dotted lines indicate boundaries of SVZ and DG. Scale bar: 50 μm. E: Mean±SEM of NBR1 puncta per SVZ and SGZ section from WT (*n*=4), *fip200* cKI (*n*=4), *tax1bp1* cKO (*n*=4), and *fip200* cKI; *tax1bp1* cKO mice (*n*=4) at P28. ****: *P*<0.0001 (one-way ANOVA with Dunnett's multiple comparisons test). F: Lysates were extracted from NSC of P28 WT, *fip200* cKI, *tax1bp1* cKO, and *fip200* cKI; *tax1bp1* cKO mice, with TAX1BP1, NBR1, and p62 protein levels analyzed by western blotting. ACTIN was used as a loading control. G: Immunofluorescence of p62 puncta and DAPI in neurospheres from WT, *fip200* cKI, *tax1bp1* cKO, and *fip200* cKI; *tax1bp1* cKO mice at P28. Scale bar: 20 μm. H: Mean±SEM of p62 puncta per neurosphere (*n*=3 independent samples). ***: *P*<0.001 (one-way ANOVA with Dunnett's multiple comparisons test). I: Immunofluorescence of NBR1 puncta and DAPI in neurospheres from WT, *fip200* cKI, *tax1bp1* cKO, and *fip200* cKI; *tax1bp1* cKO mice at P28. Scale bar: 20 μm. J: Mean±SEM of NBR1 puncta per neurosphere (*n*=3 independent samples). ***: *P*<0.001 (one-way ANOVA with Dunnett's multiple comparisons test).

452AAAA and A114Q mutants fail to degrade p62 aggregates. Furthermore, neurosphere assays confirmed that the reintroduction of WT and V143S TAX1BP1 constructs increased the size and number of neurospheres, while the YREK449-452AAAA and A114Q mutants did not significantly affect NSC potency (Figure 4G, H). These findings suggest that TAX1BP1 is required for p62 aggrephagy through FIP200, with relevance for its degradation in NSCs.

**TAX1BP1 ablation in *fip200* cKO mice exacerbates p62/NBR1 aggregation and degeneration of SVZ and DG**

Given that TAX1BP1 ablation increased p62/NBR1 aggregation and NSC deficiency in *fip200* cKI mice, we next sought to demonstrate the function of TAX1BP1 in *fip200* cKO mice. We first explored how manipulating TAX1BP1 affected NBR1 and p62 protein levels in SVZ tissues across different experimental backgrounds. Interestingly, a marked up-regulation in NBR1 and p62 was observed in the SVZ of *fip200* cKO; *tax1bp1* cKO mice (designated *2* cKO) compared to *fip200* cKO and *fip200* cKI; *tax1bp1* cKO mice (Figure 5A; Supplementary Figure S5A). NBR1 and p62 aggregates were also significantly increased in the SVZ and DG regions of *2* cKO mice (Figure 5B–E), aligning with the observations of NSC deficiency (Figure 5F–O; Supplementary Figure S5B–G). Previous studies have indicated that primary neurospheres generated from P0 *fip200* cKO mice are similar in size and number to those from WT mice (Wang et al., 2013). However, the neurosphere assays showed marked reductions in neurosphere formation in both primary and secondary SVZ cultures derived from P0 *2* cKO mice (Figure 5P, Q). For neurospheres isolated from P28 mice, no differences in sphere size or number were observed between *fip200* cKO and *2* cKO mice. Collectively, these results indicate that the degradation of p62 aggregates in NSCs via aggrephagy proceeds efficiently only when TAX1BP1 and FIP200 are co-expressed.

## DISCUSSION

The core canonical autophagy proteins form the ULK1-ATG13-FIP200-ATG101 and PI3K-BECLIN1-ATG14L1-VPS34 complexes, which are required for the induction and initiation of autophagosomes, while two ubiquitin-like conjugation systems, ATG7-ATG12-ATG5-ATG16L1 and ATG8, are involved in the elongation of autophagosomes (Galluzzi et al., 2017; He & Klionsky, 2009; Mizushima & Levine, 2010).

Previous research has shown that cells can degrade substrates via *Atg7*-independent and autophagy receptor-dependent mechanisms, namely non-canonical autophagy (Ohnstad et al., 2020). Interestingly, unlike *Fip200*, the ablation of core autophagosome elongation genes such as *Atg5*, *Atg7*, and *Atg16L1* does not significantly impair p62 aggregate degradation or NSC functionality. In *fip200*$^{hGFAP}$ cKO mice, the accumulation of p62 aggregates triggers aberrant increases in superoxide by impairing superoxide dismutase functions, which affects the fate of autophagy-deficient NSCs (Wang et al., 2016). In addition, p62 aggregates can hinder NSC differentiation by promoting increased infiltration and activation of microglia through a p53-independent, non-cell autonomous mechanism (Wang et al., 2017). This difference highlights the essential role of the non-canonical function of FIP200 in NSC maintenance and differentiation.

Aggrephagy is a specialized cellular mechanism designed to degrade protein aggregates, relying on specific cargo receptors (Lamark & Johansen, 2012). Six aggrephagy receptors —TAX1BP1, NBR1, P62, OPTN, TOLLIP, and CCT2—have been identified and implicated in the degradation of ubiquitinated protein aggregates (Gibertini et al., 2023; Ma et al., 2022; Sarraf et al., 2020; Trapannone et al., 2023). In this study, we found that among these six receptors, only TAX1BP1, NBR1, and p62 aggregates significantly accumulated in NSCs that were impaired by the absence of FIP200. Interestingly, individual knockdown of TAX1BP1, NBR1, and p62 in WT, *fip200* cKO, *fip200* cKI NSCs produced different phenotypes, with only TAX1BP1 knockdown leading to significant increases in p62 and NBR1 protein levels in *fip200* cKI NSCs. Moreover, knockdown of TAX1BP1 further impaired the self-renewal capacity of *fip200* cKO and *fip200* cKI NSCs, while knockdown of p62 largely reversed these defects. These insights suggest that autophagy receptors play different roles in NSC self-renewal, particularly under the context of canonical autophagy deficiency.

To investigate the non-canonical functions of FIP200 and its partner TAX1BP1, *fip200* cKO, *fip200* cKI, *tax1bp1* cKO, *fip200* cKI; *tax1bp1* cKO, and *fip200*; *tax1bp1 2* cKO mice were generated. The *fip200* cKI mice were designed to express a FIP200-4A mutant incapable of binding with ATG13, thus disrupting the formation of the canonical autophagy induction complex. This model allowed us to study the non-canonical interactions involving FIP200 and other proteins (Chen et al., 2016). By leveraging the differential outcomes observed in these mouse models, we demonstrated that the degradation of p62 aggregates primarily occurred via FIP200-

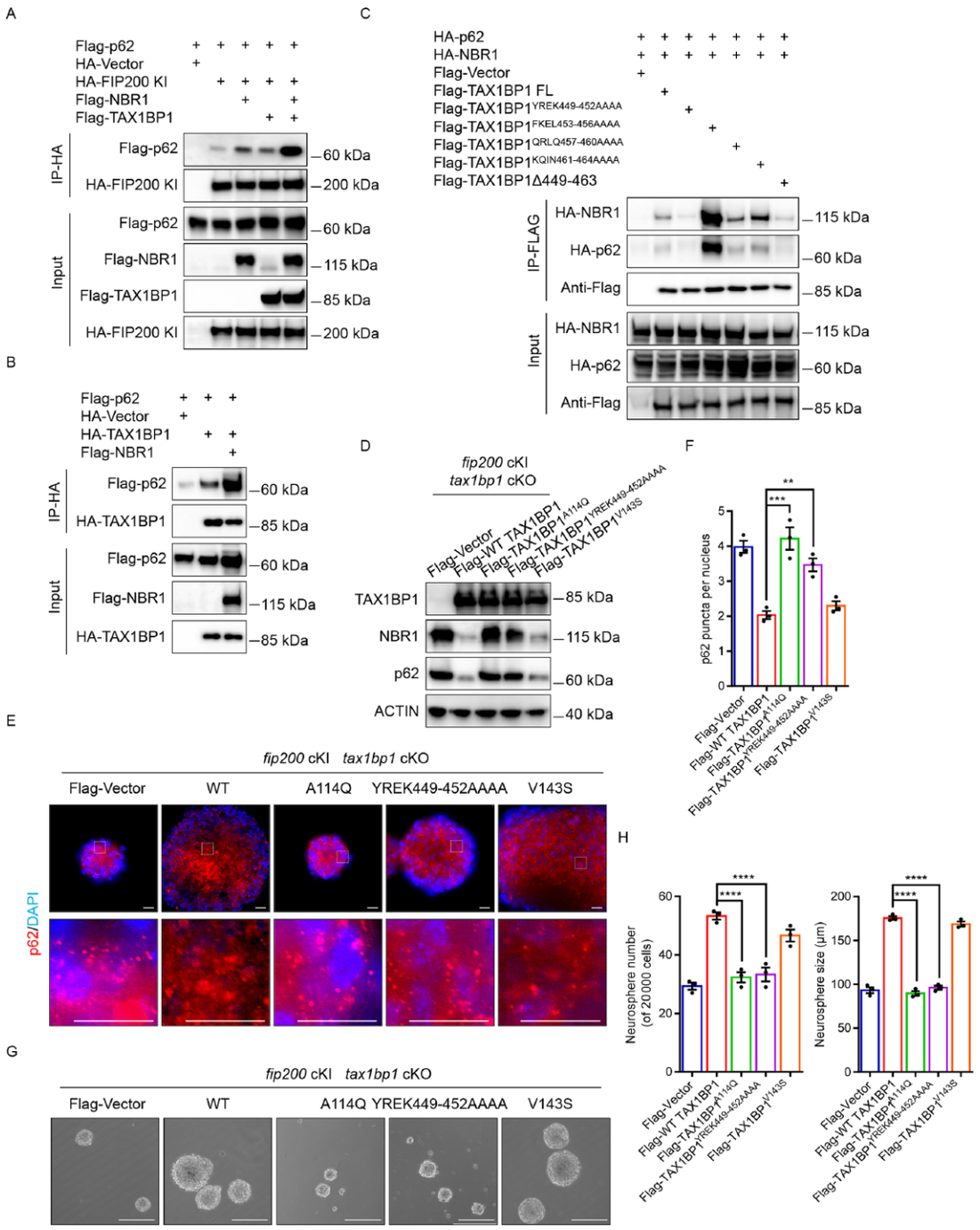



**Figure 4 TAX1BP1 mediates p62 aggregate aggrephagy by recruiting FIP200 and NBR1**

A: Co-immunoprecipitation assays in HEK293T cells after co-transfection with Flag-p62 and indicated combinations of empty HA-vector and HA-tagged FIP200 KI with or without Flag-TAX1BP1 or Flag-NBR1 before immunoprecipitation with anti-HA magnetic agarose. Immunoprecipitates (top panel) and input samples (bottom panel) were then subjected to western blotting against anti-Flag or HA. B: Co-immunoprecipitation assays in HEK293T cells after co-transfection with Flag-p62 and indicated combinations of empty HA-vector and HA-tagged TAX1BP1 with or without Flag-NBR1 before immunoprecipitation with anti-HA magnetic agarose. Immunoprecipitates (top panel) and input samples (bottom panel) were then subjected to western blotting against anti-Flag or HA. C: Co-immunoprecipitation assays in HEK293T cells after co-transfection with HA-p62, HA-NBR1, and indicated combinations of empty Flag-vector, Flag-tagged TAX1BP1 FL, YREK449-452AAAA, FKEL453-456AAAA, QRLQ457-460AAAA, KQIN461-464AAAA, and Δ449-463 before immunoprecipitation with anti-DYKDDDDK magnetic agarose. Immunoprecipitates (top panel) and input samples (bottom panel) were then subjected to western blotting against anti-HA or Flag. D: Western blotting of TAX1BP1, NBR1, and p62 protein levels in *fip200* cKI; *tax1bp1* cKO NSCs re-expressed with different TAX1BP1 mutants. ACTIN was used as a loading control. E: Immunofluorescence of p62 puncta and DAPI in *fip200* cKI; *tax1bp1* cKO NSCs re-expressed with different TAX1BP1 mutants. Scale bar: 20 μm. F: Mean±SEM of p62 puncta per neurosphere ($n$=3 independent samples). **: $P$<0.01; ***: $P$<0.001 (one-way ANOVA with Dunnett's multiple comparisons test). G: Neurosphere formation from *fip200* cKI; *tax1bp1* cKO NSCs re-expressed with different TAX1BP1 mutants. Representative phase contrast images. Scale bar: 200 μm. H: Mean±SEM of number and size of neurospheres ($n$=3 independent samples). ****: $P$<0.0001 (one-way ANOVA with Dunnett's multiple comparisons test).

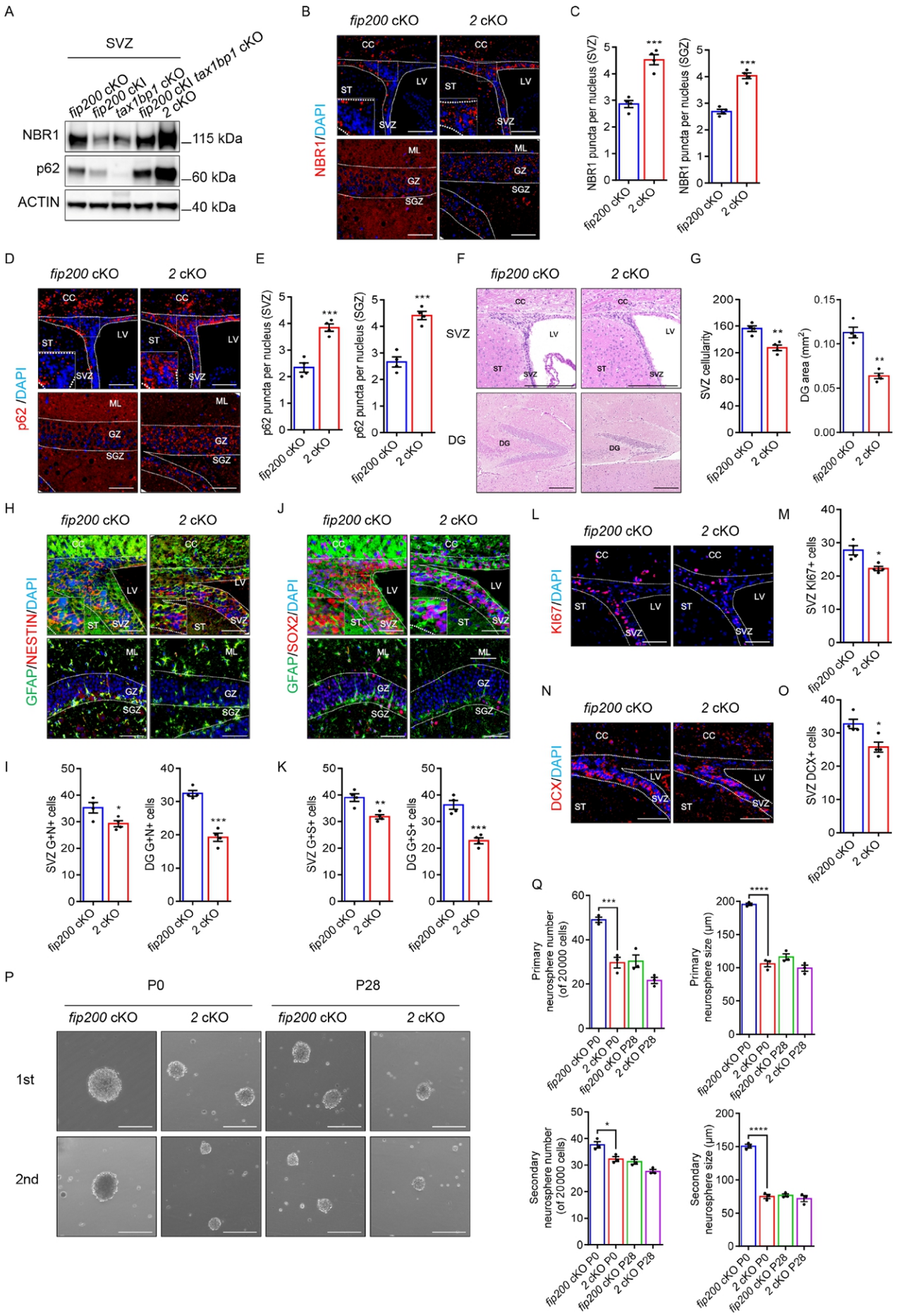

A
SVZ
fip200 cKO
fip200 cKI
tax1bp1 cKO
fip200 cKI tax1bp1 cKO
2 cKO
NBR1
p62
ACTIN
115 kDa
60 kDa
40 kDa
B
fip200 cKO
2 cKO
NBR1/DAPI
CC
ST
LV
SVZ
ML
GZ
SGZ
C
NBR1 puncta per nucleus (SVZ)
NBR1 puncta per nucleus (SGZ)
fip200 cKO
2 cKO
D
p62 /DAPI
E
p62 puncta per nucleus (SVZ)
p62 puncta per nucleus (SGZ)
F
SVZ
DG
G
SVZ cellularity
DG area (mm²)
H
GFAP/NESTIN/DAPI
I
SVZ G+N+ cells
DG G+N+ cells
J
GFAP/SOX2/DAPI
K
SVZ G+S+ cells
DG G+S+ cells
L
KI67/DAPI
M
SVZ KI67+ cells
N
DCX/DAPI
O
SVZ DCX+ cells
P
P0
P28
1st
2nd
Q
Primary neurosphere number (of 20000 cells)
Primary neurosphere size (μm)
Secondary neurosphere number (of 20000 cells)
Secondary neurosphere size (μm)
fip200 cKO P0
2 cKO P0
fip200 cKO P28
2 cKO P28

**Figure 5 TAX1BP1 ablation in *fip200* cKO mice exacerbates p62/NBR1 aggregation and degeneration of the SVZ and DG**

A: Lysates were extracted from the SVZ of P28 *fip200* cKO, *fip200* cKI, *tax1bp1* cKO, *fip200* cKI; *tax1bp1* cKO, and *2* cKO mice, with NBR1 and p62 protein levels analyzed by western blotting. ACTIN was used as a loading control. B: Immunofluorescence of NBR1 puncta and DAPI in SVZ and SGZ from *fip200* cKO and *2* cKO mice at P28. Dotted lines indicate boundaries of SVZ and DG. Scale bar: 100 μm. C: Mean±SEM of NBR1 puncta per SVZ and SGZ section from *fip200* cKO (*n*=4) and *2* cKO mice (*n*=4) at P28. ***: *P*<0.001 (unpaired Student's two-tailed *t*-test). D: Immunofluorescence of p62 puncta and DAPI in SVZ and SGZ from *fip200* cKO and *2* cKO mice at P28. Dotted lines indicate boundaries of SVZ and DG. Scale bar: 100 μm. E: Mean±SEM of p62 puncta per SVZ and SGZ section from *fip200* cKO (*n*=4) and *2* cKO mice (*n*=4) at P28. ***: *P*<0.001 (unpaired Student's two-tailed *t*-test). F: Histological analysis of sagittal sections of SVZ and DG from *fip200* cKO and *2* cKO mice at P28. Dotted lines indicate boundaries of SVZ and DG. Scale bar: 200 μm. G: Mean±SEM of SVZ cellularity and DG area per section from *fip200* cKO (*n*=4) and *2* cKO mice (*n*=4) at P28. **: *P*<0.01 (unpaired Student's two-tailed *t*-test). H: Immunofluorescence of GFAP, NESTIN, and DAPI in SVZ and SGZ from *fip200* cKO and *2* cKO mice at P28. Dotted lines indicate boundaries of SVZ and DG. Scale bar: 50 μm. I: Mean±SEM of GFAP and NESTIN positive cells per SVZ and SGZ section from *fip200* cKO (*n*=4) and *2* cKO mice (*n*=4) at P28. *: *P*<0.05; ***: *P*<0.001 (unpaired Student's two-tailed *t*-test). J: Immunofluorescence of GFAP, SOX2, and DAPI in SVZ and SGZ from *fip200* cKO and *2* cKO mice at P28. Dotted lines indicate boundaries of SVZ and DG. Scale bar: 50 μm. K: Mean±SEM of GFAP and SOX2 positive cells per SVZ and SGZ section from *fip200* cKO (*n*=4) and *2* cKO mice (*n*=4) at P28. **: *P*<0.01; ***: *P*<0.001 (unpaired Student's two-tailed *t*-test). L: Immunofluorescence of KI67 and DAPI in SVZ from *fip200* cKO and *2* cKO mice at P28. Dotted lines indicate boundaries of SVZ. Scale bar: 50 μm. M: Mean±SEM of KI67 positive cells per SVZ section from *fip200* cKO (*n*=4) and *2* cKO mice (*n*=4) at P28. *: *P*<0.05 (unpaired Student's two-tailed t-test). N: Immunofluorescence of DCX and DAPI in SVZ from *fip200* cKO and *2* cKO mice at P28. Dotted lines indicate boundaries of SVZ. Scale bar: 50 μm. O: Mean±SEM of DCX positive cells per SVZ section from *fip200* cKO (*n*=4) and *2* cKO mice (*n*=4) at P28. *: *P*<0.05 (unpaired Student's two-tailed t-test). P: Primary (first) and secondary (second) neurosphere formation from *fip200* cKO and *2* cKO mice at P0 and P28. Representative phase contrast images. Scale bar: 200 μm. Q: Mean±SEM of number and size of primary and secondary neurospheres (*n*=3 independent samples). *: *P*<0.05; ***: *P*<0.001; ****: *P*<0.0001 (one-way ANOVA with Dunnett's multiple comparisons test).

TAX1BP1-NBR1 axis-mediated non-canonical autophagy. Furthermore, the abnormal accumulation of p62 aggregates impaired NSC maintenance and differentiation. These insights fundamentally extend our understanding of autophagy in NSCs and present potential therapeutic avenues for addressing NSC maintenance and neurodegenerative conditions linked to protein aggregation.

A key innovation of our study was the use of the FIP200-4A mutant, which successfully rescued all observed phenotypes in *fip200* cKO mice, highlighting its critical role in the degradation of ubiquitinated protein aggregates. To further validate this role, we developed a model with both FIP200-4A and TAX1BP1 KO (*fip200* cKI; *tax1bp1* cKO mice), which mimicked the phenotypes observed in *fip200* cKO mice, thereby implicating TAX1BP1 as a necessary component in FIP200-4A-mediated degradation. Moreover, the *fip200* cKI; *tax1bp1* cKO mice mirrored the phenotypes of *fip200* cKO mice, suggesting that TAX1BP1 is necessary for FIP200-4A mutant-mediated degradation. The *fip200*; *tax1bp1 2* cKO mice also showed more severe phenotypes than those observed in *fip200* cKO mice at P28, indicating that TAX1BP1 also contributes to aggrephagy independently of FIP200-mediated degradation, as illustrated in our working model (Figure 6). In addition, $fip200^{hGFAP}$ cKO; $p62^{-/-}$ mice showed rescued phenotypes similar to those observed in $fip200^{hGFAP}$ cKO mice at P28, consistent with previous study (Wang et al., 2016), indicating that p62 aggregation is a major mediator for FIP200 mutant NSCs.

Beyond its central role in the autophagy initiation complex, FIP200 interacts with various proteins to direct alternative cellular functions (Yeo et al., 2020). Structural and biochemical studies have revealed that FIP200 directly interacts with p62 through its claw region to facilitate the degradation of p62-ubiquitinated protein aggregates (Turco et al., 2019a, 2019b). The FIP200 claw region is also responsible for interactions with OPTN or CCPG1 (Zhou et al., 2021). Additionally, FIP200 associates with NDP52 via its coiled-coil region, promoting NDP52-mediated xenophagy (Boyle et al., 2019; Shi et al., 2020) and mitophagy (Yamano & Youle, 2020). In *Fip200* KO cells, TBK1 is recruited to p62 aggregates via TAX1BP1, promoting p62 aggregate formation (Liu et al., 2021; Schlütermann et al., 2021), whereas, in *Atg7* KO cells, TAX1BP1 recruits FIP200 to bind to NBR1, resulting in local autophagosome formation (Ohnstad et al., 2020). Recent *in vitro* reconstitution research identified direct interactions between FIP200, TAX1BP1, NBR1, and p62, with p62 and NBR1 highlighted as major drivers of ubiquitin condensate formation, whereby NBR1 recruits TAX1BP1 to the ubiquitin condensates formed by p62. Although all three receptors interact with FIP200, TAX1BP1 is the main driver of FIP200 recruitment, thereby mediating the autophagic degradation of p62-ubiquitin condensates (Turco et al., 2021). These *in vitro* observations complement the findings in this study. To the best of our knowledge, however, this study is the first to elucidate the mechanistic basis for the degradation of p62 aggregates in NSCs via non-canonical autophagy.

Our data showed that the interactions between FIP200, TAX1BP1, NBR1, and p62 are crucial for the degradation of p62 aggregates in NSCs. We found that FIP200 preferentially binds with TAX1BP1 and NBR1, both of which enhance the interaction between FIP200 and p62. Additionally, TAX1BP1 showed a tendency to bind with NBR1, facilitating the interaction between TAX1BP1 and p62. Disrupting any of these interactions impaired degradation of p62 aggregates. Further targeted experiments revealed that similar to the phenotype observed in *fip200* cKO mice, TAX1BP1 ablation in *fip200* cKI mice caused p62 and NBR1 aggregation and degeneration of the SVZ and DG. These findings underscore the role of TAX1BP1 as a key driver of p62 aggregate degradation in canonical autophagy-defective NSCs.

In summary, our study revealed a non-canonical autophagy pathway involved in protein aggregate degradation and the regulation of postnatal NSCs. We identified TAX1BP1 as a key determinant of p62 aggregate degradation and NSC regulation in *fip200* cKI mice. Further research is required to fully elucidate the clinical relevance of this pathway in neurodegenerative diseases.

## SUPPLEMENTARY DATA

Supplementary data to this article can be found online.

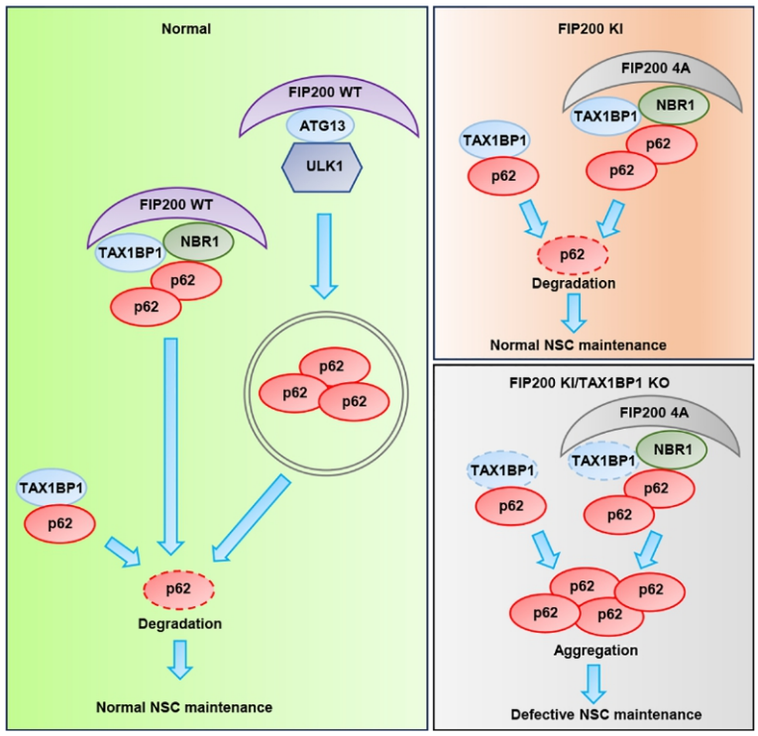



**Figure 6 Working model of FIP200-TAX1BP1 axis-mediated non-canonical autophagy of p62 aggregates, leading to normal neural stem cell (NSC) maintenance**

Schematic of differential p62 aggregate degradation in NSCs. Macroautophagy, FIP200-TAX1BP1 axis-mediated non-canonical autophagy, and TAX1BP1-mediated non-canonical autophagy mediate the degradation of p62 aggregates, leading to normal NSC maintenance.

## COMPETING INTERESTS

The authors declare that they have no competing interests.

## AUTHORS' CONTRIBUTIONS

S.C. and M.W. conceived and designed the project; S.C. and M.W. supervised the study; Y.F.Z. and R.H.Y. performed most of the experiments; S.Z., P.P.T., R.Z., Y.X.W., J.L.Z., Y.Y.W., J.M.W., M.K.L., and X.J.S. assisted with most of the cloning and mouse experiments; X.D.Z., Y.W.Z., and G.Z.L. provided reagents and resources; R.X., R.F.T, X.D.Z., S.C., and M.W. carried out data analysis. Y.F.Z., R.F.T., and S.C. wrote the manuscript. All authors read and approved the final version of the manuscript.

## ACKNOWLEDGMENTS

We would like to thank Dr. Jun-Lin Guan from the University of Cincinnati for providing *fip200* flox/KI mice. We thank Dr. Wei-Lin Jin from Lanzhou University for helpful discussions. We thank all the staff of the Laboratory Animal Center of Zhengzhou University for maintaining the animals.

## REFERENCES

Becher OJ, Holland EC. 2010. Evidence for and against regional differences in neural stem and progenitor cells of the CNS. *Genes & Development*, **24**(20): 2233–2238.

Bhutia SK, Praharaj PP, Bhol CS, et al. 2018. Monitoring and measuring mammalian autophagy. *In*: Turksen K. Autophagy in Differentiation and Tissue Maintenance. New York: Humana Press, 209–222.

Bjørkøy G, Lamark T, Johansen T. 2006. p62/SQSTM1: a missing link between protein aggregates and the autophagy machinery. *Autophagy*, **2**(2): 138–139.

Boyle KB, Ravenhill BJ, Randow F. 2019. CALCOCO2/NDP52 initiates selective autophagy through recruitment of ULK and TBK1 kinase complexes. *Autophagy*, **15**(9): 1655–1656.

Casares-Crespo L, Calatayud-Baselga I, García-Corzo L, et al. 2018. On the role of basal autophagy in adult neural stem cells and neurogenesis. *Frontiers in Cellular Neuroscience*, **12**: 339.

Chen S, Wang CR, Yeo S, et al. 2016. Distinct roles of autophagy-dependent and -independent functions of FIP200 revealed by generation and analysis of a mutant knock-in mouse model. *Genes & Development*, **30**(7): 856–869.

Deng ZQ, Lim J, Wang Q, et al. 2020. ALS-FTLD-linked mutations of SQSTM1/p62 disrupt selective autophagy and NFE2L2/NRF2 anti-oxidative stress pathway. *Autophagy*, **16**(5): 917–931.

Doetsch F, Caillé I, Lim DA, et al. 1999. Subventricular zone astrocytes are neural stem cells in the adult mammalian brain. *Cell*, **97**(6): 703–716.

Donde A, Sun MK, Jeong YH, et al. 2020. Upregulation of ATG7 attenuates motor neuron dysfunction associated with depletion of TARDBP/TDP-43. *Autophagy*, **16**(4): 672–682.

Fleming A, Rubinsztein DC. 2020. Autophagy in neuronal development and plasticity. *Trends in Neurosciences*, **43**(10): 767–779.

Friesen EL, Zhang YT, Earnshaw R, et al. 2020. BAG5 promotes alpha-synuclein oligomer formation and functionally interacts with the autophagy adaptor protein p62. *Frontiers in Cell and Developmental Biology*, **8**: 716.

Gage FH. 2000. Mammalian neural stem cells. *Science*, **287**(5457): 1433–1438.

Galluzzi L, Baehrecke EH, Ballabio A, et al. 2017. Molecular definitions of autophagy and related processes. *The EMBO Journal*, **36**(13): 1811–1836.

Gibertini S, Ruggieri A, Cheli M, et al. 2023. Protein aggregates and aggrephagy in myopathies. *International Journal of Molecular Sciences*, **24**(9): 8456.

Guo CT, Zhao Y. 2020. Autophagy and DNA damage repair. *Genome Instability & Disease*, **1**(4): 172–183.

He CC, Klionsky DJ. 2009. Regulation mechanisms and signaling pathways of autophagy. *Annual Review of Genetics*, **43**: 67–93.

Huang J, Klionsky DJ. 2007. Autophagy and human disease. *Cell Cycle*, **6**(15): 1837–1849.

Klionsky DJ, Petroni G, Amaravadi RK, et al. 2021. Autophagy in major human diseases. *The EMBO Journal*, **40**(19): e108863.

Lamark T, Johansen T. 2012. Aggrephagy: selective disposal of protein aggregates by macroautophagy. *International Journal of Cell Biology*, **2012**: 736905.

Liang CC, Wang CR, Peng X, et al. 2010. Neural-specific deletion of FIP200 leads to cerebellar degeneration caused by increased neuronal death and axon degeneration. *Journal of Biological Chemistry*, **285**(5): 3499–3509.

Liu H, Wang CR, Yi F, et al. 2021. Non-canonical function of FIP200 is required for neural stem cell maintenance and differentiation by limiting TBK1 activation and p62 aggregate formation. *Scientific Reports*, **11**(1): 23907.

Liu YH, Lai WS, Tsay HJ, et al. 2013. Effects of maternal immune activation on adult neurogenesis in the subventricular zone-olfactory bulb pathway and olfactory discrimination. *Schizophrenia Research*, **151**(1-3): 1–11.

Lyu L, Chen Z, McCarty N. 2022. TRIM44 links the UPS to SQSTM1/p62-dependent aggrephagy and removing misfolded proteins. *Autophagy*, **18**(4): 783–798.

Ma SF, Attarwala IY, Xie XQ. 2019. SQSTM1/p62: a potential target for neurodegenerative disease. *ACS Chemical Neuroscience*, **10**(5): 2094–2114.

Ma XY, Lu CJ, Chen YT, et al. 2022. CCT2 is an aggrephagy receptor for clearance of solid protein aggregates. *Cell*, **185**(8): 1325–1345. e22.

Majcher V, Goode A, James V, et al. 2015. Autophagy receptor defects and ALS-FTLD. *Molecular and Cellular Neuroscience*, **66**: 43–52.

Mizushima N, Levine B. 2010. Autophagy in mammalian development and differentiation. *Nature Cell Biology*, **12**(9): 823–830.

Oh CK, Dolatabadi N, Cieplak P, et al. 2022. S-nitrosylation of p62 inhibits autophagic flux to promote α-synuclein secretion and spread in parkinson's disease and lewy body dementia. *Journal of Neuroscience*, **42**(14): 3011–3024.

Ohnstad AE, Delgado JM, North BJ, et al. 2020. Receptor-mediated clustering of FIP200 bypasses the role of LC3 lipidation in autophagy. *The EMBO Journal*, **39**(24): e104948.

Palmer TD, Takahashi J, Gage FH. 1997. The adult rat hippocampus contains primordial neural stem cells. *Molecular and Cellular Neuroscience*, **8**(6): 389–404.

Pankiv S, Clausen TH, Lamark T, et al. 2007. p62/SQSTM1 binds directly to Atg8/LC3 to facilitate degradation of ubiquitinated protein aggregates by autophagy. *Journal of Biological Chemistry*, **282**(33): 24131–24145.

Rué L, López-Soop G, Gelpi E, et al. 2013. Brain region- and age-dependent dysregulation of p62 and NBR1 in a mouse model of Huntington's disease. *Neurobiology of Disease*, **52**: 219–228.

Sarraf SA, Shah HV, Kanfer G, et al. 2020. Loss of TAX1BP1-directed autophagy results in protein aggregate accumulation in the brain. *Molecular Cell*, **80**(5): 779–795. e10.

Schaeffer V, Goedert M. 2012. Stimulation of autophagy is neuroprotective in a mouse model of human tauopathy. *Autophagy*, **8**(11): 1686–1687.

Schlütermann D, Berleth N, Deitersen J, et al. 2021. FIP200 controls the TBK1 activation threshold at SQSTM1/p62-positive condensates. *Scientific Reports*, **11**(1): 13863.

Shi XS, Chang CM, Yokom AL, et al. 2020. The autophagy adaptor NDP52 and the FIP200 coiled-coil allosterically activate ULK1 complex membrane recruitment. *eLife*, **9**: e59099.

Thorburn A. 2018. Autophagy and disease. *Journal of Biological Chemistry*, **293**(15): 5425–5430.

Trapannone R, Romanov J, Martens S. 2023. p62 and NBR1 functions are dispensable for aggrephagy in mouse ESCs and ESC-derived neurons. *Life Science Alliance*, **6**(11): e202301936.

Turco E, Savova A, Gere F, et al. 2021. Reconstitution defines the roles of p62, NBR1 and TAX1BP1 in ubiquitin condensate formation and autophagy initiation. *Nature Communications*, **12**(1): 5212.

Turco E, Witt M, Abert C, et al. 2019a. FIP200 claw domain binding to p62 promotes autophagosome formation at ubiquitin condensates. *Molecular Cell*, **74**(2): 330–346. e11.

Turco E, Witt M, Abert C, et al. 2019b. How RB1CC1/FIP200 claws its way to autophagic engulfment of SQSTM1/p62-ubiquitin condensates. *Autophagy*, **15**(8): 1475–1477.

Vázquez P, Arroba AI, Cecconi F, et al. 2012. Atg5 and Ambra1 differentially modulate neurogenesis in neural stem cells. *Autophagy*, **8**(2): 187–199.

Wang CR, Chen S, Yeo S, et al. 2016. Elevated p62/SQSTM1 determines the fate of autophagy-deficient neural stem cells by increasing superoxide. *Journal of Cell Biology*, **212**(5): 545–560.

Wang CR, Liang CC, Bian ZC, et al. 2013. FIP200 is required for maintenance and differentiation of postnatal neural stem cells. *Nature Neuroscience*, **16**(5): 532–542.

Wang CR, Yeo S, Haas MA, et al. 2017. Autophagy gene FIP200 in neural progenitors non-cell autonomously controls differentiation by regulating microglia. *Journal of Cell Biology*, **216**(8): 2581–2596.

Wang SK, Li BG, Qiao HM, et al. 2014. Autophagy-related gene Atg5 is essential for astrocyte differentiation in the developing mouse cortex. *EMBO Reports*, **15**(10): 1053–1061.

Wang Y, Yang J, Zheng HR, et al. 2009. Expression of mutant p53 proteins implicates a lineage relationship between neural stem cells and malignant astrocytic glioma in a murine model. *Cancer Cell*, **15**(6): 514–526.

Xi Y, Dhaliwal JS, Ceizar M, et al. 2016. Knockout of *Atg5* delays the maturation and reduces the survival of adult-generated neurons in the hippocampus. *Cell Death & Disease*, **7**(3): e2127.

Yamano K, Youle RJ. 2020. Two different axes CALCOCO2-RB1CC1 and OPTN-ATG9A initiate PRKN-mediated mitophagy. *Autophagy*, **16**(11): 2105–2107.

Yang JS, Chen XL, Xu HL. 2021. SQSTM1/p62 droplet -mediated autophagosome formation: insights into Huntington disease. *Autophagy*, **17**(10): 3256–3259.

Yang Y, Zhu YF, Zhou S, et al. 2022. TRIM27 cooperates with STK38L to inhibit ULK1-mediated autophagy and promote tumorigenesis. *The EMBO Journal*, **41**(14): e109777.

Yeo SK, Wang CR, Guan JL. 2020. Role of FIP200 in inflammatory processes beyond its canonical autophagy function. *Biochemical Society Transactions*, **48**(4): 1599–1607.

Zhao CM, Deng W, Gage FH. 2008. Mechanisms and functional implications of adult neurogenesis. *Cell*, **132**(4): 645–660.

Zheng XH, Wang WW, Liu RZ, et al. 2012. Effect of p62 on tau hyperphosphorylation in a rat model of Alzheimer's disease. *Neural Regeneration Research*, **7**(17): 1304–1311.

Zhou ZX, Liu JP, Fu T, et al. 2021. Phosphorylation regulates the binding of autophagy receptors to FIP200 Claw domain for selective autophagy initiation. *Nature Communications*, **12**(1): 1570.

Fu et al. *Zool. Res.* 2024, 45(4): 951−960
https://doi.org/10.24272/j.issn.2095-8137.2024.039

ZR | Zoological Research

Article Open Access

# Tumor necrosis factor α deficiency promotes myogenesis and muscle regeneration

Yu Fu[1], Jing-Ru Nie[1], Peng Shang[2], Bo Zhang[1], Da-Wei Yan[3], Xin Hao[1,*], Hao Zhang[1,*]

[1] *State Key Laboratory of Animal Biotech Breeding*, *China Agricultural University*, *Beijing* 100193, *China*
[2] *College of Animal Science*, *Xizang Agricultural and Animal Husbandry University*, *Linzhi*, *Xizang* 860000, *China*
[3] *College of Animal Science and Technology*, *Yunnan Agricultural University*, *Kunming*, *Yunnan* 650201, *China*

## ABSTRACT

Tumor necrosis factor α (TNFα) exhibits diverse biological functions; however, its regulatory roles in myogenesis are not fully understood. In the present study, we explored the function of *TNFα* in myoblast proliferation, differentiation, migration, and myotube fusion in primary myoblasts and C2C12 cells. To this end, we constructed *TNFα* muscle-conditional knockout (*TNFα*-CKO) mice and compared them with *flox* mice to assess the effects of *TNFα* knockout on skeletal muscles. Results indicated that *TNFα*-CKO mice displayed phenotypes such as accelerated muscle development, enhanced regenerative capacity, and improved exercise endurance compared to *flox* mice, with no significant differences observed in major visceral organs or skeletal structure. Using label-free proteomic analysis, we found that *TNFα*-CKO altered the distribution of several muscle development-related proteins, such as Hira, Casz1, Casp7, Arhgap10, Gas1, Diaph1, Map3k20, Cfl2, and Igf2, in the nucleus and cytoplasm. Gene set enrichment analysis (GSEA) further revealed that *TNFα* deficiency resulted in positive enrichment in oxidative phosphorylation and MyoD targets and negative enrichment in JAK-STAT signaling. These findings suggest that *TNFα*-CKO positively regulates muscle growth and development, possibly via these newly identified targets and pathways.

**Keywords:** TNFα; Muscle-conditional knockout; Myogenesis; Regeneration; Muscle development

## INTRODUCTION

Tumor necrosis factor α (TNFα) is a cytokine that exists in secreted, membrane-bound, or intracellular soluble forms, exhibiting biological activities across various cell types (Horiuchi et al., 2010; Kriegler et al., 1988). By binding to receptors on the cell membrane, it activates different cascading signaling pathways to regulate processes such as cell growth, differentiation, apoptosis, and inflammatory responses (Jang et al., 2021). Skeletal muscle formation primarily depends on complex processes such as myoblast proliferation, migration, differentiation, cytoskeletal rearrangement, and myotube fusion, which are regulated by multiple genes. Although *TNFα* has been extensively studied in the context of immunology, recent studies have also highlighted its significant roles in skeletal muscle development, including myogenesis, muscle repair, muscle disease, and muscle atrophy (Di Credico et al., 2023; Fang et al., 2021; Li et al., 2020; Shirakawa et al., 2021).

As an endogenous muscle factor, *TNFα* is expressed in cultured myoblasts and strongly activated in injured muscle tissue (Collins & Grounds, 2001; Li & Schwartz, 2001). However, its role in myoblast proliferation and muscle regeneration remains controversial. Overexpression of *TNFα* can substantially reduce the number of $Pax7^+$ cells (Li et al., 2020). Conversely, the exogenous addition of *TNFα* protein can stimulate myoblast proliferation and satellite cell activation (Alvarez et al., 2020; Li, 2003; Shirakawa et al., 2021). Muscle regeneration is impaired in both *TNFα* knock-in mice (Li et al., 2020) and *TNFα* receptor double-knockout mice ($p55^{-/-}p75^{-/-}$) following cardiotoxin (CTX)-induced muscle injury (Chen et al., 2005). Furthermore, *TNFα* consistently inhibits the accumulation of muscle-specific proteins in differentiated C2C12 cells. Notably, it promotes MyoD degradation through the ubiquitin-proteasome pathway, reducing the half-life and abundance of the MyoD protein (Langen et al., 2004). *TNFα* also suppresses myotube formation (Meyer et al., 2015). Interestingly, low concentrations of exogenous TNFα protein can promote myogenesis, while high concentrations induce the opposite effect (Chen et al., 2007). Additionally, triptolide can prevent lipopolysaccharide-induced skeletal muscle atrophy by gradually reducing *TNFα* levels (Fang et al., 2021).

This is an open-access article distributed under the terms of the Creative Commons Attribution Non-Commercial License (http://creativecommons.org/licenses/by-nc/4.0/), which permits unrestricted non-commercial use, distribution, and reproduction in any medium, provided the original work is properly cited.

Copyright ©2024 Editorial Office of Zoological Research, Kunming Institute of Zoology, Chinese Academy of Sciences

Received: 06 February 2024; Accepted: 07 April 2024; Online: 08 April 2024

Foundation items: This work was supported by the Xizang Major Science and Technology Project (XZ202101ZD0005N), Yunnan Major Science and Technology Project (202302AE090015), National Key R&D Program of China (2023ZD04044-04), and National Natural Science Foundation of China (32060736)

*Corresponding authors, E-mail: haoxin0331@163.com; hzhang@cau.edu.cn

However, the physiological role of *TNFα* in skeletal muscle development and associated molecular mechanisms remain unclear.

Regarding immunity, there is a well-established consensus on the role of the TNFα signaling pathway. The binding of TNFα to its receptor ultimately leads to NF-κB-dependent cellular responses, cell apoptosis, or necrosis (Hsu et al., 1995; Li & Schwartz, 2001; Pasparakis & Vandenabeele, 2015; Varfolomeev & Vucic, 2018). TNFα also activates three groups of MAP kinases, including extracellular signal-regulated, p38 MAP, and c-Jun NH2-terminal kinases (Sabio & Davis, 2014). However, these known signaling pathways do not fully explain the mechanisms by which TNFα regulates muscle development. Therefore, it is plausible that additional, muscle-specific regulatory pathways remain undiscovered and warrant further research.

In the current study, we explored the role of *TNFα* and its associated mechanisms in muscle development. We systematically examined the effects of *TNFα* on myoblast proliferation, migration, differentiation, and myotube fusion. We successfully established *TNFα* muscle-conditional knockout (*TNFα*-CKO) mice *in vivo* and evaluated their skeletal muscle development, muscle regenerative capacity following CTX-induced damage, and exercise endurance. Mechanistically, we identified potential new targets and pathways influenced by *TNFα*. Our results provide a theoretical foundation for further studies on the regulation of muscle development by *TNFα* and propose a novel strategy for myopathy treatment.

## MATERIALS AND METHODS

### C2C12 cell culture and RNA interference

The C2C12 myoblast cell line (Type Culture Collection of the Chinese Academy of Sciences, China) was cultured in Dulbecco's modified Eagle medium (DMEM, Gibco, USA) with 10% fetal bovine serum (FBS, Gibco, USA) and 1% penicillin/streptomycin (Gibco, USA). To induce differentiation, the cells were incubated in DMEM supplemented with 2% horse serum (Gibco, USA) and 1% penicillin/streptomycin. To interfere with *TNFα* expression, we designed small interfering RNAs (siRNAs) based on the *TNFα* gene sequence and selected the top candidates with the highest scores (siRNA-403, siRNA-509, siRNA-631) from the design website. The number assigned to each siRNA corresponds to its position relative to the start site of *TNFα*. The *TNFα* siRNA sequences were: siRNA-403, sense: CUCAGAUCAUCUUCUCAAATT, antisense: UUUGAGAAGAUGAUCUGAGTT; siRNA-506, sense: CCAACGGCAUGGAUCUCAATT, antisense: UUGAGA UCCAUGCCGUUGGTT; and siRNA-631, sense: AGCCG AUUUGCUAUCUCAUTT, antisense: AUGAGAUAGCAAAU CGGCUTT. Cell transfection was performed using Lipofectamine 2000 in accordance with the manufacturer's instructions (Invitrogen, USA).

### Animals

The *floxed-TNFα* mouse line (C57BL/6N background) was established by Cyagen Biosciences (China) by inserting LoxP site flanking exons 1 and 4 of the *TNFα* gene. The *TNFα*-CKO were generated by crossing $TNF\alpha^{flox/flox}$ and *Myf5-Cre* mice obtained from Jackson Laboratory (USA). The mouse genotype was determined via polymerase chain reaction (PCR) using tail DNA with the following primers: *Cre*-F: 5′-AACCAGAGACTCCCCAAGGT-3′, *Cre*-R: 5′-ACGAAGTTATT AGGTCCCTCGAC-3′, *Cre*-WR: 5′-CGGCTCTTAAAGCAAT GGTC-3′, F2: 5′-GAGACCTAAGCTCTATCCCTGCTC-3′, R2: 5′-TCACATTTTCAGCCCTGTGTCTTT-3′). $Cre^{-}$ mice had an amplicon of 240 bp, while $Cre^{+}$ mice possessed an amplicon of 120 bp. Furthermore, $flox^{+/+}$ mice showed a single band at 205 bp, while $flox^{-/-}$ mice showed a single band at 138 bp. Consequently, $flox^{+/+}Cre^{-}$ mice served as control $TNF\alpha^{flox/flox}$ mice, while $floxflox^{+/+}Cre^{+}$ represented *TNFα*-CKO mice. For muscle regeneration assays, 50 μL of CTX (20 μmol/L, Sigma-Aldrich, USA) was injected into the tibialis anterior (TA) muscles of 2-month-old mice. All animal procedures were performed in accordance with the guidelines for good laboratory practice. The animals were provided with sufficient water, standard chow diet, and appropriate feeding conditions. Furthermore, the animal care and experimental procedures were conducted based on the National Research Council Guide for the Care and Use of Laboratory Animals and were approved by the Institutional Animal Care and Use Committee at China Agricultural University, Beijing, China (approval number: AW80203202-1-1).

### Primary myoblast purification and culture

Mouse primary myoblasts were isolated from 6-week-old C57BL/6N mice. Briefly, mouse muscles were minced and digested in 0.2% type II collagenase (Sigma-Aldrich, USA) and 2.5 U/mL dispase (Roche Applied Science, USA) for 1 h. After digestion, the cells were filtered and centrifuged at 1500 ×*g* for 5 min at room temperature, then cultured in growth medium (F10 supplemented with 20% FBS, 1% penicillin-streptomycin, 5 ng/mL basic fibroblast growth factor, and 1% chicken embryo extract) on collagen-coated cell culture plates at 37℃ and 5% $CO_2$.

### EdU and CCK8 assays

5-Ethynyl-2-deoxyuridine (EdU) and Cell Counting Kit-8 (CCK8) assays were conducted in accordance with the instructions provided with the EdU (Ribobio, China) and CCK8 (Solarbio, China) assay kits, respectively. In the EdU assay, cells transfected for 24 h were incubated with 50 μmol/L EdU for 2 h, then fixed with 4% paraformaldehyde (PFA), permeabilized with 0.5% Triton X-100, and incubated with Apollo reaction buffer. EdU-labeled cells and 4',6-diamidino-2-phenylindole (DAPI)-stained (Solarbio) nuclei were photographed under a microscope (ZEISS, Germany). For the CCK8 assay, transfected cells were incubated with 100 μL of 10% CCK8 solution at 37℃ for 1 h. Absorbance was measured at 450 nm using a multimode reader (Biotek, USA).

### Cell wounding and Transwell migration

For wounding, the cells (24–48 h after transfection) were scratched with a pipette tip of the same width. Floating cells were washed with phosphate-buffered saline (PBS) and the medium was then replaced with DMEM plus 2% FBS. At 24 h post-wounding, cell migration distance was recorded. For the Transwell assay, equal amounts of cells were cultured in the lower and upper Transwell chambers for 12 h, with crystal violet then used to stain the migrated cells induced by the serum gradient.

### Immunofluorescence (IF)

Myoblasts or muscle tissues were fixed in 4% PFA for 20 min and permeabilized for 15 min in 0.3% Triton X-100 with PBS. The samples were then blocked in blocking buffer (Beyotime, China) for 2 h at room temperature and incubated overnight at 4℃ with the following primary antibodies: MyHC (M4276,

1:200; Sigma-Aldrich, USA), eMyHC (F1.652, 1:50; Developmental Studies Hybridoma Bank, USA), and laminin (L9393, 1:1 000; Sigma-Aldrich, USA). After incubation, the samples were washed with PBS and incubated with fluorescently labeled secondary antibodies (SA00013-2 and SA00013-3, 1:400; Proteintech, USA) for 1 h at room temperature in darkness. The samples were then washed with PBS and the cell nuclei were labeled using DAPI for 5 min. Finally, immunofluorescence images were visualized using a fluorescence microscope (Model Q500MC; Leica Image Analysis System, Germany).

**Magnetic resonance imaging (MRI)**

MRI was performed under anesthesia using 2% isoflurane on an MRI system equipped with a 7 T/16-cm wide-bore instrument. Thus, 20 contiguous coronal slices (thickness=1 mm), covering the region from the knee to the ankle, were acquired. The scan parameters were: echo time (TE)=7.8 ms, repetition time (TR)=500 ms, field of view=100 mm×60 mm, matrix size=256×256, and acquisition time=20 min. The images were analyzed using VNMRJ v.4.0 (Varian Associates, USA).

**Hematoxylin-eosin staining (H&E)**

After fixation in 4% PFA, tissues were processed for routine paraffin histology and stained with H&E. The sections were then examined under an inverted microscope.

**Swimming exhaustion test**

Several large beakers were filled with water and maintained at a constant temperature of 28℃. The mice were fasted overnight (15 h), and a piece of metal (7% of body weight) was attached to their tails to ensure that they would sink without swimming. The duration each mouse swam until exhaustion was recorded.

**qPCR analysis**

Total RNA was isolated from myoblasts and muscle tissues using a TRNzol Universal Reagent (Tiangen, China). Subsequently, 2 μg of total RNA was reverse transcribed into cDNA using a FastKing gDNA Dispelling RT SuperMix Kit (Tiangen, China) according to the manufacturer's instructions. qPCR was then performed using the Universal SYBR Green Fast qPCR Mix system (ABclonal, China). The primer sequences used are shown in Supplementary Table S1.

**Western blot analysis**

The C2C12 cells and primary myoblasts were lysed in RIPA buffer (Beyotime, China) or a nuclear/cytoplasmic protein extraction kit (Beyotime, China). Proteins were then resolved using sodium dodecyl-sulfate polyacrylamide gel electrophoresis (SDS-PAGE) and transferred to polyvinylidene fluoride (PVDF) membranes. The membranes were then blocked in QuickBlock buffer (Beyotime, China) for 30 min at room temperature and incubated overnight at 4℃ with primary antibodies, including: mouse anti-MyoG (ab1835, 1:500; Abcam, USA), mouse anti-MyHC (M4276, 1:1 000; Sigma-Aldrich, USA), rabbit anti-TNFα (A11534, 1:1 000; ABclonal, China), mouse anti-Casz1 (sc-398303, 1:1 000; Santa Cruz Biotechnology, USA), rabbit anti-Hira (A12527, 1:1 000; ABclonal, China), rabbit anti-Diaph1 (A11596, 1:1 000; ABclonal, China), rabbit anti-Tnnt1 (A10354, 1:1 000; ABclonal, China), rabbit anti-Fgf21 (A3908, 1:2 000; ABclonal, China), rabbit anti-Map3k20 (A14513, 1:1 000; ABclonal, China), rabbit anti-Cfl2 (A8009, 1:2 000; ABclonal, China), rabbit anti-Histone H3 (A2348, 1:5 000; ABclonal, China), rabbit anti-GAPDH (2118s, 1:5 000; Cell Signaling Technology, USA), and rabbit anti-β-Tubulin (ab6046, 1:5 000; Abcam, USA). Incubation with the secondary antibodies was performed for 1 h at room temperature.

**Proteomic analysis**

*Flox* and *TNFα*-CKO primary myoblasts were induced to differentiate for 2 d. Thereafter, nuclear and cytoplasmic proteins were extracted using nuclear/cytoplasmic protein extraction kits (Beyotime, China). Briefly, the samples were sonicated three times with 1% protease inhibitor cocktail on ice using a high intensity ultrasonic processor (Scientz, China). The supernatant was then obtained via centrifugation at 12 000 ×*g* and 4℃ for 10 min. Protein concentration was measured using a BCA kit (Beyotime, China).

The protein samples were added to four volumes of pre-cooled acetone and precipitated at −20℃ for 2 h. Thereafter, they were re-dissolved in 200 mmol/L triethylammonium bicarbonate and ultrasonically dispersed. Trypsin was added at a 1:50 trypsin-to-protein mass ratio for the first digestion overnight. The samples were then reduced with 5 mmol/L dithiothreitol for 30 min at 56℃ and alkylated with 11 mmol/L iodoacetamide for 15 min at room temperature in the dark.

To dissolve and separate the tryptic peptides, an EASY-nLC 1200 UPLC system (Thermo Fisher Scientific, USA) was used at a constant flow rate of 500 nL/min. The separated peptides were then analyzed using an Orbitrap Exploris 480 mass spectrometer (Thermo Fisher Scientific, USA) with a nano-electrospray ion source. The resulting tandem mass spectrometry (MS/MS) data were processed using the Proteome Discoverer search engine (v.2.4.1.15, Thermo Fisher Scientific, USA). The MS/MS data were searched against the Mus_musculus_10090_SP_20230103.fasta database (17 132 entries) concatenated with the reverse decoy database. Trypsin (Full) was specified as the cleavage enzyme, allowing up to two missed cleavages. The false discovery rates (FDRs) for proteins, peptides, and peptide-spectrum match were adjusted to <1%. The minimum peptide length was set to 6. Label-free measurements were performed using the PTM Bio System (PTM-Biolabs, China). Data were obtained via ProteomeXchange with the identifier PXD046525.

Gene lists were analyzed using GSEA v.4.3.2 from the Broad Institute (Subramanian et al., 2005). The submitted gene list was normalized by applying the $-\log_{10}$ transformation to the count values, assigned as positive or negative based on the direction of the fold change. All other GSEA parameters were set to default. The annotated HALLMARK, DELASERNA, and KEGG gene sets obtained from the DAVID and MSigDB databases were used as enrichment inputs.

**Statistical analysis**

All data were analyzed using SPSS v.22.0 (IBM, USA) and presented as mean±standard deviation (SD). *P*-values were calculated by performing a two-tailed Student's *t*-test, and statistical significance was indicated as follows: $^{*}$: $P<0.05$, $^{**}$: $P<0.01$, and $^{***}$: $P<0.001$.

## RESULTS

***TNFα* knockdown promoted cell proliferation, migration, differentiation, and myotube fusion in C2C12 cells**

Skeletal muscle formation primarily relies on processes such as myoblast proliferation, migration, differentiation, and

myotube fusion. We successfully reduced *TNFα* expression in C2C12 cells using RNA interference fragments, with siRNA-631 showing the highest interference efficiency (Figure 1A). Regarding proliferation, the CCK8 assay showed higher absorbance for the siRNA-*TNFα* (si-*TNFα*) transfection group than for the siRNA negative control group (si-NC) (Figure 1B). *TNFα* knockdown also significantly increased the number of EdU$^+$ cells (Figure 1C) and up-regulated the expression of proliferation marker genes, *Ki67*, *Cyclin B*, and *CDK4* (Figure 1D). Cell wounding (Figure 1E) and Transwell (Figure 1F) assays demonstrated that *TNFα* knockdown enhanced myoblast migration and promoted C2C12 cell differentiation into more numerous, longer, and thicker myotubes (Figure 1G), with most myotubes exhibiting multi-nucleation (as indicated by white arrows in Figure 1H). *TNFα* knockdown also significantly up-regulated the expression of myogenic marker genes, *MyoG* and *MyoD* (Figure 1I), as well as fusion marker genes, *β-1 integrin* and *Myomaker* (Figure 1J). Muscle hypertrophy and degradation are crucial processes in muscle development (Bodine et al., 2001). Here, the qPCR results showed that *TNFα* knockdown significantly promoted the expression of muscle hypertrophy genes (*Fst* and *Nog*), while inhibiting the expression of *myostatin* and muscle degradation marker genes (*Atrogin1*, *Bmp4*, and *Foxo3*) (Figure 1K). Overall, *TNFα* knockdown promoted myoblast proliferation, migration, differentiation, and fusion in C2C12 cells, implying that *TNFα* plays a significant regulatory role in the growth and development of skeletal muscles.

**_TNFα_-CKO accelerated mouse muscle development, improved exercise endurance, and enhanced muscle regenerative capacity**

To investigate the role of *TNFα* in muscle development, we generated conditional knockout mice by selectively deleting *TNFα* in skeletal muscles using *Myf5-Cre/TNFα* and *flox/flox* alleles. The *TNFα*-CKO mice exhibited normal birth and survival, with no apparent abnormalities in appearance (Figure 2A). The male *TNFα*-CKO mice demonstrated significantly higher body weights (Figure 2B) and body lengths (Figure 2C) than the *flox* control mice, while the female *TNFα*-CKO and *flox* mice showed no significant differences in body length (Supplementary Figure S1A). Additionally, the *TNFα*-CKO mice developed more robust forelimbs and hindlimbs (Figure 2D). MRI analysis revealed an increase in hindlimb muscles and subcutaneous fat content in *TNFα*-CKO mice, with no significant changes in skeletal volume between the two groups (Figure 2E). Furthermore, the muscle weights of quadriceps (Quad), tibialis anterior (TA), extensor digitorum longus (EDL), gastrocnemius (GAS), soleus (SOL), trapezius (Trap), and triceps were higher in 2-month-old *TNFα*-CKO

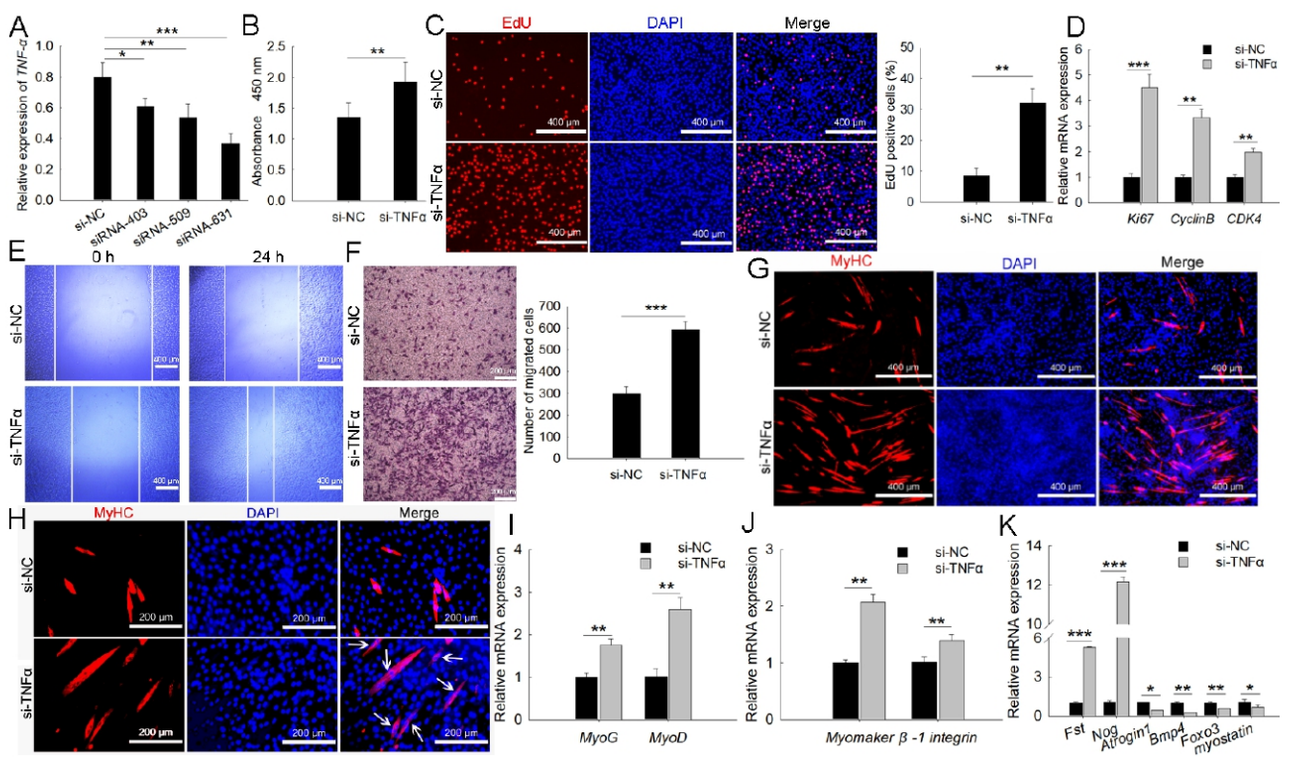



**Figure 1 Promotion of myoblast proliferation, migration, differentiation, and myotube fusion in C2C12 cells through *TNFα* knockdown**

A: Detection of interference efficiency for different siRNA-*TNFα* fragments. Cells were transfected for 24 h, then collected for qPCR. B: CCK8 assay of si-NC and si-*TNFα* C2C12 cells. C: Representative photographs of EdU-stained si-NC and si-*TNFα* cells. EdU$^+$ staining (red) of S-phase cells and DAPI staining (blue) of cell nuclei are shown (Scale bar: 400 μm), and proliferative cells were quantified as a ratio of EdU$^+$/DAPI$^+$. D: Analysis of expression levels of proliferation marker genes. C2C12 cells were transfected with si-NC and si-*TNFα* for 24 h, then collected for qPCR. E, F: Cell wounding (E) and Transwell (F) analysis of migration ability of myoblasts. Migrated cells were stained purple with crystal violet and counted. G: Immunofluorescence staining for MyHC (red) in si-NC and si-*TNFα* C2C12 cells after culturing for 4 d in differentiation medium (Scale bar: 400 μm). H: Myoblast fusion analysis via immunofluorescence staining for MyHC. White arrows represent multinucleated myotubes (Scale bar: 200 μm). I–K: Analysis of expression levels of myogenic differentiation (I), fusion (J), hypertrophy, and degradation marker genes and *myostatin* (K) in si-NC and si-*TNFα* C2C12 cells using qPCR. Transfected cells were cultured in differentiation medium for 4 d. Data are presented as mean±standard deviation (SD); $n$=3. $^*$: $P$<0.05; $^{**}$: $P$<0.01; $^{***}$: $P$<0.001 (Student's $t$-test).

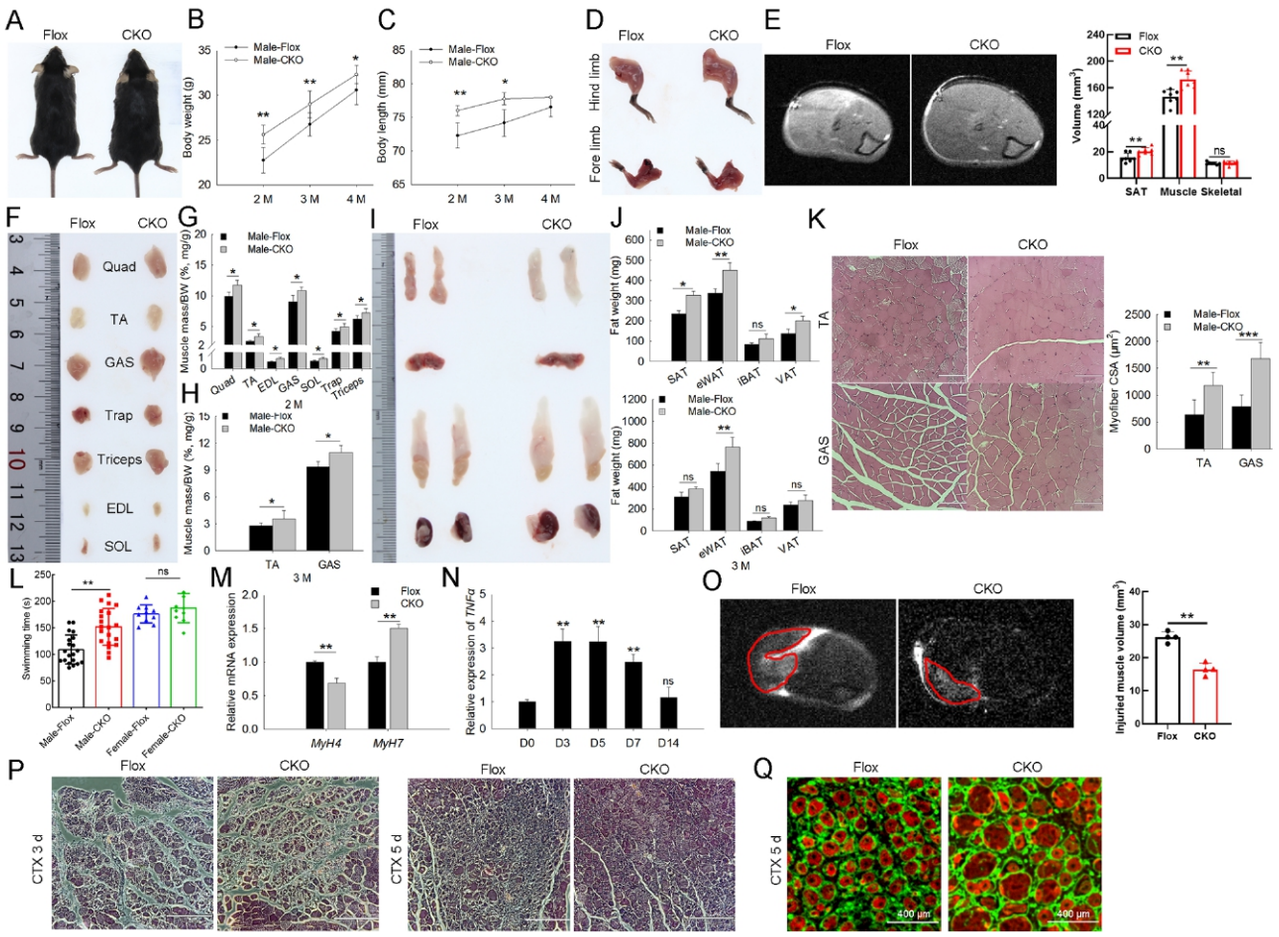



**Figure 2 Improved development speed, exercise endurance, and regeneration ability of *TNFα*-CKO mouse muscles**

A: Gross body morphology of *TNFα*-CKO and *flox* mice. B, C: Body weight (B) and length (C) of *TNFα*-CKO and *flox* male mice at 2, 3, and 4 months ($n$≥50). D: Representative photographs of forelimbs and hindlimbs of *TNFα*-CKO and *flox* mice. E: Magnetic resonance imaging (MRI) of hindlimbs, subcutaneous fat (SAT), muscle, and bone volume. F–H: Representative photographs (F) and weight analysis (G and H) of skeletal muscles of *TNFα*-CKO and flox mice. BW, body weight. I, J: Representative photographs (I) and weight analysis (J) of adipose tissue in *TNFα*-CKO and *flox* mice. K: H&E staining of TA and GAS muscles in *TNFα*-CKO and *flox* mice (Scale bar: 100 μm). CSA, cross-sectional area. L: Swimming exhaustion time assay for *TNFα*-CKO and *flox* mice (n≥10). M: Analysis of expression level of *Myh4* in EDL and *Myh7* in SOL using qPCR. Mice were sacrificed immediately after swimming exhaustion tests to collect SOL samples. N: Analysis of expression level of *TNFα* after CTX-induced injury at d 0, 3, 5, 7, and 14. O: MRI results and damage volume data 5 d after CTX-induced injury. Area circled by red line indicates damaged muscle tissue ($n$=6). P: H&E staining of GAS 3 and 5 d after CTX-induced injury (Scale bar: 210 μm). Q: Immunofluorescence staining for MyoG (red) and laminin (green) in GAS 5 d after CTX-induced injury (Scale bar: 400 μm). Data are presented as mean±SD ($n$=6). *: $P$<0.05; **: $P$<0.01; ***: $P$<0.001; ns: Not significant (Student's $t$-test).

male mice than in 2-month-old male *flox* mice (Figure 2F and 2G). Examination of TA and GAS weights in 3-month-old mice showed similar results to those obtained at 2 months (Figure 2H). Muscle weight analyses for female and male *TNFα*-CKO mice were similar (Supplementary Figure S1B). Subcutaneous fat (SAT), epididymal white adipose tissue (eWAT), and perirenal white adipose tissue (pWAT) weights were also significantly increased in 2- and 3-month-old *TNFα*-CKO mice, while differences in interscapular brown adipose tissue (iBAT) weight were not significant (Figure 2I, J). The change in fat tissue weight in female *TNFα*-CKO mice was similar to that in male mice at 3 months, although this was not the case for male and female mice at 2 months (Supplementary Figure S1C). Heart, liver, spleen, lung, and kidney weights revealed that *TNFα*-CKO did not affect the development of major visceral organs in either male or female mice (Supplementary Figure S1D, E). Thus, *TNFα*-CKO accelerated skeletal muscle development and adipose tissue formation, which may be responsible for the changes in mouse body weight observed in this study.

The H&E staining results revealed larger GAS and TA muscle fiber cross-sectional areas in *TNFα*-CKO mice (Figure 2K), consistent with the greater muscle weight observed. A well-developed skeletal muscle system is often associated with endurance. As expected, swimming exhaustion tests showed significantly improved endurance for male *TNFα*-CKO mice. Interestingly, however, no significant differences in endurance were observed between female *TNFα*-CKO and *flox* mice (Figure 2L). *TNFα*-CKO also significantly down-regulated the expression of the fast-twitch muscle fiber marker *Myh4* and up-regulated the expression of the slow-twitch muscle fiber marker *Myh7* (Figure 2M). These findings suggest that *TNFα*-CKO accelerates the development of mouse skeletal muscles and enhances endurance.

Muscle regenerative capacity after injury is an important indicator of the muscle development process, reflecting

adaptability to external stimuli and self-repair abilities. To simulate muscle damage, we injected mice with CTX. In *flox* mice, qPCR analysis revealed a significant increase in *TNFα* expression induced by CTX, accompanied by the entire regeneration process (Figure 2N). MRI analysis further revealed a smaller injury area in *TNFα*-CKO mice 5 d after CTX-induced muscle injury (Figure 2O). Both H&E (Figure 2P) and IF staining (Figure 2Q) demonstrated that, compared to *flox* mice, *TNFα*-CKO mice exhibited more intact muscle fiber structures 3 or 5 d after CTX-induced injury. This was accompanied by a clearer laminin outline and the up-regulation of embryonic myosin heavy chain (eMyHC), a key marker of muscle regenerative capacity. These observations suggest that *TNFα*-CKO mice possess a stronger muscle regenerative ability than *flox* mice.

**Functional validation of *TNFα* in primary myoblasts of *TNFα*-CKO mice**

To confirm the *in vitro* function of *TNFα*, we established primary myoblasts from *flox* and *TNFα*-CKO mice. As expected, *TNFα* mRNA and protein levels were extremely low in the *TNFα*-CKO primary myoblasts (Figure 3A), which also exhibited a higher number of EdU$^+$ cells (Figure 3B) and significantly up-regulated *CDK4* and *Cyclin B* expression (Figure 3C). Bright-field microscopy also indicated that *TNFα* deletion facilitated the formation of myotubes following the induction of primary myoblast differentiation for 2 d (Figure 3D). Furthermore, IF staining further revealed that *TNFα*-CKO led to myotube hypertrophy, as demonstrated by the formation of a greater number of longer and thicker myotubes marked by *MyHC* (Figure 3E–H). Concurrently, the mRNA and protein levels of myogenic marker genes *MyHC*, *MyoG*, and *MyoD* were significantly up-regulated (Figure 3I, J). In summary, similar to our observations for C2C12 cells, deletion of *TNFα* significantly promoted the proliferation and differentiation of primary myoblasts.

**Identification of new targets for *TNFα* in myoblast cells**

Current understanding, such as *TNFα* facilitating NF-κB nuclear entry and activating certain MAP kinases, fails to fully elucidate the role of *TNFα* in myoblasts. To explore this further, we isolated the nucleus (N) and cytoplasm (C) of *flox* and *TNFα*-CKO primary myoblasts in the early stages of differentiation to identify new targets using label-free proteomic profiles. To illustrate changes in the distribution of differentially abundant proteins (DAPs; fold-change>1.5 or <0.67, *P*-value<0.05) between the cell nucleus and cytoplasm, we presented up-regulated and down-regulated proteins

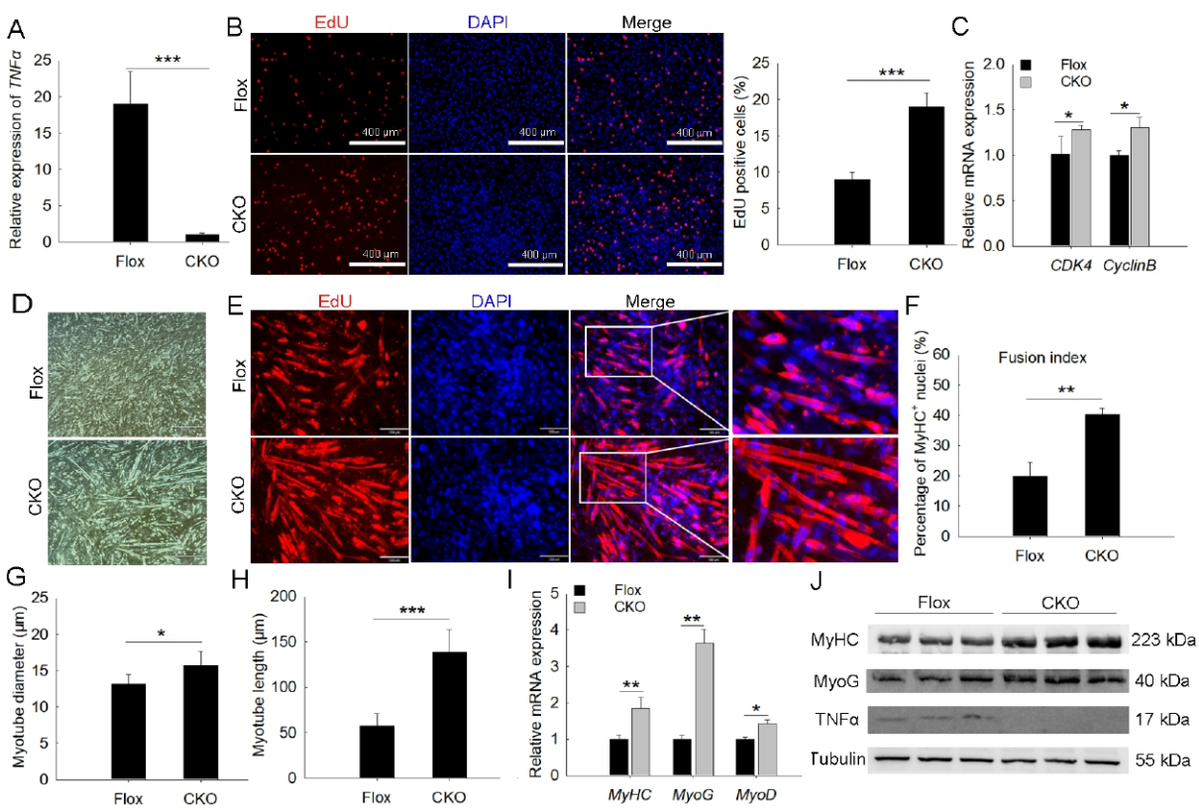



**Figure 3 Functional verification of *TNFα* expression in primary myoblasts**

A: Detection of *TNFα* mRNA level in *flox* and CKO primary myoblasts using qPCR. B: Representative photographs of EdU-stained *flox* and *TNFα*-CKO primary myoblasts. EdU$^+$ staining (red) of S-phase cells and DAPI staining (blue) of cell nuclei are shown (Scale bar: 400 μm), and proliferative cells were quantified as a ratio of EdU$^+$/DAPI$^+$. C: Analysis of expression levels of proliferation marker genes in *flox* and *TNFα*-CKO primary myoblasts using qPCR. Same number of *flox* and *TNFα*-CKO primary myoblasts were inoculated in plates and cultured in growth medium. D: Differentiation of primary myoblasts observed under a microscope 2 d after incubation in differentiation medium (Scale bar: 520 μm). E: Immunofluorescence staining of MyHC in *flox* and *TNFα*-CKO primary myoblasts 2 d after incubation in differentiation medium (Scale bar: 130 μm). Fusion index (F), myotube diameter (G), and myotube length (H) were quantified. I: Analysis of expression levels of myogenic marker genes in *flox* and *TNFα*-CKO primary myoblasts using qPCR. Myoblasts were differentiated for 2 d. J: Analysis of protein expression levels of MyHC, MyoG, and TNFα in *flox* and *TNFα*-CKO primary myoblasts. Myoblasts were differentiated for 2 d. Data are presented as mean±SD ($n$=3). $^*$: $P$<0.05; $^{**}$: $P$<0.01; $^{***}$: $P$<0.001 (Student's $t$-test).

separately. Most DAPs exhibited changes exclusively in either the cell nucleus or cytoplasm, while some exhibited synchronous changes in both compartments (Figure 4A). Notably, a small subset of DAPs, including six nucleus-down-regulated and cytoplasm-up-regulated proteins and one nucleus-up-regulated and cytoplasm-down-regulated protein, displayed a pattern reminiscent of translocation between the nucleus and cytoplasm (Figure 4A).

We used a heatmap to display changes in the abundances of selected proteins of interest, some of which may be potential targets of TNFα (Figure 4B). Compared to the *flox* group, Hira and Casz1 were significantly up-regulated in the nucleus of the *TNFα*-CKO group, with no detection in the cytoplasm, whereas Casp7, which was down-regulated, was only present in the cytoplasm. Arhgap10, up-regulated in the nucleus and down-regulated in the cytoplasm, exhibited the opposite shuttle direction to Gas1, which was down-regulated in the nucleus and up-regulated in the cytoplasm. Furthermore, Fgf21, Des, Igf2, and Igfbp5 were up-regulated in both the nucleus and cytoplasm, while fhl1, Pik3r1, and Myh4 were down-regulated in both compartments, implying corresponding changes in their total cellular levels. Map3k20, Cfl2, Tnni1, and Myom3 were significantly up-regulated, while Stat1, Stat2, Diaph1, Pdcd4, and Ripk1 were significantly down-regulated in the nucleus, with no significant changes in the cytoplasm (Figure 4B). These alterations in protein abundance in the cell nucleus suggest potential regulatory roles in myogenesis. Additionally, western blot analysis (Figure 4C) using Histone 3 and GAPDH as reference proteins for the nucleus and cytoplasm, respectively, confirmed the expression of several proteins related to muscle development. Densitometry on the western blot bands (Figure 4D) indicated that the changes in protein abundance closely matched the heatmap results, confirming the reliability of the proteomic data.

GSEA can assess the interactions between predefined gene lists and the standard hallmark collection, potentially uncovering biological pathways not limited to DAPs. As expected, *TNFα* deficiency resulted in negative enrichment of the TNF (normalized enrichment score (NES)=−1.89, $P$<0.001, FDR Q=0.004) and NF-κB (NES=−1.74, $P$=0.006, FDR Q=0.01) signaling pathways, accompanied by *TNFα*-induced apoptosis (NES=−2.12, $P$<0.001, FDR $Q$<0.001) (Supplementary Figure S2A). Furthermore, *TNFα* deficiency led to positive enrichment in MyoD targets (NES=2.39, $P$<0.001, FDR $Q$<0.001) (Figure 4E) and oxidative phosphorylation (NES=2.22, $P$<0.001, FDR $Q$<0.001) (Figure 4F). Conversely, it resulted in negative enrichment of the JAK-STAT signaling pathway (NES=−1.62, $P$=0.023, FDR Q=0.052) (Figure 4G). For instance, highly enriched and up-regulated DAPs, including Igf2, Igfbp5, Cfl2, Myh3, and Myl4, were identified in MyoD targets, while down-regulated DAPs,

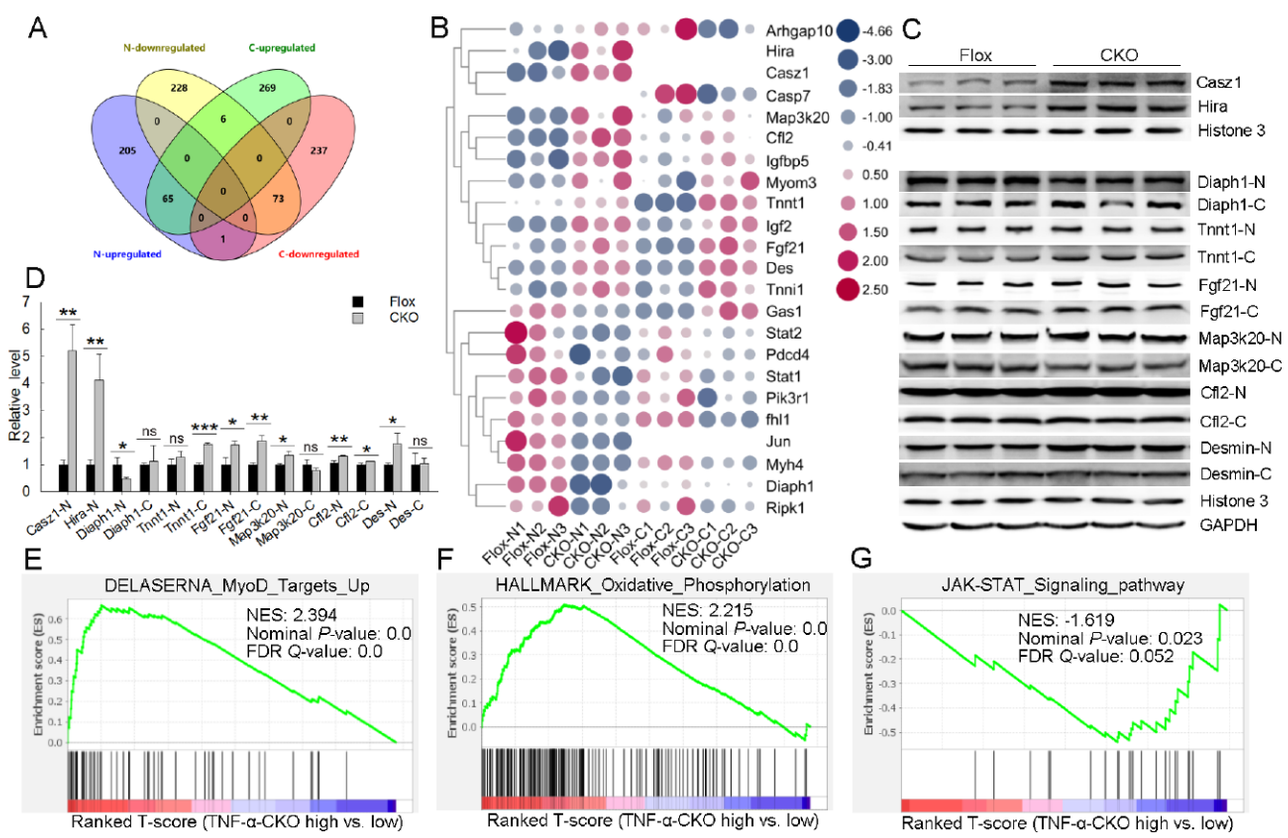



**Figure 4 *TNFα*-CKO-induced changes in protein distribution and pathway enrichment**

A: Venn diagram showing overlap between up-regulated and down-regulated differentially abundant proteins (DAPs) in nucleus (N) and cytoplasm (C) based on fold change>1.5 and $P$<0.05. B: Heatmap showing degree of changes in DAP levels due to *TNFα*-CKO. Scale size was normalized and shown by area. C: Western blots showing degree of changes in levels of certain proteins related to muscle development. *Flox* and *TNFα*-CKO primary myoblasts were induced to differentiate for 2 d. Histone 3 and GAPDH were used as reference proteins for N and C, respectively. Corresponding quantifications are shown in (D). D: Relative level indicates target protein/internal reference ratio of densitometry on western blot bands ($n$=3). Data are presented as mean±SD. *: $P$<0.05; **: $P$<0.01; ***: $P$<0.001 (Student's $t$-test). E–G: GSEA assays of proteomic data showing positive enrichment of MyoD targets and oxidative phosphorylation and negative enrichment of JAK-STAT signaling pathway following *TNFα*-CKO.

such as Jun, Stat1, Stat2, and Stat3, were observed in the JAK-STAT signaling pathway (Supplementary Figure S2B). These findings reveal novel *TNFα*-regulated targets and pathways that potentially mediate the effects of *TNFα* on muscle growth and development.

## DISCUSSION

In this study, we explored the influence of *TNFα* on myoblast proliferation, migration, differentiation, and myotube fusion. Specifically, we assessed the effects of *TNFα*-CKO on muscle development and regeneration in mice, and identified novel *TNFα*-regulated targets and pathways, which may act as critical mediators in muscle development. These findings could significantly enhance our understanding of the role of *TNFα* in muscle development and provide a theoretical basis for molecular breeding and myopathy treatment.

Our results indicated that *TNFα* knockdown promoted the proliferation of C2C12 myoblasts, which was also confirmed in primary myoblasts. Previous studies have indicated that *TNFα* overexpression significantly reduces the number of $Pax7^+$ cells (Li et al., 2020), while exogenous TNFα protein can stimulate myoblasts and satellite cell proliferation (Alvarez et al., 2020; Li, 2003; Shirakawa et al., 2021). These contrasting results may be due to the differing effects of high and low TNFα concentrations on myoblast proliferation or suggest distinct mechanisms of action between exogenously administered and endogenous *TNFα*. Additionally, we demonstrated the role of *TNFα* in myoblast migration and established *TNFα*-CKO mice to investigate the effects of *TNFα* on muscle development and regeneration, which has not been previously reported. Results indicated that the *TNFα*-CKO mice exhibited enhanced muscle regeneration after CTX-induced injury, consistent with the phenotype observed in *TNFα* knock-in mice (Li et al., 2020) but in contrast to the muscle regeneration impairment observed in TNFα receptor double-knockout mice ($p55^{-/-}p75^{-/-}$) (Chen et al., 2005). These findings, combined with the results of cell proliferation analysis, suggest the involvement of both autocrine *TNFα* and receptor-mediated *TNFα* in muscle development. Furthermore, we observed that *TNFα*-CKO accelerated fat tissue deposition in skeletal muscles, without affecting the development of bones and visceral organs. We inferred that *TNFα*-CKO influenced lipid deposition through paracrine or endocrine mechanisms. Therefore, the *TNFα*-CKO mice established in this study may serve as valuable models for further research into the roles of *TNFα* in muscle development or other physiological effects.

Identifying new targets and pathways of *TNFα* in skeletal muscle is essential for understanding its regulatory mechanisms in muscle development. In this study, we found that *TNFα* deletion significantly up-regulated the levels of histone chaperone Hira and zinc finger transcription factor Casz1 in the cell nucleus. Previous studies have suggested that Hira knockout can significantly reduce histone variant H3.3 deposition and H3K27ac modification in muscle gene regulatory regions, thereby inhibiting myoblast proliferation, differentiation, and skeletal muscle development and regeneration (Valenzuela et al., 2017). Casz1 promotes skeletal muscle differentiation by directly affecting regional epigenetic modifications, chromatin accessibility, and super-enhancer establishment (Liu et al., 2020). GSEA has shown positive enrichment of MyoD targets following Casz1 overexpression (Liu et al., 2020), consistent with our results (Figure 4E). These findings suggest that the enhancement of muscle development following *TNFα* knockout partially depends on the biological functions of Hira and Casz1. Arhgap10, identified from genome-wide selection signals in meat from goat breeds, promotes myoblast proliferation and differentiation (Yuan et al., 2023). Our results showed that *TNFα* knockout induced Arhgap10 translocation from the cytoplasm to the nucleus, indicating its activation and nuclear function following *TNFα* knockout. Conversely, Gas1 exhibited the opposite translocation direction compared to Arhgap10. Gas1 has been shown to negatively impact skeletal muscle stem cells and muscle regeneration (Li et al., 2019), consistent with the stronger muscle regeneration capacity observed in *TNFα*-CKO mice in this study. Cfl2 is an essential mediator for myogenic differentiation in C2C12 cells (Nguyen et al., 2020), and its loss leads to abnormal sarcomere formation (Balakrishnan et al., 2020). Map3k20 and Diaph1 positively and negatively regulate myogenic differentiation, respectively, by affecting MyoG expression (Saleh et al., 2019; Yan et al., 2022). Our results showed that *TNFα* knockout also resulted in the up-regulation of Cfl2 and Map3k20 and the down-regulation of Diaph1, theoretically favoring myogenic differentiation. In addition, *TNFα*-CKO significantly up-regulated slow-twitch muscle fiber markers (mRNA level of *Myh7*, protein levels of Tnnt1 and Tnni1) and down-regulated the protein and mRNA levels of the fast-twitch muscle fiber marker *MYH4* (Figure 4B). These results align with the increased endurance observed in *TNFα*-CKO male mice. The absence of similar endurance improvements in female mice requires further investigation, as their phenotypic differences were also less pronounced compared to those in males.

Muscle fibers are highly metabolically active cells. During myogenic differentiation, myoblasts undergo autophagy-mediated mitochondrial remodeling, shifting from a highly glycolytic state to a pronounced reliance on oxidative phosphorylation (Sin et al., 2016). The significant positive enrichment in oxidative phosphorylation suggests that *TNFα* deficiency may affect the energy metabolism of myoblasts, in accordance with the relatively rigid structural demands imposed by muscle contraction. *TNFα* is known to significantly activate the JAK/STAT pathway in endothelial and microglial cells (Coelho-Santos et al., 2012; Kandhaya-Pillai et al., 2022). Typically, the JAK-STAT pathway inhibits myogenic differentiation (Jang & Baik, 2013). For instance, Stat1 interacts with MEF2, repressing its transcriptional activity and thereby suppressing myogenic differentiation (Xiao et al., 2011). Similarly, circ*SVIL*, *SOCS1*, *SOCS3*, and *PIAS1* promote myogenic differentiation by inhibiting the JAK-STAT pathway (Diao et al., 2009; Yue et al., 2022). Our results showed that *TNFα* deficiency led to negative enrichment in the JAK-STAT pathway, accompanied by decreased levels of Stat1, Stat2, and Stat3 in the cell nucleus, although the down-regulation of Stat1 was only 1.32-fold and did not meet differential criteria. Further research on the impact of *TNFα* on the phosphorylation of STAT proteins, or validation using activators and inhibitors of the JAK/STAT signaling pathway, may be beneficial. These findings provide initial insights into the relationship between *TNFα* and these pathways in skeletal muscle, offering new avenues for understanding the mechanisms by which *TNFα* regulates muscle development. These findings are integrated and presented in Figure 5.

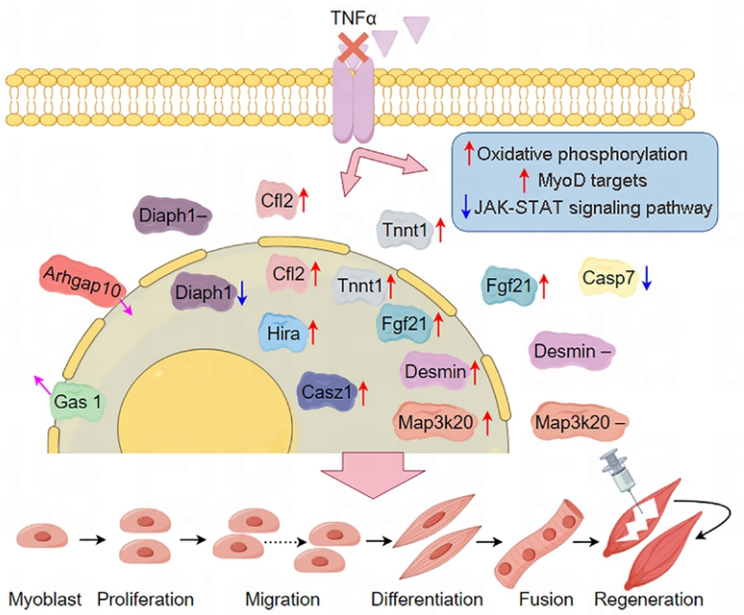



**Figure 5 Diagram showing mechanism of action of *TNFα*-CKO in regulating muscle growth and development**

Red and blue arrows indicate up-regulation and down-regulation of protein levels or pathway enrichment, respectively. Horizontal line indicates non-significant changes, pink arrow indicates direction of protein transfer. Figure was drawn by Figdraw.

## SUPPLEMENTARY DATA

Supplementary data to this article can be found online.

## COMPETING INTERESTS

The authors declare that they have no competing interests.

## AUTHORS' CONTRIBUTIONS

Y.F. and H.Z. conceived and designed the study and supervised the analyses. Y.F. and X.H. prepared the data. X.H. analyzed the data. X.H. and J.R.N. prepared the draft of the manuscript. P.S., B.Z., and D.W.Y. provided resources. X.H., Y.F., and H.Z. revised and finalized the manuscript. All authors read and approved the final version of the manuscript.

## ACKNOWLEDGMENTS

The authors are grateful to Dr. Kai Gao (Institute of Laboratory Animals Science, CAMS & PUMC) for assistance with MRI experiments.

## REFERENCES

Alvarez AM, DeOcesano-Pereira C, Teixeira C, et al. 2020. IL-1β and TNF-α modulation of proliferated and committed myoblasts: IL-6 and COX-2-derived prostaglandins as key actors in the mechanisms involved. *Cells*, **9**(9): 2005.

Balakrishnan M, Yu SF, Chin SM, et al. 2020. Cofilin loss in *Drosophila* muscles contributes to muscle weakness through defective sarcomerogenesis during muscle growth. *Cell Reports*, **32**(3): 107893.

Bodine SC, Latres E, Baumhueter S, et al. 2001. Identification of ubiquitin ligases required for skeletal muscle atrophy. *Science*, **294**(5547): 1704–1708.

Chen SE, Gerken E, Zhang YM, et al. 2005. Role of TNF-α signaling in regeneration of cardiotoxin-injured muscle. *American Journal of Physiology-Cell Physiology*, **289**(5): C1179–C1187.

Chen SE, Jin BW, Li YP. 2007. TNF-α regulates myogenesis and muscle regeneration by activating p38 MAPK. *American Journal of Physiology-Cell Physiology*, **292**(5): C1660–C1671.

Coelho-Santos V, Gonçalves J, Fontes-Ribeiro C, et al. 2012. Prevention of methamphetamine-induced microglial cell death by TNF-α and IL-6 through activation of the JAK-STAT pathway. *Journal of Neuroinflammation*, **9**: 103.

Collins RA, Grounds MD. 2001. The role of tumor necrosis factor-alpha (TNF-α) in skeletal muscle regeneration: studies in TNF-α(-/-) and TNF-α(-/-)/LT-α(-/-) mice. *Journal of Histochemistry & Cytochemistry*, **49**(8): 989–1001.

Di Credico A, Gaggi G, Izzicupo P, et al. 2023. Betaine treatment prevents TNF-α-mediated muscle atrophy by restoring total protein synthesis rate and morphology in cultured myotubes. *Journal of Histochemistry & Cytochemistry*, **71**(4): 199–209.

Diao YR, Wang X, Wu ZG. 2009. SOCS1, SOCS3, and PIAS1 promote myogenic differentiation by inhibiting the leukemia inhibitory factor-induced JAK1/STAT1/STAT3 pathway. *Molecular and Cellular Biology*, **29**(18): 5084–5093.

Fang WY, Tseng YT, Lee TY, et al. 2021. Triptolide prevents LPS-induced skeletal muscle atrophy via inhibiting NF-κB/TNF-α and regulating protein synthesis/degradation pathway. *British Journal of Pharmacology*, **178**(15): 2998–3016.

Horiuchi T, Mitoma H, Harashima SI, et al. 2010. Transmembrane TNF-α: structure, function and interaction with anti-TNF agents. *Rheumatology (Oxford)*, **49**(7): 1215–1228.

Hsu H, Xiong J, Goeddel DV. 1995. The TNF receptor 1-associated protein TRADD signals cell death and NF-κB activation. *Cell*, **81**(4): 495–504.

Jang DI, Lee AH, Shin HY, et al. 2021. The role of tumor necrosis factor alpha (TNF-α) in autoimmune disease and current TNF-α inhibitors in therapeutics. *International Journal of Molecular Sciences*, **22**(5): 2719.

Jang YN, Baik EJ. 2013. JAK-STAT pathway and myogenic differentiation. *JAK-STAT*, **2**(2): e23282.

Kandhaya-Pillai R, Yang XM, Tchkonia T, et al. 2022. TNF-α/IFN-γ synergy amplifies senescence-associated inflammation and SARS-CoV-2 receptor expression via hyper-activated JAK/STAT1. *Aging Cell*, **21**(6): e13646.

Kriegler M, Perez C, DeFay K, et al. 1988. A novel form of TNF/cachectin is a cell surface cytotoxic transmembrane protein: ramifications for the complex physiology of TNF. *Cell*, **53**(1): 45–53.

Langen RCJ, Van Der Velden JLJ, Schols AMWJ, et al. 2004. Tumor necrosis factor-alpha inhibits myogenic differentiation through MyoD protein destabilization. *The FASEB Journal*, **18**(2): 227–237.

Li LJ, Rozo M, Yue SB, et al. 2019. Muscle stem cell renewal suppressed by GAS1 can be reversed by GDNF in mice. *Nature Metabolism*, **1**(10):

985–995.
Li JB, Yi XJ, Yao ZQ, et al. 2020. TNF receptor-associated factor 6 mediates TNFα-induced skeletal muscle atrophy in mice during aging. *Journal of Bone and Mineral Research*, **35**(8): 1535–1548.
Li YP. 2003. TNF-α is a mitogen in skeletal muscle. *American Journal of Physiology-Cell Physiology*, **285**(2): C370–C376.
Li YP, Schwartz RJ. 2001. TNF-α regulates early differentiation of C2C12 myoblasts in an autocrine fashion. *The FASEB Journal*, **15**(8): 1413–1415.
Liu ZH, Zhang XY, Lei HY, et al. 2020. CASZ1 induces skeletal muscle and rhabdomyosarcoma differentiation through a feed-forward loop with MYOD and MYOG. *Nature Communications*, **11**(1): 911.
Meyer SU, Thirion C, Polesskaya A, et al. 2015. TNF-α and IGF1 modify the microRNA signature in skeletal muscle cell differentiation. *Cell Communication and Signaling*, **13**: 4.
Nguyen MT, Min KH, Kim D, et al. 2020. CFL2 is an essential mediator for myogenic differentiation in C2C12 myoblasts. *Biochemical and Biophysical Research Communications*, **533**(4): 710–716.
Pasparakis M, Vandenabeele P. 2015. Necroptosis and its role in inflammation. *Nature*, **517**(7534): 311–320.
Sabio G, Davis RJ. 2014. TNF and MAP kinase signalling pathways. *Seminars in Immunology*, **26**(3): 237–245.
Saleh A, Subramaniam G, Raychaudhuri S, et al. 2019. Cytoplasmic sequestration of the RhoA effector mDiaphanous1 by Prohibitin2 promotes muscle differentiation. *Scientific Reports*, **9**(1): 8302.
Shirakawa T, Rojasawasthien T, Inoue A, et al. 2021. Tumor necrosis factor alpha regulates myogenesis to inhibit differentiation and promote proliferation in satellite cells. *Biochemical and Biophysical Research Communications*, **580**: 35–40.
Sin J, Andres AM, Taylor DJR, et al. 2016. Mitophagy is required for mitochondrial biogenesis and myogenic differentiation of C2C12 myoblasts. *Autophagy*, **12**(2): 369–380.
Subramanian A, Tamayo P, Mootha VK, et al. 2005. Gene set enrichment analysis: a knowledge-based approach for interpreting genome-wide expression profiles. *Proceedings of the National Academy of Sciences of the United States of America*, **102**(43): 15545–15550.
Valenzuela N, Soibam B, Li LR, et al. 2017. HIRA deficiency in muscle fibers causes hypertrophy and susceptibility to oxidative stress. *Journal of Cell Science*, **130**(15): 2551–2563.
Varfolomeev E, Vucic D. 2018. Intracellular regulation of TNF activity in health and disease. *Cytokine*, **101**: 26–32.
Xiao F, Wang HX, Fu XR, et al. 2011. Oncostatin M inhibits myoblast differentiation and regulates muscle regeneration. *Cell Research*, **21**(2): 350–364.
Yan JY, Yang YL, Fan XH, et al. 2022. circRNAome profiling reveals circFgfr2 regulates myogenesis and muscle regeneration via a feedback loop. *Journal of Cachexia, Sarcopenia and Muscle*, **13**(1): 696–712.
Yuan Y, Zhang WY, Yang BG, et al. 2023. A 1.1 Mb duplication CNV on chromosome 17 contributes to skeletal muscle development in Boer goats. *Zoological Research*, **44**(2): 303–314.
Yue BL, Yang HY, Wu JY, et al. 2022. circSVIL regulates bovine myoblast development by inhibiting STAT1 phosphorylation. *Science China Life Sciences*, **65**(2): 376–386.

(Continued from inside back cover)


| | |
|---|---|
| Zhen Liu | Institute of Neuroscience, CAS, China |
| Jia-Hong Lu | University of Macau, China |
| Li Lu | Kunming Institute of Zoology, CAS, China |
| Anders Pape Møller | Université Paris-Saclay, France |
| Li Ma | Kunming Institute of Zoology, CAS, China |
| Zi-Ning Meng | Sun Yat-sen University, China |
| Masaharu Motokawa | Kyoto University Museum, Japan |
| Yong-Gang Nie | Institute of Zoology, CAS, China |
| Sang-Bing Ong | The Chinese University of Hong Kong, China |
| Saunak Pal | Indian Institute of Science, India |
| Hyun Park | Korea University, Republic of Korea |
| Julian Kerbis Peterhans | Roosevelt University, USA |
| Nikolay A. Poyarkov jr. | Lomonosov Moscow State University, Russia |
| Xiao-Guang Qi | Northwest University, China |
| Jian-Wen Qiu | Hong Kong Baptist University, China |
| Qiang Qiu | Northwestern Polytechnical University, China |
| Xiang-Guo Qiu | University of Science and Technology of China, China |
| Jing Qu | Institute of Zoology, CAS, China |
| Ming-Qiang Rong | Hunan Normal University, China |
| Christian Roos | Leibniz-Institute for Primate Research, Germany |
| Chang-Wei Shao | Yellow Sea Fisheries Research Institute, CAS, China |
| Qiong Shi | BGI Marine, China |
| Wei-Feng Shi | Shanghai Jiao Tong University, China |
| Xing-Feng Si | East China Normal University, China |
| Bing Su | Kunming Institute of Zoology, CAS, China |
| Yong-Hua Sun | Institute of Hydrobiology, CAS, China |
| Yu-Hua Sun | Institute of Hydrobiology, CAS, China |
| Chatmongkon Suwannapoom | University of Phayao, Thailand |
| Yi-Gang Tong | Beijing University of Chemical Technology, China |
| Christoph W. Turck | Max Planck Institute of Psychiatry, Germany |
| Guo-Hao Wang | National Institutes of Health, USA |
| Kai Wang | Kunming Institute of Zoology, CAS, China |
| Ke-Xiong Wang | Institute of Hydrobiology, CAS, China |
| Kun Wang | Northwestern Polytechnical University, China |
| Wen Wang | Northwestern Polytechnical University, China |
| Xiao-Qun Wang | Beijing Normal University, China |
| Yan-Jiang Wang | Third Military Medical University, China |
| Ying-Yong Wang | Sun Yat-sen University, China |
| Bin Wei | Shanghai University, China |
| Fu-Wen Wei | Institute of Zoology, CAS, China |
| Gary Wong | Institut Pasteur Shanghai, CAS, China |
| Dong-Dong Wu | Kunming Institute of Zoology, CAS, China |
| Jun-Hong Xia | Sun Yat-sen University, China |
| Hui Xiang | South China Normal University, China |
| Zuo-Fu Xiang | Central South University of Forestry & Technology, China |
| Jin-Hua Xiao | Nankai University, China |
| Shi-Jun Xiao | Jilin Agricultural University, China |
| Xiao Xiao | Fudan University, China |
| Can Xie | Hefei Institute of Physical Science, CAS, China |
| Song-Guang Xie | Hainan University, China |
| Yu-Yun Xing | Jiangxi Agricultural University, China |
| Shi-Qing Xu | Soochow University, China |
| Xiao-Hong Xu | Institute of Neuroscience, CAS, China |
| Qing-Pi Yan | Jimei University, China |
| Guang Yang | Nanjing Normal University, China |
| Xin-Wang Yang | Kunming Medical University, China |
| Xing-Lou Yang | Kunming Institute of Zoology, CAS, China |
| Zhi-Yuan Yao | Shenyang Normal University, China |
| Wen-Hua Yu | Guangzhou University, China |
| Ti-Fei Yuan | Shanghai Key Laboratory of Psychotic Disorders, China |
| Xi-Guo Yuan | Xidian University, China |
| Zhi-Yong Yuan | Southwest University, China |
| Jian-Xiong Zeng | Shanghai Jiao Tong University, China |
| Bao-Wei Zhang | Anhui University, China |
| Bo Zhang | Southern Ocean Science and Engineering Guangdong Laboratory-Zhanjiang, China |
| Guo-Jie Zhang | Zhejiang University, China |
| Jing-Song Zhang | Center for Excellence in Molecular Cell Science, CAS, China |
| Shi-Chang Zhang | Hubei University, China |
| Xin Zhang | Hefei Institutes of Physical Science, CAS, China |
| Ya-Ping Zhang | Chinese Academy of Sciences, China |
| Yan Zhang | Peking University, China |
| Yun-Wu Zhang | Xiamen University, China |
| Zhi Zhang | University of Science and Technology of China, China |
| Zhi-Jun Zhang | Southeast University, China |
| Bo Zhao | Kunming Institute of Zoology, CAS, China |
| Hui Zhao | The Chinese University of Hong Kong, China |
| Tian Zhao | Chengdu Institute of Biology, CAS, China |
| Wen-Ming Zhao | Beijing Institute of Genomics, CAS, China |
| Ya-Hui Zhao | Institute of Zoology, CAS, China |
| Ping Zheng | Fudan University, China |
| Jiang Zhou | Guizhou Normal University, China |
| Qi Zhou | Zhejiang University, China |
| Wu Zhou | The University of Mississippi, USA |
| Xin Zhou | China Agricultural University, China |
| Xu-Ming Zhou | Institute of Zoology, CAS, China |
| Xian-Jun Zhu | Sichuan Provincial People's Hospital, China |
| Kang Zou | Nanjing Agricultural University, China |

# Zoological Research Editorial Board


## EDITOR-IN-CHIEF:

| | |
|---|---|
| Yong-Gang Yao | Kunming Institute of Zoology, CAS, China |

## ASSOCIATE EDITORS-IN-CHIEF:

| | |
|---|---|
| Wai-Yee Chan | The Chinese University of Hong Kong, China |
| Xue-Long Jiang | Kunming Institute of Zoology, CAS, China |
| Yong-Tang Zheng | Kunming Institute of Zoology, CAS, China |

## ASSOCIATE EDITORS:

| | |
|---|---|
| Jiong Chen | Ningbo University, China |
| Peng-Fei Fan | Sun Yat-sen University, China |
| David Irwin | University of Toronto, Canada |
| Jia-Tang Li | Chengdu Institute of Biology, CAS, China |
| Shu-Qiang Li | Institute of Zoology, CAS, China |

## MEMBERS:

| | |
|---|---|
| Amir Ardeshir | University of California, Davis, USA |
| Yu-Hai Bi | Institute of Microbiology, CAS, China |
| Jean Philippe Boubli | University of Salford, UK |
| Wen-Jun Bu | Nankai University, China |
| Kevin L. Campbell | University of Manitoba, Canada |
| Gang Cao | Huazhong Agricultural University, China |
| Colin Chapman | McGill University, Canada |
| Ce-Shi Chen | Kunming Medical University, China |
| Liang-Biao Chen | Shanghai Ocean University, China |
| Luo-Nan Chen | Center for Excellence in Molecular Cell Science, CAS, China |
| Xiang-Jun Chen | Zhejiang University, China |
| Xue-Xin Chen | Zhejiang University, China |
| Yong-Chang Chen | Kunming University of Science and Technology, China |
| Ying Cheng | Yunnan University, China |
| Yu-Peng Cun | Chongqing Medical University, China |
| Ji Dai | Shenzhen Institute of Advanced Technology, CAS, China |
| Zhi-Fang Dong | Chongqing Medical University, China |
| Li-Na Du | Guangxi Normal University, China |
| Zhen-Yu Du | East China Normal University, China |
| Miguel Angel Esteban | BGI-Shenzhen & Guangzhou Institutes of Biomedicine and Health, CAS, China |
| He-Zhi Fang | Wenzhou Medical University, China |
| Ji-Feng Fei | Southern Medical University, China |
| Chu-Tian Ge | Zhejiang Wanli University, China |
| De-Yan Ge | Institute of Zoology, CAS, China |
| Shao-Yu Ge | SUNY at Stony Brook, USA |
| Cyril C. Grueter | The University of Western Australia, Australia |
| Shen Gu | The Chinese University of Hong Kong, China |
| Jian-Fang Gui | Institute of Hydrobiology, CAS, China |
| Xian-Guang Guo | Chengdu Institute of Biology, CAS, China |
| Shun-Ping He | Institute of Hydrobiology, CAS, China |
| David Hillis | University of Texas at Austin, USA |
| Chun-Hui Hou | Kunming Institute of Zoology, CAS, China |
| Ji Hu | ShanghaiTech University, China |
| Xiao-Xiang Hu | China Agricultural University, China |
| Jin-Lian Hua | Northwest A&F University, China |
| Lu-Sheng Huang | Jiangxi Agricultural University, China |
| William R. Jeffery | University of Maryland, USA |
| Xiang Ji | Wenzhou University, China |
| Jian-Ping Jiang | Chengdu Institute of Biology, CAS, China |
| Yu Jiang | Northwest A&F University, China |
| Le Kang | Hebei University, China |
| Laxman Khanal | Tribhuvan University, Nepal |
| Esther N. Kioko | National Museums of Kenya, Kenya |
| Randall C. Kyes | University of Washington, USA |
| Liang-Xue Lai | Guangzhou Institutes of Biomedicine and Health, CAS, China |
| Ren Lai | Kunming Institute of Zoology, CAS, China |
| Kai Lei | Westlake University, China |
| Peng Lei | Sichuan University, China |
| Cheng-Hua Li | Ningbo University, China |
| Da-Li Li | East China Normal University, China |
| Guo-Gang Li | Qinghai Normal University, China |
| Hai-Peng Li | Shanghai Institute of Nutrition and Health, CAS, China |
| Jin-Song Li | Center for Excellence in Molecular Cell Science, CAS, China |
| Ming Li | Institute of Zoology, CAS, China |
| Ming Li | Kunming Institute of Zoology, CAS, China |
| Ming Li | University of Nebraska-Lincoln, USA |
| Wei-Dong Li | Shanghai Jiao Tong University, China |
| Xiao-Jiang Li | Jinan University, China |
| Wei Liang | Hainan Normal University, China |
| Qiang Lin | South China Sea Institute of Oceanology, CAS, China |
| Wei-Qiang Lin | Zhejiang University, China |
| Huan-Zhang Liu | Institute of Hydrobiology, CAS, China |
| Jian-Hua Liu | South China Agricultural University, China |
| Lei Liu | Ningbo University, China |
| Sheng Liu | Sun Yat-sen University, China |


(Continued on previous page)

ZOOLOGICAL RESEARCH
动物学研究
Bimonthly, Since 1980
Volume 45 Issue 4, 18 July, 2024

Project for Enhancing International Impact of China STM Journals
中国最具国际影响力期刊
中国科技核心期刊
中国百强报刊

**Editor-in-Chief:** Yong-Gang Yao

**Executive Editor-in-Chief:** Xue-Long Jiang

**Editors:** Su-Qing Liu Long Nie Rong-Fu Wang

**Edited by** Editorial Office of Zoological Research

(Kunming Institute of Zoology, Chinese Academy of Sciences, 17 Longxin Road, Kunming, Yunnan, Post Code: 650201 Tel: +86 871 65199026 E-mail: zoores@mail.kiz.ac.cn)

**Sponsored by** Kunming Institute of Zoology, Chinese Academy of Sciences; China Zoological Society

**Supervised by** Chinese Academy of Sciences

**Published by** Editorial Office of Zoological Research, Kunming Institute of Zoology, Chinese Academy of Sciences©

**Printed by** Kunming Xiaosong Plate Making & Printing Co, Ltd

**Domestic distribution by** Yunnan Post and all local post offices in China

**International distribution by** China International Book Trading Corporation (Guoji Shudian) P.O.BOX 399, Beijing 100044, China

**Overseas Code:** BM358








Domestic Postal Issue No.: 64-20

Price: 25.0 USD/150.0 CNY

ISSN 2095-8137

CN 53-1229/Q






ISSN 2095-8137
